Transactions of the ASME

Technical Editor
ARTHUR J. WENNERSTROM
Senior Associate Editor
G. K. SEROVY
Associate Editors
Air Pollution Control
H. E. HESKETH
Diesel and Gas Engine Power
G. VanDeMARK
Gas Turbine
G. OPDYKE
Power
R. W. PORTER
Advanced Energy Systems
T. M. BARLOW
Fuels
H. C. ORENDER
Nuclear Engineering
J. SUSNIR

BOARD ON COMMUNICATIONS
Chairman and Vice-President
K. N. REID, JR.

Members-at-Large
W. BEGELL
W. G. GOTTENBERG
D. KOENIG
M. KUTZ
F. LANDIS
J. T. COKONIS
J. E. ORTLOFF
C. PHILLIPS
H.C. REEDER
R. E. NICKELL

President, G. KOTNICK
Executive Director,
PAUL ALLMENDINGER
Treasurer, ROBERT A. BENNETT

PUBLISHING STAFF
Mng. Dir., Publ., J. J. FREY
Dep. Mng. Dir., Pub.,
JOS. SANSONE
Managing Editor,
CORNELIA MONAHAN
Production Editor,
JACK RUMMEL
Editorial Prod. Asst.
MARISOL ANDINO

The Journal of Engineering for Gas Turbines and Power (ISSN 0742-4795) is published quarterly for $90 per year by The American Society of Mechanical Engineers, 345 East 47th Street, New York, NY 10017. Second class postage paid at New York, NY and additional mailing offices. POSTMASTER: Send address change to The Journal of Engineering for Gas Turbines and Power, c/o The AMERICAN SOCIETY OF MECHANICAL ENGINEERS, P.O. Box 3199, Grand Central Station, New York, NY 10163. **CHANGES OF ADDRESS** must be received at Society headquarters seven weeks before they are to be effective. Please send old label and new address. **PRICES:** To members, $36.00, annually; to nonmembers, $90.00. Add $6.00 for postage to countries outside the United States and Canada. **STATEMENT from By-Laws.** The Society shall not be responsible for statements or opinions advanced in papers or ... printed in its publications (B 7.1, para. 3).

INDEXED by the Engineering Index, Inc.

Journal of Engineering for Gas Turbines and Power

Published Quarterly by The American Society of Mechanical Engineers

VOLUME 106 • NUMBER 3 • JULY 1984

TECHNICAL PAPERS

(Contents Continued)

TECHNICAL BRIEFS

ANNOUNCEMENTS

Flow Phenomena in Compressor Casing Treatment

G. D. J. Smith[1]

N. A. Cumpsty

Whittle Laboratory,
Department of Engineering,
University of Cambridge,
Cambridge CB3 OEL, England

An axial skewed slot casing treatment has been tested over the tips of an isolated low-speed rotor with a hub-tip ratio of 0.4. An improvement in stall margin of 22 percent at nominal clearance was obtained. Detailed measurements of the loss pattern downstream of the rotor were made with a hot wire. Measurements were also made in the blade passage with a traversing gear moving with the rotor and in the treatment slots themselves using hot wires. The tentative conclusion is that unsteady effects in the slot are of secondary importance. Of primary importance is the selective removal of high absolute swirl, high loss fluid from the endwall near the trailing edge of the pressure surface of the blade, and reintroduction of this, with absolute swirl direction reversed, near the blade leading edge.

Introduction

In the late 1960s, it was discovered that the stall of a compressor could be delayed to smaller mass flows by having treatment over the rotor tips. Since then, many different geometries of treatmant have been tested, for example [1-12]. Such treatments can only be useful if the compressor is taken into stall by the rotor tips (i.e., is "tip critical") or stator hub, but with this proviso a large number of different treatment geometries have been found to be effective. It also appears from these tests that the flow Mach number is not critical to the behavior of the treatment, similar improvements in stall margin being produced by a given treatment at tip Mach number of, for example, 1.5 and 0.15.

The different treatments are not all equally effective. Perhaps the most successful treatment for reducing the mass flow at stall is the axial skewed slot, and this is the treatment used for the experiments described here. (The geometry is shown in Fig 1 and described more fully in section on the axial flow compressor rig.) An essential feature of the design is the inclination of the slots so that flow emerging from them would possess swirl in the opposite sense to the rotor motion. Tests by Takata and Tsukuda [2] showed that if the inclination was reversed (so that flow emerged from the slots in the rotor direction) the compressor actually stalled at a higher mass flow rate than with a solid wall.

Despite the usefulness of casing treatment for extending the unstalled operating range of compressors, it has so far found fairly limited application. One major reason for this is that the treatments most effective in extending the range usually degrade the efficiency significantly.

A treatment that will break away from this constraint would be most valuable, but a systematic approach to obtaining this requires that there should first be a good understanding of the way in which existing casing treatments operate. Most of the many past tests on treatments have looked at the effect of the treatment on the flow leaving the rotor without investigating the flow phenomena occurring in and just above the treatment, but a few, notably by Prince et al. [1], Camarata et al. [3], and Takata and Tsukuda [2], did examine the flow inside the slots grooves of the treatment. As expected, flow entered the slots near their rear and reemerged near the front where the static pressure was low. Greitzer et al. [4] showed detailed downstream profiles of relative total pressure that allowed some interpretation of the processes. The present paper describes measurements taken behind the rotor, inside the slots, and between the moving blades. From this base, most of the processes occuring can be regarded as well determined, but it must be admitted that there are aspects of the flow behavior which are not properly understood.

Part of the difficulty in understanding the operation of the treatment is the ignorance surrounding the cause of stall in even a smooth wall (i.e., no casing treatment) compressor. The most conventional view is that rotating stall is initiated by a separation from the surface of the blades; because of the high-incidence into the rotor in the annulus boundary layer separation is likely to occur first for the rotor near the casing. This view of the process of stall underpins the tentative explanation of casing treatment behavior presented by Mikoljczak and Pfeffer [5]. This was based on flow visualization experiments using a linear cascade in water with a grooved belt moving past the blade tips.

The experimental data obtained with the smooth walled build of the compressor used for the tests described here do not show any tendency for stall to be initiated on the suction side, but on the contrary, the region of low relative total pressure fluid collects by the pressure surface. This tendency, which is explainable in terms of the inlet skew and the tip clearance flow, is demonstrated below but is mentioned here to draw attention to the difference of opinion regarding stall inception.

Greitzer et al. [4] conducted a carefully thought-out experiment based on the hypothesis that stall could be initiated either on the annulus wall or on the blade. It was postulated

[1] Present address: Department of Mechanical Engineering, University of Natal, Durban, South Africa

Contributed by the Gas Turbine Division for publication in the JOURNAL OF ENGINEERING FOR GAS TURBINES AND POWER. Manuscript received by the Gas Turbine Division July 11, 1983.

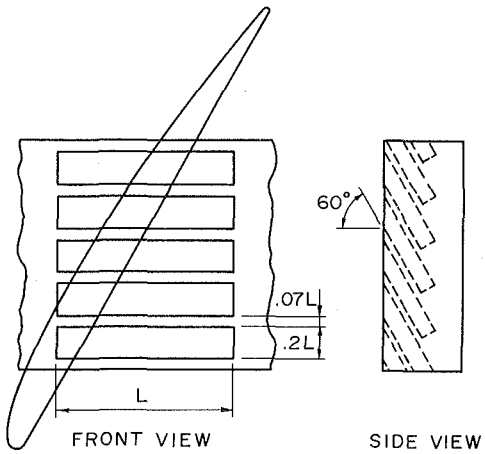

Fig. 1 Axial skewed slot treatment

that casing treatment would be effective in improving the range for the former but not the latter. The blade loading was increased (in order to produce blade stall) by removing every other blade so that the diffusion factor exceeded the normally permitted value. The hypothesis was apparently borne out very closely; a large improvement in range was produced for the high solidity blades for which the cascade diffusion factor limits were not exceeded, but no effect on stall margin was produced for the more highly loaded blades. It should be remarked that these blades were quite highly cambered (49 deg at the tip) and different behavior to that observed with low camber, high-stagger fan tip sections might be expected. The smooth walled build of low solidity showed no accumulation of loss near the pressure face of the blades but a large accumulation near the suction side. The high-solidity smooth walled build does show the loss towards the pressure side in a manner not very dissimilar to that on the present fan tip.

A recent paper by Koch [13] has succeeded in correlating stalling pressure rise for a very wide range of compressors assuming that the stalling process occurs on the endwall. Blade stall in the sense of the paper by Greitzer et al. [4] is also likely to occur close to the endwall where the incidence is high. The failure of the casing treatment to delay stall in this case appears to be contrary to the ideas presented by Mikoljczak and Pfeffer [5], who suggested that the casing treatment has its beneficial effect by drawing flow from the suction surface corner.

The confusion surrounding the process of stalling will help to explain the difficulty encountered in explaining the process even with the detailed and interlocking sets of measurements described in the present paper.

The Axial Flow Compressor Rig

An existing low-speed compressor of 1.52-m tip diameter and 0.4 hub/tip ratio was used throughout the experimental program. The research rotor was fitted with 22 blades of constant chord length 152.4 mm, giving hub and tip solidities of 1.43 and 0.47, respectively. The overall features of the rig and blading have already been described by Gregory-Smith [14]. The rotor is designed for a free-vortex flow at a flow coefficient of 0.70. The rotor tips are staggered at 60.7 deg with 7.8 deg of camber, C4 section and 8 percent thickness/chord ratio.

A 4:1 contraction ratio bellmouth formed the entry to the compressor, and this housed screens and an aluminum honeycomb flow straightener to minimize large scale flow nonuniformities. Inlet guide vanes and stators were not used, but the research rotor was run in series with an auxiliary fan positioned far downstream of the working area. Speed control on both rotors and a variable position throttle in the exhaust permitted a wide range of flow conditions to be obtained.

The treatment was the same design that Prince et al. [1] had tested, which in turn had been based on data gathered from early NASA work [6, 9]. The treatment, shown in Fig. 1, had rectangular cavities that extended axially over the middle 73 percent of the axial chord. The length of the slot, 55 mm, was five times greater than its breadth, and the depth was half the length. Like Prince's design, the depth of the slot was inclined at 60 deg to the radial in such a way that flow emerging from the slot would do so with swirl contrary to the blade direction. The slot design gave an open area to total area ratio of approximately 0.70.

Flow Measuring Equipment

A full description of the instrumentation and the measurement technique is given by Smith [15]. Radial traverses were made downstream of the rotor blades (and in a few cases upstream) using a conventional three-hole cobra probe. The probe was operated in the null-yaw mode to give flow angle and total pressure. High-frequency response measurements were taken with constant temperature hot wires and flush mounted transducers. An angled hot-wire technique, as employed by Whitfield et al. [16], was used downstream of the blade row, where the three-dimensional character of the flow was of interest. This technique can only be used in situations where the range of flow angle is known to fall within the calibration of the probe; the calibration cannot be extended to cover all flow angles, as the support pins then fall upstream of the hot wire introducing errors due to shielding. The angled hot wire was therefore not suited to flow measurements inside the treatment slots where the flow direction could vary by 180 deg. Instead a shielded hot wire, entering through the side of the slot, was used to find the velocity direction and sense, and a separate conventional hot wire, entering through the bottom of the slot, was used to measure the flow velocity. This latter probe had 20-mm-long pins supporting the wire to minimize the effects of flow blockage. The wire was aligned normal to the slot length and normal to the compressor axis.

A computerized data acquisition system was used for all the hot wire and high-response pressure transducer tests. With this system, the rapidly varying input signals could be phase locked to a physical event, in this case determined by a particular blade passing over a magnetic trigger.

For an understanding of how the treatment improved flow

Nomenclature

C_s = flow velocity in treatment slot
C_t = tangential component of absolute flow velocity
C_x = axial component of fluid velocity
CT = casing treatment build
P_o = total pressure
P_s = static pressure
SW = smooth wall build
t/c = blade tip clearance to chord ratio
U_m = Midspan blade speed
U_t = tip blade speed
β_2 = absolute outlet flow angle
ψ_{ss} = $\Delta P_s / \frac{1}{2}\rho U_m^2$, nondimensional static pressure rise across rotor
ϕ = flow coefficient, C_{x/U_M}

stability, it was important to measure the velocity and pressure in between the rotor blades and close to the casing treatment. These measurements were taken with a 5-hole probe rotating with the rotor. The probe was operated in the fixed direction mode and probe pressures were transferred to the stationary frame via a sealed-bearing, pressure-transfer device. These data were processed using a technique developed by Lewis [17] to give the total and static pressures and the three velocity components. This rotating frame probe traversed a surface bordered by the blade pressure and suction surfaces and by the passage leading and trailing edges. After such a surface had been traversed, it was necessary to stop the rig in order to move the probe to a new radial position. By repeating this process, a three-dimensional picture of the flow in the rotating passage of the blade could be developed; traverses taken at five different radial surfaces gave an adequate definition of the flow.

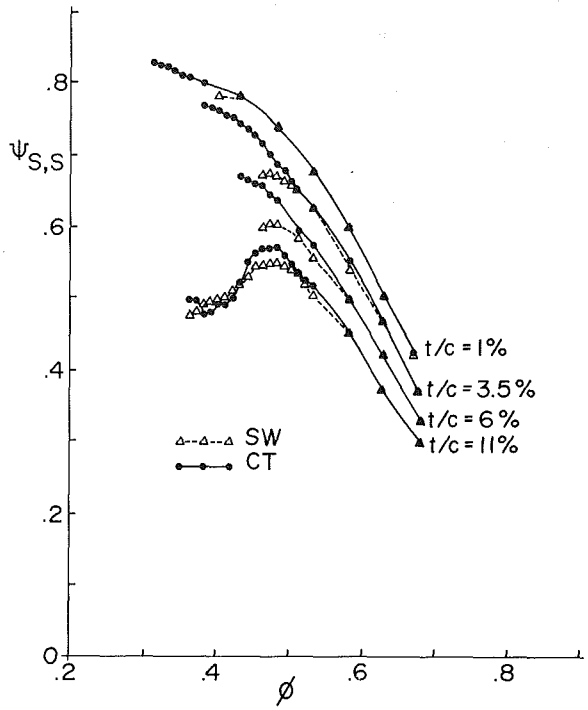

Fig. 2 Static pressure rise characteristics at various tip clearances for the solid wall and treated builds

Compressor Characteristics

Figure 2 shows nondimensional static-to-static pressure rise against nondimensional flow rate for smooth wall (sw) and casing treatment (ct) builds at a range of tip clearances expressed as a percentage of blade chord. In low-speed tests, stall margin improvement is commonly expressed as the percentage reduction in the mass flow rate just prior to stall which accompanies the fitting of the treatment. With this definition, a stall margin improvement of 21.7 percent is obtained at nominal clearance, i.e., $t/c = 1$ percent.

It is well known that increasing the blade tip clearance reduces the pressure rise and prematurely precipitates the stall. From this point of view the increase in flow area beneath the blade tips that is associated with the geometry of the treatment slots might be expected to exacerbate this loss in performance. In practice, this was not the case and substantial improvements in flow range were achieved in high tip clearance builds. The results presented in Fig. 2 show stall margin improvement to increase with tip clearance from a value of 21.7 percent at nominal clearance to 28 percent at 6 percent clearance. (The absence of a pressure discontinuity on the curve for the build of largest clearance, $t/c = 11$ percent, precludes an exact calculation of stall margin improvement, but an improvement of 20 percent is obtained at peak pressure rise.) It is noteworthy that the tip clearance of the treated rig could be increased by 5 mm (to $t/c = 3.5$ percent) without the outlet pressure dropping below the peak value realized with the solid wall compressor. It seems possible that the ability of the casing treatment to minimize the deleterious effects of tip clearance may recommend its use even more than its ability to reduce the flow at stall with nominal clearance.

The results in Fig. 2 indicate that treating the compressor has lead to a significant increase in the pressure rise just prior to the stall, but it can also be seen that the treatment has little effect on the characteristic at high flow rates near the free vortex design point. In addition, the Reynolds number dependence of the compressor unstalled behavior is slight, with the nondimensional pressure rise characteristics being almost independent of rotor speed over a factor of two. All subsequent results shown in this paper are therefore only for a single rotational speed of 450 rev/min, and these results always apply to the nominal clearance of 1 percent.

The flow behavior just prior to stall in the untreated build ($\phi = 0.4$) differed markedly from that found in the treated case at the same flow rate. The untreated rig showed a large increase in blockage near the tip critical whereas in the treated rig the only evidence of markedly increased flow blockage occurred near the hub. This information was obtained by

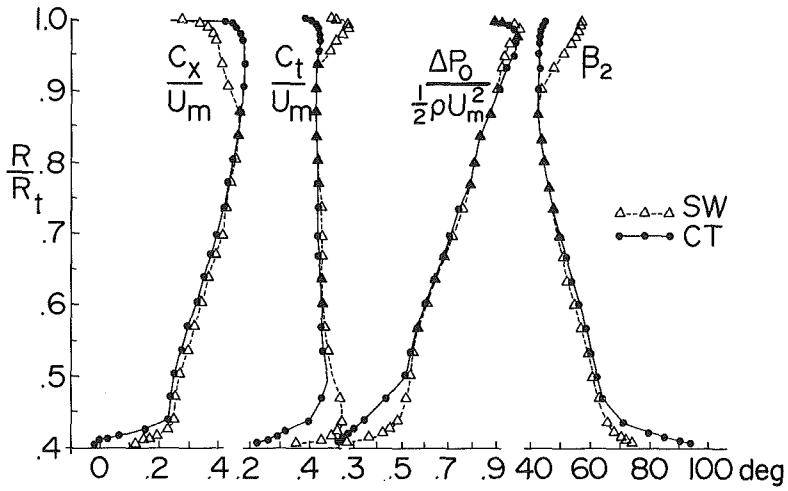

Fig. 3 Outlet flow field for the solid wall and treated builds, $\phi = 0.4$

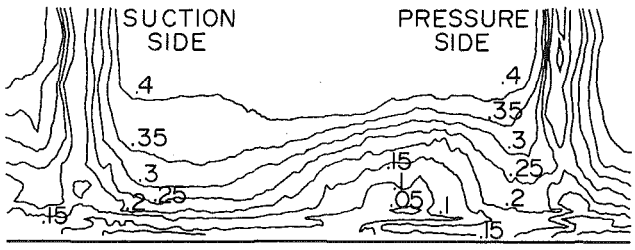

Fig. 4 Axial velocity measured in the radial-tangential plane downstream of the solid wall rotor and nondimensionalized by *Um*. $\phi = 0.32$

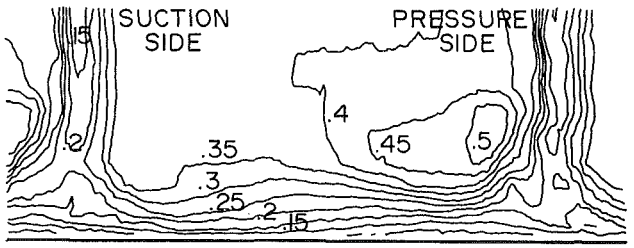

Fig. 5 Axial velocity measured in the radial-tangential plane downstream of the treated rotor and nondimensionalized by *Um*. $\phi = 0.32$

simultaneously recording the output from two hot wire probes attached near the hub and tip at identical axial and circumferential stations one axial chord downstream of the rotor. In all cases with the treated outer wall, the hot wire signals showed that a large-scale stalled region completely encircled the hub and covered approximately 10 percent of the span.

Near stall for the treated rig ($\phi = 0.32$) a low-frequency rumble normally characteristic of the presence of rotating stall was emitted, but the hot wire mounted at the hub still showed an axisymmetric pattern of unsteadiness similar to that found at $\phi = 0.4$, although the unsteady flow now extended further along the span. Even though the flow near the hub was unsteady and, close to the hub, even reversed in the axial sense, it should be stressed that the compressor was still operating stably on the unstalled part of the characteristic. Further throttling led to a conventional stall in which the pressure across the rotor dropped abruptly. The reversed or stalled flow that girdled the hub prior to this breakdown was then replaced by a single full-span rotating stall cell and a region of apparently normal flow. The stall cell speed of 0.56 times the rotor speed was unchanged by the presence of the treatment.

It was found that at any given Reynolds number the treated compressor always entered stall at a lower mass flow rate than the untreated build and the mass flow rate at the point of stall recovery was also lower. However, the treated rotor took more time to recover from a rotating stall and the noise from the stalled compressor was more severe than that heard during the stall of the solid wall build. The severity of the stall was difficult to quantify because stall appears over different regions of the pressure rise characteristic of the two builds. Nevertheless, the output from a hot wire showed that the greatest excursions in flow velocity were found during the stall of the treated build.

Downstream Flow Surveys

The results in Fig. 3 were measured one axial chord downstream of the blade trailing edge using the three hole cobra probe. The two sets of curves in this figure, one for the smooth wall rig and one for the compressor with treatment, were both obtained at a flow coefficient of 0.4, which corresponds to the flow rate marginally greater than that for stall of the untreated build. Considering the plot of axial velocity, the treatment had the effect of increasing the throughflow in the tip region and decreasing it elsewhere. (This decrease is an indirect influence of the treatment and occurs because treated and solid wall tests were performed at equal overall mass flow rates.) For the treated build, a small region of reversed flow occured near the hub, and flow is probably drawn through the blade passage into the upstream flow field. On this low hub/tip ratio machine the blade outlet angle at the hub is only 1 deg from the axial, and this feature of the free vortex design would make it easier for the direction of flow in the passage to reverse. The reversed flow encircled the hub and reduced the effective annulus through flow area by 1 percent. A conventional hot wire placed 6 mm from the hub and 10 mm downstream of the rotor revealed no clearly defined rotating stall as such, although the flow varied randomly from pitch-to-pitch as if the blades were severely stalled. This axisymmetric unsteadiness covered the first 10 percent of the span but further out the repetitive blade wakes of the normal unstalled flow were found. The extent of the unsteady reversed flow decreased as the throttle was opened until eventually clearly defined blade wakes were found down to the hub. The casing treatment results in Fig. 3 also show a marked reduction in swirl velocity and flow angle in the tip region but remarkably little alteration in total pressure rise.

At the lightly loaded free vortex condition of $\phi = 0.7$ (the flow coefficient for which the rotor was designed), the radial traverse results of the treated and solid wall builds could not be separated, indicating that the treatment is not effective at low-pressure rise conditions. This result may indicate that the efficiency penalty when using treatment as high flow rates is insignificant, but this idea has not been checked.

The velocity surveys made in the tip region with an angled hot wire covered a radial/tangential plane 10 mm downstream of the blade trailing edges. These data are presented as contours of axial velocity for the untreated and treated builds in Fig. 4 and 5 for a flow coefficient of 0.40, the value close to stall for the untreated build. These results were phase locked to the passing blades and slightly more than one blade pitch is shown. For the smooth walled compressor a buildup of low velocity fluid near the blade pressure face is very apparent in Fig. 4. This collection of low axial velocity (and also low velocity relative to the moving blades (Fig. 6)) is attributable to both the effect of inlet skew and, perhaps predominantly, to the flow through the tip clearance. This retarded flow coalesces with a well-defined wake from the blade pressure face. The retarded zone extends over half the blade pitch, but there is no evidence of a buildup of low-velocity fluid near the suction surface.

The traverse for the treated compressor at the same flow rate, Fig. 5, shows completely different features to the solid wall build. Differences are noticed in the pressure face corner, where high axial velocity flow replaces the blockage; in the suction face corner, which is deeply scoured by the free-stream; and all along the annulus wall, where the closely spaced velocity contours show that the boundary layer has been thinned.

Contours of relative dynamic head are shown in Figs. 6 and 7 for the solid wall and treated builds. The low dynamic head region near to the pressure surface is very clear in the untreated compressor but replaced by a region of higher relative total pressure in the treated case.

The cobra probe and the angled hot wire were also used to measure the outlet flow field of the treated compressor at a flow rate just above its stall point. In Fig. 8, cobra probe results of the smooth wall and treated builds are superimposed at flow rates just above their respective stall points ($\phi = 0.4$ and $\phi = 0.32$, respectively). Close to the outer wall the axial velocity profile is very similar in each case and indeed a separate investigation has shown that the axial displacement

thickness is very nearly equal for the two cases. Decreasing the mass flow rate from $\phi = 0.4$ to $\phi = 0.32$ leads to an increase in total pressure, outlet flow angle, and swirl. The increased swirl without significantly increased losses over much of the annulus leads to an increase in the outer wall static pressure, a result consistent with the performance curve shown in Fig. 2, where the static pressure on the outer wall of the treated compressor is seen to increase as the compressor is throttled from $\phi = 0.4$ to $\phi = 0.32$. The reversal of flow near the hub, where the outlet flow angles are in excess of 90 deg, is more pronounced and covers the first 5 percent of the span. The lower values of swirl velocity near the hub follow from the low speed of the reversed flow. The total pressure curve shows that losses have increased in the hub region of the treated build.

Traversing the tip region with an angled hot wire when the treated compressor was operating near to its stalling mass flow rate shows up considerable change in the position of the passage blockage, Fig. 9. This region of low axial velocity is not on the pressure side, as was the case in the smooth wall build, but appears toward the suction side, where it blends in with the collosal blade wakes. Considering that stable operation is still maintained in the treated build with this amount of blockage, it is surprising that a lesser blockage on the pressure face of the untreated compressor precipitates its stall. It thus seems that it is the position of the blockage, rather than its magnitude, that is the more crucial precursor to the stall.

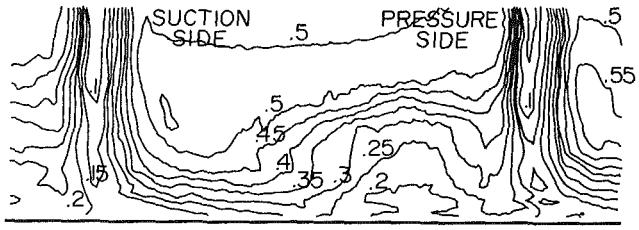

Fig. 6 Relative dynamic head measured in a radial-tangential plane downstream of the solid wall rotor and nondimensionalized by Um^2. $\phi = 0.4$

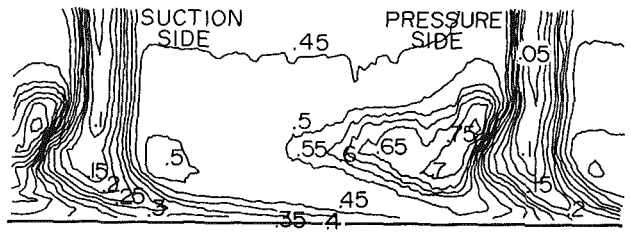

Fig. 7 Relative dynamic head measured in a radial-tangential plane downstream of the treated rotor and nondimensionalized by Um^2. $\phi = 0.32$

The blockage close to the suction surface originates, in part, from blade boundary layer flow on the suction surface streaming down toward the blade tip. This is shown by plotting the hot-wire data in vector form for a flow condition near the stall of the treated compressor, Fig. 10. The vectors represent the resultant of the radial velocity and the projection of axial and tangential velocity components on a plane perpendicular to the blade stagger angle. The blade wakes show up as regions of radial flow streaming down the blade to the outer wall where the flow either integrates with the wall boundary layer or is turned back towards the hub. Flow in the midpitch region is directed towards the hub and vortex like flow patterns are now observed in both blade corners. There is no evidence in the vector plots of flow having moved beneath the blade tip from the pressure face to the suction face. This appears to indicate that the treatment has somehow counteracted the tip leakage flow. This fact could perhaps be inferred from Fig. 2 where the treated compressor performance showed far less degradation because of tip clearance effects than the solid wall compressor. Just to the left of the blade pressure face, the flow shown in Fig. 10 is seen to ride up the blade surfaces as if the blade trailing edge region was performing like a snow plough that scoops up low absolute whirl passage flow. It must be remembered, however, that these measurements were made downstream of the rotor, and as such, they represent the aftermath of the treatment flow.

A vector plot of the outlet flow from the solid wall rig operating near its stall condition is not presented here but these results, [15], showed that the mass flow of boundary layer fluid streaming down the blades was only about a third of that found in the treated build near its stall point. At $\phi = 0.40$, the proportion of the total blockage in the endwall boundary layer that comes from radial flow along the suction surface was calculated by an approximate method in [15] to be less than 4 percent.

Even though the hot-wire technique produced detailed maps of the velocity field downstream of the tip and revealed considerable change in the flow field, it was not possible to explain the high-velocity core in the pressure face corner of

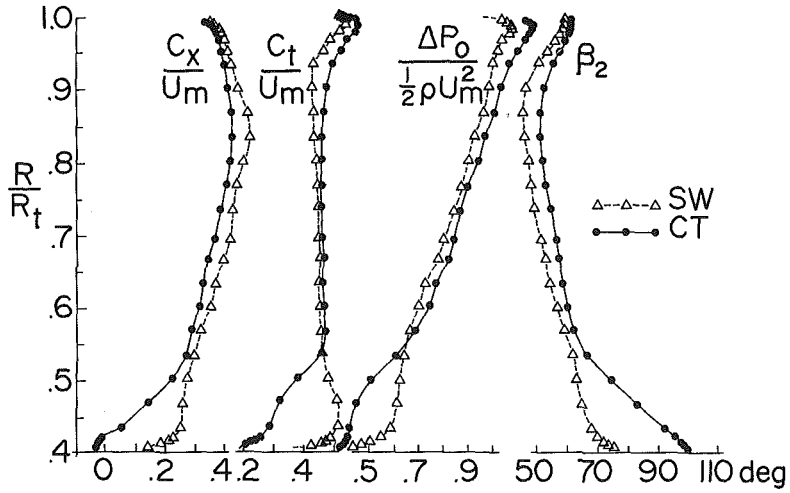

Fig. 8 Outlet flow field for the solid wall and treated builds, $\phi = 0,4$ and $\phi = 0.32$ respectively

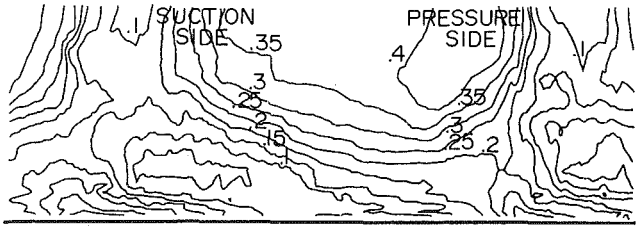

Fig. 9 Axial velocity measured in a radial-tangential plane downstream of the treated rotor and nondimensionalized by *Um*. $\phi = 0.32$

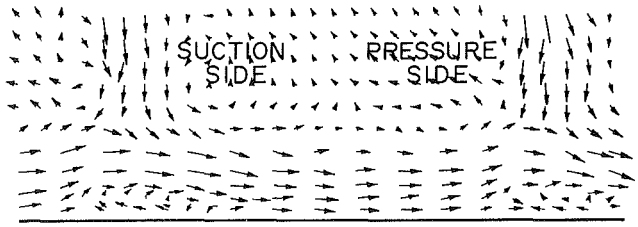

Fig. 10 Relative velocity presented in vectored form for the flow in a radial-tangential plane downstream of the treated rotor, $\phi = 0.32$

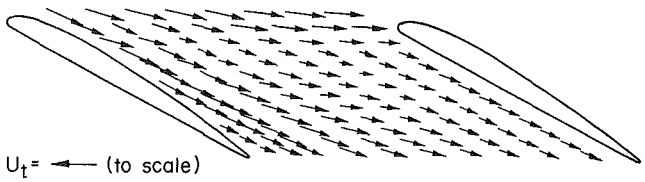

Fig. 11 Relative velocity measured in the blade passage 6 mm above the solid wall, $\phi = 0.42$

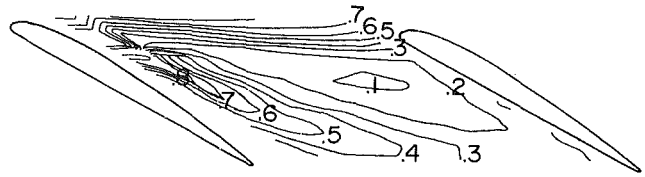

Fig. 12 Relative dynamic head measured in the blade passage 6 mm above the solid wall, $\phi = 0.42$

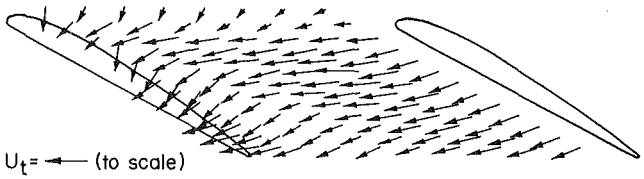

Fig. 13 Absolute velocity field in the blade passage 6 mm above the solid wall, $\phi = 0.42$

the treated compressor. The interaction of the flow entering and leaving the slot with the flow in the blade passage also remained unknown at this stage.

Flow in the Rotor Blade Passage

Measurements taken in between the rotor blades with the rotating probe were recorded at flow rates near stall, which were slightly higher than those used in previous tests, since the presence of the rotating probe increased the flow rate at which the compressor stalled.

The first set of results apply to the smooth wall build operating near its stall mass flow, $\phi = 0.42$, with the traverse plane of the probe being 6 mm above the outer annulus wall. These results are presented in Fig. 11 as a plot of relative flow vectors on a developed plan view of the blade passage. The skewed inlet flow may be seen crossing the blade passage to the pressure face corner as a flow of low relative velocity. This region of flow is shown in Fig. 12 to be part of a stream of low relative dynamic pressure fluid that migrates diagonally across the passage from the vicinity of the suction surface leading edge to approximately the midchord region of the pressure face. It is this cross-passage flow that therefore accounts for the pressure face blockage that was shown in the downstream results, Figs. 4 and 6. The velocity deficit of the inlet annulus wall boundary layers is not in itself the cause of the retarded flow that accumulates in the pressure face corner. In fact, this boundary layer flow enters the blade passage with a relative velocity magnitude no more than a few percent below that of the flow in the freestream. (A simple calculation for a particle entering with vanishingly small axial velocity shows that the relative dynamic pressure cannot be more than 8 percent below that of the freestream.) The boundary layer fluid is thus apparently reenergized by moving into the rotating frame. The major cause of the low relative total pressure fluid is probably the tip clearance flow, which is likely to be discharged approximately normal to the blade chord, that is at about 30 deg from the upstream axial direction. In addition, the high skew of the flow increases the blade loading to the extent that there may be flow separation in the blade suction surface/annulus wall corner.

The process becomes clearer when the blade passage results are referred to the absolute frame. Figure 13 is a plot of absolute velocity for the passage flow measured 6 mm from the smooth outer wall at a flow rate of $\phi = 0.42$. It is noted that the flow always has an absolute swirl component in the same direction as the blade rotation, with the areas of highest swirl appearing at the suction trailing edge and at midpitch position 10 percent of the axial chord from the blade leading edge. The pitch-averaged swirl at the latter position is 0.53 times the blade tip speed and spatially this region of the flow would correspond in the treated compressor to a position directly above the leading edge of the slot.

Measurements taken in the blade passage 6 mm above the treatment at the same flow rate, $\phi = 0.42$, revealed considerable change in the flow velocity and magnitude. As Fig. 14 shows, the flow near the leading edge of the slot is seen to be pointing 13 deg upstream (measured relative to the tangential direction and averaged over the pitch), and the relative velocity measured in the midpassage above the leading edge of the slot is roughly double that found in the same area of the smooth wall flow. This increase in velocity is most noticeable in the midpassage region where the flow has gained considerably in relative swirl. This flow is toward the pressure surface of the blade where the flow is turned and finally leaves the passage with a velocity 1.5 times greater than that measured in the solid wall build. The high-velocity core previously evident near the pressure surface in Fig. 5 and 7 can be tracked upstream along a roughly diagonal path from the blade pressure face corner at the trailing edge to a region above the leading edge of the slot. It is here that the treatment is ejecting a flow of considerable relative swirl into the blade passage. Figure 14 also shows that the flow in the treated build has the greatest relative swirl just above the leading edge of the slot. The swirl in this region is approximately equal to the blade tip speed of 24 m/s. This is an unexpected result, because flow in the absolute frame above the leading edge of the slots must therefore be almost stationary, see Fig. 16.

The results of the blade passage surveys for the treated wall in absolute coordinates, Fig. 16, show regions of high absolute velocity all along the blade suction surfaces. The flow near the trailing edge of the suction surface has a high absolute velocity because this flow, perhaps a region of

separated flow, has a low relative velocity and therefore a high absolute swirl. It is significant that the region towards the trailing edge of the blades has an absolute flow direction which favors flow entering the skewed axial slots.

The contours of relative dynamic head for the treated build, Fig. 15, do not show the extensive low head region fanning across the passage as they did for the solid wall build, Fig. 12, but towards the trailing edge conditions are comparatively uniform. Near the front of the slot, where flow emerges from it, the contours of dynamic head are more complicated.

The region of almost stagnant flow in the absolute frame is quite extraordinary, since the same region of the flow in the smooth wall build, Fig. 13, has an extremely high absolute swirl (0.5 times the blade tip speed) in the direction of blade rotation. Seemingly the effect of the treatment has been to bring this high absolute flow to a standsill, a result which is expected if flow leaves the leading edge region of the slot with equal and opposite momentum to the flow formerly found in the same region of the smooth wall build. Measurements of static pressure on the annulus walls are presented in Fig. 23 and show that a considerable and localized pressure rise is associated with this deceleration of the flow.

The previous sections considered the data from the blade passage surveys in a surface parallel to the outer annulus wall. Since a number of these surveys were taken at different distances from the outer wall, it is possible to plot these data in planes parallel to the stagger of the blade to show the nature of the spanwise flows. An example of this is shown in Fig. 17, where vectors are superimposed on a sketch of the blade and treatment. This is for $\phi = 0.42$ and on a plane approximately 25 percent of the pitch from the pressure surface. (Results for the smooth wall build are not shown because the spanwise flows were minimal for this build.) It is apparent that flow is directed towards the treatment over roughly the downstream 60 percent of the passage and away from the treatment over the remaining upstream part of the slot. In fact, these plots show flow directed away from the wall well upstream of the area actually covered by the treatment. It seems that as flow enters the blade passage it is forced to move away from the wall before passing over the jet of fluid emerging from the treatment. Above the downstream half of the treatment slot the flow is drawn towards the treatment; this radial flow direction is maintained downstream of the trailing edge of the treatment slot although the velocity magnitude is then greatly diminished. The flow pattern is only slightly different at other stations in the blade passage, except that in a small area (roughly 5 percent of the passage area) near the leading edge of the suction surface the measurements suggest that flow is directed towards the annulus wall. This finding is examined in detail in [15], where it is concluded that the extremely high shear of the flow in this region leads to unreliable measurement of the radial component of velocity.

When the treated build was operated near to its stall mass flow rate, $\phi = 0.36$, the aforementioned flow features changed in magnitude, but the trends were essentially unaltered.

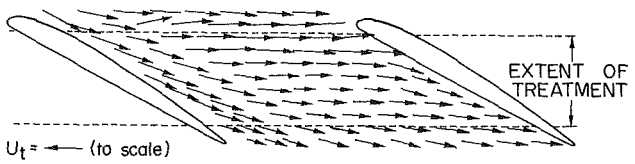

Fig. 14 Relative velocity measured in the blade passage 6 mm above the treated wall, $\phi = 0.34$

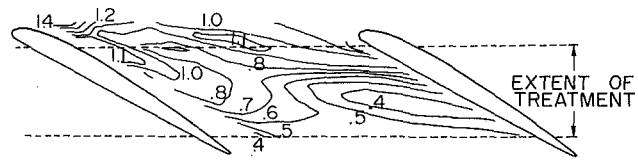

Fig. 15 Relative dynamic head measured in the blade passage 6 mm from the treated wall, $\Phi = 0.34$

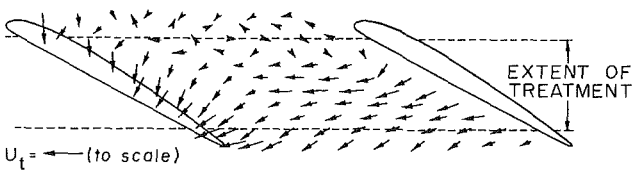

Fig. 16 Absolute velocity field in the blade passage 6 mm above the treated wall, $\phi = 0.34$

Flow Direction and Velocity Within the Slots

An instantaneous picture of the direction and sense of the

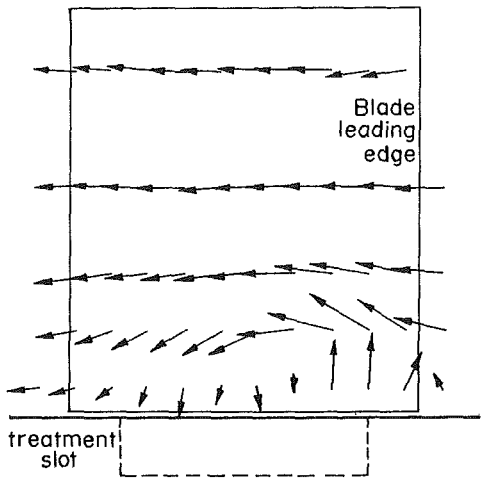

Fig. 17 Spanwise flows in the treated build 20 percent of the pitch from the pressure surface, $\phi = 0.34$

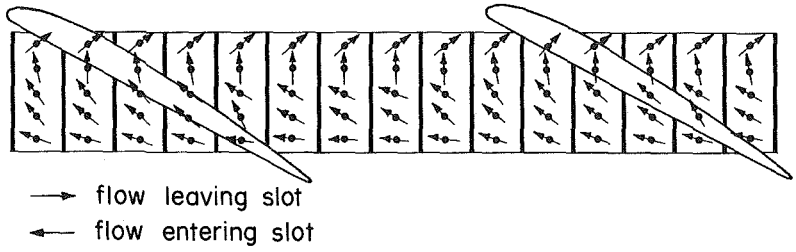

Fig. 18 Flow direction at middepth in the treatment slots, $\phi = 0.42$

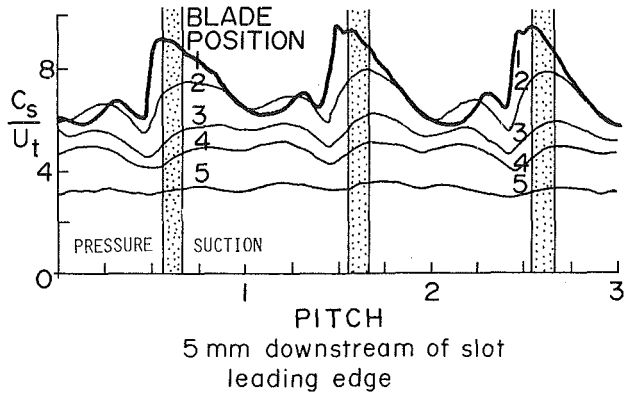

Fig. 19 Flow velocity in the treatment slot 5 mm downstream of the slot leading edge, $\phi = 0.42$. Trace 1 is for flow at the treatment lip. Traces 2-5 are at greater depths (i.e., increments of 6.5 mm).

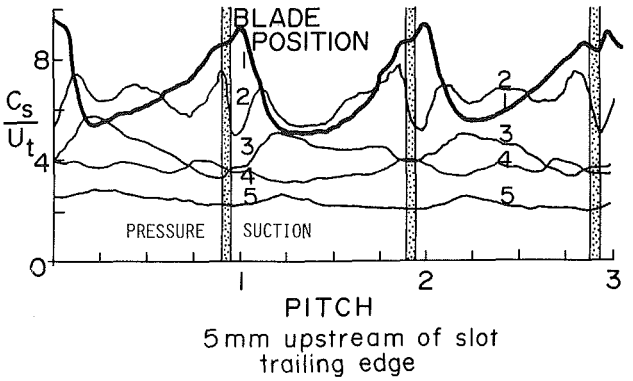

Fig. 20 Flow velocity in the treatment slot 5 mm upstream of the slot trailing edge, $\phi = 42$. Trace 1 is for flow at the treatment lip. Traces 2-5 are at greater depths (i.e., increments of 6.5 m).

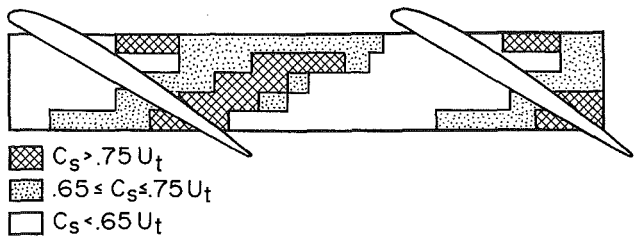

Fig. 21 Qualitative representation of the velocity of the flow in the treatment slots, $\phi = 0.42$

flow in the slot was obtained with a shielded hot-wire technique, described in [15], and these results are shown in Fig. 18 on a developed plant view of the treated outer annulus wall. Slightly more than one blade pitch is shown and the data refer to a position at mid-depth within the slot. Flow is seen to enter the cavities over approximately the downstream 60 percent of the slot and to leave the slot over approximately the upstream 20 percent of the slot. Both these findings apply to the entire blade passage. Some change in flow direction with time was detected using the hot-wire technique. The unsteadiness in flow angle was determined qualitatively and in the most extreme case was estimated at 15 deg. It must be stressed that the flow was therefore never observed to change sense, i.e., to enter the slot from a point where it had previously been emerging. The unsteadiness in direction was greatest near the front of the slot as the suction surface of the blade passed over it and near the rear at approximately blade midpassage. The magnitude of the velocity in the slot was

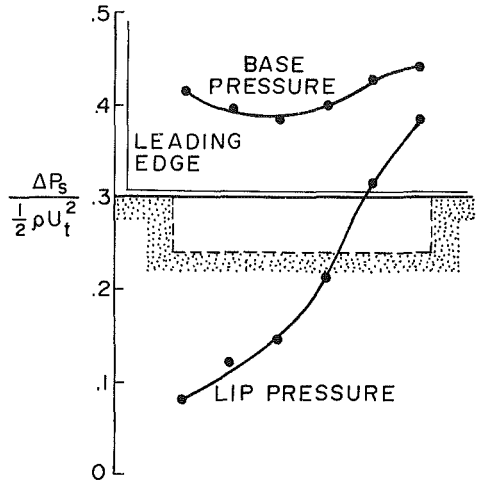

Fig. 22 Steady-state static pressure on the lip and at the base of the treatment slots, $\phi = 0.42$

measured at 24 percent (6.5 mm) depthwise intervals within the slot and ensemble averaged over 80 rotor revolutions. The last measurement station was 1 mm from the base of the slot. The results of Fig. 19 were measured 5 mm downstream from the leading edge of the slot, whilst Fig. 20 were measured 5 mm upstream from the trailing edge of the slot, both at $\phi = 0.42$. It will be recalled that these positions correspond to areas where flow emerges from and enters the slot, respectively. In both cases six vertical lines have been overlaid to indicate the position of the pressure and suction surfaces of the blades of just over two blade passages. The shading represents the blade thickness. The largest velocities with the greatest level of fluctuation are found on the lip, but this reflects the movement of the blade more than transport inside the passage and is therefore less interesting. At the front and back of the treatment the flow has a nonzero mean, superimposed on which is a fluctuating velocity component at blade passing frequency. The velocity pattern does not vary significantly from one passage to another. Both the steady and unsteady components diminish rapidly as the base of the slot is approached.

The velocity fluctuation inside the slot shown in Figs. 19 and 20 is complicated and not fully explainable. It seems very probable that it is not of first importance, the main effect being the mean transport of the fluid from the back to the front. Near the rear of the slot the flow into the slot 6.5 mm below the tip shows a pronounced peak just before the pressure side of the blade crosses it. There is, however, no corresponding peak near the front of the slot, yet being a low Mach number flow one might expect the effects to travel with negligible delay. The explanation is that much of the fluctuation observed is rotational in nature and is, to first order, convected by the mean flow. This is made rather clearer in Fig. 21 where shading is used to indicate levels of velocity 6.5 mm below the lip. The peaks in the velocity drift to the right, relative to the blades, so that a line joining the peaks would be at about 55 deg to the axial. This angle is in fact calculated if the flow inside the slots that carries the disturbance upstream is equal to 0.7 times blade speed.

At $\phi = 0.36$, close to stall for the treated compressor, the velocity pattern inside the slots was basically the same, but rather larger in magnitude.

The time-mean static pressure at the lip and base of the slot are shown in Fig. 22 superimposed on a sketch of an axial section through the blade and the casing treatment. The case shown is for $\phi = 0.42$, but the results for other flow rates are similar. The pressure on the lip reflects a local pitchwise

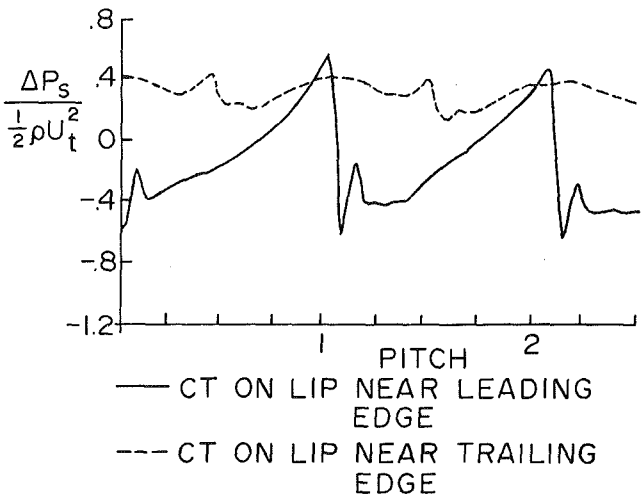

Fig. 23 Transient static pressure distribution on the lip of the treatment, $\phi = 0.42$

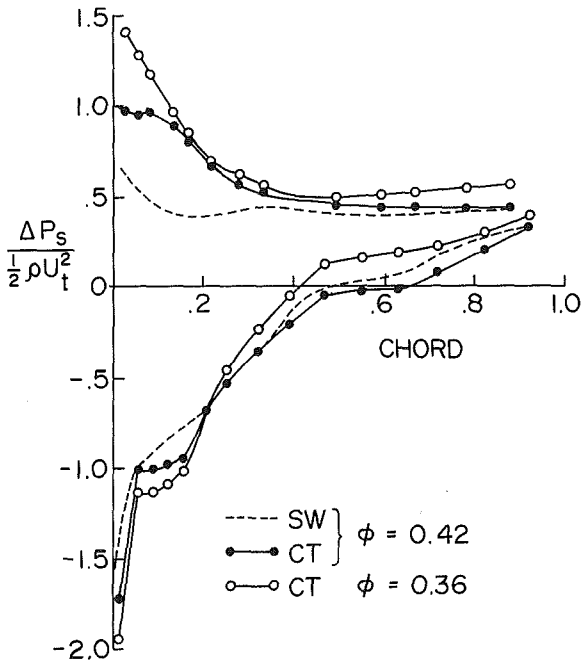

Fig. 24 Static pressure distribution on the rotor blades surface 6 mm from the outer annulus wall of the solid wall and treated rotors

average of the blade pressure field and consequently rises fairly uniformly from front to back. The pressure at the base of the slot is almost uniform and consistently higher than that at the tip. Thus where the flow enters the slot (over the rear 60 percent), the flow enters against an adverse pressure gradient. The process could, of course, be described differently by saying that the flow entering and being decelerated establishes a pressure gradient. The flow leaving near the front of the slot is accelerated out by a quite large pressure difference. The pressure difference does not help one to decide whether flow should be entering or leaving the slot and one therefore is forced to conclude that it is the direction of the flow near to the wall which determines this. As Fig. 15 shows, the absolute flow direction over the rear part of the treatment favors the flow entering. Without casing treatment, Fig. 13, the flow inclination close to the wall is such that it would enter treatment slots, if they were installed, at all axial stations. This raises the questions of why the flow configuration establishes itself in the way it does. One could imagine a casing treatment gradually opening up under a flow previously established as in Fig. 13. In this case, one would expect the flow to be less successful at entering near the front, because of the much larger pressure difference between lip and base. From this, a circulatory pattern could be established with flow entering at the back and leaving, with rather higher absolute velocity, near the front. This has accepted a more or less constant pressure along the base of the slot, which is feasible since the geometry does not lend itself to large accelerations in the axial direction. The discussion of the pressure distribution in the slot is necessarily rather intuitive because of the complicated flow, even on a mean or steady basis. In addition, the velocity measurements have shown the flow to be strongly nonuniform and rotational and one side of the passage is exposed to a nonuniform pressure across which is a high velocity nonuniform flow.

The nonsteady pressure measurements in the treatment show varying pressure with time but with the base pressure generally higher than on the lip, see [15]. Near the rear of the treatment the lip pressure was found to be briefly higher than that at the base just before the blade pressure face passes over the slot. Under such circumstances the flow can enter the slots particularly easily and the observed peak in velocity can be seen in Fig. 20.

Figure 23 shows the pressure traces of the casing treatment lip near the leading and trailing edges. The comparative uniformity of the pressure near the rear of the treatment is striking. The pressure varies strongly near the treatment leading edge and in overall terms this variation is similar with and without casing treatment. The most interesting difference that the casing treatment produces is the peak in pressure evident just past the blade suction surface. It is conjectured that this is where the swirl induced by the rotor interacts with the swirl from the casing treatment with the consequent net deceleration producing a rise in pressure. Although of general interest, this does not appear to be of importance.

The pressure distributions around the tips of the rotor are shown in Fig. 24 for three different cases. There is the smooth wall and the casing treatment builds at $\phi = 0.42$ and the casing treatment close to its stall point at $\phi = 0.36$. The general shape and included area are very similar to that further from the tip, i.e., outside the annulus boundary layer, except for the high pressure near to the pressure side leading edge. This effect is produced by the flow leaving the treatment slots and is therefore fairly local to the tip. The suction side does show abrupt changes in slope, with flat regions of low gradient, suggesting separation and reattachment. This is most clear about 10 percent chord for the casing treatment at $\phi = 0.42$, but a similar effect may be present at about 50 percent. There does not appear to be any evidence of substantial separation or blade stall, consistent with the velocity vectors in Fig. 11 and Fig. 14.

Concluding Remarks

Despite the measurements made it must be admitted that the reason for the effectiveness of casing treatment is not really understood. Fundamentally it is the ignorance regarding the precise flow mechanism leading to stall that makes this impossible. One can easily see that the rapid growth of blockage is enough to reduce the pressure rise-flow rate gradient and initiate instability, but the significance of this blockage occurring near the pressure surface is not clear.

At one level, the behavior of casing treatment seems very simple. A route is provided for flow to pass from the pressure surface to the suction surface so that a small proportion of the flow can be recirculated. The subtlety of a successful treatment like the axial skewed slot appears twofold. The boundary layer fluid tends to have high absolute swirl and therefore is suitably oriented to enter the treatment. Whereas the high

swirl velocity would be wasted in a normal smooth walled compressor, the casing treatment is capable of turning it and reintroducing it in a way which is utilizable. The casing treatment therefore selects the flow that is contributing to the blockage and then makes what would be a waste, useful. There does not seem to be any evidence other than the linear cascade flow visualization experiment described by Mikoljczak and Pfeffer [5] to suggest that aspirating the incipient or actual separation on the suction side contributes to the stall margin improvement. One can go further and say that the overwhelming trend for those casing treatments that do bring about stall margin improvement is the provision of a flow path between the pressure and suction surface. This would include circumferential grooves and blade angle slots.

The experiment by Greitzer et al. [4] can be interpreted in terms of our present tentative model. According to this, a stall margin improvement (and indeed improvement in pressure rise) due to casing treatment is only to be expected if the blading is such as to cause flow blockage to collect on the pressure surface. The high solidity blading used by Greitzer does this (see Fig. 8 of [4]) but the low solidity build does not since the low relative total pressure flow then collects in the suction surface/endwall corner. Within the usual meaning of the term the separation or stall is in the tip region for both solidities.

The present measurements have brought us to the tentative conclusion that unsteady effect in the slots are of minor importance: it is the steady or mean flow which matters. The processes in the region where the flow leaves the slot and interacts with the flow in the blade passage seems to be important, interesting, and poorly understood. One would like to know what is the optimum direction for the flow to leave the slots; it is certainly not clear that zero axial velocity and inclined to the radial at 60 deg is ideal. Short of an extensive "cut and try" exercise, this requires an understanding of the processes after the flow leaves the slot. The most obvious requirement appears to be more and better measurements in the blade passage, perhaps using rotating probes, laser measurement techniques or keeping the blade passage stationary and rotating the treatment. The latter approach was used by Takata and Tsukuda [2] and greatly simplifies the instrumentation for a minor sacrifice in flow realism.

If the axial skewed slot serves to remove blockage from the pressure surface/endwall corner and return it, turned through 180 deg, near the blade leading edge, one must remark that the rectangular geometry of the slots used is most peculiar. It is our belief that a continuously curved passage, perhaps semicircular, could be both more effective and easy to manufacture.

Because the rig used for these tests was not fitted with a torque meter it was impossible to find the loss in efficiency with casing treatment. The present experiments were unable to allow any useful conclusions to be drawn about the reasons for the loss of efficiency measured elsewhere when casing treatment has been used. It is proper to add that the cause of inefficiency in even smooth walled compressors is not understood; the sum of the profile loss, endwall boundary layer, and secondary flow is not sufficient to explain the observations, and improperly understood processes, notably those related to tip clearance flow, are probably crucial. The casing treatment might be expected to reduce the loss, by selectively removing the high loss fluid, but for reasons not explained this appears to be overwhelmed by one or more other effects.

It has been found [1] that the inclusion of a baffle half the axial distance along the casing treatment reduces the efficiency penalty whilst retaining most of the stall margin improvement. At first sight, this appears to conflict with the present conclusion that it is mean flow from the rear to the front that is basis of the stall margin improvement. This is not, however, the case. With highly staggered thin blades, such as those used in most modern compressors, and with casing treatment of typical axial length, there is ample opportunity for axial flow to occur from the pressure surface to the suction surface of the blades. The smaller efficiency penalty with this geometry probably points to undesirable levels of axial flow, or the inclusion of fluid which does not have high losses, when a baffle is absent. Still there remain many aspects that are either poorly understood or not understood at all.

Acknowledgment

The authors wish to express their gratitude to Rolls Royce Limited, who supported this research and in particular to Mr. C. Freeman for his encouragement and advice.

References

1 Prince, D. C., Jr., Wisler, D. A., and Hilvers, D. E., "Study of Casing Treatment Stall Margin Improvement Phenomena," NASA CR-134552, Mar. 1974.

2 Takata, H., and Tsukuda, Y., "Study on the Mechanism of Stall Margin Improvement of Casing Treatment," ASME Paper No. 75-GT-13, ASME Gas Turbine Conference, Mar. 1975.

3 Camarata, F. J., Greitzer, E. M., Joslyn, H. D., and Nikkanen, E. P., "Effect of Casing Treatment on the Near Tip Flow Field of a Large-Scale Rotor," United Technologies Research Publication R7512136683-1, Dec. 1975.

4 Greitzer, E. M., Nikkanen, J. P., Haddad, D. E., Mazzawy, R. S., and Joslyn, H. D., "A Fundamental Criterion for the Application of Rotor Casing Treatment," ASME *Journal of Fluids Engineering*, Vol. 101, June 1979, pp. 237–24.

5 Mikolajczak, A. A., and Pfeffer, A. M., "Methods to Increase Engine Stability and Tolerance to Distortion," AGARD LS No. 72, *Distortion Induced Instability*.

6 Osborn, W. M., Lewis, G. W., Jr., and Heidelberg, L. J., "Effect of Several Porous Casing Treatments on Stall Limit and on Overall Performance of an Axial-Flow Compressor Rotor," NASA TN D-6537, Nov. 1971.

7 Moore, R. D., Kovich, G., and Blade, R. J., "Effect of Casing Treatment on Overall and Blade-Element Performance of a Compressor Rotor," NASA TN D-6538, Nov. 1971.

8 Fabri, J., and Reboux, J., "Effect of Outer Casing Treatment on Stall Margin of a Supersonic Rotating Cascade," ASME Paper No. 75-GT-95, ASME Gas Turbine Conference, Mar. 1975.

9 Tesch, W. A., "Evaluation of Range and Distortion Tolerance for High Mach Number Transonic Fan Stages, Task IV Stage Data and Performance Report for Casing Treatment Investigations," Vol. 1, NASA CR-72862, May 1971.

10 Bailey, E. E., "Effect of Grooved Casing Treatment in the Flow Range Capability of a Single-Stage Axial Flow Compressor", NASA TM X-2459, Jan. 1972.

11 Horlock, J. H., and Lakhwani, C. M., "Propagating Stall in Compressors With Porous Walls," ASME Paper No. 75-GT-59, ASME Gas Turbine Conference, 75-GT-59, 1975.

12 Amann, C. A., Nordensen, G. E., and Skellenger, G. D., "Casing Modification for Increasing the Surge Margin of Centrifugal Compressor in an Automotive Turbine Engine," ASME *Journal of Engineering for Power*, Vol 97, July 1975, pp. 329–336.

13 Koch, C. C., "A Criterion for Stall," ASME JOURNAL OF ENGINEERING FOR POWER, Vol. 103, 1981, pp. 645–656.

14 Gregory-Smith, D. G., "Annulus Wall Boundary Layers in Turbomachines," Ph. dissertaion, University of Cambridge, 1970.

15 Smith, G. D. J., "Casing Treatment in Axial Compressor,"Ph.D. dissertation, University of Cambridge, 1980.

16 Whitfield, C. E., Kelly, J. C., and Barry B., "A Three Dimensional Analysis of Rotor Wakes," *Aeronautical Quarterly*, 1972, pp. 285–300.

17 Lewis W. E., "Fixed Direction Probes for Aerodynamic Measurements," *Proc.Instn. Mech Engrs.*, Vol. 180, pt. 3J.

D. K. Das
Associate Professor,
Division of Engineering Technology,
SUNY College of Technology,
Utica, N.Y.

H. K. Jiang
Lecturer,
Department of Jet Propulsion,
Peking Institute of Aeronautics
and Astronautics,
Peking,
People's Republic of China

An Experimental Study of Rotating Stall in a Multistage Axial-Flow Compressor

The flow field and the distribution of the flow parameters in the rotating stall regime in a three stage axial flow compressor were obtained in detail using three-hole cylindrical probes containing fast response transducers in association with a digital data acquisition system and an ensemble averaging technique. An appreciable amount of experimental data are presented in this paper with a critical discussion on those.

Introduction

The intriguing phenomenon of rotating stall in axial flow compressors has been studied extensively, both experimentally and theoretically, by various investigators. A brief review of the latest publications on this field has been given in [1]. In spite of all these efforts, however, it is recognized that the amount of information available on the stall cell structure is rather limited. Earlier Dunham [2] and later Tanaka and Murata [3] studied rotating stall cell in single stage compressors, and they were followed by an extensive investigation by Day [4] and Day and Cumpsty [5] on a multistage compressor, in which a number of excellent unconventional observations and ideas on the structure of the stall cell were put forward. However, the need for further detailed experimental investigation to understand fully the intricacies of the structure of the stall cell still exists.

This paper presents, in response to this need, finer and detailed measurements of the flow parameters in the rotating stall regime in a three-stage, low-speed axial flow compressor. The substantial amount of information provided in the paper includes information on the flow parameters at the edges of the stall cell as well as the effect of varying the axial gap between the blade rows on the stalled flow.

Test Rig and Measuring Technique

The present investigation was carried out on a three-stage axial flow compressor rig, using three-hole cylindrical probes containing fast response transducers in association with a digital data acquisition system and an ensemble averaging technique. A brief description of the test rig, the instrumentation and the data acquisition technique is given below.

Test Compressor

A schematic layout of the experimental rig is shown in Fig. 1. The compressor comprised of three identical stages and inlet guide vanes (IGV). Some of the geometric data of the compressor rig are given in Table 1.

The compressor blades were of free vortex design with the degree of reaction varying from 0.66 at the tip to 0.31 at the hub. The blade midheight reaction was 0.5. This configuration gave a design flow coefficient of $\bar{c}_x/\bar{U} = 0.5$. The axial gap between the blade rows was changeable and the present tests were carried out with gaps of 0.4 and 0.7 chord length. The flow through the system was controlled by a manually operated wooden disk mounted at the entrance of a large plenum chamber. A venturi meter was used to measure the air mass flow through the compressor, which was driven by a d-c electric motor. Most of the tests were performed at a

Table 1

Blade tip diameter	406	mm
Hub-tip ratio	0.7	
No. of blades on each rotor	38	
No. of blades on each stator	37	
Blade chord	30.5	mm
Aspect ratio	2	
Blade camber at midheight	27	deg
Blade stagger at midheight	38	deg
Blade cross-sectional profile	C4	
Design speed	50	rev/s
Bell mouth length	160	mm
Compressor length	310	mm
Downstream duct length	1000	mm
Downstream duct diameter	406	mm
Exit duct length	1800	mm
Venturi throat diameter	254	mm

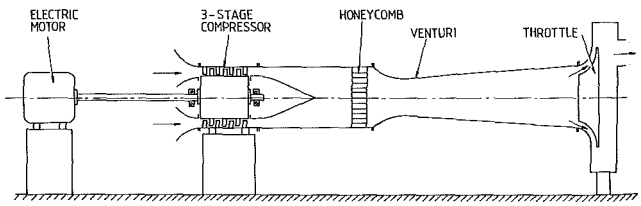

Fig. 1 Layout of compressor rig

Contributed by the Gas Turbine Division and presented at the 1983 Tokyo International Gas Turbine Congress, Tokyo, Japan, October 24–28, 1983. Manuscript received by the Gas Turbine Division July 6, 1983. Paper No. 83-GTJ-20.

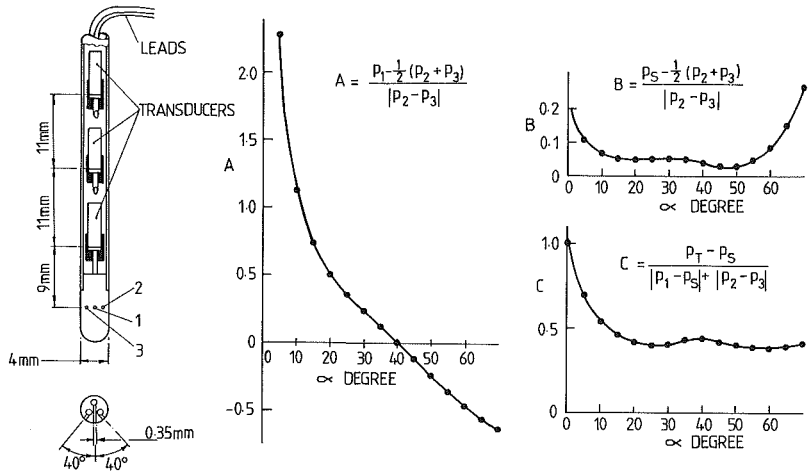

Fig. 2 Three-hole pressure probe and its calibration

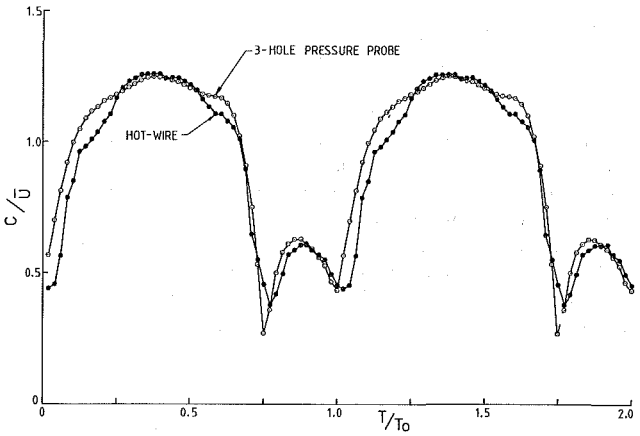

Fig. 3 Comparison between three-hole pressure probe and hot-wire results

compressor speed of 50 rev/s, which gave a Reynolds number of 10^5 based on the chord length of the blade.

Instrumentation

The rig was equipped with conventional low-response instrumentation at the inlet, the interrow gaps, and the outlet of the compressor. The data acquired from these were used to obtain the steady state overall and stage characteristics of the compressor.

The flow measurements in the rotating stall regime relied on two cylindrical three-hole probes of 4 mm dia, each containing three Kulite miniature silicon bonded pressure transducers (XCQ-080-1G) specially designed and developed for this investigation. Their construction and calibration are shown in Fig. 2. Each hole of these probes was individually connected to a transducer, the measuring range of which was 7×10^3 Pa and the natural frequency 100 KHZ. The length of the tube connecting each hole to the corresponding transducer was kept to a minimum (the maximum length being 33 mm, giving a cavity resonance frequency of about 2.5 KHZ). The frequency response of the system was found to be satisfactory for the present investigation, since the frequency of the rotating stall cell was never expected to be more than 25 HZ.

The calibration of these probes is given in the form of the coefficients A, B, and C against the flow angle α (Fig. 2), where P_1, P_2, and P_3 are the readings corresponding to the measuring holes 1, 2, and 3, respectively. Using these calibration curves as computer input, the flow angle α, the static pressure P_S, and the stagnation pressure P_T in a plane perpendicular to the axis of the cylinder of the probes were calculated. The fact that the radial component was not included in these calculations, could introduce some error into the velocity measurement. Although the centrifugal effect might be rather strong in the stalled regions, the radial component of the velocity was still fairly small as compared to the other two components. Hence the error due to the radial component would be negligible.

The calibration of the probes was carried out in a steady flow rig with a wide range of velocity (the Reynolds number range simulated was 0.2×10^4 to 1×10^4 based on the probe diameter). It was seen that the effect of varying the Reynolds number over this range on the probe calibration was small for an angle variation of ± 60 deg.

The velocity distribution obtained with the three-hole probe was compared with that obtained with a hot-wire probe (the wire being placed radially) in a real rotating stall condition. This is shown in Fig. 3, where it is obvious that the two are in reasonable agreement.

Nomenclature

a = sonic velocity, m/s
A,B,C = calibration coefficients
c = absolute flow velocity, m/s
c_x = axial velocity component, m/s
$\bar{c}_x$ = axial velocity component averaged over annulus, m/s
c_θ = absolute circumferential velocity component, m/s
P_1,P_2,P_3 = three-hole pressure probe readings
P_T = stagnation pressure (gauge pressure), Pa
P_S = static pressure (gauge pressure), Pa
ΔP_{T-S} = inlet stagnation to exit static pressure rise, Pa
T = time, s
T_o = time period of stall cell, s
$\bar{U}$ = blade speed at mean radius, m/s
ρ = air density, Kg/m^3
α = absolute flow angle, degree
ω_C = angular velocity of stall cell propagation, rad/s
ω_R = angular velocity of rotor, rad/s

Table 2

Operation points on compressor characteristics		D	A	B	C
Flow coefficient $\bar{C}_x/\bar{U}$		0.405	0.31	0.215	0.215
Stall cell speed (in percentage of rotor speed)	Gap: 0.4 chord length	35%	32.5%	30.9%	28.6%
	Gap: 0.7 chord length	41.5%	38.5%	37%	

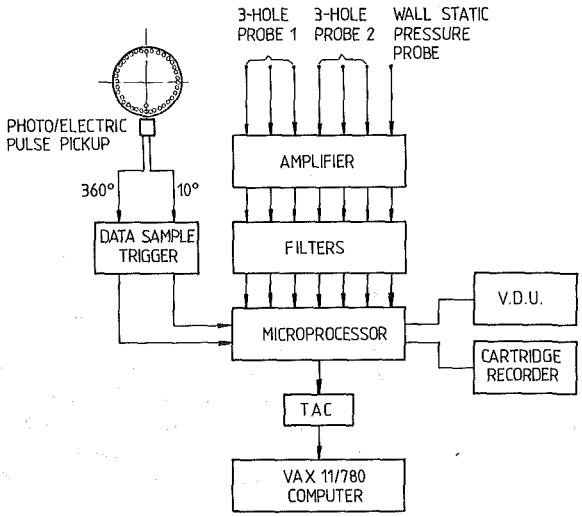

Fig. 4 Layout of data acquisition system

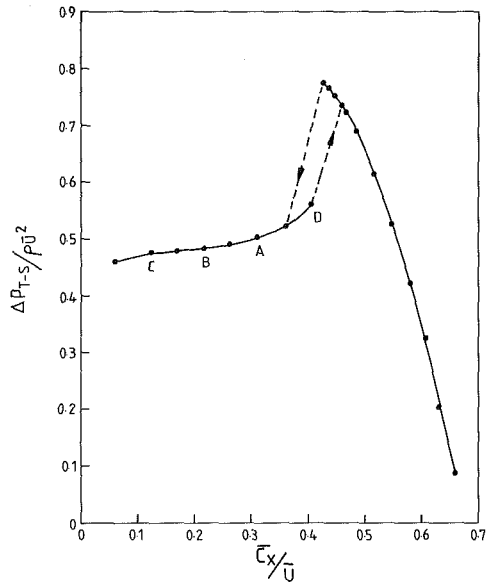

Fig. 5 Inlet total to exit static pressure rise characteristic of the three-stage compressor

In addition, the wall static pressure was measured by means of a probe containing a Kulite transducer (XCQ-080-1G).

Data Acquisition Technique

The flow through the compressor in the rotating stall regime is known to be time unsteady. However, most of the tests in the present investigation were performed in the single cell, full-span rotating stall regime, leading to highly periodic signals, which were analyzed by means of an ensemble averaging technique. This required a reference signal for defining the stall cell period. Initially, the wall static pressure probe was used for this purpose. However, the results obtained were not satisfactory and because of this a series of preliminary experiments were performed, and it was found that in the rotating stall regime, the flow angle ahead of the rotors specially near the tip had a sudden change at the edges of the stall cell. Hence one of the three-hole probes fixed immediately ahead of one of the rotors near the tip was used for the purpose of reference.

The data acquisition system is shown in Fig. 4. The output from the probes, passed through an amplifier and low-pass filters, were sampled by a microprocessor and initially recorded in a digital cartridge and then transferred to a mainframe computer via a terminal access controller for further analysis and graphical presentation. During the recording, the microprocessor was initiated by a trigger unit, which consisted of a slotted disk (mounted on the compressor shaft), a photo/electric pick-up, and a square constant pulse width generator. The output from the probes was sampled 36 times (every 10 deg) in each cycle of the compressor. Using the mainframe computer, at least 100 cycles of the data for each measuring point were averaged, each period of the stall cell containing 50 to 100 averaged data.

From the preliminary results, it was found that in the present tests, variations in the flow angle in the stalled region were always within a range of approximately 100 deg. Therefore, it was possible to use the probes with a fixed orientation (0 deg from axial ahead of IGV, 70 deg at other measuring planes). This helped to avoid any rotation of the probe about its axis, which made the measuring procedure very convenient.

Experimental Results

Compressor Characteristics and Stall Pattern. The steady-state (time-mean) overall characteristic of the compressor is shown in Fig. 5 in the nondimensional form of $\Delta P_{T-S}/\rho\bar{U}^2$ versus the mean flow coefficient $\bar{C}_x/\bar{U}$. Throttling from the fully open condition to the point of peak pressure resulted only in stronger turbulence but no stall cell. Beyond this point, however, the pressure rise as well as the flow rate fell abruptly and a single stall cell occupying about one third of the annulus covering the full blade height (full span stall) appeared. On throttling further, the pattern of the stall cell remained almost unchanged but increased in size, while the pressure rise remained more or less constant. Finally, for flow rates less than approximately 0.1, the stall cell fills up the entire annulus and the flow can then be described as axisymmetric. On opening the throttle, the characteristic maintained its original shape with the exception that the point of cessation of the stall shifted from that of its onset resulting in a hysteresis loop, as shown in Fig. 5. At the cessation of the stall cell, the stall pattern remained full-span single cell while the amplitude of fluctuation became smaller.

Tests were carried out in two builds with different axial gaps, 0.4 and 0.7 chord length, respectively. The results showed that changes in the axial gap left the compressor

characteristic unaltered, but led to certain changes in some features of the stall cell, which are discussed later.

It was also found that the stall cell speed varied with changes in the flow rate and the axial gap. Table 2 shows the stall cell speeds at different throttling positions for the two builds.

It is seen that the speed of the stall cell decreases with reduction in the flow rate and the axial gap.

Unsteady Flow Measurements

Flow measurements in the rotating stall regime were taken for the aforementioned two builds at five radial positions (90, 70, 50, 30, and 10 percent of blade height) in each of the eight axial measuring planes (six interrow gaps and another two: one ahead of the IGV and the other behind the third stator). For the build with the relatively wider gap, each interrow gap has two axial measuring planes (near rotor and near stator). Detailed measurements were obtained at the operation point A (Fig. 5) on the compressor characteristic with a flow coefficient of 0.31. Flow parameters were measured also at the points B, C, and D on the characteristic limiting the same to a fixed radius in each measuring plane with the exception that radial traverses were performed for the second stage.

The variations in the flow parameters, namely, the absolute flow angle α, the axial velocity coefficient $C_x/\bar{U}$, the absolute circumferential velocity coefficient $C_\theta/\bar{U}$, the absolute velocity coefficient $C/\bar{U}$, the stagnation pressure coefficient $P_T/\frac{1}{2}\rho\bar{U}^2$ and the static pressure coefficient $P_S/\frac{1}{2}\rho\bar{U}^2$ are presented in Figs. 6–10. In these plots, the flow parameters are plotted against T/T_o, the fraction of the stall cell time period. These plots are all directly from the computer and each plot shows two periods of the stall cell. Since all the traces in the present tests were triggered by the same fixed reference probe, the various parameters in the figures are all with one to one correspondence between the points in their plots.

Axial Variation of Flow Parameters

Figure 6 shows the flow measurements at the blade midheight in the various axial measuring planes for the build with the axial gap of 0.4 chord length at the operation point A. In these plots, the numbers 1, 3, and 5 indicate the measuring planes ahead of rotors, 2, 4, and 6 behind the rotors, 7, behind the third stator and 0, ahead of the IGV.

From Fig. 6(*a*), it is seen that in the stalled region the absolute flow angles ahead of the rotors are all approximately 100 deg or a bit more, indicating an almost tangential flow with a small negative axial component in the same direction as that of the rotor in almost the whole circumferential extent. Also, as we can see, the flow angles at the stall cell edges change very sharply. Behind rotors, the flow angles in the stall cell center are above 90 deg but change smoothly. For the build with the wider gap, plots of which are not presented in this paper, the stalled flow angles behind the rotors were always below 90 deg.

Correspondingly, Fig. 6(*b*) indicates that fairly strong reverse flow occurs in the whole stalled region ahead of the rotors and only in the central part behind. For the 0.7 chord length axial gap build, no reverse flow appeared behind the rotors, since flow angles were always below 90 deg.

In Fig. 6(*c*), it can be seen that ahead of the rotors, the absolute circumferential velocities are high (of the order of the blade speed) in the stalled regions, being even higher for the rear stages, while behind the rotors, the velocities are much lower. It is to be noted that at the edges of the stall cell ahead of the rotor, the circumferential velocities are also very low, in fact lower than the tangential component of unstalled flow as well as the stall cell speed, which is 32.5 percent of the rotor speed. This fact suggests that the highly tangential moving flow is strictly limited to the stalled region.

The absolute velocities shown in Fig. 6(*d*) are similar to those of the circumferential velocities.

Figure 6(*e*) shows that the stagnation pressure is fairly high in the stalled region ahead of the rotors, but behind the rotors and at the stall cell edges, it is much lower. Relating this to the circumferential velocity variations (Fig. 6(*c*)), it seems obvious that a great deal of work must have been exerted on the reversed stalled flow while being swirled out of the rotor in the tangential direction; but the high kinetic energy must dissipate both in the axial gap and the stator. In the vicinity of the edges of the stall cell ahead of the rotor, the loss must be very high as a result of a highly vertical motion.

The static pressure variations shown in Fig. 6(*f*) indicate that the static pressure in the stalled region ahead of the rotors is also higher than that in the unstalled flow, which should be related to the high tangential velocity. Behind the rotors, it is still a bit higher in the first stage, while in the latter stages, its distributions are not "in phase" with that of other parameters and they have maximum values at the trailing edge (in absolute frame) of the stall cell and minimum values at the leading edge.

On comparing the flow measurements for various axial planes by noting the amplitude of variation of the flow parameters, it is seen that although the stalled flow is similar in nature for each stage, actually it becomes more active gradually from stage to stage and not just repeats.

It is apparent that a close analysis of the variation of the stalled flow parameters at the exit plane of the compressor may lead to a better understanding of the process of flow reversal. In Figs. 6(*a*) and 6(*b*), we can see that unlike that ahead of the third stator, the stalled fluid at the exit plane appears reversed just like that ahead of the rotors. Figures 6(*c*) and 6(*e*) indicate that, in contrast with the unstalled flow, the circumferential velocities and the stagnation pressure of the stalled flow are all higher than those ahead of the third stator. Also we can see that the circumferential velocities and the stagnation pressure have very low values at the stall cell edges. Figure 6(*f*) shows that the static pressure also becomes higher and tends to be uniform as in the case of unstalled flow. It is thought that the unstalled flow with higher pressure may not be able to move directly into the stalled region, but the reverse flow, which comes from the unstalled region must initially occur at a distance behind the third stator.

Figure 6 also provides information on the axial shape of the stall cell. The locations of the stall cell edges are shown in the figures by vertical broken lines. It is evident that the stall cell is almost axial throughout the compressor and its circumferential extent remains almost the same from the front to the rear of the compressor. However, this is not always so as is obvious from other results obtained in the present investigation itself, which show that the circumferential extent of the stall cell decreases fractionally towards the rear of the compressor at the tip, but increases at the hub. Also the trailing edge always maintains an approximately axial line whereas the leading edge does not.

On examining the unstalled flow carefully in Fig. 6, it can be seen that the existence of the stall cell does have some effect on the unstalled flow. In front of the IGV, the flow angles and the circumferential velocities vary from a highly positive value at the leading edge of the stall cell to a highly negative value at the trailing edge. Correspondingly, the stagnation pressure and the static pressure vary from a little above atmospheric pressure to quite a negative value. The effect also appears within stages. The stagnation pressure and the static pressure near the trailing edge of the stall cell are low in the first stage but gradually become higher in the latter stages. For the build with the wider gap, this effect appears to be stronger and the results show also that near the trailing edge of the stall cell the

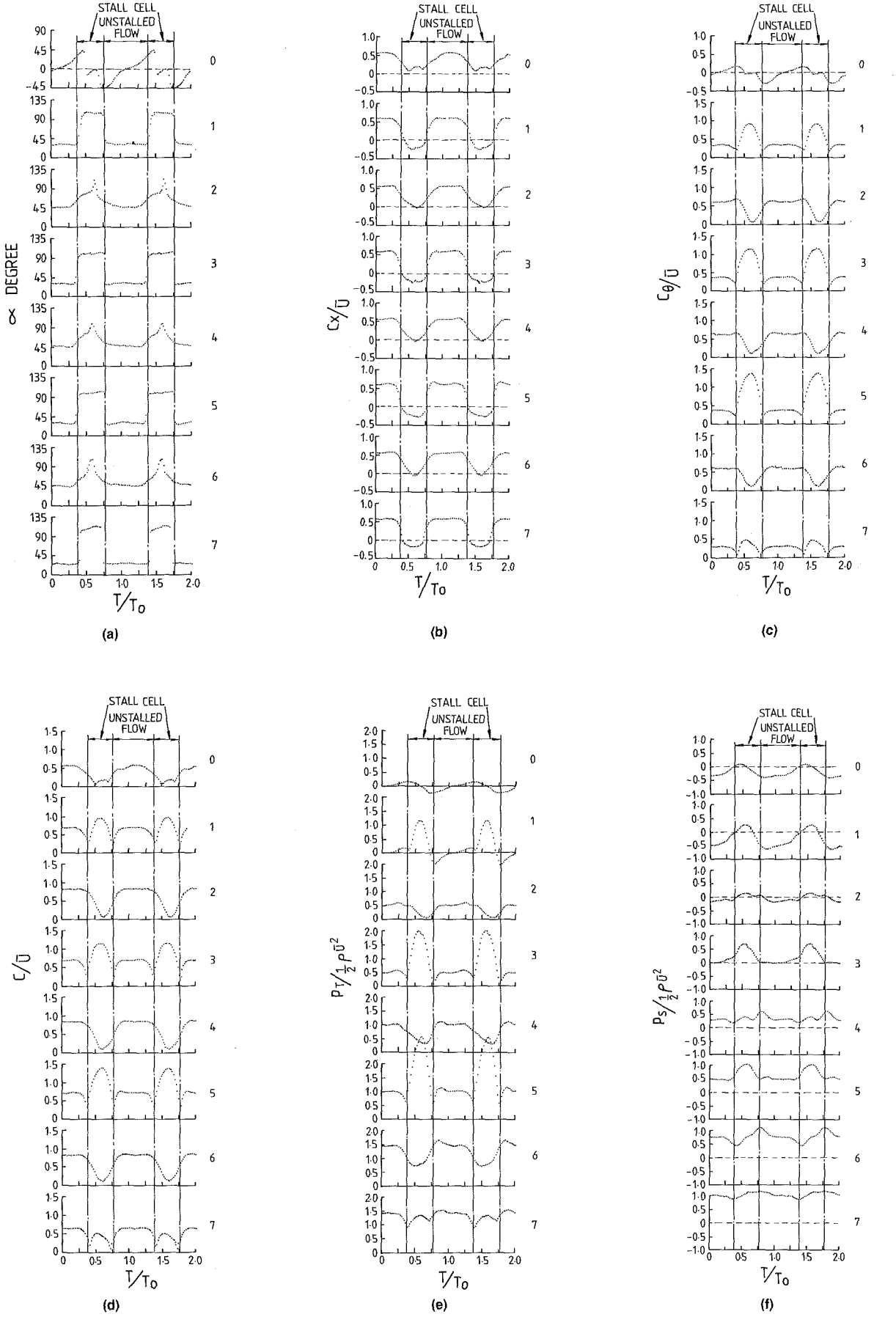

Fig. 6 Flow parameter variations at blade midheight in axial measuring planes (axial gap = 0.4 chord length)

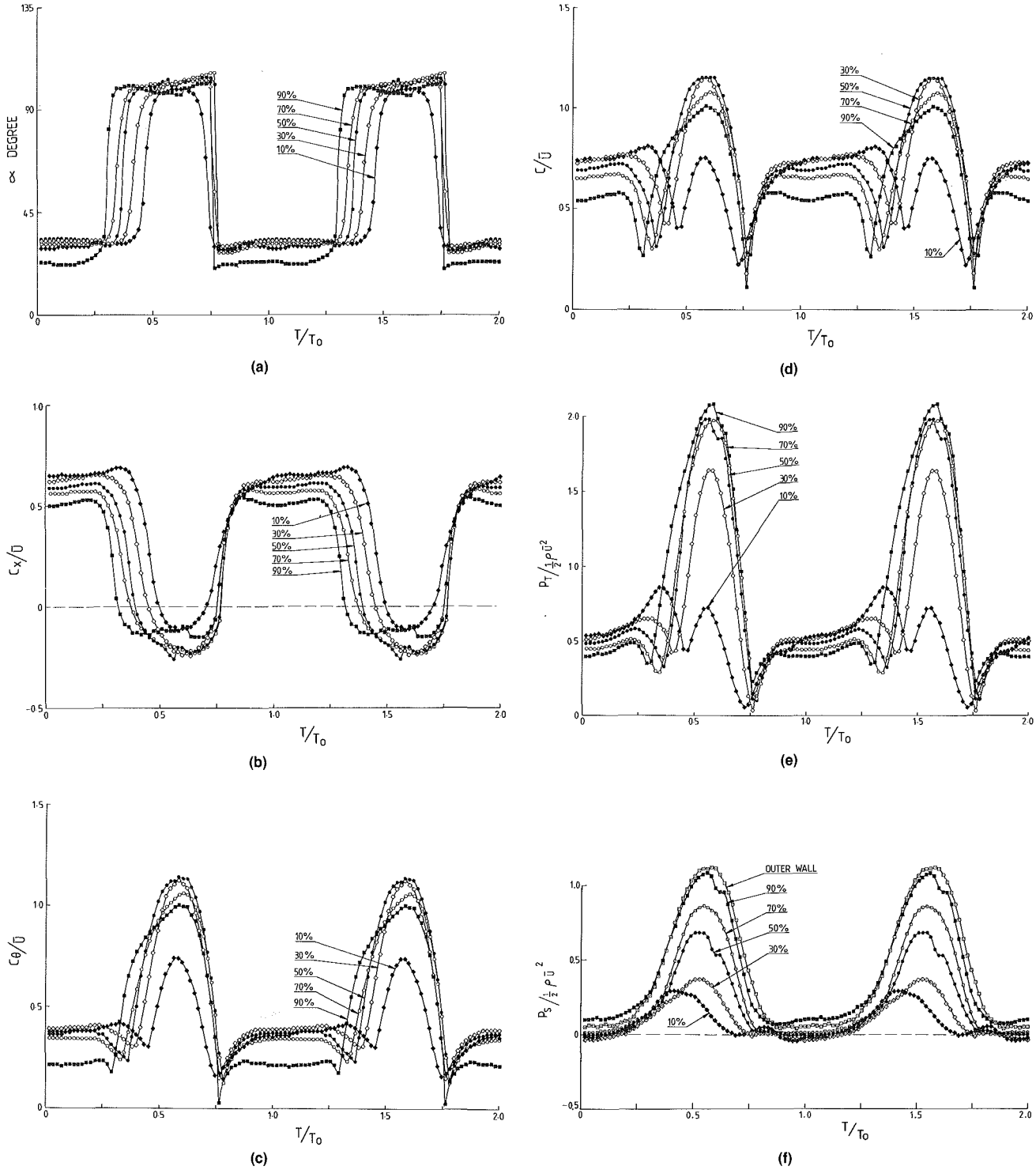

Fig. 7 Flow parameter variations at different radial positions ahead of second rotor (axial gap = 0.4 chord length)

flow angles and the circumferential velocities ahead of the rotors are always lower than those near the leading edge, but are higher behind the rotors. It suggests that the rotor exerts more work on the unstalled flow in the area near the trailing edge of the stall cell than on that near the leading edge. From these observations, the behavior of the unstalled flow can not be thought of as uniform.

Radial Variations of Flow Parameters

A Typical set of results for the second stage are presented in Fig. 7 (0.4 chord length gap) and 8 (0.7 chord length gap) to show the radial variation of the flow parameters ahead of the rotor for the operating point A, where the percentages shown are radial measuring positions with respect to the hub. Similar results are shown in Figs. 9 and 10 for the variation of some of the flow parameters behind the rotor at the 90 percent position.

Figures 7(*a*) and 7(*b*) show that the stalled flow angles and the axial velocities ahead of the rotor are almost the same in the stalled region from hub to tip, but with different cir-

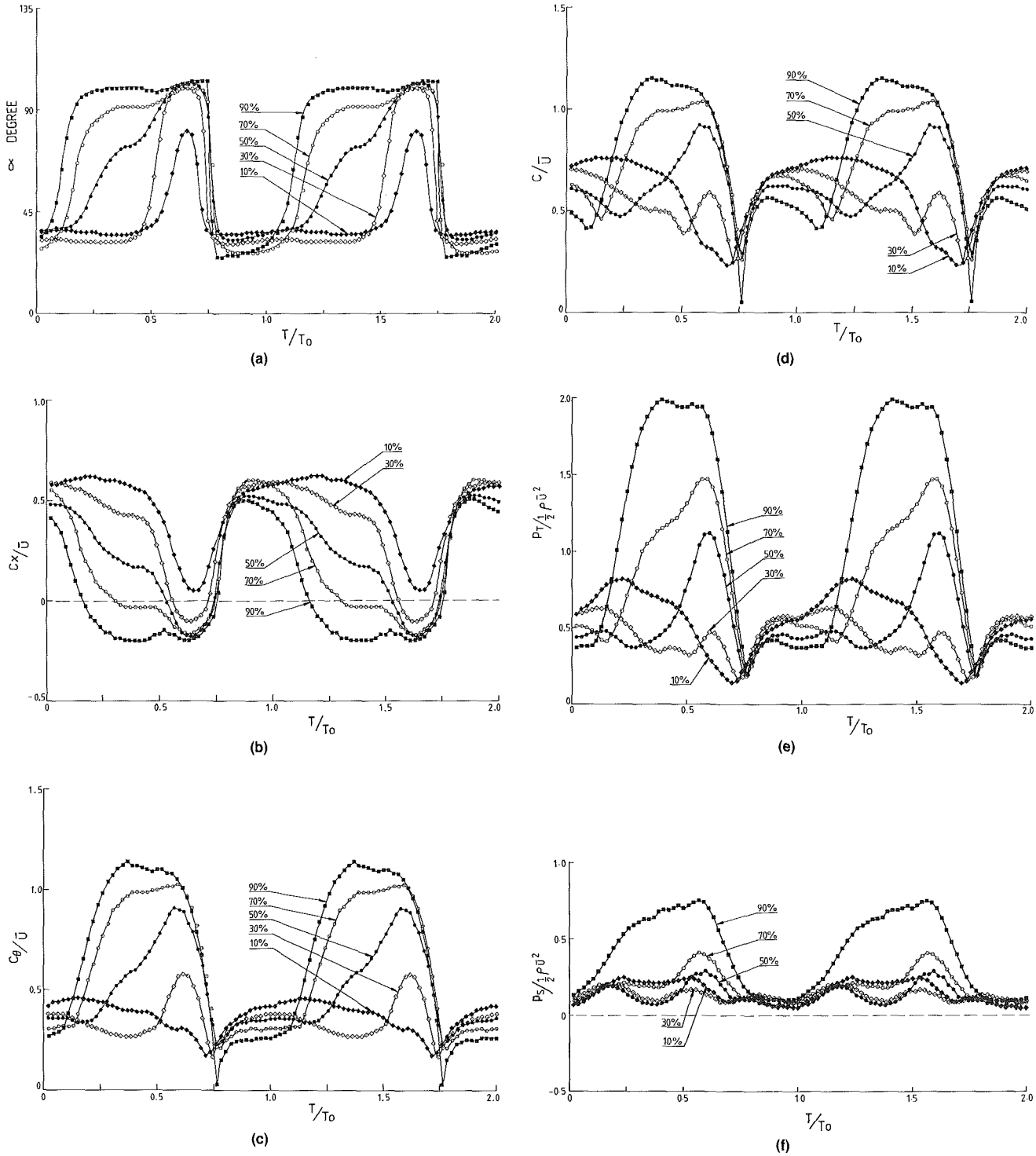

Fig. 8 Flow parameter variations at different radial positions ahead of second rotor (axial gap = 0.7 chord length)

cumferential extents. This indicates that the reverse flow appears almost in the whole radial stalled region ahead of the rotor; but the circumferential extent of the stall cell varies from relatively narrower at the hub to relatively wider at the tip with the trailing edge remaining almost radial as shown in Fig. 11. Figures 7(*c*), 7(*d*), and 7(*e*) show that the circumferential velocities, the absolute velocities and the stagnation pressure in the stalled region are all high in most parts of the span except near the hub. The fact that the velocities and the stagnation pressure at the stall cell edges are low can be clearly seen on all of these plots. Figure 7(*f*), which shows higher static pressure gradually increasing from hub to tip in the stalled region ahead of the rotor, also contains a plot of the wall static pressure obtained with the wall static pressure probe, showing good agreement with the other results obtained with the combined probe.

Figure 9 obtained with the same conditions as those for Fig. 7, shows for the tip, reverse flow ahead of the rotor and downstream flow behind it, mainly in the left part of the stall cell. Other measurements indicate that this observation holds

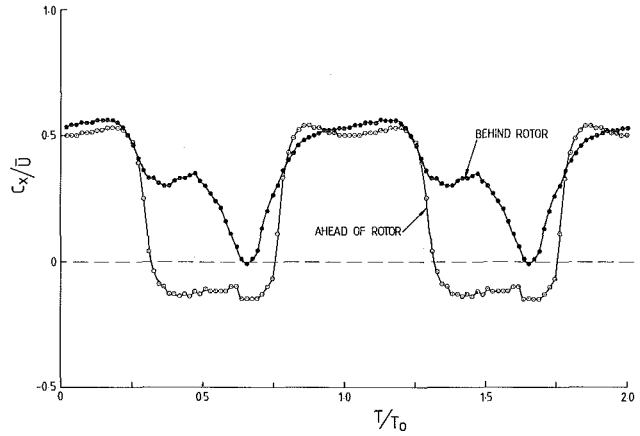

Fig. 9(*a*) Variations of axial velocity at tip (axial gap = 0.4 chord length)

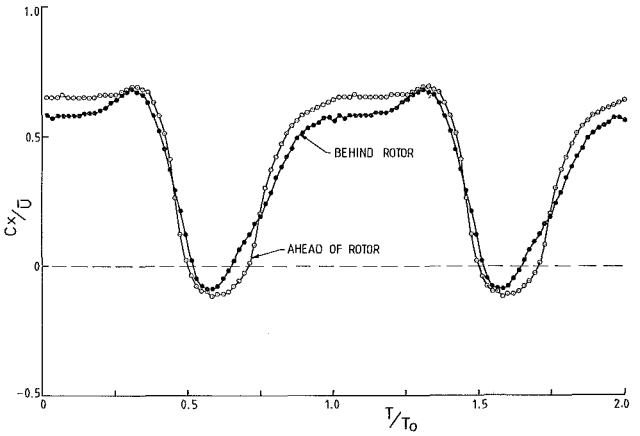

Fig. 9(*b*) Variations of axial velocity at hub (axial gap = 0.4 chord length)

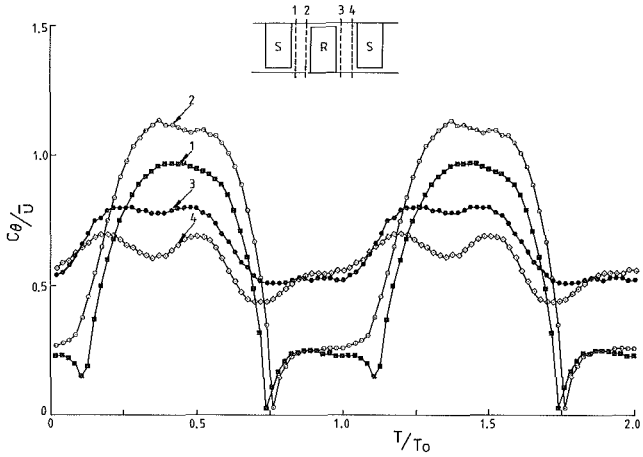

Fig. 10(*a*) Variations of circumferential velocity at tip (axial gap = 0.7 chord length)

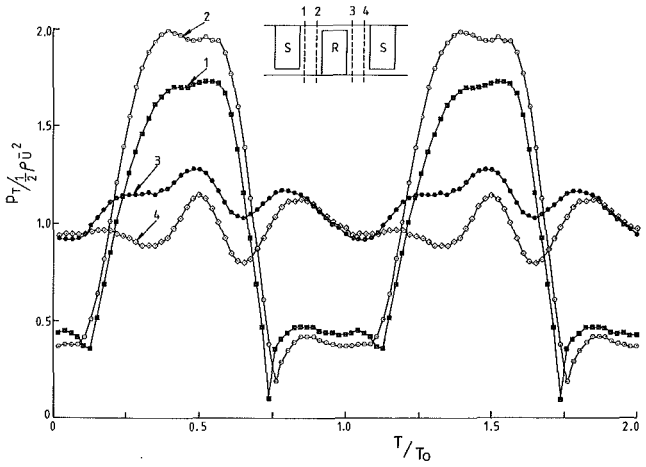

Fig. 10(*b*) Variations of stagnation pressure at tip (axial gap = 0.7 chord length)

good for all the other operation points and builds of the compressor.

Figure 10 shows that variation in the flow parameters in the gap between the blade rows at the tip for the build with 0.7 chord length gap. It is seen that the circumferential velocities and the stagnation pressure in the stalled region are higher near the rotor than near the stator both ahead of the rotor and behind it. Also it is seen that behind the rotor their variations are different from those at other radial positions in that their values are somewhat higher than those in the unstalled region. In the build with the narrower gap, these higher values of circumferential velocities and stagnation pressure behind the rotor only appear in the left part of the stall cell, while in the right part they are still lower as we can see later in Fig. 12. From Figs. 9 and 10, it is clear that in the stalled region some of the fluid leaves the rotor upstream and during this process acquires a great deal of kinetic energy from the rotor, which dissipates rapidly in the gap even before it reaches the stator. Another portion of the fluid leaves the rotor downstream especially in the left part of the stall cell, but it seems that the effect of the rotor on this part of the fluid is not as significant as that on the upstream fluid.

It can be seen from Fig. 8 that the size of the axial gap does not vary the nature of stalled flow but has some effect on the variation of the flow parameters as well as the shape and the character of the stall cell. For the build with the wider gap, the circumferential extent of the stall cell seems to be wider at the tip but narrower at the hub as shown in Fig. 11. Also the reverse and highly tangential moving flow with high pressure

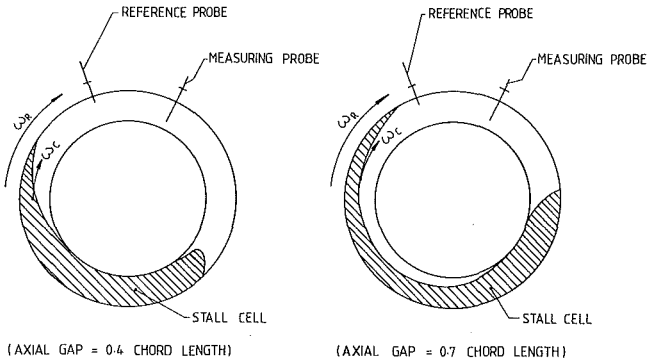

Fig. 11 Circumferential extent of stall cell

appears only in the upper part of the annulus ahead of the rotor and thus the radial flow pattern of the stall cell in this case has some differences from that in the build with the narrower gap in that no reverse flow is found behind the rotor.

Discussion

The flow structure in the single-cell, full-span rotating stall regime of the three-stage compressor can be built up from the measurements taken in the present investigation. Because of

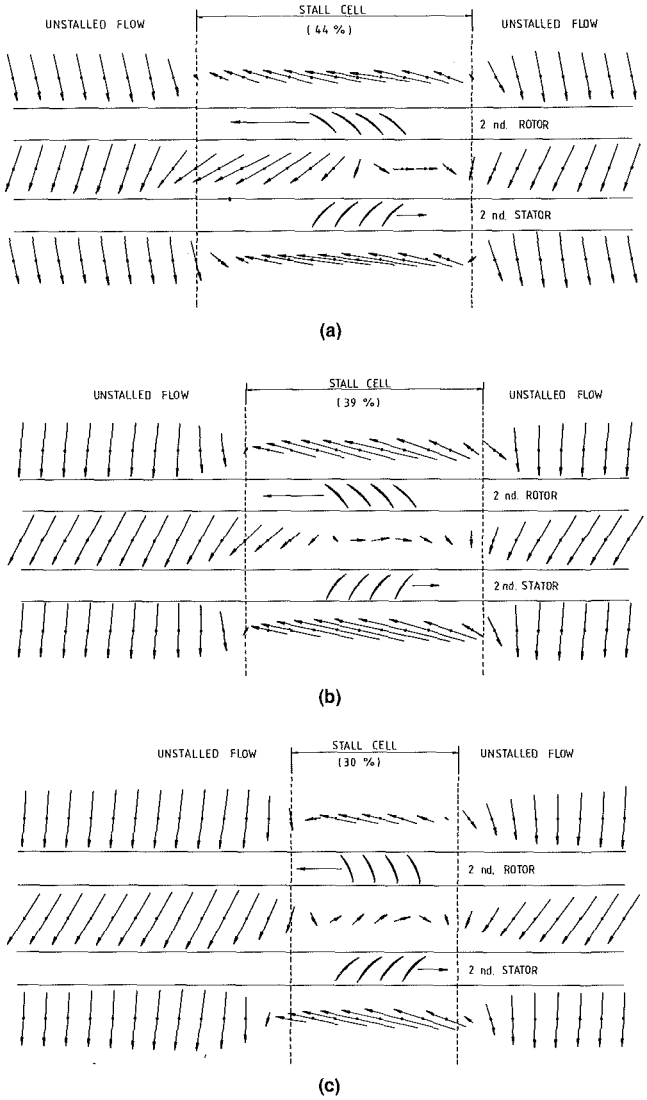

Fig. 12 Flow field (vector distribution; axial gap = 0.4 chord length; drawn in the cell reference frame)

the quite small axial gap in compressors in general, it is thought that the measurements taken from the build with the smaller axial gap should be closer to the reality.

Figures 12(*a*), (*b*), and (*c*) present the flow field in a two-dimensional form at the tip, the midheight, and the hub in the second stage of the build with the axial gap of 0.4 chord length in a coordinate system related to the stall cell. By virtue of the plots shown in Figs. 6–10 in association with Fig. 12, some general features of the flow pattern in the rotating stall regime of the compressor can be drawn.

One remarkable flow form within the stall cell is the highly tangential motion in the direction of the rotor ahead of the rotor. Figure 12 shows clearly that this kind of motion occurs in most part of the stalled area ahead of the rotor, except near the edges, where the circumferential velocities are much lower, even lower than the stall cell speed. Behind the rotor, the circumferential velocities of the stalled flow are also much lower in the center of the stall cell and the fluid in the stall cell frame appears to be moving in a direction opposite to that of the rotor. The figure suggests that although there is a highly tangential movement in the stall area, the unstalled flow cannot cross the stall cell. Thus the results of the present investigation do not seem to support the "crossing model" ([5], Fig. 14, pp. 107–109).

In the flow field behind the rotor, however, a certain

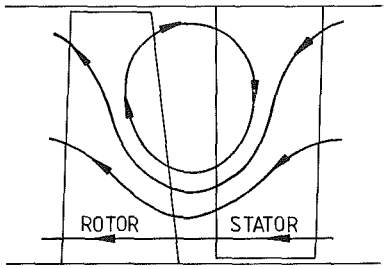

(AXIAL GAP = 0·4 CHORD LENGTH)

Fig. 13 Sketch of radial flow pattern at center of the stall cell

amount of mass transport does occur at the stall cell boundaries specially at the left one (the leading edge in the absolute frame). But on the whole, it cannot be thought of as crossing of the fluid through the stall cell. In the situation shown in Fig. 12, the fluid, which is transferred from the left part of the stall cell into the unstalled region behind the rotor, in fact comes from the lower part of the rotor blade passage by centrifugal effect as described below.

The possible radial flow pattern at the center of the stall cell can be drawn from the various plots of the axial velocity at different radial positions as shown in Fig. 13. It presents that part of the reverse stalled fluid and some unstalled fluid entering the rotor blade passage, which is centrifuged radially outwards, most of it going upstream and a relatively smaller amount of it going downstream from the tip of the rotor. In the stator blade passage, the fluid goes the other way and the fluid coming from both the present rotor and the next rotor goes inward and then moves into the present rotor again.

So far as the axial movement of the stalled fluid is concerned, the general tendency is fluid reversal. In the present measurements, reverse flow appears in all the cases, whether in different builds or at different operation points. It was found that for the builds, the smaller the axial gap, the wider the radial extent of the fluid reversal, while for the operation conditions, the deeper the throttling, the wider were both the radial and the circumferential extent of the fluid reversal. Also it was seen that in front of the rotor fluid reversal could appear in the whole span, whereas behind the rotor, it would occur in all but the tip of the blade.

An idea can be formed regarding the general cause of the tendency of the fluid reversal in the stalled region from the measurements in the various axial measuring planes from the front to the rear of the compressor and particularly from those in the exit plane. Although the fluid in the stalled region is highly tangential in motion, from the point of view of axial motion, it is very much a retarded flow. Obviously, the blade rows, which were designed for normal throughflow, are not suitable for this kind of fluid motion. Although a great amount of work has been exerted on the stalled flow (during the measurement of the compressor characteristic, it was found that from the peak pressure point, at which the power consumption was maximum, to the nearly fully closed position, the power consumption reduced by less than 5 percent), most of this flow must have dissipated within the stall cell itself as loss. Therefore, essentially the stalled region is a pressure-deficit region as shown in Fig. 6. Thus the unstalled flow with a higher pressure should have a tendency to move into the stalled area and cause fluid reversal. In fact, the measurements in the exit plane have shown that the strong fluid reversal actually occurs behind the third stator.

It may be observed that due to this tendency the rotor blades, which are inclined in the direction of rotation, move the stalled fluid in a tangential direction with a high tangential

velocity and a high pressure. Also when the stall fluid is being centrifuged in the rotor passage to reach the tip part of the annulus, the high pressure caused by the centrifugal effect of the rotor forces the fluid towards upstream rather than downstream. This may be a possible explanation for the occurrence of stronger stalled flow in the rear stages of the compressor than in the front.

Conclusion

On the basis of the results reported in the present paper, the following conclusion may be drawn:

1 The fairly simple three-hole cylindrical pressure probe containing fast response transducers in association with a digital data acquisition system and an ensemble-averaging technique has proved to be a convenient and satisfactory method for the experimental investigation of rotating stall.

2 Deep rotating stall cell is indeed a very active and intricate flow area, in which various flow motions such as highly tangential motion with fluid reversal ahead of the rotor, radial motions in both the rotor and stator passages occur. In addition, there is mass transport at the stall cell edges behind the rotor mainly occurring in the upper part of the annulus at the leading edge.

3 The pressure gradient between the unstalled and the stalled flow areas is probably the main cause of the stalled fluid reversal. It seems likely that the complex stalled flow pattern is formed by the tangential and the centrifugal effects of the rotor under the axial and the circumferential pressure gradients.

4 Although it has been confirmed that the stall cell essentially extends axially through the compressor, the unstalled flow does not pass through the stall cell. The highly tangential motion is strictly limited to the stall region ahead of the rotor and most of the kinetic energy exerted by the rotor dissipates during the motion in the axial gap and in the stator especially near the edges of the stall cell. Thus the results do not seem to support the concept of the "crossing model."

5 The variation of the axial gap between the blade rows modifies the shape of the stall cell and the flow parameter distribution in the stalled compressor. With increase in the axial gap, the strong stalled flow tends to move towards the upper part of the annulus, and its three-dimensionality becomes more pronounced.

References

1 Das, D. K., and Ozcanli, S. C., "An Experimental Study of the Unsteady Response of the Rotor Blades of an Axial Flow Compressor Operating in the Rotating Stall Regime," AIAA-83-0001, AIAA 21st Aerospace Sciences Meeting, Reno, Nevada, Jan. 10–13, 1983.

2 Dunham, J., "Observations of Stall Cells in a Single Stage Compressor," A.R.C. CP589, 1961.

3 Tanaka, S., and Murata, S., "On the Partial Flow Rate Performance of Axial Flow Compressor and Rotating Stall, Second Report," *Bulletin of the J.S.M.E.*, Vol. 18, No. 117, Mar. 1975.

4 Day, I. J., "Detailed Flow Measurements During Deep Stall in Axial Flow Compressors," AGARD, CP177, 1976.

5 Day, I. J., and Cumpsty, N. A., "The Measurement and Interpretation of Flow Within Rotating Stall Cells in Axial Compressors," *Journal of Mechanical Engineering Sciences*, Vol. 20, No. 2, 1978, pp. 101–114.

Experimental Study of a High-Throughflow Transonic Axial Compressor Stage

A. J. Wennerstrom
Aero Propulsion Laboratory,
Air Force Wright Aeronautical Laboratories,
Wright—Patterson AFB, Ohio 45433

Design information and experimental results are presented for a transonic axial compressor stage passing 40 lbs/s-ft² frontal area (195 Kg/s-m²) with a pressure ratio of 1.95 at 1500 ft/s (457 m/s) tip speed. The design incorporates several unusual features that helped it achieve a peak isentropic efficiency over 88 percent at design speed. The compressor was evaluated at three rotor tip clearances and an optimum was found. Vortex generators placed upstream on the casing proved relatively ineffective in influencing stall margin. Vortex generators installed on the rotor did improve stall margin and also increased efficiency at speeds of 90 percent and below.

Introduction

In aircraft turbine engines, there has long been a premium placed on achieving high flow per unit of compressor frontal area in order to minimize engine and installation weight. There is also substantial incentive to maximize loading in order to keep the number of required stages to a minimum, with further favorable impact on weight, cost, and ruggedness. Preliminary design studies of compressors for an advanced turbojet illustrated that the greatest aerodynamic challenge to state-of-art improvements in this area rested with the first stage. The research configuration described in this paper was conceived with the object of evaluating how far the incorporation of several advanced design concepts might permit one to progress in increasing specific flow and loading.

In addition to describing the design, this paper presents results of an extensive experimental program associated with its evaluation. The compressor was tested with three different rotor tip clearances. It was also evaluated with boundary layer control, consisting of three configurations of vortex generator mounted on the casing upstream of the rotor and one vortex generator configuration mounted on the rotor itself.

Baseline Design

Preliminary Design. Two parameters were established at the outset. The corrected specific flow goal was 39.7 lbs/s-ft² frontal area (193.8 Kg/s-m²). A corrected tip speed of 1500 ft/s (457.2 m/s) was chosen as the maximum value consistent with turbine stress considerations for a turbojet. Most of the remaining characteristics resulted from the objective of designing a multistage compressor with the minimum number of stages consistent with the application.

Peliminary design was accomplished with the axisymmetric, streamline-curvature, full radial equlibrium analysis computer program described in [1]. Losses were assumed to be equal to the sum of two components; losses due to diffusion as described by Lieblein's loss parameter versus diffusion factor relationship [2] and losses due to a normal passage shock wave as described by Miller, Lewis, and Hartmann [3]. The empirical loss parameter curves used for the rotor are shown in Fig. 1. Those for the stator were taken from [4]. A 2.0 percent rise in blockage was specified across the rotor and maintained constant across the stator. Inlet guide vanes (IGV) were excluded from consideration. Although variable IGV might be desirable to expand the part-speed operating envelope, they were not necessary for reduction of relative inlet Mach number, nor could significantly cambered IGV be tolerated at design-point because of the high flow rate and resultant danger of choking. A design approach was adopted that assumed that the stator would be a load-bearing structure supporting the front engine bearing and transmitting services. The stator was designed to turn the flow back to the axial direction.

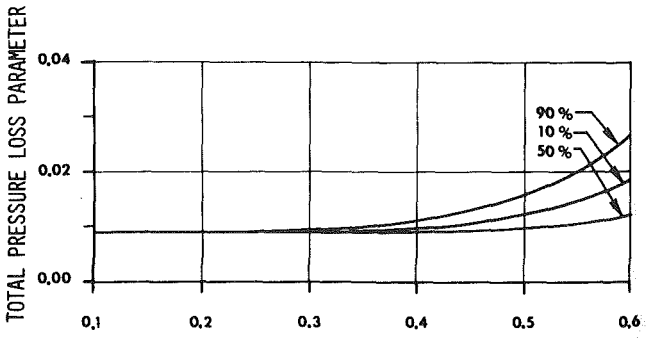

Fig. 1 Rotor diffusion loss correlation

Contributed by the Gas Turbine Division of the American Society of Mechanical Engineers and presented at the Sixth International Symposium on Airbreathing Engines, Paris, France, June 6-10, 1983. Manuscript received by the Gas Turbine Division.

Mean streamline axial velocity ratios are a principal design control variable in the preliminary design program of [1]. Values of 0.815 for the rotor and 1.206 for the stator were selected by trial-and error as choices that minimized rotor relative turning angles, and consequently shock losses, and gave a reasonable balance of diffusion between the blade rows. A constant outer diameter was specified. Aspect ratios for the stage were governed primarily by hub ramp angle, mechanical stress, and aeroelastic stability considerations. High aspect ratio tended to minimize stage weight and rotor root stresses, but tended toward steep hub ramp angles, greater flutter sensitivity, necessitating part-span dampers, and less stall margin. A compromise was chosen, resulting in a rotor hub ramp angle of approximatley 30 deg and reasonable prospects of not requiring part-span dampers. The aspect ratio of the stator was chosen such that hub ramp angle declined monotonically and smoothly from the inlet value.

Two other variables used for design control were the rotor tip diffusion factor and the spanwise rotor total pressure distribution. A limiting rotor tip diffusion factor of 0.52 was selected. The rotor total pressure distribution was iteratively adjusted until, in combination with the loss model, an approximately constant total pressure was achieved at the stage exit. The resultant rotor total pressure ratio distribution ranged from 2.07 at the hub to 1.92 at the tip. The relative turning angle at the rotor tip was limited to 2.4 deg for a relative inlet Mach number of 1.61. The foregoing choices led to a predicted stage total pressure ratio of 1.93 at an isentropic efficiency of about 0.84. The corresponding total temperature ratio ranged from 1.23 at the hub to 1.29 at the tip. At the stator hub, the Mach number was barely supersonic at 1.02 and the diffusion factor was 0.55. Test facility considerations set the outer diameter at 17 in. (432 mm) and the flow, consequently, at 62.6 lbs/s (28.4 Kg/s).

Detail Design. The detailed aerodynamic design was accomplished with an early version of the computer program described in [4], employing the streamline curvature method of computation. Although conceptually similar to the method employed for the preliminary design, much greater precision was achieved through the addition of many more axially distributed computing stations to define the flow path, including four stations within the interior of each blade row. The computational mesh employed is illustrated in Fig. 2. For the computations made within a blade row, blade-force terms were included in the momentum equation in the form of an axisymmetric body-force field assumed to act normal to the surface formed by the stacked camber lines of each blade row. "Arbitrary" airfoils were employed for both rotor and stator. The technique used consists of assuming the meridional distributions of total enthalpy through rotors and of angular momentum through stators. Then, after correcting for the internal deviation angle distribution, airfoils are fitted to the calculated relative flow angles and stacked as described in [5]. Three somewhat novel features were incorporated into this design. These were: (*i*) variable fillet radii at blade/platform interfaces, (*ii*) leading edge sweep at the stator hub, and (*iii*) an optimization criteria based upon static pressure to select the best airfoils.

The idea for variable fillets stems from experience with fillet design for the wing/fuselage juncture in aircraft. To minimize interference drag and boundary layer growth in the corner, a fillet was chosen equal to approximately one-fourth of the average local blade spacing. Then, over a distance equal to about 20 percent chord, the fillet radius was reduced to about one-fourth of its midchord value as leading and trailing edges were approached. This treatment was applied to the rotor hub and both stator endwalls.

Stator hub Mach numbers on the order of sonic and higher have normally posed problems. To handle this, the stator leading edge was swept forward toward the hub by an amount

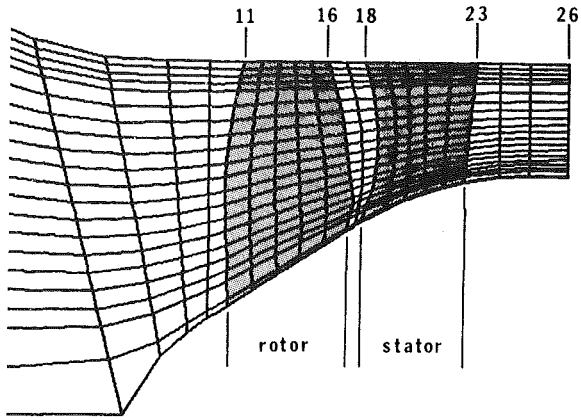

Fig. 2 Compressor design computational mesh

intended to reduce the component of Mach number normal to the leading edge to approximately 0.4. This level was chosen on the basis of cascade data, which generally showed incidence range to be a maximum for Mach numbers up to 0.4, and to then decrease as Mach number increased further. The stator leading edge was swept forward again at the tip in order to increase solidity and reduce stage length.

The pressure distribution optimization criteria was based upon the following simple logic. To achieve minimum loss airfoils, one generally would like to minimize pressure gradients on the airfoil surfaces. However, computation technology when the design was accomplished, and for that matter, even today, was not capable of accurately predicting pressure distributions on high Mach number cascades. Therefore, the next best approach appeared to be to minimize the meridional gradient in a circumferential average sense. The absolute minimum would, of course, be linear from leading to trailing edge. However, this would not be achievable because an airfoil cannot sustain loading all the way to its trailing edge. Thus the final choice was to strive for meridional gradients of static pressure that were approximately linear through the first three quarters of the blade row and then tapered off toward the trailing edge. This approach was used for both rotor and stator.

Designs involving axisymmetric computations inside blade rows require several additional assumptions to be made because of the relative lack of data concering circumferentially averaged parameters within blade rows. These are, in order of decreasing criticality, the spatial distributions of deviation angle, blockage, and loss. The interior deviation angle is the difference between the circumferentially averaged relative flow angle and the local camber line angle on an axisymmetric stream surface within a blade row. It equals the incidence at the leading edge and the conventional deviation angle at the trailing edge. If airfoil lift is to diminish to zero at the trailing edge, the rate of change of deviation angle must be approximately equal and opposite to the rate of change of camber line angle at the trailing edge. This defines its slope at the trailing edge. Finally, in the covered portion of the passage, deviation angle should be extremely small. These four considerations led to the curves shown in Fig. 3. Blockage due to boundary layers and wakes was estimated according to a simplified formula for a turbulent boundary layer on a flat plate, substituting meridional velocity and length for absolute velocity and path length. The method used is substantially as described by Jansen [6]. However, the blockage was not applied at the endwalls. The total blockage calculated at each computing station was linearly distributed from hub to tip in proportion to the spanwise solidity variation. Midspan blockage estimated in this manner rose from 1.0 percent at the rotor leading edge to 6.0 percent at the

rotor trailing edge, and remained at 6.0 percent throughout the stator. Losses were assumed to increase linearly from leading-to-trailing edge for convenience.

Incidence to the rotor was originally set at 1.0 deg with respect to the suction surface. An inviscid time-dependent cascade plane analysis of several sections showed this to be approximately 4.0 percent deficient in flow. Rotor incidence was subsequently set at 2.0 deg relative to the suction surface. Stator incidence varied linearly from 5.0 deg at the hub to zero at the tip, relative to the camber line. Trailing edge deviation angle was predicted according to the NACA method described in [7], equations (269) and (271), using a shape correction factor of 1.0. Calculated rotor values were increased by 2.0 deg.

A rotor tip solidity of approximately 1.5 was chosen such that a weak oblique passage shock attached to the leading edge and resulting from the incidence angle to the pressure surface would intersect the suction surface at about 90 percent chord. This, plus the axial depth of the stage determined through the preliminary design, set the number of rotor blades at 20. The resultant hub solidity was approximately 3.0, with a nearly linear spanwise variation. A minimum stator solidity of 1.6 at the tip was chosen because of the relatively high turning (40 to 50 deg) and high average Mach number (0.7 to 1.0). The forward-swept leading edge at the hub produced a hub solidity of 2.8. The number of stator blades was set at 31 to satisfy the solidity requirements and to avoid resonant frequencies resulting from rotor/stator interaction. Axial spacing between blade rows was kept to an absolute minimum. The closest encounter occurs at the hub due to the swept stator leading edge, where the gap is about 8 percent of rotor hub chord. The gap reaches a maximum at the tip of 23 percent of rotor tip chord.

Since the aerodynamic objectives were viewed as very ambitious at the time, the rotor structure was designed to be minimally adequate so as not to compromise the aerodynamics. Rotor blade maximum thickness varied from 6.0 percent chord at the hub to 2.5 percent chord at the tip. The chordal location of maximum thickness varied from 56 percent chord at the hub to 70 percent chord at the tip to minimize leading edge wedge angles. This led to a predicted peak combined stress of 68,000 lbs/in.^{2} (4688 N/m^2) using 6A14V titanium. Rotor leading edge radius varied from 0.431 percent chord at the hub to 0.125 percent chord at the tip, corresponding to absolute values of 0.015 in. (0.38 mm) and 0.005 in., (0.13 mm), respectively. Trailing edge thickness from one-third trailing edge span outward was equal to leading edge thickness on the same streamline. However, trailing edge thickness inboard of that point was increased to a maximum at the hub two-thirds greater than at the leading edge to compensate for a high stress region. Maximum thickness was located at 50 percent chord in the stator and varied in magnitude from 4.0 percent chord at the hub to 6.0 percent chord at the tip. Stator leading and trailing edge radii were held constant at 0.006 in. (0.15 mm) across the span.

The final design point characteristics obtained were:

Rotor inlet hub/tip radius ratio	0.312
Mean rotor aspect ratio (avg. span/avg. chord)	1.320
Mean stator aspect ratio (avg. span/avg. chord)	1.255
Rotor mass averaged total pressure ratio	1.966
Stage mass averaged total pressure ratio	1.912
Rotor tip static pressure ratio	2.169
Rotor tip relative Mach number	1.658
Rotor isentropic efficiency	0.869
Stage isentropic efficiency	0.830

Full details of the design are presented in [8].

Apparatus and Procedure

Test Facility. The compressor was tested in the 2000-hp facility at Wright-Patterson Air Force Base. This facility was operating in an open-loop mode at the time, and is a conventional, electrically driven compressor test facility. Inlet air is well filtered and conditioned to a high degree of uniformity. An axisymmetric throttle is closely coupled downstream of the compressor. Estimated measurement uncertainty is as follows:

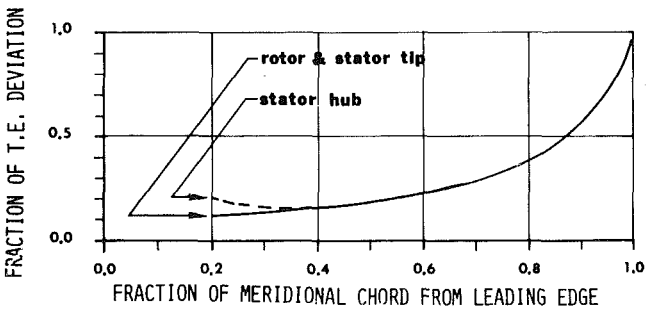

Fig. 3 Assumed within-blade deviation angles

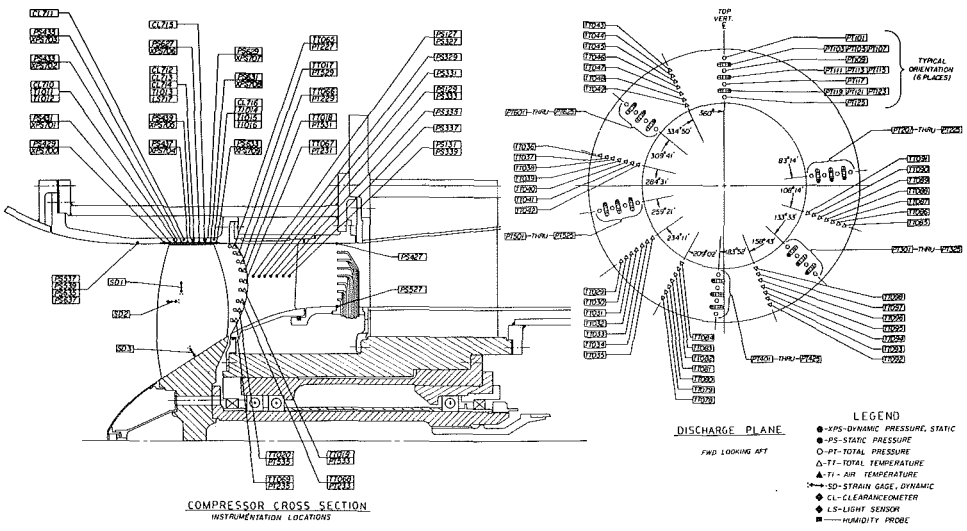

Fig. 4 Test vehicle instrumentation

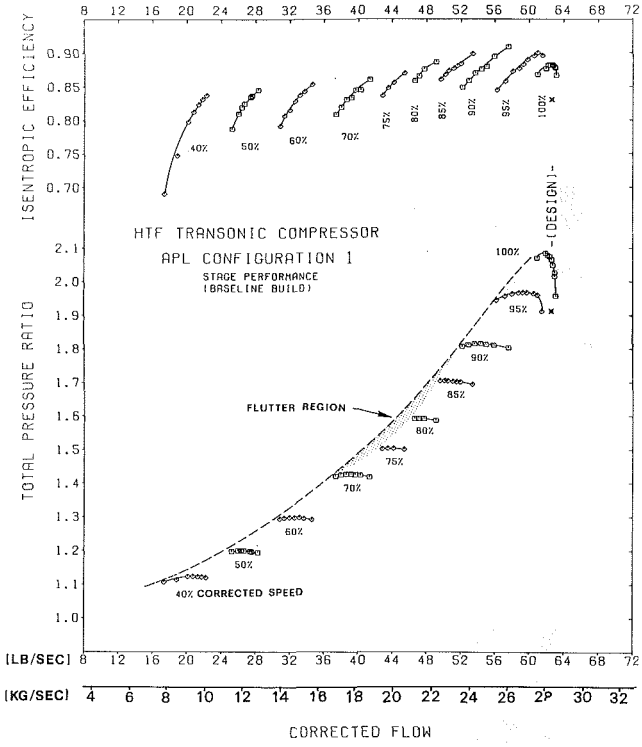

Fig. 5 Baseline compressor performance map

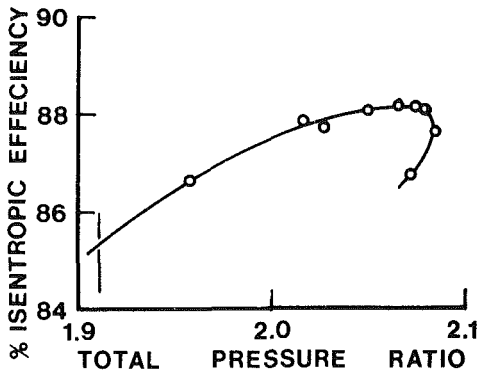

Fig. 6 Extrapolation to design point performance

Rotation speed, rpm	±30
Flow, percent	±1.0
Pressure, percent	±0.1
Temp, at 212°F (100°C) and below	±0.3°F (0.17°C)
at 346°F (175°C)	±1.0°F (0.55°C)

Compressor Test Vehicle. A cross section of the compressor test vehicle showing the type, quantity, and distribution of instrumentation is shown in Fig. 4. The exit plane instrumentation assumes a high degree of axial symmetry in the experiment. The 12 rakes, half pressure and half temperature, are indexed two and one-sixth times the angular spacing of the stator blades from one another. Thus each group of six rakes covers the equivalent of one blade passage in equal increments. The second, fourth, and sixth elements on each pressure rake were three-hole cobra configurations. All instrumentation were fixed so that one complete scan of all pressures and temperatures required less than 15 s.

Data Reduction. All data points used are the average of two consecutive complete scans of the instrumentation. The pressure ratio and efficiency numbers obtained for the compressor map are the result of complete radial equilibrium analysis using a streamline-curvature analysis comparable to the design process. For this purpose, however, the computing stations within the blade row illustrated in Fig. 2 were eliminated. All others remained. The data point having peak efficiency was evaluated in greater detail, incorporating the computing stations internal to the rotor. In this instance, within-rotor blockage and deviation angle were adjusted to match the experimental values of static pressure measured on the casing across the rotor tip. Although total temperature and total pressure were measured both at the stator leading edge and the exit plane, exit plane data were considered to be more reliable. For example, stator leading edge data could produce rotor hub efficiences several points in excess of 100 percent. Thus rotor performance was calculated using total temperatures, circumferentially mass averaged in the exit plane, and total pressures that were the peak values obtained from the circumferential distribution. The circumferentially mass-averaged total pressure was used for stage performance. Boundary layer and wake blockages were determined by iteratively adjusting the throughflow solution until calculated and measured casing static pressures coincided, interpolating blockage between planes where the static pressure was measured.

Baseline Performance

The map of stage performance from 40 to 100 percent corrected speed is shown in Fig. 5. Several points are worth noting. The choking flow could not be determined at any speed below 95 percent of design because of a facility throttle limitation. Thus one can only estimate the peak efficiences and breadth of the speed lines at 90 percent speed and below. At 75–85 percent speed, transonic stall flutter was experienced at the first bending frequency. At speeds above and below this, conventional stalls were experienced, although at 40 percent speed, stall was barely detectable. At that speed, a slight change in acoustic pitch was observed, but the compressor continued to operate stably and could be throttled to nearly zero flow. The change in pitch occurred when backflow commenced, and further throttling simply altered the ratio of the amount of flow that continued downstream to the amount of flow that recirculated very smoothly back into the inlet. This phenomenon was detected by inlet thermocouples, but was not evident by strain gage signals nor by high-frequency pressure measurements made over the rotor. The limitation in maximum throttle area also prevented a pressure ratio as low as the design value to be measured at design speed. Design point performance can best be assessed by examining Fig. 6, which plots efficiency versus pressure ratio at design speed. At design pressure ratio, maximum flow was achieved, which is about 0.8 percent in excess of design flow. This is within the measurement uncertainty, however. The efficiency at this point is estimated from Fig. 6 to be 0.854, or 2.4 points above design. Alternatively, at design flow, the pressure ratio is 2.065 versus the design value of 1.912, and the corresponding efficiency is 0.882, or 5.2 points above design. This is also the peak efficiency at design speed. The peak stage efficiency measured was 0.909, with a pressure ratio of 1.804 at 90 percent speed, although the true peak may be higher since peaks could not be determined at 90 percent speed and below. Full details concerning the test rig and data are presented in [9].

Compressor Modifications

Tip Clearance. The clearance between the rotor tip and the casing at design speed was predicted to be 0.016 in. (0.41 mm). This is equivalent to 0.415 percent of tip chord, or 0.324 percent of mean span. This was made deliberately tight initially in order to evaluate the sensitivity of the design to tip clearance. Clearance was progressively increased in two steps by grinding 0.010 in. (0.25 mm) from the tips of the rotor

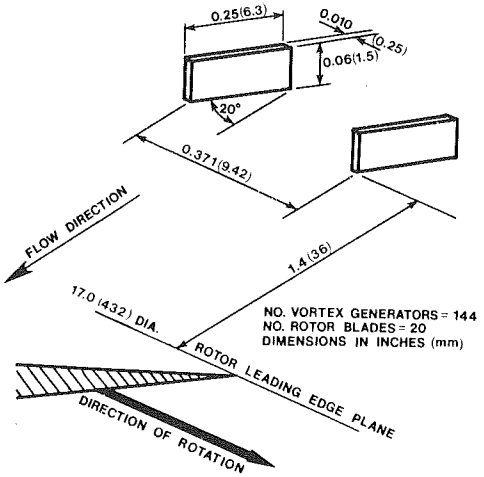

Fig. 7 Casing vortex generator configuration "A"

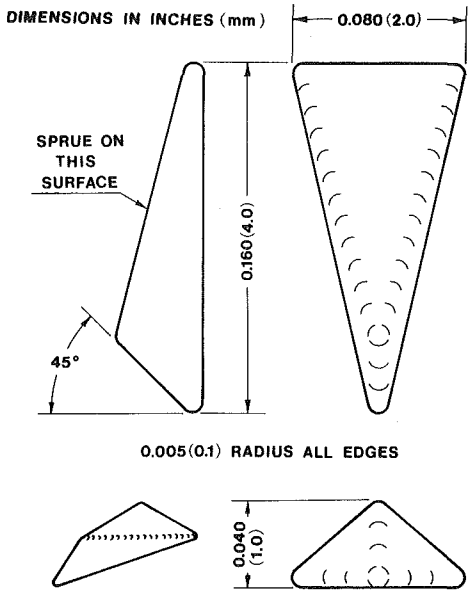

Fig. 8 Rotor vortex generator configuration

blades each time. The casing remained untouched. The resulting test matrix was:

	% Chord	% Span
Original clearance (config. 1)	0.415	0.324
First modification (config. 2)	0.675	0.524
Second modification (config. 3)	0.935	0.724

Casing Vortex Generators. Vortex generators installed on the outer casing of a compressor, just upstream of the rotor, were successful in improving the performance of a supersonic compressor, as described in [10]. Their purpose was to maintain sufficient energy in the casing boundary layer to discourage separation on the wall due to shock/boundary layer interaction or loading. The referenced supersonic compressor was not particularly efficient, and it was not difficult to improve upon its performance. The object of these experiments was to see if boundary layer control devices, specifically vortex generators, had any potential for further improvement of an already efficient compressor; also to evaluate several vortex generator configurations at different tip clearances to see if there was any optimization potential or apparent interaction between the two. Three configurations of vortex generator were evaluated, designated A, B, and C. Configuration A is pictured in Fig. 7. Configuration B consisted of half of the number of vortex generators, with a height double that of A; all other dimensions held constant.

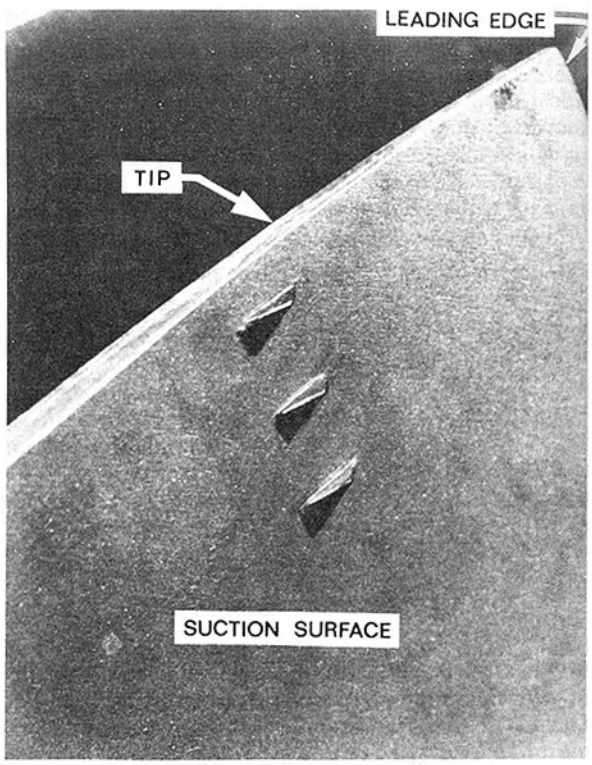

Fig. 9 Rotor vortex generator installation

Configuration C consisted of one-third of the number and triple the height with respect to A; all other dimensions held constant. The rationale applied to design of vortex generator Configuration A is described in both [10] and [11]. Configurations B and C held the ratio of vortex generator height to spacing constant, a key parameter, but deviated progressively from the initial design criteria in other respects. A potentially important detail is that the vortex generators were staggered in the same direction as the following rotor blades. Thus the direction of rotation of the vortices was such that, if the fluid in the vortices is assumed to obey gyroscopic laws of motion, its reaction to the circumferential pressure gradient would be to turn toward the casing.

Rotor Vortex Generators. Rotor mounted vortex generators in a small group near the tip were also found effective in improving the performance of a supersonic compressor in yet unpublished experiments. One of the last experiments with this transonic compressor consisted of installing such vortex generators on the rotor in the last build (i.e., with the third and largest tip clearance) to see what effect they might have, both with and without casing vortex generators, on a basically efficient compressor. The configuration of the vortex generator is illustrated in Fig. 8 and their installation is pictured in Fig. 9. For the rationale of their design, refer to [12]. A significant point is that they were aligned asymmetrically with respect to the relative local flow such that their upper surface was parallel to the streamline direction. Thus they were designed to produce one principal vortex each, corotating, as opposed to counterrotating pairs if symmetrically aligned. It was assumed that the fluid in the vortices will have less momentum in the relative flow direction than the free stream, thus will tend to be centrifuged outward. The direction of vortex rotation was chosen such that, if the vortices are again assumed to behave according to gryroscopic laws of motion, the reaction of the vortices will be to turn toward the suction surface rather than depart from the airfoil. The vortex generators were located roughly halfway between the rotor leading edge and the impingement line of a normal passage shock. They were pressure molded of glass-reinforced

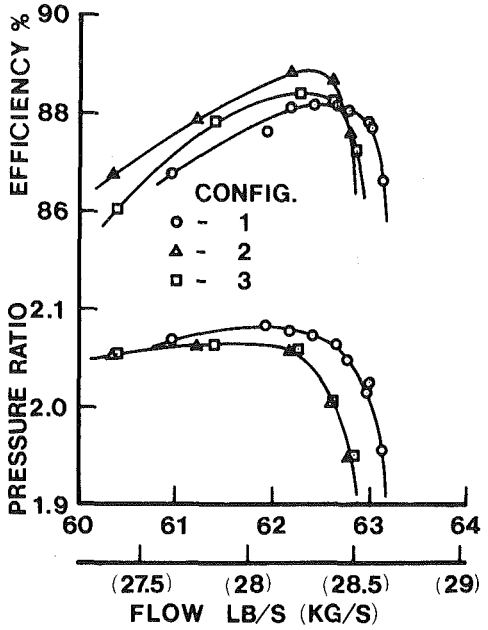

Fig. 10 Effect of rotor tip clearance changes at design speed

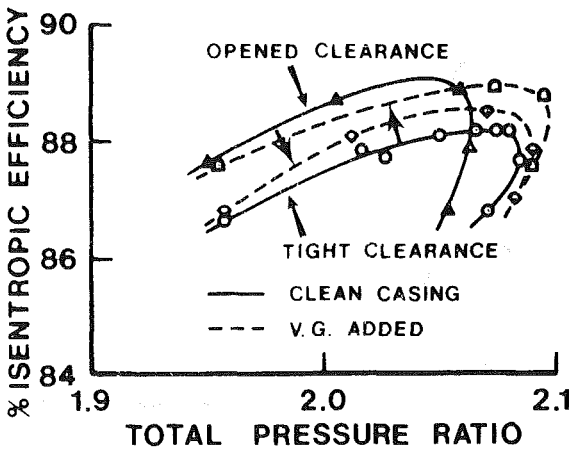

Fig. 11 Casing vortex generator interaction with rotor tip clearance at design speed

polyimide plastic and bonded to the rotor blades with an epoxy commonly used for attaching strain gages. In the course of this and other experiments, 300 of these vortex generators were installed and operated at angular velocities producing more than 100,000 g's acceleration without loss of a single one.

Results

Tip Clearance Changes. The effect of tip clearance on overall stage performance at design speed is illustrated in Fig. 10. The surprising result was discovery of an apparent optimum clearance. The intermediate value of clearance produced an increase in efficiency of about 0.7 point over the entire design speed operating range. This same level of improvement was observed at all speeds and tended to increase somewhat at low speeds; e.g., 50 percent speed. In the exit plane of the stage, the increase appeared to be relatively uniformly distributed. However, an examination of total pressure and temperatures measured at the stator leading edge showed a more localized improvement near the tip where it would be expected. The more uniform distribution in the exit plane was probably the result of mixing caused by secondary flow. The first clearance increase caused a reduction in choking flow of about 0.5 percent at design speed. The second clearance increase produced no further change, however. Complete performance data for the two increased clearance tests are presented in [13] and [14].

Casing Vortex Generators. In general, vortex generator Configurations A and B performed very similarly. Configuration C was ineffective. Configuration A was slightly more efficient with the tight clearance of rotor Configuration 1. Configuration B proved slightly more efficient with rotor Configurations 2 and 3. Another general observation which can be made is that the casing vortex generators had virtually no effect on the stall line, as viewed on a conventional compressor map, in spite of the fact that they tended to produce a higher pressure rise at each corrected speed. The stall points just shifted slightly laterally on the original stall line. The effect of the best vortex generators, in combination with rotor tip clearance changes, is illustrated in Fig. 11 on a plot of efficiency versus pressure ratio, comparing Configurations 1 and 2 at 100 percent speed. (The performance of Configuration 3 did not differ significantly from Configuration 2.) It will be observed that Configuration 1, having the original clearance, was improved in efficiency about 0.6 point and produced a higher pressure rise with vortex generators added. Configuration 2, on the other hand, was degraded in efficiency about 0.7 point with the addition of vortex generators, although it too achieved slightly higher pressure rise. More detailed data on these tests are provided in [11] and [15–21].

Rotor Vortex Generators. The influence of vortex generators installed on the rotor of Configuration 3, both with a clean casing and in combination with casing vortex generators, is illustrated in Fig. 12. Rotor-mounted vortex generators did produce an increase in stall margin of 3 percent at design speed, raising it from 11 percent to 14 percent. Adding casing vortex generators produced another 1 percent increase. In the range of 90 to 100 percent corrected speed, shown in Fig. 12, rotor vortex generators tended to increase the efficiency over most of the test range. A more significant consideration is probably the efficiency on an engine operating line. A hypothetical operating line is shown in Fig. 12, passing through the design point. Pressure ratios were taken from the intersection of the estimated operating line, with the experimental speed lines extrapolated as required. The efficiency at 100 percent speed was estimated by a slight extrapolation of a crossplot of efficiency versus pressure ratio. Through this process, the following operating line isentropic efficiences were estimated.

Percent corrected design speed	90	95	100
Configuration 3 (clean)	91.2	90.7	86.4
Configuration 3.1 (rotor V.G.'s)	92.0	90.5	85.9
Configuration 3.1B (rotor casing V.G.'s)	91.8	90.0	85.5

Although the accuracy of such extrapolation is admittedly arguable, the trends shown are believed to be representative. At 100 percent speed, rotor vortex generators incur a penalty of about 0.5 point in efficiency, whereas at 90 percent speed, a benefit of about 0.8 point appears likely. The addition of casing vortex generators penalizes the efficiency an additional 0.4 or 0.5 points at 100 percent and 95 percent speed, diminishing to 0.2 point at 90 percent speed. More detailed data on Configurations 3.1 and 3.1B are presented in [12–22].

Conclusions

Compressor Design. The higher-than-expected efficiency achieved with this stage, in combination with meeting all other overall design goals, is strong evidence in support of the more critical assumptions made for the design and some of the unusual features incorporated. For example, the high degree of sweep incorporated in the stator leading edge at the

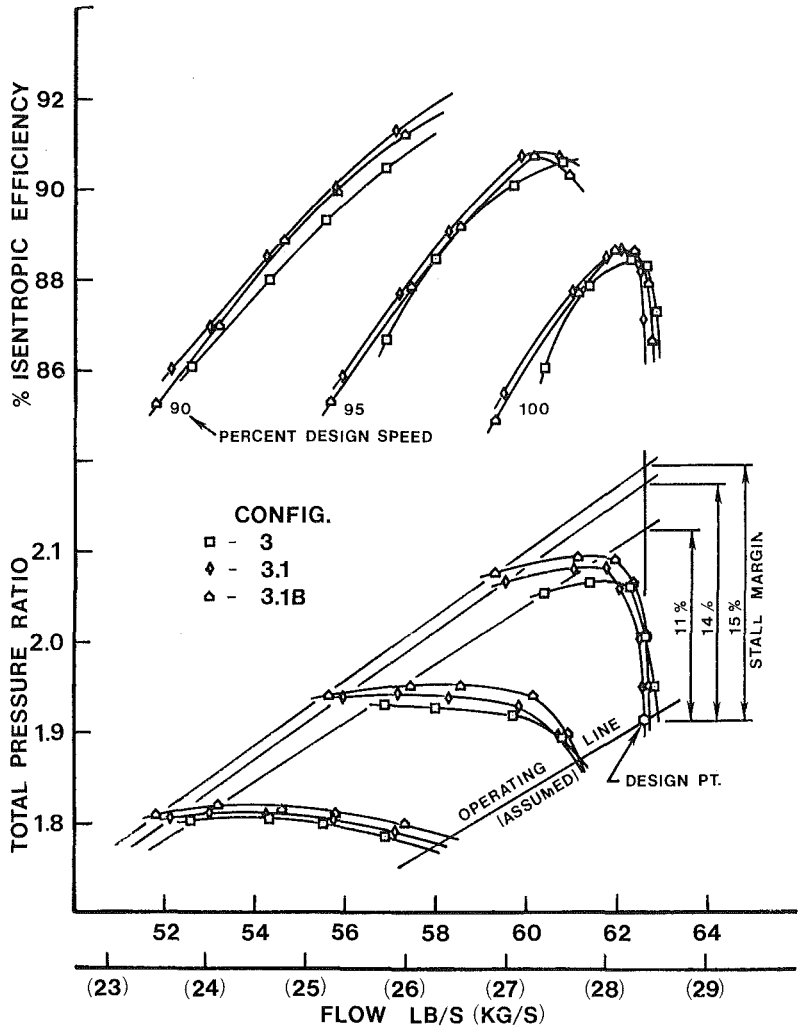

Fig. 12 Influence of rotor vortex generators

hub appeared to entirely eliminate the shock losses which otherwise might be appreciable in this region. The optimization criteria based upon the meridional static pressure gradient appeared reasonably successful for both subsonic and supersonic sections. Additional evidence to support this is shown in Figs. 13 and 14. Figure 13, extracted from [23], illustrates the static pressure distribution around a blade section, near the rotor tip, at design-point conditions when tested in a cascade wind tunnel. The relative inlet Mach number is about 1.61. On the suction surface, the static pressure remains nearly constant up to the shock impingement point. Compression waves from the negatively cambered region appear to compensate for the expansion around the leading edge, leading to a very slight precompression. After shock impingement, the pressure rises smoothly to the trailing edge. Figure 14, extracted from [9], shows the static pressure distribution measured on a midspan stream surface from the stator as installed in the compressor during operation at design speed near best efficiency. The inlet Mach number is about 0.83 at that radius. The suction surface expansion appears moderate and diffusion is smooth, tapering off as the boundary layer grows. The Mach number corresponding to the lowest pressure measured on the suction surface is about 0.94, although it is likely to have peaked between that point and the leading edge. The overall conclusion drawn relative to the airfoil optimization technique is that it is indeed a satisfactory approach applicable to airfoils operating from high subsonic through supersonic Mach numbers. More sophisticated methods using cascade plane analyses are feasible, especially at subsonic Mach numbers, but the

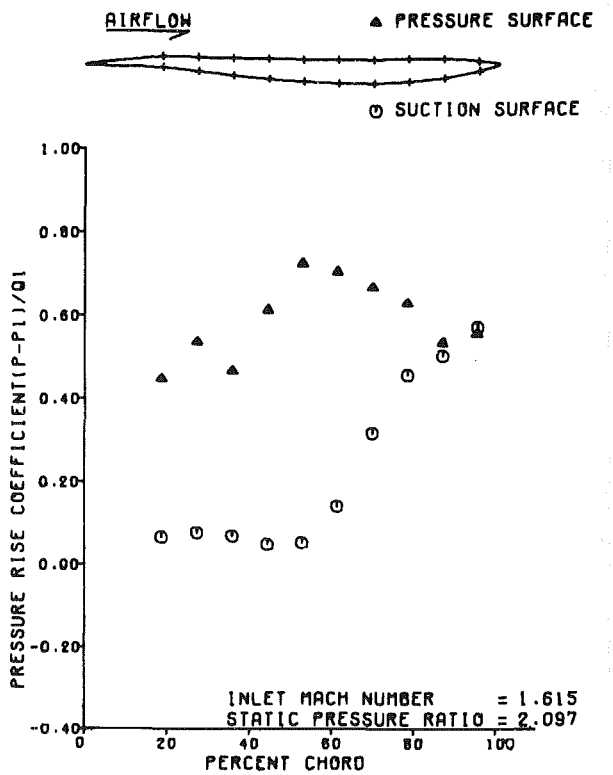

Fig. 13 Cascade pressure distribution of rotor tip section

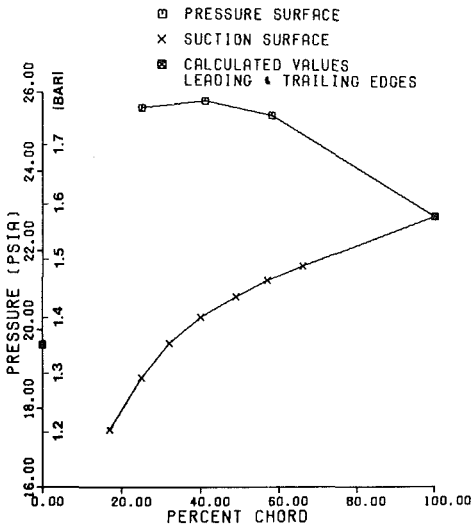

Fig. 14 Stator midspan pressure distribution at design speed and peak efficiency

method employed here, relying strictly on axisymmetric or circumferential average computations, can also produce good results. However, in combination with the optimization, one should still do an inviscid cascade-plane analysis of one or more sections operating supersonically to confirm that the incidence is correctly set to pass the flow. No firm conclusion can yet be drawn concering the unusual airfoil fillet geometry, because the compressor was not tested with more conventional fillets. However, the fillets used showed no signs of hurting the performance. Whether they helped it or not is an open question.

A further general conclusion reached is that it has proven feasible to obtain high efficiency at higher values of flow, Mach number, and loading than have heretofore been common. However, the case described does not yet represent a practical compressor for most applications because of the aeroelastic instability experienced on the stall line at part speed. Also, the first bending frequency of the rotor blades coincides with a two-per-rev excitation high within the operating range, whereas it is usually desired to place this frequency substantially above the operating range. Thus it remains to be seen what penalty, if any, is associated with the ruggedizing required for a practical application. The principal modifications required would be more rotor airfoil thickness approaching the root and somewhat thicker leading and trailing edges. If the entire design procedure was repeated with these changes, there is no reason to believe that the penalty would be excessive.

Tip Clearance. This appears to be one of those rare instances where an optimum rotor tip clearance was observed within a range of clearances feasible for operation. As pointed out by Peacock [24], "there is some evidence among the compressor and compressor cascade data that an optimum gap exists when the opposing effects of secondary flows and tip leakage with rotor/wall relative movement tend to balance." However, the documented cases are few and do not encompass the Mach number regime of this compressor. It is tentatively concluded that the optimum may occur in this compressor when the tip leakage vortex is just large enough to help stabilize the flow. At larger values, there will be excess unproductive leakage, and at smaller values, there may be insufficient energy in the vortex to produce any useful effects. The fact that an optimum was observed here, and otherwise rarely, may be a result of the severe operating conditions imposed upon the tip. At lighter loading and lower Mach numbers, the optimum may be much closer to zero.

Casing Vortex Generators. The use of vortex generators on the casing did not appear to be of significant benefit to this compressor. At the smallest rotor tip clearance, they did produce some advantage, which lends some credance to the conclusion reached above concerning the tip leakage vortex. However, it is far more attractive to run the larger clearance without vortex generators, so this result is of little practical interest. Although it was originally speculated that casing vortex generators might improve stall margin, this proved not to be the case with this compressor.

Rotor Vortex Generators. A few vortex generators located on the rotor near the tip did prove to offer a modest stall margin improvement, as well as a slight efficiency improvement, at speeds below 95 percent of design. At design speeed, the efficiency penalty was limited to 0.5 point on the operating line, which should be an acceptable order of magnitude in relation to the 3 percent added stall margin. On this basis, it is concluded that there may be practical applications for rotor mounted vortex generators. They could be manufactured integrally with blades in production quantities. Alternatively, the material and method of application used for these experiments could probably survive sustained service since they would be unlikley to be subject to much erosion or foreign object damage in the location in which they were used.

Acknowledgments

The type of effort described in this paper is, of necessity, a team effort. The following were major contributors to one or more facets of the overall program: William A. Buzzell, Robert D. DeRose, George R. Frost, Daniel J. Gurecki, Richard M. Hearsey, C. Herbert Law, Efren C. Strain, and Robert P. Wirrig.

References

1 Creveling, H. F., and Carmody, R. H., "Axial Flow Compressor Design Computer Programs Incorporating Full Radial Equilibrium, Part II—Radial Distribution of Total Pressure and Flow Path or Axial Velocity Ratio Specified (Program III)," NASA-CR-54531, Department of Commerce Clearinghouse N68-38057, June 1968.

2 Lieblein, S., Schwenk, F. C., and Broderick, F. L., "Diffusion Factor for Estimating Losses and Limiting Blade Loadings in Axial Flow Compressor Blade Elements," NACA RME53D01, 1953.

3 Miller, G. R., Lewis, G. W., and Hartmann, M. J., "Shock Losses in Transonic Compressor Blade Rows," ASME Transactions, Vol. 83, No. 3, July 1961, pp. 235–242.

4 Hearsey, R. M., "A Revised Computer Program for Axial Compressor Design," ARL-TR-75-0001, Vols. I & II, A009273 and A009157, Aerospace Research Laboratories, Wright-Patterson AFB, Ohio, Jan. 1975.

5 Frost, G. R., and Wennerstrom, A. J., "The Design of Axial Compressor Airfoils Using Arbitrary Camber Lines," ARL-TR-73-0107, AD756165, Aerospace Research Laboratories, Wright-Patterson AFB, Ohio, July 1973.

6 Jansen, W., "The Application of End-Wall Boundary Layer Effects in the Performance Analysis of Axial Compressors," ASME Paper No. 67-WA/GT-11, 1967.

7 Johnson, I. A., Bullock, R. O., et al., "Aerodynamic Design of Axial Flow Compressors," NASA SP-36, 1965.

8 Wennerstrom, A. J., and Frost, G. R., "Design of a 1500 ft/sec Transonic, High-Through-Flow, Single-Stage Axial-Flow Compressor with Low Hub/Tip Ratio," AFAPL-TR-76-59, ADB016386, Aero Propulsion Laboratory, Wright-Patterson AFB, Ohio, Oct. 1976.

9 Wennerstrom, A. J., et al., "Investigation of a 1500 ft/sec, Transonic, High-Through-Flow, Single-Stage Axial-Flow Compressor with Low Hub/Tip Ratio," AFAPL-TR-76-92, ADB016506, Aero Propulsion Laboratory, Wright-Patterson AFB, Ohio, Oct. 1976.

10 Law, C. H., Wennerstrom, A. J., and Buzzell, W. B., "The Use of Vortex Generators as Inexpensive Compressor Casing Treatment," SAE Paper No. 760925. Society of Automotive Engineers, 1976.

11 Wennerstrom, A. J., et al., "Investigation of a High-Through-Flow, Single-Stage Axial-Flow, Compressor with Casing Vortex Configuration 'A' (Configuration 1A)," AFWAL-TR-80-2042. ADB050857, Air Force Wright Aeronautical Laboratories, Wright-Patterson AFB, Ohio, June 1980.

12 De Rose, R. D., et al., "Investigation of a High-Through-Flow, Single Stage Axial-Flow Compressor with Tip Clearance Increased 0.020 Inch and Rotor Tip Vortex Generators (Configuration 3.1)," AFWAL-TR-82-2071, ADB068098, Air Force Wright Aeronautical Laboratories, Wright-Patterson AFB, Ohio, Sept. 1982.

13 Law, C. H., et al, "Investigation of a High-Through-Flow, Single-Stage Axial-Flow Compressor with Tip Clearance Increased 0.010 Inch (Con-

figuration 2),'' AFWAL-TR-80-2079, ADB059621, Air Force Wright Aeronautical Laboratories, Wright-Patterson AFB, Ohio, Apr. 1981.

14 Law, C. H., et al., ''Investigation of a High-Through-Flow, Single-Stage Axial-Flow Compressor with Tip-Clearance Increased 0.020 Inch (Configuration 3),'' AFWAL-TR-81-2029, ADB059618, Air Force Wright Aeronautical Laboratories, Wright-Patterson AFB, Ohio, Apr. 1981.

15 Wennerstrom, A. J., et al., ''Investigation of a High-Through-Flow, Single-Stage Axial-Flow Compressor with Casing Vortex Generator Configuration 'B' (Configuration 1B),'' AFWAL-TR-80-2054, ADB050858, Air Force Wright Aeronautical Laboratories, Wright-Patterson AFB, Ohio, June 1980.

16 Law, C. H., et al., ''Investigation of a High-Through-Flow, Single-Stage Axial-Flow Compressor with Tip Clearance Increased 0.010 Inch and Casing Vortex Generator Configuration 'A' (Configuration 2A),'' AFWAL-TR-80-2080, ADB059617, Air Force Wright Aeronautical Laboratories, Wright-Patterson AFB, Ohio, Apr. 1981.

17 Law, C. H., et al., ''Investigation of a High-Through-Flow, Single-Stage Axial-Flow Compressor with Tip Clearance Increased 0.010 Inch and Casing Vortex Generator Configuration 'B' (Configuration 2B),'' AFWAL-TR-81-2027, ADB059690, Air Force Wright Aeronautical Laboratories, Wright-Patterson AFB, Ohio, Apr. 1981.

18 Law, C. H., et al., ''Investigation of a High-Through-Flow, Single-Stage Axial-Flow Compressor with Tip Clearance Increased 0.010 Inch and Casing Vortex Generator Configuration 'C' (Configuration 2C),'' AFWAL-TR-81-2024, ADB059620, Air Force Wright Aeronautical Laboratories, Wright-Patterson AFB, Ohio, Apr. 1981.

19 Law, C. H., et al., ''Investigation of a High-Through-Flow, Single-Stage Axial-Flow Compressor with Tip Clearance Increased 0.020 Inch and Casing Vortex Generator Configuration 'A' (Configuration 3A),'' AFWAL-TR-81-2026, ADB059689, Air Force Wright Aeronautical Laboratories, Wright-Patterson AFB, Ohio, Apr. 1981.

20 Law, C. H., et al., ''Investigation of a High-Through-Flow, Single-Stage Axial-Flow Compressor with Tip Clearance Increased 0.020 Inch and Casing Vortex Generator Configuration 'B' (Configuration 3B),'' AFWAL-TR-81-2080, ADB059642, Air Force Wright Aeronautical Laboratories, Wright-Patterson AFB, Ohio, Apr. 1981.

21 Law, C. H., et al., ''Investigation of a High-Through-Flow, Single-Stage Axial-Flow Compressor with Tip Clearance Increased 0.020 Inch and Casing Vortex Generator Configuration 'C' (Configuration 3C),'' AFWAL-TR-81-2025, ADB060879, Air Force Wright Aeronautical Laboratories, Wright-Patterson AFB, Ohio, Apr. 1981.

22 DeRose, R. D., et al., ''Investigation of a High-Through-Flow, Single-Stage Axial-Flow Compressor with Tip Clearance Increased 0.020 Inch, Rotor Tip Vortex Generators, and Casing Vortex Generator Configuration 'B' (Configuration 3.1B),'' AFWAL-TR-82-2070, ADB068306, Air Force Wright Aeronautical Laboratories, Wright-Patterson AFB, Ohio, Aug. 1981.

23 Fleeter, S. et al., ''Experimental Investigation of a Supersonic Compressor Cascade,'' ARL-TR-75-0208, A014395, Aerospace Research Laboratories, Wright-Patterson AFB, Ohio, June 1975.

24 Peacock, R. E., ''A Review of Turbomachinery Tip Gap Effects, Part 2: Rotating Machinery,'' *International Journal of Heat and Fluid Flow*, Vol. 4, No. 1, Mar. 1983, pp. 3–16.

Three-Dimensional Structure and Decay of Vortices Behind an Axial Flow Rotating Blade Row

M. Inoue

M. Kuroumaru

Faculty of Engineering,
Kyushu University,
Fukuoka, Japan

Detailed measurements were made of the three-dimensional turbulent flow field behind an axial-flow rotating blade row. The flow was surveyed at 15 radial locations and 70 circumferential sampling points in five measuring planes parallel to the trailing edge of the rotor. Statistically accurate mean velocities as well as turbulence stresses were obtained from numerous hot-wire signals, more than 12,000 for each sampling point. Vorticities were derived by the numerical differentiation of these data. The three-dimensional structure of various kinds of vortices generated through the rotor, such as a leakage vortex, trailing vortices, scraping vortices, a horseshoe vortex, etc. were elucidated quantitatively by use of the local streamwise, lateral and normal components of vorticity. The decay characteristics of these vortices were investigated in relation to the distribution of the turbulent stresses.

Introduction

A study of the flow field behind an axial flow rotating blade row is very important since that flow contributes to the aerodynamic losses, noise production, and vibration characteristics of an axial compressor. However, this flow is exceedingly complicated due to a highly three-dimensional wake affected by centrifugal and Coriolis forces, trailing vortices shed from the blade trailing edge, horseshoe and scraping vortices caused by interaction of a blade and the annulus wall boundary layer, and tip leakage flow.

Watanabe et al. [1] and Whitfield et al. [2] took the lead in presentation of the complete map of the three-dimensional flow pattern behind a rotor by using the waveform averaging of hot-wire anemometer outputs. This measuring technique has been further developed at Cambridge University [3, 4], The Pennsylvania State University [5, 6], Vrije Universiteit Brussel [7, 8], Iowa State University [9], etc. A large number of experimental studies have been undertaken to gain some insight into the physical nature of the flow field. Most of these investigations have been concerned with the rotor wake characteristics [10–15], and more recently, have been concerned with the interaction region of the casing wall boundary layer, the rotor wake, and the tip leakage flow [16–20]. The behavior of flow fields inside and behind an axial rotor has been examined by Dring et al. [21].

However, no attempt has been made to investigate the vorticity of the entire flow field. Since various vortices are involved, the quantitative expression of the three-dimensional vortex is essential to make these complex flow phenomena clearer.

In this research, accurate measurements were made of three components of the mean flow velocity as well as six components of the turbulence stress behind an axial rotating blade row. A newly devised periodic multisampling technique with a slanted single hot-wire [22] was used. The vorticity vectors were estimated by the numerical differentiation of the mean velocity components. The expression of the flow field by streamwise, lateral, and normal components of the vorticity allowed quantitative description of the three-dimensional structure of the various vortices. The decay of typical vortices was investigated in relation to the turbulence stresses.

Experimental Equipment

A 380-mm-dia, single-stage axial fan with hub tip ratio of 0.6 was used for the experiments reported herein. A total pressure rise coefficient ($\Delta P/(1/2)\rho u_t^2$) of 0.252 at the design flow rate coefficient ($\bar{c}_z/u_t$) of 0.345 was obtained. The rotor consists of 8 blades with a tip diameter of 378 mm (tip clearance: 1 mm) and a hub diameter of 228 mm. The rotor blades are of NACA 65 series compressor blade section designed for free vortex operation with an axial inlet flow condition. The rotor row is followed by an 11-blade row of 140-mm chord stator blades of circular-arc section with maximum thickness of 3 mm. The blade row geometry and operating characteristics at representative sections are given in Table 1. The overall performance of the fan almost satisfied the design condition. An axisymmetric flow condition was confirmed by survey of a five-hole cobra probe. Figure 1(*a*) shows distributions of the inlet axial velocity and the axial and tangential components of inlet vorticity at the design flow rate. In this study, changes in this vorticity through the rotating blade row were investigated by the following measurement.

Contributed by the Gas Turbine Division and presented at the 1983 Tokyo International Gas Turbine Congress, Tokyo, Japan, October 24–28, 1983. Manuscript received by the Gas Turbine Division July 6, 1983. Paper No. 83-GTJ-21.

Table 1 Geometry and operating characteristics of the rotating blade row

	root	mid-span	tip
radius	114 mm	151.5 mm	189 mm
solidity	1.01	0.69	0.50
stagger	50.1 deg	60.4 deg	67.0 deg
camber (c_{l_0}*)	0.89	0.59	0.38
Inlet flow angle**	60.2 deg	66.7 deg	70.9 deg
Exit flow angle**	46.2 deg	60.8 deg	67.9 deg

* isolated airfoil lift coefficient of NACA 65 profile camber line at zero angle of attack in a potential flow
** angle between relative flow direction and axial direction

The measurements of the flow field behind the rotor at the design flow condition were made by a constant-temperature, hot-wire anemometer and a periodic multisampling and averaging technique with an on-line microcomputer. The hot-wire probe survey was carried out at the five measuring cross sections parallel to the trailing edge plane of the rotor as shown in Fig. 1(*b*). At each measuring cross section, the data acquisition was done for 15 radial locations and 70 circumferential sampling points. The circumferential spacing between blades corresponds to 62.5 sampling points.

The sensor is a slanted single hot wire of 5-μm dia, 1-mm effective length and 45 deg slanting angle. The probe actuator involved two stepping motors, one to rotate the probe about its axis and the other to traverse it axially as instructed by a microcomputer. The hot wire was calibrated before and after every survey at a measuring cross section, and the experiment was repeated if a considerable change in the calibration curve occurred.

The three-dimensional periodic and turbulent flow pattern phase locked to the rotor was obtained as follows: at each radial location, 12 positions of the hot-wire sensor were set by rotating the probe axis. At each sensor positions, the hot-wire signals for the 70 circumferential sampling points were acquired every rotor revolution for 1024 revs. The data acquisition was done by an A/D converter as instructed by the scanning pulses corresponding to the correct locations of the sampling point. The sum of the anemometer outputs and the sum of the squares were performed by the on-line computer for each sampling point during 1024 revolutions of the rotor, to yield the ensenble average and variance of the outputs. A set of 12 average values and 12 variances corresponding to the sensor positions were used to determine three components of the mean velocity and six components of the turbulence stress from the equation of hot-wire calibration curve by the least mean squares method. Further details of the measuring technique are given in [22].

Using this technique, it was possible to save considerable measuring time as well as calibrating time, thus preventing serious change in the hot-wire outputs owing to wire contamination. As the velocity and the turbulence stress are obtained from 12,288 (= 12 × 1024) signals, they are accurate in the statistical sense. However, inevitable scattering error of the turbulence stress occurs by ±10 to 20 percent of the maximum magnitude, since it is evaluated from the variance of the anemometer outputs. This fact was checked up by comparing the experimental and the theoretical values in the turbulent free jet.

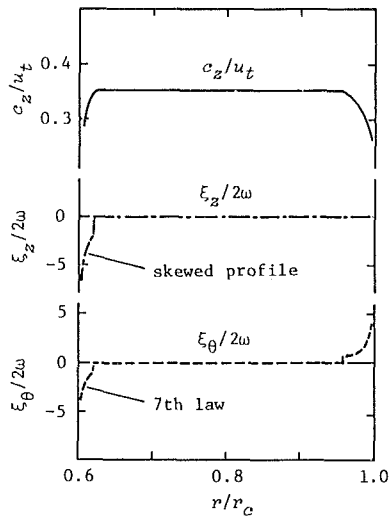

Fig. 1(*a*) Inlet flow condition of the rotating blade row

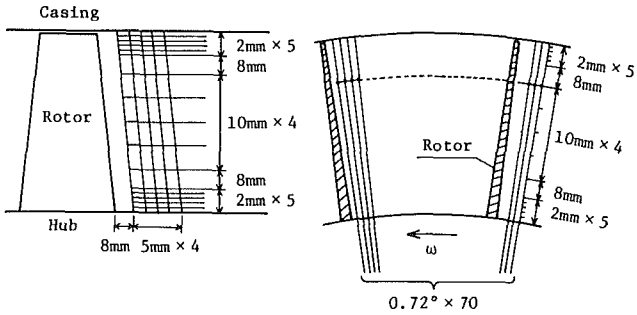

Fig. 1(*b*) Illustrations of measuring planes, measuring radial locations and sampling

Experimental Results

Average Flow Field. As typical examples of the experimental results obtained by the measuring technique described above, Figs. 2(*a*) and (*b*) show the pitchwise distributions of ensemble-average axial, peripheral, and radial velocity components, c_z, c_θ, and c_r, near the hub and the casing at $z/l_m = 0.098$ (where z equals axial distance from trailing edge of rotor and l_m equals blade chord length at midspan). All of the ensemble average velocity components are normalized by the rotor tip speed u_t. The numbers of the abscissa correspond to the relative sampling points, and the

Nomenclature

c = ensemble average absolute velocity
l_m = blade chord length at midspan
ΔP = total pressure rise
r = radius, or radial coordinate
s,τ,n = local streamwise, lateral, and normal coordinate
u_t = peripheral speed of the rotor blade tip
w = mean relative velocity
z = axial distance from the trailing edge of rotor, or axial coordinate
β = yaw angle of the relative flow
γ = pitch angle
ζ_D = kinetic energy defect of the relative flow
θ = peripheral coordinate
ξ = vorticity
ρ = density
ω = angular velocity of the rotor blade

Subscript

s,τ,n = components in s, τ, n-direction
z,θ,r = components in z, θ, r-direction
= fluctuating velocity component

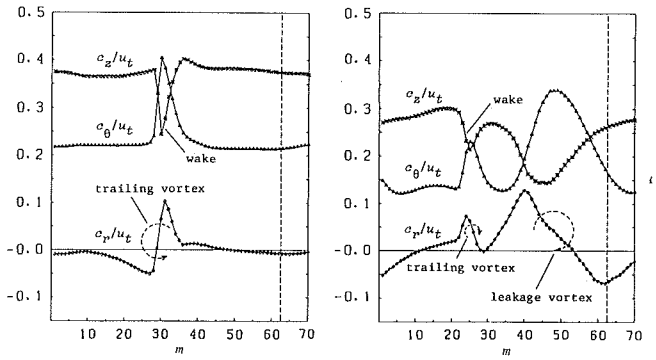

(a) near the hub (r/r_c = 0.642) (b) near the casing (r/r_c = 0.968)

Fig. 2 Distribution of ensemble average velocity components

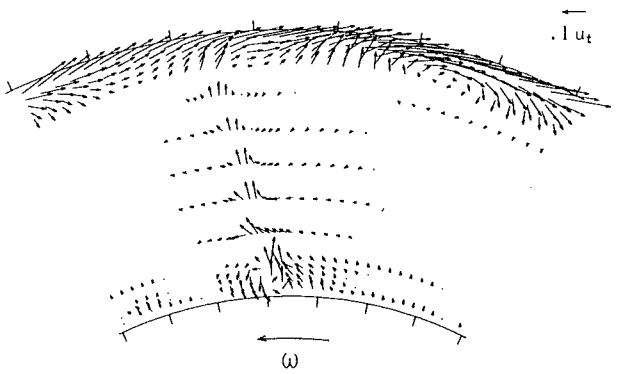

Fig. 3 Secondary flow map

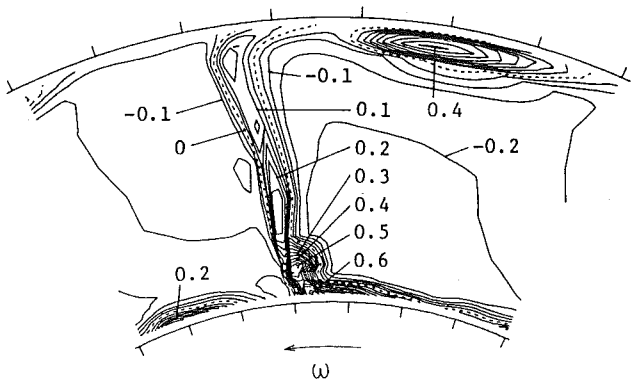

Fig. 4 Contour map of kinetic energy defect

distance from the ordinate and a vertical broken line corresponds to the length of blade spacing. In spite of considerably high turbulence level (see Fig. 12), the measured velocity changes smoothly, since it was obtained from 12,288 signals. The region of sudden decrease in axial velocity indicates the blade wake, of which the left side corresponds to the pressure side and the other the suction side. The positive and negative radial velocities inside the wake near the hub (at r/r_c = 0.642, where r_c equals casing radius) are mainly due to a trailing shed vortex sheet resulting from the interaction of the blade and the hub wall boundary layer. Higher magnitude of the radial velocity on the suction side may show existence of corner stall where centrifugal force acts on fluid more strongly [21]. Inside the wake near the blade tip (at r/r_c = 0.968), a small trailing shed vortex can also be recognized. On the right side of the wake, a large depression of the axial velocity appears where a large vortex can be noticed from the radial velocity distribution. This is the leakage vortex due to rolling-up of tip leakage flow.

Such flow phenomena as described above are more clearly seen by drawing maps on the measuring plane. Figure 3 is the map of secondary flow which is defined by a velocity component perpendicular to the design relative flow direction. The short radial segments on the hub and casing boundaries are drawn every tenth sampling point (corresponding to θ = 7.2 deg). The radial flow in the wake, the trailing vortex near the hub and the rolling-up of leakage flow near the casing can be observed in this map with a single glance. Figure 4 shows the contour map of kinetic energy defect defined by

$$\zeta_D = (w^2 - w^{*2})/w^{*2}$$

where w and w^* denote the measured and design relative flow velocity, respectively. Negative values of ζ_D are due to the displacement effect of wake and boundary layer flows as well as due to the large velocity defect in the leakage vortex. In the tip leakage flow and at the corner between the hub wall and the suction side of wake, the kinetic energy defect becomes nearly twice as large as the value in the midspan wake. The increase of ζ_D in the latter region may be caused by accumulation of the boundary layer fluid resulting from the secondary flow inside the rotor. This accumulation appears to hasten the corner stall. On the left side of the wake near the hub wall, a depression region of kinetic energy can be recognized. This region will be discussed in terms of vorticity in the following section.

Representation of the Flow Field by Vorticity. Similar physical descriptions of the foregoing interpretation of the average flow field have been obtained by other investigators. However, a quantitative expression of the three-dimensional structure of the flow field has not been successful as yet. A new trial employed in this research is to represent the flow field by vorticity on the basis of the local relative streamwise direction.

Since the smooth distribution of the average velocity has been obtained by the statistically accurate method, the axial, peripheral, and radial components of the vorticity can be evaulated by the numerical differentiation of the following equations.

$$\xi_z = (1/r)\,\partial(rc_\theta)/\partial r - (1/r)\,\partial c_r/\partial\theta$$

$$\xi_\theta = \partial c_r/\partial z - \partial c_z/\partial r$$

$$\xi_r = (1/r)\,\partial c_z/\partial\theta - \partial c_\theta/\partial z$$

The resultant vorticity vector is split by the streamwise, lateral, and normal components, ξ_s, ξ_τ, and ξ_n, which are determined locally by the following definition of the coordinates:

s = direction of the relative streamline
τ = perpendicular to the streamline on the local stream surface which is obtained by revolving the streamline about the rotating axis
n = normal to the local stream surface

Namely, (ξ_z, ξ_θ, ξ_r) is transformed into (ξ_s, ξ_τ, ξ_n) by the relation of

$$\begin{pmatrix} \xi_s \\ \xi_\tau \\ \xi_n \end{pmatrix} = \begin{pmatrix} \cos\beta\cos\gamma, & -\sin\beta, & \cos\beta\sin\gamma \\ \sin\beta\cos\gamma, & \cos\beta, & \sin\beta\sin\gamma \\ -\sin\gamma, & 0, & \cos\gamma \end{pmatrix} \begin{pmatrix} \xi_z \\ \xi_\theta \\ \xi_r \end{pmatrix}$$

where β is the local yaw angle defined by $\cos^{-1}(\sqrt{w_z^2 + w_r^2}/w)$, and γ is the local pitch angle defined by $\tan^{-1}(w_r/w_z)$. As it is expected that ξ_s, ξ_τ, and ξ_n become dominant in the secondary vortex region, in the annulus wall boundary layers and inside the blade wake, respectively, the nature of the local flow field can be described quantitatively by drawing the maps in terms of these vorticity components.

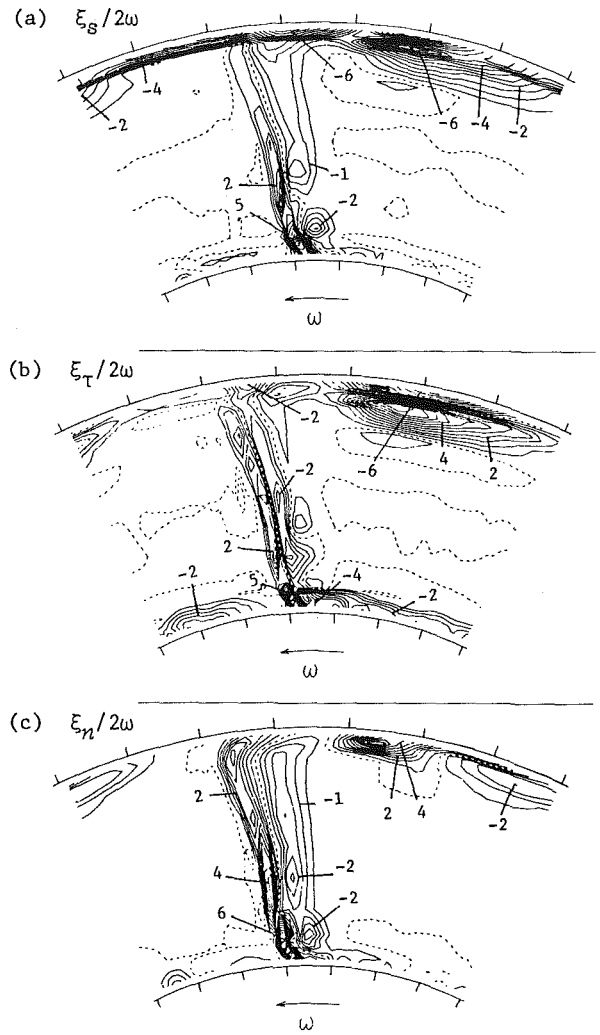

Fig. 5 Ensemble average vorticity distribution just behind the rotor

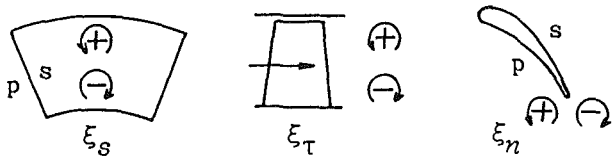

Fig. 6 Illustration of sign of vorticity

Figures 5(*a–c*) involve the absolute vorticity map just behind the rotor ($z/l_m = 0.098$). The vorticity components are normalized by twice the angular velocity of the rotor, 2ω. The interval between two adjacent contour lines corresponds to 0.5 of the dimensionless value. The dotted lines indicate zero vorticity and the relation of the sign (positive or negative) is illustrated in Fig. 6.

Inside the blade wake, the contour line of $\xi_n = 0$ is regarded as the wake center. It is bent near the tip region toward the counterrotating direction due to the skewed boundary layer on the casing wall. On the pressure side, the magnitudes of ξ_n and ξ_s, which correspond to the gradients of velocity defect and radial velocity in the wake, respectively, are much larger than those on the suction side. The considerable magnitude of ξ_τ is caused by three-dimensional skewing of the wake.

In the leakage vortex, the magnitude of ξ_s becomes remarkably high. Because of the depression of relative velocity (Fig. 4), the regions of opposite signs of ξ_n come into

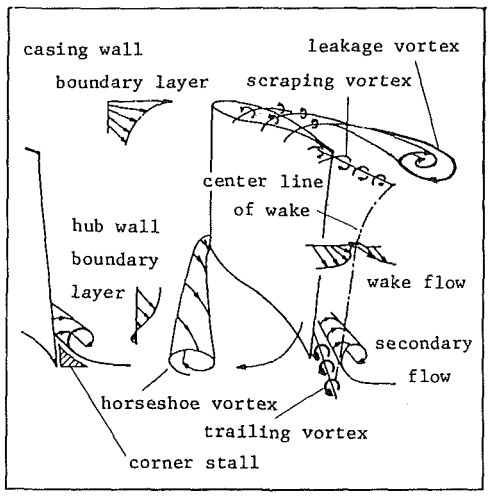

Fig. 7 Illustration of structure of the vortices generated through the rotor

existence on both sides of the leakage vortex. For the same reason, the region of positive ξ_τ appears below it. The negative value of ξ_τ above it increases with radius due to the casing wall boundary layer. The negative value of ξ_s also increases near the casing due to the skewed boundary layer. An appreciable amount of increase in $|\xi_s|$ and $|\xi_\tau|$ is recognized at the interaction region of the blade wake and the casing wall boundary layer ($\xi_s = -6$ and $\xi_\tau = -2$). This region is located on the pressure side of the wake according to the contour line of $\xi_n = 0$. Therefore, it is estimated that this increase is caused by scraping of the casing wall boundary layer.

In the trailing shed vortex near the hub, not only ξ_s but also ξ_τ and ξ_n are large. This fact indicates that the direction of the trailing shed vortex does not coincide with the streamwise direction due to the interaction with the wall boundary layer and the wake. At the corner between the hub wall and the suction side of wake, $|\xi_s|$ becomes large since the secondary streamwise vorticity in the Squire-Winter sense is concentrated at this corner in the actual flow. Consequently, the accumulation of boundary layer increases the absolute values of ξ_τ, which may produce a corner stall as stated earlier. Another accumulation comes into existence on the left side of the wake near the hub, where a substantial amount of $|\xi_\tau|$ as well as an appreciable amount of $|\xi_n|$ and $|\xi_s|$ is recognized. It is considered that this accumulation shows the existence of the horseshoe vortex resulting from the blade-wall boundary layer interaction.

Judging from the facts described above, the structure of the vortices generated behind the rotor is illustrated as shown in Fig. 7.

Decay of Vortices. Figures 8(*a–c*) show the vorticity map at the downstream measuring section ($z/l_m = 0.342$). Inside the blade wake, $|\xi_s|$ and $|\xi_\tau|$ attenuate remarkably, except near the hub wall, while considerable value of $|\xi_n|$ remains. This fact shows that the structure of the wake turns into two-dimensional one. The magnitudes of $|\xi_n|$ on both sides of wake are getting closer in magnitude as the flow proceeds downstream, i.e., the wake becomes symmetrical.

The leakage vortex keeps the same structure as is shown in Figs. 5(*a–c*). However, the magnitude of vorticity reduces considerably, and the distance from the wake increases due to interaction of the casing wall.

The trailing shed vortex, the secondary flow in the Squire-Winter sense, and the horseshoe vortex are still observed clearly near the hub wall, as if they decay slowly. But attention is paid to the difference of the effective flowing distance between the tip region and the hub region.

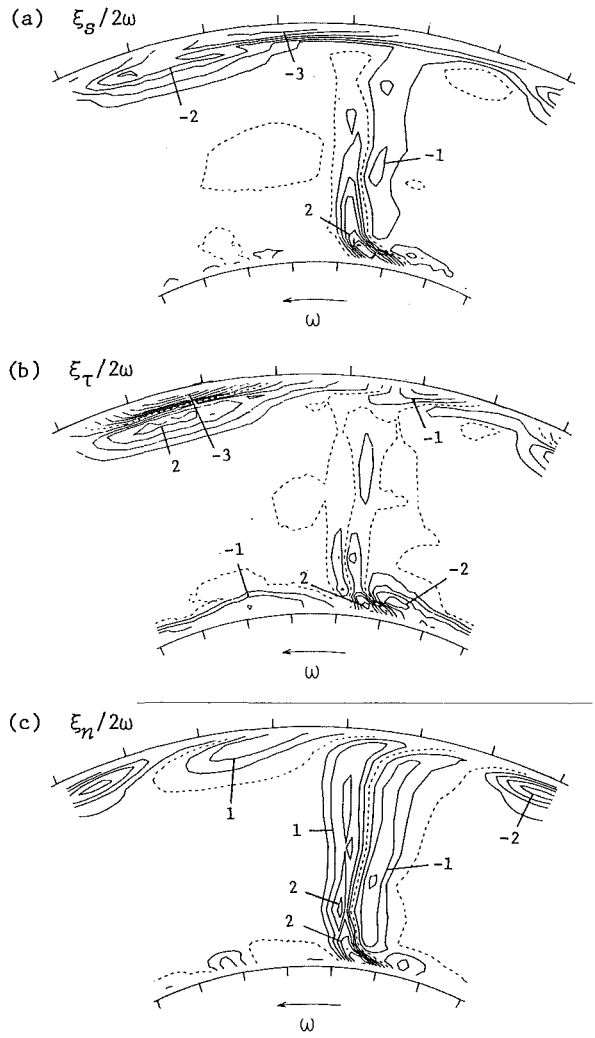

Fig. 8 Ensemble average vorticity distribution far downstream of rotor

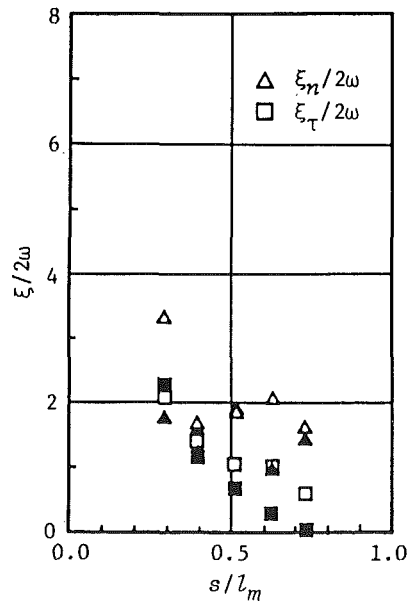

Fig. 9 Decay characteristics of vorticities inside the wake

In order to investigate the decay rate of these vortices, the absolute values of normalized vorticity at representative points are plotted against the nondimensional effective flowing distance s/l_m (Figs. 9–11).

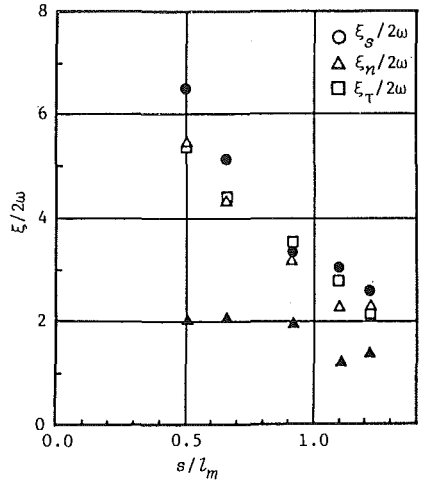

Fig. 10 Decay characteristics of vorticities in the leakage vortex

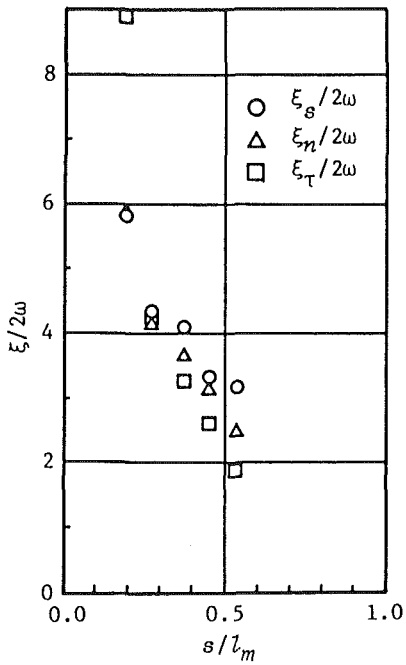

Fig. 11 Decay characteristics of vorticities in the trailing shed vortex

Figure 9 shows the streamwise variation of the maximum values of $|\xi_n/2\omega|$ and $|\xi_\tau/2\omega|$ on the both sides of the wake at midspan. The open and filled-in symbols indicate positive and negative values, respectively. The normal vorticity $|\xi_n|$ decays rapidly to $s/l_m = 0.4$, thence reducing slowly. On the other hand, the lateral vorticity $|\xi_\tau|$ is decreasing nearly to zero at $s/l_m = 0.7 \rightarrow 0.8$; the vorticity component which indicates the three-dimensional nature of the wake decays rapidly, as described earlier.

Figure 10 shows the streamwise variation of the vorticity in the leakage vortex. The filled-in circle symbol denotes the streamwise vorticity at the vortex center, the open and the filled-in triangle symbols denote the maximum values of the normal vorticity on the pressure and the suction side of the leakage vortex, and the square symbol is the lateral vorticity below the vortex. The latter three symbols indicate the gradients of the velocity defect in w. Decay rate of $|\xi_s|$ is almost the same degree of the decay of the velocity gradient around the vortex, except on the suction side of it. Unlike the other vorticities, the suction side normal vorticity $|\xi_n|$ is much smaller (gentler gradient) and its decay is by far the slowest.

Figure 11 shows the decay rate of the trailing shed vortex near the hub. All of the vorticity components show very high values just behind the rotor; however, they decay more rapidly compared to the leakage vortex. The reason for this is that the trailing vortex is shedding into the wake flow with low energy, while the leakage vortex moves farther away from the wake due to the leakage jet flow at blade tip before rolling up [17].

The decay characteristics of the vorticity will be discussed further in relation to the turbulent characteristics.

Turbulence Characteristics. The six components of turbulent stress have been derived from the 12 sets of variances of the anemometer outputs by changing the position of the slanted single hot wire [22]. The components have been converted from the cylindrical coordinate system ($z - \theta - r$) to the local streamwise system ($s - \tau - n$) by the following relation.

$$\begin{bmatrix} \overline{w_s'^2} \\ \overline{w_\tau'^2} \\ \overline{w_n'^2} \\ \overline{w_\tau' w_n'} \\ \overline{w_n' w_s'} \\ \overline{w_s' w_\tau'} \end{bmatrix} = \begin{bmatrix} A_1^2A_3^2 & A_2^2 & A_1^2A_4^2 & -A_4A_6 & A_1^2A_8 & -A_3A_6 \\ A_2^2A_3^2 & A_1^2 & A_2^2A_4^2 & A_4A_6 & A_2^2A_8 & A_3A_6 \\ A_4^2 & 0 & A_3^2 & 0 & -A_8 & 0 \\ -\frac{1}{2}A_2A_8 & 0 & \frac{1}{2}A_2A_8 & A_1A_3 & A_2A_7 & -A_1A_4 \\ -\frac{1}{2}A_1A_8 & 0 & \frac{1}{2}A_1A_8 & -A_2A_3 & A_1A_7 & -A_2A_4 \\ \frac{1}{2}A_3^2A_6 & -\frac{1}{2}A_8 & \frac{1}{2}A_4^2A_6 & A_4A_5 & \frac{1}{2}A_6A_8 & A_3A_5 \end{bmatrix} \begin{bmatrix} \overline{w_z'^2} \\ \overline{w_\theta'^2} \\ \overline{w_r'^2} \\ \overline{w_\theta' w_r'} \\ \overline{w_r' w_z'} \\ \overline{w_z' w_\theta'} \end{bmatrix}$$

where $A_1 = \cos\beta$, $A_2 = \sin\beta$, $A_3 = \cos\gamma$, $A_4 = \sin\gamma$, $A_5 = \cos 2\beta$, $A_6 = \cos 2\beta$, $A_7 = \cos 2\gamma$, and $A_8 = \sin 2\gamma$.

Figure 12 shows the contour map of the turbulence level (the root mean square of three normal stresses) at the measuring cross section. The turbulence level has been normalized by the blade tip velocity u_t instead of the local mean velocity so as to relate it to the magnitude of turbulence.

$$\text{T.L.} = \sqrt{(\overline{w_s'^2} + \overline{w_\tau'^2} + \overline{w_n'^2})/3}/u_t$$

In general, the distribution of the turbulence level resembles that of kinetic energy defect (Fig. 4). It is noted, however, that the magnitude becomes high on both sides of the leakage vortex. This phenomenon is probably caused by peripheral swaying of the leakage vortex.

Figures 13(*a–c*) are the maps of the turbulence shear stresses (cross correlation terms). The stresses have been normalized by u_t^2 instead of w^2 so as to relate them to the magnitude of momentum transfer due to the turbulence mixing effect.

Inside the wake, the distributions of $\overline{w_s' w_\tau'}$ and $\overline{w_\tau' w_n'}$ show the expected reversal of stress at the wake center. This positive and negative distribution results from opposite gradients of streamwise and radial mean velocity about the wake center. The distributions are asymmetrical about the wake center corresponding to the velocity gradients on both sides of wake. The same results have been obtained in [15, 16, 20].

Near the casing, the shearing stresses are not so large except in the leakage vortex because the magnitude of the relative velocity changes little. In the leakage vortex, the measured shear stresses are vague as the vortex is swaying in the peripheral direction (Fig. 12). However, all of the components of shear stress exhibit a tendency to vanish in the center of vortex and have high magnitude outside of it. This fact shows that the center region has the nature of a solid vortex. The value of $\overline{w_\tau' w_n'}$ is positive on the pressure and the suction side of it and becomes negative below it. This trend indicates the nature of a free vortex. Corresponding to the velocity defect in the leakage vortex (Fig. 4), it is seen that $\overline{w_s' w_\tau'} \leq 0$ on the pressure side, $\overline{w_s' w_\tau'} > 0$ on the suction side, and $\overline{w_n' w_s'} > 0$ below the vortex center.

For the trailing shed vortex, the values of all stress components change their sign at its center and become high around it. Near the hub wall, $\overline{w_s' w_\tau'}$ and $\overline{w_\tau' w_n'}$ are negligibly small except in the horseshoe vortex. The stress of $\overline{w_n' w_s'}$, which implies the momentum transfer in the hub wall boundary layer, has a considerable amount especially in the regions of the boundary layer accumulation due to the secondary flow and horseshoe vortex.

Figures 14(*a–c*) are the maps of the turbulence shear stress in the downstream measuring section ($z/l_m = 0.341$). Inside the wake, the magnitude of the shear stresses becomes very low except $\overline{w_\tau' w_n'}$ on the pressure side. In the tip leakage vortex, considerably high values of turbulence stresses remain in spite of long effective flowing distance. This is probably due to the conversion of mean vortex energy into turbulence energy. On the hub wall, $\overline{w_s' w_\tau'}$ and $\overline{w_\tau' w_n'}$ are negligibly small except near the wake. However, considerable magnitude of $\overline{w_n' w_s'}$ is observed in the interaction region of the wake and the hub wall boundary layer, because of the accumulation of low energy fluid resulting from secondary flow, which may contribute to the rapid decay of the trailing shed vortex.

In this section, the discussion is restricted to the behavior in relation to the decay of vorticity. As to the detail characteristics of the wake, the reader should refer to the laborious works by Lakshminarayana and his fellow workers, who have discussed turbulence intensities and stresses by normalizing the local mean velocity [15, 16, 20].

Correlation Between Vorticity and Turbulent Shear Stress. The correlation between the turbulence shear stress and the mean vorticity has been investigated on the basis of a local streamwise coordinate system. Figures 15, 16, and 17 show typical examples of the turbulence stress-vorticity correlation in the wake, near the hub wall, and the casing boundary layer, respectively.

Inside the wake, $\overline{w_s' w_\tau'} - \xi_n$ and $\overline{w_\tau' w_n'} - \xi_s$ correlations are obvious since the normal and the streamwise vorticities are mainly caused by the streamwise and radial velocity gradients respectively. As shown in Fig. 15, the gradient of $\overline{w_s' w_\tau'} - \xi_n$ correlation on the pressure side is steeper than that on the suction side. This fact implies that the ability for momentum transfer due to turbulent mixing is higher on the pressure side, thus the wake becomes symmetrical downstream. The gradient of $\overline{w_\tau' w_n'} - \xi_s$ correlation is steeper than that of $\overline{w_s' w_\tau'} - \xi_n$ correlation. These phenomena coincide with those obtained by Davino and Lakshminarayana [16] and are due to the effect of rotation. This is probably why the

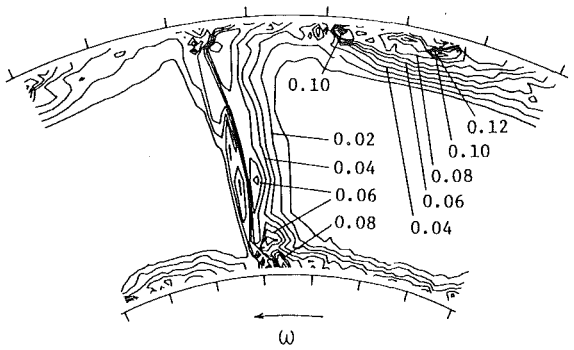

Fig. 12 Contour of turbulence level

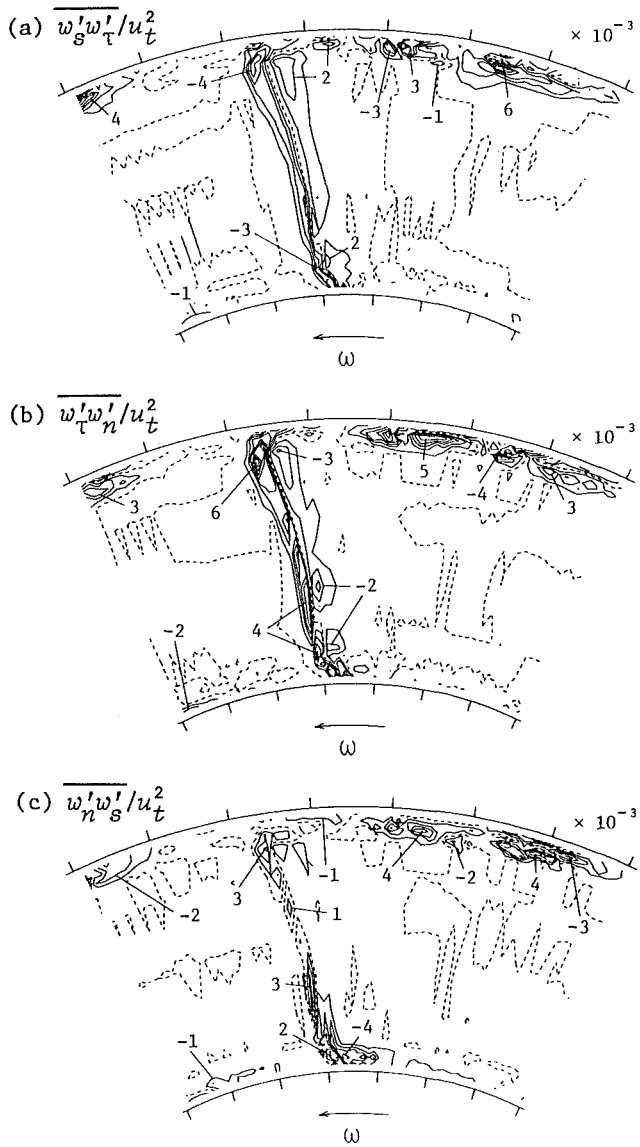

Fig. 13 Distribution of turbulence shear stress just behind the rotor

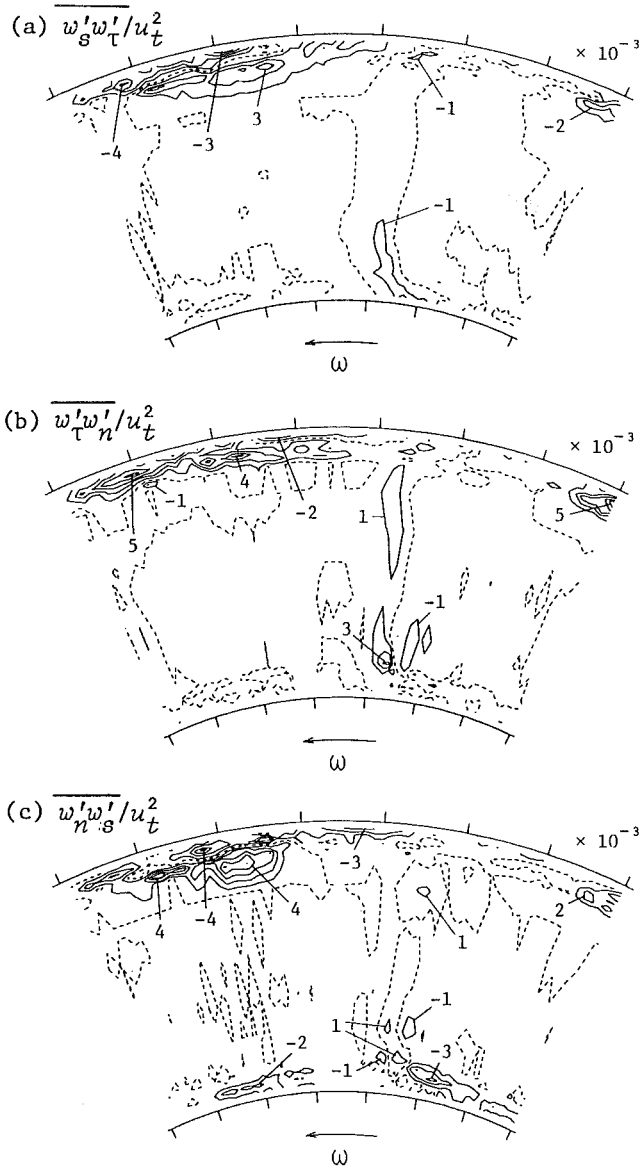

Fig. 14 Distribution of turbulent shear stress in the downstream

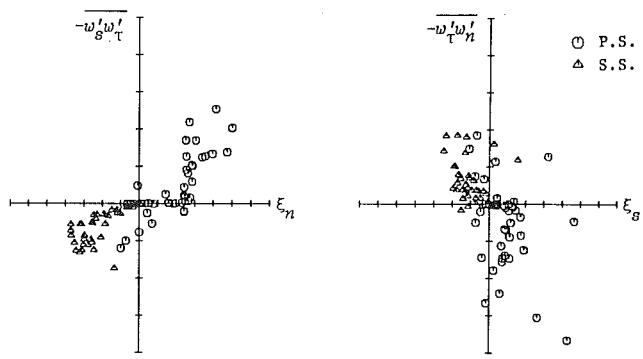

(a) $\overline{w_s'w_\tau'} - \xi_n$ correlation (b) $\overline{w_\tau'w_n'} - \xi_s$ correlation

Fig. 15 Turbulence stress-vorticity correlations inside the wake

streamwise vorticity decays more quickly than the normal vorticity to turn the wake from a three-dimensional nature to a two-dimensional one as described earlier.

In Fig. 16, $w_n'w_s'$ is correlated to ξ_τ near the wall surface (W.S.) and on the suction side of the wake (S.S.) where the boundary layer accumulates. There is considerable correlation between $\overline{w_s'w_\tau'}$ and ξ_n on the pressure side (P.S.) and the suction side (S.S.). Namely, the characteristics of boundary

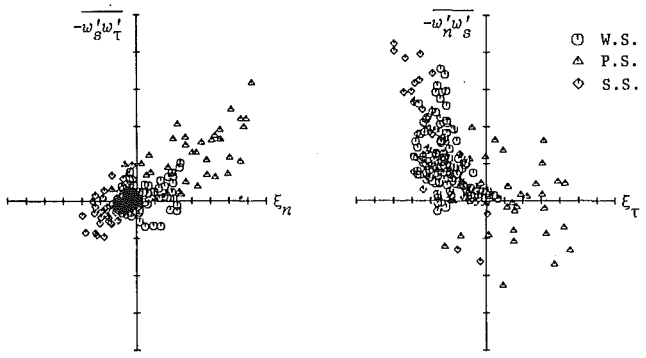

(a) $\overline{w_s' w_\tau'} - \xi_n$ correlation (b) $\overline{w_n' w_s'} - \xi_\tau$ correlation

Fig. 16 Turbulence stress-vorticity correlation near the hub wall

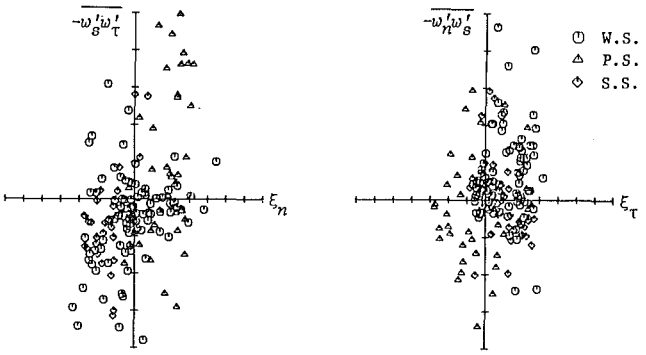

(a) $\overline{w_s' w_\tau'} - \xi_n$ correlation (b) $\overline{w_n' w_s'} - \xi_\tau$ correlation

Fig. 17 Turbulent stress-vorticity correlation near the casing wall except in the leakage vortex

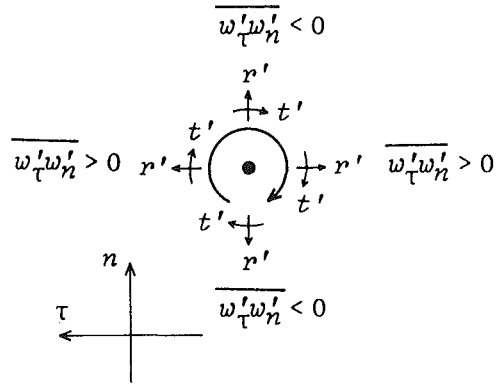

Fig. 18 Illustration of cross correlation of fluctuating velocity components which concerns with attenuation of the leakage vortex

layer and wake flows are observed to coexist together behind the blade root, where the trailing vortex is shedding. This is closely related to the rapid decay of the trailing vortex (Fig. 11).

In Fig. 17, the data in the leakage vortex have been omitted for the following reason: in a vortex, the streamwise vorticity is attenuated by the cross correlation of tangential and radial components of the velocity fluctuations referred to the vortex center ($t' - r'$ correlation in Fig. 18). Therefore, the turbulent velocity correlation varies from positive to negative around the vortex if it is expressed in terms of the local streamwise coordinate system. In spite of this data omission, there are not obvious correlations between the turbulence stress and the vorticity as there are near the hub. This is probably due to the unstable swaying effect of the leakage vortex. But the same trend is recognized in the $\overline{w_s' w_\tau'} - \xi_n$ correlation and the opposite trend in the $\overline{w_n' w_s'} - \xi_\tau$ correlation.

Conclusions

The statistically accurate mean velocities as well as the turbulence properties of the flow field behind an axial rotor have been obtained by use of the periodic multisampling and averaging technique with a slanted single hot wire. The major conclusions derived from the experimental results are as follows:

1 The complex flow phenomena behind the rotor could be grasped easily by drawing both maps of the secondary flow and the kinetic velocity defect at the measuring plane.

2 By use of the local streamwise, lateral, and normal components of vorticity, it is possible to elucidate quantitatively the three-dimensional structure of various kinds of vortices generated behind the rotor, such as a leakage vortex, trailing shed vortices, scraping vortices, a horseshoe vortex, etc.

3 Among the various vortices, the leakage vortex near the casing and the trailing shed vortex near the hub had a remarkable magnitude of vorticity. The decay characteristics of these vortices as well as those of the three dimensional wake were investigated in relation to the turbulence characteristics.

4 The blade wake, which is asymmetrical and three-dimensional just behind the rotor, becomes symmetrical and two-dimensional as the flow proceeds downstream due to the asymmetric and noniostropic nature of the turbulence shear stresses resulting from the effect of rotation.

5 Turbulence properties are considerably higher in the leakage vortex at the downstream section, because turbulence energy is generated by the mean vortex motion.

6 The trailing shed vortex decays more quickly than the leakage vortex, since the former is affected by the turbulent viscous effects of the wake and the boundary layer accumulation while the latter is rolling up separately from the wake.

References

1 Watanabe, T., Kawahito, A., Nakase, T., and Ohshima, S., "Three-Dimensional Measurement of Internal Flow in an Axial Turbomachine by use of Hot-Wire Anemometer" (in Japanese), Preprint of JSME, 43rd Kansai-branch meeting, Mar. 1968, pp. 54–56.

2 Whitfield, C. E., Kelly, J. C., and Barry, B., "A Three-Dimensional Analysis of Rotor Wakes," *Aeronautical Quarterly*, Vol. 23, No. 4, Nov. 1972, pp. 285–300.

3 Evans, R. L., "Turbulence and Unsteadiness Measurements Downstream of a Moving Blade Row," ASME JOURNAL OF ENGINEERING FOR POWER, Vol. 97, No. 1, Jan. 1975, pp. 131–139.

4 Gostelow, J. P., "A New Approach to the Experimental Study of Turbomachinery Flow Phenomena," ASME JOURNAL OF ENGINEERING FOR POWER, Vol. 99, No. 1, Jan. 1977, pp. 97–105.

5 Lakshminarayana, B., and Poncet, A., "A Method of Measuring Three-Dimensional Wakes in Turbomachinery," ASME *Journal of Fluids Engineering*, Vol. 96, No. 2, June 1974, pp. 87–91.

6 Lakshminarayana, B., "Techniques for Aerodynamic and Turbulence Measurements in Turbomachinery Rotors," *Proceedings of Symposium and Measurement Method in Rotating Components of Turbomachinery*, ASME, New York, Nov. 1980, pp. 5–29.

7 Hirsch, C., and Kool, P., "Measurement of the Three-Dimensional Flow Field Behind an Axial Compressor Stages," ASME JOURNAL OF ENGINEERING FOR POWER, Vol. 99, No. 2, Apr. 1977, pp. 168–180.

8 Kool, P., "Determination of the Reynolds-Stress Tensor with a Single Slanted Hot-Wire in Periodically Unsteady Turbomachinery Flow," ASME Paper No.79-GT-130, Mar. 1979.

9 Okiishi, T., and Schmidt, D. P., "Measurement of the Periodic Variation of Turbomachine Flow Fields," *Proceedings of Dynamic Flow Conference 1978 on Dynamic Measurements in Unsteady Flows*, Edited by B. W.. Hansen, Sept. 1978, pp. 249–269.

10 Raj, R., and Lakshminarayana, B., "Three-Dimensional Characteristics of Turbulent Wakes behind Rotors of Axial Flow Turbomachinery," ASME JOURNAL OF ENGINEERING FOR POWER, Vol. 98, No. 2, Apr. 1976, pp. 218–228.

11 Schmidt, D. P., and Okiishi, T. H., "Multistage Axial-Flow Turbomachine Wake Production, Transport, and Interaction," *AIAA Journal*, Vol. 15, No. 8, Aug. 1977, pp. 1138–1145.

12 Kool, P., DeRuyck, J., and Hirsch, C., "The Three-Dimensional Flow and Blade Wake in an Axial Plane Downstream of an Axial Compressor Rotor," ASME Paper No. 78-GT-66, Apr. 1978.

13 Reynolds, B., Lakshminarayana, B., and Ravindranath, A., "Characteristics of the Near-Wake of a Compressor or Fan Rotor Blade," *AIAA Journal*, Vol. 17, No. 9, Sept. 1979, pp. 959–967.

14 Ravindranath, A., and Lakshminarayana, B., "Mean Velocity and Decay Characteristics of the Near and Far Wake of a Compressor Rotor Blade of Moderate Loading," ASME JOURNAL OF ENGINEERING FOR POWER, Vol. 102, No. 3, July 1980, pp. 535–548.

15 Ravindranath, A., and Lakshminarayana, B., "Structure and Decay Characteristics of Turbulence in the Near- and Far-Wake of a Moderately Loaded Compressor Rotor-Blade," ASME JOURNAL OF ENGINEERING FOR POWER, Vol. 103, No. 1, Jan. 1981, pp. 131–140.

16 Davino, R., and Lakshminarayana, B., "Turbulence Characteristics in the Annulus-Wall Boundary Layer and Wake Mixing Region of a Compressor Rotor Exit," ASME JOURNAL OF ENGINEERING FOR POWER, Vol. 104, No. 3, July 1982, pp. 561–570.

17 Lakshminarayana, B., Pouagare, M., and Davino, R., "Three-Dimensional Flow Field in the Tip Region of a Compressor Rotor Passage—Part I: Mean Velocity Profiles and Annulus Wall Boundary Layer," ASME Paper No. 82-GT-11, Apr. 1982.

18 Pandya, A., and Lakshminarayana, B., "Invesitgation of the Tip-Clearance Flow Inside and at the Exit of a Compressor Rotor Passage—Part I: Mean Velocity Field," ASME Paper No .82-GT-12, Apr. 1982.

19 Hunter, I. H., and Cumpsty, N. A., "Casing Wall Boundary-Layer Development Through an Isolated Compressor Rotor," ASME Paper No. 82-GT-18, Apr. 1982.

20 Lakshminarayana, B., Pouagare, M., and Davino, R., "Three-Dimensional Flow Field in the Tip Region of a Compressor Rotor Passage—Part II: Turbulence Properties," ASME Paper No. 82-GT-274, Apr. 1982.

21 Dring, R. P., Joslyn, H. D., and Hardin, L. W., "An Investigation of Axial Compressor Rotor Aerodynamics," ASME JOURNAL OF ENGINEERING FOR POWER, Vol. 104, No. 1, Jan. 1982, pp. 84–96.

22 Kuroumaru, M., Inoue, M., Higaki, T., Abd-elaziz, F. A., and Ikui, T., "Measurements of Three-Dimensional Flow Field behind an Impeller by Means of Periodic Multi-Sampling of a Slanted Hot Wire," *Bulletin of the JSME*, Vol. 25, No. 209, Nov. 1982, pp. 1674–1681.

Tip Clearance Flow in a Compressor Rotor Passage at Design and Off-Design Conditions

B. Lakshminarayana
Director of Computational Fluid Dynamics Studies and Professor of Aerospace Engineering.

A. Pandya[1]

Department of Aerospace Engineering, The Pennsylvania State University, University Park, PA. 16802

The flow field in the tip clearance region of a compressor rotor at an off-design condition is reported in this paper. The earlier data at the design condition have also been reinterpreted and correlated with the blade and the flow parameters. The measurements inside the rotor tip region are acquired using a miniature hot-wire sensor of "V" configuration. The instantaneous velocity data are analyzed by the ensemble-averaging technique to derive the blade-to-blade velocity field at various axial and radial locations between the rotor tip and the casing. The flow and the blade pressure data at the design condition are compared with the data at the off-design condition (lower blade loading). In addition to a reduction in the leakage velocities, its chordwise variation is also altered substantially at the lower blade loading.

Introduction

It is known [1, 2] that the leakage velocities in the clearance region of a turbomachinery rotor are strongly dependent on the blade loading. This paper discusses the effect of the change in the blade loading on the tip leakage flow. This discussion is based on an experimental investigation carried out as part of a systematic program underway at The Pennsylvania State University to study the endwall flow in a compressor rotor. The characteristics of the mean flow in the tip clearance region of a compressor rotor at the design condition are discussed by Pandya and Lakshminarayana [3]. The mean flow and the turbulent flow characteristics at the off-design condition and the significant changes in the leakage flow properties that occur as a result of changes in the blade loading are presented and discussed in this paper.

Experimental Facility, Instrumentation, and Program

A detailed discussion of the facility used in this investigation is given by Lakshminarayana [4] and a brief description is given in [3]. The hub/annulus wall diameter ratio of the facility is 0.5, with the diameter of the annulus wall equal to 0.932 m. The inlet guide vane row, which consists of 43 blades, is followed by the 21-bladed rotor. The rotor is followed by a stator vane row of 25 blades. Some of the other operating conditions and rotor specifications are as follows: flow coefficient based on tip speed, 0.60; speed of rotor, 935 rpm. Blade element data at the tip are NASA 65 series, chord 15.41 cm, spacing 14.12 cm, maximum thickness 5.10 percent of chord, stagger angle 45.0 deg, and a maximum camber height 8 percent chord. The blade elements are NACA 65-010 basic profile on a circular arc camber. The design and the off-design conditions at which the clearance data were acquired are indicated on the performance characteristics of the stage (Fig. 1). The data at the design condition are reported in [3]. The data at the off-design condition ($\bar{\phi}$ = 0.60, $\bar{\psi}$ = 0.375, $\bar{\eta}$ = 65 percent) are reported in this paper. Both the data are correlated with the blade and flow geometry.

All the flow field measurements reported in this paper were carried out using a stationary two-sensor, hot-wire probe in combination with the ensemble-averaging technique [3]. Unlike the conventional two-sensor, hot-wire probe (x configuration), the present sensor is a "V" type of probe where both the sensors are in the same plane and the included angle between the two sensors is 90 deg. With this arrangement, it was possible to measure two components of the velocity at the same radial location with the least spatial

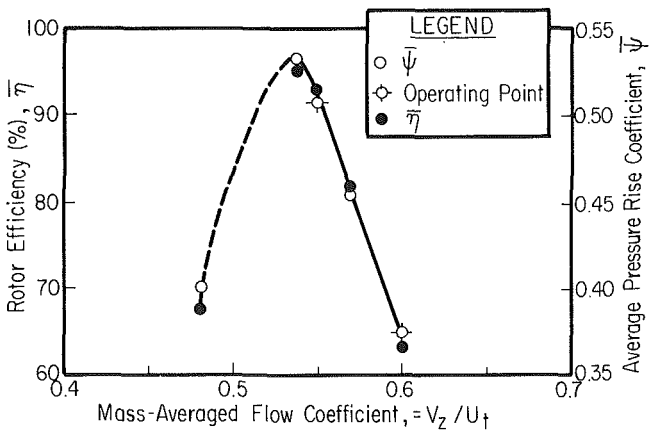

Fig. 1 Performance curve and operating conditions of the axial flow compressor

[1] Presently at Memorex Corporation, RTC Division, Santa Clara, Calif.

Contributed by the Gas Turbine Division of the American Society of Mechanical Engineers and presented at the Sixth International Symposium on Airbreathing Engines, Paris, France, June 6-10, 1983. Manuscript received by the Gas Turbine Division.

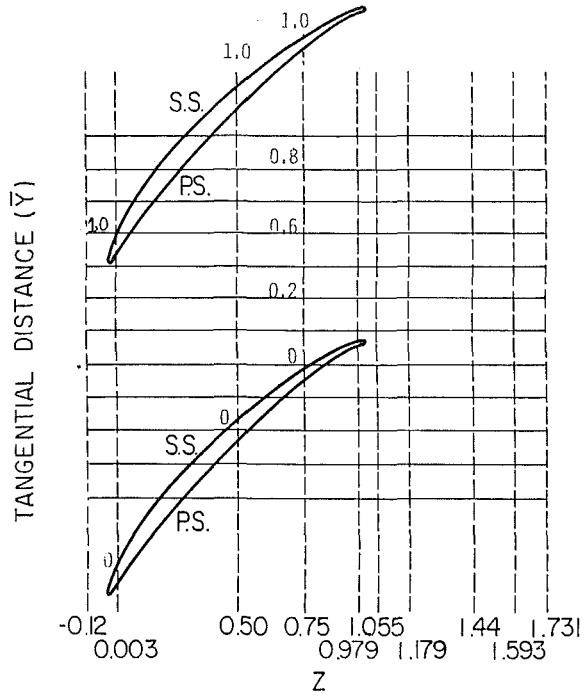

Fig. 2 Axial stations of measurement

error. A micrometer-type probe traverse mechanism with an accuracy of ± 0.002 cm is used to traverse the probe through the casing. Details of the measurement technique can be found in [3] and [5].

Experimental measurements consisted of two parts: (*a*) clearance measurements and (*b*) flow field measurements. An accurate measurement of the clearance for all the 21 rotor blades at various axial locations was necessary in order to acquire data as near the blade tip as possible. The measurement of clearance was carried out with a fotonic sensor at four axial stations. The clearance varied from 2 mm at the leading edge to 1.5 mm at the trailing edge [5]. the maximum variation of clearance from blade to blade was 20 percent. The variation was large near the blade leading edge. There was no difference between the static and dynamic clearance for the same blade, even though the clearance varied from blade to blade at all the axial stations.

The axial stations of measurement was well as blade geometry are shown in Fig. 2. Details of the measurement technique, locations, steps involved in the data processing are given in [3].

Table 1 Compressor parameters at design and off-design conditions

	Design Condition	Off-Design Condition
rpm	1110	935
Inlet velocity	28.37 m/s	26.28 m/s
Flow coefficient $\bar{\phi}$	0.55	0.60
Average pressure rise coefficient $\bar{\psi}$	0.51	0.375
Blade tip speed	51.5 m/s	43.8 m/s

Experimental Results

The results at only selected locations are presented and compared with the data at the design condition, the complete set of data is presented in [5]. The velocity components presented in this paper are in the absolute system and are normalized by the corresponding blade tip speed. The operating conditions are shown in Table 1.

The data presented in this paper include the blade static pressure near the blade tip, axial and the tangential velocity components. Some of the earlier data [3, 5] at the design condition are reinterpreted and correlated in this paper.

Blade Pressure Measurements. The static pressure distribution on the rotor blade was measured at the design (ϕ

Nomenclature

C = chord length
C_L = section lift coefficient derived from blade pressure distribution (based on local inlet relative velocity and tip chord)
C_{LR} = retained lift coefficient at the tip of the blade
C_P = blade pressure coefficient based on local inlet dynamic head of relative flow and inlet static pressure
C_l = local lift coefficient $[(C_p)_p - (C_p)_s]$
P.S. = pressure surface
R = radius ratio (r/r_t), $R = 1$ at tip of the blade, $R = 0.5$ at hub
$\bar{R}$ = distance from the annulus wall in the radial direction normalized by the clearance at the leading edge
$\bar{r}$ = distance from the annulus wall normalized by (*i*) clearance at L.E. for rotor inlet flow, (*ii*) local clearance for flow inside the passage, and (*iii*) clearance at T.E. for rotor exit flow
S = blade spacing
S.S. = suction surface
t_{max} = maximum thickness of the blade at the tip
U = blade speed
V = mean velocity in stationary frame of reference (Fig. 10) normalized by U_t
$\bar{V}$ = passage-averaged velocity in stationary frame of reference normalized by U_t
W = mean velocity in relative frame of reference normalized by U_t
W_{No} = W_N at the inlet of the rotor normalized by U_t (Fig. 10)
X = chordwise distance
$\bar{Y}$ = distance from the suction surface in the tangential direction normalized by the blade spacing (Fig. 2).
z,θ,r = axial, tangential, and radial directions
Z = axial distance from the rotor blade leading edge normalized by the axial chord
β = relative flow angle measured from the axial direction
Ω = rotational speed rpm
ϕ = mass-averaged flow coefficient $(\bar{V}_z)/(U_t)$
ρ = fluid density
τ = tip clearance height
$\bar{\eta}$ = mass-averaged rotor efficiency (Euler) = $\bar{\psi}/\bar{\psi}_{\text{Euler}}$
$\bar{\psi}$ = mass-averaged stagnation pressure rise coefficient normalized by $\rho U_t^2/2$

Subscripts

max = maximum value in the passage
t = value at the tip of the rotor blade
z,θ = value in axial and tangential directions, respectively
1 = inlet
p,s = pressure and suction surfaces, respectively
2d = two-dimensional value away from the influence of annulus wall boundary layer
$\sim$ = gap-averaged values

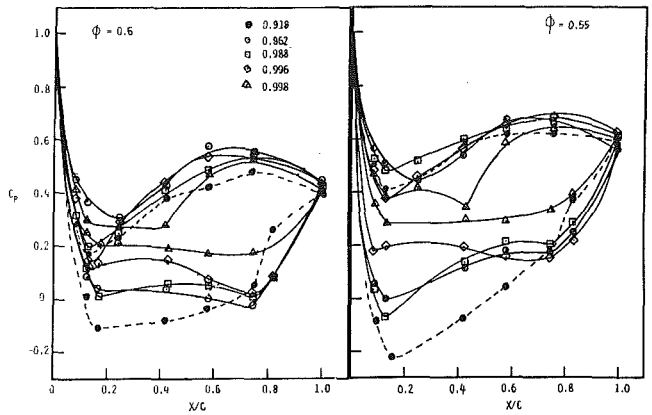

Fig. 3 Blade static pressure distribution

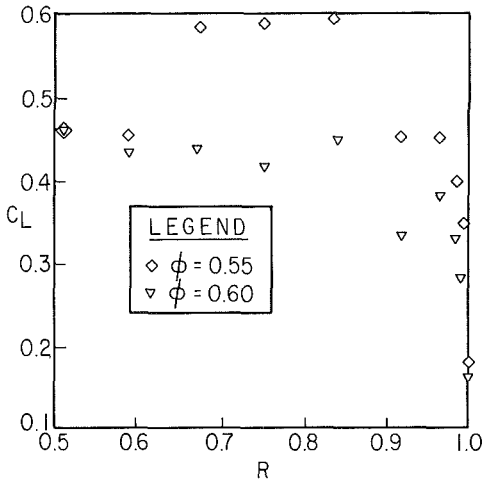

Fig. 4 Radial variation of section lift coefficient (C_L)

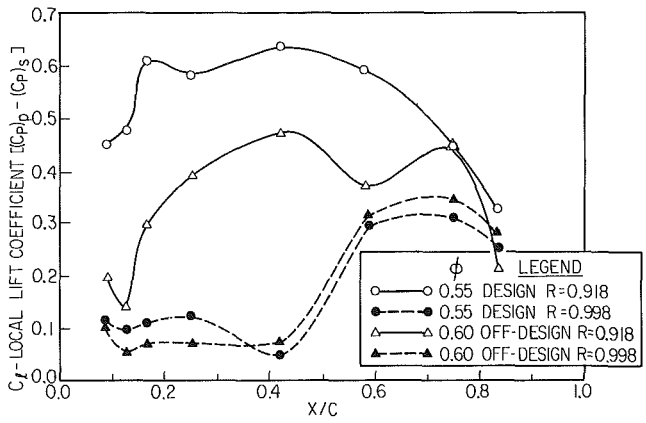

Fig. 5 Chordwise distribution of local lift coefficient (C_l)

= 0.55) and the off-design (ϕ = 0.6) conditions at various chordwise and radial locations, including several locations very near the blade tip (R = 0.998, 0.996, 0.988, 0.962, 0.918, etc.). The last radial location is about 0.4 percent of the span or 0.9 mm from the tip of the blade, whose span is 22.85 cm. The method of measurement as well as the data at all the locations and the operating conditions are presented in [6]. The pressure distribution at the design and the off-design conditions at various radial locations near the blade tip are shown in Fig. 3. A plot of the lift coefficient (based on the inlet relative velocity and the chord at the blade tip) at these operating conditions is shown plotted in Fig. 4. At R = 0.918,

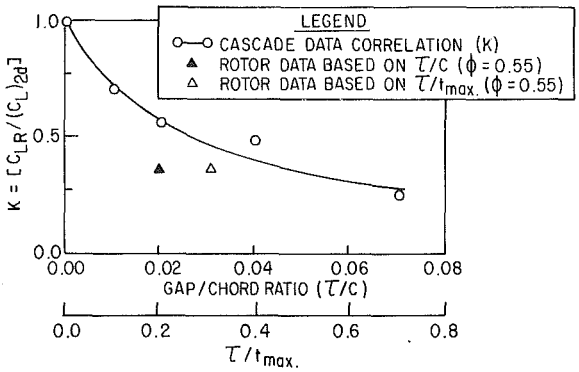

Fig. 6 Retained lift at the blade tip

the flow is nearly inviscid with very little influence of the annulus wall boundary layer on the flow field. The blade loading decreases rapidly as the tip is approached. Even though C_L at ϕ = 0.55 is higher than the off-design condition, the pressure distribution and the lift coefficients are almost identical for both cases at the tip for R = 0.998. The suction peak moves closer to the trailing edge as the blade tip is approached. This is in conformity with the cascade data reported in [7]. A possible reason for this is the presence of tip vortex or low pressure region on the suction side near the trailing edge.

The local pressure difference (or local lift coefficient = $[(C_p)_p - (C_p)_s]$, which is a measure of the leakage velocity, at both the operating conditions is plotted in Fig. 5 for R = 0.918 (inviscid region) and R = 0.998 (at the tip). The data at R = 0.918 indicate that the local pressure differences are much lower for ϕ = 0.6 up to Z = 0.25, beyond which the differences between the design and the off-design values, even though appreciable, decrease reaching almost identical values beyond Z = 0.75. The local lift coefficient has a major influence on the leakage velocity, and this will be discussed in a later section. The local lift coefficient is almost identical at the tip at both operating conditions at all chordwise locations.

The correlation based on the "retained lift concept," developed in [2] and [7] has been employed by many investigators for the prediction of the tip clearance effect in turbomachinery. A correlation for K, which is the lift retained at the tip $[C_{LR}/(C_L)2d]$, derived from the measurement in a cascade [7] is shown in Fig. 6. The correlation in [2] and [7] utilizes the solid curve in the figure. The rotor data, based on the measurements (Fig. 5) is also shown in Fig. 6. The value of $(C_L)_{2d}$ is based on the data at R = 0.918. The data point based on the τ/C (tip clearance height normalized by the maximum blade chord) does not seem to agree well with the correlation. At small clearances encountered in practice, the thickness of the blade should influence the leakage velocities. Since the resistance to the leakage flow, or the retention of the lift on the blade at the tip, depends on the length of the leakage flow path, the proper normalizing factor for this clearance height seems to be that based on the maximum blade thickness at the tip. The rotor data normalized by t_{max} seem to show better agreement with the cascade correlation. Even though the authors do not have sufficient data to draw conclusions on the proper normalizing factor, future research should be directed in confirming or disproving this trend.

Mean Velocity Profiles and Flow Angles Inside the Tip Clearance Region. The notations used and the nature of leakage flow are shown in Fig. 7. W_N is the leakage velocity in the terminology used in this paper, and W' is the resultant velocity in the clearance region. The blade-to-blade variation of the axial velocity (V_z), the absolute tangential velocity (V_θ), and the relative flow angle (β) are plotted in Figs. 8–12

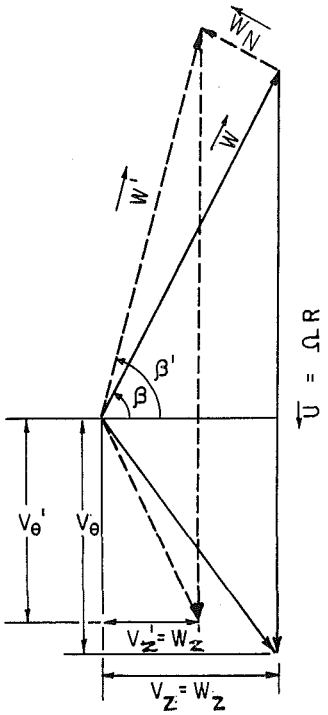

Fig. 7 Velocity triangles with and without the leakage flow

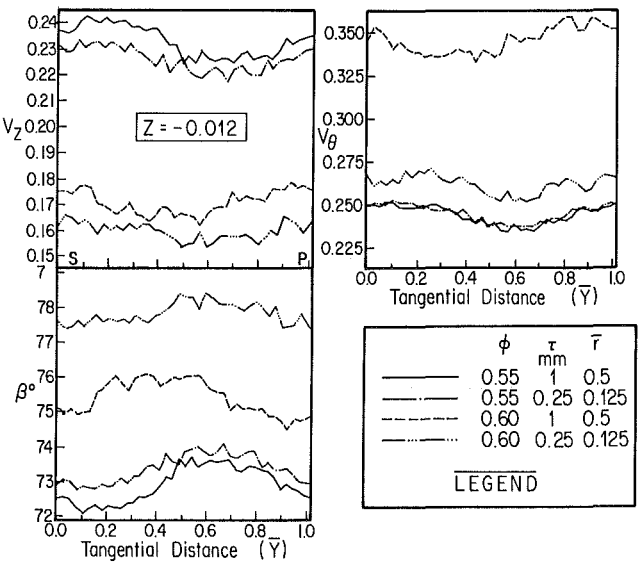

Fig. 8 Axial and absolute tangential velocity profiles and relative flow angles at $Z = -0.012$

for various chordwise locations inside the passage. The pressure and suction surface locations as well as tip clearance regions are marked on these figures. All the velocities are normalized by the corresponding blade tip speed. Measurements are compared at two typical locations, one near the wall and one near the blade tip.

At $Z = -0.012$, which is located upstream of the leading edge, the axial velocities are generally lower and the tangential velocities are higher at the off-design condition, relative flow

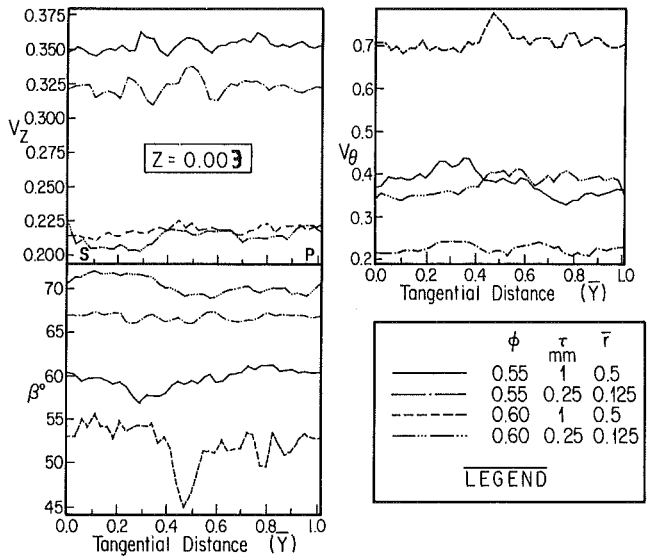

Fig. 9 Axial and absolute tangential velocity profiles and relative flow angles at $Z = 0.003$

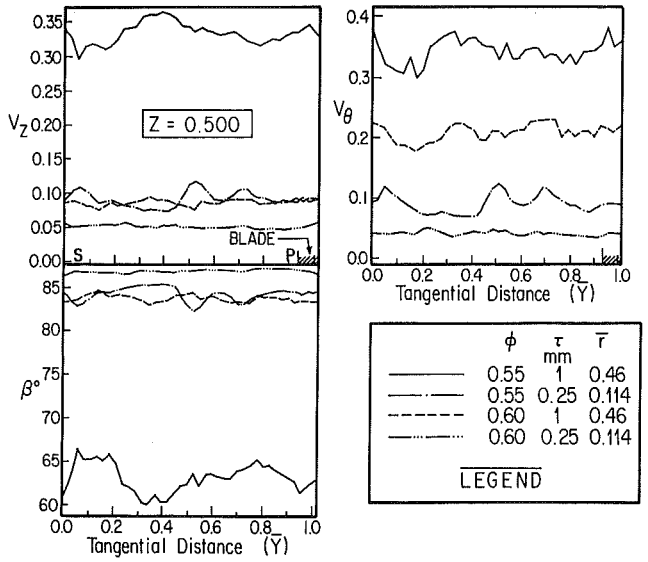

Fig. 10 Axial and absolute tangential velocity profiles and relative flow angles at $Z = 0.5$

angles are also higher at the off-design condition. The velocity distribution shows some nonuniformity in the circumferential direction. However, the maximum variation is less than 7 percent. This trend in the flow behavior is similar even at the leading edge ($Z = 0.003$) as shown in Fig. 9. Due to the scraping effect of the blade, the tangential velocities generally show a dramatic increase near the leading edge, especially at $\bar{r} = 0.5$ and the off-design condition. At the off-design condition, the axial velocities are generally lower and this is likely to increase the absolute tangential velocity. The flow turning is also larger between $Z = -0.012$ and $Z = 0$ at $\bar{r} = 0.5$ and $\phi = 0.6$.

The axial and absolute tangential velocity profiles at $Z = 0.5$ are shown in Fig. 10. The axial velocities generally decrease from $Z = 0$ to $Z = 0.5$, and this is more pronounced at the off-design condition. This seems to indicate that the annulus wall boundary layer growth is more rapid at the off-design condition. The tangential velocities also show dramatic decreases at the off-design condition. The inlet swirl generated near the leading edge of the blade is drastically

reduced as the flow proceeds from $Z = 0$ to 0.5, with relative flow angles nearly tangential at the off-design condition. The leakage flow tends to increase the relative flow angles and decrease the absolute tangential and axial velocities as shown in Fig. 7. The local lift coefficient shown in Fig. 5 seems to indicate that the leakage flow should be substantial in the region $0.25 < Z < 0.75$ at both the operating conditions.

The leakage velocities at the off-design condition should be smaller and hence its effect on the velocity distribution should be mild. The observed profile indicates (Fig. 10) that the circumferential nonuniformity of the axial, tangential velocity profiles and the relative angles are much smaller at the off-design condition. High leakage velocities produce a vortex due to the roll up of this crossflow and its interaction with the annulus wall boundary layer. This produces a circumferential nonuniformity in the velocity profiles and angles. The wakelike profile observed at the design for $\bar{r} = 0.46$ is probably caused by this effect. Absence of this effect at the off-design condition seems to indicate decreased leakage velocity.

The dominant influence of the leakage flow is felt at $Z = 0.75$ (Fig. 11). The axial velocity increases at all the locations. This is probably caused by the spanwise flow towards the tip due to the leakage flow. The axial velocities are generally lower inside the gap region. Large circumferential nonuniformity exists in this region. The axial and tangential components of velocity are very high upstream of the pressure side of the tip clearance region and low downstream of the suction side of the tip clearance region. A similar, but opposite trend is observed in the outlet angle distribution, at both the design and off-design conditions. This indicates that major effects of leakage flow and mixing exist in this region. The nonuniformities are very severe at $\bar{r} = 0.66$ and more pronounced at the design condition. A large change in the relative flow angle inside the gap at $\bar{r} = 0.66$ (increase from 54 to 75 deg across the tip clearance for the design, and increase from 67 to 80 deg for the off-design condition), reveal the major effects of leakage flow. Even though the blade is not unloaded completely in this region (see Fig. 5), the leakage velocities seem to be high. It is possible that the effects observed here are caused by the leakage flow which originated upstream (say, $Z \leq 0.5$), due to the stagger angle of the blade.

The tangential and the axial velocity distribution at $Z = 0.75$ (Fig. 11) indicates the presence of wakelike profiles near the midpassage at $\phi = 0.55$ and $\bar{r} = 0.66$. One possible reason for this dip, which is also observed [8] inside the passage and inward from the blade tip, is that the leakage flow travels farther away from the suction side (than in a cascade) due to the blade relative motion before mixing with the main flow. This mixing results in a loss of angular momentum (rV_θ), and kinetic energy in the mean flow. This phenomena, observed mainly at the design flow condition, seems to confirm

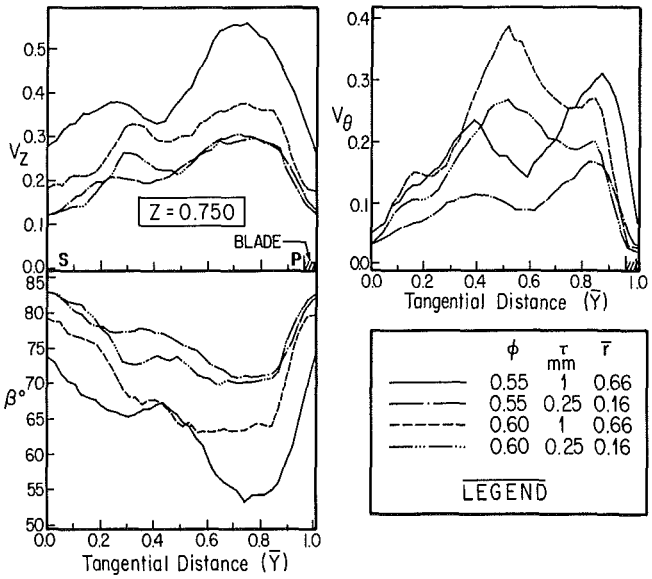

Fig. 11 Axial and absolute tangential velocity profiles and relative flow angles $Z = 0.75$

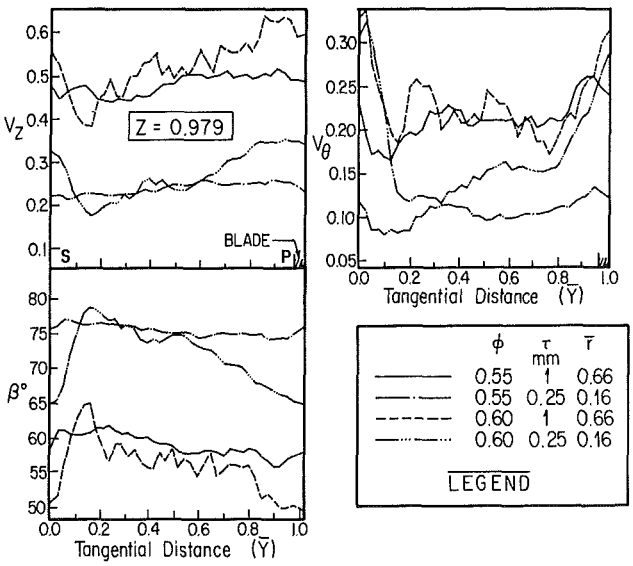

Fig. 12 Axial and absolute tangential velocity profiles and relative flow angles at $Z = 0.979$

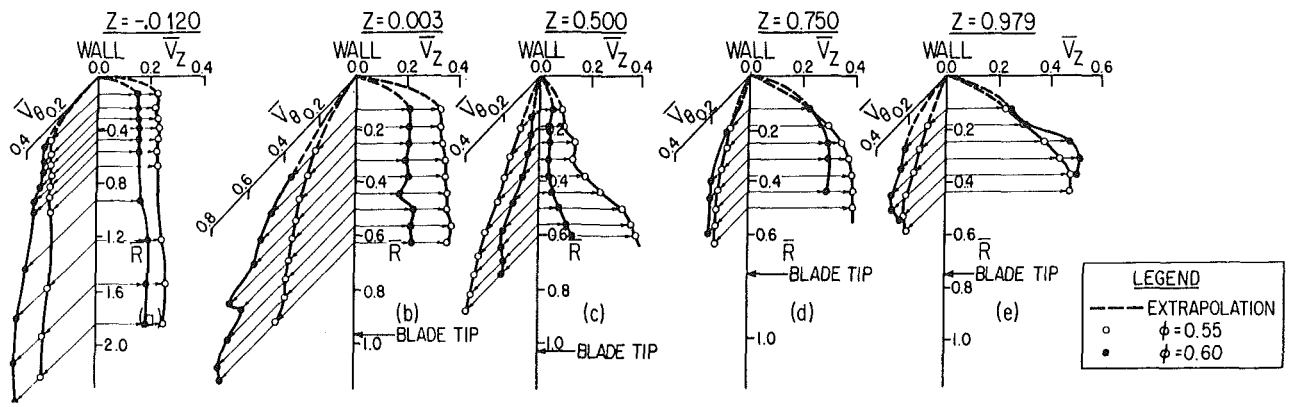

Fig. 13 Radial variation of passage-averaged axial and tangential velocity

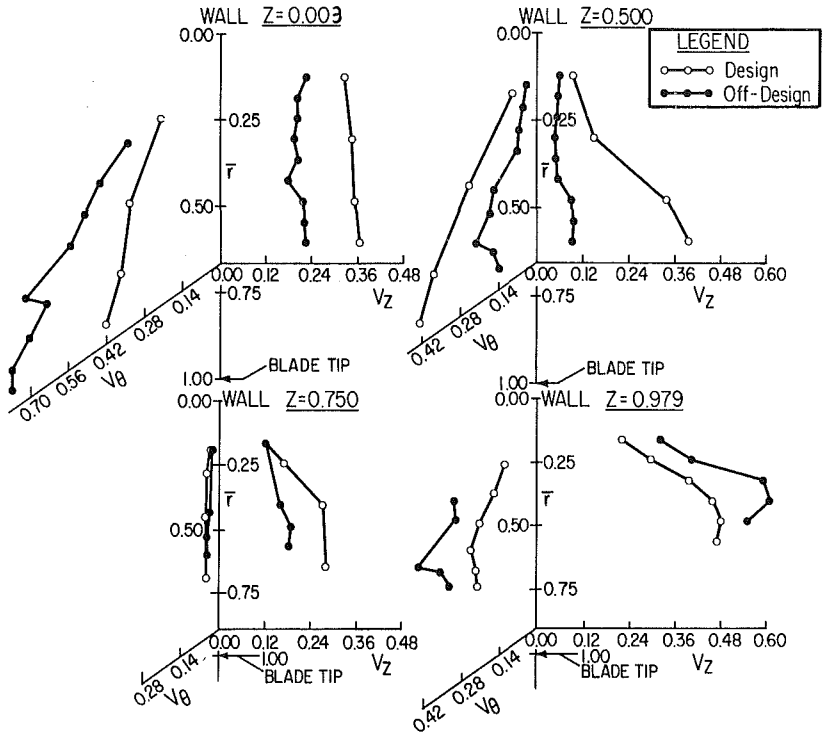

Fig. 14 Radial variation of axial and absolute tangential velocities inside the tip clearance region

stronger leakage flow and eventual roll up at $\phi = 0.55$. The dip at the center can also be interpreted as those caused by a leakage vortex. The magnitude of the defect in axial velocities near the midpassage at the off-design condition is not as severe as the design condition. The influence of leakage is reduced as the annulus wall is approached.

Substantial redistribution of the velocities and relative flow angles occur as the flow progresses from $Z = 0.75$ to $Z = 0.979$, as indicated in Fig. 12. The velocities at the design condition become nearly uniform across the passage, with a general increase in their values at most passage locations. However, the velocity profiles at the off-design conditions show that the effects of leakage flow persists even at this axial location, even though the effects are not as pronounced as those observed at $Z = 0.75$. The differences in the observed phenomena between the design and off-design conditions may be due to the type of blade pressure distribution observed.

The velocity profiles at the exit are found to be very similar at both design and off-design conditions. The data at the design condition can be found in [3] and the off-design condition in [5].

Annulus Wall Boundary Layer Development. The radial variation of the axial and the absolute tangential velocities, averaged over the blade passage at various axial locations, are plotted in Fig. 13 for $\phi = 0.55$ and 0.6. A detailed interpretation of the growth of the wall boundary layer in the clearance region at $\phi = 0.55$ is given in [3]. Major differences are observed in the development of the passage-averaged velocity profiles between $\phi = 0.6$ and 0.55. At $Z = 0.5$, both the velocity components are much smaller for $\phi = 0.6$. The axial velocities are generally lower for $\phi = 0.6$. This may be due to faster boundary layer growth and the resulting larger velocity defects in the clearance height region.

The boundary layer profiles are very unconventional (neither law of the wall or power law profile seem to be valid) due to complex interaction between the annulus wall boundary layer, the leakage flow, and the spanwise transport of the blade boundary layer and mixing of these flows downstream. It should be remarked here that $\bar{R} = 2$ or less represents a fraction of the annulus wall boundary layer thickness and the data shown in Fig. 13 represent the inner region of the annulus wall boundary layer.

Velocity Profiles Inside the Gap. The radial variation of the axial and the tangential velocity components inside the gap (midway between the pressure and the suction surfaces) is shown in Fig. 14. No measurement is available very close to the blade tip. As expected, the presence of the annulus wall boundary layer and the resulting defect in velocity is observed from the annulus wall to midclearance height ($\bar{r} \sim 0.5$). The data seem to indicate that the maximum velocity inside the gap occurs between the blade tip and the midclearance height. A decrease in axial velocity is observed between $Z = 0$ to $Z = 0.750$, and an increase from $Z = 0.75$ to 0.979, at both the operating conditions. These effects are more pronounced at the off-design condition. The axial velocities at $\phi = 0.6$ are lower than the values for $\phi = 0.55$, everywhere except at the trailing edge.

The tangential velocities, however, decrease rapidly from $Z = 0$ to $Z = 0.75$ (leakage flow region) reaching negligible values at $Z = 0.75$, it increases beyond $Z = 0.75$. As mentioned earlier, very high values of the tangential velocity component measured at the leading edge is probably due to blade scraping or "dragging" effects. The decrease in the tangential velocity in the clearance region in the axial direction is much more rapid at $\phi = 0.6$. Absence of any swirl at $Z = 0.75$ seems to indicate that the maximum leakage flow (which has a tendency to under turn the flow and guide the absolute flow more towards the axial direction) occurs upstream of this region.

The velocity components and the "force defect," averaged over the clearance height, are derived from the following equations

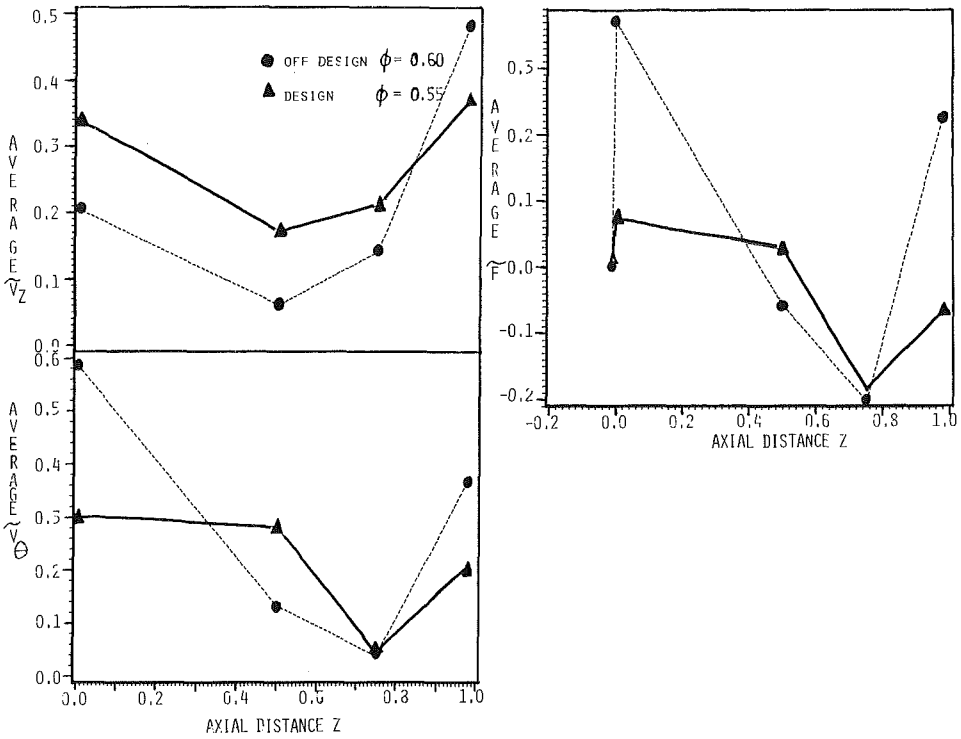

Fig. 15 Axial variation of the gap-averaged values of $\tilde{V}_z, \tilde{V}_\theta, \tilde{F}$

$$\tilde{V}_z = \frac{1}{\Delta r}\int_{\bar{r}_{\min}}^{\bar{r}_{\max}} V_z d\bar{r}, \quad \tilde{V}_\theta = \frac{1}{\Delta r}\int_{\bar{r}_{\min}}^{\bar{r}_{\max}} V_\theta V_z d\bar{r} \Big/ \tilde{V}_z$$

$$\tilde{F}_\theta = \frac{S}{\Delta r}\int_{\bar{r}_{\min}}^{\bar{r}_{\max}} (V_\theta - V_{\theta 1}) V_z d\bar{r} \Big/ S\tilde{V}_z$$

$\Delta r = \bar{r}_{\max} - \bar{r}_{\min}$, which are respectively the maximum and minimum location of $\bar{r}$ at which the data are available. The last quantity, termed "force defect" in this paper, is a measure of the loss in lift or force. Negative values of $\tilde{F}$ indicates a loss and positive values indicates a gain. Since there is no blade at this location, this quantity should be zero under ideal conditions. It should be remarked here that these gap-averaged quantities are approximate to the extent that there are no data close to the blade tip.

It is evident from Fig. 15 that the total mass flow through the gap decreases continuously till the midchord location and then increases. The increase in the mass flow beyond midchord could be attributed to the spanwise transport of the blade boundary layer toward the blade tip. The large increase in the mass flow for $\phi = 0.6$ beyond $Z = 0.75$ may be attributed to larger spanwise flow in the blade boundary layer associated with the off-design operation. The average tangential velocity also decreases continuously till $Z = 0.75$ (except for the design condition between $Z = 0$ to 0.5) and then increases. This trend seems to be consistent with the local lift coefficient (at the tip) plotted in Fig. 5.

The "force defect" $\tilde{F}$ increases (rapidly for the off-design condition) from $Z = -0.012$ to 0.003 due to blade dragging effect and then decreases continuously, reaching very high negative values up to $Z = 0.75$. This is an indication of the loss in the work done due to the blade leakage. But an increase in $\tilde{F}$ from $Z = 0.75$ to 1.0 seems to indicate that the leakage effects have subsided and the clearance flows have some turning. This concept of clearance flow sustaining lift and circulation has been postulated in [2] and [7].

Leakage Velocity. In the absence of any clearance between the rotor blade and the annulus wall, the flow should follow the blade contours near the blade surfaces, and the velocity component in the direction normal to the blade should be zero. Any deviation of the flow from the blade contour in the

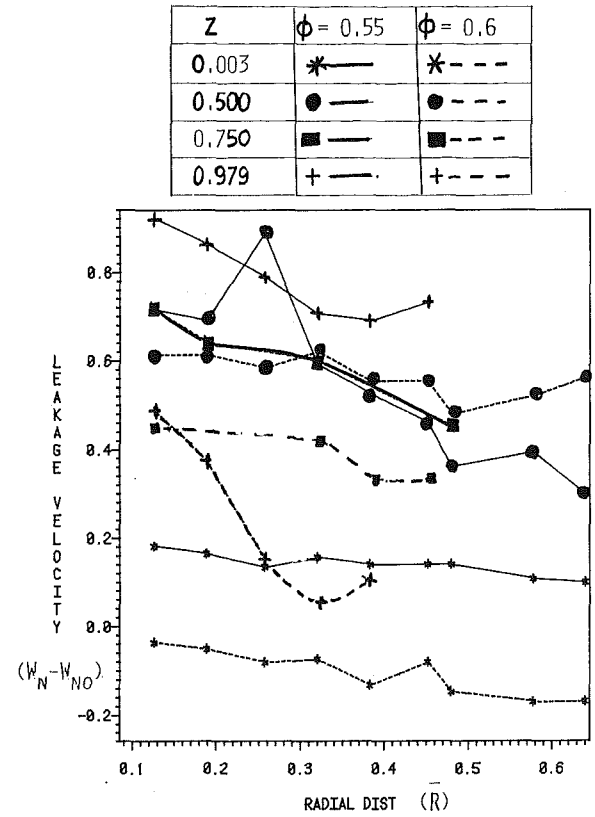

Fig. 16 Radial variation of leakage velocity on the suction side of the blade

tip-clearance region will give rise to a component normal to the blade, which is termed as the leakage velocity in this paper. A true representation of the leakage flow should take into account the normal component of the velocity at the inlet (W_{No}). The change in velocity triangle due to leakage flow is shown in Fig. 7. W_N is the leakage velocity in the terminology adopted in this paper; W' is the resultant velocity in the clearance region. In deriving the values of W_N near the blade surfaces, the value of β in Fig. 7 is taken to be respective blade surface angles.

Figure 16 shows the variation of the leakage velocity at the suction surface ($W_N - W_{No}$) in the radial direction at four axial locations inside the passage for $\phi = 0.55$ and 0.6. The velocities are normalized by the blade-tip speed and the inlet-component substracted from it. Near the leading edge, the leakage velocity is very small for $\phi = 0.6$ and small for $\phi = 0.55$, which is in accordance with the pressure gradient across the blade in this region (Fig. 5). A considerable jump in the leakage velocity at $Z = 0.50$ is due to the existence of a large pressure gradient across the blade in this region. The values at $\phi = 0.55$ are higher in the outer part of the clearance, otherwise they are generally of the same order of magnitude.

There is no appreciable change in the leakage velocity between $Z = 0.5$ and 0.75 at $\phi = 0.55$, but a substantial reduction in leakage velocity occurs for the off-design case ($\phi = 0.6$). This is consistent with the local lift coefficient (Fig. 5), where smaller values of C_l are observed for $X/C = 0.6$ and $\phi = 0.6$. But there is a drastic reduction in the leakage velocity for the off-design case as the flow approaches the trailing edge, but a small increase for the design case. The results at $Z = 0.979$ should be viewed with caution as the blade angle changes in this region are substantial. It is evident that the maximum leakage velocity occurs close to the mid-chord for $\phi = 0.6$, while for the design case large values are observed throughout the entire blade length, except very near the leading edge.

An estimate of the leakage flow that exists in an inviscid flow is made by applying the Bernoulli equation across the gap

$$W_N^2 = W_S^2 - W_p^2 = \frac{2(P_p - P_s)}{\rho U_t^2}$$

$$W_N = \sqrt{C_l}\,\frac{W_1}{U_t} \tag{1}$$

where subscripts s and p refer to local values on the suction and pressure sides, respectively. The local lift coefficient (at $R = 0.918$) plotted in Fig. 5 is used for this estimation. The measured values at $\bar{R} = 0.3$ (away from the wall and the blade tip, where the viscous effects are likely to be small) is compared with the estimated values in Fig. 17. The agreement is good everywhere, except near the trailing and leading edge regions of the blade. Good agreement between the estimated and the measured values should not be construed as a validation of the inviscid prediction method, as the viscous effects near the blade tip and the annulus wall are likely to affect the gap-averaged leakage velocity. But a preliminary analysis based on local lift coefficient should provide an estimate of the magnitude of the leakage velocity. Another word of caution is also in order. At very small clearance heights, the "retained lift," which is neglected in equation (1) may introduce inaccuracy in the estimation of the leakage velocity. In this particular case, the local lift coefficient (or k) at the tip is very small up to the midchord (Fig. 5), and this may account for the good agreement between the estimated and the measured values.

Concluding Remarks

It is evident from the measurements presented in this paper that the local lift coefficient or pressure difference, which is modified under off-design condition, has a significant effect on the leakage velocities in a rotor. The leakage velocities are substantial at most chordwise locations at the design condition. Dominant effect of the leakage flow is felt near $Z = 0.75$ at both operating conditions. A substantial redistribution in both the velocity components occur beyond $Z = 0.75$. The gap-averaged velocities and the "force defect thickness" in the gap decreases from the leading edge to about $Z = 0.75$, beyond which an increase is observed. This effect is more dominant at the off-design condition.

To understand the leakage phenomena and the eventual roll up of this flow into a vortex, it is essential to carry out detailed three-dimensional measurement of the flow field by nonintrusive techniques in the gap region as well as away from it.

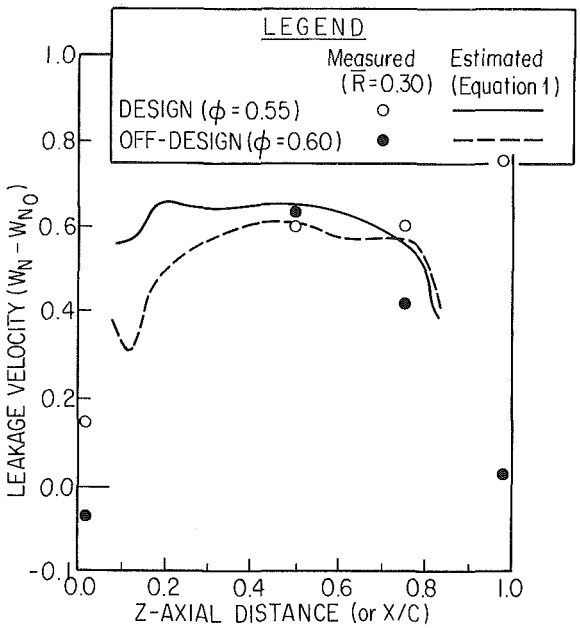

Fig. 17 Estimated and measured leakage velocity inside the gap

Acknowledgments

This work was supported by the National Aeronautics and Space Administration through Grant No. NsG 3212, with P. M. Sockol as the Project Monitor. Assistance from M. Pouagare and K. N. Sachidananda Murthy in the preparation of this paper is gratefully acknowledged.

References

1 Rains, D. A., "Tip Clearance Flow in Axial Flow Compressors and Pumps," California Inst. Tech. Mech. Eng. Lab. Report 5, 1956.

2 Lakshminarayana, B., "Methods of Predicting the Tip Clearance Effects in Axial Flow Turbomachinery," ASME *Journal of Basic Engineering*, Vol. D92, Sept. 1970, pp. 467-482.

3 Pandya, A., and Lakshminarayana, B., "Investigation of the Tip Clearance Flow Inside and at the Exit of a Compressor Rotor Passage: Parts 1 & 2, JOURNAL OF ENGINEERING FOR POWER, Vol. 105, 1983, pp. 1-17.

4 Lakshminarayana, B., "An Axial Flow Research Compressor Facility Designed for Flow Measurement in Rotor Passages," ASME *Journal of Fluids Engineering*, Vol. 10, No. 4, Dec. 1980, pp. 402-411.

5 Pandya, A., "Investigation of the Tip Clearance Flow Inside and at the Exit of a Compressor Rotor Passage," M. S. thesis, Department of Aerospace Engineering, The Pennsylvania State University, Mar. 1982.

6 Sitaram, N., and Lakshminarayana, B., "End Wall Flow Characteristics and Overall Performance of an Axial Flow Compressor Stage," NASA CR 3671, 1983.

7 Lakshminarayana, B., and Horlock, J. H., "Leakage and Secondary Flows in Compressor Cascades," British ARC R&M 3483, 1967.

8 Lakshminarayana, B., Pouagare, M., and Davino, R., "Three-Dimensional Flow Field in the Tip Region of a Compressor Rotor Passage," JOURNAL OF ENGINEERING FOR POWER, Vol. 104, 1982.

F. A. H. Breugelmans

Y. Carels

M. Demuth

von Karman Institute for Fluid Dynamics,
B-1640 Rhode Saint Genese, Belgium

Influence Of Dihedral on the Secondary Flow in a Two-Dimensional Compressor Cascade

Introduction

The secondary flow is important in the accurate prediction of the flow field in turbomachines. It arises from annulus wall boundary layer buildup, blade end clearance effects, blade-to-blade pressure gradients producing a crossflow, relative motion between blade and wall, and centrifugal effects resulting in an accumulation of low energy boundary layer material.

The development of secondary flow is governed by the balance of forces acting on the fluid. The type of vortex law chosen for a given meridional flow path produced the radial equilibrium and more in particular the positioning in space of the blade elements generates additional radial force components. This results from the relative freedom in choosing of the stacking line within the mechanical constraints. Sweep and dihedral may be introduced to exert a control on the secondary flow evolution.

The dihedral or lean angle effect on the radial equilibrium are discussed by Vavra [1] and Smith [2, 3], who showed that the effect on the radial pressure gradient is proportional to the tangent of the dihedral angle. Smith discusses in detail the dihedral and sweep effects and advises on incidence angle and solidity to be considered for the cascade. The dihedral effect is smaller than the sweep influence and the downwash (flow turning) perturbation changes sign along the blade chord. The meridional curvature tends to be important in the axisymmetric stream surface solution when dihedral is introduced. This effect will show up in the yaw and bank angle of the flow in a rectilinear cascade. The constraint of matching the endwall may result in significant flow angle variations. Novak [4] discusses the lean angle effect on a turbine nozzle configuration in which a reversal of the spanwise distribution of the mean static pressure in the blade is predicted with and without 10 deg lean angle. At the trailing edge plane, only a slight difference between the two cases is observed, since there the transverse pressure gradient becomes zero. The effect of fillet geometry studied by Debruge [5] included also the considerations of dihedral in the prediction of the boundary layer development in the corner.

Numerous experimental investigations of secondary flow development have been performed. Salvage [6] derived his conclusions on longitudinal and crosswise boundary layer development and on secondary flow magnitude and distribution based on 43 different compressor cascade experiments. Dejc and Trojanowski [7] describe experiments in annular turbine nozzle cascade where positive and negative dihedral angles (Δ) of $+13$ and -14 deg produce large variation of the loss in the hub region. Other experiments with $\Delta = +20$ to -20 deg show a symmetric influence on tip and hub with an increase of the midspan loss. In this case, the model has a small aspect ratio. It is mentioned that meridional contouring has to be combined with leaning the blades and this geometrical freedom provides a larger control on the degree of reaction. It is suggested to use a curved blade in order to obtain a beneficial effect at the root and tip radius. The experiments are carried out on curved blade with 0 deg dihedral at the tip. An improvement is observed over the lower 2/3 of the span when compared to the radial blades. The aspect ratio and hub-tip ratio seem to be a factor in the loss distribution, since they determine the relative importance of the secondary flow with respect to main flow as defined by the radial pressure gradient.

The experiments reported herein are concerned with the dihedral effect in a rectilinear compressor cascade at nominal incidence.

Experimental Facility and Instrumentation

The Facility. The experimental rig is the low-speed cascade tunnel C-1 of the von Karman Institute. It is a continous flow facility with a rectangular cross section of 127 × 500 mm (Fig. 1). A large centrifugal blower pumps air into the settling chamber, which is equipped with screens. A large contraction guides the flow into the rectangular duct towards the rectilinear cascade model. The inlet duct is equipped with slots in the endwalls and with porous and deformable walls at the top and bottom in order to remove the boundary layer buildup in and control the axial velocity ratio across the cascade. However, suction through the slots is not applied and solid endwalls are used in order to avoid any recirculation through porous walls for these tests.

The inlet velocity can be controlled by the continous speed adjustment of the 18-kW d-c blower. The amount of suction, when applicable, can be controlled independently by valves in

Contributed by the Gas Turbine Division and presented at the 1983 Tokyo International Gas Turbine Congress, Tokyo, Japan, October 24–28, 1983. Manuscript received by the Gas Turbine Division June 9, 1983. Paper No. 83-GTJ-12.

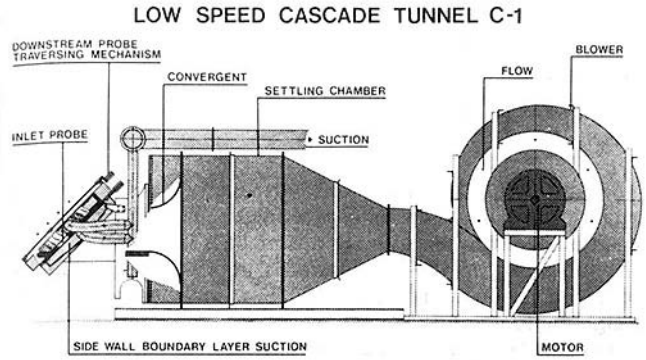

Fig. 1 Low-speed cascade tunnel

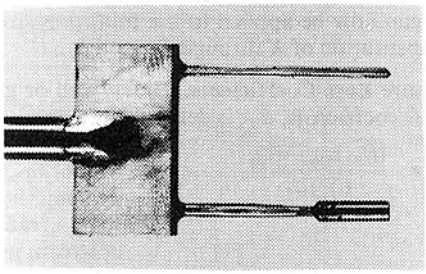

Fig. 2 Combined pressure probe

the piping to the 45-kW a-c suction blower. The inlet flow survey plane is fixed at 120 mm in front of the blade midchord position; the downstream surveys can be performed in the span- and pitchwise directions in planes parallel to the blade trailing edges. The maximum air speed is 40 m/s, and the tunnel is of the nonreturn type, discharging into the atmosphere. Compressor and turbine cascades can be accommodated.

The Instrumentation. The upstream flow field is measured with a directional probe, NACA short prism type, for which the calibration procedure is described in [8]. The downstream surveys are performed with a multihead probe (Fig. 2) in which the total pressure sensing port was separated from the directional sensing holes by 20 mm. The stagnation pressure is obtained and no calibration corrections are needed due to the vented shield around the measuring tube. The 20 mm separation minimizes the interference with the four-hole probe head for yaw and pitch angle detection. All tubes are of 1 mm dia. The probe is fully described in [6].

The calibration curves are determined using the technique of [9, 10] in which yaw, pitch, static, and dynamic coefficients are determined for yaw and pitch angle variations of ±30 deg. This calibration confirmed the insensitivity to angular

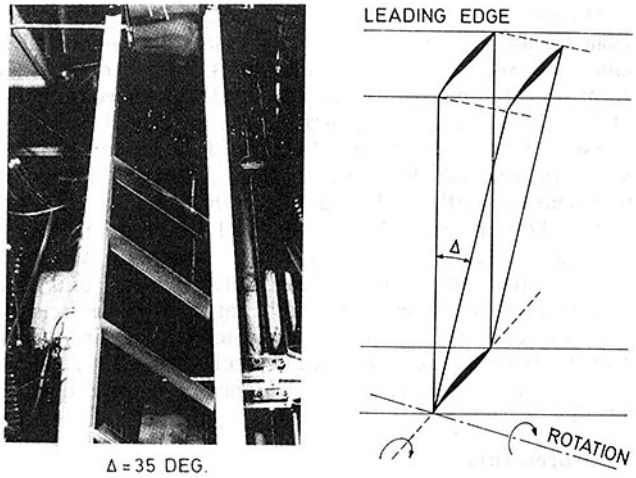

Fig. 3 Cascade model with dihedral-no sweep

variations of the total pressure reading. The pressure tappings are connected to strain gage pressure transducers, whose signal is amplified and stored on a magnetic tape using a microprocessor-controlled eight-channel data logger.

The Compressor Cascade Model. The blades are NACA 65-12 A_{10} −10 airfoils as described in [11] with a chord of 127 mm, solidity and aspect ratio of unity, a stagger angle of 28.9 deg and a nominal air inlet angle of 45 deg, corresponding to an incidence angle of −1.1 deg when dihedral is zero. This configuration has been extensively investigated in [6]. The effect of dihedral is investigated for dihedral angles from 0 deg (reference) to 35 deg. Dihedral, or the blade not normal to the endwall, is introduced by rotation of the two-dimensional blade around the chordwise direction. This operation introduces a change of the incidence angle, adds a slight sweep angle to the cascade model and modifies slightly the aspect ratio and solidity. The incidence angle is corrected by a modification of the stagger angle according to Table 1 [12]:

Table 1

$$\Delta_\gamma = (\beta_1' - \gamma)_{\Delta=0} - \text{ARCTG}\frac{tg(\beta_1' - \gamma)_{\Delta=0}}{\cos\Delta}$$

or

Δ	Δγ	Δ	Δγ
0°	reference	25°	−1.5°
15°	−.5°	35°	−3.1°

Nomenclature

AVR = axial velocity ratio
DF = diffusion factor
q = dynamic pressure
Re = Reynolds number
V = velocity
i = incidence angle
α = angle of attack
β = flow angle = ATAN(V_θ/V_x)
γ_2 = exit yaw angle-ATAN(V_s/V_x)
δ = boundary layer thickness
δ^* = boundary layer displacement thickness
Δ = dihedral angle
ϵ = sweep angle
θ = boundary layer momentum thickness
θ_2 = exit bank angle = ATAN(V_s/V_θ)
σ = solidity
ω = total pressure loss coefficient

Subscripts

0 = stagnation conditions
1 = inlet
2 = outlet
BL = boundary layer
c_1 = based on chord and inlet velocity
MS = midspan
PROF = profile
s = spanwise with Δ = 0 deg as reference direction
sec = secondary flow related
T = overall
x = axial component
θ = pitchwise direction

Superscripts

—— = pitchwise integrated
═══ = pitch- and spanwise integrated
= tangent to camberline

The sweep angle, formed by the projection of the leading edge on an axial plane and the normal to the endwall is eliminated by a rotation around an axis normal to the plane formed by leading edge and chord. The 35 deg dihedral model and the sweep angle compensation are illustrated in Fig. 3. These rotation angles are 9.2, 14.9, and 19.8 deg for the three value of the dihedral. The solidity increases from 1.0 (reference) to 1.01, 1.03, and 1.06 with an aspect variation from 1.0 (reference) to 1.02, 1.06, and 1.14 for the increasing dihedral angle. The effective blade maximum thickness changes from 10 to 10.3 percent, 11.0 percent, and 12.2 percent as well as the effective camber angle. These effects are not corrected for in the blade construction since two-dimensional blades are cast and the ends cut to fulfill the no sweep requirement with a zero clearance fit at the end walls, 127 mm apart.

Measurements

The measurements are performed in planes parallel to the cascade leading and trailing edge plane. The inlet flow survey is performed at a plane 56 mm axially in front of the leading edges; the inlet boundary layer on both endwalls is measured with a boundary layer probe, which is exchanged for a NACA prism-type probe for the midspan traverses of the cascade and control of the tunnel speed. The outlet flow field is measured at 21 equally spaced traversing planes 10 mm axially downstream of the trailing edges. This distance is kept constant for all spanwise measurements. Two inlet boundary layers are used: the naturally developed one and an artifically thickened one using triangular vortex generators of 7 mm edge and fixed on the end walls, 1 m upstream of the central blade. The boundary layer parameters on the end wall are given in Table 2. These values are averages of the measurements on both endwalls and the boundary layer thickness difference between the two sides is 1 mm, with almost identical velocity profiles. The vortex generators have been interchanged in order to prove that the dihedral effects are not masked by an eventual disymmetry in the inlet flow

Table 2

	Reference	Artificially thickened
δ	18 mm	32 mm
δ^*	2.3 mm	3.5 mm
θ	1.7 mm	2.1 m

Turbulence levels in the inlet plane at the midspan position of Tu = 0.8 percent and 1.25 percent are measured for the two inlet boundary layer thickness. No special effects on the pitchwise periodicity are observed when comparing the dihedral with the reference case.

The local total pressure loss coefficient and the downstream flow vector are obtained through the calibration curves of the multiple head probe. Mass-and area-averaged quantities are calculated for each pitchwise survey. The following procedure is used in defining these values: the average value, $\bar{\bar{X}}$, of the parameter $X(s,\theta)$ a function of two variable, is given by

$$\bar{\bar{X}} = \frac{\int_{\theta_1}^{\theta_2}\int_{S_1}^{S_2} X(s,\theta)W(s,\theta)dsd\theta}{\int_{\theta_1}^{\theta_2}\int_{S_1}^{S_2} W(s,\theta)dsd\theta}$$

where $W(s,\theta)$ is a weighting function dependent, in general, upon the two spatial variables. A double bar(=) over a flow property indicates the results of averaging over the entire half-plane of measurement. For s equal to a constant, the equation degenerates into the form

$$\bar{X}(s) = \frac{\int_{\theta_1}^{\theta_2} X(s,\theta)W(s,\theta)d\theta}{\int_{\theta_1}^{\theta_2} W(s,\theta)d\theta}$$

Thus, a single bar (−) over a flow property indicates that the quantity results from pitchwise averaging. The spanwise position at which this average was made is indicated by either the subscript MS if the midspan is implied or by (s) if the spanwise position is arbitrary. For area averaging, the weighting function W is given by: $W = 1$, everywhere.

For mass flow averaging in incompressible flows: $W(s,\theta) = \rho V(s,\theta)\cos\beta(s,\theta)$, since density is constant and where $V\cos\beta$ is the axial component of the velocity vector at (s,θ). This procedure can now be applied to the total pressure and flow angle by substitution of X through P_{02} and β_2.

Total Pressure Loss Coefficients. The overall or global total pressure loss coefficient, $\bar{\bar{\omega}}_T$, is defined by

$$\bar{\bar{\omega}}_T = \frac{(\overline{P_{01}})_{MS} - \bar{P}_{02}}{(\bar{q}_1)_{MS}}$$

where $(\bar{q}_1)_{MS}$ is the dynamic head at mid span read on the upstream probe.

A local coefficient, $\omega(s,\theta)$, may be defined as

$$\omega(s,\theta) = \frac{(\overline{P_{01}})_{MS} - P_{02}}{(\bar{q}_1)_{MS}}$$

local loss coefficient

Average results for $\bar{\omega}(s)$

$$\bar{\omega} = \frac{(\overline{P_{01}})_{MS} - \overline{P_{02}}_{(s)}}{(\bar{q}_1)_{MS}}$$

pitchwise integrated loss coefficient

Loss in total pressure attributed to secondary flow is here defined as follows: $\bar{\omega}_{sec} = \bar{\omega}_T(s) - \bar{\omega}_{BL}(s)$ where $\bar{\omega}_{BL}(s)$ is the loss measured at the same plane due to the boundary layer, when the blades are not installed. In the same way: $\bar{\bar{\omega}}_{sec} = \bar{\bar{\omega}}_T - \bar{\bar{\omega}}_{BL}$.

Outlet Flow Angle Averaging. Two types to outlet flow angle are encountered:

β_2: Local

$\bar{\beta}_2$: Pitchwise mass average, obtained with the above described method.

Experimental Results

All experiments are performed at an inlet Reynolds number Re_{c1} of 2.1×10^5, exploring the central passage, while allowing for a suitable overlap to provide for the physical separation of the different heads on the probe and for the dihedral angle. No suction is applied through the upstream slots, and the endwalls are solid. The results are presented as isolines for the parameter to be considered, remembering that the blade suction surface is facing downwards when looking into the exit flow field. The blade dihedral has been chosen such that an acute corner is formed between the endwall and the suction surface on the left-hand side.

Total Pressure Losses. The total pressure loss coefficient (ω) contours for the 0, 15, 25, and 35 deg dihedral with the reference and artificially thickened inlet boundary layer are shown in Fig. 4. The aspect ratio is exagerated in the plottings due to the different scale factors for the span- and pitchwise directions. The accumulation of losses in the suction surface

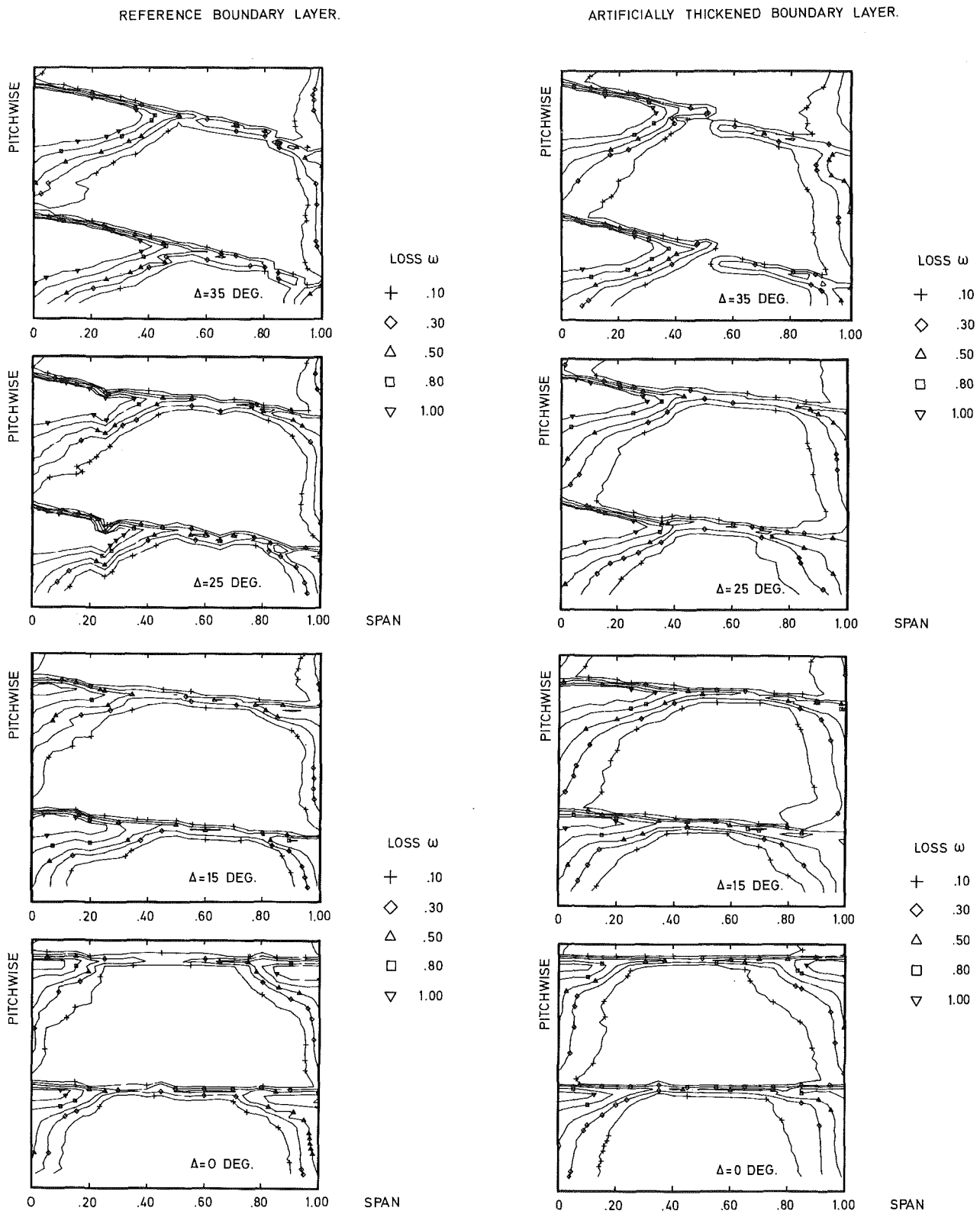

Fig. 4 Iso-loss contours for 0 to 35 deg dihedral

endwall corner are shown, and slight differences are caused by the nonidentical inlet boundary layer on the left- and right-hand side (0 deg dihedral). A small amount of dihedral (15 deg) produces a sufficient spanwise pressure gradient to suppress almost completely the development of a large loss zone in the large corner. The losses along the endwall, between two successive blades, equal the inlet boundary layer loss on the right-hand endwall when excluding the blade wakes. On the opposite wall, a large secondary flow loss zone develops, spreading out to midspan and covering 100 percent of the pitch at the endwall for 35 deg dihedral case.

The pitchwise integrared loss values are compared in Fig. 5 on which the inlet boundary layer loss profile is also shown. The difference is caused by the secondary flow development

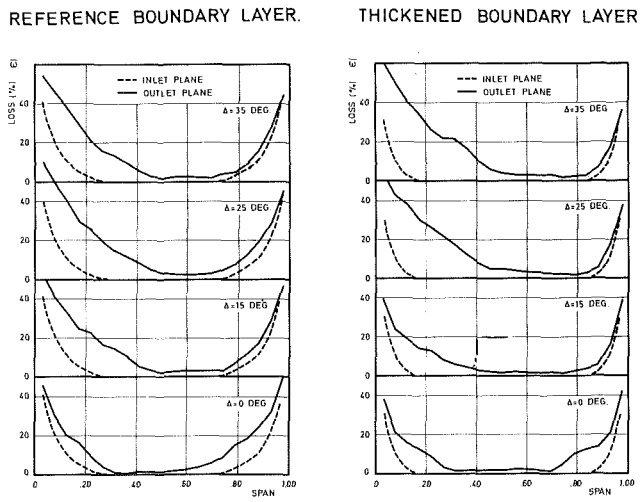

Fig. 5 Pitchwise integrated total pressure loss

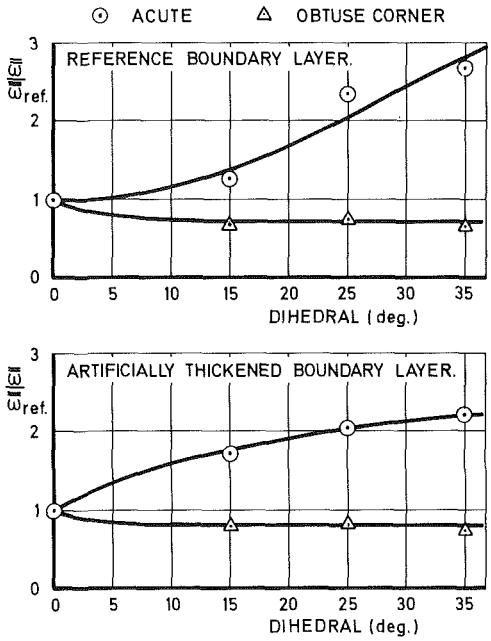

Fig. 6 Spanwise integrated total pressure loss

through the blading. The application of dihedral changes this spanwise distribution in an important manner. Very quickly, a doubling of losses occurs on the acute angle side, while one approaches the inlet loss distribution on the right-hand side for 15 to 35 deg dihedral. The losses at 25 and 35 deg dihedral reached a level where the inlet boundary layer effect does not modify the distribution, and the high loss region occupies 25 percent of the area.

The overall loss is compared in Fig. 6 to the 0 deg, dihedral configuration, using the left-and right-hand side of the blade span. The overall losses are rapidly reduced on the half-span with the obtuse corner and this at moderate diheral angles for both inlet boundary layer thicknesses. The blade half-span with the acute corner demonstrates a sharp increase in loss with respect to the reference case as shown and the beneficial effect cannot compensate the detrimental evolution on the opposite end wall.

The diffusion factor, *DF*, is calculated at the spanwise minimum loss position using the expression

$$\mathrm{DF} = 1 - \frac{\bar{V}_2}{V_1} + \frac{\bar{V}_{\theta_1} - \bar{V}_{\theta_2}}{2\sigma V_1}$$

where the inlet midspan velocity and the pitchwise-averaged outlet velocity components are used. The axial velocity ratio is calculated using the pitchwise-averaged velocity components $\bar{V}_{x2}$. The DF increases from 0.29 ($\Delta = 0$ deg) to 0.33 ($\Delta = 35$ deg) and AVR from 1.15 to 1.19 for the reference inlet boundary layer case. A lower DF of 0.24 and higher AVR 1.21 is observed for the artificially thickened inlet boundary layer.

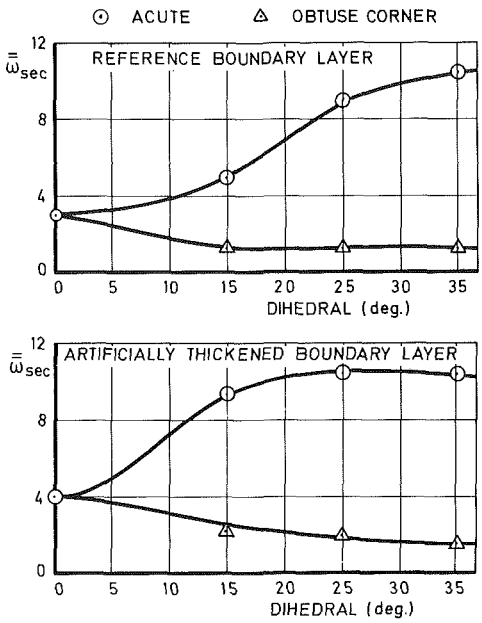

Fig. 7 Secondary flow loss

The secondary loss is that part of the total loss which is not present in the inlet wall boundary layer and in the mid span blade wake, under the assumption that the sidewall flows have not merged over the blade suction surface. The inlet boundary layer profiles are shown in Fig. 5, together with the pitchwise averaged total pressure losses. The secondary loss (Fig. 7) is reduced already by almost 50 percent for a moderate dihedral of 15 deg and little or no benefit is obtained on the obtuse angle side of the cascade model for a further increase in dihedral. The large increase in secondary loss on the opposite side is strongly dependent on inlet boundary layer thickness and dihedral as shown. The evolution towards a limit loss level, as for the total loss, seems to occur. The severity of the secondary loss for $\Delta = 35$ deg and reference inlet boundary layer is equal to the $\Delta = 25$ deg and thickened inlet boundary layer case. The local maximum of $\bar{\omega}_{sec}$ is located at 12 percent span of the high-loss side.

Exit Flow Angle. The exit flow angle distributions of $\overline{\beta_2}$, results of mass averaging in the pitchwise direction, are shown in Fig. 8. The two dimensional value of 21.4 deg is obtained over the central part of the span for the reference case. The secondary flow develops as the dihedral angle increases and the left-hand side degrades until, at $\Delta = 35$ deg, such a large corner separation has occurred that the results in that area are less reliable. The overturning, limited to roughly the inlet boundary layer thickness for $\Delta = 0$ deg, spreads towards the midspan and influences the total field at the highest dihedral $\Delta = 35$ deg investigated. The reference mechanical angle β_2 at the trailing edge is 13.9 deg for the 30 deg equivalent camber angle, the slope at the trailing edge as calculated from the coordinates provides $\beta_2 = 9.8$ deg. The deviation angle predictions are 7.5 deg (NACA-2D method) and 8.1 deg (Carter's rule for circular camberline), which results into an exit flow direction of 21.6 to 22 deg. The compensating correction to the stagger angle (Table 1) decreases the outlet flow angle predicted to 21.5 deg ($\Delta = 15$ deg); 20 deg ($\Delta = 25$ deg) and 18.9 ($\Delta = 35$ deg), respectively. This trend is experimentally observed at midspan.

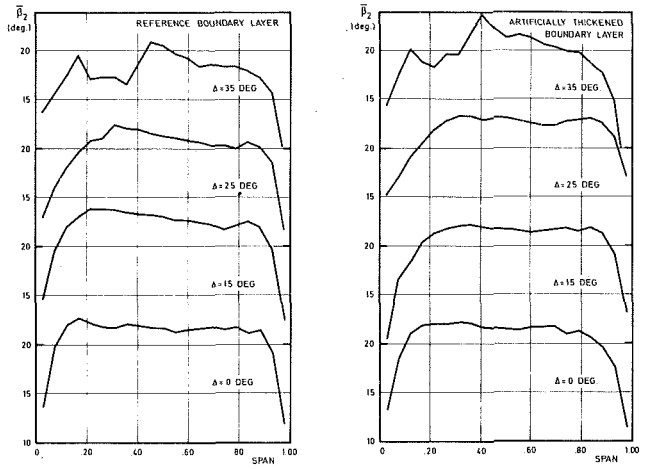

Fig. 8 Pitchwise integrated exit flow angle

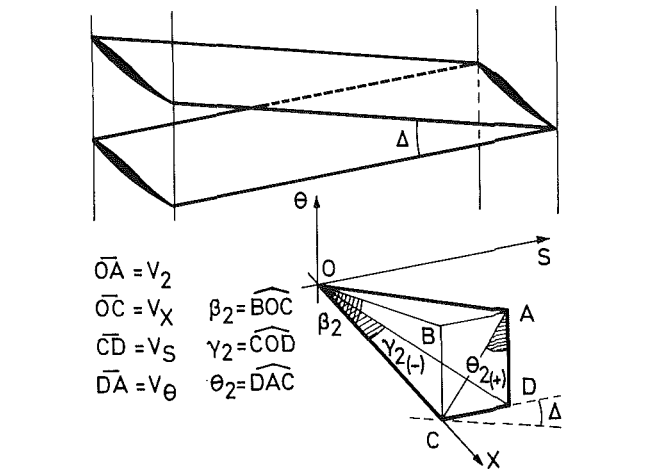

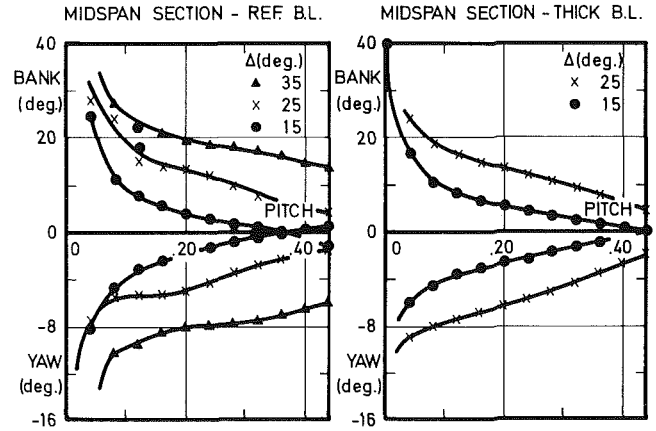

Fig. 9 Yaw and bank angle at midspan

Three velocity components are calculated from the measurements: V_x, V_θ, V_s which provide the exit flow angle β_2, the yaw angle γ_2, and the bank angle, θ_2 as defined in Fig. 9. The bank and yaw angle are compared at the midspan position for the different dihedral angles. The center of the wake is at position 0, and a bank angle equal to the complement of the dihedral corresponds to an exit velocity vector in a plane parallel to the blade trailing edge. Large bank angles are observed near the suction surface and the spanwise motion is demonstrated in the vicinity of the suction surface. The skewing of the exit velocity profile, observed in the pitchwise direction, extends over 30 percent for the smallest dihedral and almost a complete pitch is required at 35 deg dihedral as shown.

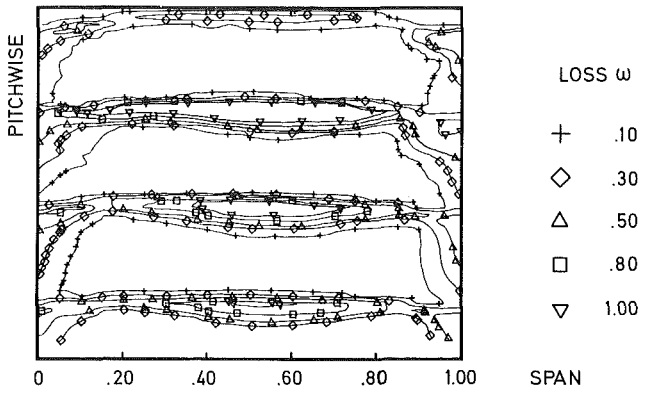

Fig. 10 C-7 curved airfoil. Iso-loss contours

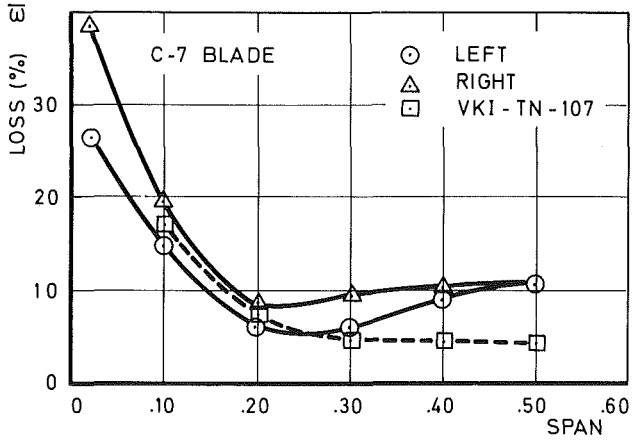

Fig. 11 C-7 pitchwise integrated total pressure loss

Comparison. The downwash perturbation is predicted in function of the chordwise direction for $\Delta = +30$ to -40 deg. The cascade model of this investigation has a positive and negative dihedral on either endwall and different perturbations are remarked at the 100 percent chord position. This effect shows up in the averaged outlet flow angle by the slope of the curves for $\Delta = 15$ and 25 deg in Fig. 8. The large loss zones mask the effect near the wall. The effect is small, as predicted by Smith [2]. The artificially thickened inlet boundary layer case is on the borderline where low aspect ratio effects influence the secondary flow development as presented by Salvage [6]. This could be an indication to the differences observed in the results with the two inlet boundary layers. The observation in [6] that inlet boundary layer thickness does not influence the secondary flow loss under certain assumptions, such as no corner stall and a sufficient aspect ratio, is not verified for all Δ values investigated.

Curved Blade. The beneficial effect of the obtuse corner, observed in the previously described experiments, could be introduced on both endwalls by using a curved stacking line. The C-7 blade section of [6] is chosen for constructional reasons and an arc of a circle forming a 20 deg dihedral angle with the walls is defined. The midspan, being the symmetry plane, corresponds to the endwall where the large loss development occurred. This 8-C-7 blade has a chord of 85 mm, camber of 45 deg, stagger equals 23 deg, solidity and aspect ratio are respectively 1.0 and 1.53. The reference inlet wall boundary layer is applied. The iso-loss lines show a variable wake thickness in the spanwise direction, with a double of the wake extension at the midspan location as shown in Fig. 10.

The pitchwise-averaged total pressure loss is shown in Fig. 11 and compared with the results of the reference configuration as given in [6]. The losses at the endwall do not

demonstrate the beneficial effect of the dihedral, while the midspan loss is doubled. The spanwise motion enhanced the secondary flow development in one endwall. This is translated at the midspan position of this curved 8-C-7 blade by an increased diffusion on the highly cambered blade. The inlet Reynolds number of 1.40×10^5 is in the critical region and additional effects such as laminar separation or bubble bursting may be enhanced by the geometrical modifications.

A critical Reynolds number for sudden secondary loss increase has been determined at 1.55×10^5 [6]. The partially curved blade described by Dejc did not yield better results at the outer radius when compared to the radial blades when the tests on a low aspect ratio nozzle do suggest that an obtuse angle between end wall and suction surface does improve the secondary loss situations [7].

Conclusions

Dihedral influences strongly the development of the secondary flow in a rectilinear compressor cascade model at nominal incidence.

The overall loss and loss distributions in the spanwise direction are modified in an important way by the dihedral effect and additional correction are needed in detailed flow prediction methods.

Opposite effects are observed on both endwalls. The secondary flow in the acute angle, between suction surface and endwall, develops into a large corner stall. On the side of the obtuse angle, the secondary flow is suppressed.

The combination of obtuse angles at both end walls did not yield the expected improvements.

References

1 Vavra, M. H., *Aero-Thermodynamics and Flow in Turbomachines*, J. Wiley & Sons, 1960.

2 Smith, L. H., and Yeh, H., "Sweep and Dihedral Effects in Axial Flow Turbomachinery," ASME *Journal of Basic Engineering*, Vol. 85, No. 2, Sept. 1963, pp. 401–416.

3 Smith, L. H., "The Radial Equilibrium Equation of Turbomachinery," ASME JOURNAL OF ENGINEERING POWER, Vol. 88. No. 1, Jan. 1966, pp. 1–12.

4 Novak, R. A., and Hearsey, R. M., "A Nearly Three-Dimensional Intra-Blade Computing System for Turbomachinery," ASME *Journal of Fluids Engineering*, Vol. 99, No. 1, March 1977, pp. 154–166.

5 Debruge, L. L., "The Aerodynamic Significance of Fillet Geometry in Turbocompressor Blade Rows," ASME JOURNAL ENGINEERING POWER, Vol. 102, No. 4, Oct. 1980, pp. 984–993.

6 Salvage, J. W., "Investigation of Secondary Flow Behavior and Endwall Boundary Layer Development Through Compressor Cascades," VKI TN 107, June 1974.

7 Deich, M. E., and Trojanowski, B. M., "Untersuchung und Berechnung axialer Turbinestufen," Berlin, *VEB Verlag Technik*, 1977, pp. 405–413.

8 Erwin, J. R., "Experimental Techniques," *Aerodynamics of Turbines and Compressors*, Vol. X of High Speed Aerodynamics and Jet Propulsion, Princeton University Press, 1964, pp. 167–269.

9 Shepperd, I. C., "A Four-Hole Pressure Probe for Fluid Measurement in Three-Dimensions," ASME *Journal of Fluids Engineering*, Vol. 103, No. 4, Oct. 1981, pp. 590–594.

10 Treaster, A. L., and Yocum, A. M., "The Calibration and Application of Five-Hole Probes," Pennsylvania State U., TM 78-10, Jan. 1978.

11 Felix, A. R., and Emery, J. C., "A Comparison of Typical NGTE and NACA Axial Flow Compressor Blade Sections in Cascade at Low-Speed," NACA TN 3937, 1957, p. 25.

12 Carels, Y., and Breugelmans, F. A. E., "Influence of Dihedral on the Secondary Flow in a NACA 65 Series Compressor Cascade," VKI PR 1982-25.

Experimental Measurement of Alford's Force in Axial Flow Turbomachinery

J. M. Vance
Professor of Mechanical Engineering,
Texas A&M University,
College Station, Texas 77843

F. J. Laudadio
Mechanical Engineer,
Motorola Corporation.

This paper presents the results of experimental measurements made on a small, high-speed, axial-flow test apparatus to verify the existence of Alford's force and to investigate the validity of his mathematical prediction model. The measurements show that the cross-coupled aerodynamic force is linearly proportional to rotor eccentricity, and to stage torque, as predicted by Alford's theory. However, it was found that the force is also speed-dependent, and that the inlet flow conditions to the stage have a pronounced effect. For some special combinations of rotor speed and stage torque, the direction of the force is reversed.

Introduction

In 1965, J. S. Alford published a theory and mathematical model [1] which predicted that rotor eccentricity in axial-flow turbomachinery would produce cross-coupled (normal to the eccentricity) aerodynamic forces on the rotor as a result of the circumferential variation of blade-tip clearance. Ever since then, the theory has been used (without experimental verification) by rotor dynamicists as one of the few mathematical models available to calculate the cross-coupled aerodynamic stiffness coefficients required for rotordynamic stability analysis of axial-flow turbomachinery.

This paper presents the results of experimental measurements made on a small, high-speed, axial-flow test apparatus to verify the existence of Alford's force and to investigate the validity of his mathematical prediction model.

There are a number of excitation mechanisms which cause rotordynamic instabilities in turbines and compressors [2]. An instability in turbomachinery is said to occur when the shaft precesses about the bearing centerline (whirling) with unacceptable amplitudes, at frequencies nonsynchronous with shaft speed. In many instances, the amplitude of whirl is large enough to damage bearings and seals.

Rotor unbalance is not a primary source of excitation for rotordynamic instability, since the centrifugal force from unbalance rotates at shaft speed. Rather, most of the destabilizing excitations come from fluid forces around the bearings, seals, and bladed disks on the rotor. Alford's force is one of these.

In mathematical terms, an instability occurs when an eigenvalue of the equation that describes the motion of the rotor has a positive real component. This implies a linearized stability analysis, with the unstable solution growing exponentially with time. Experience has shown, however, that the nonsynchronous vibration observed in turbomachinery often has bounded amplitudes. Reference [3] shows how a linearized stability analysis can usually predict the onset of the motion, since the initial small amplitudes are compatible with the assumption of the analysis.

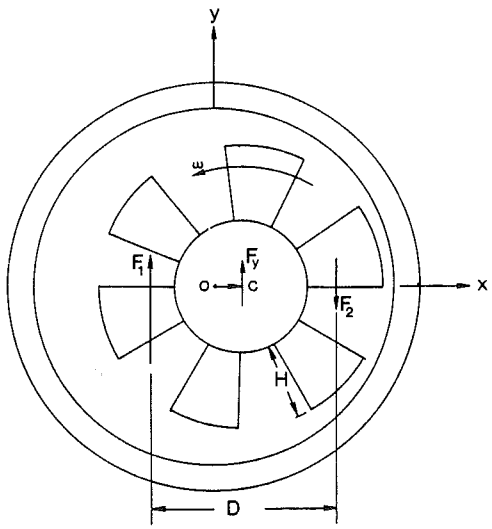

Fig. 1 Unequal aerodynamic blade forces caused by rotor eccentricity

Consequently, computer programs are now available [4] that can predict whirling frequencies and threshold speeds, provided that accurate values for the destabilizing coefficients are used as input. The destabilizing coefficients usually take the form of a linearized cross-coupled stiffness term, but sometimes are expressed as negative damping, depending on the mechanism producing the instability [2].

Reference [1] describes two different destabilizing mechanisms which can act in aircraft turbojet engines. One is associated with labyrinth seals, and the other with blade forces in axial-flow turbine or compressor wheels. It is the

Contributed by the Gas Turbine Division of THE AMERICAN SOCIETY OF MECHANICAL ENGINEERS and presented at the 29th International Gas Turbine Conference and Exhibit, Amsterdam, The Netherlands, June 4-7, 1984. Manuscript received at ASME Headquarters January 9, 1984. Paper No. 84-GT-140.

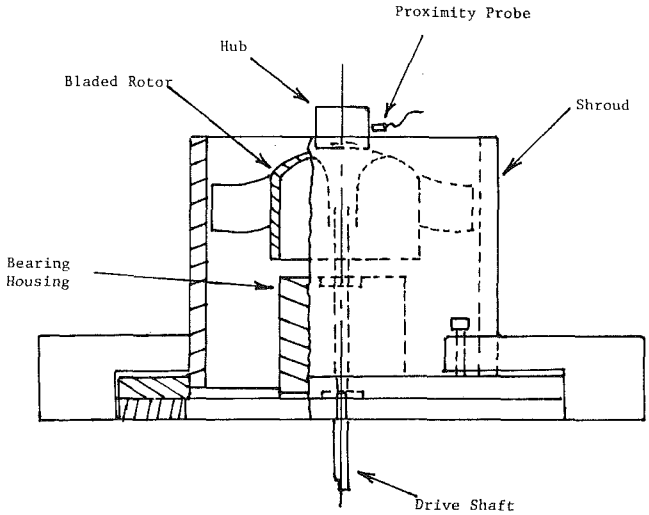

Fig. 2 Section of bladed test rotor and movable shroud

latter that is the subject of this paper, that is, the aerodynamic excitation due to circumferential variation of blade clearance in axial flow compressors and axial flow turbines. An objective of the work reported here was to verify the theory due to Alford that predicts the existence of an aerodynamic cross-coupled stiffness caused by variation of local efficiency around the bladed wheel.

Rotordynamic instabilities in axial-flow steam turbines have been described in the technical literature as "steam whirl" [5]. It seems likely that many of these cases are actually the same phenomenon as described by Alford.

Winter made experimental measurements on a laboratory model in 1968 [6]. He used ball bearings in his test rig to eliminate the instability caused by hydrodynamic bearings, and applied external damping elements to the bearings since ball bearings have little inherent damping. Winter demonstrated the presence of a load-dependent instability, but was not able to quantify his results.

In the work reported here, a small high-speed, single-stage, axial-flow blower was mounted on soft supports in a housing with adjustable eccentricity. The aerodynamic force normal to the eccentricity was measured, along with the driving torque and rotor speed. Figure 1 illustrates how the difference in tangential blade forces can produce a net force on the rotor that is normal to the radial displacement (eccentricity) of the wheel, according to [1]. The drawing is for a compressor, as opposed to a turbine. Note that, if the local efficiency decreases with increased tip clearance, force F_1 must be larger than force F_2 for a compressor or blower. For a compressor, lower efficiency is associated with larger driving torques and, hence, larger tangential blade forces.

The induced aerodynamic force on the rotor is

$$F_y = F_1 - F_2 \tag{1}$$

Since F_y is caused by rotor displacement in the x-direction, cross-coupled stiffness K_{yx} can be defined by the equation

$$F_y = -K_{yx}X \tag{2}$$

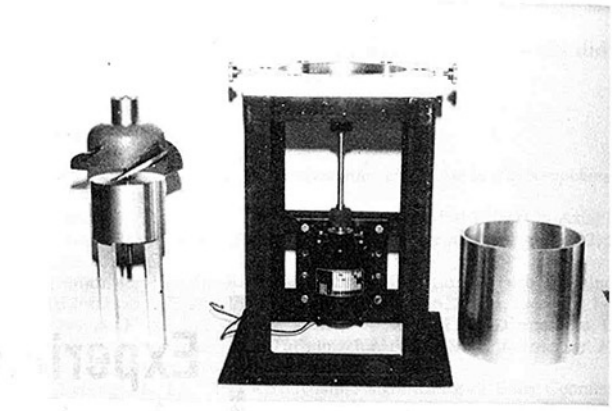

Fig. 3 Subassemblies of the test apparatus, with rotor and blades at left, support frame and drive at center, and shroud at right

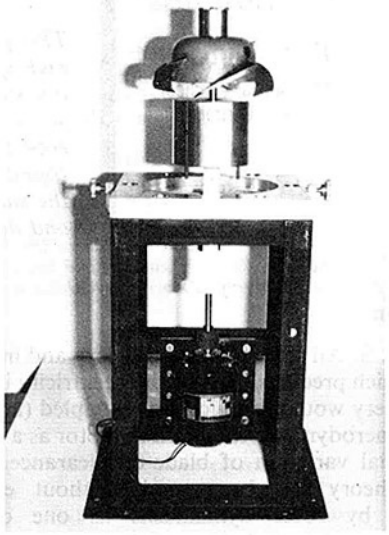

Fig. 4 Assembled test apparatus, shroud removed

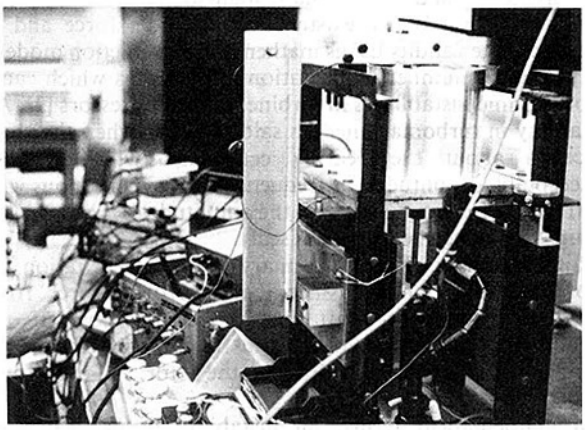

Fig. 5 Assembled test apparatus, shroud in place but no inlet duct

Nomenclature

C = y-intercept of force-torque curves (g)
D = blade pitch diameter (in.)
F = measured cross-coupled force (g)
F_1, F_2 = tangential blade forces (lb)
F_y = cross-coupled force predicted by Alford's equation (lb)
H = blade length (in.)
K_{yx} = cross-coupled stiffness coefficient (lb/in.)
N = rotor speed (rpm)
T = aerodynamic stage torque (in.-lb)
V = inlet velocity (in/s)
X = rotor eccentricity produced by offset housing (in.)
β = local aerodynamic efficiency factor (dimensionless)

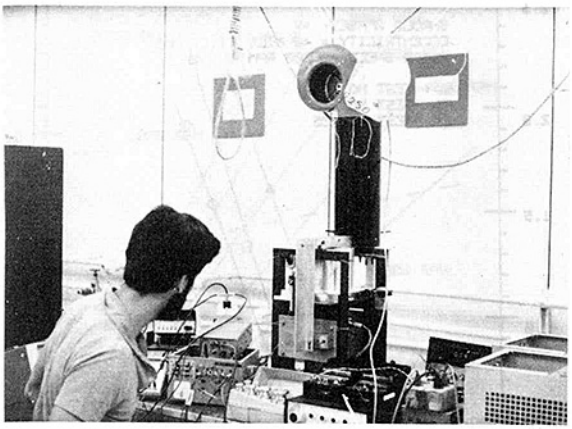

Fig. 6 Test apparatus and instrumentation with inlet duct and auxiliary blower installed

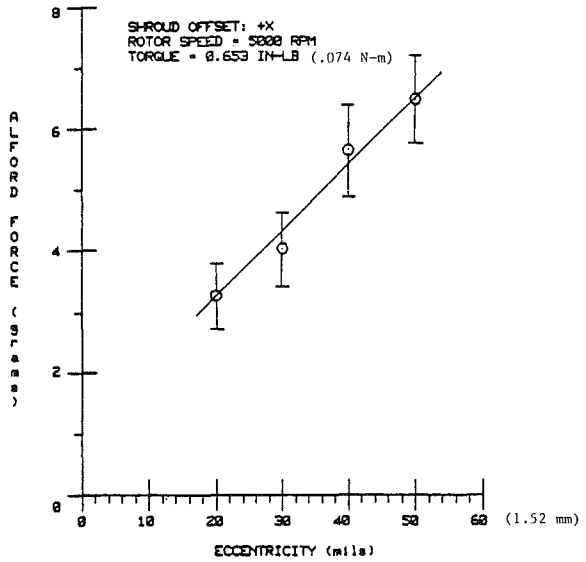

Fig. 7 Alford force as a function of rotor eccentricity, showing ± 2 standard deviations (shroud offset: + X)

According to Alford's theory [1], the cross-coupled stiffness is a function of the stage torque, T, the blade length, H, the pitch diameter, D, and the local efficiency, β, as follows

$$K_{yx} = -\frac{\beta T}{DH} \qquad (3)$$

The Test Apparatus

The test apparatus used in the experiments consists of a flexibly mounted bladed rotor driven by a variable speed electric motor and a movable shroud as illustrated in Fig. 2. The blade o.d. is 6 in. The motor is rated 1/7 hp at 10,000 rpm.

An offset of the bladed rotor within the shroud clearance circle is produced by translating the shroud laterally. The shroud is mounted on slides and is translated laterally by turning a threaded rod.

Figures 3–6 are photographs of the test apparatus hardware in various stages of disassembly.

The lateral stiffness of the rotor bearing support is made low enough so that very low levels of Alford's force (3–10 g) produce a measurable rotor deflection. The rotor deflection is measured with an eddy-current proximity probe and calibrated to lateral force in g/mil.

The speed of the rotor can be varied independently from the torque over a range of 0 to 7000 rpm by changing the voltage supplied to the electric motor and simultaneously adjusting

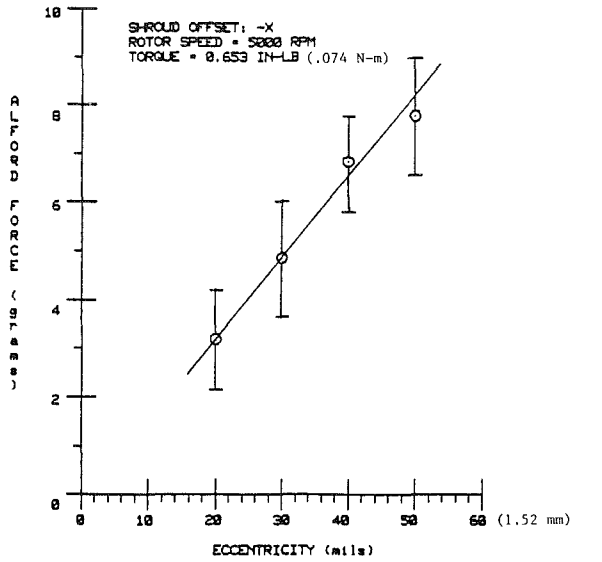

Fig. 8 Alford force as a function of rotor eccentricity, showing ±2 standard deviations (shroud offset: − X)

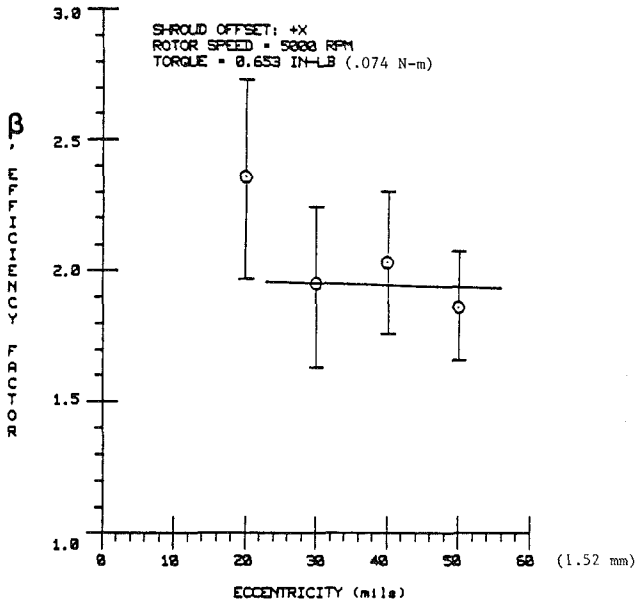

Fig. 9 Efficiency factor β as a function of rotor eccentricity, showing ±2 standard deviations (shroud offset + X)

the air velocity at the rotor inlet with an auxiliary blower. This method allows the rotor speed to be changed while holding the torque constant, or vice versa. Many combinations of speed, torque, and shroud eccentricity can thus be obtained.

Rotor speed is measured by feeding a once-per-revolution keypasor signal into an electronic counter.

The aerodynamic torque is measured with a strain gage dynamometer. The driving torque of the electric motor is entirely reacted by a steel rod in torsion, with torsional strain gages calibrated to torque.

Experimental Procedures

For each set of the data taken, a base measurement was made with the shroud in the center position (i.e., with the lateral eccentricity nominally zero). With the shroud in this position, the rotor was run up to the selected measurement speed, and measurements were made of rotor deflection, speed, and torque.

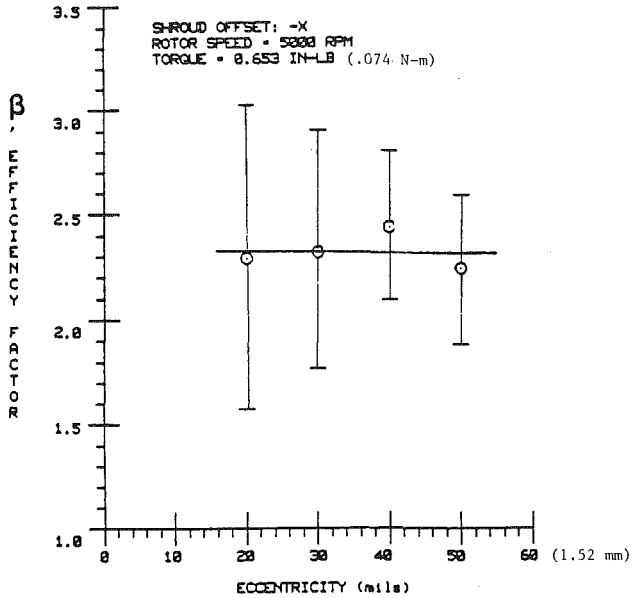

Fig. 10 Efficiency factor β as a function of rotor eccentricity, showing ± 2 standard deviations (shroud offset: $-X$)

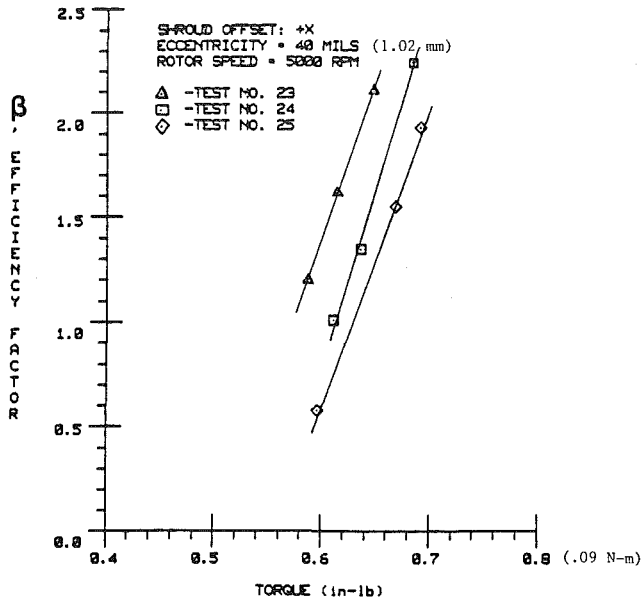

Fig. 12 Efficiency factor β as a function of developed rotor torque (for three different tests)

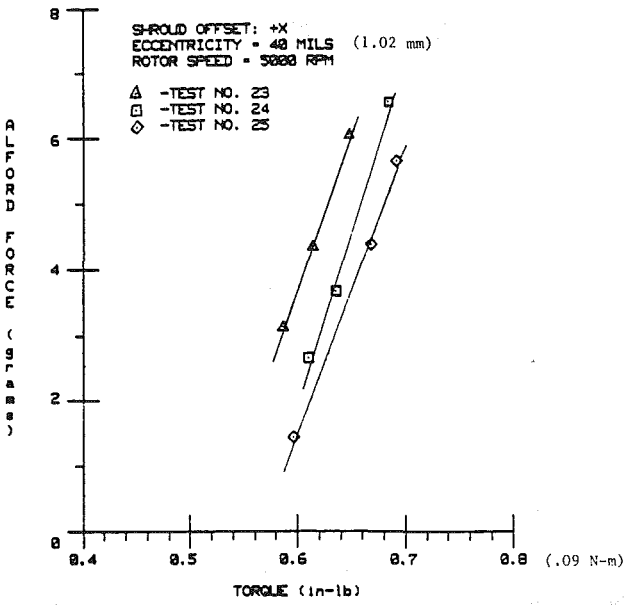

Fig. 11 Alford force as a function of developed rotor torque (for three different tests)

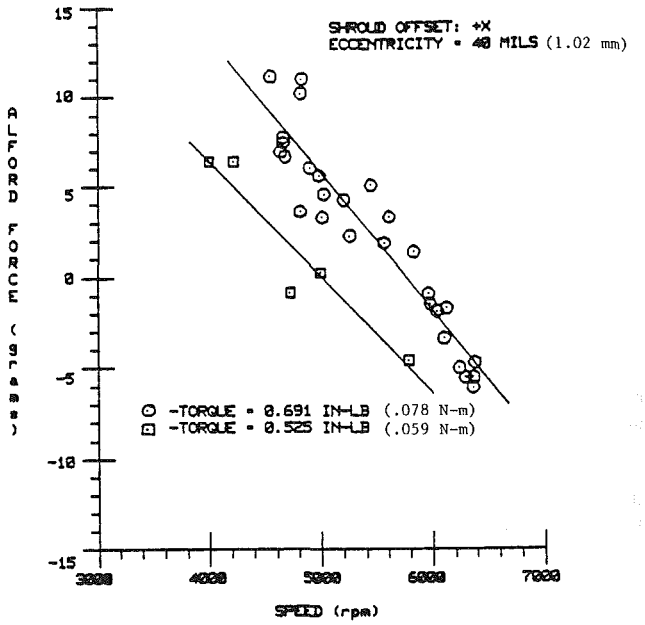

Fig. 13 Alford force as a function of rotor speed (for two different values of torque)

Immediately after completing the base measurements, an eccentricity was imparted to the shroud (adjusting screws translate the shroud laterally) and new values of rotor deflection and torque were measured at the same speed as for the base measurement. Since the direction, as well as the magnitude, of shroud offset was found to have an effect on the measurements, the procedure was repeated for an equal shroud eccentricity in the negative (opposite) direction.

One of the most challenging and time-consuming aspects of the project was the measurement of rotor deflection (d-c signal) in the presence of a relative large a-c signal produced by rotor runout, synchronous vibration, and ball bearing roughness. This was finally accomplished by passing the probe signal through a very effective low-pass filter.

Large quantities of data were taken and averaged, since the repeatability was found to be relatively poor (typically ± 20 percent for two successive measurements of the same variable under the same conditions). The poor repeatability was partially due to apparent aerodynamic instabilities (surging) under some conditions of speed and torque.

Results

The results of the experiments are shown in Figs. 7–18.

Since the cross-coupled force developed in the test rig was very small, it was measured and is presented in grams. As described, the test rotor force-deflection characteristic was measured to produce a calibration constant in grams per mil of rotor deflection (1 mil = .001 in. = .0254 mm).

Denoting the measured cross-coupled force in grams by F and applying a unit conversion factor to equations (2) and (3) gives the prediction equation as

$$F = 453.6F_y = (453.6)\frac{\beta Tx}{DH} \tag{4}$$

Figures 7 and 8 show how the measured cross-coupled force

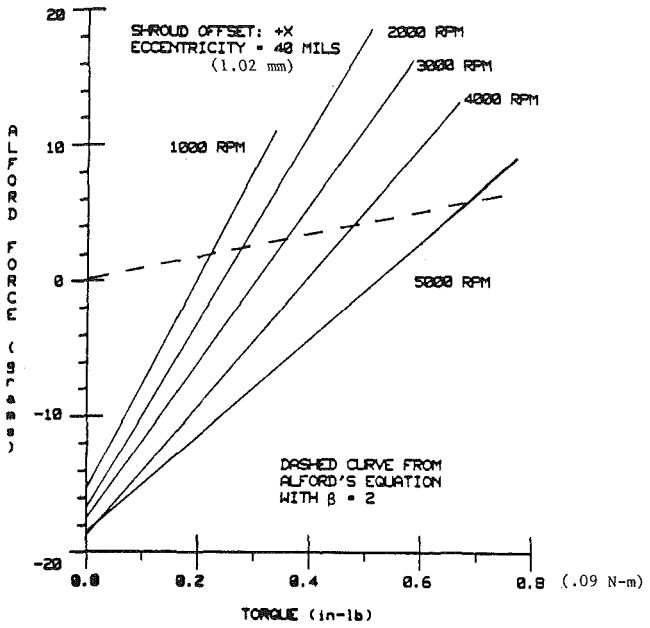

Fig. 14 Alford force as a function of developed rotor torque: for different values of speed

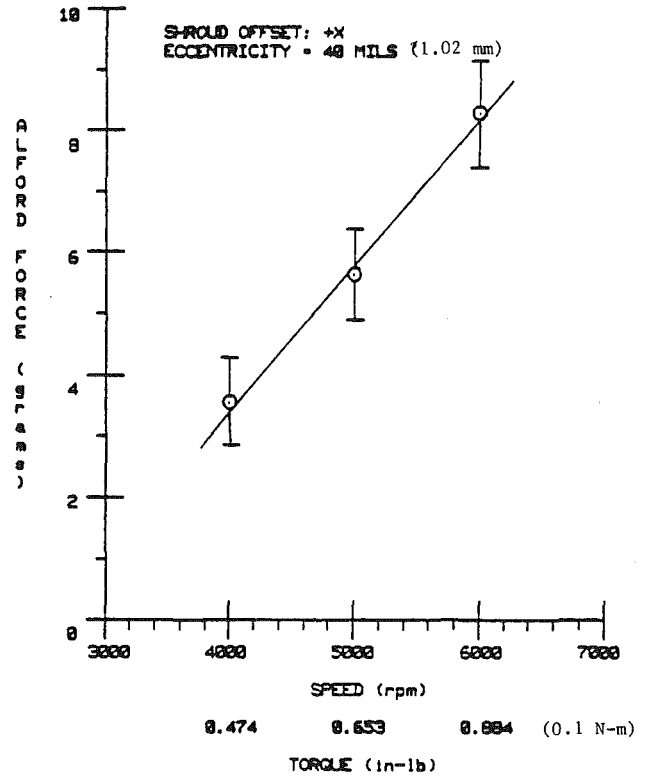

Fig. 15 Alford force as a function of developed rotor speed, showing ±2 standard deviations (shroud offset: + X)

varied with rotor eccentricity. The vertical line through each point shows the range of ±2 standard deviations of the measured data. The lines connecting the points were plotted using a least squares fit to the measured data. The only difference between the two graphs (Figs. 7 and 8) is in the direction that the eccentricity was imparted.

Figures 9 and 10 show the magnitude of the efficiency factor β and how it varies with rotor eccentricity. The difference between the two figures is the direction that the eccentricity was imparted. The efficiency factor was calculated from equation (4).

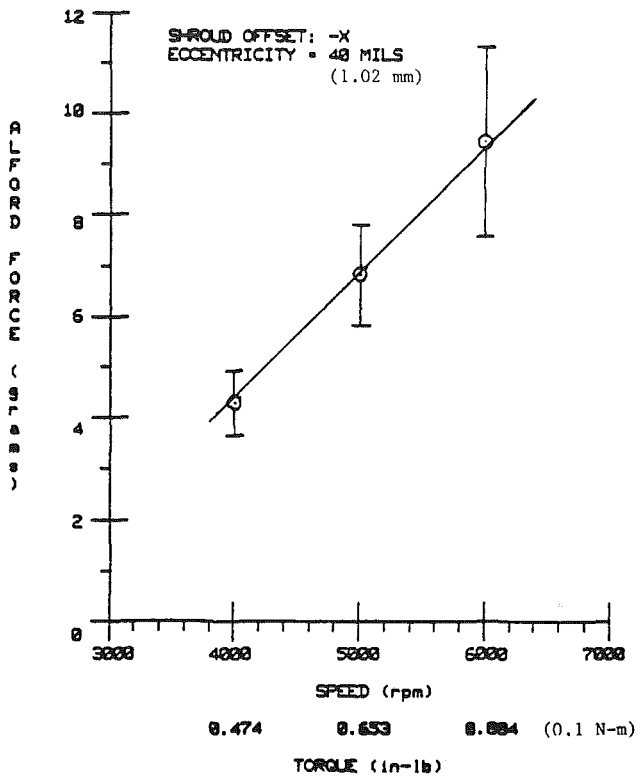

Fig. 16 Alford force as a function of developed rotor torque and rotor speed, showing ±2 standard deviations (shroud offset: − X)

Equation (4) implies that β remains constant for varying eccentricity. Figure 7 confirms this. Therefore, it was felt that the point on Fig. 9 corresponding to 20 mils eccentricity was not representative and should not be included in the least squares fit.

Figures 11 and 12 show how Alford's force and β vary with torque. Again β was calculated using equation (4). Figure 13 shows how the measured Alford force varied with speed holding the rotor torque constant. Figure 14 was derived from Figs. 11 and 13. The curve corresponding to 5000 rpm was derived using a least-squares fit to the data from all 3 tests in Fig. 11. The four remaining curves on Fig. 14 were derived from this one curve and Fig. 13, using extrapolation techniques. Figures 15, 16, 17, and 18 show how the measured Alford force and efficiency factor varied with rotor speed and torque.

Discussion

One of the remarkable features of Alford's theory is its simplicity. Figures 7, 11, and 14 verify the predicted linearity of Alford's force with rotor eccentricity and stage torque. However, Fig. 11 shows that Alford's force does not appear at all until a certain level of stage torque is reached: then it suddenly appears and increases steeply with torque. Alford mentions, in [1], that "large power inputs to the compressor rotor appear to increase the hazard of whirl. The vibration problem was encountered only at the full 100 percent power rating of the engine." Figure 11 is compatible with this observation, since extrapolation shows that the y-intercept is not zero.

Figures 12 and 13 also reveal other limitations of equation (4), principally that the efficiency factor β actually varies with the aerodynamic load torque and that the developed Alford's force is speed-dependent as well as torque-dependent.

To obtain an improved prediction model, the speed must be included as a pertinent variable. Dimensional analysis shows that if the speed is pertinent, then the inlet velocity is also

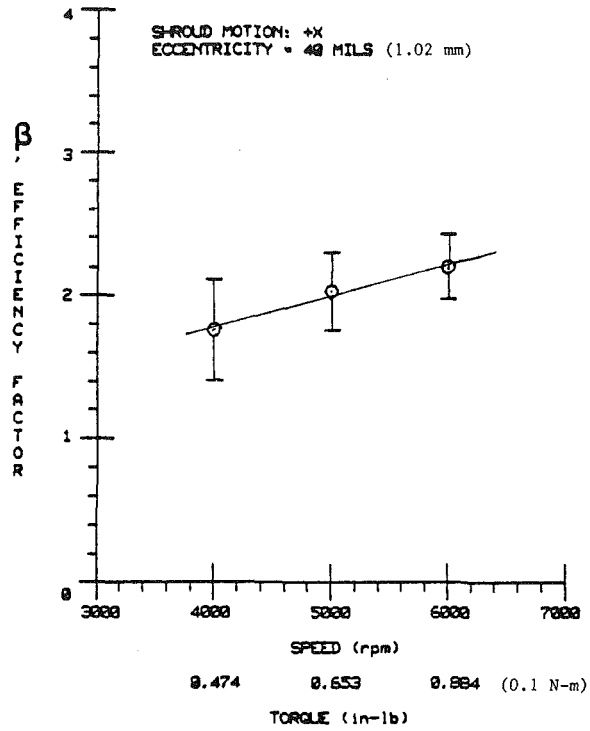

Fig. 17 Efficiency factor β as a function of developed rotor torque and rotor speed, showing ± 2 standard deviations (shroud offset: + X)

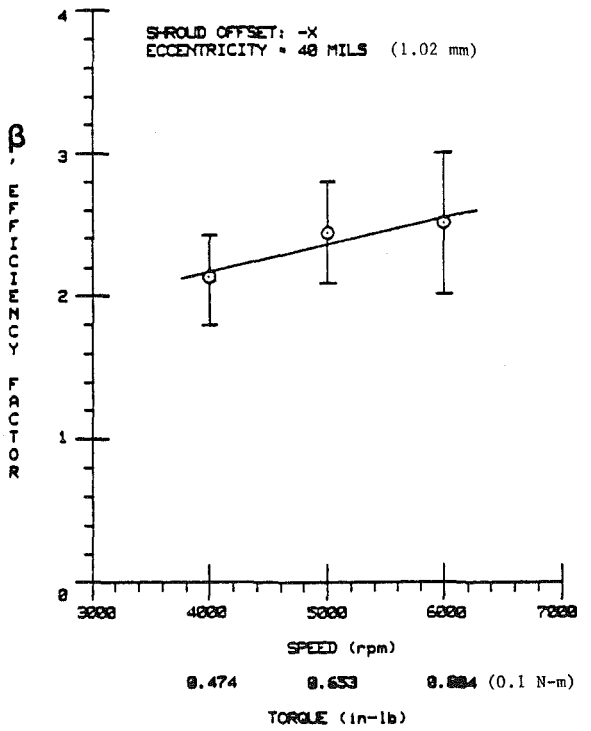

Fig. 18 Efficiency factor β as a function of developed rotor torque and rotor speed, showing ± 2 standard deviations (shroud offset: − X)

pertinent. In dimensionless groups, the prediction equation takes the form

$$\frac{F_y D}{T} = f\left(\frac{x}{H}, \frac{D}{H}, \frac{V}{ND}\right) \tag{5}$$

where N = speed, rpm; V = inlet velocity, in/s; and the other variables are as previously defined.

In the experiments reported here, measurements of the inlet velocity, V, were not made, therefore the functional form of equation (5) cannot be determined. Until the functional form of a dimensionally homogeneous prediction equation has been determined, any improved prediction model must be purely empirical, to fit available test data for a particular machine.

Equation (4) can be modified to include a y-intercept, which gives

$$F_y = \frac{T\beta x}{DH} + C \tag{6}$$

For the small test apparatus used in the experiments reported her, the constant, C, is evaluated as $C = -17.37$ grams, by taking the average y-intercept of the five curves from Fig. 14. In addition, Fig. 13 shows that the slope of the curve is affected by the rotor speed, which supports the form of equation (5).

Conclusions and Suggestions for Future Research

Due to the small size of the test rig and the lack of measurement capability for aerodynamic velocities and pressures, the conclusions which can be made from this research are mainly qualitative. They are as follows:

1 The aerodynamic force postulated by Alford for axial flow turbomachinery does exist and can be measured experimentally.

2 Alford's force is speed-dependent as well as torque-dependent and is probably also a function of the gas velocity entering the stage.

3 Although the relationship of Alford's force to the stage torque is fairly linear at a given speed, the y-intercept is not zero. That is, no aerodynamic force is generated until a certain level of stage torque is reached.

The authors believe that these conclusions are significant, since rotordynamics engineers have used Alford's theory for a number of years with little or no experimental verification.

However, it is easy to see why rotor dynamic stability thresholds cannot be accurately predicted at present by computer analyses that use Alford's unmodified equation as a model for the destabilizing coefficients. Improved prediction models for the aerodynamic force will either require experimental meausurements on full-scale turbomachinery components, such as an axial-flow stage from the compressor in a turbojet aircraft engine, or measurement of a complete set of variables in a small-scale test apparatus so that the functional form of equation (5) can be determined and extrapolated to the machine of interest.

References

1 Alford, J. S., "Protecting Turbomachinery from Self-Excited Rotor Whirl," ASME JOURNAL OF ENGINEERING FOR POWER, Vol. 87, No. 4, Oct. 1965, pp. 333-334.

2 Vance, J. M., "Instabilities in Turbomachinery," *Proceedings of the 5th Annual Vibration Institute Seminar on Machinery Vibration Analysis*, Apr. 9, 1981, New Orleans, La.

3 Vance, J. M., and Tison, J. D., "Analysis and Interpretation of Non-synchronous Whirling in Turbomachinery," ASME Paper No. 78-PET-26, presented at the Energy Technology Conference, Houston, Texas, Nov. 5-9, 1978.

4 Murphy, B. T., and Vance, J. M., "An Improved Method for Calculating Critical Speeds and Rotor-dynamic Stability of Turbomachinery," ASME JOURNAL OF ENGINEERING FOR POWER, July 1983, pp. 591-595.

5 Thomas, H. J., "Unstable Oscillations of Turbine Rotors Due to Steam Leakage in the Clearance of the Sealing Glands and the Buckets," *Bulletin Scientifique*, A.J.M., Vol. 71, 1958, pp. 1039-1063.

6 Winter, C. J., "Instabile Bewegungen von Turbinenlaeufern infolge lastabhaengiger Erregerkraefte," *Energie and Technik*, Jan. 1969, pp. 7-13.

A Study of Axial Turbine Loss Models in a Streamline Curvature Computing Scheme

R. K. Sullerey
Assistant Professor,
Aeronautical Engineering Department,
Indian Institute of Technology,
Kanpur, India

S. Kumar
Scientist,
Defence Research and Development
Organization,
Hyderabad, India

This paper describes a study of the suitability of various loss models for axial turbines as assessed with a streamline curvature computing scheme for the meridional flow involved. The important loss models in this study include the Balje/Binsley loss correlation and its modification, and a recently modified form of the Ainley/Mathieson/Dunham/Came loss correlation. Test cases for the application of the computing scheme include single-, three-, and four-stage turbines for which extensive design and measured data are available. The computed results have been compared with test results for design and off-design mass flow rates and design pressure ratio. The results indicate that the Balje/Binsley profile loss correlation with the modified Dunham/Came secondary loss correlation give results that compare best with measured data. A modified form of the Ainley/Mathieson/Dunham/Came loss model is nearly as accurate.

Introduction

For the calculation of meridional flows in axial compressors and turbines, two commonly used methods are the streamline curvature and the matrix throughflow methods. The streamline curvature method can handle mixed (sub- and supersonic) flows and has modest computer memory requirements. A formulation for streamline curvature method was proposed by Novak [1]. Subsequently, the method has been used by Davis and Miller [2] and Denton [3], among others. Even though the preparation of numerical procedures for the streamline curvature method is of importance in itself, the accuracy of flow prediction depends considerably on the correlations used to evaluate the losses in the elements of blading [3].

Majumdar [4] has reviewed the various loss correlations for axial compressors suitable for streamline curvature or other throughflow prediction methods. A systematic presentation of information on blade element losses for axial compressors is available in [5]. However, for the case of axial turbines, it appears that the commonly used loss correlations have been the Ainley and Mathieson one [6] for profile losses and the Dunham and Came method [7] for secondary losses. An analysis for some axial turbine test cases was carried out by Sullerey and Govindan [8] using these correlations. It was observed that the efficiencies predicted using these correlations were lower than the measured values.

Kacker and Okapuu [9] have recently modified the Ainley/Mathieson/Dunham/Came (AMDC) loss correlations. Denton [10], in a review of various correlation and prediction methods for profile losses, has also pointed out that Ainley/Mathieson method overpredicts the losses. According to his study, and Balje and Binsley [11] loss correlation is the best as far as profile losses are concerned.

Contributed by the Gas Turbine Division and publication in the JOURNAL OF ENGINEERING FOR GAS TURBINES AND POWER. Manuscript received by the Gas Turbine Division February 7, 1984.

In the present work, a comparative study of axial turbine loss models for a streamline curvature computing scheme has been carried out. The formulation of equations presented by Novak [1] has been used, although the computing procedure is similar to Carter et al. [12]. The blade element losses are calculated using one of the loss correlations as part of the computing scheme. Secondary losses are distributed in a parabolic fashion from hub to tip on a mass-averaged basis. The loss models considered in the present study are (*a*) the modified AMDC loss correlation of Kacker and Okapuu [9], (*b*) the Balje and Binsley loss model [11], (*c*) the Balje and Binsley profile loss model with the modified Dunham and Came correlation of Kacker and Okapuu [9], and (*d*) Carter's loss model [12]. The test cases [13–15] for the analysis have been so chosen that a large amount of design and measured data are available for comparisons. The results obtained using various loss models have been compared with each other and with the measured results. Some comparisons are also made with previous predictions of Sullerey and Govindan [8] using the AMDC loss model.

Theoretical Formulation

The basic model in the streamline curvature method of analysis consists of a series of streamlines which trace the path of the flow from the known conditions of the inlet flow to the first stage of the turbine to the final design station at the exit of the last blade row. A small portion of a streamline is shown in Fig. 1, together with the various components of flow velocity.

The flow pattern for an irreversible adiabatic flow on a prescribed stream surface can be determined by the following set of equations:

1 Continuity—conservation of mass
2 (*a*) Motion (*r*-direction)—conservation of momentum

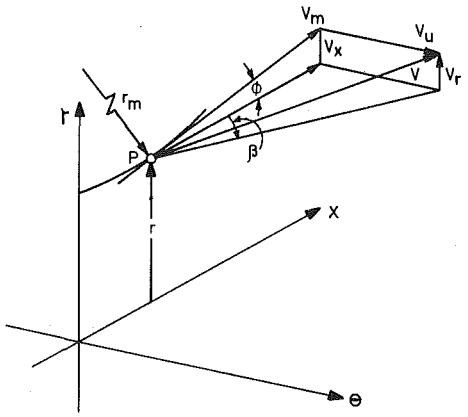

Fig. 1 Nomenclature for the flow

(*b*) Entropy (loss model)—second law of thermodynamics
(*c*) Geometrical condition—velocity triangle angle distribution scheduling

3 Energy—First law of thermodynamics
4 State

The Radial Equilibrium Equation. The equation of motion in the *r*-direction is the well-known radial equilibrium equation describing the equilibrium of flow along the radius. It can be expressed in terms of components of absolute velocity in the following way

$$\frac{1}{\rho}\frac{\partial p}{\partial r} = \frac{V_u^2}{r} + \cos\phi\frac{V_m^2}{r_m} - V_m \sin\phi\frac{DV_m}{D_m} \tag{1}$$

where m is the meridional direction.

The foregoing equation can also be expressed in terms of stagnation pressure and temperature as follows:

$$\frac{V_u^2+V_m^2}{2}\frac{1}{T_0}\frac{dT_0}{dr} - V_u\frac{dV_u}{dr} - \tfrac{1}{2}\frac{dV_m^2}{dr} + RT_0\left[1-\frac{V_u^2+V_m^2}{2C_pT_0}\right]\frac{1}{p_0}\frac{dp_0}{dr} = \frac{V_u^2}{r} + \frac{V_m^2}{r_m}\cos\phi - V_m\sin\phi\frac{DV_m}{D_m} \tag{2}$$

The term DV_m/D_m can be expressed in terms of meridional path line slope and curvature by making use of the laws of thermodynamics, equation of state, and continuity equation. Thus

$$\sin\phi\frac{DV_m}{D_m} = \frac{V_m\left[\left(1+M_u^2+\frac{r}{r_m\cos\phi}\right)\frac{\sin^2\phi}{r}+\tan\phi\frac{\partial\phi}{\partial r}\right]}{1-M_m^2}$$

The continuity equation for an axisymmetric flow passing through an axial section of arbitrary annulus can also be expressed in terms of stagnation pressure and temperature as follows

$$\dot{m} = \frac{2\pi}{R}\int_{r_h}^{r_t}\frac{p_0}{T_0}\left[1-\frac{V_u^2+V_m^2}{2\,C_pT_0}\right]^{1/\nu-1} V_m\cos\phi\, r\,d\nu \tag{4}$$

The Loss Equation. The irreversibility of flow is more conveniently expressed in terms of the stagnation presure loss, since the principal variables chosen for the analysis are total pressure and the meridional velocity. The total pressure loss coefficient for the stator blade row is defined as

$$Y_N = \frac{p_{00}-p_{01}}{p_{01}-p_1}$$

or

$$p_{01} = \frac{p_{00}}{1+Y_N\left(1-\frac{p_1}{p_{01}}\right)} \tag{5}$$

For the rotor

$$Y_R = \frac{p'_{02s}-p'_{02}}{p'_{02}-p_2}$$

or

$$p'_{02} = \frac{p'_{02s}}{1+Y_R(1-p_2/p'_{02})} \tag{6}$$

Where p'_{02s} is upstream relative stagnation pressure corrected for change in blade speed due to the change in the streamline radius between inlet and outlet of the blade row.

The values of loss coefficients Y_N and Y_R are obtained from internal loss correlation used. From known values of these coefficients, the foregoing equations, (5) and (6), can be used to obtain downstream stagnation pressure.

The Geometrical Condition. At the stator exit, the tangential velocity is related to the meridional velocity from a specification of the exit flow angle.

$$V_u = V_m\cos\phi\tan\beta \tag{7}$$

In like manner, the tangential velocity at rotor exit can also be related to the meridional velocity in terms of specified rotor exit angle. The Euler work equation can then be used to evaluate the total temperature drop through a stage and hence stage exit total temperature

$$C_p\Delta T_0 = V_{u1}u_1 - V_{u2}u_2 \tag{8}$$

The stator and rotor exit angles are input to the program. Their values are taken from appropriate references giving the design details of the turbines.

The Method of Solution

The essential part of the solution of the flow field consists of obtaining the values of total pressure, total temperature, and the two components of the absolute velocity at each

Nomenclature

A,B,C = constants
C_p = specific heat at constant pressure
M = Mach number
p = static pressure
p_0 = stagnation pressure
R = gas constant
r = radius
r_m = streamline radius of curvature
T_0 = total temperature
u = blade speed
V = velocity
m = mass flow rate
Y = pressure loss coefficient
ρ = density
ϕ = streamline slope
β = flow angle
ν = ratio of specific heats

Subscript

h = hub
m = meridional component
N = stator
R = rotor
s = secondary
u = tangential component
0 = stage inlet
1 = stator exit/rotor inlet
2 = stage exit

Superscript

= relative to the rotor

selected design station. Other parameters such as static pressure, Mach numbers, efficiencies, etc., can then be calculated from these principal variables.

For the purpose of solution, the radial equilibrium equation is written in the form

$$C_{11}\frac{dV_m^2}{dr}+C_{12}\frac{1}{p_0}\frac{dp_0}{dr}+C_{13}\frac{dV_u}{dr}=C_{14} \tag{9}$$

where C_{11}, C_{12}, etc., are certain coefficients. The differentiation of the appropriate stagnation pressure loss equation (equations (5) or (6)) also leads to a differential equation of the form

$$C_{21}\frac{dV_m^2}{dr}+C_{22}\frac{1}{p_0}\frac{dp_0}{dr}+C_{23}\frac{dV_u}{dr}=C_{24} \tag{10}$$

The third equation of the set is obtained by differentiating equation (7) (the geometrical condition).

$$C_{31}\frac{dV_m^2}{dr}+C_{32}\frac{1}{p_0}\frac{dp_0}{dr}+C_{33}\frac{dV_u}{dr}=C_{34} \tag{11}$$

The coefficients C_{11}, C_{12}, etc., in the foregoing three equations can be expressed in terms of appropriate parameters for the first stator inlet, stator exit, and the rotor exit. They can be calculated once a value of meridional velocity is selected.

The slope of a streamline is initially obtained by interpolation from its values at the hub and tip. Subsequently, it is checked by a quadratic fit of values at different stations.

The Loss Distribution. The stagnation pressure loss coefficient Y is composed of the profile loss coefficient Y_p and the secondary loss coefficient Y_s. The profile losses are calculated at a given radius according to the profile loss correlation used. For secondary losses qualitative explanations and measurements (Hanley [16], Tabakoff and Hosney [17]) suggest that these losses are largest in the hub and tip regions and negligible near the midradius. Therefore, the secondary losses were distributed across the annulus in a parabolic manner. Thus the secondary loss coefficient $Y_s(r)$ at any radius r is given by

$$Y_s(r)=Ar^2+Br+C \tag{12}$$

The constants A, B, and C in the foregoing equation are evaluated by imposing the following conditions:

1 The mass-averaged secondary loss coefficient obtained using equation (12) has the same value as obtained from the secondary loss correlation used.

2 The secondary loss coefficient is zero at the mean streamline.

3 The slope of the $Y_s(r)$ distribution curve is also zero at the mean streamline.

For want of a better method of distributing tip clearance losses, the loss coefficient calculated for these losses was added to the secondary loss coefficient.

The specific heat and the ratio of specific heat values are corrected for the effect of temperature variation in turbine.

The problem of solution consists of obtaining a meridional velocity distribution which simultaneously satisfies the radial equilibrium equation and the continuity equation. A process of iteration is used to achieve this objective beginning with an initial estimate of meridional velocity at the mean streamline position. A total of 13 streamlines are used from hub to tip, although this number can be varied. The standard Runge-Kutta-Gill method is used for solving the ordinary differential equations to obtain the meridional velocity at an adjacent streamline.

Loss Models. The equations of flow used in the streamline curvature method are for an inviscid flow. The basic purpose of the loss model is to take into account the change in entropy due to viscosity. Hence for realistic flow predictions, incorporation of an accurate and simple loss correlation is an essential part of the computing scheme. The important role of the loss model has been emphasized by several investigators [2–4]. In the present investigations, losses are calculated using the following different loss correlations.

(*i*) *Modified Ainley/Mathieson and Dunham and Came Correlations.* Kacker and Okapuu [9] have critically reviewed and modified the Ainley/Mathieson/Dunham/Came profile and secondary loss correlations. Correction factors have been introduced in the original formulation of the Ainley/Mathieson profile loss correlation. The first and major correction is to reduce the profile loss coefficient by a factor of 2/3 to account for the improvement in blade design over the years since the original formulation in the fifties. This factor is consistent with the analysis of Denton [10], who observed that the profile losses using the Ainley and Mathieson correlation are overpredicted by a factor of 1.308 compared to test data. Additional correction factors have been introduced for exit Mach number, channel flow acceleration, and Reynolds number effects.

The correction factors for the Dunham and Came [7] secondary loss correlation correct for Mach number effects and low aspect ratio effects.

(*ii*) *Balje and Binsley Loss Model.* Denton [10] has observed that the Balje and Binsley profile loss correlation with a standard deviation of 0.36 (difference between predicted and experimental loss coefficients) is the best among the various correlations. Balje and Binsley [11] calculate the loss coefficient from an expression for momentum thickness. This expression is obtained on the basis of an assumed trapezoidal surface velocity distribution. Their secondary loss correlation, however, basically provides the value of minimum secondary loss coefficient obtainable for given geometrical conditions.

In view of the fact that the Balje and Binsley [11] secondary loss correlation underpredicts these losses, a modified total loss correlation was also used in the present analysis. This consisted of the Balje Binsley profile loss correlation and the modified Dunham/Came secondary loss correlation (BBDC).

(*iii*) *Loss Correlation of Carter et al. [12].* This is a loss correlation in which the losses are considered principally a function of deflection. The loss coefficients here are expressed as a function of tangents of inlet and exit angles and of the ratio of inlet to outlet velocities. The constants in this expression are obtained by correlating with Smith's data [18] on attainable turbine efficiencies.

Application of Loss Correlation in Computing Schemes. Each of the loss correlations used forms a separate subroutine in the computer program. The subroutines are called in the program according to the loss option used. The profile and secondary loss coefficients are separately calculated and added to obtain the total loss coefficient for the blade row. The loss coefficient is used to evaluate the stagnation pressure at the row exit and the coefficients C_{21}, C_{22}, and C_{23} in equation (10). The derivative of the loss coefficient is calculated from its values at different radial stations by a SLOPE subroutine. The input to the subroutine includes the blade row exit angles and the meridional velocity in the current iteration. The aspect ratio, pitch/chord ratio and the clearance/height ratio, etc., are also specified. For the Ainley/Mathieson method, the data points of the original Ainley/Mathieson correlation curves are stored in the program and loss coefficients for intermediate angles and pitch/chord ratio are obtained by interpolation.

Table 1

	Experimental	Carter's model	Balje/ Binsley loss model	Kacker/ Okapuu loss model	BBDC loss model
1 Spool work (KJ/Kg)	44.67	45.08	48.68	46.29	45.45
2 Turbine total-to-total efficiency	0.92	0.922	0.958	0.95	0.934

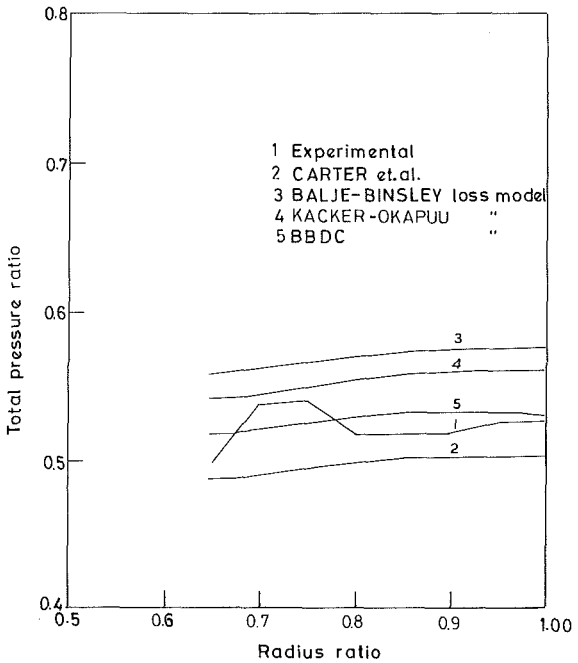

Fig. 2 Stage exit total pressure distribution for the test case 1

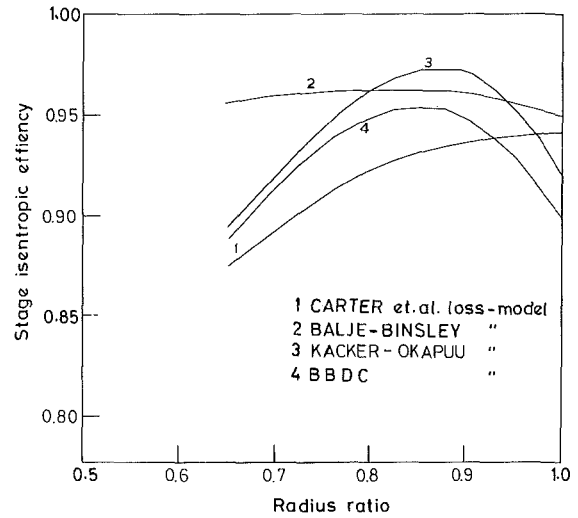

Fig. 3 Radial distribution of total to total efficiency for test case 1

Results and Discussion

The results obtained from the computer program have been plotted using a graphic terminal along with the experimental data points for test turbines.

Test Case 1. The first test case is a single-stage turbine for which the design details are given in [13]. At the equivalent design speed and pressure ratio, the measured value of total efficiency was 0.92. Under these conditions, mass flow was 1.6 percent higher than the design value. The radial variation of measured total pressure ratio is given in [13]; however, the radial distribution of efficiency was not available.

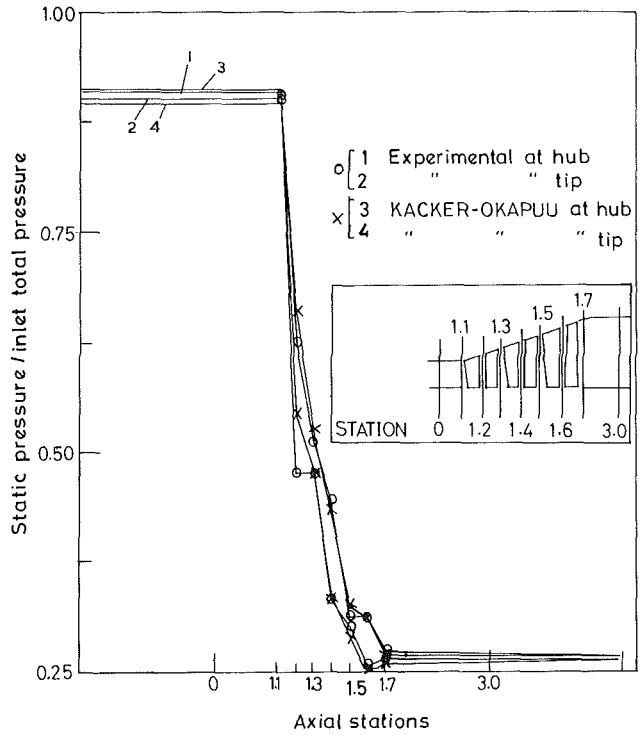

Fig. 4 Hub and tip static pressure distribution for test case 2

Figure 2 shows the distribution of the stage exit total pressure ratio with the radius ratio. The Balje-Binsley profile loss correlation with Dunham and Came secondary loss correlation is closest to the experimental results. Figure 3 presents the radial distribution of the total-to-total efficiency. The resulting distribution using loss models in which the secondary losses are parabolically distributed is more consistent compared to Carter's loss model where secondary losses are not parabolically distributed. The Balje/Binsley correlation underpredicts the losses (Table 1) and hence points out the need to combine the Balje-Binsley profile loss correlation with the Dunham/Came secondary loss model (BBDC). The data presented in Table 1 is for equivalent design speed and pressure ratio.

From Table 1, it appears that the best results are obtained with the BBDC loss model. To obtain results with design pressure ratio, the mass flow rate was adjusted till the output had the same pressure for which the turbine is designed and tested. The maximum change in mass flow rate was ±3 percent of the design mass flow rate for all the loss models. The comparison of results with same pressure ratio is more appropriate than with same mass flow rate, according to [3].

Test Case 2. In the second test case, data for a three-stage turbine [14] were used. This turbine has been designed for high-stage-loading and high-blade-loading for application in high bypass ratio turbofan engines. The design details for the turbine are presented in [14] and detailed experimental results are reported in [19]. The flow path and the measurement stations are shown in Fig. 4. The experimental data available in [19] include the stage performance, radial efficiency

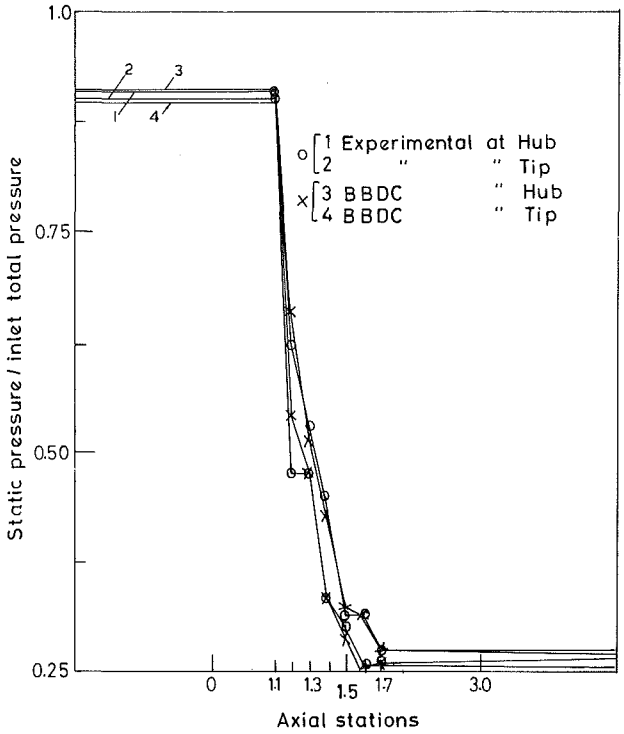

Fig. 5 Hub and tip static pressure distribution for test case 2

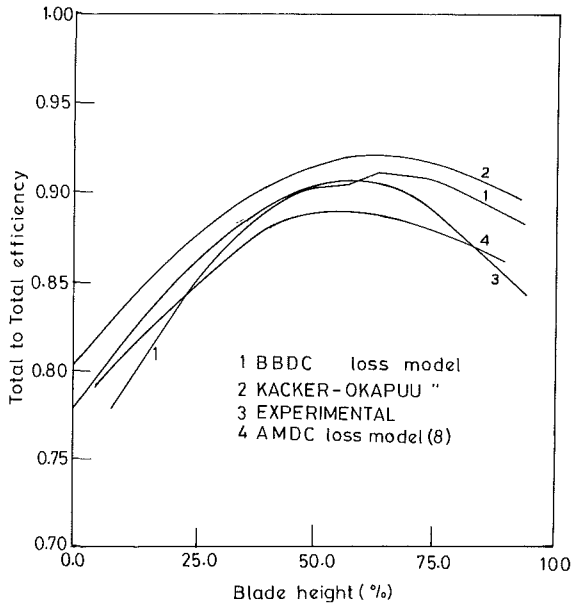

Fig. 6 Total-to-total efficiency distribution at stage 2 exit for test case 2

profiles, and exit swirl angle distributions for a wide range of pressure ratios. The experimental results taken for comparison are for a plain blade configuration.

Figures 4 and 5 present the static pressure distribution at the hub and tip obtained using Kacker/Okapuu and BBDC loss models. In both these cases, the results are in very good agreement with measured results [19]. For Carter's loss model, the agreement is less satisfactory and results are not presented here.

Figure 6 compares the total-to-total efficiency distribution with percentage blade height. The results indicate that while the AMDC loss model used in [8] underpredicts the efficiency, the modified AMDC loss model of Kacker and Okapuu [9]

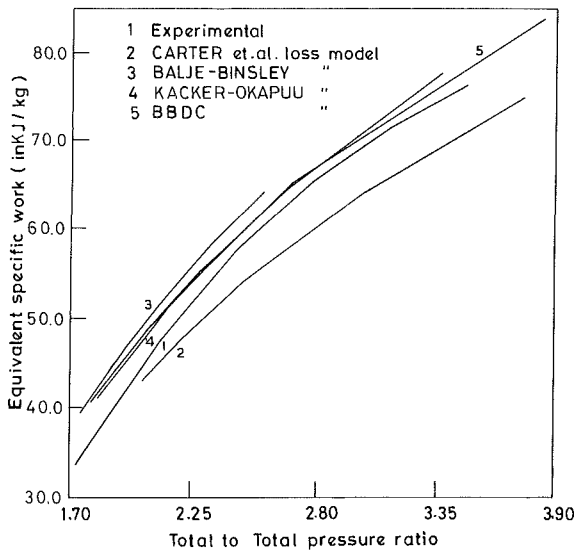

Fig. 7 Equivalent specific work versus total-to-total pressure ratio for test case 2

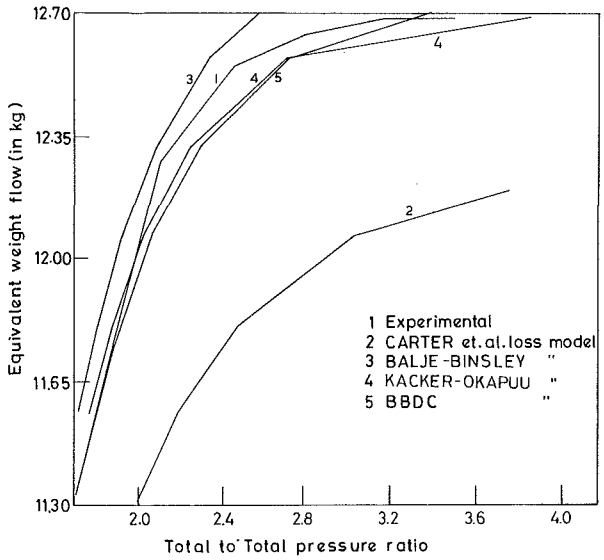

Fig. 8 Equivalent mass flow versus total-to-total pressure ratio for test case 2

predicts slightly higher efficiency values. The results with the BBDC loss model are closest to experimental data in the midradius region. The secondary losses in a turbine are concentrated closer to the endwalls and are negligible in the midradius region. The parabolic distribution is an attempt to approximate this secondary loss distribution. However, it is likely that the parabolic distribution may result in higher than actual losses at 1/4- and 3/4-span regions of high-aspect-ratio blades. The discrepancy between calculated and experimental efficiency profiles in Fig. 6 may be partly due to this reason.

Figures 7 and 8 present the distribution of equivalent specific work and equivalent weight flow as a function of total to total pressure ratio. No additional correlation was introduced for incidence angle losses. However, results for the Kacker/Okapuu and BBDC loss models are in fair agreement with measured results.

Table 2 presents the predictions of the overall parameters. The results with the Kacker and Okapuu loss model [9] are close to measured results [19], although overall efficiency is predicted 2 percent higher. For the BBDC loss model, the design mass flow rate was reduced by 0.7 percent to obtain the

Table 2

	Experimental	Carter's loss model	AMDC loss model	Balje/ Binsley loss model	Kacker/ Okapuu loss model	BBDC loss model
1 Spool work (KJ/kg)						
(*a*)With design pressure ratio	103.589	94.239	101.32	108.34	104.35	103.83
(*b*)With design mass flow rate	103.589	--	--	86.90	104.35	112.67
2 Turbine total-to-total efficiency						
(*a*) With design pressure ratio	0.886	0.882	--	0.921	0.91	0.90
(*b*)With design flow rate mass flow rate	0.886	--	0.867	0.943	0.91	0.905
3 Total to total pressure ratio						
Design mass flow rate	3.48	--	3.42	2.56	3.368	3.83

Table 3

	Experimental	Carter's loss model (12)	Balje/ Binsley loss model	Kacker/ Okapuu loss model (9)	BBDC loss model
1 Spool work(KJ/Kg)	83.63	73.64	87.35	84.47	83.11
2 Turbine total-to-total efficiency	0.858	0.745	0.917	0.867	0.853

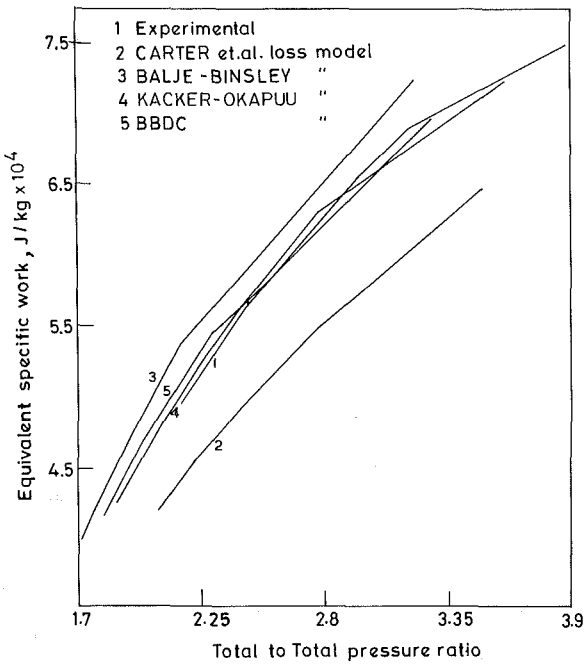

Fig. 9 Equivalent specific work versus total-to-total pressure ratio for test case 3

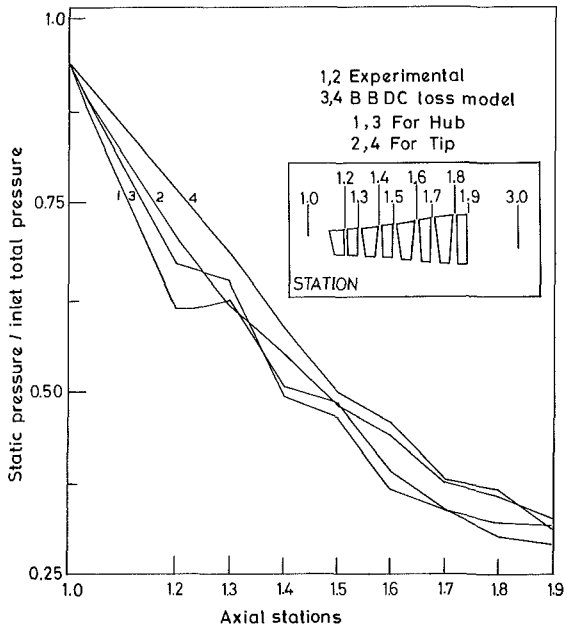

Fig. 10 Hub and tip static pressure distribution for test case 3

design pressure ratio. For this case, the results with this loss model compare best with experimental results. A 6 percent reduction in mass flow rate was required with Carter's loss model to obtain the design pressure ratio.

Test Case 3. This consists of a four-stage turbine for which design details have been taken from [15]. This turbine is also a part of an investigation program for fan drive turbines utilizing very high stage loading. However, the design equivalent specific work for this turbine is lower than in test case 2, and therefore its stage loading is lower than that of three-stage turbine. Comprehensive details of measured turbine performance over a wide range of pressure ratios is given in [20].

Figure 9 presents the equivalent specific work as a function of total-to-total pressure ratio. The results of the BBDC and Kacker-Okapuu loss models agree well with the measurements [20]. A comparison of measured hub and tip static pressure distributions with the predictions using BBDC loss model is shown in Fig. 10. A sketch of turbine flow path and the measuring stations (from [20]) is also given in Fig. 10. There is a fair agreement between the two. The radial variation of outlet flow angles at the turbine exit is compared in Fig. 11. The results of Kacker-Okapuu loss correlation are closest to the measured values. It was also observed that Mach number values at intermediate stations were in good agreement with design Mach numbers for both BBDC and Kacker and Okapuu loss models [9].

The overall results for this test case are summarized in Table 3 for the pressure ratio corresponding to design equivalent work [20].

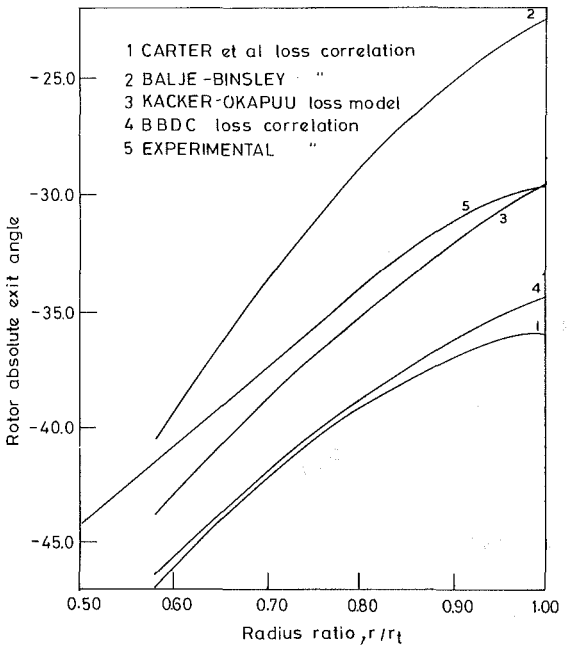

Fig. 11 Outlet flow angle distribution at turbine exit for test case 3

If the results are compared for the same pressure ratio, the BBDC loss model has slightly better predictions than the modified Ainley/Mathieson/Dunham/Came loss model of Kacker and Okapuu [9].

Conclusions

Four different loss models have been used in a streamline curvature computing scheme to study their suitability in predicting the performance of axial turbines. The analytical results have been compared with experimental results for three test cases that include three- and four-stage turbines. The modified AMDC loss model proposed by Kacker and Okapuu [9] has been found to give results in good agreement with measured results. The BBDC loss model, which combines the Balje/Binsley profile loss correlation with modified Dunham/Came secondary loss correlation is equally satisfactory and in certain cases better than Kacker-Okapuu loss model. Both these loss models can be used in throughflow analysis programs for satisfactory results. However, the BBDC loss model does not require use of figures in calculating profile loss coefficient. For very highly loaded turbines such as in test case 2, a slight adjustment in the factor of 2/3 used in profile loss correlation in Kacker-Okapuu loss model may further improve the predictions. The original AMDC loss model underpredicts the efficiency values. Carter's loss formulation [12] is basically suited for analysis of single-stage turbines having high hub-to-tip radius ratio. Thus these two loss models and the Balje/Binsley loss correlations (without Dunham/Came secondary loss correlation) should be considered less satisfactory.

References

1 Novak, R. A., "Streamline Curvature Computing Procedures for Fluid Flow Problems," ASME JOURNAL OF ENGINEERING FOR POWER, Vol. 89, No. 4, 1967.

2 Davis, W. R., and Millar, D. A. J., "A Comparison of the Matrix and Streamline Curvature Methods of Axial Turbomachinery Analysis, From a User's Point of View," ASME JOURNAL OF ENGINEERING FOR POWER, Oct. 1975.

3 Denton, J. D., "Through Flow Calculations for Transonic Axial Flow Turbines," *Turbomachinery Development in Steam and Gas Turbines*, ASME, New York, 1977, pp. 11-19.

4 Majumdar, A. S., "A Review of Recent Computational Procedures for Off-Design Analysis of Axial Compressors," *Journal of the Aero. Soc. of India*, Vol. 27, No. 1.

5 "Aerodyanamic Design of Axial Flow Compressors," NASA-SP-36, 1965.

6 Ainley, D. G., and Mathieson, G. C. R., "A Method of Performance Estimation for Axial Flow Turbines," H.M.S.O., A.R.C., R&M, 2974, 1957.

7 Dunham, J., and Came, P. M., "Improvements to the Ainley/Mathieson Method of Turbine Performance Prediction," ASME JOURNAL OF ENGINEERING FOR POWER, July 1970, pp. 252-256.

8 Sullerey, R. K., and Govindan, T. R., "A Meridional Flow Analysis of Axial Turbines Using Streamline Curvature Method," *Proceedings of 11th National Conference on Fluid Mechanics and Fluid Power*, Hyderabad, India, 1982, pp. CF 58-63.

9 Kacker, S. C., and Okapuu, U., "A Mean Line Prediction Method for Axial Flow Turbine Efficiency," ASME Paper No. 81-GT-58.

10 Denton, J. D., "A Survey and Comparison of Methods for Predicting the Profile Loss of Turbine Blades," *Institution of Mechanical Engineers Conference Publication 3*, Paper C 76/73, 1973, pp. 204-212.

11 Binsley, R., and Balje, O. E., "Axial Turbine Performance Evaluation, Loss Geometry Relationship-Part A," ASME, JOURNAL OF ENGINEERING FOR POWER, Vol. 90, No. 4, Oct. 1968.

12 Carter, A. F., Platt, M., and Lenherr, F. K., "Analysis of Geometry and Design Point Performance of Axial Flow Turbines, Part I—Development of the Analysis Method and the Loss Coefficient Correlation," NASA CR-1181.

13 Kofskey, M. G., Roelke, J. R., and Haas, Ec.Jo, "Turbine for Low-Cost Turbojet Engine, Part II-Opened Stator," NASA TND-7626.

14 Evans, D. C., and Wolfmeyer, G. W., "Highly Loaded Multistage Fan Drive Turbine-Plain Design Configuration," NASA CR 1964, 1972.

15 Evans, D. C., and Hill, J. M., "Experimental Investigation of a 4½ Stage Turbine With Very High Stage Loading Factor, Part I—Turbine Design," NASA CR-2140, 1974.

16 Hanley, W. T., "A Correlation of Endwall Losses in Plane Compressor Cascades," ASME JOURNAL OF ENGINEERING FOR POWER, July 1968.

17 Tabakoff, W., and Hosney, W., "An Experimental Investigation on Loss Reduction in Small Guide Vanes," AIAA Paper No. 76-617, 1976.

18 Smith, S. F., "A Simple Correlation of Turbine Efficiency," *J. Aero. Soc.*, Vol. 69, July 1965, pp. 467-470.

19 Wolfmeyer, G. W., and Thomas, M. W., "Highly Loaded Multistage Fan Drive Turbine—Performance of Initial Seven Configurations," NASA CR-2362, 1974.

20 Walker, N. D., and Thomas, M. W., "Experimental Investigation of a 4½-Stage Turbine With Very High Loading Factor, Part II—Turbine Performance," NASA CR-2363, 1974.

A Systematic Computational Design System for Turbine Cascades, Airfoil Geometry, and Blade-to-Blade Analysis

Z.-Q. Ye[1]
Visiting Scientist,
Department of Mechanical Engineering,
Iowa State University,
Ames, Iowa 50011

This paper describes a systematic computational design system for two-dimensional turbine cascades. The system includes a sequence of calculations in which airfoil profiles are designed from velocity diagram requirements and specified geometric parameters, followed by an inviscid global streamline curvature analysis, a magnified reanalysis around the leading edge, and a transitional profile boundary layer and wake mixing analysis. A finite area technique and a body-fitted mesh are used for the reanalysis. The boundary layer analysis is performed using the dissipation-integral method of Walz which has been modified in the present application. Several turbine airfoil profile geometry designs are presented. Also two sample cascade design cases and their calculated performance for a range of Mach numbers and incidence angles are given and discussed.

Introduction

A successful design system for turbomachinery cascades would provide a calculational tool by which cascade geometry could be computed from certain design input and provide a subsequent procedure by which optimum geometries may be determined and chosen. The design procedure usually starts from known flow conditions ahead of and behind the cascade, the thermodynamic states and flow velocities at the inlet and the outlet of a cascade having been calculated in advance. The quite successful simplification of an axisymmetric flow field and the separation of hub-to-tip and blade-to-blade flows is still widely used, although three-dimensional throughflow methods are already available. The design of a cascade is, therefore, to find airfoil profiles that lie on a surface of revolution and that satisfy imposed design requirements.

There appears to be a consensus among turbomachinery designers to classify two-dimensional cascade design methods as either "indirect" or "direct." The "indirect" design approach is an inverse calculation design, and extensive work on this approach has been carried out by LeFoll [1], Huo [2], Papailiou [3], Henderson [4], Boiko and Kozhevnikov [5], Schmidt [6], and Thompkins and Tong [7]. The "direct" design approach, on the other hand, involves a sequence of calculations in which the airfoil profile in cascade is designed from velocity diagram and structural constraint requirements, followed by analysis of the aerodynamic and profile boundary layer performance. The "direct" method is gaining in popularity with the appearance of fast computer codes to perform the different calculations requried. Examples of "direct" design systems have been reported by Thomas and Piendel [8], Monello et al. [9], and Hobbs and Weingold [10].

It is the purpose of this paper to report on a rapid numerical procedure that is useful in the context of a "direct" design system for axial flow turbine cascades. In this procedure, the design system enables the user to design turbine cascades satisfying design specifications of velocity triangle and loading requirements while incorporating analysis of the aerodynamic and profile boundary layer performance. The design system as developed is an automated and interactive computational one by which cascades approaching optimum performance under high subsonic to transonic flow conditions and transitional boundary layer behavior can be designed.

Sample cascade design cases are computed, and the design results are discussed in the paper.

Outline of the Design Analysis Procedure

A general flow diagram of the design procedure is shown in Fig. 1 in which the sequence of the main calculations and the techniques employed are pointed out. The interaction stations are noted where the user can branch back to the beginning of the procedure if the design is found to be unsatisfactory.

Airfoil Geometry. In the design of turbomachinery cascades, it is highly desirable that the curvature of the profile contour be continuous in order to avoid severe velocity changes [11, 12]. The analytical description of the profile must not restrict the freedom of the designer in choosing appropriate profile shapes, and it should be possible to introduce local changes without substantially affecting the remaining part of the profile. The power-law polynomials

[1] On leave from Gansu University of Technology, Lanzhou, China.

Contributed by the Gas Turbine Division and presented at the Joint Power Generation Conference, Indianapolis, Indiana, September 25–29, 1983. Manuscript received by the Gas Turbine Division June 30, 1983. Paper No. 83-JPGC-GT-7.

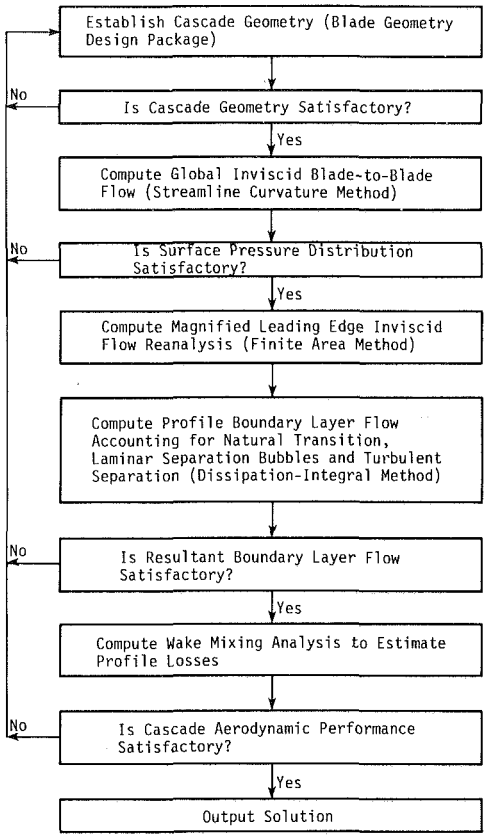

Fig. 1 Turbine cascade design system flow diagram

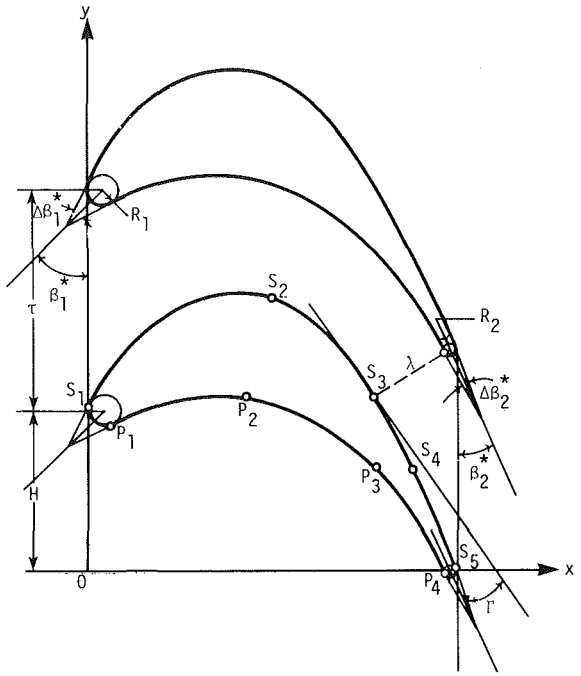

Fig. 2 Coordinate system and cascade geometric parameters

adequately meet these requirements. The airfoil profile is fitted by segments of nth degree polynomials while maintaining continuous curvature variation.

The basic profile data for the design problem as shown in Fig. 2 are: R_1 and R_2 are the leading and trailing edge radii; H is a camber distance; β_1^* and β_2^* are the metal angles at leading and trailing edge; $\Delta\beta_1^*$ and $\Delta\beta_2^*$ are the leading and leaving edge wedge angles; τ is the pitch; β_λ is the gaging angle ($\beta_\lambda = \sin^{-1}(\lambda/\tau)$); Γ is the uncovered turning; S_2, S_4, P_2, P_3 are suction and pressure surface defining points. A Cartesian coordinate system is used with the y-axis passing through the cascade leading edge and the x-axis through the center of the trailing edge circle. All input lengths are normalized on axial chord.

The governing equations for determining the polynomials are:

$$
\begin{aligned}
Y_{S1} &= H + R_1 \sin\left(\beta_1^* - \frac{\Delta\beta_1^*}{2}\right)\\
X_{S1} &= R_1\left[1 - \cos\left(\beta_1^* - \frac{\Delta\beta_1^*}{2}\right)\right]\\
Y'_{S1} &= \tan\left(\frac{\pi}{2} - \beta_1^* + \frac{\Delta\beta_1^*}{2}\right)\\
Y_{S3} &= \tau - (\tau\sin\beta_\lambda + R_2)\sin(\Gamma + \beta_2^*)\\
X_{S3} &= B_X - (\tau\sin\beta_\lambda + R_2)\cos(\Gamma + \beta_2^*) - R_2\\
Y'_{S3} &= \tan\left(\Gamma + \beta_2^* - \frac{\pi}{2}\right)\\
Y_{S5} &= R_2 \sin\left(\beta_2^* - \frac{\Delta\beta_2^*}{2}\right)\\
X_{S5} &= B_X - R_2\left[1 - \cos\left(\beta_2^* - \frac{\Delta\beta_2^*}{2}\right)\right]\\
Y'_{S5} &= \tan\left(\beta_2^* - \frac{\Delta\beta_2^*}{2} - \frac{\pi}{2}\right)
\end{aligned}
\qquad (1)
$$

Nomenclature

A,B = column vector
B_X = airfoil axial chord
C = coefficient matrix
C_{pi} = pressure coefficient, $2(P - P_1)/\rho_1 v_1^2$
H = camber distance parameter
k = number of polynomials
M = Mach number, or number of q-os
M_L = number of q-o just in front of leading edge
M_T = number of q-o through trailing edge
m = number of given points on suction or pressure surface
N = number of streamlines
n = degree of polynomial
P = pressure
R_1, R_2 = radii of leading and trailing edge circles
x, y = Cartesian coordinates
$Y(x)$ = polynomial
β_λ = gaging angle
β_1^*, β_2^* = metal angles at leading and trailing edges
$\Delta\beta_1^*, \Delta\beta_2^*$ = wedge angles at leading and trailing edges
Γ = uncovered turning
λ = throat length
τ = cascade pitch
ψ = stream function
ψ_T = loading coefficient
$\bar{\omega}_2$ = pressure loss coefficient $(P_{T1} - P_{T2})/(P_{T1} - P_2)$

Subscripts

1 = upstream station, or leading edge
2 = downstream station, or trailing edge
T = total

$$
\left.
\begin{aligned}
Y_{P1} &= H - R_1 \sin\left(\beta_1^* + \frac{\Delta\beta_1^*}{2}\right) \\
X_{P1} &= R_1\left[1 + \cos\left(\beta_1^* + \frac{\Delta\beta_1^*}{2}\right)\right] \\
Y'_{P1} &= \tan\left(\frac{\pi}{2} - \beta_1^* - \frac{\Delta\beta_1^*}{2}\right) \\
Y_{P4} &= -R_2 \sin\left(\beta_2^* + \frac{\Delta\beta_2^*}{2}\right. \\
X_{P4} &= B_X - R_2\left[1 + \cos\left(\beta_2^* + \frac{\Delta\beta_2^*}{2}\right)\right] \\
Y'_{P4} &= \tan\left(\beta_2^* + \frac{\Delta\beta_2^*}{2} - \frac{\pi}{2}\right)
\end{aligned}
\right\} \quad (2)
$$

The polynomial $Y(x)$ of degree n is of the form:

$$
\begin{aligned}
Y(x) &= a_0 x^n + a_1 x^{n-1} + \ \ldots\ + a_{n-1}x + a_n \\
&= \sum_{i=0}^{n} a_i x^{n-i}
\end{aligned} \quad (3)
$$

with first and second derivatives:

$$
\left.
\begin{aligned}
Y'(x) &= \sum_{i=0}^{n-1} (n-i)\, a_i x^{n-i-1} \\
Y''(x) &= \sum_{i=0}^{n-2} (n-i)\,(n-i-1) a_i x^{n-i-2}
\end{aligned}
\right\} \quad (4)
$$

In the design, polynomials of degrees three and four are used to fit segments of the profile to the set of geometry conditions describing the cascade.

For the suction or pressure surface, the total number k of the polynomials that describe the profile depends on the number m of given points (including defining points $k = m - 1$). In order to have a continuous curvature, the function should be twice continuously differentiable at interior match points ($k = 2 \ldots m - 1$), i.e.,

$$
\left.
\begin{aligned}
Y_{k-1}(x_k) &= Y_k(x_k) \\
Y'_{k-1}(x_k) &= Y'_k(x_k) \\
Y''_{k-1}(x_k) &= Y''_k(x_k)
\end{aligned}
\right\} \quad (5)
$$

We apply the design and matching conditions to defining polynomials for the profile segments. A system of equations for the suction or pressure side in unknown coefficients of polynomials is obtained in matrix form as

$$
C\mathbf{A} = \mathbf{B} \quad (6)
$$

Here the unknown vector **A** is composed of the coefficients of the polynomials used and the right-hand vector **B** is made up of the design and match point conditions.

Gaussian elimination is used to solve an 18 × 18 linear system of equations for the suction surface and a 12 × 12 linear system for the pressure surface of the profile. The degree of the polynomials used between indicated profile points are:

Suction surface: S_1 to S_2, 4th degree; S_2 to S_3, 4th degree; S_3 to S_4, 3rd degree, S_4 to S_5, 3rd degree.

Pressure surface: P_1 to P_2, 3rd degree; P_2 to P_3, 3rd degree; P_3 to P_4, 3rd degree.

If the auxiliary points S_2, S_4 and P_2, P_3 are not used (entered in the input as zero), reduced systems of equations for suction and pressure surface and correspondingly altered polynomial fits are employed. Refer to Ye and Kavanagh [13] for details.

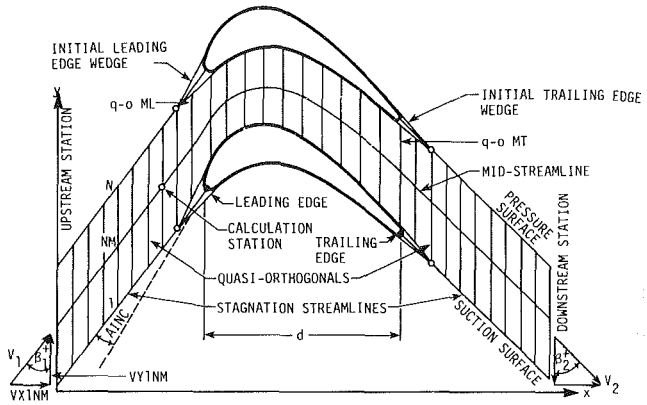

Fig. 3 Cascade flow field for streamline curvature calculation

Global Inviscid Analysis. The present streamline curvature analysis (SCA) method for two-dimensional cascade adiabatic flow solution is an implementation of techniques using "quasi-orthogonals" (q-os) recommended by Wilkinson [14, 15]. The objective of the SCA is to provide a global inviscid analysis of blade-to-blade flows used in conjunction with cascade geometry design procedures. The governing equations to be solved are a velocity gradient equation and the continuity equation. The velocity gradient relationship along a q-o, which for this application coincides with the y-axis (see Fig. 3), is obtained by combining the equations of momentum, energy, and entropy.

The computational flow field for the global streamline curvature calculation is shown in Fig. 3. The total number of q-os (M) is divided evenly among the upstream, cascade passage, and downstream regions. The q-o just ahead of the leading edge is q-o number M_L; the q-o passing through the trailing edge is q-o number M_T. The spacing is arranged so that the leading edge lies midway between q-o M_L and q-o $M_L + 1$. The total number of streamlines (N) must be odd, and the midstreamline is number NM.

In the analysis, up to 39 q-os and 9 streamlines are used for the solution. A quartic is fitted through a point on q-o and its four neighbor points on either side for the same streamline and is subsequently differentiated at the point to calculate slopes and second derivatives needed in the analysis. As is generally true in streamline curvature analysis methods, damping of the calculations is required for convergence in high subsonic or transonic flow cases and in cases of high pitch-to-chord ratios. With damping applied, extensive calculations may be required.

In the programmed method, limits are placed on the number of iterations performed, and specific tolerances are applied for convergence in the continuity, channel, and stagnation streamline shaping solutions (see Alarcon and Kavanagh [16] for details).

Inviscid Reanalysis of Leading Edge. The reanalysis procedure developed in this investigation for two-dimensional adiabatic flow is based on the finite area techniques presented by Caspar et al. [17] and by McDonald [18]. The body-fitted orthogonal mesh grid constructed from the known airfoil geometry shown in Fig. 4 is used and the solution is obtained in the physical plane in terms of the stream function, directly using the information provided by the global streamline curvature analysis. The continuity equation and the irrotationality condition are combined to obtain the equation to be approximated with the finite area technique. Finite area computational elements used are noted in Fig. 4. Details of the development of the analysis are given by Alarcon [19].

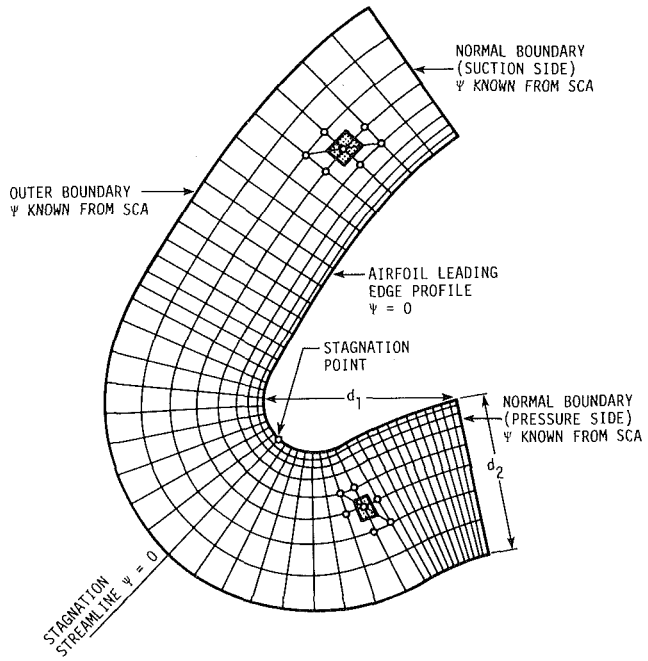

Fig. 4 Reanalysis computational mesh and solution domain for the reanalysis boundary value problem. Two example computational elements are shown.

The reanalysis mesh is made up of 45 lines normal to the airfoil and 9 transverse curves (including airfoil contour) around the airfoil. The point spacing along the normals is exponental, increasing from the airfoil toward the outer boundary. The spacing along the airfoil is uniform around the leading edge circle and then exponential from the circle tangency points to the normal mesh boundaries.

Finite area equations are written at each mesh point in terms of quantities at the point and six neighbor points, such as shown for representative elements in Fig. 4.

Integral Boundary Layer Analysis. The dissipation-integral boundary layer calculation procedure presented by Walz [20] was used in this investigation to perform the profile layer calculation. The method and solution procedure applies to both laminar and turbulent boundary layers, with or without heat transfer.

In this application, the dissipation-integral method has been extensively modified to include improved empirical auxiliary relations for turbulent boundary layer calculations. Also, since the profile boundary layer is highly transitional, the laminar and turbulent calculations were linked through appropriate transition models: laminar starting, natural transition, laminar separation bubbles, and turbulent separation. In addition, the important effects of wall curvature and free stream turbulence level on the development of the turbulent boundary layers were included. Wake mixing calculation methods determine the losses due to the profile boundary layer and wake mixing (see Alarcon [19] for details).

The approach used here for cascade design analysis is comparable to that which might employ methods such as TSONIC developed by Katsanis [21] for blade-to-blade flow analysis and BLAYER developed by McNally [22] for profile boundary layer calculations (refer to [13] for details).

Design Problems

Determination of Input for the Design. Fifteen geometric parameters are required as input by the turbine cascade geometry design (TCGD) program. Figure 2 should be referred to for the airfoil and cascade geometric parameters.

The cascade design can be initiated by selecting a pitch to axial chord ratio, τ/B_X, from loading considerations. In the expression for loading coefficient ψ_T given below, the gas angles are given and a value of ψ_T is selected for design experience (refer to Horlock [23]).

$$\psi_T = 2\frac{\tau}{B_X}\sin^2\beta_2(\cot\beta_1 + \cot\beta_2) \tag{7}$$

Therefore, τ/B_X can be solved for from equation (7). Typical values for ψ_T may range from 0.6 to 1.2 with the final choice being determined by the satisfactory performance of the cascade.

A value of H can now be selected which determines the camber distribution and stagger of the airfoil. This parameter plays a role, along with wedge angle $\Delta\beta_1^*$, in determining the channel area variation with chord and, therefore, the loadng distribution.

The cascade gaging angle β_λ is determined from the given exit gas angle β_2 and Mach number M_2, using experimental correlations accounting for flow deviation. The cascade throat or gaging length λ is calculated from

$$\lambda = \tau\sin\beta_\lambda \tag{8}$$

The inlet metal angle β_1^* coincides with the inlet gas angle at zero incidence; normally, the incidence is set negatively to reduce overspeeding around the leading edge on the suction side. The exit metal angle β_2^* and the uncovered turning Γ are finally decided on by finding an acceptable pressure distribution and satisfactory profile boundary layer performance for the design.

The trailing edge radius R_2 is selected according to manufacturing or airfoil cooling requirements and trailing edge blockage considerations. The leading edge radius R_1 generally tends to increase with blade loading and turning.

The wedge angles $\Delta\beta_1^*$, $\Delta\beta_2^*$ and the auxiliary points (X_{S2}, Y_{S2}), (X_{S4}, Y_{S4}), (X_{P2}, Y_{P2}), (X_{P3}, Y_{P3}) (see Fig. 2) on the suction and pressure sides are determined in a trial and error procedure to give an acceptable airfoil shape. These variables strongly influence the cross-channel area variation and hence the pressure distribution. Design experience shows that $\Delta\beta_2^*$ generally ranges from 0–10 deg.

The designer first uses the TCGD program to design the airfoil profile and to obtain a graphical output of the profile. He then uses the package of programs for blade-to-blade analysis consisting of the global blade-to-blade inviscid analysis, the inviscid reanalysis of the leading edge, and the profile integral boundary layer analysis to analyze the cascade flow performance. This package includes a main program and 56 subroutines. The designer can run the whole program to get all the performance at one time or run parts of the program to get analysis as desired.

Airfoil Profile Solution. The geometry design program TCGD is operated in an interactive mode by which the input geometric parameters are adjusted according to intermediate results put out by the program upon the request of the user.

This approach allows the designer to modify the design rapidly and continuously until he is satisfied. To facilitate the initial specification of a profile, the input is reduced to quantities that are known. All the auxiliary points S_2, S_4 and P_2, P_3 do not need to be included as input; i.e., for the first iteration they can be set to zero. The computer produces a profile in dashed outline as shown in Fig. 5. Of course, the first profile has to be improved. Comparison of the actual shape with what the designer has in mind gives a clear indication of the necessary changes. The designer can then modify the profile wherever necessary by assigning values to the auxiliary points. For example, in Fig. 5, the dotted and dashed outline shows how the profile is modified by setting the points S_2 and P_2. The profile in solid outline is the final design in which all the values of the auxiliary points are given.

Table 1 Geometry design parameters for turbine cascade profiles

Profile	R_1	R_2	H	β_1^*, deg	$\Delta\beta_1^*$, deg	β_2^*, deg	$\Delta\beta_2^*$, deg	τ	β_λ, deg	Γ deg
A	0.0555	0.0220	0.8051	38.5	30	15.92	2	1.1817	15.4075	8
B	0.0662	0.0228	1.2155	40.15	30	17.07	2	1.4740	15.7987	6
C	0.1567	0.0160	2.4420	90	90	10.43	4	2.5350	9.6890	12

Table 2 The input data for turbine geometry design program

Profile	R_1	R_2	H	β_1^* deg	$\Delta\beta_1^*$ deg	β_2^* deg	$\Delta\beta_2^*$ deg	X_{S2}	Y_{S2}
D	0.0325	0.0135	0.4600	44.5	40	21.8	4.0	0.65	0.67554
E	0.038	0.0225	0.6878	90	27.5	34.992	6.5	0.525	0.6065

Profile	X_{S4}	Y_{S4}	X_{P2}	Y_{P2}	X_{P3}	Y_{P3}	τ	β_λ deg	Γ deg
D	0.85	0.3589	0.475	0.4773	0.80	0.2655	0.825	24.4424	14.8
E	0.675	0.4598	0.35	0.5475	0.72	0.2695	0.99	34.6865	12.2

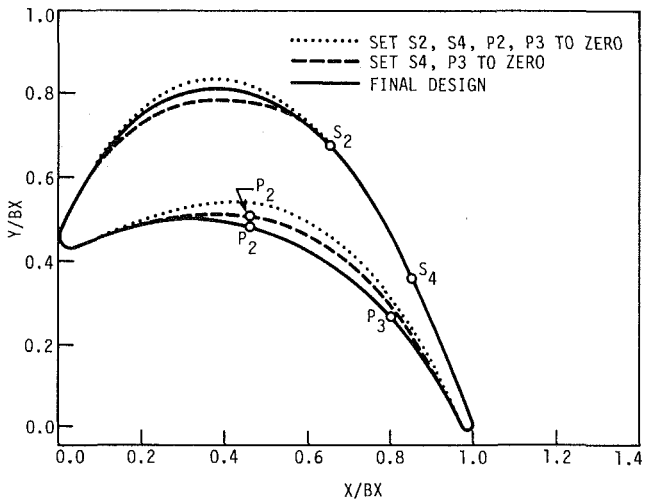

Fig. 5 Airfoil profile design of turbine cascade

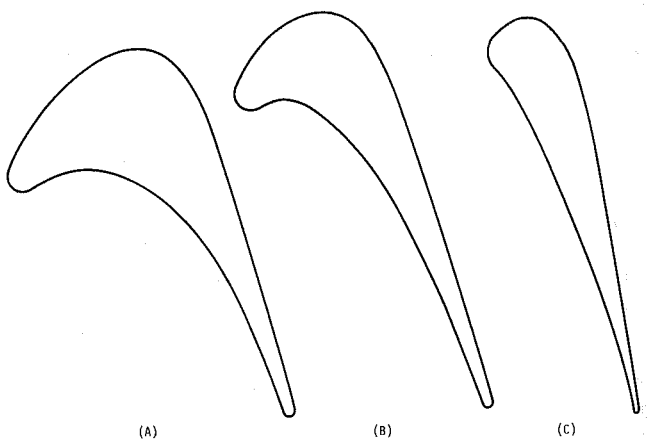

Fig. 6 Computer generated profiles

Design Results and Comparisons

The geometry design program TCGD has been developed to design the airfoil profile in cascade in an interactive fashion. Rapid graphing capabilities are essential to the method. To verify the advantages of the proposed profiling method, a study of several airfoil profiles, representative of high-performance blading requirements, was carried out. The cases and their design parameters are given in Table 1, and computer-generated plots of the profiles are shown in Fig. 6. Experience with the geometry design program TCGD has shown, in general, that arbitrary turbine profiles can be easily and rapidly designed.

Two turbine cascade designs obtained with the TCGD program, followed by global inviscid analysis, reanalysis of the leading edge flow region, and transitional boundary layer analysis are presented next. Design profile D is a turbine rotor blade, while design profile E is a turbine guide vane. The design data used with program TCGD, including auxiliary points for the profiling process, are listed in Table 2.

Figure 7(*a*) is the computer-generated graph of the resultant design of the turbine blade (profile D). This profile was assigned a loading coefficient $\psi = 0.8$ with 0 deg incidence and moderate subsonic exit flow ($M_2 = 0.58$, $M_{max} = 0.62$). Figure 8(*a*) shows the resultant design for the turbine guide vane (profile E), which was assigned a loading coefficient $\psi_T = 0.94$ with 0 deg incidence. The velocity triangle and exit Mach number requirements determined the gaging angle in both profile design cases.

Figures 7(*b–d*) and 8(*b–d*) display the midstreamline velocity distributions, the pressure coefficient distributions along the profiles, and the natural transition, fully turbulent, laminar separation, and turbulent reattachment locations. These results were obtained from the global inviscid analysis, leading edge reanalysis, and boundary layer analysis. As can

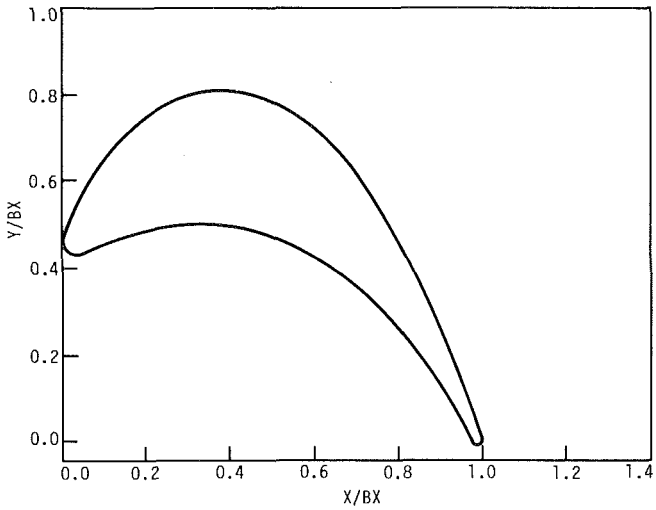

Fig. 7(*a*) Computer generated design for the turbine blade

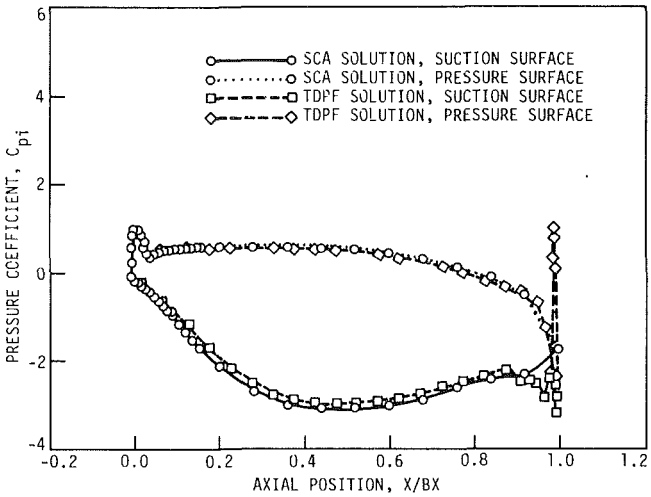

Fig. 7(*d*) Comparison of pressure coefficient distributions between SCA and TDPF methods in incompressible case

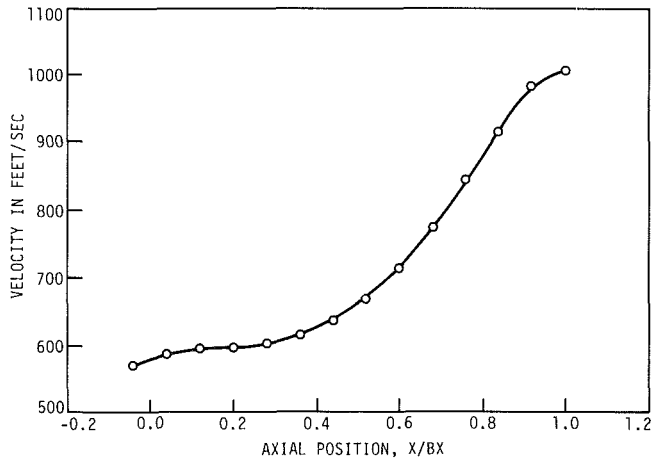

Fig. 7(*b*) Mid-streamline velocity distribution

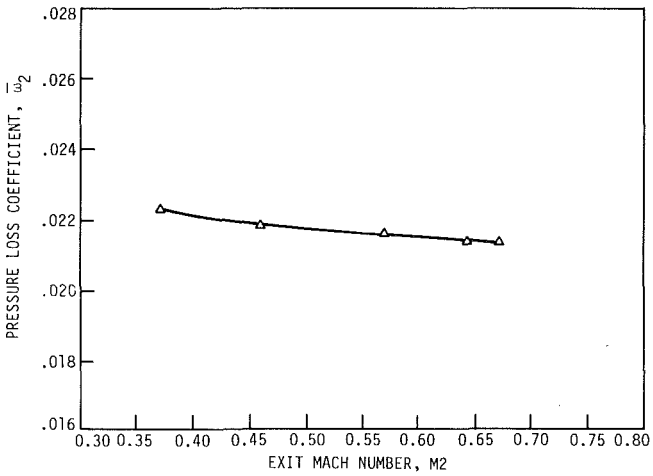

Fig. 7(*e*) Pressure loss coefficient $\bar{\omega}_2$ variation with exit Mach number M_2.

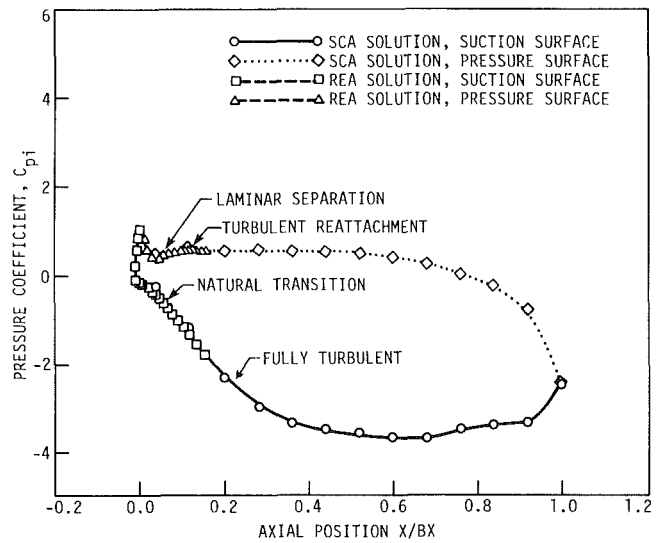

Fig. 7(*c*) Pressure coefficient distribution.

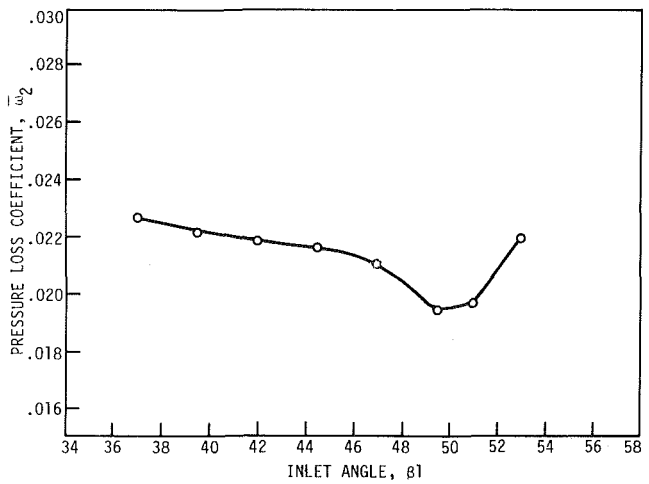

Fig. 7(*f*) Pressure loss coefficient $\bar{\omega}_2$ variation with inlet angle β_1

Fig. 7 Turbine blade cascade design case

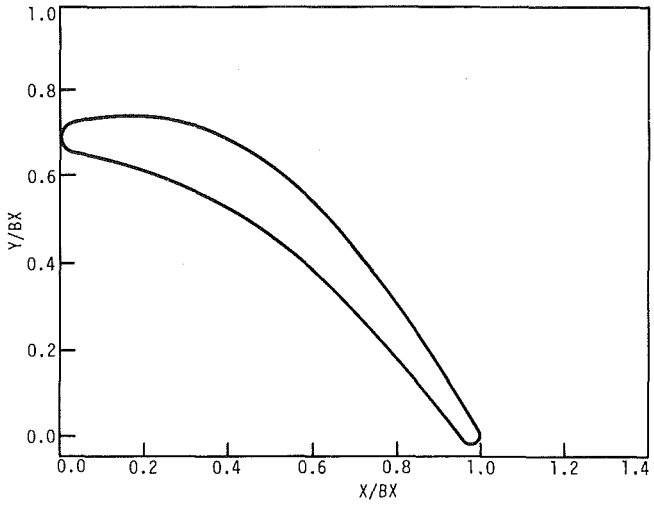

Fig. 8(*a*) Computer generated design for the turbine guide vane

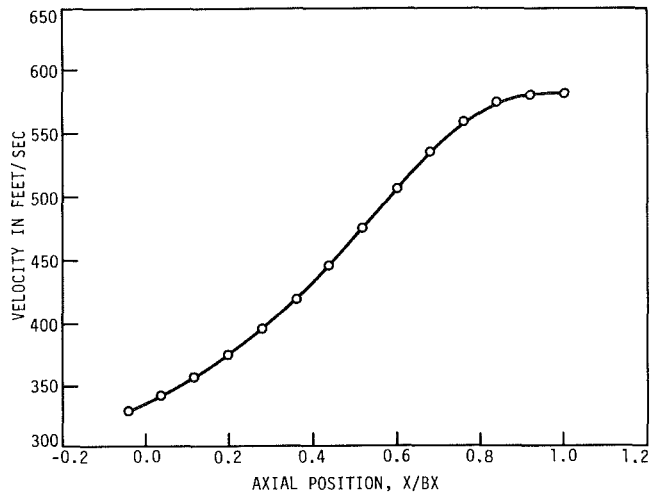

Fig. 8(*b*) Mid-streamline velocity distribution

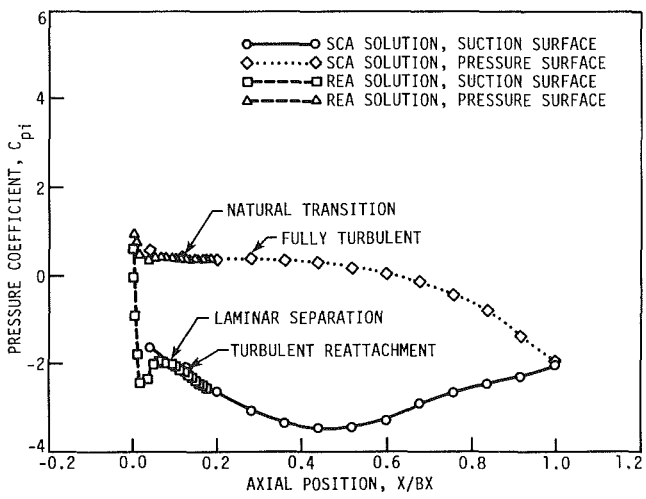

Fig. 8(*c*) Pressure coefficient distribution.

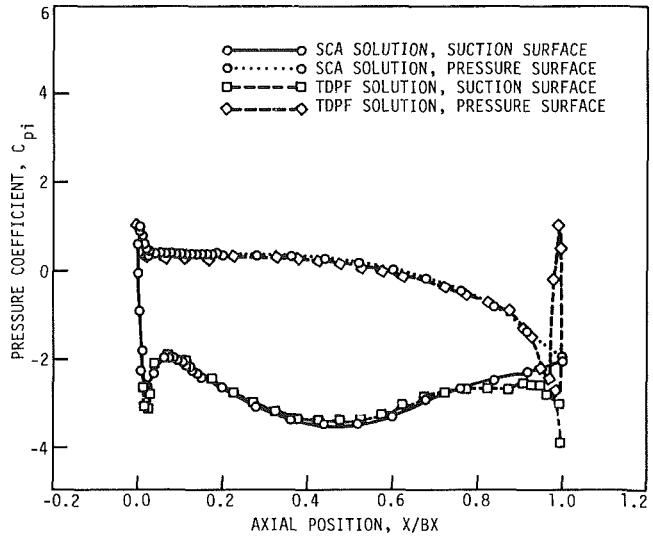

Fig. 8(*d*) Comparison of pressure coefficient distributions between SCA and TDPF methods in incompressible case

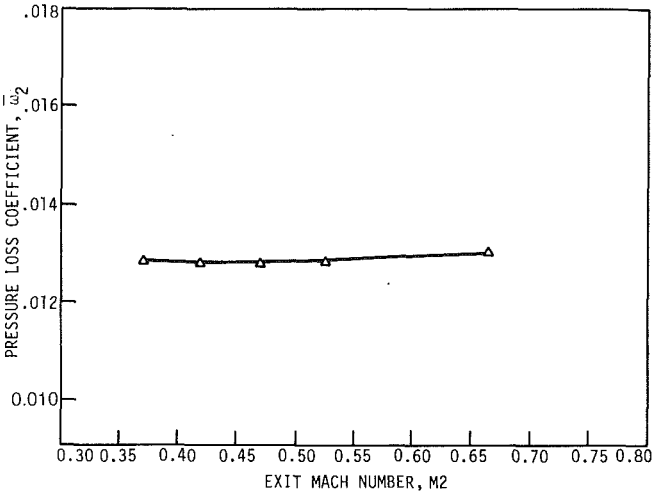

Fig. 8(*e*) Pressure loss coefficient $\bar{\omega}_2$ variation with exit Mach number M_2.

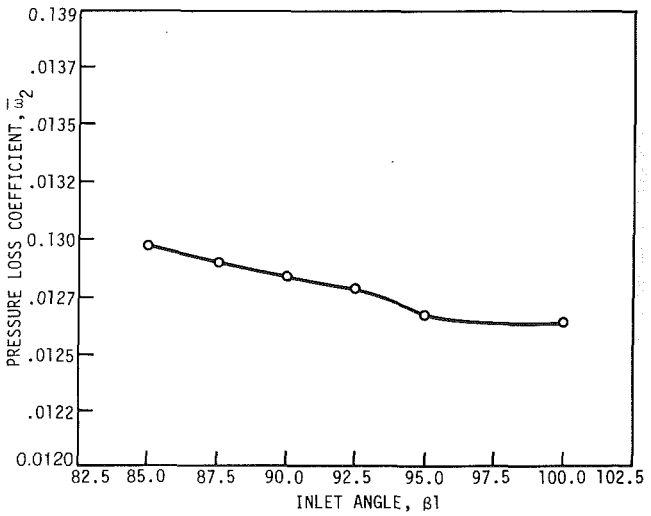

Fig. 8(*f*) Pressure loss coefficient $\bar{\omega}_2$ variation with inlet angle β_1

Fig. 8 Turbine guide vane cascade design case

be seen, the midstreamline velocities continually increase with chord in Figs. 7(*b*) and 8(*b*). Also the pressure coefficient curves in Figs. 7(*c*) and 8(*c*) are smooth and the peak pressure coefficients are low to minimize the diffusion and to avoid excessive boundary layer growth.

The pressure coefficent distributions calculated by the global inviscid analysis combined with a local reanalysis around the leading edge are compared with those calculated by a two-dimensional potential flow (TDPF) procedure based on distributed singularities for the same profile design cases. The results are shown in Figs. 7(*d*) and 8(*d*). Agreement between the two methods is good except near the inviscid trailing edge stagnation point. This shows the usefulness of the method to the actual problems.

The pressure loss coefficient variation with exit Mach number for two cases is shown in Figs. 7(*e*) and 8(*e*), and with inlet angle in Figs. 7(*f*) and 8(*f*). From the calculated cascade performance in design cases, it is observed that little change in loss coefficient with Mach number or incidence occurs.

Conclusions

The systematic computational design system can be used rapidly and effectively for the design of turbine cascades. The procedure is widely applicable, accurate, and economical.

A geometry design procedure is developed to accomplish the design of turbine cascade from given velocity triangle requirements in an interactive fashion. Experience with the geometry design program has shown that the turbine profile can be easily and rapidly designed.

The developed streamline curvature for global inviscid analysis, a leading edge reanalysis, and the developed transitional boundary layer calculation are found to be accurate, fast and flexible. The results obtained from the SCA method are compared with those obtained from two-dimensional potential flow method based on distributed singularities. They are shown to be in good agreement.

Acknowledgments

This work was done by the author during his stay at the Turbomachinery Components Research Laboratory in the Department of Mechanical Engineering, Iowa State University. The opportunity to work in the Laboratory as a Visiting Scientist and advice and direction provided by Professors P. Kavanagh, G. Serovy, and T. Okiishi in carrying out this work is gratefully acknowledged.

References

1 LeFoll, J., "A Theory of the Representation of the Properties of Boundary Layer on a Plane," *Proceedings of the Seminar on Advanced Problems in Turbomachinery Part I*, edited by K. Cassady and J. Chauvin, von Karman Institute, Belgium, 1965.

2 Huo, S., "Blade Optimization Based on Boundary Layer Concepts," *AGARD AGARograph* 164, 1972, pp. 141–170.

3 Papailiou, K., "Boundary Layer Optimization for the Design of High Turning Axial Flow Compressor Blades," ASME JOURNAL OF ENGINEERING FOR POWER, Vol. 93, 1970, pp. 147–155.

4 Henderson, M. L., "Inverse Boundary-Layer Technique for Airfoil Design," NASA Conference Publication No. 2045, pt. 1, Vol. 1, 1978.

5 Boiko, A. V., and Kozhevnikov, S. N., "Designing Subsonic Turbine Profiles of Optimal Aerodynamic Shape," *Teploenergetika*, Vol. 25, 1978, pp. 55–57.

6 Schmidt, E., "Computation of Supercritical Compressor and Turbine Cascades With a Design Method for Transonic Flows," ASME JOURNAL OF ENGINEERING FOR POWER, Vol. 102, 1980, pp. 68–74.

7 Thompkins, W. T., Jr., and Siu Shing Tong, "Inverse or Design Calculations for Nonpotential Flow in Turbomachinery Blade Passages," ASME JOURNAL OF ENGINEERING FOR POWER, Vol. 104, 1982, pp. 281–285.

8 Thomas, K. M., and Piendel, J. J., "An Automated Interactive Design System for Advanced Gas Turbines," ASME Paper No. 74-GT-82, 1974.

9 Monello, J. A., Mitchell, W. S., and Tall, W. A., "Application of Nonseries Airfoil Design Technology to Highly Loaded Turbine Exit Guide Vanes," ASME JOURNAL OF ENGINEERING FOR POWER, Vol. 101, 1979, pp. 202–211.

10 Hobbs, D. E., and Weingold, H. D., "Development of Controlled Diffusion Airfoils for Multistage Compressor Application," ASME Paper No. 83-GT-211, 1983.

11 Engeli, M., Zollinger, H. J., and Alleman, J. C., "A Computer Program for the Design of Turbomachinery Blades," ASME Paper No. 78-GT-36, 1978.

12 Boiko, A. V., and Kozhevnikov, S. N., "Analytic Design of Aerodynamically Advanced Subsonic Turbine Profiles with the Aid of High-Order Polynomials," *Energomashinostroenie*, No. 11, 1980, pp. 9–11.

13 Ye, Z.-Q., and Kavanagh, P., "Axial-Flow Turbine Cascade Design Procedure and Sample Design Cases," TCRL-28, Engineering Research Institute, Iowa State University, 1983.

14 Wilkinson, D. H., "Stability, Convergence, and Accuracy of Two-Dimensional Streamline Curvature Method Using Quasi-Orthogonals," *Proc. Inst. Mech. Eng.*, Vol. 184, Pt. 3G(1), 1970, pp. 108–119.

15 Wilkinson, D. H., "Calculation of Blade-to-Blade Flow in a Turbomachine by Streamline Curvature," Aero. Res. Council Reports & Memoranda No. 3704, 1970.

16 Alarcon, G. A., and Kavanagh, P., "Streamline Curvature Methods for Cascade Flow Analysis," ISU-ERI-Ames-80218, TCRL-15, Engineering Research Institute, Iowa State University, 1980.

17 Caspar, J. R., Hobbs, D. E., and Davis, R. L., "The Calculation of Two-Dimensional Potential Cascade Flow Using Finite Area Methods," *AIAA Journal*, Vol. 18, 1979, pp. 103–109.

18 McDonald, P. W., "The Computation of Transonic Flow Through Two-Dimensional Gas Turbine Cascades," ASME Paper No. 71-GT-89, 1971.

19 Alarcon, G. A., "Design of Turbine Cascades with Transitional Profile Boundary Layers," Ph.D. thesis, Iowa State University, Ames, Iowa, 1980.

20 Walz, A., *Boundary Layers of Flow and Temperature*, The M.I.T. Press, Cambridge, Mass., 1969.

21 Katsanis, T., "FORTRAN Program for Calculating Transonic Velocities on a Blade-to-Blade Stream Surface of a Turbomachine," NASA TN D-5427. 1969.

22 NcNally, W. D., "FORTRAN Program for Calculating Compressible Laminar and Turbulent Boundary Layers in Arbitrary Pressure Gradients," NASA TN D-5681, 1970.

23 Horlock, J. H., *Axial Flow Turbines*, Robert E. Krieger Publishing Company, New York, 1973.

Effectiveness Measurements for a Cooling Film Disrupted by a Single Jet

B. L. Button
Reader,

Department of Mechanical Engineering,
Coventry (Lanchester) Polytechnic,
Coventry, CV1 5FB, England

Experimental measurements of the effectiveness downstream of a slot airflow with the jet airflow normal to the wall have been performed in a wind tunnel. The separate and combined contributions of the slot and jet airflows to the effectiveness are established for a range of airflow conditions relevant to gas turbine combustors. Generally, the jet reduces the effectiveness. The major interactions between the airflows occur just downstream of the jet. Visualization studies using tufts and velocity and turbulence intensity profiles are reported.

Introduction

The walls of gas turbine combustors are usually maintained at acceptable temperatures by cooling films of air injected parallel to the wall through slots. However, air needs to be added to the primary, secondary, and tertiary zones of the combustor. This is achieved by injecting jets of air normal to the wall, which inevitably disrupts the cooling film and give rise to high-temperature areas and hot spots downstream of the jets.

In order to seek a detailed understanding of some of the phenomena involved, a program of research has been partially completed [1]. This covers flow visualization, effectiveness, and heat transfer coefficient measurements downstream of a slot exit, for various combinations of slot and single-and multiple-jet geometries and airflow conditions some of the flow visualization and effectiveness results for a single jet disrupting a cooling film from a slot. For the majority of these results the jet centerline is positioned one jet diameter downstream of the slot exit but some results are given for two other positions of the jet. A brief description of the airflow rig and measurement techniques used and the preliminary experiments carried out is included. A comprehensive description of these and the design and construction of the airflow rig and its instrumentation and verification data acquisition and analysis used to carryout the research can be found in [1].

Airflow Rig and Measurement Techniques

The airflow rig is shown schematically by Fig. 1. It consists of three separate system, each supplying an airflow to the working section. For the main system, or wind tunnel, ambient air is drawn in through filters by a centrifugal fan with a variable speed drive. The air then passes through a diffuser, a settling chamber containing a honeycomb and five screens and a contraction used to meter the flow. Although different in size the slot and jet systems prepare the airflows in a similar way, but they are metered by orifice plate assemblies built to conform to BS 1042 [2]. A flexible coupling is included in each system to isolate the working section from vibrations. The air temperatures are measured using copper-constantan thermocouples and the relative humidity by a capacitive type sensor. Pressures are measured using a micromanometer [3].

The working section is 300 mm square and 710 mm long. It has fixed walls, an adjustable roof and the base contains the slot for the boundary layer bleed, the exit of the slot and jet airflows, and the test specimen for the effectiveness measurements. These are shown by Fig. 2, which also includes the details of the slot geometry used. This is based on the pulse drilled designs that are now in use in some combustors. The jet pipe is 925 mm long. To a first approximation the outlet velocity and turbulent intensity profiles leaving it resemble those found in combustors.

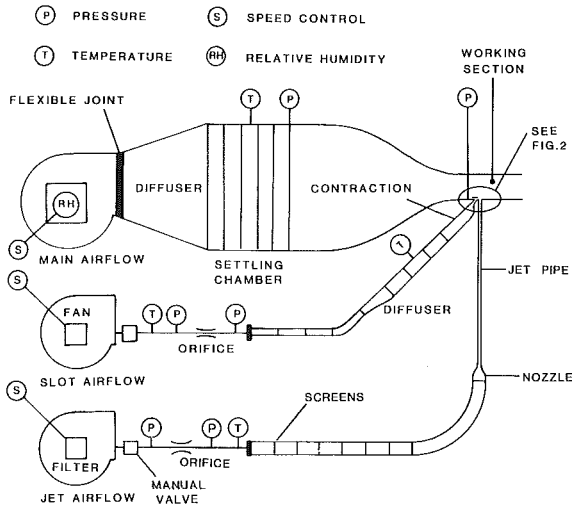

Fig. 1 Schematic of the airflow rig

Contributed by the Gas Turbine Division of THE AMERICAN SOCIETY OF MECHANICAL ENGINEERS for presentation at the 28th International Gas Turbine Conference and Exhibit, Phoenix, Arizona, March 27-31, 1983. Manuscript received at ASME Headquarters January 18, 1983. Paper No. 83-GT-250.

The flow visualization studies were made using tufts and DISA hot-wire anemometry with miniature probes. Initially the tufts were nylon wool 25 mm long, but subsequently it was found cotton thread 15 mm long was more sensitive.

The impermeable-wall effectiveness was determined from helium concentrations at the wall and at a the point of injection for the slot and jet separately, i.e., $\eta_j = c_{ij}/c_{cj}$ and $\eta_s = c_{is}/c_{cs}$. About 2 percent of helium in air by volume was used. For each test, 48 samples were measured with a katharometer. They were selected automatically every 20 s by a multiport valve at a sampling flow of 2.5 cm^3/s. The samples were drawn from the test specimen through the valve, katharometer, and rotameter by a vacuum pump.

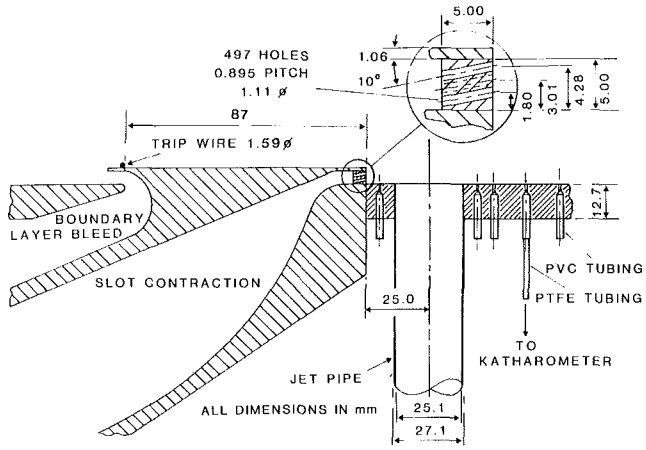

Fig. 2 Slot and jet geometry

Experimental Measurements

Preliminary Experiments. The results of the preliminary experiments include the following:

(*a*) A calibration of the temperature, pressure, relative humidity and hot-wire sensors and the katharometer detector;

(*b*) Verification that the mean velocity obtained from using the contraction and two orifice plate assemblies are the same as the results of the pitot tube surveys made at the entry of the three airflows into the working section, respectively.

(*c*) The main airflow in the working section, excluding peripheral boundary layers, at 16 m/s varies by < 0.5 percent and the turbulence intensity distribution < 0.3 percent.

(*d*) For the turbulent boundary layer from the trip wire in a zero pressure gradient, the lateral variation about the mean for δ^* and θ is 3.5 percent and for H is < 2 percent. $\delta^*/D = 0.048$ at the leading edge of the jet exit. The velocity and turbulence profiles are in good agreement with those given by Klebanoff and Diehl [4] and those quoted by Schlichting [5], repectively.

(*e*) The velocity and turbulence profiles downstream of the

Table 1 Tests and airflow conditions

$\bar{U}_m$/(m/s)	16 (Ma = 0.05)								
$\bar{U}_s$/(m/s)	8			16			24		
M_s	0.5			1.0			1.5		
$\bar{U}_j$/(m/s)	8	16	32	8	16	32	8	16	32
M_j	0.5	1.0	2.0	0.5	1.0	2.0	0.5	1.0	2.0
(*a*)&(*d*)		*		*	*	*		*	
(*b*)&(*c*)	*	*	*	*	*	*	*	*	*

* Test
(*a*) Velocity and turbulence measurements
(*b*) Tuft measurements
(*c*) η_s and η_j measurements with $x_{sj} = 25.0$ mm
(*d*) η_s and η_j measurements with $x_{sj} = 50.0$ and 75.0 mm

Nomenclature

c_{cj} = helium concentration in jet airflow at exit
c_{cs} = helium concentration in slot airflow at exit
c_{ij} = helium concentration at wall for jet airflow
c_{is} = helium concentration at wall for slot airflow
D = jet diameter
H = shape factor
Ma = main airflow Mach number
M_j = mass velocity ratio for jet $(\rho_j \bar{U}_j/\rho_m \bar{U}_m)$
M_s = mass velocity ratio for slot $(\rho_s \bar{U}_s/\rho_m \bar{U}_m)$
$\bar{U}_j$ = mean jet airflow velocity
$\bar{U}_m$ = mean main airflow velocity
$\bar{U}_s$ = mean slot airflow velocity
x = distance downstream from slot exit
x_{sj} = distance between slot exit and jet center line
y = lateral distance form the jet center line
z = distance measured vertically from wall

Greek Symbols

β = angle of wool tuft or cotton thread to direction of main airflow
δ^* = displacement boundary layer thickness
η_j = impermeable-wall jet effectiveness
η_s = impermeable-wall slot effectiveness
η_{sj} = $\eta_s + \eta_j$
θ = momentum boundary layer thickness
ρ_j = jet airflow density
ρ_s = main airflow density
ρ_m = slot airflow density

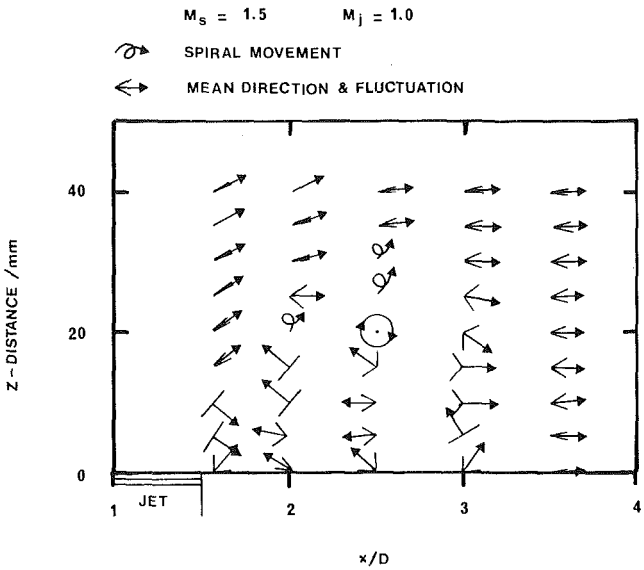

Fig. 3 Sketch of cotton threads for M_s = 1.5 and M_j = 1.0

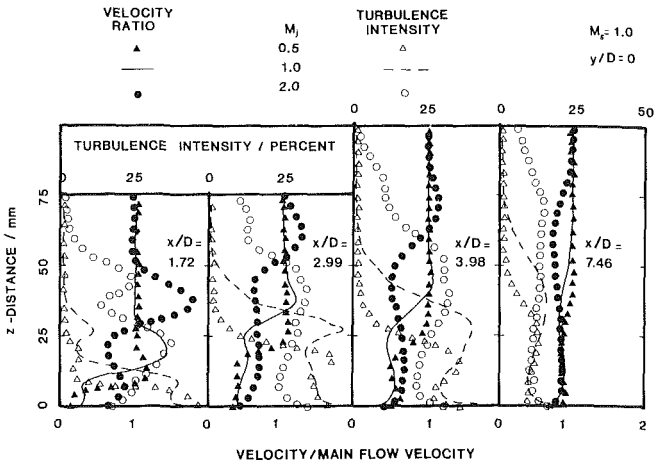

Fig. 4 Velocity and turbulent intensity profiles with x/D and z for y/D = 0, M_s = 1.0 and variations in M_j

slot resemble those for boundary layerlike flow for M_s = 0.5 and wall jetlike flow for M_s = 1.0 and 1.5.

(*f*) The velocity and turbulence profiles of the jet airflow at exit from the jet for M_j = 0.5, 1.0, and 2.0 all resemble those for fully developed turbulent pipe flow.

(*g*) The effectiveness is unchanged when the sample flow varies from 0.26 to 3.73 cm^3/s.

(*h*) The effectiveness measurements made for an unobstructed slot and a single jet downstream of a turbulent boundary layer are in good agreement with those of Kacker and Whitelaw [6] and Goldstein et al. [7], respectively.

(*i*) Separate effectiveness measurements were made for the slot geometry shown in Fig. 2 but without the jet.

Main Experiments. Table 1 summarizes the tests, airflow conditions, measurements positions, and estimated 95 percent confidence intervals for the velocity and turbulence intensity profiles, tuft and effectiveness measurements.

For boundary layer at upper lip of slot exit δ^* = 1.1 mm. Downstream of slot exit the airflow close to the wall is boundary layerlike for M_s = 0.5 and wall jetlike for M_s = 1.0 and 1.5. At the jet exit, the airflow resembles fully developed turbulent pipe flow. The pressure gradient is zero in the working section with no slot or jet airflow present.

Measurement Positions (All Dimension in mm). (*a*) x = 43.3, 75.0, 100.0 and 187.5; y = 0, and $0 < z < 100$. (*b*) As (*a*) but y = 0 and every 25 up to 100, and wool tufts every 10 with z and immediately upstream, downstream, and on either side of the jet exit. For a few tests a cotton thread was used at more positions. (*c*) and (*d*) A selection of 45 coordinates from x every 6.25 up to 75, every 12.5 up to 125, and then every 25.0 up to 187.5; y = 0 and every ± 12.5 to ± 50.

Estimates of 95 Percent Uncertainty Intervals. $\bar{U}_m < 0.1$ percent; $\bar{U}_s$ and $M_s < 2$ percent, $\bar{U}_j$ and $M_j < 3$ percent; $\beta <$ 5 deg; η_j and $\eta_s < 1$ percent; $\eta_{sj} < 2$ percent; x, y, and $z <$ 0.1 mm and low turbulence intensity < 12 percent. For turbulence intensities of 10,25, and 50 percent based on [8] the uncertainties are 10.4, 12.5, and 20.0 percent, respectively.

Discussion of Results

Tufts. These results provided primarily some indication of the direction and extent of the separate and combined airflows at the different test conditions. They show that these airflows are affected for any jet airflow by changes in the slot airflow. The general behavior of the jet airflow is consistent with the description given by Ramsey and Goldstein [9] for an almost identical jet geometry covering the same values of M_j, but subject only to a main airflow with a turbulent boundary layer adjacent to the wall. The most significant contribution indicated by the wool tuft results, and confirmed for some cases by using a cotton thread, is the position and size of the zone where reverse flows occur downstream of the jet, e.g., see Fig. 3. Some of the other detailed results are included in the subsequent sections where they assist in the understanding of the interacting airflows.

Velocity and Turbulence Intensity Profiles. So that all the velocity and turbulence intensity profiles at y/D = 0 can be shown clearly, the profiles for $M_s = M_j$ = 1.0 are given on Figs. 4 and 5 not experimental points, but by a continuous line and a broken line, respectively. Since these profiles are typical of the other profiles, they will be discussed first. At x/D = 1.72, there is a region of low velocity and high turbulence intensity that extends to $z \simeq 10$ mm and is characteristic of wake flow. Above this region, the velocity is similar to the fully developed turbulent pipe flow of the entering jet airflow, but distorted downwards and accelerated. The turbulence intensity "peaks" above and below this profile at the mixing region between the top of the jet airflow and the main airflow, and at the bottom of the jet airflow between the slot and main airflows. From the tuft results at z = 0, 20, 30, 40, and 50 mm, β is 90, 40, 20 10 and 0 deg respectively. These results show clearly the turning and distortion of the jet airflows. At x/D = 2.99, the wake airflow has moved out to $z \simeq 25$ mm, and the airflow above it has decelerated considerably, while the airflow adjacent to the wall has accelerated slightly. The direction of the resultant airflow at z = 10, 20, 30, and 40 mm indicated by the tuft angles corresponds to 30, 10, 5, and 0 deg. Between x/D = 2.99 and 3.98 and on to 7.46, the development of the resultant airflow can be divided into two regions, one above and the other below the locus of the maximum turbulence intensity away from the wall. Above the locus, the mixing of the main and the jet airflows continues to move outwards. At x/D = 3.98, the tufts still show that the direction of the airflow is moving away from the wall as at z = 10, 20, 30, 40, and 50 mm, β = 20, 20, 10, 5, and 5 deg, respectively. Between x/D = 3.98 and 7.46 and below $z \simeq 20$ mm, the velocity and turbulence intensity profiles undergo a significant development towards those for a turbulent boundary layerlike flow. Above this height, the mixing region continue to spread upward into the main airflow and has reached z = 70 mm at x/D = 7.46. At this position, $\beta \simeq 10$ deg for all zs.

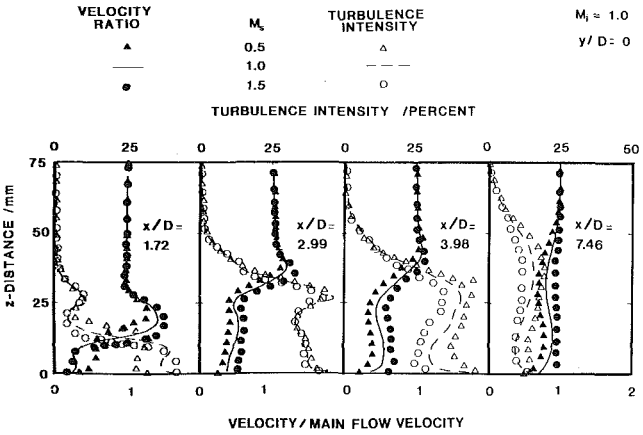

Fig. 5 Velocity and turbulent intensity profiles with x/D and z for $y/D = 0$, $M_j \approx 1.0$ and variations in M_s

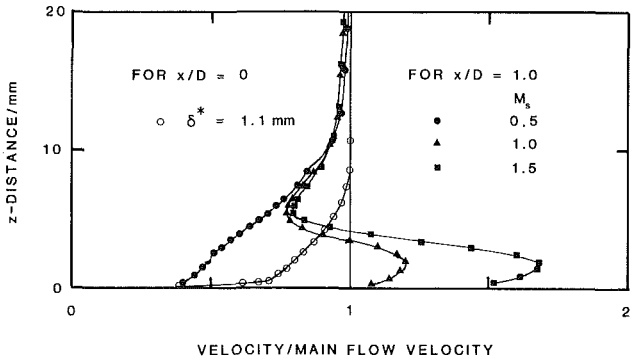

Fig. 6 Velocity profiles without the jet

Figure 4 shows how the resultant airflow from the jet at $M_j = 1.0$ changes as the slot airflow is increased from $M_s = 0.5$ to 1.5. At $x/D = 1.72$ increasing the slot airflow reduces the penetration of the jet airflow. The relative position of the velocity profiles to one another remains the same as the airflow develops to $x/D = 7.46$. Between $x/D = 1.72$ and 2.99, more of the main airflow enters the wake as M_s increases. Downstream of this wake at $x/D = 3.98$, the slot airflows seem to have reached the centerline as the velocity profiles adjacent to the wall are boundary layerlike or wall jetlike. These increases in wake flow and slot airflow augmenting the resulting airflow adjacent to the wall are responsible for the boundary layerlike flow at $x/D = 7.46$ being more advanced with increases in M_s.

Figure 5 shows how the resultant airflow from the slot airflow at $M_s = 1.0$ changes as the jet airflow is increased from $M_j = 0.5$ to 2.0. The profiles confirm the well-known fact that the penetration of the jet airflow increases with M_j. At $x/D = 1.72$, the wake flows for $M_j = 0.5$ and 1.0 are very similar. This indicates that the lobes of the kidney-shaped jet airflow are still attached to the wall on either side of $y/D = 0$, giving no access to the main or slot airflows. Whereas for $M_j = 2.0$, a significant influx of main and slot airflows occur, with a marked reduction in turbulence intensity at the wall. For this jet airflow by $x/D = 2.98$, the boundary layerlike velocity profile at the wall indicates the slot airflow has reached $y/D = 0$. For $M_j = 0.5$ and 1.0, this occurs after $x/D = 2.98$ but before $x/D = 3.98$. by $x/D = 7.46$ and below $z = 25$ mm, the resultant airflow for all M_js are very similar; as expected for $M_j = 0.5$, the profiles at the wall have not developed as quickly.

Figure 6 shows the type velocity profiles of the slot airflows that can be expected to first approach the jet airflows as they issue from the wall. These can only be an indication, because they are measured without the jet being present. The velocity profile of the turbulent boundary layer at the upper lip of the slot exit is included for comparison.

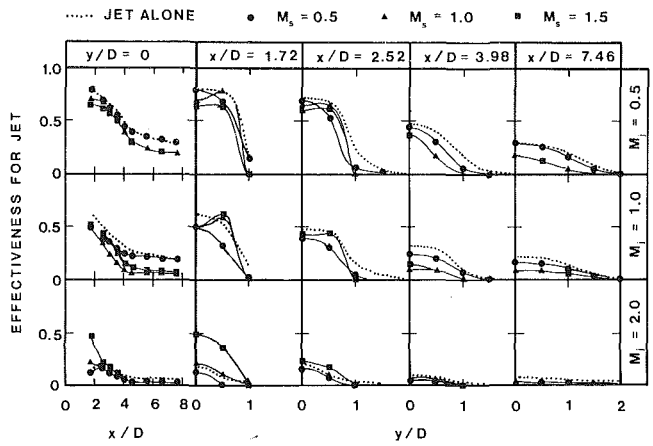

Fig. 7 η_j with x/D and y/D for $x_{sj}/D = 1.0$ and variations in M_s and M_j

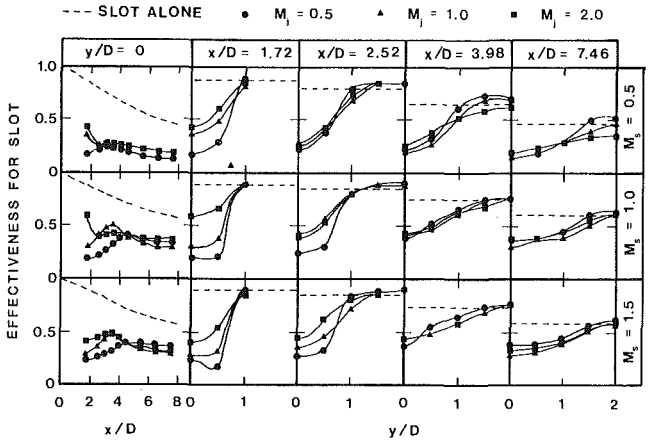

Fig. 8 η_s with x/D and y/D for $x_{sj} = 1.0$ and variations in M_s and M_j

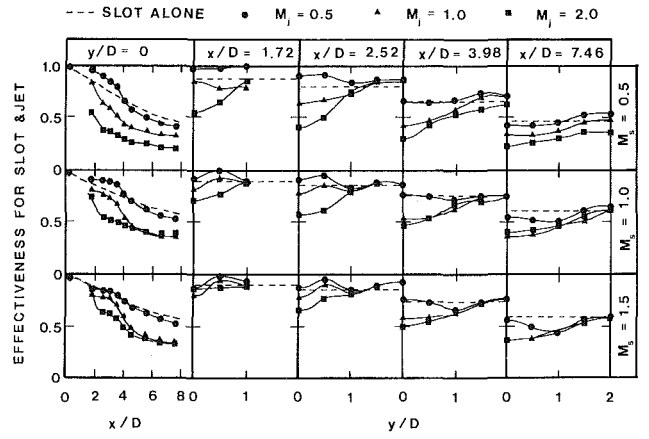

Fig. 9 η_{sj} with x/D and y/D for $x_{sj} = 1.0$ and variations in M_s and M_j

Effectiveness. The results for η_j, and η_{sj} ($\eta_j + \eta_s$) with x/D and y/D are shown by Figs. 7, 8, and 9, respectively. These are for $x_{sj}/D = 1.0$ and cover all combinations of $M_s = 0.5$, 1.0, and 1.5 with those of $M_j = 0.5$, 1.0, and 2.0. It is of relevance to note that by presenting η_j, η_s, and in effect $1 - \eta_{sj}$, the composition changes of the resultant airflow at the

wall can be apportioned to the jet, slot, and main airflows, respectively.

Figures 10 and 11 are examples to show how η_{sj} is affected by moving the jet further downstream of the slot to $x_{sj} = 2.0$ and 3.0.

Included in Figs. 7–11 for comparison are the effectiveness results for the slot without the jet, or the jet without the slot, ie., a flat surface from the trip wire to the jet. These are respectively referred to as for the "slot alone" or the "jet alone."

Jet Effectiveness. The results in Fig. 7 show that the slot airflow does affect η_j when compared with the results for the jet alone. The most striking differences occur between the jet exit and $2.54 < x/D < 3.98$. These relate to the zone where reverse flow was found to occur. Downstream of this zone the development of jet airflows seem to be the same. In all cases the jet airflow remains in contact with the wall, even though it is only just perceptible when $M_j = 2.0$ and $x/D = 7.46$.

The results for η_j with x/D for $M_s = 0.5$ and $M_j = 0.5$ are shown to be almost identical to those for the jet alone at $y/D = 0$. However differences do occur at other y/Ds. It is suggested that these occur because the momentum of the airflow at the wall approaching the jet is reduced (see Fig. 6). This enables the jet airflow when $M_s = 0.5$ to penetrate further away from the wall. Then the slot airflow has more access underneath the jet airflow which reduces η_j. The access being insufficient to reach $y/D = 0$. In the case of $M_j = 1.0$ and 2.0 when $M_s = 0.5$, the slot airflow does appear to reach $y/D = 0$, because η_j is reduced below the results for the jet alone at $y/D = 0$. As would be expected the differences between all the η_j results for $M_s = 0.5$ and those for the jet alone diminish as x/D increases.

The tuft photographs for $M_s = 1.0$ and $M_s = 1.5$ with $M_j = 0.5$ and 1.0, not shown, do illustrate that the distorted jet is initially forced closer to the wall; see also Fig. 4 for $M_j = 1.0$. This can cause the lobes of the kidney-shaped jet airflow to come into contact with the wall. Where this occurs η_j first increases with y/D before it decreases. This is evident for the η_j results given $x/D = 1.72$ and 2.53. For three of the results the lobes are still in contact with the wall at $y/D = 2.52$. By x/D both jet airflows have moved far enough away from the wall for the slot airflows to gain access to $y/D = 0$. This is consistent for $M_s = 1.5$ and $M_j = 1.0$ with the zone of reverse flow shown by Fig. 3. After the slot airflows, coming from either side of the jet meet at $y/D = 0$, it is hardly possible to distinguish between the η_j results for $M_s = 1.0$ and 1.5.

For $M_j = 2.0$, the η_j results for $M_s = 1.0$ and 1.5 do not follow the same trend with x/D as those for $M_s = 0.5$ and the jet alone. For the latter two cases η_j with x/D at $y/D = 0$ first increases then decreases with a maximum at $x/D = 2.5$. This probably occurs because the horizontal momentum of the crossflow is not sufficient to bring the underside of the jet airflow flow to the lowest point straight away; as it appears to do for $M_s = 1.0$ and 1.5. This explanation is supported by the measurement of β for a tuft positioned at the downstream edge of the jet which for $M_s = 0.5$, 1.0, and 1.5 fluctuates between 95 to 80, 90 to 60 and 45 to 0 deg respectively

Slot Effectiveness. To discuss the main features of the results those for $M_s = 1.5$ and $M_j = 1.0$ will be discussed first. These are shown by Fig. 8. They show that η_s with x/D and y/D resembles a "valley" when compared to those for the slot alone. Downstream of the jet exit at $x/D = 2.52$ η_s is higher than the results for the slot alone when $y/D > 1.5$. Although not shown, this also applies to η_s upstream and in the vicinity of the jet exit. This indicates that the slot airflow is forced to move out at the wall to go around the obstruction caused by the jet airflow and its wake. At $y/D = 0$ and x/D

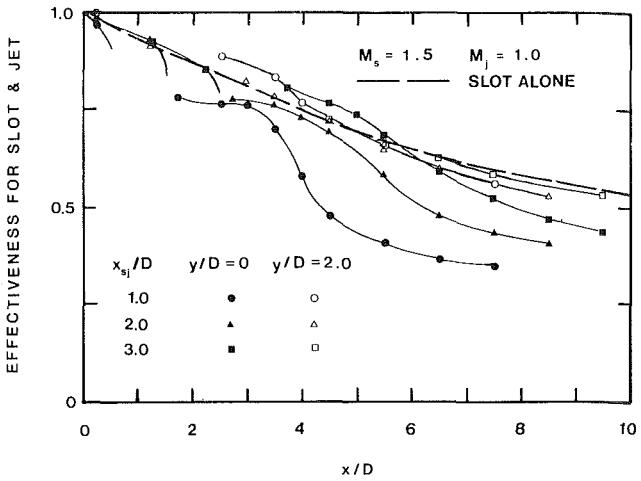

Fig. 10 η_{sj} with x/D at $y/\Delta = 0$ and 2.0 for $M_s = 1.5$ and $M_j = 1.0$ and variations in x_{sj}/D

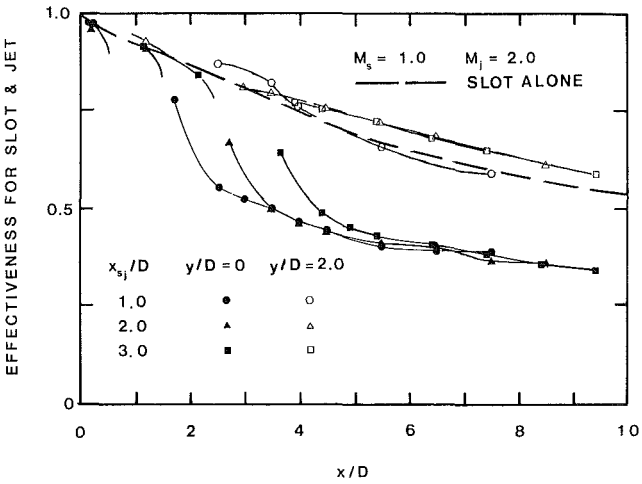

Fig. 11 η_{sj} with x/D at $y/D = 0$ and 2.0 for $M_s = 0$ and $M_j = 2.0$ and variations in x_{sj}/D

$\simeq 3\ \eta_s$ is a maximum. This position is about coincident with the end of the zone containing reverse flow shown by Fig. 3. It is suggested that the increases in η_s that occur with x/D at $y/D = 0$ and 0.5 from $x/D = 1.5$ are caused by the slot airflow as it moves downstream entering progressively the sides of the zone. After which the slot airflow moves in behind the zone and underneath the developing jet airflow. Then increasing x/D gradually decreases η_s.

Based on the previous discussion all the results for η_s with x/D at $y/D = 0$, with one exception, indicate a zone exists downstream of the jet exit. The exception occurs at $M_s = 0.5$ and $M_j = 1.0$ and the two tuft results just downstream of the jet exit did show some reversed flow indicating that perhaps the zone is very small at this flow condition. It will be observed that a sudden decrease in η_s occurs with x/D from $x/D = 1.72$ at $y/D = 0$ for $M_j = 2.0$ with $M_s = 0.5$ and 1.0. This is consistent with slot airflow being drawn up behind the jet airflow. The η_s result for $M_s = 0.5$ is higher than the one for $M_s = 1.0$. Probably this is because the horizontal momentum of the slot airflow is lower and as already pointed out in the previous section the underside of the jet airflow is not as close to the wall.

Combined Effectiveness for Slot and Jet. The η_{sj} results shown by Fig. 9 with x/D at $y/D = 0$ when compared to those for the slot alone are only ever higher when $M_j = 0.5$ in the

region $1.72 < x/D < 3.98$, but then by no more than 0.1; otherwise they are lower by as much as 0.4. Predominantly, η_{sj} with x/D is greater than the results for the jet alone, again when $M_j = 0.5$ but there are some other instances when this occurs. After $X/D \simeq 4$, the results for η_{sj} with x/D at $y/D = 0$ have the same trend as those for the slot alone, i.e., the results for $M_s = 1.0$ and 1.5 being very similar to one another and higher than those for $M_s = 0.5$.

Two examples of the effect of moving the jet further downstream of the slot exit from $x_{sj}/D = 1$ to 2 and 3 on η_{sj} with x/D at $y/D = 0$ and 2 are shown by Figs. 10 and 11. The η_j and η_s results and those for other η_{sj}s can be found in [1]. For all the results given the limit of the lateral disruption by the jet airflow to the slot airflow is very similar and is about $y/D = \pm 2$.

Figure 10 shows a typical result for when the jet airflow is close to the wall. Under these flow conditions the contribution of η_j downstream of the jet is substantial and remains very similar for all three x_{sj}s. Whereas as x_{sj} increases, more of the slot airflow remains undisturbed upstream of the jet and there is less slot airflow downstream of the jet to be disturbed. This is shown for $y/D = 0$ and results in an increase in η_{sj} position for position as x_{sj} increases.

Figure 11 shows a typical result for when the jet airflow is away from the wall and above the slot airflow. Although, as before, the distribution of η_{sj} with x/D at $y/D = 0$ downstream of the jet is very similar for all x_{sj}s, the influence of η_j is much smaller and confined to about $1D$. Overall this resutls of the slot airflow upstream of the jet is larger as x_{sj} increases.

Only Odgers and Son [10], using a heated main airflow, have reported results for η_{sj} with x/D and y/D for a cooling film disrupted by a single jet. For similar slot and jet dimensions and with $x_{sj} = 2.7$, they also reported increases and decreases in η_{sj} relative to η_s. Their recommendation when $(\rho U_j^2)/(\rho_m U_m^2) > 1$ that η_s for the slot alone should be reduced by 0.1 to account for the disruption of the cooling film caused by the jet is insufficient based on the results presented here where changes up to 0.3 occur. The reason for the difference or further comparisons are not possible because neither M_s nor M_j can be calculated from the data that they give.

Conclusions

1 The results show that the major interactions between the three airflows occur in a small region just downstream of the jet centerline ($\pm 3D$ by $\pm 1D$ wide).

2 The combined and separate contributions of the slot airflow and of the jet airflow to the η_{sj} have been established.

3 Like η_s for the slot alone, which decreases with x/D, where η_s for $M_s = 1.0$ and 1.5 are very similar to one another and are higher than for $M_s = 0.5$, η_{sj} with x/D and along any y/D, has the same trend for any M_j.

4 For most practical combustors, where $M_j >> 1$ and $M_s \geq 1$, η_{sj} is lower than η_s for the slot alone by as much as 0.3 and a higher x_{sj} is to be preferred.

Acknowledgments

The research reported here was carried out in the Department of Mechanical Engineering at Coventry (Lanchester) Polytechnic with a grant from the Science and Engineering Research Council. The use of the facilities and the financial support are gratefully acknowledged.

References

1 Button, B. L., "Jet Penetration of a Cooling Film," PhD thesis, CNAA—Coventry (Lanchester) Polytechnic, 1980.

2 "Measurement of Fluid Flow in Pipes, Part 1: Orifice Plates, Nozzles and Venturi Tubes," British Standards 1042, 1964.

3 Arnold, B. and Button, B. L., "Micromanometer for Zero to 10 000 N/m^2," *Electron. Eng. (London)*, Vol. 48, No. 582, 1976, p. 11.

4 Klebanoff, P. S., and Diehl, Z. W., "Some Features of Artificially Thickened Fully Developed Turbulent Boundary Layers with Zero Pressure Gradient," NACA TR-1110, 1952.

5 Schlichting, H., *Boundary-Layer Theory*, McGraw-Hill, New York, 1968.

6 Kacker, S. C., and Whitelaw, J. H., "The Effect of Slot Height and Slot-Turbulence Intensity on the Effectiveness of the Uniform Density, Two-dimensional Wall Jet," ASME JOURNAL OF HEAT TRANSFER TRANSACTIONS, Vol. 90, 1968, pp. 469–475.

7 Goldstein, R. J., Eckert, E. R. G., and Ramsey, J. W., "A Film Cooling With Injection Through a Circular Hole," NASA CR-54604, 1968.

8 Ramsey, J. W., "The Interaction of a Heated Air Jet with a Deflecting Flow," PhD thesis, University of Minnesota, 1969.

9 Ramsey, J. W., and Goldstein, R. J., "Interaction of Heated Jet with a Deflecting Stream," ASME JOURNAL OF HEAT TRANSFER, Vol. 93, 1971, pp. 365–372.

10 Kadotani, K., and Goldstein, R. J., "Effect of Mainstream Variables on Jests Issuing From a Row of Inclined Round Holes," ASME Paper No. 78-GT-138, 1978.

On the Nature of Jets Issuing From a Row of Holes Into a Low Reynolds Number Mainstream Flow

T. Yoshida
National Aerospace Laboratory,
Tokyo, Japan

R. J. Goldstein
Mechanical Engineering Department,
University of Minnesota,
Minneapolis, Minn. 55455

Measurements are reported of the temperature and velocity fields above an adiabatic flat plate through which air is injected via a row of circular injection holes inclined at an angle of 35 deg to the surface. A mainstream flow of air over the plate is present, with Reynolds number based on stream velocity and injection tube diameter of 3.4 × 10^3 throughout the experiments. The boundary layer approaching the row of holes is either laminar or turbulent and either fully developed laminar or turbulent pipe flow is present in the injection hole (in the absence of the mainstream). The jets emanate from the holes at a mass flux rate from 0.2 to 2.0 times that of the mainstream flow. Key findings are: (i) a laminar jet can penetrate into the main flow with a smaller mass flux than a turbulent jet; and (ii) a turbulent-approaching boundary layer generates a wider domain of interaction between the jets and the mainstream than a laminar-approaching boundary layer for the same blowing rate.

Introduction

Many analyses of a jet in the presence of a crossflow have been reported in connection with diffusion from stacks and the jet wake from V/STOL aircraft [1]. In these applications, the ratio of jet velocity to mainstream velocity is generally much higher than unity. Some researchers present experimental results of jet trajectories for various injection angles and comparisons with empirical equations [2–5].

Another application in which jet–mainstream interactions are important occurs in film cooling [6]. In this process, one or more rows of jets of cooling air are introduced through a surface exposed to a high-temperature gas stream. The relative mass flux of the jets to that of the mainstream (the blowing rate, M) is preferably small to prevent the jets from penetrating the boundary layer and moving away from the surface. Studies of jet-mainstream flows related to such applications are described in [7], in which injection through a single tube normal or inclined at an angle of 35 deg to a plate surface is used; a similar study used a row of holes [8]. Both of these studies considered turbulent-approaching boundary layer and fully developed turbulent flow in the hole from which the jet emanates. An experimental and theoretical work [9] considers a similar geometry with emphasis on an analysis close to the injection holes.

In many applications, particularly near the leading-edge region of turbine blades, the mainstream boundary layer may be laminar. In addition, at low blowing rates, the Reynolds number in the injection holes may be quite small. Thus it is important to study the effect of the nature (laminar or turbulent) of the boundary layer and injected flow on the flow field in the vicinity of injection holes and on the film-cooling performance.

The present report describes measurements of the velocity and temperature fields above an adiabatic flat plate containing a row of round holes spaced 3 diameters apart across the span and incined at an angle of 35 deg to the surface. The mainstream Reynolds number is low, and by use or absence of trip, the wall boundary layer can be maintained turbulent or laminar. Use of trips and varying the flow rate through the injection holes provides either laminar or turbulent essentially fully developed tube flow in the injection holes in the absence of the mainstream flow. The Reynolds number based on the free-stream velocity and the injection hole diameter is 3.4 × 10^3 throughout the present experiments, which is close to that found in the leading-edge region of turbine blades [10]. A companion study [11] describes film-cooling effectiveness and heat transfer measured in the apparatus.

Experimental Apparatus

The experiments are conducted in a low-speed open-circuit, suction-type wind tunnel at the University of Minnesota (Fig. 1). A detailed description of the wind tunnel is given elsewhere [12, 13]. The approach section downstream of the contraction has been shortened in length to reduce the mainstream Reynolds number. Trips are absent when a laminar boundary layer is desired and put in place to provide a turbulent one. The area of the cross section is virtually constant along the

Contributed by the Gas Turbine Division and presented at the 1983 Tokyo International Gas Turbine Congress, Tokyo, Japan, October 24–28, 1983. Manuscript received by the Gas Turbine Division May 25, 1983. Paper No. 83-GTJ-8.

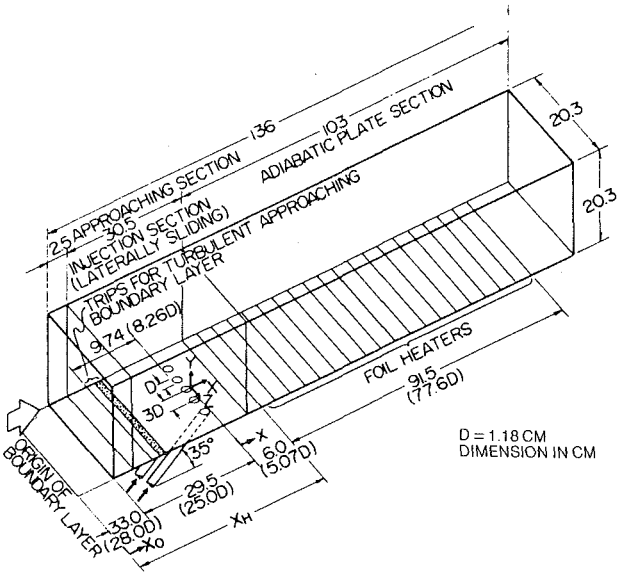

Fig. 1 Schematic of test section

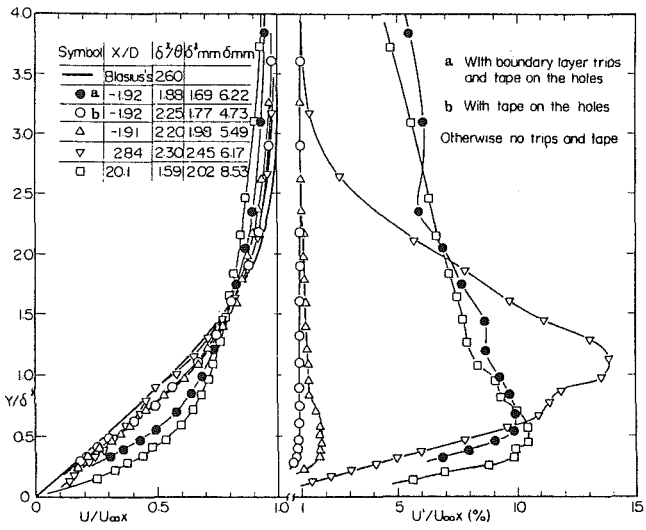

Fig. 2 Boundary layer profiles without injection: (*a*) velocity profiles; (*b*) turbulence intensity profiles

flow direction to maintain a near-zero freestream pressure gradient.

Test Procedure and Experimental Conditions

All the experments are conducted under steady-state conditions. When heated, the jets have a temperautre approximately 55°C higher than that of the mainstream (at ambient temperature, ~21°C), providing a density ratio $\rho_2/\rho_\infty \simeq 0.85$. The temperature probe used consists of a thermocouple stretched across two supports. The junction is made large, 0.13 cm diameter or approximately 10 wire diameters, to minimize conduction effects in the three-dimensional temperature field to be surveyed. For velocity measurements, a hot-film probe with a 0.051-mm-dia × 1.0-mm-long sensor is used with unheated jets and mainstream. Due to the restrictions of probe dimensions, data at positions closer to the wall surface than Y/D of 0.02 for the velocity and 0.06 for the temperature are not used.

The free-stream velocity, u_∞, is maintained at 4.5 m/s. The free-stream turbulence intensity, Tu_∞, is the order of magnitude of 1 percent, and the free-stream Reynolds number, Re_D, is 3.4×10^3. The blowing rate, M, employed in the present study ranges from 0.2 to 2.0. At a position 2 mm upstream from the leading edges of the injection holes, the normalized displacement thickness of the approaching boundary layer, δ_0^*/D, is 0.16 with the laminar boundary layer and 0.14 with the turbulent one. The acceleration parameter, K, is approximately 1.2×10^{-7} over the length of the test section.

Experimental Results

Mainstream Boundary Layer Profiles With No Injected Flow. The boundary layer is examined without injection—i.e., $M = 0$. Figure 2 shows dimensionless velocity and turbulence intensity profiles above the wall surface at various streamwise sections with the free-stream velocity, u_∞,

Nomenclature

D = inner diameter of injection tube
I = momentum flux ratio (integral mean of momentum of jet at tube exit/$\rho_\infty u_\infty^2$)
K = acceleration parameter, $(\mu_\infty/\rho_\infty)(1/u_\infty^2)(dU_\infty/dx)$
L = laminar flow
M = blowing rate, $\rho_2 \bar{u}_2/\rho_\infty u_\infty$
M_0 = fictitious blowing rate in the absence of free stream corresponding to actual $\bar{u}_2$ and assumed value of u_∞ = 4.5 m/s
Re = Reynolds number, ($Re_D = \rho_\infty u_\infty D/\mu_\infty$, $Re_j = \rho_2 \bar{u}_2 D/\mu_2$)
T = turbulent flow
T = temperature
T_{1max} = maximum temperature in fluid at $X/D = 1$
T_2 = temperature measured on outer wall of injection tube, ≃ temperature of injected flow
T_∞ = temperature of free stream
Tu = turbulence intensity
U = time-averaged velocity of flow measured with hot-film probe
U' = time-averaged rms fluctuating velocity
$U_{\infty x}$ = local U outside of boundary layer
$\bar{u}_2$ = mean velocity of injected flow
u_∞ = free-stream velocity in the X-direction at inlet of test section
X = distance downstream of downstream edge of injection hole, see Fig. 1
X_H = distance from effective origin of boundary layer to start of heating section.
X_0 = distance downstream of effective origin of wall boundary layer
Y = distance upward, normal to test wall surface
Z = lateral distance from center line of injection hole

Greek Symbols

β = angle of injection tube inclined to wall surface in the X-direction
δ = boundary layer thickness at which the velocity reaches 95 percent of $U_{\infty x}$
δ^* = boundary layer displacement thickness
δ_0^* = boundary layer displacement thickness 2 mm upstream of leading edge of injection holes
θ = dimensionless temperature defined in equation (1)
$\theta_{1\,max}$ = dimensionless temperature defined in equation (2)
μ_∞ = viscosity of free stream air
μ_2 = viscosity of injected gas
ρ_∞ = density of free stream air
ρ_2 = density of injected gas

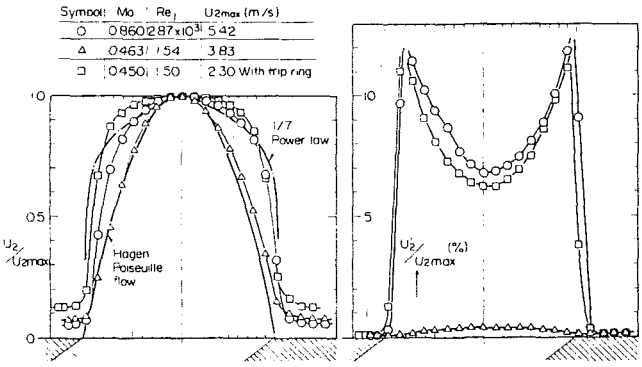

Fig. 3 Jet flow without mainstream: (*a*) velocity profiles; (*b*) turbulence intensity profiles

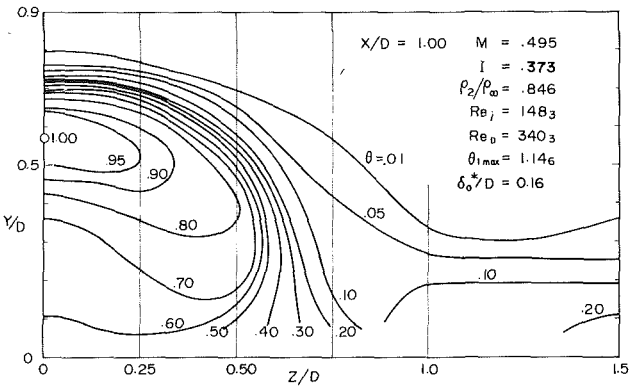

Fig. 4 Contours of constant temperature (θ) for M = 0.5, Main:*L*, Jet:*L*, X/D = 1.0

of 4.5 m/s. In the figure, the theoretical laminar boundary layer profile by Blasius is indicated as a reference.

At the location $X/D = -1.9$, and $Z/D = 0$, 2 mm upstream of the center injection hole leading edge, the results are summarized as follows. A laminar boundary layer exists when no trips are present, regardless of the existence of a thin tape on the injection holes. A deviation of the experimenal profiles from the theoretical curve is partly due to the constant cross-sectional area of the test section, which produces a slight acceleration of the mainstream. The turbulence intensity near the wall is smaller than that in the free stream for closed (thin tape covered) holes, while a slight increase is observed for open holes. When trips are attached to the wall, the boundary layer becomes turbulent. The location of the trips has been selected in order to provide about the same displacement thickness for the laminar and turbulent boundary layers. The normalized displacement thickness, δ_0^*/D, is about 0.16 for the laminar-approaching boundary layer and 0.14 for the turbulent one.

Downstream of the holes at $X/D = 2.84$ and $Z/D = 0$, the boundary layer velocity profile is still a laminar one in the absence of trips and for the open holes; however, some distortions are observed in the velocity profile. This is due to the presence of the open holes. An increased magnitude of turbulence intensity can be observed in the figure. Further downstream at $X/D = 20.1$, the boundary layer becomes turbulent for the open holes even without a trip on the wall. Although not indicated on the figure, at this section, the boundary layer is still laminar if the tape is attached over the holes.

Jet Flow Without Mainflow. Figure 3 shows dimensionless velocity and turbulence intensity profiles at the exit of the center injection hole, $Z/D = 0$ and $Y/D = 0.02$, for the injected jet in the absence of the mainstream. The jet flow is not heated and the hot-film probe is used for the measurements. M_0 in the figure indicates a fictitious blowing rate assuming a mainstream velocity of 4.5 m/s.

When the jet Reynolds number, Re_j, is 1.5×10^3 without a trip ring, the velocity profile is close to that of a fully developed laminar pipe flow and agrees with the Hagen-Poiseuille flow profile. The turbulence intensity is smaller than 0.4 percent everywhere across the tube exit. On the other hand, the velocity profile approaches that of a fully developed turbulent pipe flow under the same jet Reynolds number when a trip ring is attached on the inner surface of the tube, 10 tube diameters upstream of the tube exit. As for turbulence intensity, consistent with results of [8] and [14], when the trip ring is used a relatively high intensity is observed near the edge of the jet, and it decreases gradually toward the center of the hole, still remaining relatively high compared to that in the laminar jet. It is therefore possible to obtain either a laminar or turbulent jet flow under the same jet Reynolds number of around 1.5×10^3.

At a larger Reynolds number (for example, $Re_j = 2.87 \times 10^3$), the velocity profile is close to that of a fully developed turbulent pipe flow. The profile is already more full than that predicted by a 1/7th power law, but its trend is very similar to that shown in [15]. Further, the profile of turbulence intensity distinctively indicates turbulent flow. For this jet Reynolds number, the trip rings are not used.

Temperature Field Above Wall. The temperature of the flow with unheated mainstream and heated jets is measured with the thermocouple probe. The temperature is normalized by the following equations:

$$\theta = (T - T_\infty)/(T_{1\max} - T_\infty) \quad (1)$$

$$\theta_{1\max} = (T_{1\max} - T_\infty)/(T_2 - T_\infty) \quad (2)$$

where $T_{1\max}$ is a maximum temperature among data taken at the section $X/D = 1$. Results are discussed in terms of the dimensionless temperature θ.

Figure 4 shows constant temperature contours at $X/D = 1$ for $M = 0.5$ with the combination of the laminar-approaching boundary layer and the laminar jets. A kidney-shaped distribution is observed in the near downstream region for injection through a round hole with a turbulent (jet)-turbulent (boundary layer) combination—see [1, 7, 8]; this is also found with the laminar-laminar combination in the present study. The center of the laminar jet penetration is slightly below $Y/D = 0.6$. This penetration height is higher than that of the turbulent jet shown in the following figure. The laminar jet tends to penetrate more fully into the mainstream than a turbulent jet with the same blowing rate. In the upper part of the laminar jet, the distribution of contours is dense—that is, the mixing between the jet and the mainstream is rather poor at this section. In contrast, the distribution of contours is quite coarse under the jet.

The contours with the turbulent combination (Fig. 5) show considerably different features at the same measurement section and with almost the same experimental conditions of M, ρ_2/ρ_∞, δ_0^*/D, and Re than those with the laminar flows. Comparing the results in Fig. 5(*a*) to those in Fig. 4, the jet center stays lower, and yet the region of interaction between the jet and the mainstream spreads more widely with the turbulent-turbulent combination. Due to the difference in velocity profiles, for the same blowing rate, M, the momentum flux ratio, I, for the turbulent jet is smaller than that of the laminar one by 14 percent. The behavior in a jet-mainstream interaction depends considerably on the momentum flux ratio. Further downstream at $X/D = 6.14$, the contours (see Fig. 5(*b*)) spread wider and come close to circular shape in the center region of the jet; furthermore, the jet center is slightly lower compared to those in the section $X/D = 1$. According to [16], a kidney shape turns into a

nearly asixymmetric shape for a small momentum flux ratio. The present results correspond to the latter case.

The temperature profiles at four downstream sections, all at $Z = 0$, are shown in Fig. 6 under the following conditions: $M = 0.5$, $Z/D = 0$, $\rho_2/\rho_\infty = 0.85$, and $\mathrm{Re}_D = 3.4/10^3$. At each downstream location, four profiles are shown for the different combinations among the laminar- or turbulent-approaching boundary layer and the laminar or turbulent jets. It is clear that the type of jet flow governs the jet trajectory decisively while the effect of the approaching boundary layer is observed mainly in the mixing zone surrounding the jet flow. At this blowing rate, laminar jets penetrate somewhat into the mainstream while turbulent jets are closer to the wall regardless of the type of the approaching boundary layer. This is due to the larger momentum flux of a laminar jet compared to that of a turbulent jet both with the same blowing rate, M.

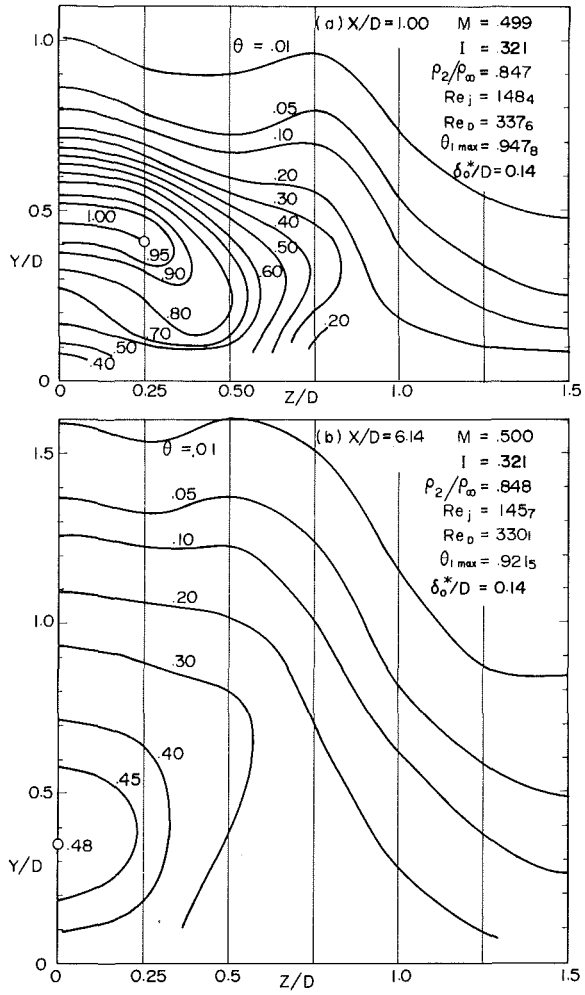

Fig. 5 Contours of constant temperature (θ) for $M = 0.5$, Main:T, Jet:T, (a) $X/D = 1.0$; (b) $X/D = 6.14$

The turbulent-approaching boundary layer generates a wider mixing region in the upper part of the jet than does a laminar boundary layer regardless of the type of jet flow, as can be observed in the near downstream section, $X/D = 1.0$ and 3.99. Comparing the temperature field near the wall for a turbulent-approaching boundary layer with that for a laminar one in the region near $X/D = 1$, the turbulent mainstream appears to interact more strongly with the jet flow, which leads to lower temperatures. On the other hand, the temperature slightly above the wall is higher for the turbulent jets than for the laminar ones in most downstream sections due to the better attachment of the turbulent jets. The interaction between the mainstream and the jet flows is least for the laminar–laminar combination among all the combinations. Therefore, the enthalpy in the jet core is relatively unchanged until the far downstream region.

Figure 7 shows trajectories corresponding to maximum temperature in the symmetry plane $Z/D = 0$. The laminar jets, indicated by solid symbols, attach to the wall surface and flow along the surface for blowing rates up to 0.35 but have penetrated into the mainstream when $M = 0.5$. The turbulent jets indicated by open symbols remain near to the wall surface at $M = 0.5$, regardless of the type of approaching boundary layer; they do penetrate into the mainstream for $M \geq 1.0$. When the jet remains attached to the surface, it is difficult to determine the maximum temperature height because the temperature gradient is small above the wall as seen in Fig. 6(c) and 6(d) and also shown in Fig. 7 by a mini-sketch. However, the height of maximum temperature does appear slightly greater close to injection than further downstream whenever the jet remains attached to the wall.

In the near downstream region, the trajectory of the laminar jet with $M = 0.5$ shows a similar trend to that of a jet which is attached to the wall, though, for $M = 0.5$, the jet is

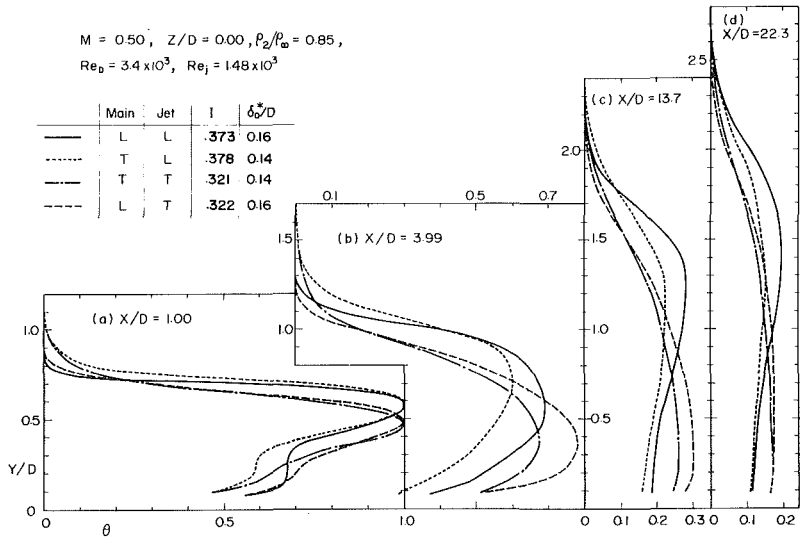

Fig. 6 Comparison of temperature (θ) profiles at $M = 0.5$ for laminar and turbulent flows

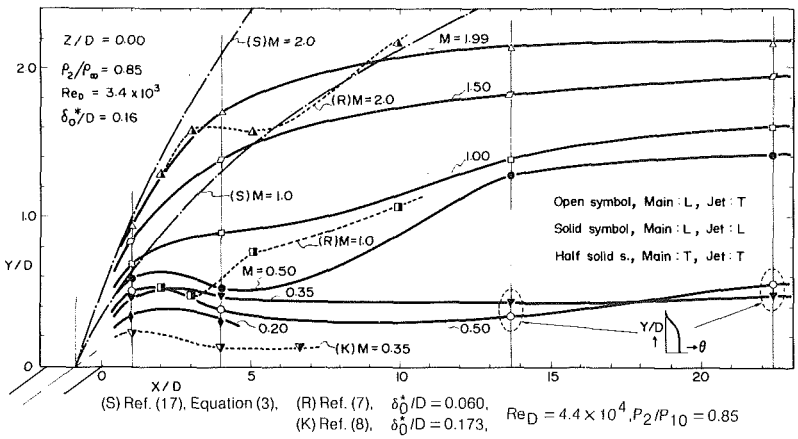

Fig. 7 Location of maximum temperature in flow field downstream of jet injection

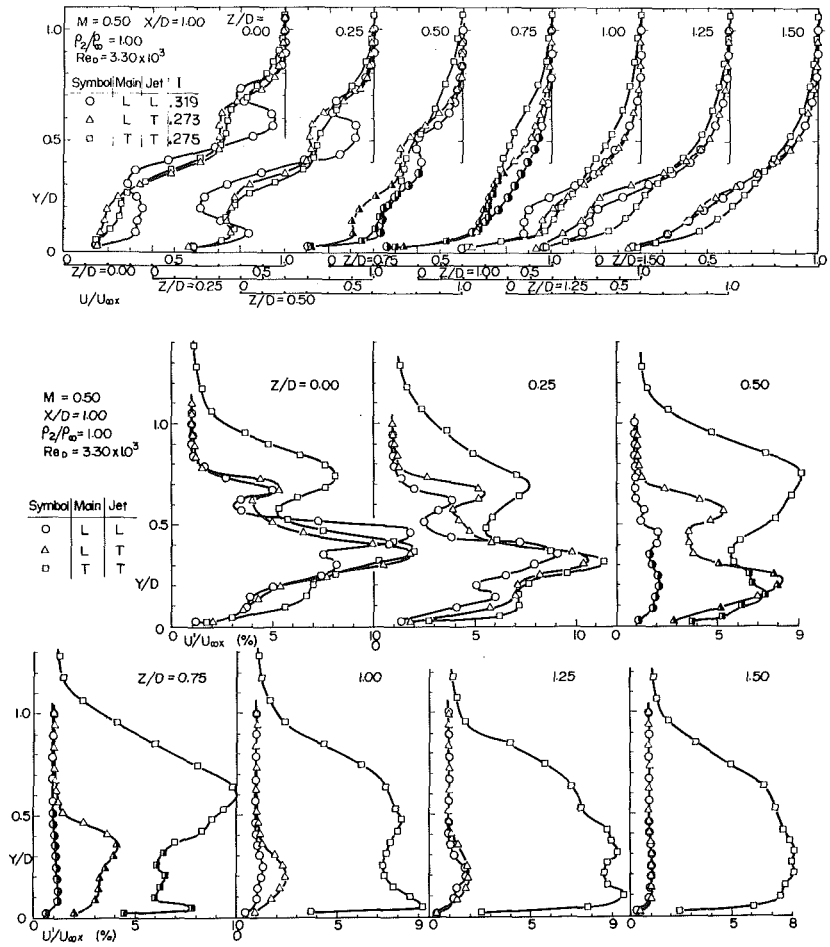

Fig. 8 Flow field at section X/D = 1: (*a*) mean velocity profiles; (*b*) turbulence intensity profiles

slightly higher. Even at X/D = 1.0, the laminar jet for M = 0.5 has a very distinct profile (see Fig. 6) showing a tendency to lift off and penetrate into the mainstream. This is confirmed in Figs. 6 and 7 of [11], where fairly small values of film cooling effectiveness occur in this region. Thus, for a blowing rate of 0.5, the laminar jet is very close to—but still over—a critical value of blowing rate for jet lift-off.

In Fig. 7, results from earlier works [7, 8] are shown for comparison. These results were obtained with the same experimental apparatus as used in the present study, but the mainstream Reynolds number is different. The results for M = 0.35 from [8] are compared to the present results for M = 0.5—both for turbulent-turbulent flows; both curves (Fig. 7) show the same trend. The turbulent jet for M = 0.35 [8] shows a higher trajectory than the present results for a laminar jet of M = 0.2. The curve for M = 1.0 (from [7] represents a penetrating (lift-off) jet flow. This curve is located lower than that of the present curve, M = 1.0 (laminar jet boundary layer-turbulent jet) due to a considerably small displacement thickness in the earlier ex-

periment. The curve from [7] for $M = 2.0$ with a turbulent boundary layer and turbulent jet is situated roughly at the same height as the present results for $M = 1.99$ (laminar boundary layer–turbulent jet). At high M, there is a very large momentum flux in the jet flow compared to that in the mainstream; the jet trajectory is barely affected by the boundary layer thickness.

An empirical equation [17] describing the trajectory of a jet through a round hole in the presence of a cross flow can be used for comparison purposes. The equation for the position of the jet is

$$X/D = (1/I)\,(Y/D)^{2.55} + [1 + (1/I)]\cos\beta\,(Y/D) \qquad (3)$$

This was derived from results for $2 \le I \le 22$, $1 \le \rho_2/\rho_\infty \le 3$, and 45 deg $\le \beta \le$ 90 deg. The mainstream conditions, u_∞ and δ^*/D, are not given in [17]. The predictions of this equation are shown on Fig. 7 for $M = 1.0$ and 2.0 $\rho_2/\rho_\infty = 0.85$, and $I = 1.28$ and 5.12. As is already recognized, valid conditions for the equation are considerably different from those in the present study. According to [7] and [16], a temperature trajectory for $\rho_2/\rho_\infty < 1$ is below the velocity trajectory throughout the downstream region for the same blowing rate [7] or the same momentum flux ratio [16], except in the very vicinity of a hole where both trajectories are the same. From the view point of film cooling, a prediction of the trajectory of the jet as indicated by a maximum temperature which penetrates into a mainstream cross flow is not so important; it is important, however, in enabling prediction of critical jet flow conditions for attachment to a wall under given mainstream conditions and geometry.

Flow Field Above Wall. The velocity and turbulence intensity profiles above the wall surface at $X/D = 1$ and for $M = 0.5$ are presented in Fig. 8(*a*) and (*b*), respectively. At each location (Z) across the span, three flow conditions—laminar jet and laminar mainstream, turbulent jet and laminar mainstream, and turbulent jet and turbulent mainstream—are represented. Since tests are conducted with the hot-film probe axis in the Z-direction, the measurements represent vector summations primarily of the X and Y-components of the flow quantities. These summations are represented by upper case U and U' in the figures to set them apart from lower case u and u', which refer to mean velocity and velocity fluctuations in the X-direction. The injected flow is not heated, consequently $\rho_2/\rho_\infty \simeq 1$. The momentum flux of the jets is lower than that for $\rho_2/\rho = 0.85$ in the temperature field investigation by about 15 percent for the same blowing rate.

As indicated by the velocity and turbulence intensity profiles in the plane of symmetry, $Z/D = 0$, the center of the three individual jets is at a height of $Y/D = 0.6$, but the laminar jet appears slightly higher than the two turbulent jets, consistent with the temperature measurements. As observed in the turbulence intensity profiles at $Z/D = 0$ and 0.25, the relative maxima near the wall in the region of the lower edge of the jet core, are much larger than maxima in the upper edge of the jet and the interaction between the mainstream and the jet flow is stronger in the top of the jet than below the jet.

Kidney-shaped jet cores are present in the center region, $0 \le Z/D < 0.75$, consistent with the results of temperature measurements, Figs. 4 and 5. Under the jet cores, relative maxima of the velocity and turbulence intensity profiles are observed, especially for the laminar jet. This may imply reverse flows due to the blockage effect of the jet flow in the mainstream, which was pointed out in earlier works [7, 8]. With turbulent jets, this flow is rather weak because the diffusion in the circumference of the jets is more active than with laminar jets. For the turbulent-approaching boundary layer, the turbulence intensity is high at the upper edge of the jet core at $Z/D = 0.5$ and 0.75. This is attributed to a high turbulence intensity which existed originally in the boundary layer before coming across the jet flow (see solid symbols in Fig. 2).

In the planes $Z/D = 0.50$ and 0.75, the velocities just above the wall are larger than those at $Z/D = 1.50$, for the corresponding height and type of flows. These data are marked with half-solid symbols in Figs. 8(*a*) and (*b*). Flow characteristics at $Z/D = 1.50$ are essentially those for the mainstream without the injected flow. Therefore, the higher velocities come from the existence of injected flow and flows from the jet core lower edge.

In the planes $Z/D = 1.0$ and 1.25, the velocity and turbulence intensity profiles are similar to those in the absence of injection in the uppermost region, however, a strong influence of the injected flows is observed in the vicinity of the wall. Gentle variations of velocity and relatively high turbulence intensity in this region suggest the existence of a flow that may be due to a pair of vortices. This is strongly related to the results of cooling effectiveness measurements in the same region (see Fig 5 in [11]). Such vortices have been observed [18] with a similar film cooling configuration using flow visualization with dye injection in a water tunnel.

In the midplane between the neighboring two injection holes, $Z/D = 1.5$, the velocity and turbulence intensity profiles are scarcely affected by the injected flows, at least at $X/D = 1.0$.

Concluding Remarks

An inclined laminar jet injected through a wall separates from the surface and penetrates into the mainstream at a smaller blowing rate than a similarly inclined turbulent jet, mainly because of the larger momentum flux of the laminar jet compared to that of the turbulent one.

A turbulent-approaching boundary layer causes a wider region of interaction between the jet and the mainstream than a laminar-approaching boundary layer at the same blowing rate. In the upper part of the jet core, the region of the interaction extends further upward for the turbulent-approaching boundary layer, while, in the lower part of the jet core, mixing between the turbulent mainstream and the jet is more active compared to the laminar-approaching boundary layer, resulting in a lower temperature of the flow near the wall surface. This trend is especially realized in the near downstream region of the injection holes.

When the jet flow attaches to the wall surface, the maximum temperature at a given X/D is at a slightly higher location immediately downstream of injection than it is further downstream.

There exists a reverse flow under the jet core around the symmetry planes $Z/D = 0$ at $X/D = 1$, while a pair of vortices or, under some conditions, flow with strong turbulence intensity occur under and/or beside the jet at $Z/D =$ 1.0 and 1.25.

Acknowledgment

Support from the Air Force Office of Scientific Research was helpful in the completion of this work.

References

1 "Analysis of a Jet in a Subsonic Crosswind; A Symposium" NASA SP-218, Sept. 1969.

2 Margason, R. J., "The Path of a Jet Directed at Large Angles to a Subsonic Free Stream," NASA TN D-4919, 1968.

3 Ziegler, H., and Wooler, P. T., "Multiple Jets Exhausting into a Crossflow," J. Aircraft, Vol. 8, 1971, pp. 414–20.

4 Platten, J. L., and Keffer, J. F., "Deflected Turbulent Jet Flows," ASME *J. Appl. Mech.*, Vol. 38, 1971, pp. 756–58.

5 Le Grives, E., and Benoit, A., "A New Theoretical Model for Representing Jet Penetration into a Subsonic Stream," *La Recherche Aerospatiale*, No. 3, 1972, pp. 133–42.

6 Goldstein, R. J., "Film Cooling," *Advances in Heat Transfer*, Vol. 7, Academic Press, New York, 1971, pp 321–379.

7 Ramsey, J. W., and Goldstein, R. J., "Interaction of a Heated Jet with a Deflecting Stream," ASME *Journal of Heat Transfer*, Vol. 93, 1971, pp 365-372.

8 Kadotani, K., and Goldstein, R. J., "On the Nature of Jets Entering a Turbulent Flow, Part A: Jet-Mainstream Interaction," JOURNAL OF ENGINEERING FOR POWER, Vol. 101, 1979, pp. 459-465.

9 Bergeles, G., "Three-Dimensional Discrete-Hole Cooling Processes: An Experimental and Theoretical Study," Ph.D. thesis, Imperial College, July 1976.

10 Matsuki, M., "Recent Status on Research and Development of FJR 710 Turbofan Engine," *Proceedings of the 1977 Tokyo Joint Gas Turbine Congress (May 1977)*, pp. 1-11.

11 Goldstein, R. J., and Yoshida, T., "The Influence of a Laminar Boundary Layer and Laminar Injection on Film Cooling Performance," *Journal of Heat Transfer*, Vol. 104, 1982, pp. 355-362.

12 Goldstein, R. J., Eckert, E. R. G., and Ramsey, J. W., "Film Cooling with Injection Through a Circular Hole," University of Minnesota HTL TR No. 82, 1968; NASA CR-54604, 1968.

13 Eriksen, V. L., "Film Cooling Effectiveness and Heat Transfer With Injection Through Holes," University of Minnesota HTL TR No. 102, 1971; NASA CR-72991, 1971.

14 Laufer, J., "The Structure of Turbulence in Fully Developed Pipe Flow," NACA TR-1174, 1954.

15 Nikradse, J., "Gesetzmaessigkeiten der turbulenten Stroemung in glatten Rohren," VDI-Forschungsheft, 356, 1932.

16 Kamotani, Y., and Greber, I., "Experiments on a Turbulent Jet in a Cross Flow," *AIAA Journal*, Vol. 10, 1972, pp. 1425-1429.

17 Abramovich, G. N., *The Theory of Turbulent Jets*, MIT Press, Cambridge, Mass., 1963.

18 Le Grives, E., private communication, Nov. 1977.

Liquid Crystal Visualization of Surface Heat Transfer on a Concavely Curved Turbulent Boundary Layer

J. C. Simonich
United Technologies Research Center,
East Hartford, Conn. 06108

R. J. Moffat
Stanford University,
Stanford, Calif. 94305

An experimental heat transfer study on a concavely curved turbulent boundary layer has been performed. A new, instantaneous heat transfer measurement technique utilizing liquid crystals was used to provide a vivid picture of the local distribution of surface heat transfer coefficient. Large scale wall traces, composed of streak patterns on the surface, were observed to appear and disappear at random, but there was no evidence of a spanwise stationary heat transfer distribution, nor any evidence of large scale structures resembling Taylor-Gortler vortices. The use of a two-dimensional computation scheme to predict heat transfer rates in concave curvature regions seems justifiable.

Previous Research on Concave Curvature

One of the uncertainties in the prediction of heat transfer from the pressure surfaces of gas turbine blades concerns the possible effects of concave curvature. A considerable amount of attention has been focused on the curvature problem in recent years, both experimentally and theoretically.

The fact that streamwise curvature affects a boundary layer flow has been recognized for many years. The early work of Wilcken [1], Wendt [2], Wattendorf [3], Schmidbauer [4], and the Clausers [5] demonstrated that even small amounts of curvature had large effects on the hydrodynamics. As a result of these works, by the late 1930s, many important curvature effects were already known. It was known that concave curvature increases turbulent activity while convex curvature reduces it. Mean velocity profiles were greatly influenced and mixing lengths were seen to increase in concave and decrease in convex curvature. Increases in boundary layer thickness were noted in concave curvature, as were decreases in convex curvature. The transition from laminar to turbulent flow was enhanced by concave curvature and retarded by convex. In all of these early experiments the flow over both the concave and convex surfaces was assumed to be two-dimensional, and no flow visualization was reported. It was not until Gortler's classical work in 1940 [6] that longitudinal vortices in concave laminar boundary layers were hypothesized analytically and not until 1962 was their presence confirmed experimentally by Tani [7]. The presence of longitudinal vortices similar to the Taylor-Gortler vortices in laminar flow were sought in turbulent boundary layers as well. The first experimental evidence of stationary Taylor-Gortler roll cells in turbulent flow was presented by So and Mellor in 1972 [8, 9]. Sets of velocity profiles, spaced apart in the spanwise direction, indicated stationary structures in the flow. The debate over whether or not a spanwise, stationary vortex pattern exists along the streamwise direction in concavely curved turbulent boundary layers has been raging ever since. Experiments that have indicated the presence of stationary structures include So and Mellor [8, 9], Merony and Bradshaw [10], Hoffman and Bradshaw [11], Ellis and Joubert [12], and Prabhu and Rao [13]. Those experiments that did not indicate stationary structures include Thomann [14], Ramaprian and Shivaprasad [15–17], Jeans and Johnston [18], and the present study.

Although a preliminary study was made by Kreith in 1955 [19], the first systematic study of turbulent boundary layer heat transfer in the presence of streamwise curvature was performed by Thomann in 1968 [14]. His work was performed at a Mach number of 2.5 and curvature effects may have been amplified by the compressible flow. His results show a 20 percent increase and a 15 percent decrease in Stanton number for concave and convex curvature compared to flat-plate behavior. Surface flow visualization with lamp black did not show any signs of longitudinal structures on the concave surface.

The first experiment on incompressible turbulent boundary layer heat transfer with longitudinal curvature was performed by Mayle, Blair, and Kopper in 1979 [20]. For the two cases studied, convex curvature decreased heat transfer by 20 percent and concave curvature increased heat transfer by 33 percent at the end of the test section (compared to a flat plate correlation). Spanwise periodic variation in dynamic pressure profiles appeared to indicate the presence of stationary Taylor-Gortler vortices.

The Hoffman and Bradshaw work employed vortex generators in the wind tunnel contraction to hold the structures stationary. As much as a 20 percent variation in skin

Contributed by the Gas Turbine Division and presented at the 1983 Tokyo International Gas Turbine Congress, Tokyo, Japan, October 24–28, 1983. Manuscript received by the Gas Turbine Division May 16, 1983. Paper No. 83-GTJ-7.

friction between the valleys and the troughs of the vortex structures was noted by Hoffman and Bradshaw [11].

In both of the previous heat transfer studies on concave curvature, conventional heat transfer measurement techniques were used. These techniques average the measured heat transfer both in the spanwise direction and in time. Any local effect that a Taylor-Gortler roll cell might have on heat transfer cannot be detected with these techniques.

The purpose of the present study was to determine whether or not such structures were present, and if present, to what extent they affected the local heat transfer.

Liquid Crystals

In order to map out the distribution of heat transfer coefficient over a large area in the curved region, a new technique for heat transfer measurement was developed. It used an electrically heated sheet covered with a layer of liquid crystal paint to visualize the distribution of heat transfer coefficient on the surface.

Liquid crystals are amazing substances. Organic compounds derived from esters of cholesterol, chloresteric liquid crystals exhibit several unique properties. Liquid crystals have two distinct melting points. One occurs when the substance changes from a solid to a cloudy liquid, and a second when the cloudy liquid changes to a clear liquid. The molecules are arranged in layers with the long axis of the molecules parallel to each other in the plane of the layer. Each layer is slightly rotated, compared to its neighbor, forming a helical pattern. Positive interference occurs whenever the layers are aligned. The distance between aligned layers can be altered by a number of external stimuli, including temperature, electric and magnetic fields, shear stress, and chemical vapors. Modern fabrication techniques for microencapsulation produce gelatin spheres of 5 to 30 microns in diameter containing liquid crystal. These techniques greatly reduce contamination due to shear stress, chemical vapors, and ultraviolet light and result in a substance which changes color mainly in response to temperature. The color change is brilliant and reproducible and can be calibrated to accurately measure temperature. It is this property that makes liquid crystals a valuable tool for heat transfer research.

Several experimentalists have used liquid crystal packaging arrangements for aerodynamic visualization and heat transfer measurement. The earliest aerodynamic use was reported by Klein in 1968 [21]. He used unencapsulated liquid crystals to study the transition process on an aerodynamic model. Lemberg [22] used liquid crystals for the visualization of unsteady boundary layers in 1970.

The first experiment to employ liquid crystals for convective heat transfer was reported by Vennemann and Butefisch in 1973 [23]. Models coated with liquid crystals were aerodynamically heated in a high-speed flow and a transient technique was used to calculate the heat transfer coefficient.

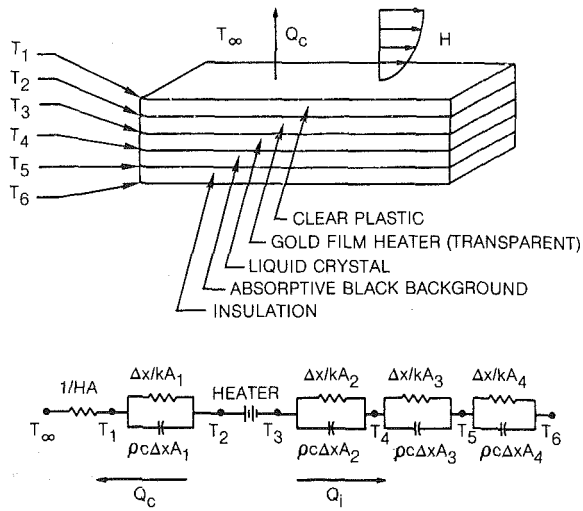

Fig. 1 Schematic diagram and thermal circuit for the liquid crystal packaging arrangement

The first steady-state heat transfer measurement technique employing liquid crystals was performed by den Ouden and Hoogendoorn in 1974 [24]. They used a constant-temperature heat source and measured the stagnation heat transfer from a jet impinging on a flat plate.

Cooper [25, 26] and later Kelleher [27] used a constant heat flux surface and liquid crystals to measure the heat transfer around cylinders, in a concave, laminar duct, and around turbomachinery blades in air. Only steady-state measurements were reported.

An evaluation of two different liquid crystal techniques was presented by Hippensteele, Russell, and Stepka in 1981 [28]. They evaluated two different constant heat flux heater arrangements in various flow situations. Only qualitative heat transfer results were reported.

The Present Configuration. Several different packaging arrangements for liquid crystal heat transfer surfaces are possible. Both uniform temperature and uniform heat flux surfaces can be constructed, each in a variety of different geometries. The system chosen for this study is shown schematically in Fig. 1. The top surface is a thin layer of polycarbonate material (0.1 mm) upon which has been vapor deposited a thin, gold film that is used as a constant heat flux, Joulean heater. The gold is only a few Angstroms thick and is

Nomenclature

$C_f/2$ = skin friction coefficient, $\tau_w/\rho U_\infty^2$
c_p = specific heat
H,h = heat transfer coefficient
l = mixing length
l_0 = flat-wall mixing length
Pr = Prandtl number
Q'' = heat flux per unit area
R = radius of curvature
Re_θ = Reynolds number based on momentum thickness, $U_\infty\theta/\nu$
Ri = Richardson number
St = Stanton number, $Q''/\rho C_p U_\infty (T_w - T_\infty)$
T = temperature, time
T_w = wall temperature
U = mean streamwise velocity
U_∞ = mean free stream velocity
u_τ = shear velocity, $\sqrt{\tau_w/\rho}$
y = distance normal to wall
y^+ = nondimensional distance from the wall, $U_\tau y/\nu$
β = log region correction constant
δ = boundary layer thickness
δ_{99} = thickness of the boundary layer where mean velocity is 99 percent of the potential flow mean velocity
θ = momentum thickness

$$\int_0^\infty \frac{\rho U}{\rho_\infty U_\infty}\left(1-\frac{U}{U_\infty}\right)dy$$

κ = Von Karman constant
λ_{th} = wavelength of thermal streaks
λ^+ = nondimensional spanwise streak spacing, $U_\tau\lambda/\nu = \sqrt{C_f/2}U_\infty\lambda/\nu$
λ_{th}^+ = nondimensional spanwise thermal streak spacing, $\sqrt{\mathrm{St}}U_\infty\lambda_{th}/\nu$
ν = kinematic viscosity
ρ = density
τ_w = surface shear stress

nearly transparent. This makes it possible to see the liquid crystal paint, the next layer underneath, through the gold film. A black absorptive layer under the liquid crystal absorbs light not reflected by the liquid crystal paint. The package is completed by a layer of insulation that reduces heat loss out the back of the package.

The technique is as follows: a measured amount of electric power is supplied to the uniform heat flux heater of known size. After correction for heat loss from the back side, this provides a known and uniform heat flux per unit area. The temperature at the back surface of the polycarbonate is indicated by the color of the calibrated liquid crystal. After correction for the temperature drop through the polycarbonate, the front face temperature is known. The freestream temperature is measured independently. These three measured quantities are necessary and sufficient to define the heat transfer coefficient. Contours of constant color (isochromes) are not only contours of constant temperature (isotherms) but also contours of constant heat transfer coefficient (isostantons). The technique is therefore useful for quickly mapping out contours of heat transfer coefficient on surfaces.

Qualification of the Technique. As with any new technique, the liquid crystal technique had to be qualified before applying it to a new flow situation. Details of the qualification procedures were reported by Simonich and Moffat in 1982 [29]. A summary of the results will be given here.

By using a spectral light source, such as a mercury vapor light, the temperature of a given color can be calibrated to $\pm 0.25°C$. This technique reduces the ambiguity temperature band by a factor of 3 compared to use of an incandescent or "white" light source.

The uniformity of heat release from the gold film heater was measured by two different techniques. One was a direct measurement of local heat flux while the other inferred heat release from local measurements of gold film resistance. Both methods showed that the uniformity was typically ± 10 percent.

The frequency response of the liquid crystal package was determined both analytically and experimentally. A linear perturbation analysis was used to study two different boundary conditions: (*i*) a sinusoidally varying heat transfer coefficient with a constant heat flux at the heater; and (*ii*) a sinusoidally varying heat flux at the heater with a constant heat transfer coefficient. The second boundary condition case could be established experimentally. For the former case, it was predicted that a disturbance with an amplitude of 13.5 percent could be seen if its frequency were 1.3 Hz or less, at the conditions which we expected for these tests. The response would be higher for larger values of heat transfer coefficient or amplitude. While this level of frequency response would only be useful for steady-state measurements in typical air flows, it is high enough to show most of the important dynamic processes in low-speed turbulent boundary layer flows in water. Experiments with sinusoidally varying power applied to the heater confirmed the predictions. This established that the prediction method was accurate, hence it is felt that variations in h of 13.5 percent could also be seen if they occurred at 1.3 Hz or less.

An important measure of the near wall time scales in a turbulent boundary layer is the mean period between burst events. Kim et al. [30] measured the distribution of time between bursts for a turbulent boundary layer in water. Their flow conditions were similar to those used here: $U_\infty = 0.5$ ft/s, $\delta_{99} = 3$ in., and $Re_\theta = 1100$. They found the average time interval between bursts was 2.27 s, implying a frequency of 0.44 Hz. Their maximum frequency was 1.0 Hz. It seems unlikely that any large-scale structure would change position with frequencies higher than the streak structure. Therefore,

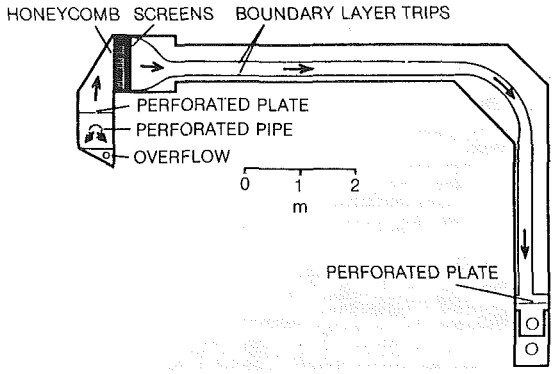

Fig. 2 Schematic diagram of basic channel layout, from Jeans and Johnston [18]

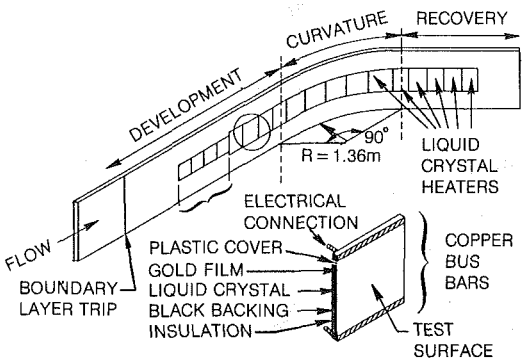

Fig. 3 Schematic diagram of the test section

the liquid crystal package was judged to be fast enough to see the most important dynamic events.

In order to qualify the technique and compare it against conventional heat transfer techniques, the package was tested in three simple flat-plate flow regimes: laminar free convection, laminar forced convection, and turbulent forced convection. Comparison between the measured heat transfer coefficients and empirical and analytic predictions of the flow was found to be good.

Experimental Apparatus

The experiment was performed in a large-scale water tunnel especially designed for this study. A schematic diagram is shown in Fig. 2. The flow length was divided into three main parts: a flat-plate development section, a concave curve, and a flat-plate recovery. The rig was an open-channel, closed-circuit water rig. Water was recirculated from a 13,000 gal (49,000 L) storage tank by a 1200 galpm (4500 Lpm) pump. The tunnel had plexiglass walls supported by steel frames, which provided excellent visibility for flow visualization. The boundary layer entering the test section was tripped by a 3/16 in. (4.8 mm) square rod 3 ft (.91 m) downstream of the 4 to 1 contraction. The boundary layer developed for another 3 m downstream before the first measurement station. The pressure gradient in the streamwise direction was held negligibly small by varying the width of the channel in the straight portions. A control wall opposite to the curved test wall was designed using potential flow solutions to provide a zero streamwise pressure gradient in the curved region, measured at the test surface. Fourteen independently controlled, waterproof, liquid crystal packages were used in the test: 3 in the flat-plate approach region, 7 in the curved region and 4 in the flat-plate recovery region.

A schematic diagram of the test section and a blow up of one heater is shown in Fig. 3. The waterproof liquid crystal

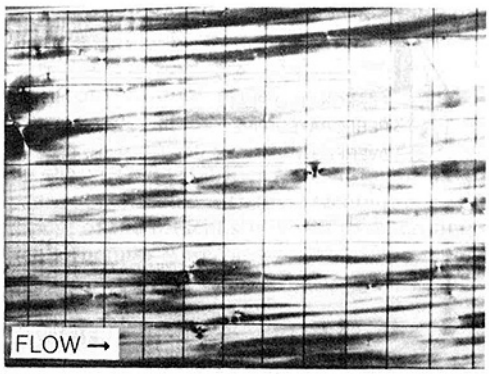

Fig. 4 Photograph of streamwise streak patterns obtained in a turbulent boundary layer using the liquid crystal technique. Grid lines are 25 mm apart. Flow is from left to right.

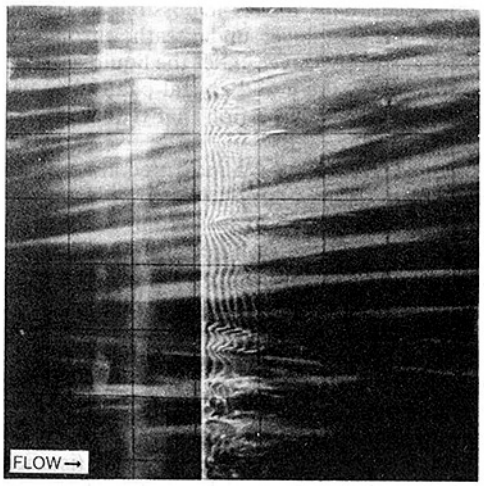

Fig. 5 Photograph of visualized thermal streak pattern beneath concavely curved turbulent boundary layer, also showing hydrogen bubble trace from a wire at $y^+ = 10$

packages were inserted into cavities in the test section so that the liquid crystal surface was mounted flush with the test wall, at the midheight of the test section. The physical aspect ratio of the water tunnel was 4.8 to 1. Since there was a free surface, the apparent aspect ratio was twice this 9.6 to 1. The beginning and end of curvature were placed in the middle of two liquid crytsal packages, rather than at the interface between packages. In addition, 4 preheaters were installed upstream of the first measurement station. No experimental data were taken from these preheaters. They were used only to develop a thermal boundary layer prior to the first measurement station.

Results

Heat Transfer and Flow Visualization Observations. In addition to the liquid crystal technique outlined above for visualizing the surface heat transfer, the flow was also visualized with dye and hydrogen bubbles. Dye injected from an extended hypodermic syringe was used for casual observation, but the main visualization tool was hydrogen bubbles. The hydrogen bubbles were generated from a .004-in.-dia (.1-mm) platinum wire suspended in the boundary layer, above and parallel to the surface.

The following section describes what was observed in the flow and on the surface, presenting observations only. Interpretation is reserved for the discussion section of the paper.

The Flat-Plate Approach Region. From all observations, the flat-plate region upstream of the curvature was a normal, zero pressure gradient, turbulent boundary layer. The nominal free-stream velocity was 15 cm/s, and the momentum thickness Reynolds number was about 1300. If a hydrogen bubble wire was placed very near to the wall, within y^+ of 10, the streaky structure of the boundary layer was observed. Low-speed streaks and high-speed sweeps were apparent, and the structure appeared normal. For an excellent review of the structure of turbulent boundary layers, see Cantwell [31].

When power was applied to the liquid crystal test surfaces, streaks, similar in general appearance to the hydrodynamic streaks, were observed on the surface. These thermal streaks, marked by a single color in the liquid crystal, indicated an area of uniform heat transfer coefficient. A typical photograph of the flat-plate streak pattern is shown in Fig. 4. These streaks were uniformly distributed across the surface and were generally parallel to the free-stream direction, in the direction of the hydrodynamic streaks. The streaks appeared and disappeared randomly in space and time. Streaks were never observed to cross one another, but often two or more merged to form one which extended both the length and the lifespan of the streak. The width of a streak was .3–.6 cm or 25–50 in inner or wall coordinates (i.e., nondimensionalized by u_τ/ν). The streaks were much longer than they were wide. The longitudinal streak length was 12.5–25 cm (1000 to 2000 in inner coordinates). The spanwise streak spacing was found to be 89 in inner coordinates, based on skin friction measurements from the concurrent hydrodynamic study by Jeans and Johnston [18]. This is slightly lower than the generally accepted hydrodynamic streak spacing of 100 reported in a review of several studies by Cantwell [31]. Unlike hydrogen bubble techniques, which generate bubbles near the surface and which are then carried away from the wall, the liquid crystal technique provides information directly on the surface. A recent study by Smith and Metzler [32] found that the observed hydrodynamic streak spacing from hydrogen bubble wire visualization decreases as the wire approaches the wall. The streak spacing observed in the present work seems reasonable.

When observed as a whole, the overall pattern formed by the streaks looks like eel grass in a slowly moving river. Individual streaks were observed to be "born" by gradually widening in cross section. The streaks "died" by necking down in cross section or by being washed out from the upstream end. The total area covered by the streaks was 28 to 56 percent (found by dividing the streak width by the streak spacing).

The hydrodynamic spacing was best observed by using a plan view (a view whose line of sight is perpendicular to the wall) with a transversely mounted wire. To view the vortical structure of the flow, a mirror was placed in the flow downstream of the hydrogen bubble wire. The view thus provided, from outside the rig, was a head on view of the bubbles coming directly at the observer. Streamwise vorticity was observed in the flat-plate region, but no large-scale structures were observed.

The Concavely Curved Region. The heat transfer and flow patterns visualized in the curved region were far different from the flat plate region and from our preconceived notions about what the flow would look like. From previous hydrodynamic studies of concavely curved boundary layers, it was thought that stationary roll cells or Taylor-Gortler vortices would exist in the curve. It was imagined that their effect on heat transfer would be to produce stationary longitudinal streamwise ribbons of color in the liquid crystal surface marking regions of high and low heat transfer coefficient.

No such patterns were detected in the heat transfer distribution. What were found instead were isolated, large-

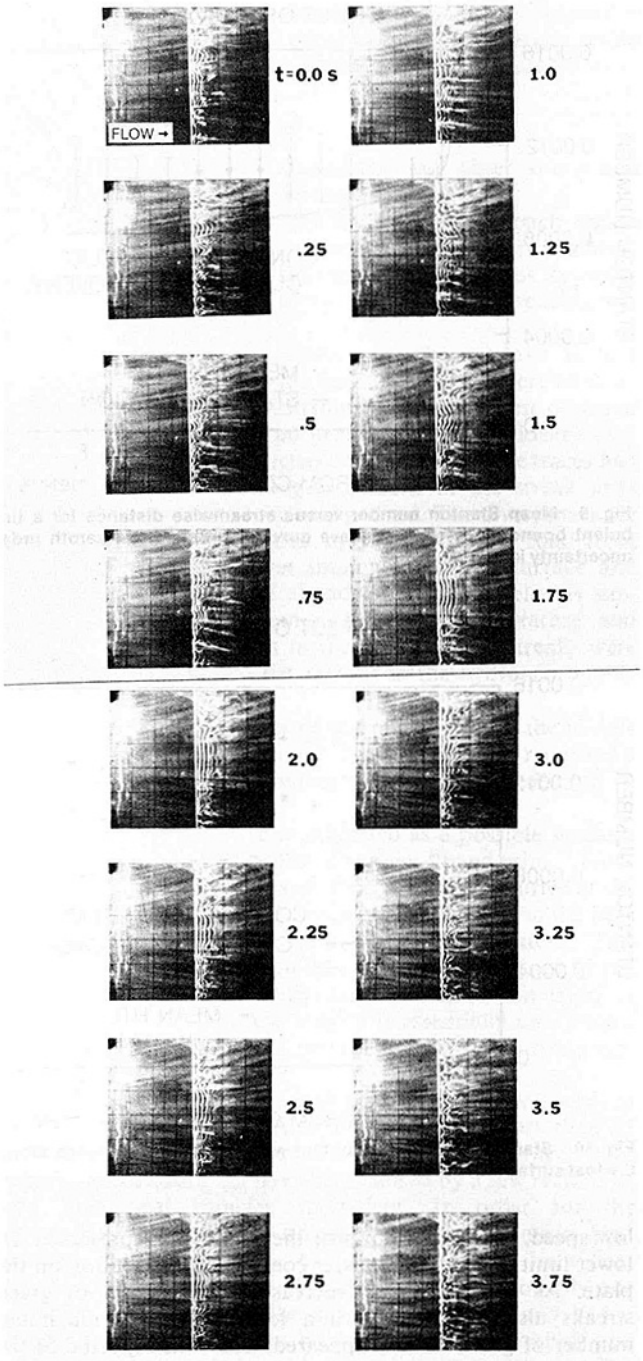

Fig. 6 Sequence of movie frames showing birth, life, and death of a divergence

scale wall traces that appeared and disappeared randomly in space and time with no preferred location. A wall trace was defined as a set of streaks on the liquid crystal surface that formed an identifiable, large-scale pattern distinguishably different from the background streak pattern. A photograph of a typical streak pattern in the curved region is shown in Fig. 5. The diverging wall traces, or "divergences," have diverging streak patterns in the streamwise direction and form a "V" with the apex pointing upstream. These divergences do not appear to be convected downstream during their lifetime. They form all at once at a particular location, bloom out with a crisp streak pattern with a maximum 20 deg angle of the streaks from the downstream direction and then "die." They "die" by having their crisp streak pattern broaden out and disappear. The divergences are about 10 × 20 cm in the

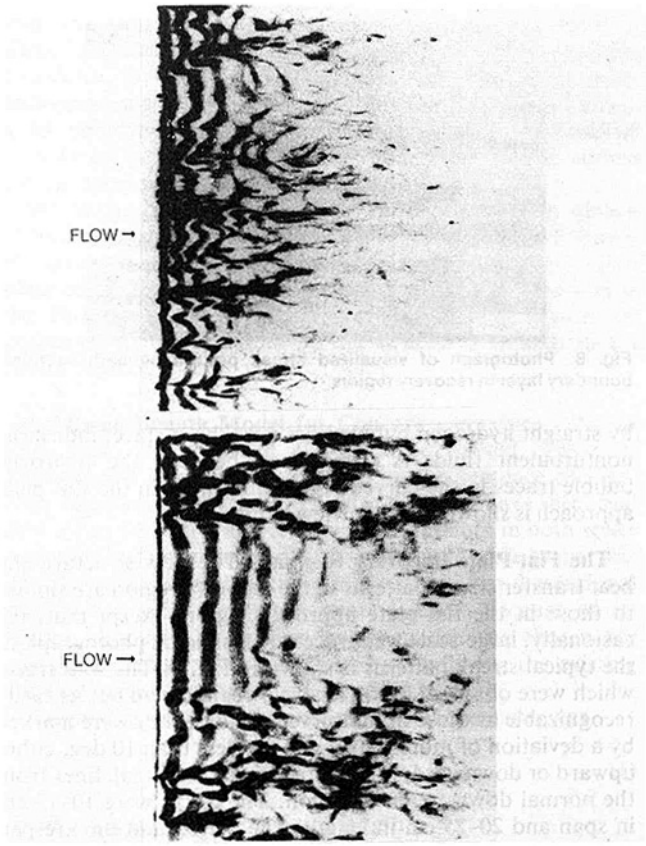

Fig. 7 Photographs of hydrogen bubble traces for flat-plate (top) and concavely curved region (bottom). Wire at $y^+ = 10$.

spanwise and streamwise directions, respectively. The period and the lifetime of the concave wall traces were determined by analyzing frames from a 16-mm movie. The average period between occurrences (over a 17 by 15 cm area) was 13.1 s with a standard deviation of 6.9 s. The average lifetime was 4.4 s with a standard deviation of 1.9 s. If these times are normalized by outer layer variables U_∞ and δ, as is done with wall bursting, the results are

$$\frac{T_p U_\infty}{\delta} = 20 \text{ for the period}$$

$$\frac{T_l U_\infty}{\delta} = 6.9 \text{ for the lifetime}$$

A sequence of photos taken from a 16-mm movie showing the birth, life, and death of a divergence is shown in Fig. 6.

A .003-in.-dia (.0756-mm) chromel-alumel thermocouple boundary layer probe was used to conditionally sample the thermal boundary layer. The probe was positioned on the wall in the flow and a long-term average temperature was determined. An audible tone was then produced whenever the temperature was less than the average. It was then possible to view the liquid crystal streak patterns and simultaneously hear the signal indicating low fluid temperature. A strong correlation between low temperature at the probe and the appearance of divergences was noted.

Based on the difference in the average color of liquid crystal inside and outside of the divergence, the difference in heat transfer coefficient between the center of a divergence and outside was found to be less than 25 percent. The spanwise spacing of the thermal streaks in the curve, nondimensionalized by the mean Stanton number, was 3.7 percent larger than in the flat-plate approach region. That was not felt to be significant, since the standard deviation of that measure was 14 percent. The divergences were often marked

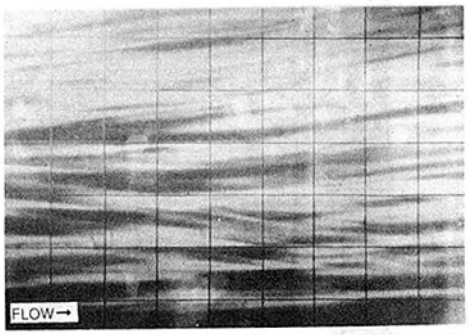

Fig. 8 Photograph of visualized streak pattern beneath turbulent boundary layer in recovery region

by straight hydrogen bubble lines near the surface, indicating nonturbulent fluid. A comparison between the hydrogen bubble traces in the curved region and those in the flat plate approach is shown in a plan view in Fig. 7.

The Flat-Plate Recovery Region. The flow structure and heat transfer streak patterns in the recovery region are similar to those in the flat-plate approach region, except that, occasionally, large-scale wall traces are visible. A photograph of the typical streak patterns is shown in Fig. 8. The wall traces which were observed in the recovery region were not as easily recognizable as those in the curved region. They were marked by a deviation of more than 5 deg and less than 10 deg, either upward or downward, in the direction of the streak lines from the normal downstream direction. The traces were 10–15 cm in span and 20–25 cm in length. The period and the lifespan were found from single-frame movie analysis to be 11.1 and 3.9 s, respectively. The wall traces were "born" by appearing all at once with either an upward or a downward streak pattern. The traces "died" by either (*i*) a broadening of the streaks, (*ii*) by streaks changing direction, or (*iii*) by being washed out from upstream. There appeared to be less lateral movement of either the hydrodynamic or the thermal streaks in this region compared to the flat-plate approach region. The difference in heat transfer coefficient between the middle of the traces and the rest of the surface was negligible. The longitudinal streak spacing, nondimensionalized by Stanton number, was 17.5 percent larger in the recovery region than in the approach region.

Mean Heat Transfer Results. The spanwise and temporally averaged Stanton number distribution was measured along the test surface. The results of a typical case are shown in Fig. 9. These are compared to a flat-plate prediction of the flow by the two-dimensional finite difference computer program, STAN5 [33]. The heat transfer decreases slowly in the approach region and then increases abruptly to a level 20 percent above the flat-plate prediction. It then remains relatively constant, even after the withdrawal of curvature in the recovery region.

In addition to providing heat transfer streak patterns in turbulent flow and spanwise averaged heat transfer coefficients, the liquid crystal technique provides information about the peak to peak variation of heat transfer coefficient about the mean. To explain how this is done, the data taking procedure must be outlined.

When the liquid crystal is above or below its event temperature band, it is colorless. As the temperature is raised through the event band, the apparent color of the liquid crystal continuously changes from red through violet. Green was chosen as the calibration event temperature. During a test run, the power to the liquid was increased slowly, until the first signs of green streaks appeared on the surface. These streaks represented the lowest heat transfer coefficient on the surface and hence represented "low speed streaks," areas of

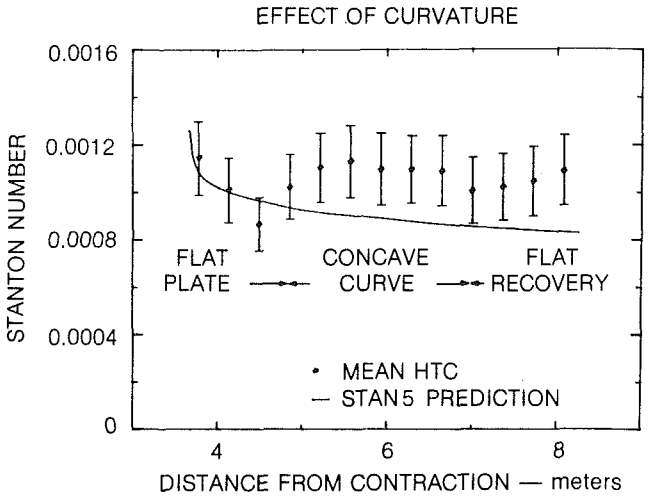

Fig. 9 Mean Stanton number versus streamwise distance for a turbulent boundary layer in concave curvature. Bars show zeroth order uncertainty intervals.

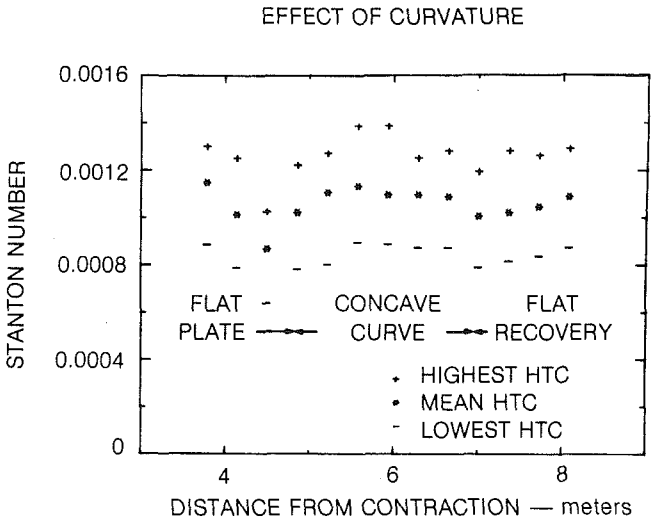

Fig. 10 Stanton number distribution as a function of distance along the test surface

low speed, hot fluid from near the wall. This represented the lower limit of the heat transfer coefficient distribution on the plate. As the power was increased, the number of green streaks also increased until a level where the maximum number of green streaks appeared. This was reported as the average heat transfer coefficient. As the power was increased still further, the number of green streaks decreased until a level was reached where only a few remaining green streaks were present. These represented the highest heat transfer coefficient streaks on the plate: high-speed sweeps of cold fluid from outside the boundary layer. The peak to peak variation of Stanton number throughout the test section is shown in Fig. 10. The variation is about ±20 percent about the mean and is approximately the same in the approach, in the recovery and in the concave regions.

All interpretations of color were done by eye. Tests were conducted in order to ascertain the repeatability of the data. Tests with a single observer and tests with two different observers were conducted. The tests were conducted by having a second person adjust the power level to give a particular color pattern responding to verbal orders from the observer. A single observer was able to repeat the same point within a standard deviation of 3 percent of the Stanton number. Two different observers, with an agreement on objective, repeat to

a standard deviation of 6 percent. A 15 percent difference in power setting was very easy to detect. The average zeroth order uncertainty in Stanton number was 12.8 percent.

Discussion

The following section summarizes our observations and gives our interpretation of the results.

All indications are that the flow in the approach region upstream of curvature was a normal, zero pressure gradient, turbulent boundary layer. The momentum thickness Reynolds number was about 1300 and the spanwise streak spacing was 89 in inner coordinates.

The heat transfer distribution on the concave surface showed occasional large-scale wall traces which were of short duration and had a limited streamwise extent. These occurred randomly with no preferred location, and no evidence of a stationary pattern was detected on the surface. The traces had the appearance of a divergent pattern in the streak lines distinctly different from the background. The divergences are believed to have been caused by sweeps of cold fluid from outside the boundary layer impinging on the surface and "squishing out" the fluid already there. This belief is supported by conditional sampling of the temperature and velocity field. Divergences in the heat transfer streaks were often accompanied by quiet regions in the hydrogen bubble traces near the wall.

A decrease in the number of thermal streaks in the middle of a divergence was often noted. This is believed to represent a reduction in near wall bursting and tied to a reduction in turbulence production.

The following sequence is suggested as a possible scenario for the formation of a thermal, divergent "hand print." First, a large "pocket" of outer layer fluid is suddenly hurled at the wall. This causes a radially directed outward flow in the near wall region and starts to form a star burst pattern. This pattern is swept downstream into a fanlike divergence by the local convective flow. Only the local flow direction is changed, however, and the local h is essentially unaffected. After a short lifespan, the thermal trace of the divergence disappears.

The difference in average heat transfer coefficient between the region inside a divergence and outside was less than 25 percent. The 20 percent increase in spanwise averaged heat transfer noted could not have been caused by a few regions of very high heat transfer coefficient. In order for the divergences to cause the observed increase in mean heat transfer, they would have had to have a very high heat transfer coefficient. The wall traces were spaced roughly one boundary layer apart in the spanwise direction and had a roughly triangular footprint on the wall with a length of two boundary layers and a width of one boundary layer. The maximum active area of a wall trace was then 1/2 of the total area. From the lifetime and period, 4.4 and 13.1 s, respectively, the wall traces were active only 1/3 of the time (4.4/13.1). Therefore, the wall traces contribution to the average heat transfer coefficient was only 1/2 × 1/3 or 1/6. In order to produce a 20 percent increase in average heat transfer, the local heat transfer coefficient in the divergences would have to be 6 × 20 percent or 120 percent higher than the mean. Measurements of local heat transfer coefficient inside the diverging region could not have failed to detect levels anywhere near this high. Therefore, the 20 percent increase in mean heat transfer could not have been caused by concentrated regions of high heat transfer coefficient inside the divergent regions.

It is suggested that the increase in the mean heat transfer was caused by two factors: (*i*) large scale interchanges of regions of hot and cold fluid from the inner and outer boundary layer and (*ii*) higher turbulence intensity, at medium and fine scales, leading to increased local mixing. Both of these effects could have been caused by the large-scale structures in the curved region. In the companion hydrodynamic study, Jeans and Johnston [18] showed about a 15 percent increase in spanwise averaged, longitudinal turbulence intensity across the whole layer in the curved region, compared to the flat plate approach.

While the introduction of curvature produces an almost immediate response in the mean heat transfer, the withdrawal of curvature has a very small effect. The full recovery to flat-plate conditions may be very slow indeed. The structures in the flow and the wall traces in the recovery region are presumed to be remnants of the structures created in the curved region.

A Mixing Length Model for Concave Curvature. As we have seen, the flow in the concave curved region is distinguished from flat-plate flows by the presence of transient, large-scale structures. The structures we have seen, and their effect on heat transfer, have been random in both space and time, and no evidence of stationary large-scale events was seen. It seems justifiable, therefore, to use a two-dimensional scheme to predict the mean heat transfer. Because of its relative simplicity, a mixing length model was chosen for concave curvature. This was done by modifying the existing finite difference computer program STAN5 [33].

The mixing length model chosen for the inner layer was

$$\frac{l}{l_0} = e^{-\beta\,\mathrm{Ri}} \tag{1}$$

where l_0 is the flat plate mixing length;
β is an inner layer mixing length constant;
Ri is the Richardson number $= S(1+S)$

where $$S = \frac{2\kappa U/h}{dU/dy - \kappa U/h}$$

and $$h = 1 + y/R$$

This Richardson number definition was first proposed by So [34]. The first two terms of the Taylor expansion of equation (1) are identical to an inner layer model first proposed by Bradshaw [35]

$$\frac{l}{l_0} = 1 - \beta\,\mathrm{Ri} \tag{2}$$

Equation (1) has the advantage that it can never predict a negative mixing length for strong concave curvature.

A cubic equation was chosen to specify the mixing length in the outer layer

$$\frac{l}{R} = 0.086\left(\frac{\delta}{R}\right) + 2\frac{(\alpha - 0.086)}{\delta/R_{\mathrm{lim}}}\left(\frac{\delta}{R}\right)^2 + \frac{(0.086-\alpha)}{\delta/R_{\mathrm{lim}}^2}\left(\frac{\delta}{R}\right)^3 \tag{3}$$

where α is the asymptotic slope of the l/R versus δ/R correlation
δ/R_{lim} is the value of δ/R where α is specified

The validity of this outer layer model is seen by examining a cross plot of mixing length data from the concave experiments of Hoffman and Bradshaw [11] and Prabhu and Rao [13] in Fig. 11.

Adams and Johnston [36] recently proposed a model for convex curvature which includes an asymptotic limit for strong convex curvature.

$$\frac{l}{R} = 0.0025 \tanh\left[\frac{34.5\,\delta}{R}\right] \tag{4}$$

A comprehensive mixing length model for curvature is shown in Fig. 12. This model predicts outer layer mixing

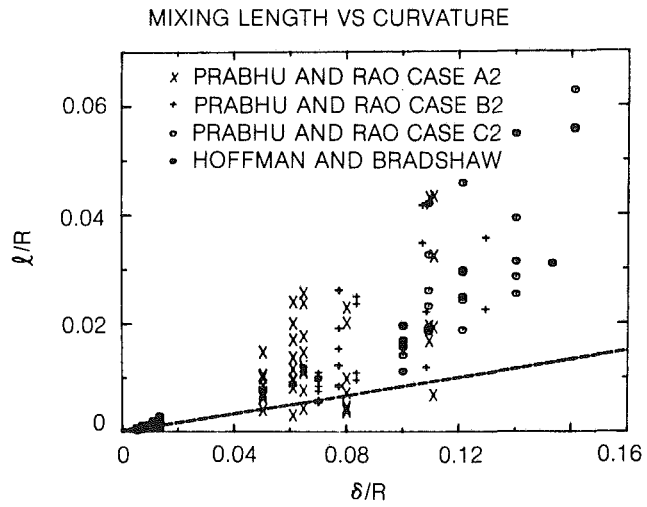

Fig. 11 Mixing length distribution from Hoffman and Bradshaw [11] and Prabhu and Rao [13]. Dashed line shows flat plate, outer layer mixing length.

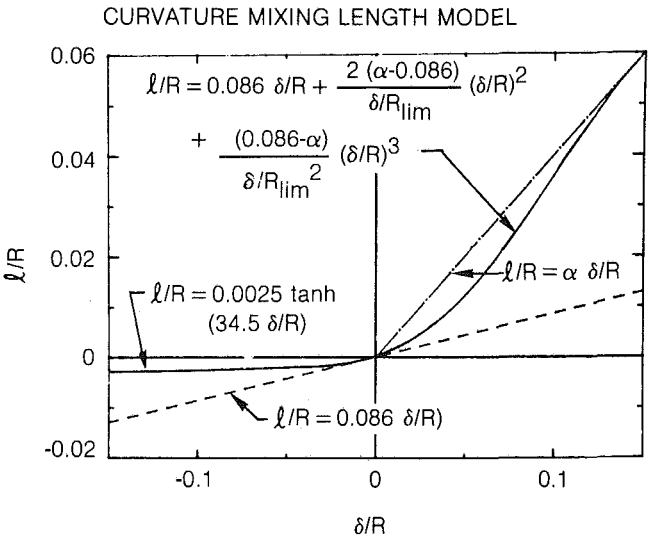

Fig. 12 Outer layer mixing length model for convex and concave curvature

lengths from strong convex curvature through flat-plate flows to strong concave curvature.

A lag equation for an effective radius was used for the transition from the curvature region to the recovery region. The form employed was

$$\frac{1}{R_{\text{eff}}} = \frac{1}{R_{\text{old}}} \exp\left[-C\frac{(xd-xu)}{\delta}\right] \tag{5}$$

where $1/R_{\text{old}}$ is the curvature at the last integration step
$(xd-xu)$ is the integration step size
δ is the boundary layer thickness
C is a lag constant

Results obtained using this model for the present experiment are shown in Fig. 13. The values chosen for the empirical constants were

$$\begin{aligned} \beta &= 4.5 \\ \alpha &= 0.4 \\ \delta/R_{\text{lim}} &= 0.15 \\ C &= 0.05 \end{aligned}$$

Conclusions

The curved region showed random isolated, large-scale wall traces, characterized by a divergence of the longitudinal

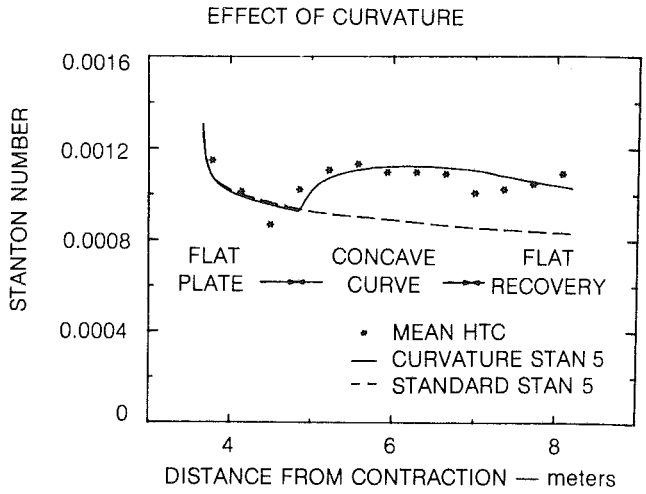

Fig. 13 Stanton number prediction from curvature version of STAN5

streaks on the wall. These wall traces last several seconds, but are limited in streamwise extent. The locally averaged heat transfer coefficient inside a region of divergence is not markedly higher than the surrounding area, even though the spanwise-averaged heat transfer is 20 percent higher than a flat-plate prediction. These wall traces are believed to be the thermal footprints of the "sweeps" found by Jeans and Johnston [18]. They are thought to be caused by sweeps of cold fluid from outside the boundary layer bringing lower turbulence fluid closer to the wall. This observation was confirmed by conditional sampling of the temperature field in the boundary layer.

The distribution of heat transfer coefficient showed no evidence of stationary Taylor-Gortler vortices or roll cells in the concave regions. Large-scale wall traces were observed, but they were not stationary. They appeared and disappeared in a random fashion and had no preferred location. These observations confirm the hydrodynamic findings of Jeans and Johnston [18].

The spanwise- and timewide-averaged heat transfer coefficient over the entire concave region was about 20 percent higher than flat-wall predictions for the same flow conditions. This increase is believed to be due to large-scale interchanges of hot and cold fluid and increased local mixing from higher turbulence intensity at medium and small scales, rather than a few regions of very high heat transfer coefficient. The increased scale and intensity are probably a consequence of the large-scale events.

The distribution of the surface heat transfer in the recovery region is similar to that in a flat-plate flow, except that occasionally remnants of structures created in the curved region upstream are carried downstream. These remnants create small divergences in the thermal streak lines.

The withdrawal of concave curvature appears to produce a slower response to heat transfer than the introduction of curvature. The recovery of mean Stanton number to flat-plate values appears to take a long distance to accomplish.

A two-dimensional, finite-difference computer program with a modified Beta Richardson inner-layer mixing length model appears to predict adequately the spanwise-averaged heat transfer. Since no stationary vortices were observed in either the hydrodynamics or in the heat transfer studies, there does not appear to be a need for a three-dimensional code. The outer-layer mixing length does not appear to be an important parameter for modeling concavely curved turbulent boundary layer heat transfer at least for water.

Acknowledgments

The authors would like to thank Prof. J. P. Johnston and

his research assistant, Dr. Albert Jeans, who performed the concurrent hydrodynamic study on the same flow facility, for many hours of thought provoking discussion. We also thank Prof. S. J. Kline for his many useful suggestions and coments.

The financial support of the U. S. Air Force of Scientific Research is gratefully acknowledged.

References

1 Wilcken, H., "Turbine Grenzschichten an Gewoelbten Flaechen," Berlin, Vol. 1, No. 4, Sept. 1930, translated as NASA TT-F-11, 421, Dec. 1967.

2 Wendt, F., "Turbulente Stromungen Zwischen zesi rotierenden honaxialen Zylindren," *Ing.-Arch.*, Vol. 4, 1933, p. 577.

3 Wattendorf, F. L., "A Study of the Effect of Curvature on Fully Developed Turbulent Flow," *Proc. Royal Soc.*, Vol. 148, 1935.

4 Schmidbauer, H., "Behavior of Turbulent Boundary Layers on Curved Convex Walls," NACA-TM No. 791, 1936.

5 Clauser, M., and Clauser, F., "The Effect of Curvature on the Transition from Laminar to Turbulent Boundary Layer," NACA-TN No. 613, 1937.

6 Görtler, H., "On the Three-Dimensional Instability of Laminar Boundary Layers on Concave Walls," NACA Tech. Memo. 1375, June 1954, translated from Ges d. Wiss. Gotteningen, Nachr. a. d. Math., Bd. 2, Nr. 1, 1940.

7 Tani, I., "Production of Longitudinal Vortices in the Boundary Layer Along a Concave Wall," *Journal of Geophysical Research*, Vol. 67, No. 8, July 1962, pp. 3075–3080.

8 So, R. M. C., and Mellor, G. L., "An Experimental Investigation of Turbulent Boundary Layers Along Curved Surfaces," NASA-CR-1940, Apr. 1972.

9 So, R. M. C., and Mellor, G. L., "Experimental on Turbulent Boundary Layers on a Concave Wall," *The Aeronautical Quarterly*, Vol. 16, No. 25, Feb. 1975.

10 Meroney, R. N., and Bradshaw, P., "Turbulent Boundary Layer Growth Over a Longitudinally Curved Surface," *AIAA Journal*, Vol. 13, No. 11, Nov. 1975.

11 Hoffman, P. H., and Bradshaw, P., "Turbulent Boundary Layers on Surfaces of Mild Longitudinal Curvature," Imperial College Aero. Rept. 78-04, (submitted to JFM), 1978.

12 Ellis, L. B., and Joubert, P. N., "Turbulent Shear Flow in a Curved Duct," *JFM*, Vol. 62, pt. 1, 1974, pp. 54–84.

13 Prabhu, A., and Rao, B. N. S., "Effect of Concave Streamline Curvature on Turbulent Boundary Layers," AIAA Paper No. 81-1193, presented at the AIAA 14th Fluid and Plasma Dynamics Conference, June, 1981.

14 Thomann, H., "Effect of Streamwise Wall Curvature on Heat Transfer in a Turbulent Boundary Layer," *JFM*, Vol. 33, pt. 2, 1968, pp. 283–292.

15 Ramaprian, B. R., and Shivaprasad, B. G., "Mean Flow Measurements in Turbulent Boundary Layers Along Mildly Curved Surfaces," *AIAA Journal*, Vol. 15, No. 2, 1977, pp. 189–196.

16 Ramaprian, B. R., and Shivaprasad, B. G., "Turbulence Measurements in Boundary Layers along Mildly Curved Surfaces," *J. of Fluids Engineering*, Vol. 100, No. 1, Mar. 1978, pp. 37–46.

17 Ramaprian, B. R., and Shivaprasad, B. G., "The Structure of Turbulent Boundary Layers along Mildly Curved Surfaces," *JFM*, Vol. 85, 1978, pp. 273–303.

18 Jeans, A. H., and Johnston, J. P., "The Effects of Streamwise Concave Curvature on Turbulent Boundary Layer Structure," Report MD-40, Thermosciences Division, Mech. Engrg. Dept., Stanford University, June 1982.

19 Kreith, F., "The Influence of Curvature on Heat Transfer to Incompressible Fluids," ASME *Transactions*, Vol. 77, No. 11, 1955, pp. 1247–1256.

20 Mayle, R. E., Blair, M. F., and Kopper, F. C., "Turbulent Boundary Layer Heat Transfer on Curved Surfaces," ASME *Journal of Heat Transfer*, Vol. 101, No. 3, Aug. 1979.

21 Klein, E. J., "Liquid Crystals in Aerodynamic Testing," Astronautics and Aeronautics, Vol. 6, No 7, 1968, pp. 70–73.

22 Lemberg, R., "Liquid Crystals for the Visualization of Unsteady Boundary Layers, AFOSR Scientific Report, AFOSR-TR-71-2622, 1971.

23 Vennemann, D., and Bütefisch, K. A., "The Application of Temperature-Sensitive Crystals to Aerodynamic Investigations," European Space Agency, ESRO-RR-77, translation of DLR-FB-73-121, 1973.

24 den Ouden, C., and Hoogendoorn, C. J., "Local Convective-Heat-Transfer Coefficients for Jets Impinging on a Plate; Experiments Using a Liquid-Crystal Technique," *Proceedings of the Fifth International Heat Transfer Conference*, Vol. V. AIChE, New York, 1974, pp. 293–297.

25 Cooper, T. E., Field, R. J., and Meyer, J. F., "A Liquid Crystal Thermographic Study of a Heated Cylinder in Crossflow," Naval Postgraduate School Report NPS-59Cg74111, Nov. 1974.

26 Cooper, T. E., Field, R. J., and Meyer, J. F., "Liquid Crystal Thermography and Its Application to the Study of Convective Heat Transfer," ASME *Journal of Heat Transfer*, Vol. 97, Aug. 1975, pp. 442–450.

27 Kelleher, M. D., Flentie, D. L., and McKee, R. J., "An Experimental Study of the Secondary Flow in a Curved Rectangular Channel," ASME Paper No. 79-FE-6, presented at the Joint ASME/CSME Appiled Mechanics, Fluids Engineering and Bioengineering Conference, June 1979.

28 Hippensteele, S. A., Russell, L. M., and Stepka, F. S., "Evaluation of a Method for Heat Transfer Measurements and Thermal Visualization Using a Composite of a Heater Element and Liquid Crystals," NASA Tech. Memo. 81639; also ASME Paper No. 81-GT-93, 1981.

29 Simonich, J. C., and Moffat, R. J., "New Technique for Mapping Heat Transfer Coefficient Contours," *Rev. Sci. Instrum.*, Vol. 53, No. 5, May 1982, pp. 678–683.

30 Kim, H. T., Kline, S. J., and Reynolds, W C., "An Experimental Study of Turbulence Production Near a Smooth Wall in a Turbulent Boundary Layer with Zero Pressure Gradient," Report MD-20, Thermosciences Div., Mech. Engrg. Dept., Stanford University, Jan. 1968.

31 Cantwell, B. J., "Organized Motion in Turbulent Flow," *Ann. Rev. Fluid Mech.*, Vol. 13, 1981, pp. 457–515.

32 Smith, C. R., and Metzler, S. P., "The Characteristics of Low-Speed Streaks in Near-Wall Region of a Turbulent Boundary Layer," *JFM*, Vol. 129, 1983, pp. 27–54.

33 Crawford, M. E., and Kays, W. M., "STAN5—A Program for Numerical Computation of Two-Dimensional Internal and External Boundary Layer Flows," NASA CR-2742, Dec. 1976.

34 So, R. M. C., "On the Curvature/Buoyancy Analogy for Turbulent Shear Flows," ZAMP, Vol. 31, Facs. 5, 1980, pp. 628–633.

35 Bradshaw, P., "The Analogy Between Streamwise Curvature and Buoyancy in Turbulent Shear Flow," *JFM*, Vol. 36, pt. 1, 1969, pp. 177–191.

36 Adams, E. W., and Johnston, J. P., "A Mixing Length Model for the Prediction of Convex Curvature Effects on Turbulent Boundary Layers," Internal Lab Report, IL-42, Thermosciences Div., Mech. Engrg. Dept., Stanford University, July 1981.

L. M. C. Gato
Assistant Lecturer.

A. F. de O. Falcão
Professor.

Department of Mechanical Engineering,
Instituto Superior Técnico,
1096 Lisboa Codex, Portugal

On the Theory of the Wells Turbine

A theoretical investigation is presented concerning the aerodynamic performance of the Wells turbine, a self-rectifying, axial-flow turbine suitable for energy extraction from a reciprocating air flow. A two-dimensional analysis is developed, and expressions, based on potential flow, are derived for the blade shape maximizing the turbine efficiency. Three-dimensional effects and profile losses are then accounted for by means of an actuator disk theory, which shows that large radial distortions of axial velocity profile can occur, depending on blade shape, with important implications on the extent of the stall-free conditions.

1 Introduction

A problem, encountered in some devices for sea-wave energy conversion, consists in transforming a reciprocating flow of air into unidirectional rotational motion, which can be used to drive an electrical generator. This requirement is met, without the need of any rectifying valves, by the turbine invented some years ago by Dr. A. A. Wells. It is an axial-flow turbine, constituted essentially by a rotor with untwisted aerofoil blades of symmetrical cross section, set radially at a 90-deg angle of stagger. Versions with and without guide vanes are known to have been tested. The main feature of the turbine is its capability of producing a time-averaged positive power from a cyclically reversing air flow with a fairly high efficiency and a large blade-to-air velocity ratio.

The performance of the Wells turbine has been object of theoretical investigations using the two-dimensional cascade flow model [1–3]. Experimental data have been published only for turbines with rotor blades of constant chord. Grant et al. [2, 4] used a turbine of 0.4-m rotor dia, with guide vanes on both sides of the rotor, whereas Raghunathan et al. [3, 5, 6] tested a turbine of 0.2-m dia without guide vanes.

The main purpose of this paper is to develop a more comprehensive and exact analysis, including three-dimensional effects, and to find out how the blade shape affects the turbine performance. The turbine is supposed to have long cylindrical walls and no guide vanes, and the flow is considered incompressible. A two-dimensional analysis is first developed, in section 2, and expressions, based on potential flow, are derived for the blade shape, allowing maximum efficiency for given values of the hub-to-tip diameter ratio, flow rate coefficient, and exit-loss coefficient. Three-dimensional effects and profile losses are considered, in section 3, by means of an actuator disk flow model, which is used to obtain numerical results showing the effect of blade shape upon turbine performance.

Contributed by the Gas Turbine Division of THE AMERICAN SOCIETY OF MECHANICAL ENGINEERS and presented at the 29th International Gas Turbine Conference and Exhibit, Amsterdam, The Netherlands, June 4–7, 1984. Manuscript received at ASME Headquarters December 6, 1983. Paper No. 84-GT-5.

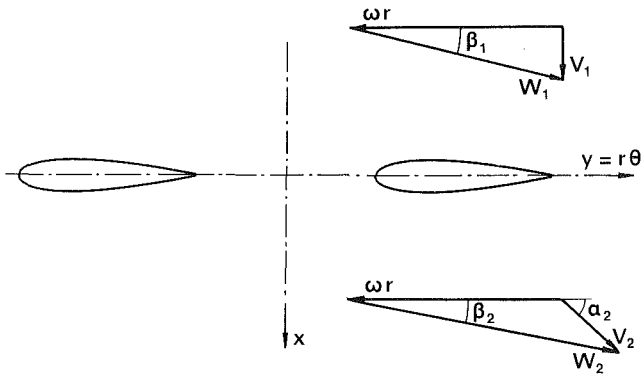

Fig. 1 Two-dimensional cascade geometry

2 Two-Dimensional Analysis

2.1 Basic Assumptions. We introduce a system of cylindrical coordinates (r, θ, x) and consider the annular flow through the turbine to be incompressible and bounded by two coaxial walls of revolution. For the sake of simplicity of the analysis, the duct enclosing the rotor blades is assumed to have cylindrical walls, at $r=R_i$, $r=R$ $(R_i<R)$, long enough so that we may ignore the disturbing end-effects upon the flow pattern about the blades. The rotor has angular speed, ω, and comprises a set of N untwisted blades, of chord, $c(r)$, and symmetrical profile, located radially at the plane $x=0$. In the present analysis, the effect of the annular wall boundary layers is neglected, and the incoming flow is supposed uniform and swirl-free, with positive axial velocity, U.

As a first approximation, we ignore the flow interference between different radii, which means that the radial velocities are neglected. In this case, the flow at each cylindrical streamsurface may be adequately represented by the two-dimensional flow about a rectilinear cascade of blades in the (x, y) plane, where we take $y=r\theta$.

We consider, in the (x, y) plane, a cascade of symmetrical aerofoils set at 90-deg angle of stagger along the y-axis (tandem cascade), with chord, c, and pitch, $t=2\pi r/N$, and moving with velocity, ωr, along the negative y-direction (Fig.

1). The incoming flow velocity, $\mathbf{W}_1$, relative to the blades, has components $W_{1x}=U$ and $W_{1y}=\omega r$. Far downstream, it is $W_{2x}=U$ and $W_{2y}=\omega r+V_{2y}$. We define the lift and drag directions as perpendicular and parallel, respectively, to the relative mean velocity vector, $\mathbf{W}_m=(\mathbf{W}_1+\mathbf{W}_2)/2$, and introduce the lift and drag coefficients, c_L and c_D, referred to the relative mean flow dynamic pressure. It can easily be found that the work, $E(r)$, done by the fluid on the blades, per unit mass of fluid, is given by

$$E=\frac{1}{2}c_L\frac{c}{t}\omega r\,U\frac{\sin(\beta_m-\gamma)}{\sin^2\beta_m\cos\gamma} \tag{1}$$

where $\gamma=\arctan(c_D/c_L)$, and β_m is the angle of $\mathbf{W}_m$ with the y-direction. Applying the momentum theorem, we obtain

$$\tan\beta_m=\frac{U}{\omega r+\dfrac{E}{2\omega r}} \tag{2}$$

which, together with equation (1), allows β_m and E to be determined if c_L and c_D are known as functions of β_m (or β_1). The pressure drop through the cascade is then given by

$$p_1-p_2=\frac{1}{2}c_L\frac{c}{t}\rho\,U^2\frac{\cos(\beta_m-\gamma)}{\sin^2\beta_m\cos\gamma} \tag{3}$$

In order to define the turbine efficiency, η, we assume that the swirl kinetic energy at exit is lost, as well as a fraction $KU^2/2$ ($K\le 1$) of the axial-velocity kinetic energy. It follows that $\eta=P/T$, where

$$\left.\begin{aligned} P&=2\pi\rho U\int_{R_i}^{R}E(r)\,r\,dr \quad \text{and}\\ T&=2\pi U\int_{R_i}^{R}\left(p_1-p_2+K\rho\frac{U^2}{2}\right)r\,dr \end{aligned}\right\} \tag{4}$$

are the power output of, and the power available to, the turbine, respectively.

In unstalled conditions, β_m is a small angle, of the order of magnitude of γ, which means that the work, E, is expected to depend strongly on the drag coefficient, more markedly than in conventional cascade flows. (In particular, it is $E<0$ if $\beta_m<\gamma$.) Experimental data on tandem-cascade flow are relatively scarce. The only published results [7] were obtained for a Reynolds number of about 10^5, which is one to two orders of magnitude smaller than what is expected to occur in full-scale Wells turbines for sea wave-energy conversion. Aerofoil drag coefficients, and to a lesser extent lift coefficients, are known to change substantially for large Reynolds number variations over these ranges [8], which means that those data are probably unreliable to predict the performance of full-scale turbines. An alternative approach, which will be followed here, consists in using isolated aerofoil experimental data, modified by interference factors derived from cascade potential flow theory. Although this method still does not allow an accurate evaluation of the drag coefficient (which could be affected by interference between aerofoils in an unpredictable manner), it constitutes a fairly reliable way of determining the lift coefficient for a large variety of aerofoil profiles and a wide range of Reynolds numbers, provided the chord-to-pitch ratio is not too close to unity.

We introduce the cascade interference factor, $k=c_L/c_{Lo}$, where c_{Lo} is the isolated aerofoil lift coefficient at the angle of incidence, β_m, and assume that, for the geometries and Reynolds numbers of interest, k is not substantially affected by viscous and thickness effects. Consequently, we will take, for k, the corresponding value calculated for a cascade of flat plates in potential flow. An exact solution for the plane potential flow about an infinite row of flat plates with arbitrary angle of stagger is well known [9–11], and the theoretical value of the interference factor is found to be independent of the angle of incidence, β_m. For the special case of 90-deg angle of stagger, it is simply

$$k=\frac{2t}{\pi c}\tan\frac{\pi c}{2t} \tag{5}$$

2.2 Potential Flow. Before dealing with the case of aerofoils in real flow, we derive some theoretical results for the potential flow about blades of negligible thickness (flat plates). In this case, it is $\gamma=0$, and $c_{Lo}=2\pi\sin\beta_m$. The angle α_2, of the downstream velocity $\mathbf{V}_2$, is given by

$$\tan\alpha_2=\frac{U}{V_{2y}}=\frac{1}{2}\operatorname{cotan}\frac{\pi c}{2t} \tag{6}$$

which shows α_2 to depend only on the cascade solidity. Introducing the dimensionless quantities $[r^*, R^*, c^*]=[r, R_i, c]/R$, $U^*=U/(\omega R)$, $[P^*, T^*]=[P, T]/(\rho\omega^3R^5)$, we obtain, for the efficiency, $\eta=P^*/T^*$, where $T^*=P^*+L_x^*+L_y^*$

$$P^*=4\pi U^{*2}\int_{R^*}^{1}r^{*2}\tan\frac{Nc^*}{4r^*}\,dr^* \tag{7}$$

Nomenclature

c = blade chord
c_D, c_L = drag, lift coefficient
c_{Lo} = isolated aerofoil lift coefficient
E = blade work per unit mass of fluid
k = cascade interference factor
K = fraction of axial kinetic energy lost at exit
L_x, L_y = exit energy losses due to axial, tangential velocity
N = number of rotor blades
p = pressure
$\Delta p, \Delta p_o$ = drop in static, stagnation pressure across the disk
P = turbine power output
Q = volume flow rate
(r,θ,x) = cylindrical coordinate system
R_i, R = inner, outer radius
S = solidity, total blade area/annular area
t = cascade pitch
T = power available to the turbine
U = inlet flow velocity
v = velocity perturbation to radial equilibrium
V, W = absolute, relative flow velocity
(x, y) = cartesian coordinate system (Fig. 1)
α, β = angle of absolute, relative velocity
γ = arctan (c_D/c_L)
η = turbine efficiency
ρ = density
ω = rotor angular speed

Subscripts

av = time-averaged value in oscillating flow
o = conditions of maximum flow rate in oscillating flow
op = optimum value for maximum efficiency
1,2 = upstream, downstream of blade row
$+\infty, -\infty$ = radial equilibrium conditions, at $x=\pm\infty$

Superscripts

$*$ = dimensionless value
$-$ = time-averaged value in oscillating flow

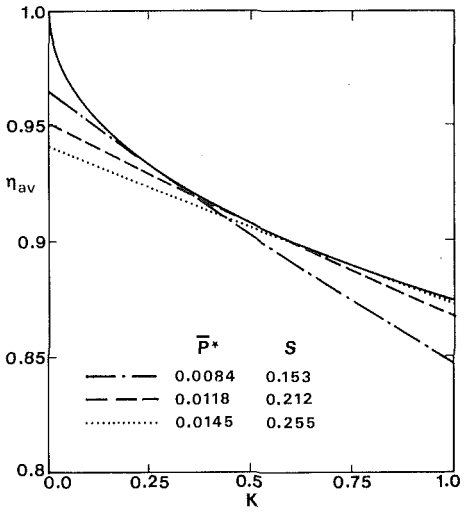

Fig. 2 Results from two-dimensional potential flow theory for blades of optimum shape

$$L_x^* = \frac{\pi}{2} K(1-R^{*2})U^{*3},\ L_y^* = 4\pi U^{*3}\int_{R^*}^{1} r^* \tan^2 \frac{Nc^*}{4r^*}\, dr^* \qquad (8)$$

L_x^* and L_y^* being dimensionless coefficients for the exit losses due to axial and swirl velocity components, respectively.

Since the Wells turbine is intended primarily for applications with oscillating flow, it is convenient, at this stage, to introduce time-averaged values. Assuming sinusoidally varying flow rate, we may write $U(t) = U_o \sin \Omega t$. Then, since the average values of $\sin^2 x$ and $\sin^3 |x|$ over a cycle are equal, respectively, to 1/2 and $4/(3\pi)$, it follows that $\bar{P}^* = P_o^*/2$ and $[\bar{L}_x^*, \bar{L}_y^*] = [L_{xo}^*, L_{yo}^*]4/(3\pi)$, where the superscript bar and the subscript, o, indicate time-averaged and maximum flow rate conditions, respectively. The following relation holds for the corresponding efficiencies

$$\eta_{av} = \frac{\bar{P}^*}{\bar{T}^*} = \left[1 + \frac{8}{3\pi}\left(\frac{1}{\eta_o} - 1\right)\right]^{-1} \qquad (9)$$

from which it can be found that $\eta_{av} > \eta_o$, a result which should be expected, since η decays with increasing flow rate as a consequence of the losses rising faster than the power produced (see equations (7) and (8)). (Note that η_{av} is *not* the time-averaged value of η.)

For given values of R^*, U^*, and K, η can be considered as a functional of $\mu(r^*) = Nc^*(r^*)$, and to find the function $\mu(r^*)$ that gives a maximum of η is a problem of variational calculus. We shall deal with this question first by looking for the function $\mu(r^*)$ that yields a minimum of L_y^* (i.e., a maximum of η) for fixed P^*. This is the classical isoperimetric problem (see e.g. [12]) and its solution in this case can easily be found to be

$$Nc^* = 4r^* \arctan \frac{r^* P^*}{\pi U^{*2}(1-R^{*4})} \qquad (10)$$

from which we obtain

$$L_y^* = \frac{P^{*2}}{\pi U^*(1-R^{*4})} \qquad (11)$$

Equation (10) gives the optimum chord distribution for a given power coefficient, P^*. (This will be referred to hereafter as blade shape A.) From equation (11), we obtain the expression of the function $\eta = f(P^*)$ giving the maximum efficiency for each value of P^*. Then, by setting $f'(P^*) = 0$, we find the optimum value of P^*

$$P_{op}^* = \pi U^{*2}(1-R^{*2})\left[\frac{K}{2}(1+R^{*2})\right]^{1/2} \qquad (12)$$

Table 1 Highest efficiency conditions for several blade shapes

	S	$\bar{P}_{op}^*$	$(\eta_{av})_{max}$
Shape A	0.212	0.0118	0.908
c/r = const	0.216	0.0116	0.906
Shape B	0.212	0.0110	0.901
c = const	0.208	0.0108	0.901

which turns out to give $L_x^* = L_y^*$, and finally yields the following expression for the maximum value, η_{max}, of the efficiency η, for fixed R^*, U^*, and K

$$\eta_{max} = \left[1 + U^*\left(\frac{2K}{1+R^{*2}}\right)^{1/2}\right]^{-1} \qquad (13)$$

The time-averaged efficiency, η_{av}, in oscillating flow, is plotted in Fig. 2 versus the loss coefficient K, for $R^* = 0.5$, $U_o^* = 0.134$, and several values of $\bar{P}^* = P_o^*/2$ (or of the solidity S, i.e. total blade area divided by annular area), it being assumed that the radial distribution of the chord satisfies equation (10) for each value of P_o^* (blade shape A). In the same figure, the solid line represents the maximum time-averaged efficiency, $(\eta_{av})_{max}$, as given by equations (13) and (9), and may be considered as the envelope of the curves for each value of P_o^*.

It is to be noted that the power coefficient, P_{op}^*, for maximum efficiency, increases with K (see equation (12)), and also that it is $(\eta_{av})_{max} = 1$ for $K = 0$, but the latter condition implies vanishingly small values of P^* and S.

Equations (10–13) define the blade shape and solidity, and the turbine performance, for fixed R^*, U^*, and K, if maximizing the efficiency is the dominating design condition. It is of interest to know how the efficiency is affected if other blade shapes are chosen instead, which may be more convenient from other points of view, namely manufacturing and blade stresses. It can easily be found that, instead of equation (13), we have

$$\eta_{max} = \left[1 + \frac{3}{2} U^* \sqrt{K} \frac{1-R^{*2}}{1-R^{*3}}\right]^{-1}$$

for c/r = constant (constant chord-to-pitch ratio), and

$$\eta_{max} = \left[1 + 2U^*\left(\frac{K}{2}\frac{\ln R^*}{R^{*2}-1}\right)^{1/2}\right]^{-1}$$

for constant blade work, E (which will be referred to as shape B and gives c increasing with r). Table 1 compares these cases, and also the turbine with constant blade chord, for $K = 0.5$, $U_o^* = 0.134$, and $R^* = 0.5$. The results show the maximum attainable efficiency, and the optimum power coefficient and solidity, to be only slightly affected by the blade shape. We recall that this conclusion is based on two-dimensional, blade-element inviscid flow model. More marked differences are found if three-dimensional effects and profile losses are included in the analysis, as shown in section 3.

3 Three-Dimensional Analysis

3.1 Actuator Disk Theory. The assumption of zero radial velocity, which is a condition for the validity of the two-dimensional analysis, is exact only in the special case of incompressible irrotational flow and constant blade circulation (or constant blade work). In the general case of blade circulation varying with the radius, the shed vorticity induces radial velocities which make the stream surfaces deviate from the circular cylindrical shape. In order to account for this effect, we use the well known actuator-disk flow model, which assumes the shed vorticity to be axisymmetrically distributed [13]. Moreover, we consider the shed vortex lines to have approximately the shape of semi-infinite true helical

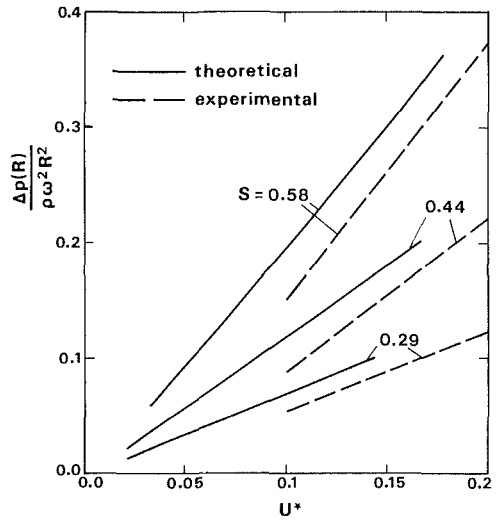

Fig. 3 Theoretical and experimental pressure drop across blade row versus inlet flow velocity

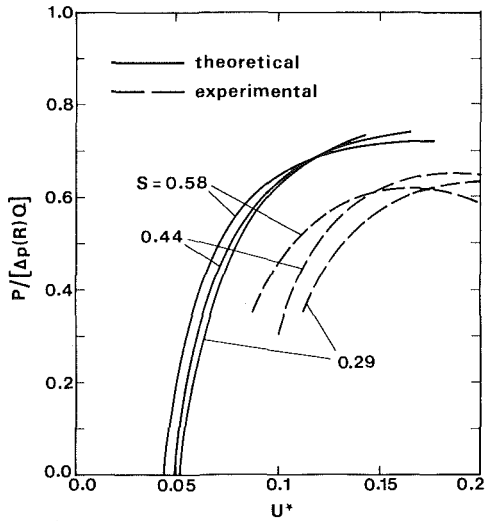

Fig. 4 Theoretical and experimental rotor efficiency versus inlet flow velocity

lines (linear actuator disk theory). This requires the radial velocity, and hence the shed vorticity, to be everywhere small, which in turn implies that the blade circulation should not be allowed to vary strongly with the radius. (We will however apply our analysis to cases when this condition is not satisfied, the consequence being that the results shall not then be expected to be fully accurate.) The actuator disk equations yield the (radially varying) axial velocity at the disk, which will then allow the flow deflection and the pressure drop to be known from two-dimensional cascade data.

We assume inviscid, incompressible, axisymmetric flow and write, for the velocity $\mathbf{V}$ (with radial, tangential and axial components V_r, V_θ, V_x),

$$\mathbf{V} = \mathbf{V}_{\pm\infty} + \mathbf{v} \text{ for } x \gtrless 0, \tag{14}$$

$\mathbf{V}_{\pm\infty}$ being the velocity far away from the blade row, at $x = \pm\infty$, where the flow is in radial equilibrium and so $V_{-\infty x} = U$ = constant, $V_{-\infty\theta} = V_{-\infty r} = V_{+\infty r} = 0$. The velocity, $\mathbf{v}$, represents the perturbation from radial equilibrium flow, and, under the assumptions above, is known to be an irrotational vector field [13].

The continuity equation, together with the tangential component of $\nabla \times \mathbf{v} = 0$, gives the following differential equation for $v_x(r, x)$

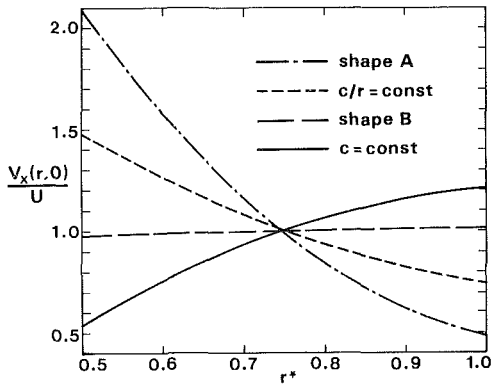

Fig. 5 Axial velocity profile at disk for several blade shapes

$$\frac{1}{r}\frac{\partial}{\partial r}\left(r\frac{\partial v_x}{\partial r}\right) + \frac{\partial^2 v_x}{\partial x^2} = 0$$

a solution of which is

$$v_x(r,x) = \pm \sum_{n=1}^{\infty} A_n e^{\mp\lambda_n x} F_n(r) \quad \text{for} \quad x \gtrless 0 \tag{15}$$

where $F_n(r) = J_0(\lambda_n r) + b_n\, Y_0(\lambda_n r)$, J_0 and Y_0 being Bessel functions. The eigenvalues λ_n, b_n ($n = 1,2, \ldots$) can be found from the boundary condition $v_r = 0$, or equivalently $F_n'(r) = 0$, for $r = R_i$ and R. The condition of continuous axial velocity across the disk yields

$$v_x(r,-0) = -v_x(r,+0) = \frac{1}{2}[V_{+\infty x}(r) - U] \tag{16a}$$

$$= -\sum_{n=1}^{\infty} A_n\, F_n(r). \tag{16b}$$

In order to solve the problem, we consider the radial component of Euler equation

$$V_r\frac{\partial V_r}{\partial r} + V_x\frac{\partial V_r}{\partial x} - \frac{V_\theta^2}{r} = -\frac{1}{\rho}\frac{\partial p}{\partial r}$$

which can be written, at the exit from the disk, $x = +0$, as

$$\frac{d}{dr}v_x(r,+0) = \frac{1}{2V_x(r,0)}\frac{V_\theta(r,+0)}{r}\frac{d}{dr}[rV_\theta(r,+0)] - \frac{1}{\rho}\frac{d}{dr}\Delta p_o \tag{17}$$

where Δp_o is the drop in stagnation pressure across the disk. A solution is then worked out iteratively as follows. We start by assuming a radial distribution for the axial velocity at the disk, $V_x\ (r,\ 0) = U + v_x\ (r,\ -0)$. From two-dimensional cascade data, we obtain Δp_o, and also the swirl velocity downstream of the cascade, which we take as the value of $V_\theta\ (r,\ +0)$. Then equation (17) allows $dv_x\ (r,\ +0)/dr$ to be known as a function of r. The coefficients A_n can now be computed by taking into account that

$$\frac{d}{dr}v_x(r,+0) = -\sum_{n=1}^{\infty} A_n\, \lambda_n[J_1(\lambda_n r) + b_n\, Y_1(\lambda_n r)]$$

and using the orthogonality properties of the Bessel functions. So, from equation (16*b*), we obtain the new value of $V_x(r, 0)$ which completes the iterative cycle.

3.2 Numerical Results. Figures 3 and 4 show a comparison between results from our actuator disk analysis and experimental data obtained by Raghunathan and Tan [6] for a turbine with $R = 0.1$ m, $R^* = 0.62$ and blade chord in-

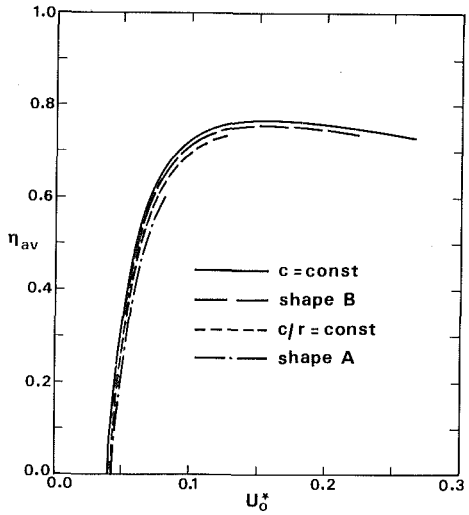

Fig. 6 Time-averaged turbine efficiency in oscillating flow versus inlet velocity amplitude, for several blade shapes

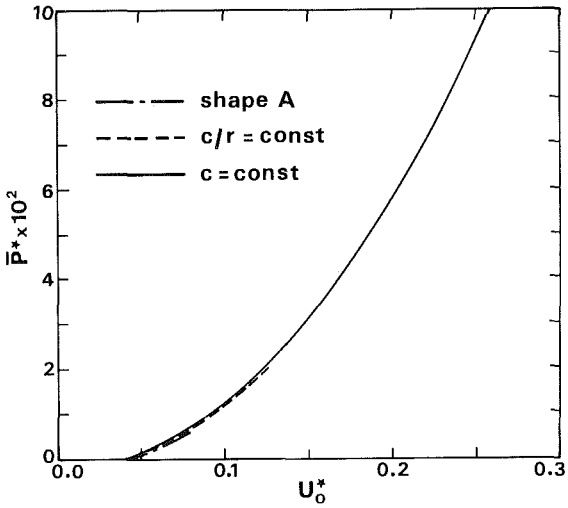

Fig. 7 Time-averaged power output in oscillating flow versus inlet velocity amplitude for several blade shapes

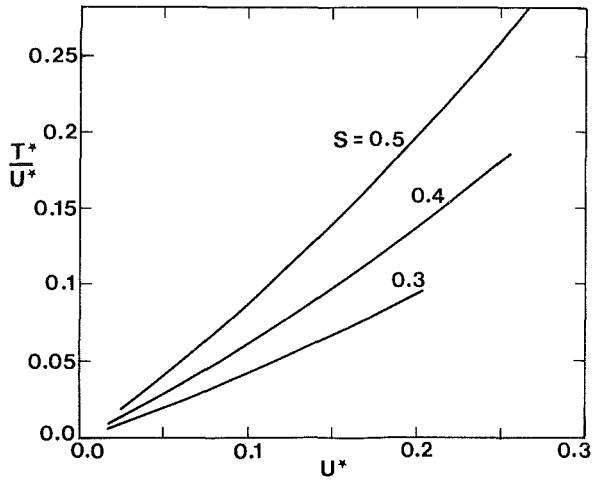

Fig. 8 Dimensionless plot of overall pressure drop across the turbine versus flow rate, for constant-chord blades

dependent of radius. The experiments were performed with blade profile NACA 0021 at Reynolds number of about 2.3×10^5 (based on relative velocity at blade tip). The values of c_{Lo} and c_D for the calculations were taken from [8], for NACA 0018 (since no available data were found for NACA 0021 at such low Reynolds numbers). Figure 3 represents the variation of the static pressure drop across the blade row (or disk), $\Delta p(R)$, measured or calculated at the outer wall, versus inlet flow velocity. Figure 4 shows a plot of the efficiency, defined here as $P/[\Delta p(R)Q]$ (i.e., ignoring exit losses). In both figures, each theoretical curve ends at the value of U^* for which the maximum value of $\beta_m(r)$ equals about 11 deg; this value, for the corresponding Reynolds number and isolated aerofoil, is the highest angle of incidence for stall-free conditions (see [8]). The discrepances between theoretical and experimental results are possibly due, in part, to joint effects of the following factors.

(*a*) Annular-wall boundary layers, blade-tip clearance and mechanical losses (all of which are believed to affect significantly the performance of a small turbine) are not accounted for by the theory.

(*b*) The theoretical calculations were based on c_D and c_{Lo} data for NACA 0018 instead of 0021. (For $\mathrm{Re} \sim 2 \times 10^5$, c_{Lo} is known to decrease with increasing relative thickness, see [8].) In addition, we mention again that no attempt was made in the analysis to correct the drag coefficient for cascade interference effects.

The results plotted in Figs. 5–8 were based on aerofoil data from [8] for NACA 0018 and $\mathrm{Re} \sim 10^7$ (considered representative of a full-scale industrial turbine), and computed for $R^* = 0.5$, $K = 0.5$. Figures 5–7 illustrate the effect of blade shape upon turbine performance, for constant solidity, $S = 0.5$. Figure 5 shows the radial distribution of the axial velocity component at the disk. Blades of shape A (defined as in section 2.2) and, less strongly, of c/r = const, induce a distortion in axial velocity profile that tends to aggravate the appearance of blade stall at the hub (in comparison with what should be expected from two-dimensional analysis), whereas constant-chord blades perform favorably in this respect. This effect is clearly illustrated in Fig. 6, where the efficiency curves for different blades shapes terminate at different values of U_o^* (which are taken as the limit of stall-free conditions and are those for which the maximum value of $\beta_m(r)$ equals 16 deg).

Figure 6 shows a plot of the time-averaged efficiency, η_{av}, for sinusoidally varying flow rate, versus (dimensionless) amplitude of the inlet flow velocity. Here, we define, as before, $\eta_{av} = \bar{P}/\bar{T}$, where now it is

$$T = 2\pi \int_{R_i}^{R} V_x(r,0)\left[\Delta p(r) + \frac{K\rho}{2} V_x^2(r,0)\right] r\, dr$$

A similar plot is given in Fig. 7 for the time-averaged power output. It is interesting to notice that the positions of the various blade shapes, on what concerns efficiency, as shown in Fig. 6, are inverted in comparison with the results of Table 1, where three-dimensional effects and profile losses are not accounted for.

The Wells turbine has often been referred to as satisfying a relationship of proportionality between flow rate and overall pressure difference (or gross available energy per unit mass of fluid). Figure 8 shows this to be only approximately true.

4 Conclusions

The results of the theoretical analysis show that fairly high values of the mean efficiency, of the order of 70–80 percent, are expected to be attainable in reciprocating flow with properly designed Wells turbines.

Three-dimensional flow effects, which were ignored in previous analyses, are found to be large, depending strongly on blade shape, and to be especially important in connection with the extent of the stall-free conditions. Except for blades

which do not differ much from shape B (constant-circulation blades), the present actuator-disk linear analysis is believed to be unable to give an accurate representation of the flow field. This will require a nonlinear, three-dimensional theory.

Finally, we mention that the presently available experimental data concerning tandem cascades of blades are not sufficient as a basis for an accurate prediction of the performance, and a reliable design, of full-scale Wells turbines. Steps towards improving this situation are desirable.

Acknowledgment

The authors wish to thank CTAMFUTL/INIC, Lisbon, for the support of this research.

References

1 Sturge, D. P., "Turbine for an Oscillating Water Column Wave Power System," CEGB Report No. MM/MECH TA 41, 1977.

2 Grant, R. J., Johnson, C. G., and Sturge, D. P., "Performance of a Wells Turbine for Use in a Wave Energy System," *Future Energy Concepts*, IEE Publication No. 192, 1981.

3 Raghunathan, S., Tan, C. P., and Wells, N. A., J., "Theory and Performance of a Wells Turbine," *Journal of Energy*, Vol. 6, No. 2, 1982, pp. 157–160.

4 Grant, R. J., and Johnson, C. G., "Performance Tests on a Single Stage Wells Turbine," CEGB Report No. MM/MECH TF 207, 1979.

5 Raghunathan, S., and Tan, C. P., "Performance of the Wells Turbine at Starting," *Journal of Energy*, Vol. 6, No. 6, 1982, pp. 430–431.

6 Raghunathan, S., and Tan, C. P., "Aerodynamic Performance of a Wells Air Turbine," *Journal of Energy*, Vol. 7, No. 3, 1983, pp. 226–230.

7 Raghunathan, S., Tan, C. P., and Wells, N. A. J., "Wind Tunnel Tests on Airfoils in Tandem Cascade," *AIAA Journal*, Vol. 19, No. 11, 1981, pp. 1490–1492.

8 Jacobs, E. N., and Sherman, A., "Airfoil Section Characteristics as Affected by Variations of the Reynolds Number," NACA Report No. 586, 1937.

9 von Kármán, T., and Burgers, J. M., *Aerodynamic Theory*, Vol. 2, edited by W. F. Durand, Springer, Berlin, 1935.

10 Weinig, F. S., *Aerodynamics of Turbines and Compressors,"* edited by W. R. Hawthorne, Oxford University Press, London, 1964.

11 Scholz, N., "Aerodynamics of Cascades," AGARD-AG-220, 1977.

12 Smirnov, V. I., *A Course of Higher Mathematics*, Vol. 4, Pergamon Press, Oxford, 1964.

13 Hawthorne, W. R., and Horlock, J. H., "Actuator Disc Theory of the Incompressible Flow in Axial Compressors," *Proceedings of the Institution of Mechanical Engineers*, Vol. 176, No. 30, 1962, pp. 789–814.

Spray Characteristics of Plain-Jet Airblast Atomizers

N. K. Rizk
Visiting Professor.

A. H. Lefebvre
Reilly Professor of Combustion Engineering.

The Combustion Laboratory,
Thermal Sciences and Propulsion Center,
School of Mechanical Engineering,
Purdue University,
West Lafayette, Ind. 47907

The effects of air and liquid properties and atomizer dimensions on the spray characteristics of plain-jet airblast atomizers are examined. Mean drop size and drop-size distribution are measured using an improved form of light scattering technique. The test range includes wide variations in air velocity, air pressure, air/liquid ratio, and liquid viscosity. The experimental data generally confirm the results of previous studies on prefilming types of airblast atomizers. They show that increases in air velocity, air pressure, and air/liquid ratio all tend to produce a more uniform spray and a lower mean drop size. It is also observed that any change in air properties, liquid properties, and atomizer geometry that lowers the mean drop size also produces a more uniform distribution of drop sizes in the spray.

Introduction

The merits of the airblast atomizer have led to its installation in a wide range of industrial and aircraft gas turbines. Most of the systems now in service are of the "prefilming" type, in which the fuel is first spread out into a thin, continuous sheet and then subjected to the atomizing action of high velocity air. In other designs, the fuel is injected into the high-velocity airstream in the form of one or more discrete jets. A drawback to the thin-sheet airblast atomizer is that it is fully effective only when both sides of the liquid sheet are exposed to the air. This requirement introduces a complication in design, since it usually means arranging for two separate air flows through the atomizer. For this reason, the plain-jet type of airblast atomizer, in which the fuel is not transformed into a thin sheet, but instead is injected into the high-velocity airstream in the form of discrete jets, is sometimes preferred. Much less is known about the performance of this type of atomizer, since the only previous investigations of significance are those of Nukiyama and Tanasawa [1], Weiss and Worsham [2], Gretzinger and Marshall [3], Kim and Marshall [4], Lorenzetto and Lefebvre [5], and Jasuja [6]. Although these studies did much to elucidate the key factors involved in plain-jet airblast atomization, the range of variables studied was incomplete. For example, almost all the experiments were conducted at normal atmospheric pressure. Jasuja's test program included measurements at higher levels of pressure, but no attempt was made to determine the distribution of drop sizes in the sprays.

The present investigation represents an attempt to remedy these deficiencies. In common with previous studies, it covers fairly wide ranges of atomizing air velocity, fuel viscosity, air/fuel ratio, and atomizer size. However, attention is focused on the effects of ambient pressure on mean drop size and drop-size distribution. Considerable importance is attached to the latter effect, since it is the drop-size distribution in a spray that determines its evaporation history. For example, sprays with a nonuniform drop-size distribution evaporate more rapidly in the initial phase than do uniform sprays of the same mean diameter [7, 8], due to the presence of a larger number of small drops. For gas turbine combustors, therefore, a nonuniform spray has definite advantages in terms of wider burning limits and better ignition performance, especially at high altitudes where failure to relight is often due to an inadequate supply of fuel vapor in the spark zone. However, a nonuniform spray necessarily contains some larger drops [9] which take longer to evaporate. If the residence time in the combustion zone is insufficient to ensure complete evaporation and combustion of these large drops, they will lower the level of combustion efficiency and raise the concentrations of carbon monoxide and unburned hydrocarbons in the exhaust gases. Another interesting feature of the evaporation history of fuel sprays is that the drop-size distribution changes during evaporation in such a way that the mean diameter of the remaining drops increases for moderately or highly nonuniform sprays and decreases for more uniform sprays. This is again due to the existence of more small drops in the former case. From these and other considerations, it is clearly of practical importance to acquire more knowledge on the drop-size distribution of sprays and the manner and extent to which the drop-size distributions obtained with airblast atomizers are influenced by air properties, liquid properties, and atomizer design features.

Experimental

The liquids selected for this study are:

Aviation kerosine: $\mu = 0.00129$ kg/(ms), $\sigma = 0.0275$ kg/s^2, $\rho = 780$ kg/m^3

Gas oil: $\mu = 0.003$ kg/(ms), $\sigma = 0.0281$ kg/s^2, $\rho = 810$ kg/m^3

Blended fuel: $\mu = 0.0183$ kg/(ms), $\sigma = 0.0285$ kg/s^2, $\rho = 840$ kg/m^3

A cross-sectional schematic drawing of the plain-jet

Contributed by the Gas Turbine Division of THE AMERICAN SOCIETY OF MECHANICAL ENGINEERS and presented at the 28th International Gas Turbine Conference and Exhibit, Phoenix, Arizona, March 27-31, 1983. Manuscript received at ASME Headquarters July 11, 1983. Paper No. 83-GT-138.

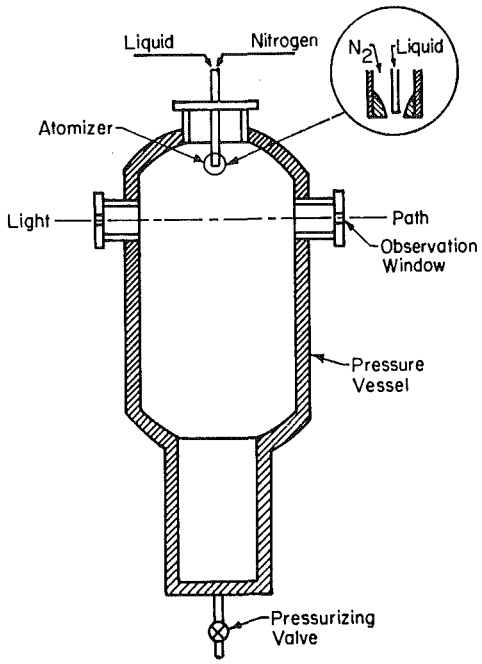

Fig. 1 Schematic diagram of test rig

atomizer is shown in Fig. 1. Essentially, it comprises a means for producing a round jet of liquid and surrounding this jet by a coaxial, coflowing stream of high-velocity air. The apparatus for studying spray characteristics is also shown schematically in this figure. The main component is a cylindrical pressure vessel which is mounted on a stand with its axis in the vertical position and it is 120 cm long and 75 cm in diameter. The atomizer under test is located centrally at the top of the cylinder and sprays downward into the vessel which is pressurized to the desired level using gaseous nitrogen that is tapped from a large liquid nitrogen storage/evaporator system. Gaseous nitrogen from this same source also provides the atomizing "air" for airblast atomizers. The reason for using nitrogen instead of air is to avoid the risk of explosion at high pressures. As the physical properties of nitrogen are very similar to those of air, the results obtained with nitrogen are considered valid for systems using air.

After atomization, a gentle downdraft of nitrogen conveys the droplets downward into a collection tank at the bottom of the chamber, from whence the liquid is returned to the storage tank. Any fuel that is entrained into the nitrogen flowing out of the test chamber is also separated out and returned to the storage tank. The objective is partly to conserve fuel, especially those fuels of which only a limited supply is available, and also to avoid any pollution problems created by the escape of droplets or mists into the atmosphere.

Drop sizes are measured using the light-scattering technique first proposed by Dobbins, Crocco, and Glassman [10] and later developed at Cranfield [5]. It is based on a direct measurement of the scattered light intensity profile

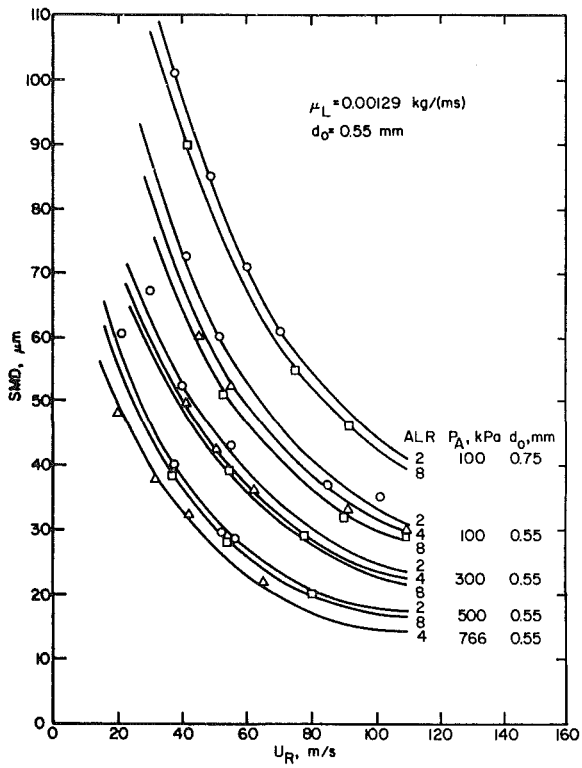

Fig. 2 Variation of mean drop size with air pressure, air/liquid ratio, and fuel nozzle diameter, for a low viscosity liquid

after the monochromatic light beam has passed through the spray. The SMD is obtained directly from measurement of intensity versus radius in the focal plane of the receiving lens. In practice, this is accomplished by measuring the traverse distance (r) between the optical axis and a point on the profile at which the light intensity is equal to 1/10 of the normalized intensity in the scattered profile. The SMD of the spray can then be determined using the relationship between r and SMD as derived by Roberts and Webb [11]. Recently, Rizk and Lefebvre [17] have used the method advocated by Swithenbank et al. [13] to extend the light-scattering technique to include measurements or drop-size distribution.

Tests were conducted using two geometrically similar atomizers, having fuel nozzle diameters of 0.55 mm and 0.75 mm, over the following ranges of test conditions.

Atomizing "air" velocity	10 to 120 m/s
Ambient "air" pressure	100 to 766 kPa
Air/liquid ratio	2 to 8
Fuel viscosity	0.0013 to 0.0183 kg/ms

Mean Drop Size

At the outset of the investigation, it was anticipated that the effects of air and liquid properties on mean drop size would be very similar to previous findings in regard to general trends

Nomenclature

A,B = constants in equations (1) and (2)
ALR = air/liquid ratio by mass
d_o = fuel nozzle diameter
L = atomizer dimension in equation (11)
L_c = characteristic dimension of atomizer
P = pressure
q = drop-size distribution parameter
SMD = Sauter mean diameter of drops in spray
U = velocity
v = volume (or mass) fraction of spray in drops of diameter less than x
x = drop diameter
$\bar{x}$ = drop-size parameter
μ = liquid dynamic viscosity
ρ = liquid density
σ = surface tension

Subscripts

A = air
L = liquid
R = relative, air to fuel

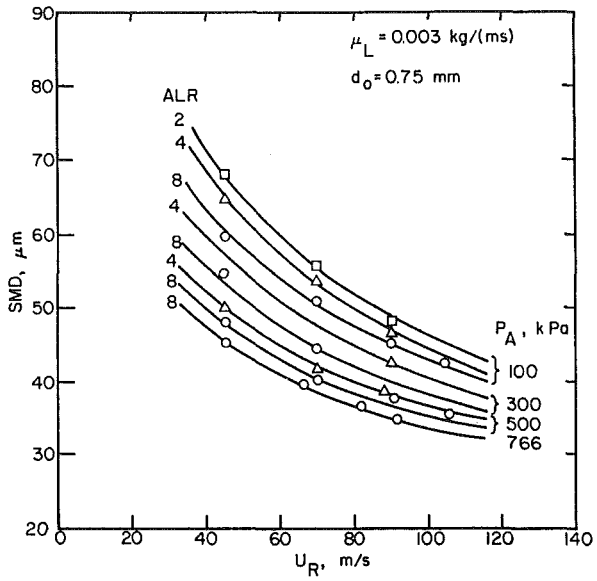

Fig. 3 Variation of mean drop size with air pressure and air/liquid ratio for a medium viscosity liquid

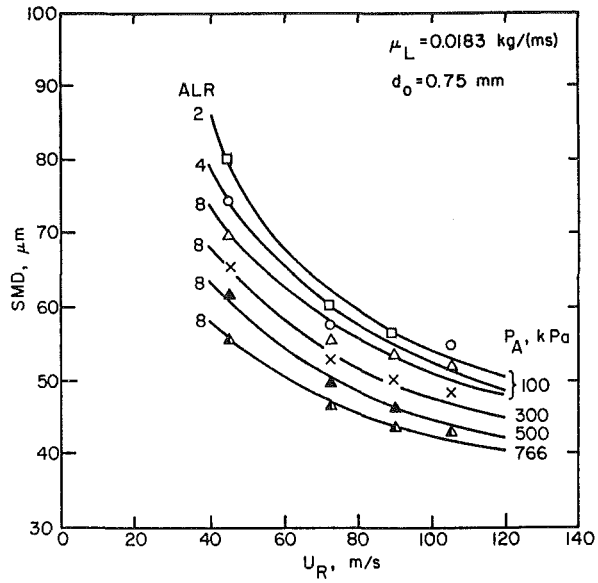

Fig. 4 Variation of mean drop size with air pressure and air/liquid ratio for a high viscosity liquid

[1-6, 9, 12, 14], and this was confirmed by the experimental data. Some typical results are shown plotted in Figs. 2-5. Figure 2 illustrates the effects of air velocity, air/liquid ratio, air pressure, and atomizer dimensions on mean drop size. Similar data for liquids of higher viscosity are given in Figs. 3 and 4. These data show that SMD increases with increase in liquid viscosity and/or atomizer size and decreases with increase in air/liquid ratio. SMD diminishes rapidly with increase in air velocity, according to the relationship SMD α $U_R^{-0.8}$. The influence of air pressure on SMD is less marked, in fact, SMD α $P_A^{-0.4}$. This relationship between SMD and P_A is illustrated more directly in Fig. 5.

It has been shown elsewhere [14] that the basic drop-size equation for airblast atomizers is

$$\frac{\text{SMD}}{L_c} = A\left(\frac{\sigma}{\rho_A U_A^2 L}\right)^{0.5}\left(1+\frac{1}{\text{ALR}}\right) + B\left(\frac{\mu_L^2}{\sigma\rho_L L}\right)^{0.5}\left(1+\frac{1}{\text{ALR}}\right) \quad (1)$$

where A and B are constants whose values depend on atomizer design features and must be determined experimentally. L_c is a characteristic dimension that represents the scale of the atomizer. The term L represents the atomizer dimension at the point or surface where the liquid first contacts the air stream. For prefilming airblast atomizers $L=D_p$, the prefilmer lip diameter. For plain-jet atomizers $L=d_o$, which is also appropriate for the characteristic dimension, L_c. Substituting in equation (1) for $L=L_c=d_o$, gives

$$\frac{\text{SMD}}{d_o} = A\left(\frac{\sigma}{\rho_A U_A^2 d_o}\right)^{0.5}\left(1+\frac{1}{\text{ALR}}\right) + B\left(\frac{\mu_L^2}{\sigma\rho_L d_o}\right)^{0.5}\left(1+\frac{1}{\text{ALR}}\right) \quad (2)$$

In practice, some secondary factors, such as liquid-stream Reynolds number and airstream Mach number, affect the atomization process in a manner that is not yet fully understood. Thus, it is found that the ability of equation (2) to correlate SMD can be improved by reducing the exponent of the term $\sigma/\rho_A U_A^2 d_o$ from 0.5 to 0.4. Also, if relative velocity, U_R, is substituted for air velocity, U_A, then the diminished influence of air/liquid ratio on SMD should be accounted for by reducing the exponent of the term

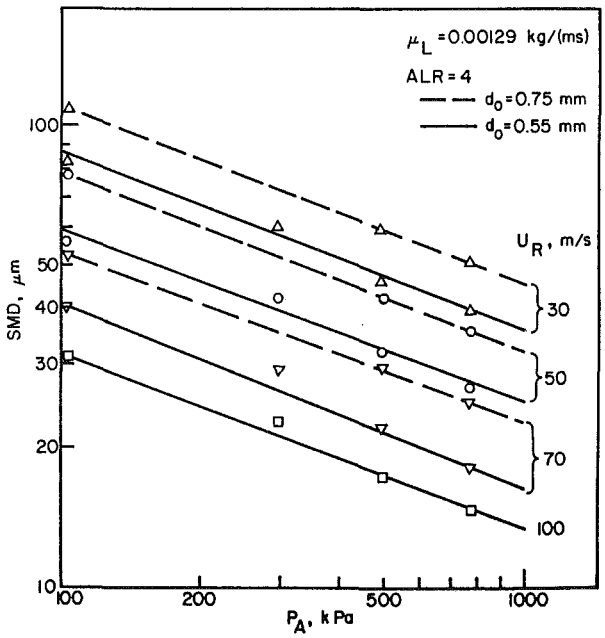

Fig. 5 Graphs illustrating the effect of ambient air pressure on mean drop size

(1 + 1/ALR). These considerations lead to the following modified form of equation (2), which now includes the experimentally determined values of A and B

$$\frac{\text{SMD}}{d_o} = 0.48\left(\frac{\sigma}{\rho_A U_R^2 d_o}\right)^{0.4}\left(1+\frac{1}{\text{ALR}}\right)^{0.4} + 0.15\left(\frac{\mu_L^2}{\sigma\rho_L d_o}\right)^{0.5}\left(1+\frac{1}{\text{ALR}}\right) \quad (3)$$

The ability of equation (3) to correlate the values of SMD obtained experimentally is illustrated for low-viscosity liquids in Fig. 6 and for high viscosity liquids in Fig. 7. An excellent correlation is demonstrated for low viscosity liquids. For liquids of high viscosity, the correlation is inferior but still quite satisfactory. Comparison with the results obtained by other workers is hindered by the different methods adopted for presenting the data. However, a comparison is possible

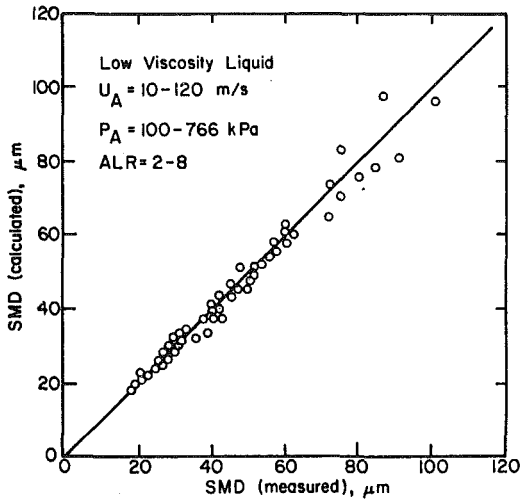

Fig. 6 Comparison of calculated and experimental values of mean drop size for low viscosity liquids

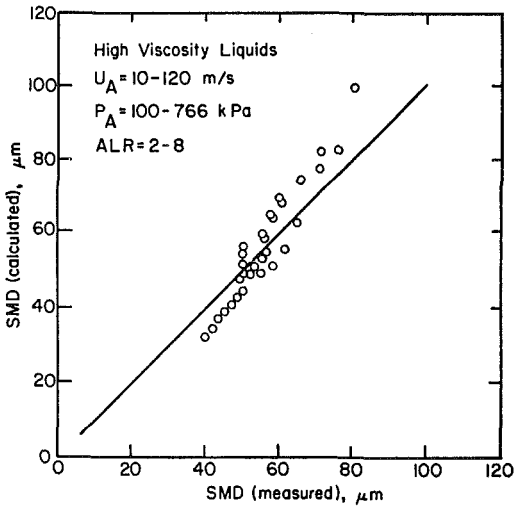

Fig. 7 Comparison of calculated and experimental values of mean drop size for high viscosity liquids

Table 1 Summary of data on effect of variables on mean drop size for liquids of low viscosity

Investigators	Power dependence of mean drop size on			
	Air velocity U_A	Air density ρ_A	Surface tension σ	Dimension d_o
Nukiyama and Tanasawa [1]	−1.0	0	0.5	0
Weiss and Worsham [2]	−1.33	−0.30	–	0.16
Gretzinger and Marshall [3]	−0.40	−0.40	0	–
Kim and Marshall [4]	−1.14	−0.57	0.41	–
Lorenzetto and Lefebvre [5]	−1.00	−0.30	0.33	0
Jasuja [6]	−0.90	−0.45	0.45	0.55
Ingebo [16] Theoretical	−0.67	−0.33	0.17	0.5
Experimental	−0.75	−0.25	0.25	0.5
Present Study	−0.80	−0.40	0.40	0.60

for liquids of low viscosity, as illustrated in Table 1. The values of the exponents for air pressure, air velocity, surface tension, and liquid viscosity listed in this Table show appreciable differences, as might be expected in view of the

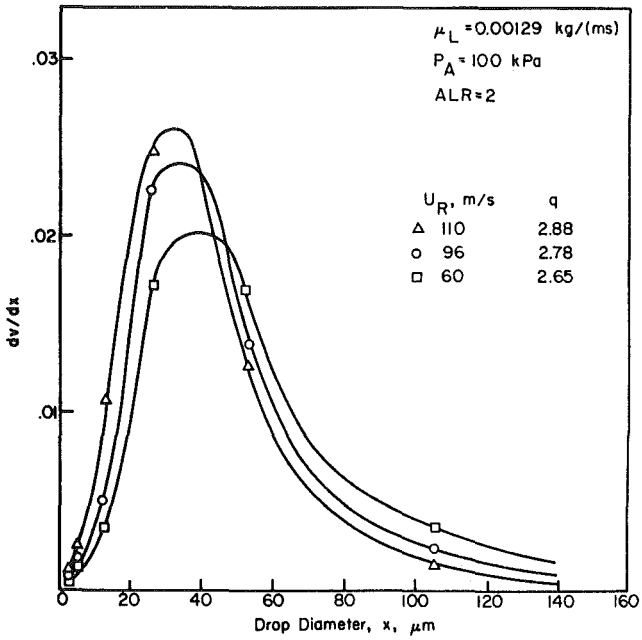

Fig. 8 Influence of air velocity on drop-size distribution

different types of atomizer represented and the different methods used to measure mean drop size. However, there is a close similarity between the results of Jasuja [6] and those obtained in the present study. To some extent, this may be due to the fact that both investigations employed the same light-scattering method for the measurement of mean drop size.

Drop-Size Distribution

One of the most fundamental and important properties of a liquid spray is the frequency of occurrence of the various sizes of droplets, or the drop-size distribution in the spray. It is also the property that is most difficult to predict theoretically and to determine experimentally. This is why so little information on drop-size distribution is available in the literature.

Several mathematical expressions have been derived to represent drop-size distribution. Usually they contain two independent parameters, one of which is a mean diameter of some kind and the other is a measure of the dispersion of the spray, or the deviation from the mean. The Rosin-Rammler expression [15] is perhaps the most widely used at the present time. Although developed originally for powders, it has been applied with success to liquid drops. It can be expressed in the form

$$1 - v = \exp - (x/\tilde{x})^q$$

where v is the volume fraction of the spray occurring in drops of diameter less than x, $\tilde{x}$ is a size parameter, and q is a distribution parameter. The higher the value of q, the more uniform is the spray. Values of q were determined over the entire range of test conditions. Some typical results are shown in Figs. 8 and 9.

The beneficial effect of increasing relative velocity at a constant air/liquid ratio from 60 to 96 m/s, and then to 110 m/s, is shown in Fig. 8. The number of large drops in the spray diminishes rapidly with increase in air velocity. Figure 9 illustrates a significant shift in distribution toward lower drop sizes with reduction in d_o. In general, the results obtained on the influence of air and liquid properties on drop-size distribution in the present investigation, using a plain-jet airblast atomizer, are fully consistent with those obtained in a recent study conducted on a prefilming type of airblast atomizer [12]. Thus, it is found that any change in liquid

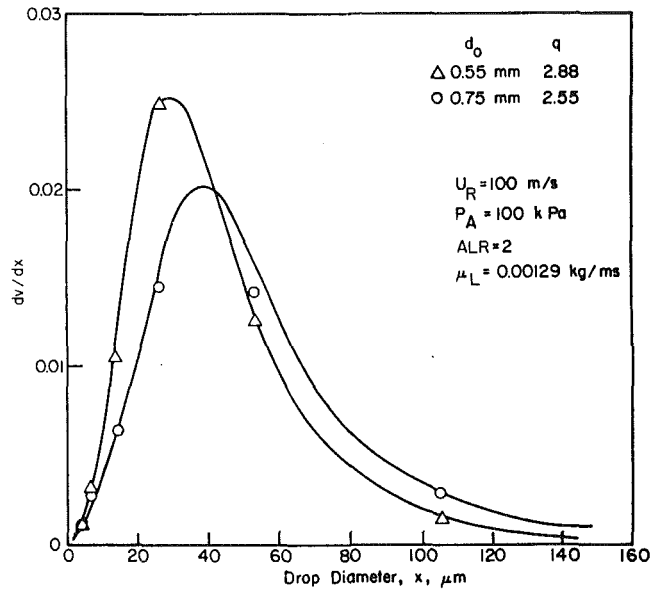

Fig. 9 Influence of liquid nozzle diameter on drop-size distribution

properties, air properties, atomizer geometry, and atomizer size that tends to produce a finer spray will also yield a higher value of q, i.e., a more uniform spray. This point is clearly brought out in Fig. 10, which shows that increases in air pressure, air velocity, and air/liquid ratio all produce a more uniform drop size. However, increases in fuel viscosity and fuel nozzle diameter both result in coarser sprays.

Conclusions

From a series of measurements carried out on a coaxial, coflowing, plain-jet airblast atomizer, it is found that the effects of the main air and liquid properties on mean drop size follow closely the trends observed previously with prefilming airblast atomizers, although the exponents of air pressure and velocity are slightly lower for the plain-jet type.

The experimental data collected in this study are correlated with good accuracy by the dimensionally correct equation.

$$\frac{\text{SMD}}{d_o} = 0.48\left(\frac{\sigma}{\rho_A U_R{}^2 d_o}\right)^{0.4}\left(1+\frac{1}{\text{ALR}}\right)^{0.4} + 0.15\left(\frac{\mu_L{}^2}{\sigma\rho_L d_o}\right)^{0.5}\left(1+\frac{1}{\text{ALR}}\right)$$

The results also confirm previous findings for prefilming airblast atomizers in regard to the effects of air and liquid properties on drop-size distribution. The measurements show that any change in atomizer geometry, liquid properties, or operating conditions that reduces the mean drop diameter will also increase the uniformity of drop sizes in the spray.

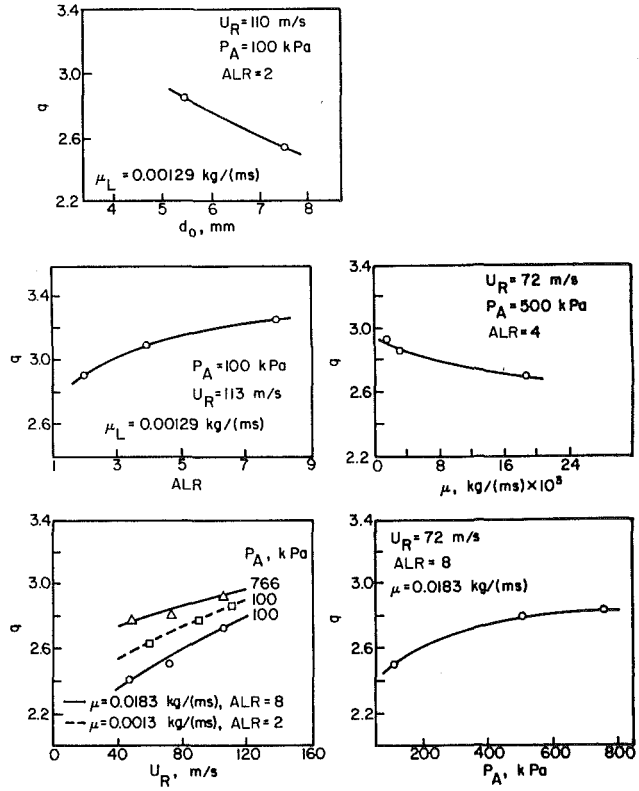

Fig. 10 Influence of liquid nozzle diameter, liquid viscosity, air pressure, air velocity and air/liquid ratio on drop-size distribution parameter, q

References

1 Nukiyama, S., and Tanasawa, Y., "Experiments on Atomization of Liquids," *JSME*, 6 parts, English translation by the Department of National Defence, Canada, 1950, pp. 1938–40.

2 Weiss, M. A., and Worsham, C. H., "Atomization in High-Velocity Airstreams," *ARS Journal*, Vol. 29, No. 4, 1959, pp. 252–259.

3 Gretzinger, J., and Marshall, W. R., "Characteristics of Pneumatic Atomization," *AIChE Journal*, Vol. 7, No. 2, June 1961, pp. 312–318.

4 Kim, K. Y., and Marshall, W. R., "Drop-Size Distributions from Pneumatic Atomizers," *AIChE Journal*, Vol. 17, No. 3, 1971, pp. 575–584.

5 Lorenzetto, G. E., and Lefebvre, A. H., "Measurements of Drop Size on a Plain-Jet Airblast Atomizer," *AIAA Journal*, Vol. 15, No. 7, July 1977, pp. 1005–1010.

6 Jasuja, A. K., "Plain-Jet Airblast Atomization of Alternative Liquid Petroleum Fuels Under High Ambient Air Pressure Conditions," ASME Paper No. 82-GT-32, 1982.

7 Dickinson, D. R., and Marshall, W. R., "The Rates of Evaporation of Sprays," *AIChE*, Vol. 14, No. 4, July 1968, p. 541.

8 Chin, J. S., Durrett, R., and Lefebvre, A. H., "The Interdependence of Spray Characteristics and Evaporation History of Fuel Sprays in Stagnant Air," *to be published*.

9 Simmons, H. C., "The Correlation of Drop-Size Distribution in Fuel Nozzle Sprays," ASME JOURNAL OF ENGINEERING FOR POWER, Vol. 99, No. 3, July 1977, pp. 309–319.

10 Dobbins, R. A., Crocco, L., and Glassman, I., "Measurement of Mean Particle Sizes of Sprays from Diffractively Scattered Light," *AIAA Journal*, Vol. 1, No. 8, 1963, pp. 1882–1886.

11 Roberts, J. M., and Webb, M. J., "Measurement of Droplet Size for Wide Range Particle Distribution," *AIAA Journal*, Vol. 2, No. 3, 1964, pp. 583–585.

12 Rizk, N. K., and Lefebvre, A. H., "Influence of Airblast Atomizer Design Features on Mean Drop Size," presented at AIAA/SAE/ASME 18th Joint Propulsion Conference, Cleveland, Ohio, June 1982.

13 Swithenbank, J., Beer, J. M., Abbott, D., and McCreath, C. G., "A Laser Diagnostic Technique for the Measurement of Droplet and Particle Size Distribution," AIAA Paper No. 76-69, 14th Aerospace Sciences Meeting, Washington, D.C., Jan. 26–28, 1976.

14 Lefebvre, A. H., "Airblast Atomization," *Prog. Energy Combust. Sci.*, Vol. 6, 1980, pp. 233–261.

15 Rosin, P., and Rammler, E., "The Laws Governing the Fineness of Powdered Coal," *Journal of the Institute of Fuel*, Vol. 7, No. 31, October 1933, pp. 29–36.

16 Ingebo, R. D., "Capillary and Acceleration Wave Breakup of Liquid Jets in Axial-Flow Airstreams," NASA Technical Paper No. 1791, 1981.

17 Rizk, N. K., and Lefebvre, A. H., "Measurement of Drop-Size Distribution by a Light-Scattering Technique," presented at Symposium on Liquid Particle Size Measurement Techniques, June 23–24, 1983, Kansas City, Mo.

The Interdependence of Spray Characteristics and Evaporation History of Fuel Sprays

J. S. Chin
Visiting Professor.

R. Durrett
Graduate Student.

A. H. Lefebvre
Reilly Professor of Combustion Engineering.

The Combustion Laboratory,
Thermal Sciences and Propulsion Center,
School of Mechanical Engineering,
Purdue University,
West Lafayette, Ind. 47907

Previously developed calculation procedures [1, 2] based on evaporation analysis are used to predict the variation of JP-5 fuel spray characteristics (mean drop diameter, D_m, and drop-size distribution parameter, n) with time during evaporation in hot air. The method takes full account of transient effects occurring during the heat-up period. The results show that both D_m and n increase with time, but the changes are more significant for sprays having small initial values of n. The time to vaporize a certain percentage of spray mass is proportional to the square of the initial mean diameter, D_{m_o}. The effect of the initial value of n, is that a spray having a larger value of n_o will reach its 90 percent evaporation point faster, but a smaller value of n_o will give a shorter 20 percent evaporation time. Based on these calculations, a general method for estimating the time required for any liquid fuel to attain any given percentage of spray mass evaporation is proposed. Although the method was developed for quiescent mixtures of fuel drops and air, it can be applied to many practical combustion devices (for example, a gas turbine combustor fitted with airblast atomizers) where it is reasonable and sufficiently accurate to assume a low relative velocity between the fuel drops and the surrounding air or gas.

Introduction

In two previous papers [1, 2] calculation procedures were developed for estimating the steady-state value of evaporation constant and the length of the heat-up period of fuel drop evaporation, and the proposed methods were used to evaluate these properties for a number of commercial engine fuels. In a subsequent publication [3], these methods were extended to cover a wide range of liquid hydrocarbon fuels. By introducing the concept of an "effective" evaporation constant which takes full account of the effects of convection and the heat-up period on overall evaporation rates, the estimation of drop lifetimes for fuel drops evaporating under various conditions of fuel type, ambient pressure and temperature, and initial drop size, was made quite straightforward [3]. However, although the evaporation characteristics of a single fuel drop provide useful guidance to the evaporation history of a complete spray, there are certain key features of an evaporating fuel spray that can only be explored by considering the spray as a whole [4, 5]. For example, from an ignition standpoint, it is the *initial* rate of evaporation that is important, whereas for high combustion efficiency the time required for complete evaportion of the fuel spray is the dominant factor. Another interesting example is provided by the lean premix/prevaporize combustor. A key feature of this concept is the attainment of complete evaporation of the fuel and complete mixing of the fuel vapor and air prior to combustion. Failure to fully vaporize the fuel results in higher NO_x emissions. It is important, therefore, to know how the fraction or percentage of fuel evaporated varies with time, so that the best compromise can be made between the conflicting requirements of minimum NO_x emissions and minimum length of premixing chamber.

It is also of interest to ascertain how the initial mean drop size (D_{m_o}), and the drop-size distribution (as defined by the Rosin-Rammler distribution parameter, n) affect the subsequent evaporation history. Rao and Lefebvre [6] conducted an experimental investigation into fuel spray evaporation under controlled conditions, but their findings shed little light on the initial rate of evaporation. Neither do they allow the fraction of fuel evaporated to be estimated for fuels other than the kerosine employed in their tests. In the present paper attention is focused on the evaporation history of JP5 fuel sprays. (The physical properties of JP5 and the other fuels investigated are provided in [1]). The results are presented in a manner which allows the time required to vaporize any given percentage of the initial spray mass to be estimated for other fuels at any stipulated conditions of ambient pressure and temperature.

It should be noted that no account is taken of the enhanced evaporation rates that occur with pressure atomizers due to the initial relative motion between the drops and the surrounding air. Since the small drops decelerate rapidly while the large drops maintain their momentum, the evaporation constant for the larger drops is higher, and this affects the evaporation history of the spryay including the change in drop-size distribution parameter. However, the results ob-

Contributed by the Gas Turbine Division of THE AMERICAN SOCIETY OF MECHANICAL ENGINEERS and presented at the 28th International Gas Turbine Conference and Exhibit, Phoenix, Arizona, March 27-31, 1983. Manuscript received at ASME Headquarters July 11, 1983. Paper No. 83-GT-7.

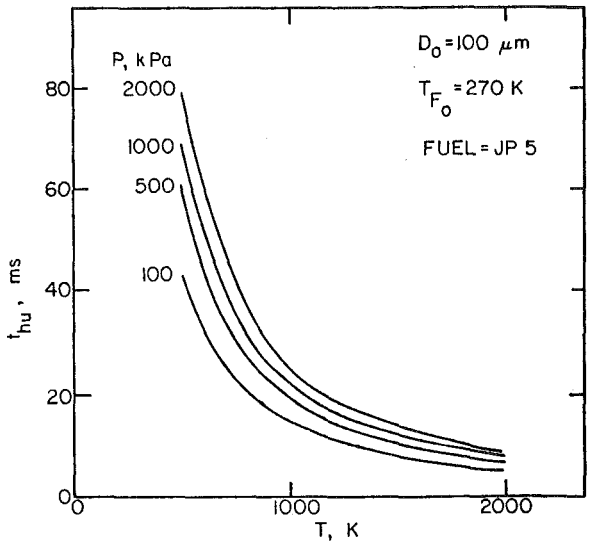

Fig. 1 Effect of ambient pressure and temperature on duration of heat-up period [2]

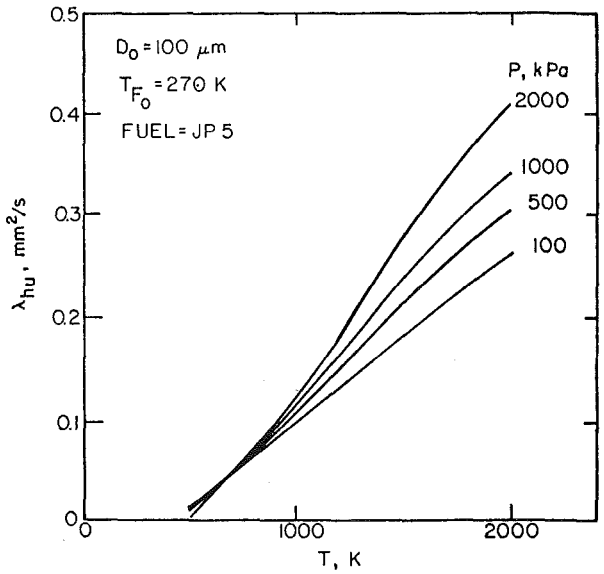

Fig. 2 Influence of ambient pressure and temperature on average evaporation constant during heat-up period [2]

tained are valid for airblast atomizers and, in fact, for all fuel injection systems that are characterized by a low relative velocity between the fuel drops and the surrounding air stream.

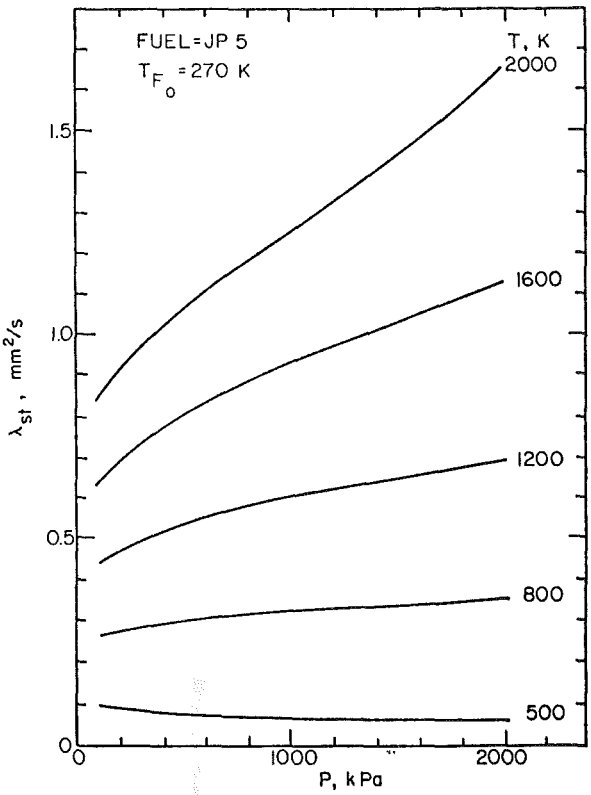

Fig. 3 Influence of ambient pressure and temperature on steady-state evaporation constant [1]

Evaporation Calculations

When a liquid spray is injected into warm air the initial rate of evaporation is quite low, and most of the heat transferred to the drop from its surroundings is used in heating up the drop. As the liquid temperature rises, the vapor concentration at the drop surface increases and a larger proportion of the heat transferred to the drop is used to supply the latent heat of vaporization. Eventually, the drop attains its wet-bulb temperature, $T_{s_{st}}$, and from then on the rate of evaporation remains constant at its steady-state value.

In [2], a simple procedure was outlined for calculating the duration of the heat-up period, t_{hu}, and the effective value of evaporation constant during this period. Figure 1, which is reproduced from [2], shows the effect of ambient pressure and temperature on the duration of the heat-up period of JP 5 fuel. It was found that t_{hu} is proportional to the square of the drop diameter. So, from Fig. 1, the heat-up period of JP 5

Nomenclature

D = drop diameter, m
D_i = mean drop diameter of group i, m
D_{it} = mean drop diameter of group i after time, Δt, m
D_m = mass (volume) mean diameter (MMD), m
D_{m_o} = initial value of D_m, m
D_o = initial drop diameter, m
ΔD = drop-size increment, m
n = Rosin Rammler drop-size distribution parameter
n_o = initial value of n
P = ambient air pressure, kPa
Q = volume fraction contained in drops of diameter less than D
Q_t = volume fraction of liquid contained in drops of diameter less than D after time, Δt
ΔQ_i = volume fraction contained in group i
ΔQ_{it} = volume fraction contained in group i after time, Δt
T = ambient air temperature, K
T_{F_o} = initial fuel temperature, K
$T_{s_{st}}$ = steady-state value of drop surface temperature, K
t = time, s
Δt = time increment, s
t_{hu} = duration of heat-up period, s
$t_{90\%}$ = time required to evaporate 90 percent of fuel spray, s
x = fraction of fuel in vapor form
λ_{hu} = effective average value of evaporation constant during heat-up period, m^2/s
λ_{st} = effective average value of evaporation constant during steady-state period, m^2/s

fuel drops can readily be determined for any given values of pressure, temperature, and drop size. The effective, average value of evaporation constant during the heat-up period, λ_{hu}, is independent of drop size [2]. Values of λ_{hu} for JP 5 at different levels of pressure and temperature are shown in Fig. 2, from [2]. Figure 3 shows the variation of λ_{st} with pressure and temperature for JP 5, from [1].

For an initial drop diameter, D_o, the change of diameter with time can be expressed by the follwing equations

(*a*) During the heat-up period

$$D^2 = D_o^2 - \lambda_{hu} t \tag{1}$$

(*b*) During steady-state evaporation

$$D^2 = D_o^2 - \lambda_{hu}\, t_{hu} - \lambda_{st}\,(t - t_{hu}) \tag{2}$$

At any time period between t and $t + \Delta t$, when

$$t < t_{hu} < (t + \Delta t)$$

the change of diameter is given by

$$\Delta(D^2) = \lambda_{hu}\,(t_{hu} - t) + \lambda_{st}\,(t + \Delta t - t_{hu}) \tag{3}$$

Drop-Size Distribution

Calculations of drop-size distribution are based on the well-known equation due to Rosin and Rammler [7]

$$Q = 1 - \exp[-0.693\,(D/D_m)^n] \tag{4}$$

where Q is the volume fraction of the spray contained in drops of diameter less than D, and D_m is the mean diameter; (for $D = D_m$, $Q = 0.5$). The exponent n provides a measure of the spread of drop sizes; the higher the value of n, the more uniform is the spray. For most practical sprays, the value of n lies between 2 and 4.

The calculation procedure for drop-size distribution is carried out in the following steps:

1 Calculate the initial drop size distribution for a given combination of D_{m_o} and n_o. Divide the total drop-size distribution into a number of groups, using different size intervals for different D_{m_o} values, as shown in the following table:

D_{m_o}, μm	30	50	70	90	120
ΔD, μm	1	2	3	4	5
Δt, ms	0.1	0.3	0.5	0.8	1

The volume fraction increment for each drop size group is calculated as

$$\Delta Q_i = \exp[-0.693\,(D_i/D_{m_o})^n] - \exp[-0.693\,(D_{i+1}/D_{m_o})^n] \tag{5}$$

taking 0.5 ($D_i + D_{i+1}$), the average drop size in the group, as the representative diameter. Note that all of the volume fraction increment in any group is regarded as being associataed with the average drop diameter in this size group.

2 For the first time period, Δt_1, calculate the drop-size change for each averaged drop size at the end of Δt_1, using equations (1-3), in which λ_{hu}, λ_{st}, and t_{hu} are determined from Figs. (1-3).

3 Calculate the volume fraction relative to the initial total spray volume remaining in each group at the end of Δt_1.

$$\Delta Q_{it} = \Delta Q_i\,(D_{it}/D_i)^3 \tag{6}$$

where D_{it} is the drop size of i group after time Δt_1.

4 Calculate the volume fraction evaporated (relative to initial spray volume) as

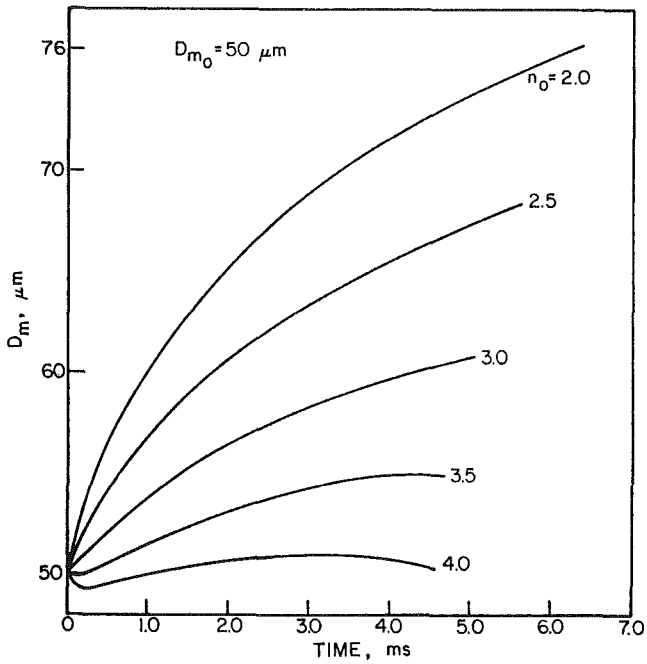

Fig. 4 Change of mean diameter (MMD) with evaporation time for different values of n_o: fuel = JP 5, P = 2000 kPa, T = 2000 K

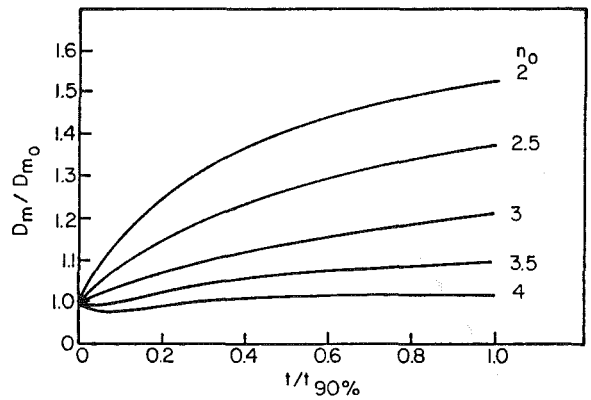

Fig. 5 Nondimensional diameter plotted against nondimensional evaporation time for various values of n_o

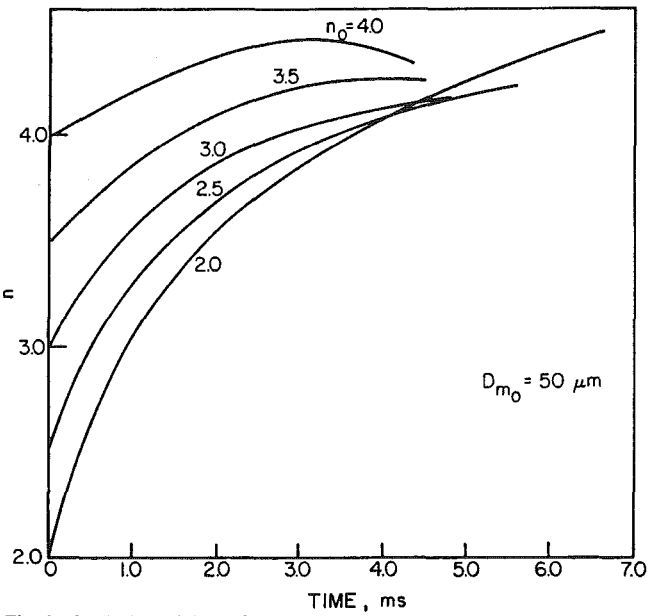

Fig. 6 Variation of drop-size distribution parameter n with evaporation time for different values of n_o: fuel = JP 5, P = 2000 kPa, T = 2000 K

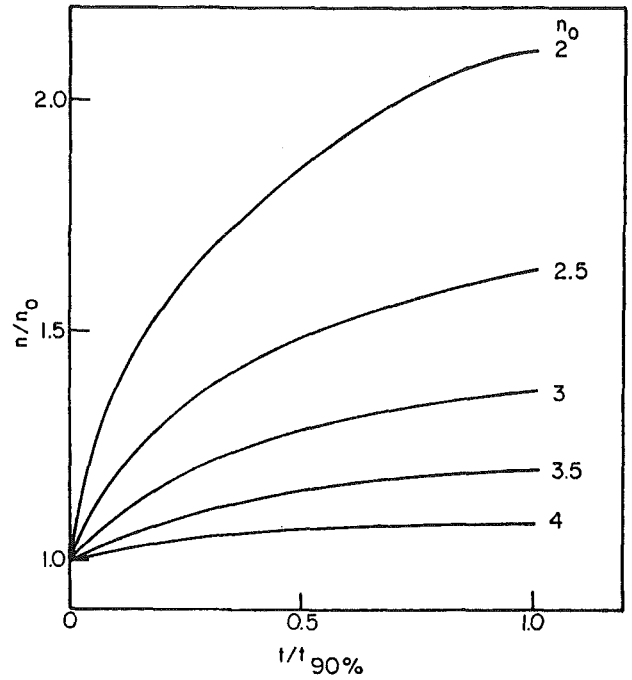

Fig. 7 Relative change of drop-size distribution parameter with nondimensional evaporation time for various values of n_o

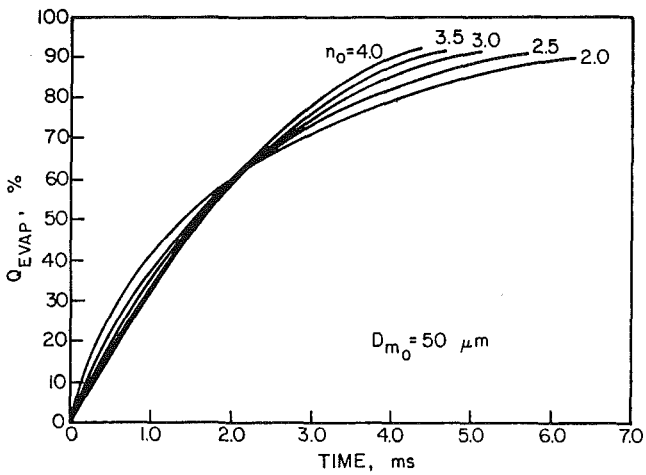

Fig. 8 Evaporation history of a JP 5 fuel spray for different values of n_o: P = 2000 kPa, T = 2000 K

$$Q_{\text{evap}} = 1 - \Sigma\Delta Q_{it} \tag{7}$$

In subsequent time increments, Δt_2, Δt_3, etc., the volume fraction evaporated (relative to the initial spray) should be $(1 - \Sigma\Delta Q_{it})$ multiplied by the total liquid volume fraction (relative to the initial spray) at the beginning of the time period.

5 Calculate the new liquid volume in each size group after time, Δt_1, expressed as a fraction of the total liquid volume in the spray after time, Δt_1.

$$\Delta Q'_{it} = (\Delta Q_{it} / \Sigma\Delta Q_{it}) \tag{8}$$

6 The new accumulative distribution, Q_t', can be calculated from

$$Q_t = \Delta Q'_{1t} + \Delta Q'_{2t} + \ldots . \Delta Q'_{it} \tag{9}$$

7 Rewriting equation (4) as

$$\ln D = \frac{1}{n} \ln \left[\frac{\ln (1-Q)^{-1}}{0.693} \right] + \ln D_m \tag{10}$$

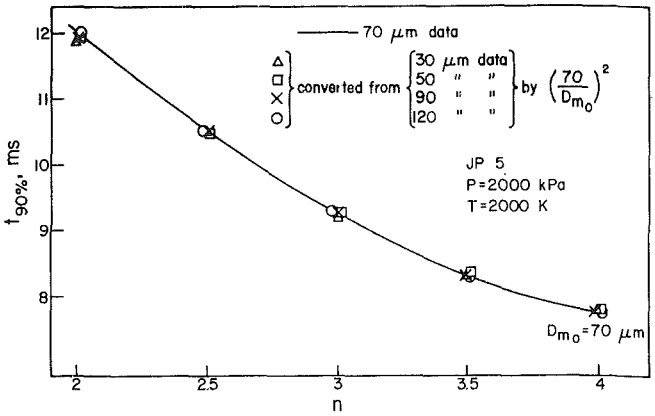

Fig. 9 Data illustrating that evaporation time is proportional to $D_{m_o}^2$

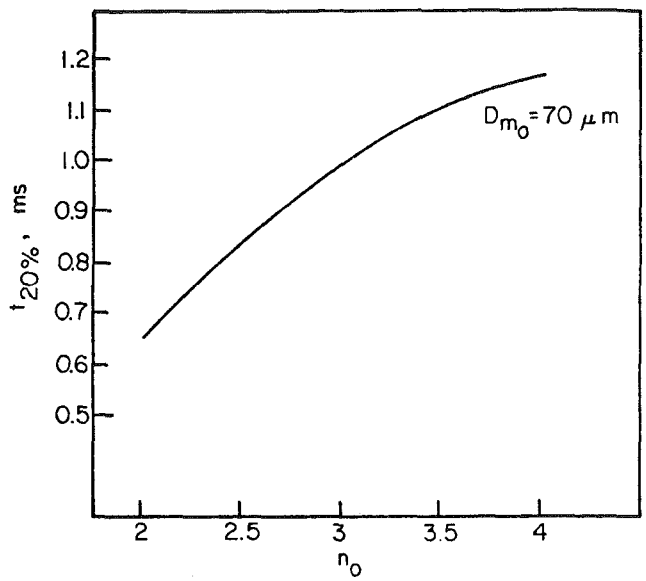

Fig. 10 Time to vaporize 20 percent of spray mass (volume) for different values of n_o: fuel = JP 5, P = 2000 kPa, T = 2000 K

and using the least squares method for ln D and ln [(ln(1 $-Q)^{-1}$)/0.693], the new drop-size distribution parameter, n, and the new mean diameter, D_m, are determined.

Results

The changes of mean diameter, D_m, with evaporation time for different values of initial mean diameter, D_{m_o}, and initial drop-size distribution parameter, n_o, are shown in Fig. 4 for a JP-5 fuel spray at T = 2000 K, and P = 2000 kPa. It is apparent that the mean diameter, D_m, increases with evaporation time. The general trend is that the change of D_m is more significant for sprays having smaller n_o values. If we nondimensionalize time, t, by using $t_{90\%}$, which is the time required to vaporize 90 percent by mass of the spray, and divide D_m by its initial value D_{m_o}, we can plot the nondimensional mean diameter D_m/D_{m_o} against nondimensional time $t/t_{90\%}$, as shown in Fig. 5, where the curves for different values of D_{m_o} combine to form a single curve. Since the evaporation time is now nondimensionalized, Fig. 5 can be seen as characteristic for the spray evaporation of various hydrocarbon fuels. It is perfectly general and applies equally well for all practical values of pressure, temperature, and D_{m_o}. The variation of drop-size distribution parameter, n, with evaporation time for a JP 5 fuel spray at T = 2000 K, P = 2000 kPa is shown in Fig. 6. It is of interest to note that if the relative change of n, i.e., n/n_o, is plotted against non-

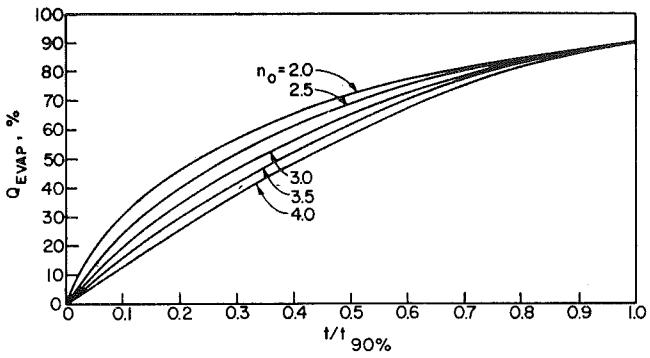

Fig. 11 Curves illustrating the variation of evaporation history with n_o

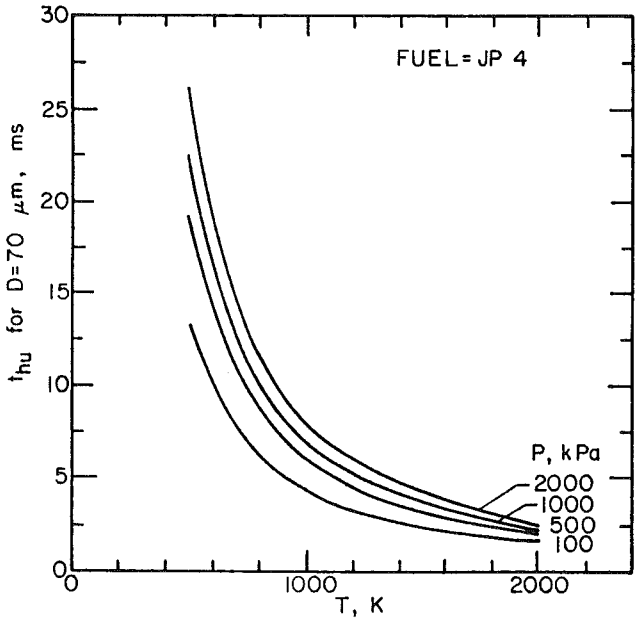

Fig. 12 Graphs illustrating the variation of the heat-up period with pressure and temperature for JP 4

dimensional evaporation time, $t/t_{90\%}$, then the results for different D_{m_o} values fall onto a single curve, as shown in Fig. 7. The general trend is for n to increase with evaporation time, and the effect is more significant for sprays having low values of n_o. Figure 7 is plotted in dimensionless form, so it is valid for all practical values of D_{m_o}, pressure, and temperature. The evaporation histories of JP fuel sprays at $T = 2000$ K and $P = 2000$ kPa are shown for $D_{m_o} = 50$ μm and various values of n_o in Fig. 8. It is clear that the time required to vaporize a certain percentage of the fuel spray is proportional to the square of D_{m_o}, as shown in Fig. 9. The curve drawn in this figure represents calculated results for the time to vaporize 90 percent of the spray mass for $D_{m_o} = 70$ μm. Other data points are converted from the calculated data for $D_{m_o} = 30$ μm, 50 μm, 90 μm, and 120 μm, by multiplying by the ratio of $(70/D_{m_o})^2$. The time required to vaporize 20 percent of the spray mass for $D_{m_o} = 70$ μm is shown in Fig. 10. From Figs. 9 and 10, it is apparent that a spray of large n_o will have a low 90 percent evaporation time and a high 20 percent evaporation time. Thus, from a combustion efficiency viewpoint, it is desirable to have a spray with a high value of n_o, but for ignition it is better to have a low n_o value. Since the evaporation curves shown in Fig. 8 tend to flatten out in the final stage of evaporation, this implies that combustion systems which demand a fully prevaporized fuel-air mixture, may require considerable prevaporization time in order to achieve this goal. This is especially true for low values of n_o, as illustratred in Fig. 8.

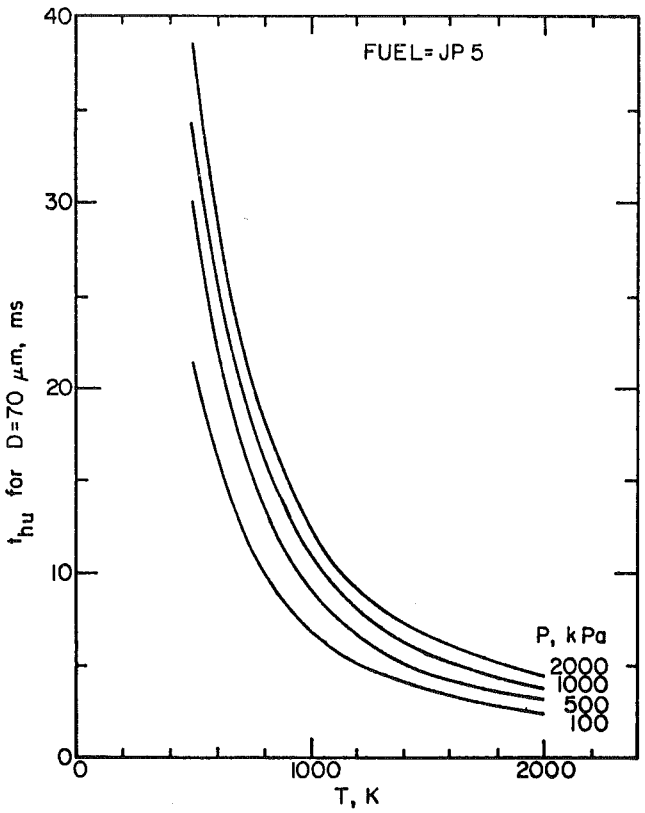

Fig. 13 Graphs illustrating the variation of the heat-up period with pressure and temperature for JP 5

Evaporation Time Estimations for Various Fuels

If evaporation history is plotted against nondimensional evaporation time $t/t_{90\%}$, the curves for different values of D_{m_o} combine into a single curve, as shown in Fig. 11. Since the evaporation time is nondimensionalized, Fig. 11 is valid for different fuel sprays at different pressures and temperatures. Based on Figs. 9 and 11, the following general method for estimating the time required to vaporize any given fraction of a hydrocarbon fuel spray in stagnant air, at any stipulated values of pressure and temperature, is proposed.

We have

$$t = (t/t_{90\%}) \cdot (t_{90\%})$$

JP 5
$P = 2000$
$T = 2000$
$D_{m_{o\times 10^{-6}}}$

$$\cdot (D_{m_o}/70\times 10^{-6})^2 \cdot \lambda_{\text{eff}} \qquad /\lambda_{\text{eff}}$$

JP 5	FUEL
$P = 2000$	P
$T = 2000$	T
x	x

where x is the fraction of the total fuel in the form of vapor and λ_{eff} is the effective evaporation constant. At the start of the evaporation process ($x = 0$), $\lambda_{\text{eff}} = \lambda_{hu}$. At the end of evaporation ($x = 1$), λ_{eff} is given by

$$\lambda_{\text{eff}_{x=1}} = \frac{D_o^2}{t_{hu} + (D_o^2 - \lambda_{hu}\, t_{hu})/\lambda_{st}}$$

$$= \frac{\lambda_{st}}{1 + (t_{hu}/D_o^2)\ (\lambda_{st} - \lambda_{hu})} \tag{11}$$

Since $t_{hu} \propto D^2$, the ratio t_{hu}/D^2 is independent of drop size.

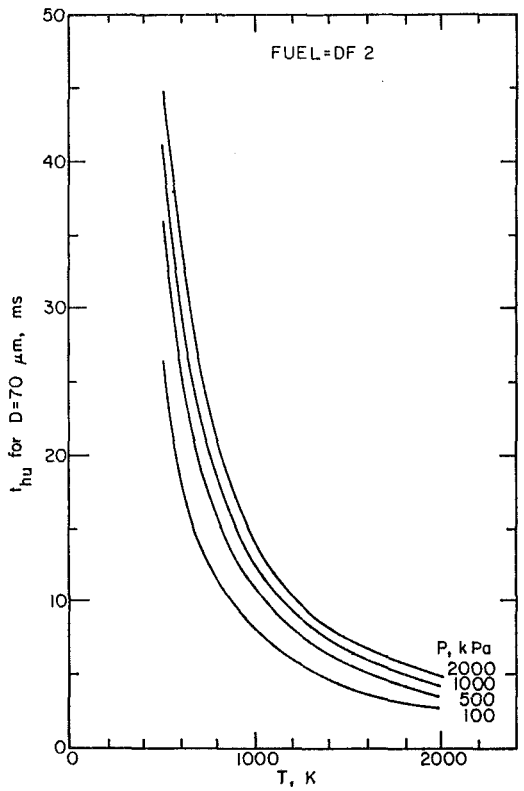

Fig. 14 Graphs illustrating the variation of the heat-up period with pressure and temperature for DF 2

For any stipulated conditions of pressure, temperature, and fuel type, it has a constant value which applies equally well both to individual drops and to the spray as a whole.

The influence of the heat-up period varies with the value of x. The value of λ_{eff} always lies between λ_{hu} and $\lambda_{\text{eff}_{x=1}}$, being larger for high values of x. If it is assumed that λ_{eff} varies as a linear function of x between λ_{hu} and $\lambda_{\text{eff}_{x=1}}$, then

$$\lambda_{\text{eff}_x} = (1-x)\,\lambda_{hu} + x \cdot \lambda_{\text{eff}_{x=1}}$$

$$= (1-x)\lambda_{hu} + \frac{x \cdot \lambda_{st}}{1 + (t_{hu}/D_o^2)\,(\lambda_{st} - \lambda_{hu})} \qquad (12)$$

Substituting into equation (12) appropriate values of λ_{hu}, λ_{st}, and (t_{hu}/D_o^2) for JP 5, at $P = 2000$ kPa, $T = 2000$K, and $D_o = 70 \times 10^{-6}$, gives

$$\lambda_{\substack{\text{eff} \\ \text{JP 5} \\ P=2000 \\ T=2000 \\ x}} = (1-x)\ 0.4077 + \frac{1.638\,x}{1 + 0.907(1.638 - 0.4077)}$$

$$= 0.4077 + 0.3664 \text{mm}^2/\text{s} \qquad (13)$$

The equation for estimating the time required to evaporate a fraction x of the volume of any given fuel spray in quiescent air, at any stipulated values of pressure and temperature, is then obtained as

$$t_{\substack{\text{FUEL} \\ P \\ T \\ x}} = (t/t_{90\%}) \cdot (t_{90\%})_{\substack{\text{JP 5} \\ P=2000 \\ T=2000 \\ D_{m_o} = 70 \times 10^{-6}}} \cdot (D_{m_o}/70 \times 10^{-6})^2$$

$$\cdot \frac{0.4077 + 0.3664\,x}{\left[(1-x)\lambda_{hu} + \dfrac{x \cdot \lambda_{st}}{1 + 0.204\, t_{hu_{70\times10^{-6}}}(\lambda_{st} - \lambda_{hu})}\right]_{\substack{\text{FUEL} \\ P \\ T \\ x}}} \qquad (14)$$

The following points should be noted in connection with the foregoing equation:

1 For computational convenience, the units employed for t_{hu} and λ in equation (14) and in the figures are ms and mm^2/s, respectively.

2 Values of $t_{hu_{70\times10^{-6}}}$ can be obtained from Figs. 12, 13, and 14 for JP 4, JP 5 and DF 2, respectively.

3 $(t/t_{90\%})$ is determined from Fig. 11, for any given values of evaporation percentage and n_o.

4 $(t_{90\%})_{\substack{\text{JP 5} \\ P=2000 \\ T=2000 \\ D_{m_o} = 70 \cdot 10^{-6}}}$ is the time required to vaporize 90 percent of a JP 5 fuel spray for $D_{m_o} = 70$ μm, $P = 2000$ kPa, and $T = 2000$ K (see Fig. 9).

The term $(D_{m_o}/70 \times 10^{-6})^2$ represents the effect of initial mean diameter on the time required to vaporize a certain percentage of the fuel spray.

Conclusions

1 Spray evaporation time is proportional to the square of the initial mass mean diameter (MMD) of the spray.

2 As evaporation proceeds, the mean drop diameter and distribution parameter n both increase with time. This effect is especially pronounced for sprays having low values of n_o.

3 The time required to evaporate any given fraction of a fuel spray in stagnant air can be estimated for different pressures and temperatures by the simple method proposed in this paper.

4 The evaporation histories of sprays having different values of distribution parameter, n, show that a spray which is optimum from a combustion efficiency viewpoint may not be desirable from an ignition standpoint.

5 Further work is needed to elucidate the effects of convection on spray evaporation.

References

1 Chin, J. S., and Lefebvre, A. H., "Steady-State Evaporation Characteristics of Hydrocarbon Fuel Drops," AIAA Paper No. 82-1176, 1982.

2 Chin, J. S., and Lefebvre, A. H., "The Role of the Heat-up Period in Fuel Drop Evaporation," presented at AIAA 21st Aerospace Sciences Meeting, Reno, Nevada, Jan. 1983.

3 Chin, J. S., and Lefebvre, A. H., "Effective Values of Evaporation Constant for Hydrocarbon Fuel Drops," *Proceedings of the Twentieth Automotive Technology Development Contractors Meeting*, SAE P-120, 1983, pp. 325-331.

4 Swithenbank, J., Turan, A., and Felton, P. G., "Two-Phase Mathematical Modelling of Gas Turbine Combustors," *Gas Turbine Combustor Design Problems*, edited by A. H. Lefebvre, Hemisphere, 1980, pp. 249-314.

5 Chigier, N., "*Energy, Combustion and Environment*," McGraw Hill, 1981.

6 Rao, K. V. L., and Lefebvre, A. H., "Evaporation Characteristics of Kerosine Sprays Injected into a Flowing Air Stream," *Combustion and Flame 26*, 1976, pp. 303-309.

7 Rosin, P., and Rammler, E., "The Laws Governing the Fineness of Powdered Coal," *J. Inst. Fuel*, Vol. 7, No. 31, Oct. 1963, pp. 29-36.

Combined Diesel and LM2500 Gas Turbine Propulsion Enhances Corvette/Frigate Missions

P.A. Dupuy
Marine and Industrial Engine Projects Department,
General Electric Company,
Cincinnati, Ohio 45215

The LM2500 Gas Turbine is used for propulsion of naval ships from 220 tons to 14,000 tons displacement. Those ships from 220 to 4000 tons have used combined diesel or gas turbine (CODOG) systems in all but one ship class. Destroyers and larger ships, 7000 tons and up, have all used solely LM2500 turbines as Combined Gas Turbine and Gas Turbine (COGAG). Recently, the diesel engine industry has announced the advent of technological developments whereby diesel engine specific power can be significantly increased. Thus it is being suggested that with this new technology, all diesel propulsion (CODAD) can replace various propulsion systems currently using combined diesels with gas turbines. This paper explores the desired mission objectives for corvette/frigate class ships and develops an analytical comparison of all diesel and combined propulsion abilities to satisfy the ship's missions. The comparison assesses the system's relative impact upon propulsion system acquisition and life operating cost, system operational flexibility, ship's detectability, and overall ability of the ship to perform the broadest range of mission requirements.

Introduction

In the 1960s, the aircraft engine derivative marine gas turbine revolutionized the design of naval escort vessels. The first generation gas turbine systems, primarily cruise or boost turbine systems (COGOG), reduced propulsion system weight, improved maneuverability, shortened underway time (from cold iron), reduced complexity of auxiliary systems, reduced on-board maintenance and thus crew manning requirements, increased ship availability and afforded modest reduction in fuel usage when compared to the then prevalent steam systems.

During the 1960s and 70s, ship weapon systems, detection systems, and countermeasures technology advanced so rapidly that naval ship designers were forced to satisfy expanding ship mission requirements while reducing ship size in order to help compensate for the rising cost of ships which accommodate the more compact and functional fighting systems. In the early 1970s, the General Electric LM2500 was introduced into naval service as the initial second-generation marine gas turbine. The term second-generation, as compared to first-generation marine turbines introduced up through the 1960's, signifies a substantial increase in engine performance and efficiency due to higher cycle pressure ratio, higher gas temperatures made possible by advanced cooling methods and better materials, and by improved component efficiencies. These changes result in the second-generation turbine having higher efficiency (lower specific fuel rate) across the full range of power output and greater specific power in three respects: more power per unit of engine mass, more power per unit of engine volume, and more power per unit of gas mass flow.

The potential for the second-generation LM2500 to provide greater power with smaller propulsion machinery volume was quickly recognized by ship designers. Briefly these features were

- Smaller inlet air and exhaust ducts
- COGAG rather than COGOG, which deleted the need for turbines used only for cruise purposes
- Lower output rpm allowing smaller main reduction gearboxes
- Lower ship fuel storage requirements
- Higher availability and longer intervals between engine repair.

The ships using LM2500 turbines are plotted on Fig. 1 by ship displacement and total power. The grid is blocked into two areas: ships using CODOG and ships using COGAG.

Figure 1 shows several distinct trends in propulsion selection. Ships from 220 to 4000 tons displacement are basically CODOG systems and ships above 4000 tons (the next larger class vessel is a 7800 ton destroyer) are COGAG.

LM2500 CODOG has been the propulsion system choice for patrol/gunboats, corvettes, and frigates where the combination of high speed and long endurance, the optimum design balance of any naval ship, militates for the use of small cruise diesels (e.g., cruising power requirements can be less

Contributed by the Gas Turbine Division of THE AMERICAN SOCIETY OF MECHANICAL ENGINEERS and presented at the 29th International Gas Turbine Conference and Exhibit, Amsterdam, The Netherlands, June 4-7, 1984. Manuscript received at ASME Headquarters January 16, 1984. Paper No. 84-GT-195.

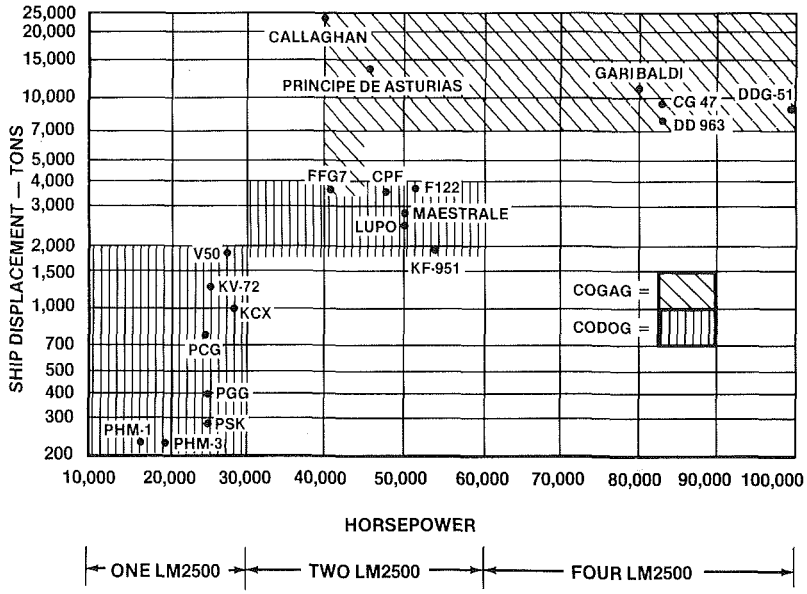

Fig. 1 LM2500 powered ships

than 2000 bhp). All of the applications up to 1950 tons use single LM2500 propulsion and all over 2000 tons use two LM2500's. At 2000 tons displacement one LM2500 gives a typical maximum speed of 28 knots, while two LM2500's give a typical maximum speed of 36 knots. Thus at approximately 2000 tons, there has been a significant transition from one to two propulsion gas turbines.

During the 1970s, the alternative system to LM2500 CODOG for ships to 2000 tons displacement has been the use of four high-speed diesels. Generally the lightweight models of these diesels were limited to continuous power of less than 4500 kW (6000 British hp) with time limited overload ratings in the order of 5000 kW (7000 bhp). These diesels, in groups of four, provided a lower continuous power capability than an LM2500 CODOG system at a notably greater propulsion machinery weight, both characteristics causing a lower ship speed capability. While some high-speed diesel models had modestly higher power, these models added substantial additional weight.

During 1982, most of the major manufacturers of high-speed marine diesels announced the development of a supercharging technique whereby the power output of their current models can be substantially increased with little additional weight or volume. As a sweeping simplification of the various manufacturers' individual techniques, their method is to reduce the cylinder pressure ratio and increase the supercharger pressure. This produces a larger mass of air per stroke and increased mean effective pressure for a simliar peak ignition pressure, and results in higher power capability per cylinder across the engine output rpm range. Publications indicate that these new models, which will be henceforth generalized as low compression ratio (LCR) engines, will have continuous power capabilities in the order of 6200 kW (8300 bhp) and time limited overload capabilities up to 7400 kW (10,000 bhp) per engine. With the announcement of a method which provides a significant increse in diesel engine specific power has come various speculations that CODAD could be able to match the features of combined diesel-gas turbine systems.

Since a propulsion system's ultimate criterion of merit is how well it satisfies propulsion system design requirements without unduly burdening the overall ship design, the purpose of this paper is to compare CODAD using LCR diesels with combined diesel-gas turbine systems for a specific ship.

Marine practice has demonstrated that 2000 tons has been the displacement above which LM2500 CODOG systems transition from one to two gas turbines. Thus 2000 tons appears the logical displacement for comparing systems where the continuous power of four LCR diesel power challenges the continuous power of one LM2500. At lower displacements, the ship becomes more sensitive to the added weight of the CODAD system and at higher displacement the 30,000 kW CODAD is competing with 44,000 kW CODOG, and these would be ships of different speed cababilities.

The 2000-Ton Ship Mission Criteria

The modern 2000-ton ship represents a classic example of the trend to achieve multimission capabilities with a smaller ship. Such a ship would likely be called upon to operate autonomously and be equipped for surface to air, surface to surface, and surface to undersea search and attack, as well as escort missions requiring long range capability. The following are the likely roles called for while maintaining a high degree of self protection.

- Escort—Traveling long distances with a convoy, splitting off to perform active sonar searches and sprinting to catch up to the convoy
- Picket Duty—The off-shore towing at slow speed of submerged array passive listening devices at slow speed
- Coastal and River Patrol—Economic zone protection, search and rescue, smuggling interdiction, training exercises

As a basis for the comparative analysis, the General Electric Co., Marine & Industrial Engine Projects Department contracted with Yard Ltd., Consulting Engineers, Glasgow, Scotland to specify the particulars of a multimission capable ship with 30 knots speed capability, a range of 4000 N. miles at 18 knots and low detectability signatures. Particulars of the baseline ship are

Displacement-nominal	2000 metric tons
Maximum speed	30 knots
Range	4000 N. miles @ 18 knots
Propellers	Two C&RP with prairie
Installed power	30 MW (40,000 bhp)
Ship service generators	Four 500 kW sets
Nominal electric load	900 kW @ 240 kg fuel/hr
Structureborne noise	Attenuated for ASW missions
Infrared radiation	Cooled stack liners
Airborne noise	Suppressed for ASW purposes and crew habitability

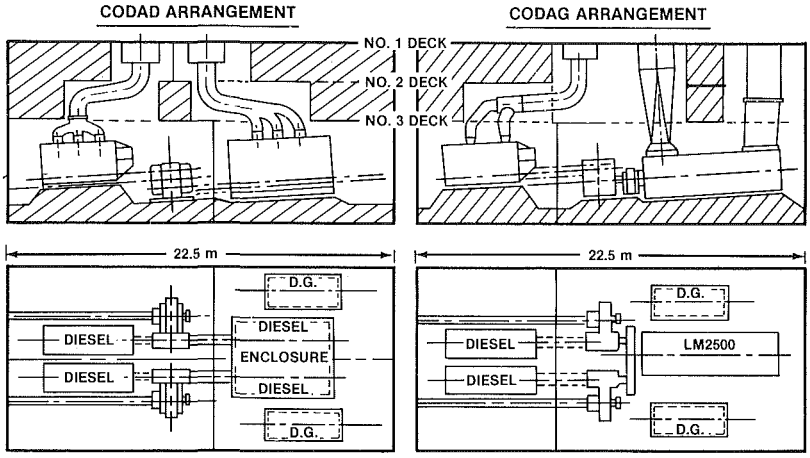

Fig. 2 Propulsion machinery arrangements

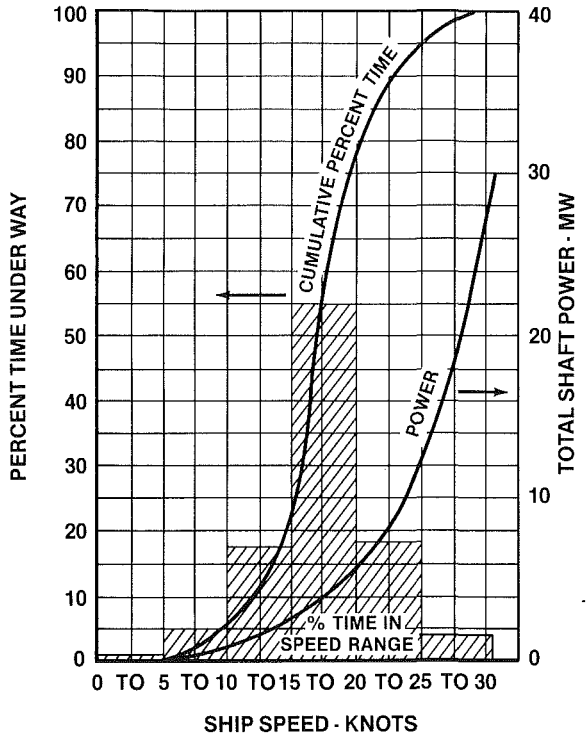

Fig. 3 Ship operating profile

The Alternative Propulsion Arrangements

For the CODAD arrangement, four LCR 7.4-MW class diesels are used, two driving into each of two combining gear boxes. One diesel on each shaft is installed in an acoustically treated encosure with double noise isolating mounting to strike a balance of quiet ASW capability in the cruise mode with minimum installation weight and cost. Based upon MTU diesels currently having the most well-defined system features of LCR, high power to weight ratio and noise isolating mounting and enclosures, MTU engines were chosen to typify what may be possible for a 30-MW propulsion system.

Since the maximum power of the LM2500 can be applied continuously through a mission, one LM2500, rated at 22 MW for this study comes close to matching the 24.5-MW total continuous power of the four LCR 7.4 MW diesels. The four diesels have a limited overload power capability of 30.0 MW. To match this power level without going to the expense of putting in a second gas turbine, a CODAG system can be used which combines the power of cruise diesels with the gas turbine when the ship goes to maximum speed.

By using two cruise diesels rated about 4 MW each in conjunction with one LM2500, the 30 MW required for 30 knots can be achieved as CODAG while affording the benefits of a conventional CODOG system. Layout arrangements of the two systems are shown in Fig. 2.

To provide maximum study continuity, MTU conventional cycle diesels were selected for the CODAG cruise engines. CODAG systems have been used successfully for many years in Navy ship applications. Examples listed in Jane's Fighting Ships 1979–80 show at least three different classes of CODAG ships, introduced into naval service in the late 1950s, the 1960s and the late 1970s.

Based upon the probable mission requirements for a typical 2000 ton ship, comparative analysis was made betwen CODAD and CODAG systems for the following ship characteristics:

- Engine and transmission system characteristics
- Annual fuel usage
- Fuel storage to meet range
- Space requirements—effects on layout
- Machinery plus fuel weight
- Maintenance requirements and manhours
- Propulsion and related machinery acquisition costs
- Life cycle costs of fuel, lube oil, and maintenance and repair parts
- Infrared relative detectability
- Acoustic relative detectability

In general, the overall results of these analyses would also be applicable for a CODOG versus CODAD comparison for ship displacement and speed requirements met by 15 MW to 22 MW installed power.

A study was also made of a CODAG control system to determine the proper matching and sequencing of the loading of the diesels and gas turbine.

Ship Power and Duty Cycle

The plot of ship shaft power and operating profile as a function of ship speed in knots is shown in Fig. 3. Ships operating time underway is assumed at 3000 hrs per year. The dominant ship operation is in the 15 to 20 knot zone.

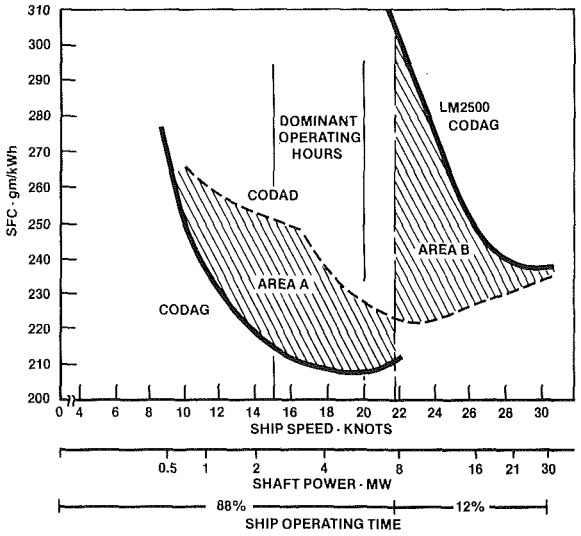

Fig. 4 Engine specific fuel consumption (SFC)

Engine and Transmission System Characteristics

CODAD system

Engines	Four MTU 20V1163TB93
MCR (each)	6120 kW @ 1220 rpm
Max. sprint power	7400 kW @ 1300 rpm
Max. two engine	5000 kW @ 990 rpm = 23.5 kts
Fixed ratio gear	4.64:1

MTU estimates this diesel TB0 to be 6000 hrs for the power duty cycle profile shown in Fig. 3.

The minimum diesel unlimited duration speed of 500 rpm produces a ship speed of 11.5 knots at full propeller pitch.

CODAG system

Gas turbine	One GE LM2500 module
Continuous rating	22 MW at 3600 rpm
Cruise diesels	Two MTU 20V1163TB82
MCR	4045 kW @ 1160 rpm
Two ratio gear	Diesel only 5.83:1, CODAG 4.17:1
Mode of operation	2 diesels to 21.8 knots 1 LM2500 to 28 knots All 3 engines to 30.3 knots

MTU estimates this diesel TB0 to be 9000 hrs for the power duty cycle profile shown in Fig. 3.

The minimum diesel unlimited duration speed of 500 rpm produces a ship speed of 9 knots at full propeller pitch. The LM2500 can drive the ship at a minimum speed of 5 knots without reducing propeller pitch.

Annual Fuel Usage

One of the reactions of those unfamiliar with combined diesel-gas turbine systems is concern that the gas turbine will cause significant additional fuel operating cost. While the diesel engine is known for a relatively flat curve of specific fuel consumption across its load range, CODOG-CODAG applications allow the cruise mode diesels to be selected for the maximum economy in the cruise power range, whereas the CODAD application diesels are selected to produce maximum ships power and therefore the greatest part of their operating time is below peak efficiency. Figure 4 shows the specific fuel consumption curves of the engines of the two systems, without installation losses or ship service fuel requirements, to illustrate this phenomenon.

Figure 4 shows that 88 percent of the time the ship is operating in the cruise mode, the CODAG plant provides a fuel savings shown by Area A which approximately offsets (as a function of each operators actual operating profile) the CODAG added fuel usage in the boost mode as shown in Area B. For the study, plots were developed of total installed fuel flow for each system as a function of ship speed. For 3000 hrs annual sea time operation (to the Fig. 3 profile), the CODAD annual fuel usage is 4030 tons, and the CODAG system is 4008 tons. If it is assumed that 50 percent of the operation below 9 knots were ASW passive mode where minimum noise is necessary, using the LM2500 with full propeller pitch would increase annual fuel usage by about 25 tons. Many CODOG ships today perform quiet operations on gas turbine for lowest possible propeller and machinery noise detectability.

Table 1 Machinery weight summary

Item	CODAG	CODAD
Gas turbine	26.0	–
Diesel engines	39.0	138.25
Main gearing	68.5	64.0
Shafting and CPP equipment	28.6	28.6
Propeller	15.4	15.4
Intake air supply system	5.75	4.25
Exhaust gas system	17.0	26.5
Fuel oil system	6.0	5.7
Lube oil system	6.25	9.5
Total tons (M)	212.5	292.2

Fuel Storage to Meet Range

To meet a range requirement of 4000 N. miles at 18 knots with a 10 percent margin, the CODAG ship will require 290 tons fuel storage, and the CODAD ship 310 tons.

Space Requirements—Effects on Layout

As seen in Fig 2, the machinery would occupy the same length (22.5M) for the two compartments. In each system these compartments accommodate the auxiliary machinery and two 500-kW ship service generator sets. An additional 7 m length compartment aft accommodates two additional 500-kW generator sets. The total deck area above either system machinery space including generator room is 325 m^2. The CODAG system requires about 14.5 m^2 more floor area at No. 3 deck level for the ducting penetrations, but this diminishes to 5.5 m^2 area difference at the No. 2 deck to accommodate the CODAD engine exhaust silencers. Since LM2500 ducting area has been accommodated in 290 ton gunboats and 220 ton hydrofoils, it does not present a significant inconvenience in a 2000-ton ship.

Machinery Plus Fuel Weight

Table 1 below lists the propulsion system comparative weights. The machinery plus fuel to make a 4000 mile range at 18 knots is 502.5 ton for CODAG compared to 602.5 tons for CODAD. The weight fractions are CODAG 25 percent, CODAD 30 percent. If the CODAG weight savings were used for additional fuel, range would increase 35 percent or to 5400 N. miles. Alternatively, the 100 tons may be used for added payload.

Maintenance Requirements and Manhours

During a 25-year life cycle, the maintenance manhours for engine preventative and corrective maintenance and shoreside repair/overhaul is calculated to be 33,700 hrs for CODAG and 42,800 for CODAD. During the 25 years there would be 14 diesel engine removals and one gas turbine removal for the CODAG system compared with 24 diesel engine removals for the CODAD system, for shoreside overhauls.

Acquisition and Through Life Costs

Budgetary estimates were made for the machinery initial cost and for machinery operating costs for 25-year service life. The propulsion machinery included in the acquisition cost are:

- Propulsion engines
- Main gearing
- Shafting and propellers
- Combustion air systems
- Exhaust gas sytems
- Fuel oil systems
- Lube oil systems

Machinery acquisition costs are in present day values, fuel cost is assumed to escalate 5 percent above inflation. Future fuel, lube, and parts cost are discounted 5 percent per year to assess them at present worth. Present worth equals Future Value $\times (1 + i)^{-n}$ where i is the discount percent and n is the number of years.

(*Millions* $ U.S.)	CODAG	CODAD
Initial machinery	8.86	8.17
25 year fuel	27.72	27.89
25 year lube oil	.57	.77
Replacement parts	2.31	5.11
Total 1983 present worth	39.46	41.94

Replacement parts include: expendables used during scheduled preventative maintenance, parts and components replaced during unscheduled shipboard corrective maintenance, and parts used at shoreside repair and overhaul.

Infrared Relative Detectability

Periodicals frequently allude to infrared detectability risk with gas turbines because they exhaust more and frequently higher temperature exhaust gases than diesels for a given power level. GE contracted Yard Ltd.[2] to do a comparison of the total ship IR detectability for CODOG/CODAG and CODAD systems. The study considered the three radiation signature components; hull and structure, exhaust gas uptakes, and exhaust gas plumes.

The study assumed typical or conventional values for: water and air temperatures; sunny, cloudy and night operation; wind velocity, structure paint finish; uptakes with and without uptake cooling; and exhaust from clean burning (nonfouled) engines.

Since atmospheric absorption effectivity limits IR radiation transmissions in many frequencies, the two strongest wavebands of transmission were compared, 3–5 μm and 8–14 μm. Due to security, the conventional spectral radiant intensity (SRI) measurements, Watts/Steradian, have been converted to arbitrary nondimensional "Spectral Radiant Intensity Units."

The threat of a high IR signature is detection by a heat seeking enemy missile. Heat seeking missiles sense differences in the infrared radiation of an object from that of its surroundings. Countermeasures include: (*i*) decoys that emit high levels of IR radiation and thus lure misisles to false targets; (*ii*) electric jammers that emit spurious signals to confuse the missile and loose lock on; and (*iii*) propulsion unit suppressors that lower engine exhaust system emissions. Typically, these missiles are radar-homing at long range and switched to IR seeking at close range. The missile span of angle of sight, as shown in Fig. 5, is 0 to 50 deg and believed representative of protection limits required by most navies. Since most missiles fly low (sea skimmers) to reduce the detection of their approach, angle of sight is usually less than 20 deg. On the basis of study data, it evolves that the total

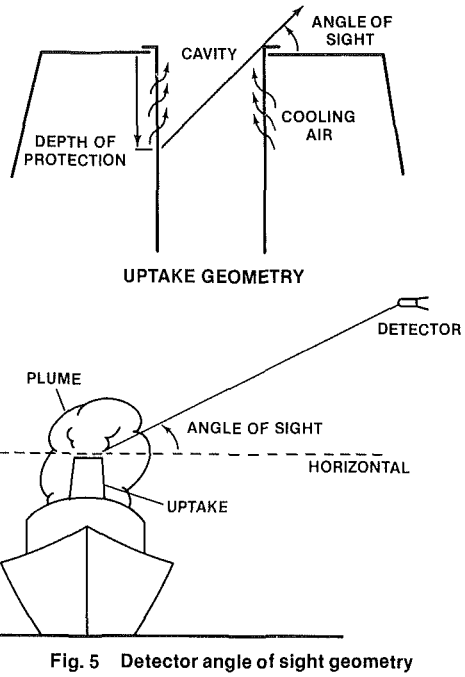

Fig. 5 Detector angle of sight geometry

ship signature is greatest at maximum speed, and the greater the angle of sight, the greater the signature. Therefore Table 2 has been compiled to show the radiant intensity for the three components of the signature, ship structure, exhaust cavity, and exhaust plume.

Highlighted in Table 2 is the radiation intensity of a typical IR decoy. The objective is to project a ship signature less than that of the decoy. The standard for evaluating detectability is for a cloudy day and thus comparisons are made on this basis. As a calibration to the effect of a sunny day, the last line of Table 2 shows the ship signature on a sunny day at full speed. At lesser ship velocities, the structure signature is slightly greater but engine caused signatures are substantially less. The standard for evaluating detectability is therefore a cloudy day, full speed. The exhaust cavity data are given for two conditions, uncooled and cooled cavity. Figure 5 shows the exhaust cavity using a method of cooling the stack metal sometimes referred to as "Bliss" cooling.

Table 2 indicates that without exhaust liner metal cooling, either propulsion system will greatly exceed the decoy, but with cooling the signature is greatly reduced. Exhaust liner cooling to achieve the cooled signatures in Table 2 requires a totol flow of ambient air of 12.8 m^3/s for a CODAD system and 11.6 m^3/s for a CODAG system. At about 1 in. H_2O liner pressure drop, such a total flow for all installed engines would require less than 10 hp (7.5-kW) fan power. Thus it can be seen that cooled exhaust cavity is essential when IR detectability is of concern. Once cooling is used, the sum of the exhaust cavity and the plume signature are miniscule compared to the ship signature. This would still be true at night because the total mass of the ship will change temperature faster than the sea water and usually produces a signature difference from its surroundings only somewhat lower than for a cloudy day. Figure 6 is a plot of the total ship signature versus angle of sight for the two selected wave bands. From Table 2 and Fig. 6 it may be seen that below 30 deg sight angle, which are the most prevalent missile homing conditions, the CODAG ship has marginally less detectability and at the higher angle of sight, the CODAD is marginally less.

The conclusions are that within the most probable angle of sight, with cooled exhaust, neither ship has a significant difference and the ship can effectively deploy IR decoys. Without cooling, on sunny day conditions, or for extremely

Table 2 Spectral radiant intensity units (cloudy day-30 knots)

Detector angle of sight		20 deg		50 deg	
Waveband		3-5 μm	8-14 μm	3-5 μm	8-14 μm
Ship structure		0.6	9.8	0.72	11.8
CODAD uncooled exhaust		18.0	7.2	40.5	15.7
CODAG uncooled exhaust		19.5	9.3	42.0	21.0
CODAD cooled exhaust		0.02	.12	0.14	0.75
CODAG cooled exhaust		0.03	.28	0.25	1.26
CODAD plume		0.08	.35	0.08	0.35
CODAG plume		0.03	.16	0.03	0.16
Typical decoy		3.0	11.25	3.0	11.25
Ship total (with	*CODAD*	*0.7*	*10.32*	*0.94*	*12.89*
cooled exhaust)	CODAG	0.66	10.24	1.0	13.22
Ship structure (sunny day)		6.7	72.0	8.0	85.0

Table 3 Antinoise installation features

COMPONENT	CODAG	CODAD
LM2500	enclosed-mounts shaft	-
CODAG diesels	single mount bare engines	
CODAD diesels	-	2 enclosed-double mount 2 - bare - single mount
Diesel GenSets	4 enclosed double mount	same
Gearboxes	Quiet design hard mount	same
Prairie(Agouti)	yes	yes
Hull mask air	no	no

Table 4 Machinery modes

Speed-knots	CODAG	CODAD
4-11.5	LM2500-CRP full pitch	two diesels-CRP partial pitch
11.5-23.5	LM2500-CRP full pitch	two diesels-CRP full pitch
23.5-28	LM2500-CRP full pitch	four diesels-CRP full pitch
28-30+	LM2500 + 2 diesels full pitch	four diesels-CRP full pitch

high angles of sight (a satellite may view at well over 50 deg) the total ship IR signal is so great that the difference between propulsion systems become irrelevant.

Acoustic Relative Detectability

In order that the acoustic signature of the ship and its susceptibility to detection may be compared on a total ship basis, GE contracted with Yard Ltd. for a noise detectability study comparison of CODAG and CODAD [3].

To compare acoustic properties and isolation requirements, equipment octaveband vibration levels were compared as functions of frequency. Then the extent of this energy concentrated in tonals was evaluated in order to identify frequency ranges that govern isolation system requirements.

To provide a quiet ASE base within reasonable cost, the selected noise attenuating features selected for the machinery components are shown in Table 3.

Table 4 shows the machinery "ASW Quiet" operating modes as a function of ship speed for the two propulsion systems.

On a broad band basis, source vibration levels of each diesel will exceed that of one LM2500, particularly in centerband frequencies from 250 Hz to 1 kHz.

LM2500 gas turbine tonals are significant at its rotational frequencies, 0–60 Hz for the power turbine and 80–150 Hz for the gas generator, depending upon power output. Tonals

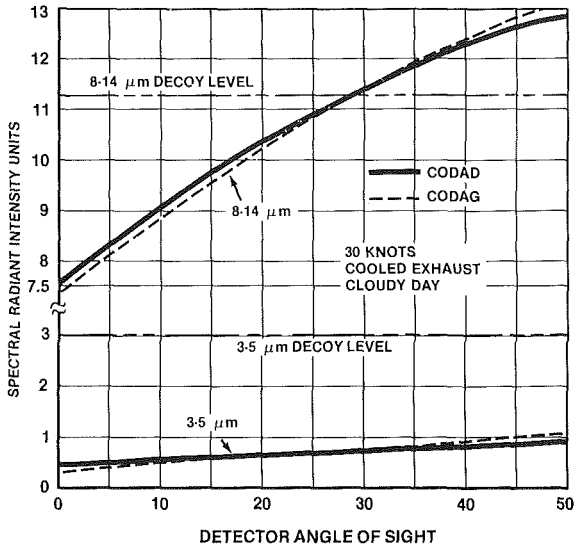

Fig. 6 Total ship IR signature

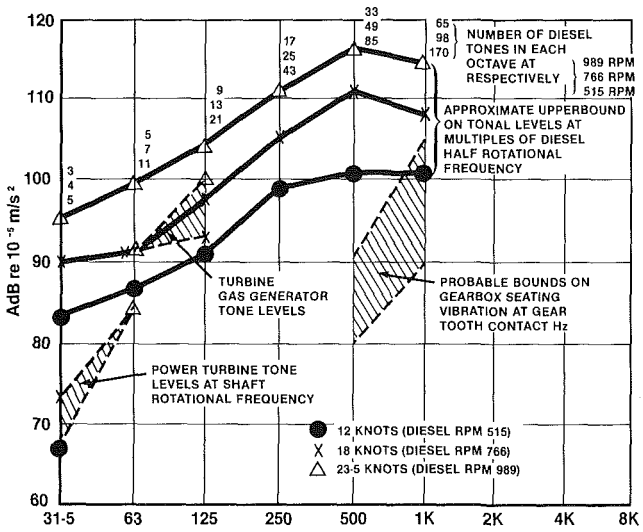

Fig. 7 Above mounts vibration levels

associated with interaction of rotor and stator blades are in the kHz range.

Diesel tonals are concentrated at multiples of one-half the rotational frequency for four stroke engines. Figure 7 shows the typical magnitude levels of vibration above the mounts for the LM2500 and a representative diesel. It assumes the highest spatially averaged tonal level of diesel vibration is 5 log (number of tonals in octave band) dB beneath the octave band level. For the gas turbine, the measured levels of vibration in the 1/3 octave containing rotational frequencies are assumed equal to the tonal levels at these frequencies.

The LM2500 module has a system of 32 mounts between the module base and the ship. For the diesel engines, double mounting is required incorporating a two-stage system with an intermediate high mass raft system. In addition to mounting, design care must be exercised for diesels and turbines in isolating noise path via piping connections to the engines and via coupling shafts into the hard mounted gearboxes. The diesel drive coupling which will not degrade the low-frequency isolation of the double mount system is considered a difficult and unpredictable design task. The LM2500 and the noise quiet diesels have noise isolating enclosures.

Two diesels of the CODAD system will provide up to 23.5 knots. It is estimated that propeller cavitation inception will occur by this ship speed and therfore noise isolation is not considered a requirement for the other two diesels and they are single mounted and unhooded.

The unlimited operation idle speed of the CODAD diesels limits minimum ship speed to about 11 knots at design propeller pitch. To perform ASW quiet tasks at lower speeds requires reduction in propeller pitch which reintroduces propeller cavitation and considerable increase in underwater noise. The LM2500 can realize a continuous minimum ship speed of about 5 knots at idle power with propeller design pitch.

Using the noise attenuating systems as described above, and on the basis of the mounting transmission radiated noise differences between one LM2500 module and two double-mounted and hooded diesels, and assuming that other noise paths and machinery (drive shafts, flex connections for cooling water, gas ducting, etc.) are made insignificant compared to mounting paths, the comparative ship detectability of the two propulsion systems is assessed as follows:

- At speeds from minimum to 20 knots, ship service diesel generator (DG) sets that are not enclosed and double mounted would be more detectable than either propulsion engines. Therefore, double mounted and enclosed DG sets were selected.
- Above propeller cavitation speeds, machinery noise becomes irrelevant from a detectability point of view. Therefore, Prairie is specified to raise the speed of propeller cavitation inception. It is estimated that with Prairie, 20 knots is achievable before propeller cavitation.
- Because the CODAG ship can maintain design propeller pitch from 5 to 11.5 knots, the CODAG ship has distinctly less detectability in this speed range by broad band sonar.
- At ship speeds from 11.5 to propeller cavitation inception (probably about 20 knots), the diesel has a greater noise energy in the critical octave bands at 250 Hz, 500 Hz and 1 kHz, and is thus likely to be more discernible by sonar arrays which are designed for high gain in the region. Lower frequency noise is generally predominated over by ocean background noises and higher frequency noises are rapidly diminished by propagation losses.

CODAG Propulsion System Control

In order to enhance diesel engine and propeller efficiency, two ratio diesel gearboxes were selected. The schematic of the transmission is shown in Fig. 8. The inboard friction clutches are engaged in the diesel cruise mode and the outboard clutches in the CODAG mode.

To assure proper control of the CODAG, General Electric contracted Yard Ltd. to provide a control study [4] defining a control system that coordinates, according to demand, the diesel engines, gas turbines, and propeller pitch, protects the propulsion machinery, and facilitates operating mode changeover.

The CODAG system operates in three modes: diesel-only (0–21 knots), gas turbine only (0 to 28 knots), and CODAG (28 to 30.3 knots). Two of these modes are identical to CODOG control in current use. The control system maintains approximately linear ship speed/throttle control lever relationship over full range of power range while protecting the propulsion machinery under transient conditions and transitioning from one drive mode to another.

In the diesel-only mode, the shafts operate independently and a separate speed demand is provided to each engine (droop) governor. The control schedules speed demand versus lever position, limits speed demand rate, and controls the load on the engine by adjusting propeller pitch rate as a function of engine speed and fuel rack position.

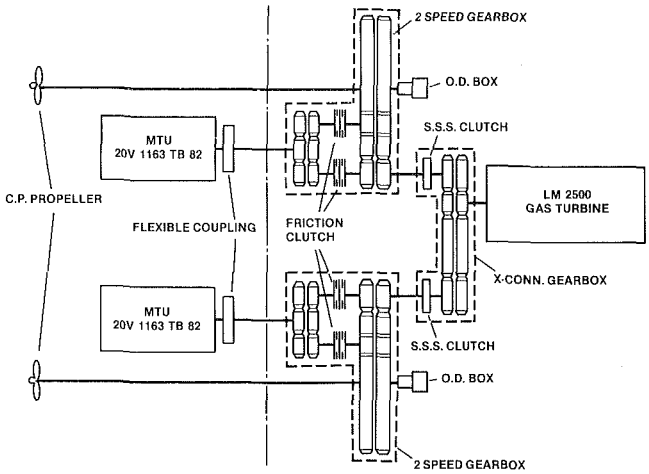

Fig. 8 CODAG transmission

For the gas turbine only mode, lever position is inputted to the engine control as an open-loop power demand, with closed-loop trim on shaft speed and on overspeed topping governor. Average power demand from both levers is used to limit power demand under asymmetric loading conditions (e.g., sharp ship turn).

Changeover, as with CODOG, is permitted below full diesel power if the shaft throttles are aligned. During drive mode changeover from diesel to gas turbine the demand signal to the turbine will be increased to the changeover level at a slow rate to prevent exceeding the permissible differential acceleration for the clutches. Once the clutches have engaged, the diesel fuel racks will reduce, and when below about 15 percent, the diesel clutches will be depressurized. In changing from gas turbine to diesel, the diesel speed demand is increased to changover demand and the friction clutches are engaged and the gas turbine power is then reduced to idle at a rate selected to avoid overloading the diesels.

Transition to CODAG operating mode is always from gas turbine only drive to permit the diesel engines to be unloaded and the CODAG gear ratio engaged at shaft speeds below the equivalent diesel idle speed. In CODAG, an additional function is required to ensure that the diesel engines share load equally. This is a slow-acting speed demand trim function which will match the diesel fuel racks to an average fuel rack value. A revised diesel speed demand schedule is required for CODAG to enable the diesels to follow the desired shaft speed schedule.

The gas turbine power trim function for shaft speed control is not required as the diesel governors will adjust the contribution of diesel power to match the desired shaft speed. Diesel load control is required to prevent overloading the diesels during maneuvering transients and the greater of the two fuel rack signals will be used to reduce pitch on either propeller to preclude diesel overload.

By employing power control (open loop) for the gas turbine and speed control with load sharing for the diesel engines, distribution of load in the CODAG drive is accomplished. The gas turbine will supply power according to its demand schedule and the diesel engines operating to a speed demand schedule based on the desired shaft speed, will share the additional load ensuring operating at that shaft speed. Any changes in load (due to transients, turning, broaching etc.) on one or both shafts will result in a change in system speed to which both diesel governors are designed to respond.

A reduction in load of a magnitude greater than the current diesel power (including power absorption at zero fuel rack of roughly 10 percent), will result in a power turbine overspeed to which the gas turbine topping governor will respond. Any

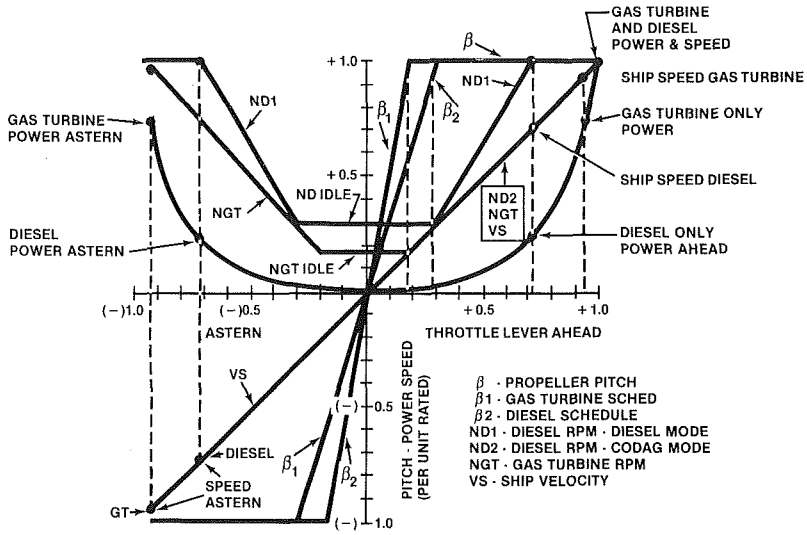

Fig. 9 CODAG control integration

increase in load above the available diesel power (or at a rate greater than the rate of diesel torque increase) will result in a reduction in pitch on both shafts due to diesel load limiting control until the overload is removed or the diesel torque has increased sufficiently to match the load.

Selecting gas turbine drive from CODAG mode, the diesel speed demand would be set to idle and the diesel clutches disengaged. The gas turbine power trim function would be restored at the start of the changeover to maintain the scheduled shaft speed throughout.

If, when in CODAG drive, the throttle is reduced below the equivalent minimum diesel speed position, the control system will automatically depressurize the diesel clutches to prevent underspeeding the diesel engine.

Integration of the system component variables for the various modes of operation is shown in Fig. 9.

The study concludes that the LM2500 CODAG control system is similar to that for CODOG and not significantly more complex. The differences to accommodate the CODAG mode are: CODAG diesel speed demand schedule, diesel load sharing function, revised load control settings and additional changeover logic.

With the described system, the gas turbine *power*, diesel engine *speed*, and propeller pitch are coordinated according to demand schedules, thus ensuring correct distribution of load throughout the power range. Other functions within the control system, such as overspeed governing, propeller pitch variation, etc., protect the machinery during transients.

Reliability and Availability

During the ASME review procedure for suitability of this paper for presentation, several commenters felt the comparative reliability and availability needed to be addressed.

The paper fundamentally considers that there is a large, established, world population of ships using CODAD with conventional supercharged high-speed diesels and a large, established, worldwide population of ships using CODOG with LM2500 gas turbine(s) and high-speed diesels. Since the CODAD has prevailed so long and continues to prevail, a very simple but logical conclusion is that they by and large have quite acceptable reliability and availability. By the same rationale, since the LM2500 CODOG has had a very fast acceptance (86 ships in about 10 years with more orders impending), their reliability and availability must be key qualities of their acceptance. Thus as a baseline, we have two established types of propulsion with good reliability-availability records.

Next we have a proposed innovation for each of these systems. Thus the question would seem to reduce to: "What impact does the proposed innovations have on the reliability and availability of the basis systems?"

The CODAD innovation is the replacement of conventionally supercharged diesels with LCR diesels. The CODOG innovation is to make it CODAG by changing the diesel reduction gears to two ratios. In both cases the end result is more horsepower for small change in equipment weight and volume.

The question was asked: "Since two ratio gears enhance CODAG performance, why were they not considered for the CODAD system?" Our reason is that in the long history of CODAD, that industry has not considered them to provide due benefits and with the increase in low-speed torque characteristics of the LCR diesels, this increases the ship cruise speed attainable on two of four diesels, thus lessening their benefit to CODAD.

The LCR innovation to CODAD introduces new state-of-the-art equipment. It includes, typically, five times the number of supercharger elements per engine, control of the sequencing of the supercharging which includes cylinder bank cutout and associated inactivation of that bank of injectors, charge air transfer system, and the valving upstream of the turbocharger turbines and anti-blow back valves upstream of the turbo compressors.

The CODAG two ratio gear introduces nothing new in propulsion systems. Two ratio gears for CODAG are in marine service. There are added control functions, but these functions can be accommodated in any vintage technology propulsion control desired.

Both LCR CODAD and LM2500 CODAG introduce additional control functions but do not introduce any new technological requirements to already well-established propulsion control systems. The LCR CODAD concept introduces technological innovations to the fundamental prime mover machinery and unit power levels which have never been in a ship. The LM2500 CODAG introduces a gear element and clutching, which are simply functions which use existing marine propulsion hardware.

Assuming the new control sequencing dynamics design for both systems are of similar magnitude, it would appear that the LCR CODAD system will introduce a higher order of probable surprise situations to be worked out thru service experience than LM2500 CODAG.

There is an inclination for some people when concerned about battle damage to equate high reliability to CODAD due

to the number (and presumed redundancy) of diesels. For slow speed operation, CODAD offers four options and CODOG or CODAG three options of prime movers. However, to achieve high speed, a quality probably most desired when battle damage is likely, the quantity of engines required for CODAD diminishes its probability to perform. For example, for the ship to reach a speed between 23 and 28 knots would require the four CODAD engines or the one LM2500 in CODOG or CODAG. If the probability of one engine providing rated power is .99, the probability of the CODAD system reaching speeds over 23 knots becomes .99 [4] or .96, while that of the CODOG or CODAG system is .99 [1] or .99.

Conclusions

Since 1978, the combination of the LM2500 gas turbine and diesel engines have provided highly advantageous propulsion systems for commissioned Navy ships from 220 to 4000 tons displacement.

This paper summarizes four studies, which conclude that the advent of new diesel low compression ratio developments will not eclipse the CODOG-CODAG system advantages. The comparative advantages of CODAG demonstrated herein for a specific 2000 ton ship are generally applicable for other ship displacements and are valid for LM2500 CODOG systems, the choice between CODOG and CODAG being a function of the ship size and speed requirements.

CODAG benefits compared to CODAD systems include:

- Less weight propulsion system, which increases ship payload or if used for fuel increases ship range
- A lower acquisition plus life cycle total costs
- Substantially fewer engine removals with subsequent reduction in overhaul and on-board maintenance man hours
- Lower ship noise detectability
- A propulsion system which contributes very little to IR detectability and is comparable or lower than CODAD at normal missile angles of sight

The combination of diesel and gas turbine propulsion offers distinct advantages for ship propulsion. LM2500 CODOG systems have and are currently demonstrating these daily. LM2500 CODAG can provide an economical and space efficient means to achieve these same operational characteristics for ships where 2 to 3 knots more speed are required than LM2500 CODOG would provide.

References[1]

1 "Installation Assessment of LM2500 CODAG and CODAD Propulsion for a 2000-Ton Frigate," Yard Ltd. Report YR2857, Oct. 1983.

2 "Infrared Radiation Detectability of LM2500 CODAG and CODAD Powered 2000-Ton Frigate," Yard Ltd. Report YR2856, Sept. 1983.

3 "Noise Detectability of LM2500 CODAG and CODAD Powered 2000-Ton Frigate," Yard Ltd. Report YR2870, Oct. 1983.

4 "LM2500 CODAG Propulsion System Control Feasibility Study," Yard Ltd. Report YR2862, Sept. 1983.

[1] Copies of these references may be requested from General Electric through the author.

Flow Distribution Characteristics and Control in Marine Gas Turbine Diffusers

M. K. Ellingsworth
Program Manager,
Office of Naval Research,
Arlington, Va. 22217

Ho-Tien Shu
Research Engineer.

S. C. Kuo
Manager.

United Technologies Research Center,
East Hartford, Conn. 06108

The object of this study was to investigate flow distribution characteristics and control in the marine gas turbine diffusers most suitable for waste heat recovery systems. The major technical problems associated with nonuniform flow distributions in heat-exchanger or flow-equipment systems were reviewed. Various means to alleviate or minimize these undesirable problems were evaluated. Four sets of candidate flow-distribution data were selected from the measured exhaust velocities of typical marine gas turbines for input to the present study. A two-dimensional turbulent flow model for diffusers was developed and computerized, and five diffuser geometries suitable for marine gas turbine waste-heat recovery applications were investigated, based on the actual inlet velocity data. The exit flow distribution characteristics (velocity, mass-flux, pressure recovery, and temperature) and diffuser performance with and without flow-distribution controls were analyzed using the computer programs developed. It was found that nonuniform flow distribution in the gas turbine exhaust can reduce diffuser efficiency to half of that attainable with uniform flow, and that the diffuser exhaust velocities will be more uniform by using guide vanes and/or flow injection than merely using nonsymmetric diffusion angles. The diffuser efficiency can be improved 20 to 36 percentage points by using these contorl means.

Introduction

The successful implementation of open-cycle gas turbines (OCGT) as a ship propulsion engine in the United States and abroad has stimulated interest in various means for further improvements in propulsion efficiency. The OCGT propulsion system indeed has many unique advantages, such as being lightweight, having a small volume, and responding quickly to power variations. However, because of some basic design requirements, constraints, and/or inherent performance characteristics, the specific fuel consumption (sfc) of the current OCGT propulsion systems have been equal to or greater than 0.42 lb/shp-hr [1, 2], which may still be too high for some advanced naval ship applications. One of the inherent performance characteristics is that the sfc of an OCGT when operated at part-load increases almost inversely proportionally to the power rating. This undesirably high part-load sfc is of major concern to the Navy, because most naval ships are operated under part-load conditions (such as cruise) for most of the time. Therefore, many alternative propulsion concepts have been proposed and investigated in the past to improve their part-load performance [3]. One of these concepts is to use Rankine-Cycle Energy Recovery (RACER) system to recover waste-heat from the gas turbine exhaust [4]. However, in order to implement this concept in a practical propulsion systems the flow distribution characteristics of the gas turbine exhaust and their effect on the waste-heat exhanger performance must be properly assessed before designing and building this altenative propulsion system.

A thorough knowledge of flow distribution problems and the necessity of being able to quantitatively analyze problems involving flow distribution has become increasingly important in modern fluid flow and heat transfer systems. Of particular concern is the impact of flow-distribution nonuniformity on thermal performance, component design, and the reliability of a flow system. In general, the incentives for flow-distribution control studies include: (*i*) providing a better understanding of the flow dynamics; (*ii*) establishing guidelines for selecting the design concept and flow system geometry; (*iii*) predicting the actual (not just idealized) system performance; and (*iv*) defining the research and development for the flow system identified. Therefore, the objectives of this paper are to discuss the basic understanding of flow-distribution problems found in many existing COGAS components, and also to provide some guidelines for designing more reliable and efficient marine gas turbine waste-heat recovery systems.

Characteristics of Flow Maldistribution

Flow distribution nonuniformity occurs almost in every real flow system. There are several mechanisms which can

Contributed by the Gas Turbine Division of THE AMERICAN SOCIETY OF MECHANICAL ENGINEERS and presented at the 28th International Gas Turbine Conference and Exhibit, Phoenix, Arizona, March 27–31, 1983. Manuscript received at ASME Headquarters December 20, 1982. Paper No. 83-GT-51.

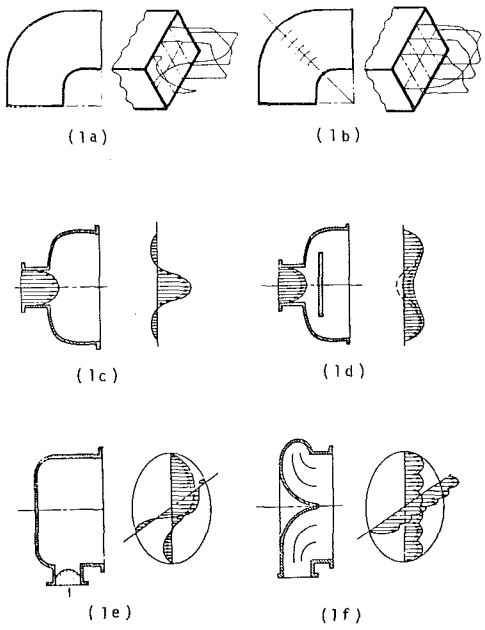

Fig. 1 Typical flow distribution control methods

cause maldistribution of fluid flow. These mechanisms which can be attributed to single or multiple factors are either related to flow properties (such as viscosity or body force effects), flow geometry (such as a sharp-edged orifice, square-shouldered expansion or contraction, nozzle diffuser, bond, etc.), or a flow control device (such as a baffle, blockage, flow injection or extraction, local heating or cooling, etc.).

Nonuniform Flow Problems and Control Methods. The most important and obvious consequence of flow maldistribution is on the pressure loss. Excessive pressure loss means that the system will require more pumping power otherwise its mass flow rate will be lower than the design value. If the flow distribution across a heat transfer matrix is nonuniform, it would not only reduce the heat transfer performance but also create thermal/mechanical stress concentrations and local overheat, dryout, or freezing problems [5, 6]. The acute difficulties created by hot spots in nuclear reactors and in coal-, oil-, and gas-fired boilers are typical examples of the consequences of flow maldistribution In addition, the tube fouling and inlet-end erosion problems of marine heat exhangers and power plant condenser waterboxes represent another type of flow-distribution problem. The combined effect of flow rotation and excessive turbulence induced by pumps, and poor inlet piping configurations or waterbox design can also result in serious operating problems [7].

The combined effects of abrupt turning, wall friction, and the flow-jet swirling from the free turbine often generate a highly turbulent and nonuniform flow-distribution inside and at the exit of the exhaust elbow (collector box). For gas turbines alone, this nonuniform flow has been a critical problem in efforts to improve the gas turbine performance, particularly at high engine power settings [8]. Experience shows that flow maldistribution is always accompanied by undesirable high pressure loss, and that a 1 percent increase in pressure loss is approximately equivalent to a 1 percent loss in engine power. For a combined gas and steam turbine (COGAS) system, the severe flow distribution nonuniformity at the exit of the collector box not only affects the diffuser design and performance but also can significantly impair the waste-heat boiler performance and life expectancy [8, 9].

Numerous flow-distribution control methods have been

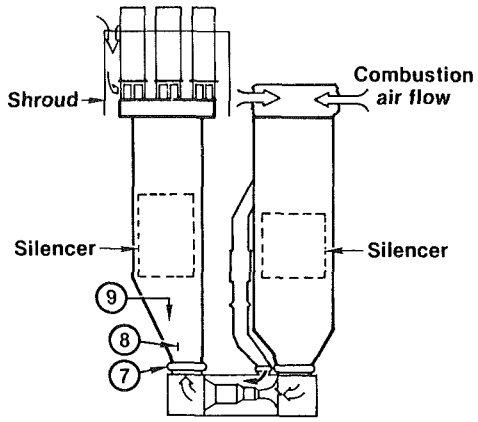

Fig. 2 DD963-class destroyer propulsion engine combustion air and exhaust ducting system

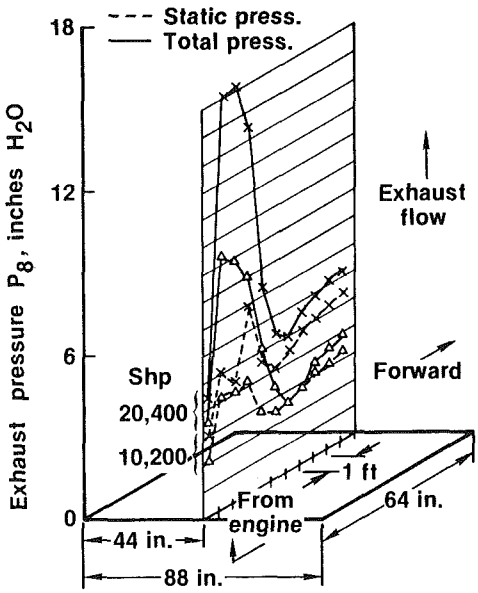

Fig. 3 Exhaust pressure map of DD963-class prototype gas turbine—module 2B

used by various designers in the past to achieve specific goals for a given flow system. These methods can be generally classified into two categories: one employs internal guiding or disturbing mechanisms (such as flow guide vanes, louvers, baffles, screens, wedges, buffer plates, or agitators), and the other uses external means of control, such as changing the flow boundary through variation of flow area, flow injection, flow suction, local heating, local cooling and shaking. The internal control methods, in general, are more efficient than the external methods. The selection of any particular flow distribution control method should depend on the characteristics of the flow system being investigated.

The velocity distribution immediately downstream of a bend is always irregular due to the flow separation and secondary flow inside of the bend (Fig. 1(*a*)). A typical case is seen in the design of wind tunnels. To improve the flow distribution, the turning vanes as shown in Fig. 1(*b*) are commonly used. The velocity distribution through a heat transfer matrix may be affected by the manner in which fluid enters the inlet plenum chambers. If a high-velocity fluid stream enters a plenum chamber axially (Fig. 1(*c*)), it is apparent that a high-velocity jet will shoot across the plenum chamber and impinge on the center of the heat transfer matrix, thus the velocity through the center of the matrix will be higher than that through the outer annular zone. Flow

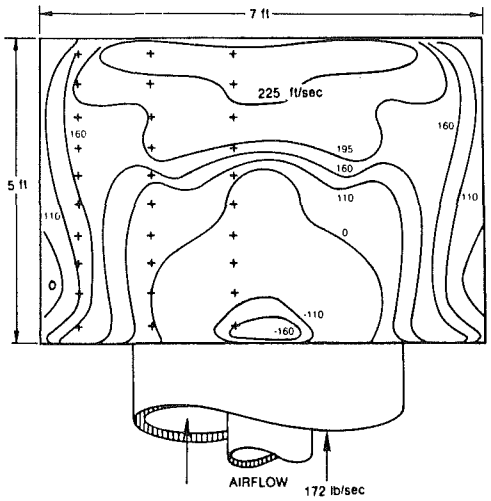

Fig. 4 Typical velocity profiles at the exit of gas turbine—FT4 test model

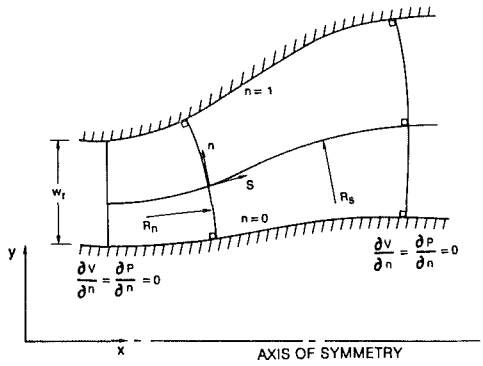

Fig. 5 Orthogonal streamline coordinate system

distribution control devices such as those shown in Fig. 1(*d*) can be used to reduce the jet effect before the flow is discharged into the plenum. This flow distribution method is simple and effective and has been employed widely in the design of gas-to-gas recuperators. The apparent disadvantage of this arrangement is the creation of a stagnation region in the center as well as eddies behind the two outer edges of the baffle, with the consequent increase in pressure loss and pumping power. If the fluid is brought into the plenum of the heat exchanger from the side, significantly different effect may occur. The velocity distribution of this configuration is depicted in Fig. 1(*e*). This undesirable flow maldistribution can be avoided by redesigning the plenum chamber as shown in Fig. 1(*f*). This method has been successfully used as the exchanger head in many air heater designs and other flow systems.

Acquisition of Turbine Exhaust Flow-Distribution Data. The study reported here was based on actual flow distribution data measured at the exit of the exhaust elbow of two typical marine gas turbines (Fig. 2, Points 1 or 2). The flow data needed for the study include the velocity profiles, the temperature, and the pressure.

Figure 3 and 4 represent the typical velocity maps obtained from two existing marine gas turbines. Figure 3 contains two sets of flow distribution data provided by ONR for two different power levels of a current marine gas turbine. The pressures are presented in terms of inches of water head. The gas temperatures were identified to be 837° F (447°C) for full-load operation and 790° F (421°C) for part-load operation. The dimensions of the diffuser inlet cross section are approximately 5 ft by 7 ft. Figure 4 shows a typical velocity map obtained at UTRC from a scale model of exhaust elbow with a special shape of inserts inside the collector box. The corresponding gas temperature for the flow distribution is 885° F (474° C).

The results presented in Figs. 3 and 4 show a unique phenomena: the flow distributions at the exit of the exhaust elbow are highly irregular and nonuniform. The results also show that the majority of the flow was concentrated at the rear end of the elbow and that reversed flow was observed in the regions near the front end. No two similar velocity-distribution maps were found. It should also be noticed that because the exhaust flow is subsonic, these velocity distribution profiles will change when the downstream condition changes. The actual flow distribution data with the RACER installed were not available at the time of this investigation. Therefore, the results shown in Figs. 3 and 4 were used as inputs to the diffuser model developed, as described in the following section.

Two-Dimensional Turbulent Flow Model

The flow-distribution characteristics investigated for a two-dimensional diffuser include the velocity, the mass flux, the pressure, and the temperature. These flow-distribution characteristics can be described by a set of governing equations derived from conservation of mass, momentum, and energy, and the equation of state. The procedure of formulating a working model for the present study consists of three steps: (*i*) constructing an orthogonal curvilinear coordinate system for two-dimensional diffusers (Fig. 5); (*ii*) formulating a two-dimensional turbulent flow model based on orthogonal curvilinear coordinate systems; and (*iii*) manipulating the analytical model to obtain a set of equations that can be solved numerically by computer. While detailed descriptions of this working model are given in [10], only a brief discussion is presented here.

Let "*s*" and "*n*" represent the velocity potential in the streamwise direction and the stream function in the normal direction, respectively (Fig. 5). Then, the equation of motion for a two-dimensional, steady-state compressible flow in the (*s*,*n*) coordinates can be expressed as

Continuity equation

$$\frac{\partial}{\partial s}\left(\frac{w\rho u_s}{V}\right)+\frac{\partial}{\partial n}\left(\frac{w\rho u_n}{V}\right)=0 \tag{1}$$

s-momentum equation

$$\rho\left[u_s V\frac{\partial}{\partial s}(u_s)+u_n V\frac{\partial}{\partial n}(u_n)-\frac{u_n^2}{R_n}+\frac{u_s u_n}{R_s}\right]=-\frac{V}{w}\frac{\partial}{\partial s}\left(\frac{w\mathbb{P}}{V}\right)+\frac{V^2}{w}\left[\frac{\partial}{\partial s}\left(\frac{w\sigma'_{ss}}{V}\right)+\frac{\partial}{\partial n}\left(\frac{w\sigma_{ns}}{V}\right)+\frac{w\sigma_{sn}}{R_s}-\frac{w\sigma'_{nn}}{R_n}\right] \tag{2}$$

n-momentum equation

$$\rho\left[u_s V\frac{\partial}{\partial s}(u_n)+u_n V\frac{\partial}{\partial n}(u_n)+\frac{u_s u_n}{R_n}-\frac{u_s^2}{R_s}\right]=-\frac{V}{w}\frac{\partial}{\partial n}\left(\frac{w\mathbb{P}}{v}\right)+\frac{V^2}{w}\left[\frac{\partial}{\partial s}\left(\frac{w\sigma_{sn}}{V}\right)+\frac{\partial}{\partial n}\left(\frac{w\sigma'_{nn}}{V}\right)+\frac{w\sigma_{sn}}{R_n}-\frac{w\sigma'_{ss}}{R_s}\right] \tag{3}$$

Energy equation

$$\rho\left[u_s V\frac{\partial}{\partial s}(C_p T)+u_n V\frac{\partial}{\partial n}(C_p T)\right]=\frac{V^2}{w}\left[\frac{\partial}{\partial s}\left(\frac{wq_s}{V}\right)+\frac{\partial}{\partial n}\left(\frac{wq_n}{V}\right)\right]+\Phi \tag{4}$$

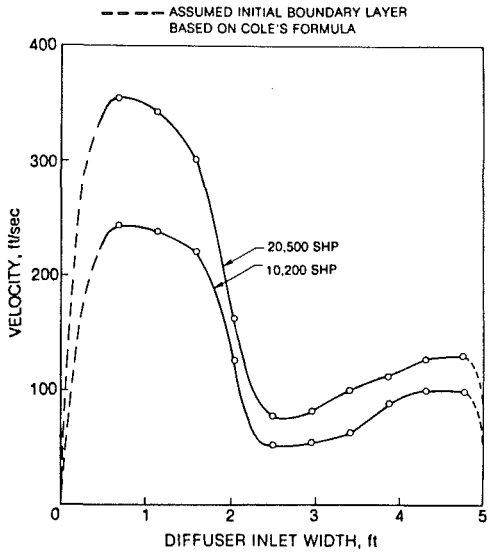

Fig. 6 Calculated exhaust gas velocity profiles for DD963-class prototype gas turbine module 2B

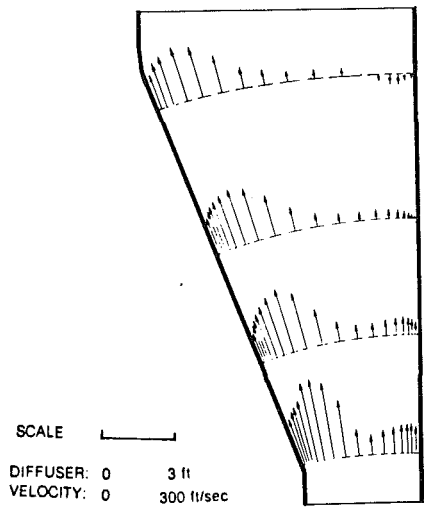

Fig. 7 Calculated velocity distribution in a diffuser without flow distribution control

Equation of state

$$\mathbb{P} = \rho \mathbb{R}\, T \tag{5}$$

In equations (1–5), V represents metric scalar coefficient or potential flow velocity, w represents the width of diffusers, $\sigma's$ and Φ are the stress tensors and dissipation functions. This set of governing equations are used to solve for five unknowns, ρ, u_s, u_n, $\mathbb{P}$, and t, which stands for density, velocity components along the s- and n-coordinates, static pressure and temperature, respectively. Mathematically this set of equations is classified as elliptic and can be solved if all the boundary conditions at the inlet, the exit, and the walls of diffusers are provided. However, the computation procedure would require extremely large data storage and computational time. Therefore, these equations were parabolized by employing the so-called "thin channel assumption," and the parabolized equations were then solved by the numerical forward-marching method. The boundary conditions for the parabolized equations should reflect that both normal and streamwise velocities are zero at the wall, and that the velocity, temperature, and pressure distributions are given at the diffuser inlet (Fig. 5).

The turbulent flow models which were used in the computation of the Reynolds stress in stress tensors ($\sigma's$) and dissipation function (Φ), are the same as that used by Smith [11], who assumed that the inner layer region of the turbulent flow is governed by Prandtl's mixing length theory with a Van Driest damping factor, and that the outer layer region is governed by an eddy model proposed by Clauser [12]. Based on this assumption, the effective viscosity for the inner and outer region of the flow fields are given, respectively, as

$$\mu_{\text{eff}} = \mu\left\{1 + 0.16 y_t [1 - \exp(-y_t\sqrt{\tau_t}/26)]^2 \frac{du_t}{dy_t}\right\} \tag{6}$$

$$\mu_{\text{eff}} = 0.008\, \mu N_R\, \rho\, w\, (u_\infty - \bar{u}) \tag{7}$$

where μ represents the molecular viscosity, and u_t, y_t and τ_t are defined as

$$\left.\begin{aligned} u_t &= u/\sqrt{\tau_w/\rho} \\ y_t &= n\sqrt{\tau_w \rho/\mu} \\ \tau_t &= \tau/\tau_w \end{aligned}\right\} \tag{8}$$

The subscripts ∞ and w represent the maximum and wall values at a given streamline station, respectively. $\bar{u}$ represents the averaged velocity across the diffuser width, w. N_R stands for Reynolds number which is calculated based on average flow properties. The empirical constants, 0.16, 26, and 0.008 which appear in equations (6) and (7) are the values suggested in [13].

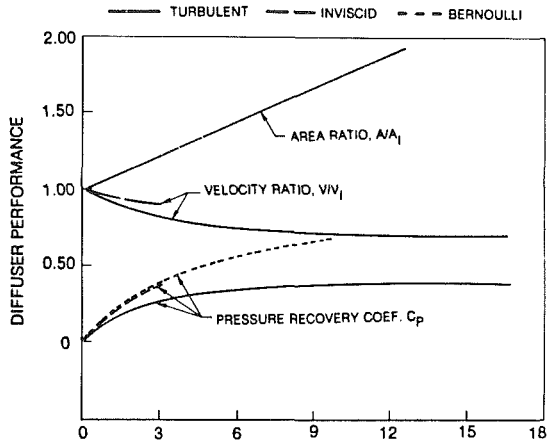

Fig. 8 Comparison of performance characteristics for a two-dimensional diffuser

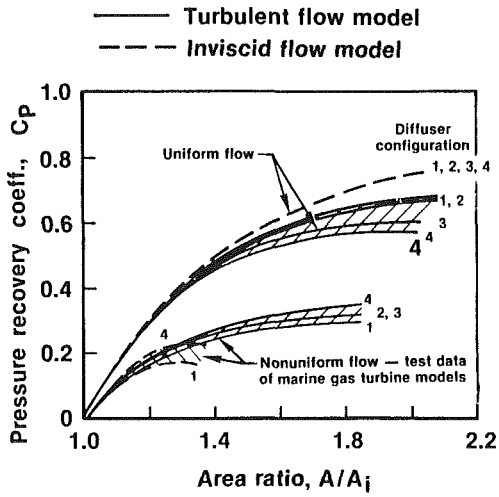

Fig. 9 Comparison of performances for two-dimensional diffusers

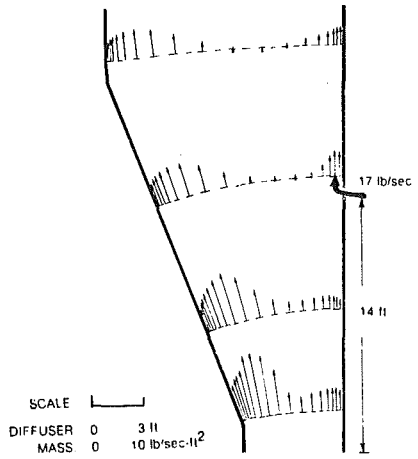

Fig. 10 Mass-flux profiles for a typical diffuser with one flow injection

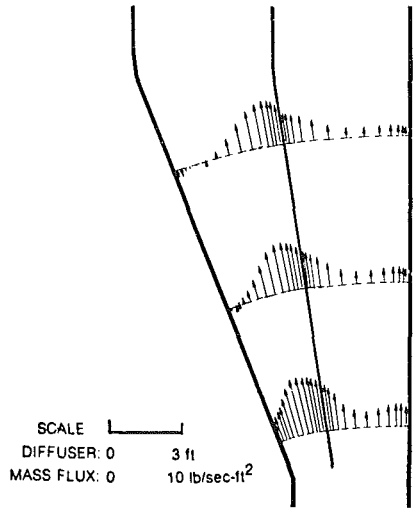

Fig. 11 Mass-flux profiles for a typical flow system with one flow-distribution vane

By using equations (6–8), the parabolized governing equations are further reduced to finite-difference form so that they can be solved by computer. The finite-difference equations were rearranged and expressed in matrix form which were solved by standard block-elimination method [10].

The flow model discussed above has been implemented in FORTRAN language on a UNIVAC 1110/80 computer system.

Performance Analysis

The computer program developed was used in the diffuser performance analyses and the results obtained are presented herein. The selection of a baseline diffuser configuration is essentially based on the geometric configuration of the engine exhaust elbow, the type of waste-heat boiler, and the space available for installation. Because the current Navy interest in recovering the waste-heat is essentially for the main propulsion engine, and because most of the marine propulsion gas turbines have rectangular exhaust elbows, a two-dimensional diffuser with rectangular cross section was selected as the baseline configuration. It was found that the exhaust collecting box was a 5-ft by 7-ft exit cross section which was then used as the inlet dimension of the diffuser. The length of the diffusers was assumed to be 18 ft for easy installation on the ship. The diffuser angles were varied to investigate its impact on diffuser performance using different inlet flow distribution data.

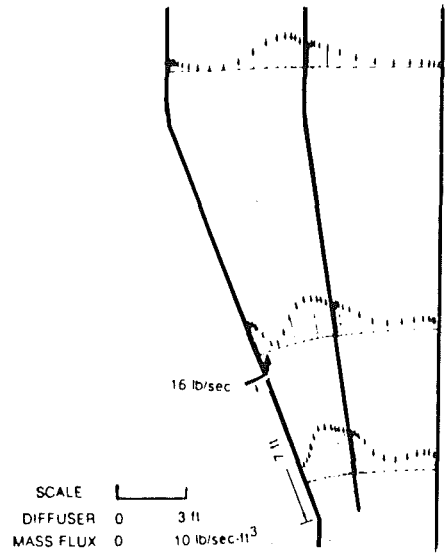

Fig. 12 Mass-flux profiles for a typical flow system with one flow-guide vane and one flow injection

Diffuser Performance. A total of twenty-five cases were analyzed, consisting of five different diffusion angles with five sets of flow distribution data. The flow distribution characteristics investigated are the velocity profiles, the mass flux distribution, the pressure-recovery, and the temperature profiles. The two typical inlet velocity profiles used in the analyses are shown in Fig. 6 and typical results obtained are shown in Fig. 7.

The results shown in Fig. 7 were plotted using the scale factor given in the lower left corner. The arrows represent the magnitude of the flow-distribution data, and the dash lines represent the actual location of the streamline station. It was found (Fig. 7) that without implementing an effective flow-distribution control device, the flow-distribution non-uniformity remains almost unchanged throughout the flow field. Boundary layer separation exists in all the nonuniform flow cases and the separation always occurs on the wall of the lower velocity side. Figure 7 also shows that the sluggish flow, which appears near the centerline region of the diffuser in the initial profile, has become more uniform as the fluid flows along the diffuser. This is due to the viscosity effect which would slow down the fast-moving fluid elements and speed up the slow-moving elements.

Figure 8 shows the velocity ratio and pressure-recovery coefficient as a function of diffuser length. The results were obtained by integrating the velocity profile and pressure-recovery profiles along the velocity-potential line at each streamline station and then weighted by the mass-flow rate. It was found that most kinetic energy has been converted into pressure in the first half (approximately 10 ft) of the diffuser length. In the second half of the diffuser, because boundary layer separation occurred, diffuser efficiency remains constant. This phenomenon was seen in all nonuniform flow cases. Figure 8 also presents the pressure-recovery coefficient calculated from inviscid flow theory and also from the Bernoulli theory. The difference between the two curves represents the effect of nonuniform flow distribution on the diffuser performance.

Comparisons of two-dimensional diffuser efficiencies for different cases are shown in Fig. 9. In this figure, the solid line

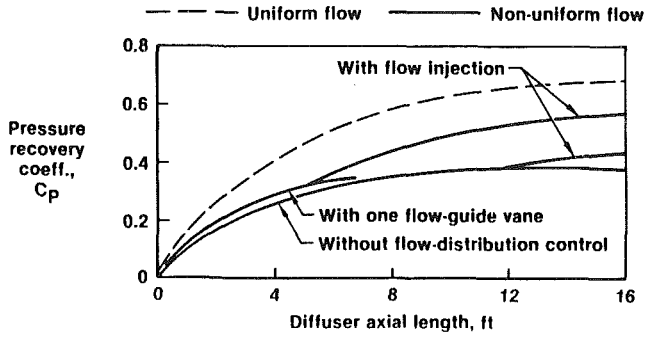

Fig. 13 Comparison of a diffuser performance for a typical configuration with and without flow-distribution control

and dotted line represent the results obtained based on turbulent flow theory and inviscid flow theory, respectively. These results can be classified into two groups: the upper group is for uniform flow cases; and the lower one is for the nonuniform flow cases. For the uniform flow cases the results from the inviscid flow models fall on top of each other, and the values are found to be almost equal to those obtained from the Bernoulli equation. The results obtained from turbulent flow models varied among the four diffusers, and the values are significantly lower than those from the inviscid flow model.

For the nonuniform flow cases, the performance results of the inviscid flow model are computed only up to an area ratio of approximately 1.3; beyond that point, reverse flow developed in the core region and the governing equations are not valid. On the other hand, the turbulent flow model does provide performance results up to an area ratio as high as 2.0. The results of this study indicated that the diffuser efficiency based on the actual flow-distribution data of marine gas turbine exhaust is approximately 50 percent lower than that based on an assumption of uniform flow.

Flow Distribution Control. Results of parametric analyses for diffuser performance presented above indicate that the nonuniform flow distribution at the diffuser inlet would remain nonuniform in the absence of flow-distribution control as the fluid travels through the diffuser. The nonuniform flow distribution would cause as much as a 50 percent reduction in diffuser efficiency (or the pressure recovery coefficient) as compared with the uniform flow case. This would definitely offer the incentives for developing and implementing suitable flow distribution control devices for diffusers.

Among those flow-distribution control methods mentioned earlier, three flow-distribution control methods judged to be more effective were investigated: (*i*) flow injection; (*ii*) flow-distribution vanes; and (*iii*) a combination of methods (*i*) and (*ii*). The injection flow could be the cooling flow from the casing of the gas turbine.

Figure 10 shows the mass flux distribution characteristics for the candidate diffuser with one point of flow injection on the right sidewall of the diffuser. The flow injection slot was located approximately 14 ft from the diffuser inlet, which is the location where boundary layer separation occurred. The flow rate of injection was approximately 17 lb/s (or 10 percent of the main stream). It was found that the boundary layer separation was completely suppressed, and that the diffuser performance improved slightly (to be discussed later in conjunction with Fig. 13). However, flow distribution at the exit of the diffuser was not improved significantly.

To use flow-distribution vanes, it was assumed that the mass flow rate and the flow area at the diffuser exit were both equally divided into two channels. The mass flux profiles at three selected streamline stations are shown in Fig. 11. This figure also shows the development of boundary layer flow separation actually started approximately 4 ft from the diffuser inlet. The numerical calculation was continued and finally interrupted due to numerical instability at approximately 15 ft from the diffuser inlet. Again, the flow distribution at the diffuser exit for this case is still not quite sufficiently uniform.

The last method to control the flow distribution was to combine the above two methods, namely, flow injection and a flow-guide vane. Results of this study are selectively presented in Fig. 12 for the mass flux distribution. The flow injection was made on the left-hand wall of the diffuser at approximately 7 ft from the diffuser inlet. The rate of injection was approximately 16 lb/s (approximately 9 percent of the main stream). Figure 12 clearly shows that the flow distribution at the diffuser exit for this case is much more uniform as compared with those shown in Figs. 10 and 11.

Comparisons of diffuser performance with and without flow distribution control for the diffuser configuration considered are shown in Fig. 13. In this figure, the dotted curve represents the diffuser efficiency obtained from a uniform flow assumption and has a maximum value of approximately 75 percent, while the bottom curve represents the efficiency of the same diffuser based on nonuniform flow at the inlet without flow-distribution control. This curve has a peak value of approximately 36 percent. The results of diffuser performance analysis with three flow-distribution control methods fall between the above extremes as expected. It was found that with one point of flow injection and one flow-distribution guide vane, an improvement of more than 20 percentage points in diffuser efficiency can be expected as compared with the results from the case without flow-distribution control.

Conclusions

The flow distribution in marine gas turbine exhausts is highly irregular and nonuniform. This nonuniform flow will remain nonuniform through a two-dimensional diffuser unless an effective means of flow distribution control is implemented. The method of using nonsymmetric diffusion angles alone will not improve either the flow distribution or the diffuser efficiency. However, this nonuniform flow distribution can be made more uniform for waste-heat recovery applications by using a specially designed diffuser which incorporates appropriate guide vanes and, if necessary, additional flow injection methods. Other methods, such as internal modifications of the elbow with different shapes of inserts, turing vanes or baffling, may also be considered. With properly designed flow-distribution control, an improvement of approximately 20 to 36 percentage points in diffuser efficiency can be expected.

The boundary layer separation caused some difficulties in analyzing the diffuser performance when using the nonuniform velocity distribution data. These difficulties disappeared when flow injection was considered for velocity distribution control.

Acknowledgment

The work described in this paper was performed by the United Technologies Research Center as part of the research program sponsored by the Office of Naval Research under Contract N00014-80-C-0476, Mod. No. P00002.

References

1 Critelli, F. X., and Rowen, W. L., "Five Year's Experience in Applying Heavy-Duty Gas Turbines to Marine Propulsion," The Society of Naval Architects and Marine Engineers, Annual Meeting, New York, Nov. 1975.

2 Rains, D. A., DD-963 Power Plant, Marine Technology, Jan. 1975.

3 Kuo, S. C., Horton, T. L. O., and Shu, H. T., "Lightweight Propulsion Systems for Advanced Naval Ship Applications, Part I-Systems Studies," UTRC Report R77-952566-5, May 1977.

4 Marron, H. D., "Gas Turbine Waste Heat Recovery Propulsion for U.S. Navy Surface Combatants," *Naval Engineers Journal*, Oct. 1981.

5 Chiou, J. P., "The Effect of Nonuniform Fluid Flow Distribution on Thermal Performance of Crossflow Heat Exchanger," ASME Paper No. 77-WA/HT-3, Nov. 27-Dec. 2, 1977.

6 Frass, A. P., and Ozisik, M. N., *Heat Exchanger Design*, John Wiley & Sons, Inc., 1965.

7 Richard, C. C., "Flow Patterns and Velocity Measurements in a Power Plant Condenser Waterbox," Naval Systems Engineering Department, U. S. Naval Academy, Annapolis, Md., 1979.

8 Colombo, R. M., "FT4 Rectangular Exhaust Duct Investigation," UAC Report H233877-1, May 1969.

9 Bauver, W. P., II, and McGowan, J. G., "Modeling the Distribution and Effects of Steam Flow in Marine Superheaters," *Combustion*, Mar. 1980, pp. 36-44.

10 Shu, H. T., and Kuo, S. C., "Flow Distribution Control Characteristics in Marine Gas Turbine Waste-Heat Recovery Systems, Phase I—Flow Distribution Characteristics and Control in Diffusers," UTRC Report R81-955200-4, Aug. 1981.

11 Smith, A. M. O., and Cebici, T., "Numerical Solutions to the Turbulent Boundary Layer Equations," Douglas Aircraft Report No. DAC 33735, May 1967.

12 Anderson, O. L., "Calculations of Internal Viscous Flow in Axisymmetric Ducts at Moderate to High Reynolds Number," *Computers and Fluids*, Vol. 8, 1980, pp. 391-411.

An Experimental Study of Local and Mean Heat Transfer in a Triangular-Sectioned Duct Rotating in the Orthogonal Mode

R. J. Clifford
Head of High-Temperature Technology Department, Rolls-Royce, Ltd, Bristol, England

W. D. Morris

S. P. Harasgama

Department of Engineering Design and Manufacture, University of Hull, Hull, England

This paper presents a selection of experimental results that examines the influence of orthogonal-mode rotation on local and mean heat transfer in a triangular-sectioned duct with potential application to cooled turbine rotor blades. It is shown that Coriolis acceleration can have a beneficial influence on mean heat transfer relative to the nonrotating case at the lower range of turbulent pipe flow Reynolds numbers studied. Also, rotational buoyancy has been shown to have a noticeable effect over this same Reynolds number range in that progressively increasing buoyancy brings about an attendant reduction in heat transfer. As the Reynolds numbers are increased, say, beyond 30,000, buoyancy effects were found to have little influence on mean heat transfer over the speed range covered. Local axial variations in heat transfer along the duct were also measured, and severe reductions in local heat transfer were detected under certain operating circumstances.

Introduction

Recent trends in the design of aero, industrial and marine gas turbines have reflected the economic prizes that can be realized by improvements to the specific fuel consumption. In this respect, the well known thermo-economic advantages of utilizing high levels of turbine entry temperature, with the inevitable and consequential attendant problems of material degradation, necessitates that extremely complex air cooling channels are designed into the heavily loaded stator and rotor blades. The complexity of these cooling channel geometries is typified in Fig. 1, which illustrates the evolution of local cooling enhancement methods that are commonly in current use inside stator and rotor blades. These enhancements in cooling have enabled turbines to operate with gas temperatures well in excess of the maximum allowable metal temperature as indicated in Fig. 1. In the past, much effort was directed at measuring and understanding the gas side heat transfer, but only rudimentary studies were carried out on internal cooling geometries. This seemed reasonable at the time, because the cooling side heat transfer had only a minor influence on the heat balance and metal temperatures tended toward that of the hot gas. However, as turbine entry temperatures increased, the coolant side heat transfer coefficients played a significant role in the heat balance (Fig. 1) and the lack of understanding in this area is only now being redressed. Morris and Ayhan [1, 2] have assessed the influence of

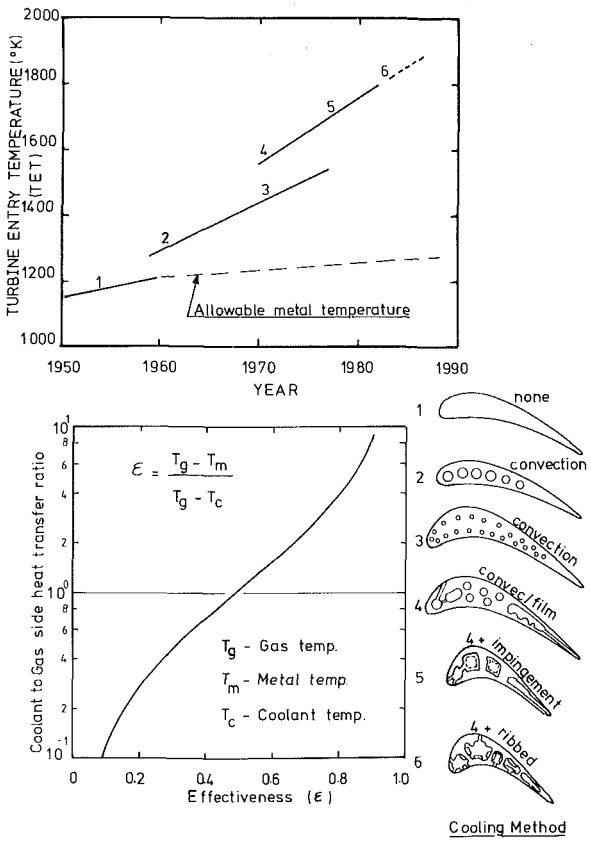

Fig. 1 Influence of cooled blades on TET and effectiveness

Contributed by the Gas Turbine Division of THE AMERICAN SOCIETY OF MECHANICAL ENGINEERS and presented at the 29th International Gas Turbine Conference and Exhibit, Amsterdam, The Netherlands, June 4-7, 1984. Manuscript received at ASME Headquarters January 9, 1984. Paper No. 84-GT-142.

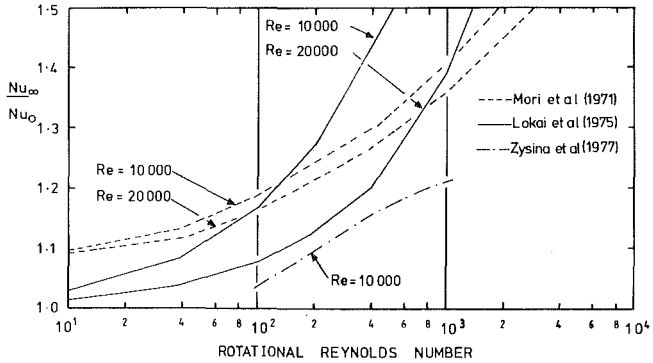

Fig. 2 Correlations for turbulent heat transfer enhancement

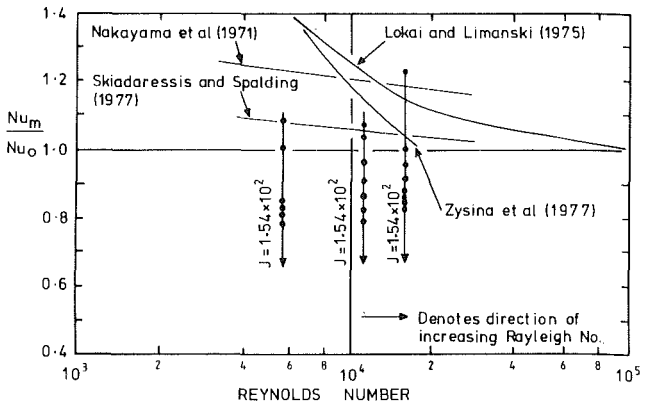

Fig. 3(*a*) Influence of rotation on turbulent relative mean Nusselt number with radially outward flow after Morris and Ayhan [1] circular duct, rotational speed = 1000 rpm

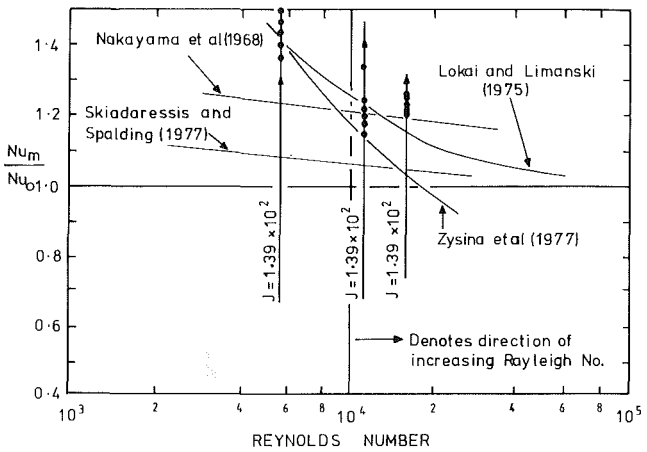

Fig. 3(*b*) Influence of rotation on turbulent relative mean Nusselt number with radially inward flow after Morris and Ayhan [2] circular duct, rotational speed = 1000 rpm

rotation on the heat transfer within a circular passage, while Clifford et al. [3] have conducted static tests on complex passage shapes.

In addition to the geometrical complexities, the determination of either local or mean heat transfer inside rotor blades is further complicated by the fact that the coolant passages are themselves rotating. This means that in general three additional inertial-type forces may influence the flow field and consequently the heat transfer. These are concerned with the well-known Coriolis and centripetal components of acceleration and, if the rotor speed is unsteady, the rotor's angular acceleration.

The present paper reports the results of some preliminary investigations into the overall influence of rotation on heat transfer inside a straight triangular-sectioned duct that rotates about an orthogonal axis. Channels of triangular section are often located in the trailing edge region of the blades. This study forms part of a longer term project to systematically identify the parameters likely to affect heat transfer performance inside turbine rotor blades and relatively simple geometries are being considered in the first instance.

Prior to presenting data for the triangular-sectioned duct, previous work with circular-sectioned ducts will be briefly reviewed in order to clarify the background material against which the present study was planned.

With orthogonal-mode rotation, Coriolis components of acceleration act as a source term for the generation of secondary flows that interact, via the energy equation, with the wall to fluid convective mechanism. Theoretical studies which attempt to account for this effect in the turbulent regime of interest to the turbine application have all predicted an enhancement in heat transfer, and experimental studies have to some extent confirmed that Coriolis acceleration has a beneficial effect on heat transfer (see for example Mori et al. [4], Skiadaressis and Spalding [5], Lokai and Limanski [6], Zysina et al [7]). Figure 2 illustrates the outcome of using the recommendations resulting from such studies for quantifying the influence of Coriolis acceleration. The data are presented in a form which assumes that the ratio of developed Nusselt number for rotating conditions to that obtained when stationary, but with the same throughflow Reynolds number can be expressed as

$$\frac{\mathrm{Nu}_\infty}{\mathrm{Nu}_0} = \phi[\mathrm{Re}, J] \tag{1}$$

where Nu_∞ is the developed Nusselt number with rotation, Nu_0 is the developed Nusselt number when stationary but operating with the same pipe flow Reynolds number. Because the results given are for air only, no Prandtl number has been included.

Although all proposals (see original texts for precise details) imply that heat transfer is enhanced with increases in the

Nomenclature

A = duct cross-sectional area
Cp = specific heat at constant pressure
d = equivalent hydraulic diameter
h = heat transfer coefficient
H = midspan eccentricity
J = rotational Reynolds number $= \Omega d^2/\nu$
k = conductivity of test section material
$\dot{m}$ = mass flow
Nu = Nusselt number $= hd/k$
Nu_m = mean Nusselt number
Nu_0 = mean Nusselt number at zero speed
Nu_∞ = developed mean Nusselt number
Pr = Prandtl number $= \mu \mathrm{Cp}/\mathrm{k}$
Ra = rotational Rayleigh number

$$= \frac{H\ \Omega^2\ \beta\ d^3\ (\Delta T)}{\nu^2} \mathrm{Pr}$$

Re = Reynolds number based on equivalent hydraulic diameter $= \dot{m}d/\mu A$
ΔT = difference between wall and fluid temperatures

Greek Symbols

β = volume expansion coefficient
ν = kinematic viscosity
μ = dynamic viscosity
Ω = rotational speed

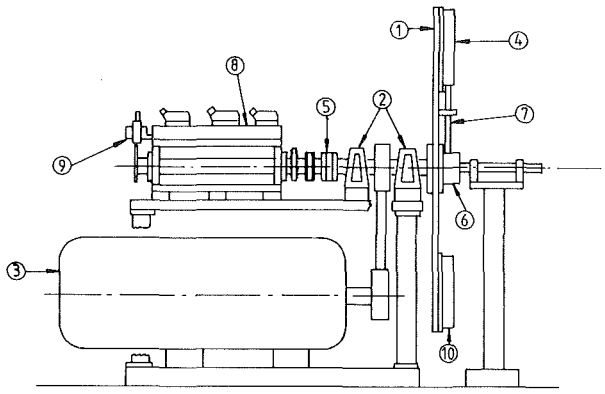

Fig. 4 Test rig

Table 1 Range of test variables

Length of test section (mm)	150.0
Conductivity of Test section (W/mK)	111.0
Cross section (Triangular)	10 mm base with 30^0 apex angle
Equivalent diameter (mm)	7.67
Mid span eccentricity (mm)	250.0
Mid span centripetal acceleration	$0 - 1.1 \times 10^4$
Air coolant	with radially outward flow
Flow rate range (Kg/s)	$1.4 \times 10^{-3} - 1.02 \times 10^{-2}$
Rotational speed range (rev/min)	0 - 2000 nominally
Heater power range (W)	15.0 - 200.0
Through flow Reynolds number range	6500 - 45500
Rotational Reynolds number range	$2.0 \times 10^2 - 1.23 \times 10^3$
Rotational Rayleigh number range	$5.0 \times 10^4 - 8.0 \times 10^6$

rotational Reynolds number, there is serious quantitative discrepancy in absolute terms.

The recognition that large fluid density variations would be present in the rotor blade application with a simultaneous extremely large artificial body force field due to the centripetal accelerations, led Morris and Ayhan [1, 2] to attempt a systematic investigation of the complex interaction likely to exist between the Coriolis source for secondary flow generation and centripetal buoyancy. Further, because the influence of centripetal buoyancy is to cause the warmer and, consequently, less dense regions of fluid to move towards the axis of rotation, the interaction of this effect with the customary forced convection mechanisms, owing to the throughflow Reynolds number, would be dependent on whether the throughflow was radially outward or inward: a further complication in an already complex flow field. Figures 3(*a*) and 3(*b*) illustrate the salient features that emerged from this earlier study of Morris and Ayhan [1, 2], which, it should be noted, was conducted with circular-sectioned ducts fitted with calming sections to permit some degree of flow development prior to the onset of heating.

In Fig. 3(*a*), the relative mean Nusselt number variation with throughflow Reynolds number for radially outward flow has been plotted for one value of the rotational Reynolds number, J, but with a variety of values of the representative wall to fluid temperature difference. Centripetal buoyancy may be characterized by a Rayleigh number that uses the centripetal acceleration at the midspan location of the heated channel and the average value of the wall to bulk fluid temperature differential as the motivating potential for heat transfer. For the range of experiments covered two important features were highlighted. First, for radially outward flow Coriolis acceleration was found to improve heat transfer so that, for a given throughflow Reynolds number increasing the rotational Reynolds number produced an attendant heat transfer enhancement. However, whereas all other available information from the technical press tended to propose only enhanced heat transfer, it was found that a systematic impediment was brought about as the rotational Rayleigh number was increased. This is clearly shown in Fig. 3(*a*) where regimes of enhanced or impeded heat transfer may be identified dependent upon the combination of operating parameters. The important feature from the design viewpoint is that prediction of heat transfer using either theoretical or empirical data that includes the influence of Coriolis acceleration alone could result in severe overestimation of heat transfer. When this experimental program was repeated over the same range of variables, but with radial inward flow, it was found that centripetal buoyancy had a converse effect in that a systematic improvement in heat transfer was found with increases in the rotational Rayleigh number as depicted in Fig. 3(*b*). It was also found that increasing the rotational Reynolds number in this instance impaired the heat transfer. This feature has not yet been fully explained.

We note therefore that information currently available via the technical literature for the prediction of heat transfer in the complex passages of turbine rotor blades leaves much to be desired, for even with the relatively simple circular-sectioned tube fitted with a settling section and rotating in the orthogonal-mode, there is much discrepancy between the results of numerous workers.

In a further attempt to identify the overall influence of rotation on heat transfer in channels relevant to turbine rotor blades, the present authors have undertaken a repeat of the work performed by Morris and Ayhan [1, 2], but with the added complexity of a triangular-section duct fitted with a "sharp entry" inlet. This was a decision taken on the grounds that, in the real engine application, ducts of noncircular section would be encountered without the academic luxury of a hydrodynamically developed flow. Because of its real engine relevance, coolant flows that produced turbulent conditions with a stationary duct were considered.

Apparatus

A schematic diagram of the test facility is shown in Fig. 4. An overhung rotor arm (1) is supported on bearings (2) and driven by a controlled electric motor (3) via a toothed pulley.

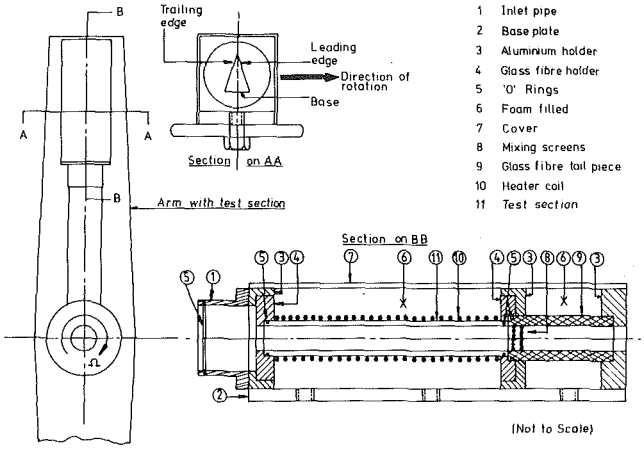

Fig. 5 Detail of test section

The test section (4) was fabricated from sheet brass 3 mm thick, so that the internal cross-sectional dimensions corresponded to an isosceles triangle having a base of 10 mm with an apex angle of 30 deg. The active heated length of the test section was 150 mm. Since the hydraulic or equivalent diameter of the test section was 7.67 mm, this gave a nominal length/effective diameter ratio of 19.55. The test section was mounted so that the 10-mm base was located in the plane of rotation.

The test section was held between two thermal insulating blocks, which were themselves bolted to a lightweight base plate to form a removable subassembly. The outer surface was electrically heated by means of spirally wound resistance wire powered via a Variac transformer and power slipring (5) mounted on the rotor shaft. This test subassembly was encased in a light sheet metal box, with the internal voids filled with insulating foam to minimize external heat loss and subsequently bolted on to the rotor arm so that the duct axis was perpendicular to the shaft axis with a midspan eccentricity of 250 mm. The temperature of the test section wall was measured by means of chrome/alumel thermocouples embedded midway along each wall. Eleven equispaced thermocouples were used on the leading edge of the section and six equispaced thermocouples each on the trailing edge and base. Further constructional details of the test section are given in Fig. 5.

Air was used as the test fluid and this was pumped through the test section via a rotating seal assembly (6) (see Fig. 4) and a plenum cylinder (7) in direct contact with the sharp inlet station of the test section. The ratio of the inlet plenum cross-sectional area to that of the test section was 12:1.

The air temperature at inlet to and exit from the test section was also measured with chrome/alumel thermocouples. A single thermocouple centrally located was used for the inlet. In the case of the coolant exit temperature, an insulated tailpiece (see Fig. 5) was fitted with a pair of staggered grids to "mix" the flow prior to venting to atmosphere and the mixed temperature checked with two thermocouples.

All thermocouple signals were taken from the rig to a Solatron System 35 computer logger via a silver/silver graphite slip ring assembly (8). Raw experimental data were written on magnetic disk storage for subsequent processing and analysis.

Rotor speed was measured by means of a digital interval meter coupled to a magnetic shaft encoder (9). Thermal dissipation in the heated test section was measured with a Cambridge Instruments analogue wattmeter and the air flow rate by means of a Fisher 2001 rotameter flow meter.

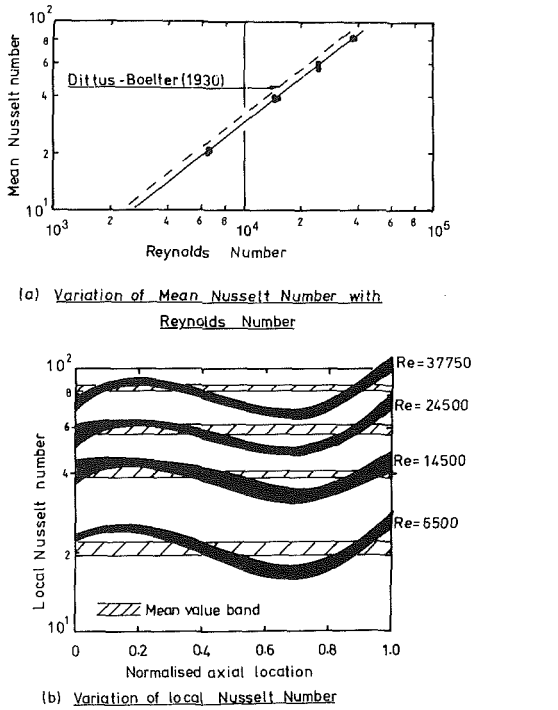

Fig. 6 Mean and local heat transfer variations at zero rotational speed

Experimental Program and Data Analysis

Before undertaking the main experimental program, a series of tests was undertaken to establish the external heat loss characteristics of the test section. For this purpose, the interior of the heated tube was filled with insulating material to inhibit any internal convection and the wall temperature measured over a range of heater power settings and rotational speeds. It was found that, in the steady state, the external heat loss (defined as the heater power dissipated corrected to allow for end conduction effects) could be correlated well as a linear function of the difference between the mean temperature of the wall and the ambient value. In this respect, it was found that there was no significant or systematic variation in temperature of the wall material in the girthwise direction. Consequently, calibration constants of proportionality linking the expected heat loss to the wall temperature history were determined for each of the rotational speeds used for production tests.

Actual convection tests were conducted over the range of operating conditions depicted in Table 1. By organizing the test program into series of tests at fixed throughflow Reynolds number and rotational speed, but with varying heater power settings, it was possible to systematically vary the rotational Rayleigh number while other parameters of a nondimensional nature were held to within 2 percent of the stated nominal values. For each production test (i.e., with convection) the previously determined heat loss calibration constants were used to check that the measured exit coolant temperature was consistent with that calculated using the measured flow rate and wall temperature history. Again it was found that even with rotation no significant girthwise variation in wall temperature was evident. When the energy accountancy check, including axial wall conduction, was deemed satisfactory, mean values of the Nusselt number, throughflow Reynolds number, rotational Reynolds number, and rotational Rayleigh number were evaluated.

Using the heat loss calibration constants on a local basis together with local allowance for axial wall conduction (obtained numerically via the axial wall temperature history),

Table 2

Legend	Nominal Reynolds number
A	6500
B	14500
C	24500
D	45500

it was subsequently possible to determine the variation axially of local heat flux and hence a local Nusselt number along the duct defined in terms of the equivalent diameter and the local value of wall to bulk fluid temperature difference. Further details of the analysis procedures used are cited in Morris and Ayhan [1, 2]. The data reduction and heat balance technique provided results which, as presented in this paper, are deemed to be within 10 percent uncertainty.

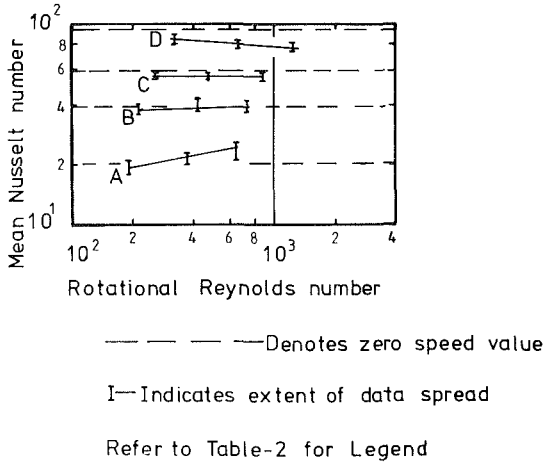

Fig. 7 Variation of mean Nusselt number with rotational Reynolds number

Results and Discussion

Previously published experiments aimed at investigating the effect of orthogonal-mode rotation on heat transfer have tended in the main to be concerned with circular-sectioned tubes fitted with calming sections to give a good approximation to developed flow prior to the commencement of heating. However, the present investigation has been deliberately undertaken with a test section involving a sharp-edged entry from a plenum chamber, itself directly influenced by rotation. Also the duct is severely noncircular in section. For these reasons, it is necessary to consider the local and mean variations of heat transfer in the ensuing discussion.

To establish a ground state with which to compare test data obtained with orthogonal-mode rotation, an initial series of experiments were undertaken at zero rotational speed. Figure 6(*a*) shows the variation of mean Nusselt number with throughflow Reynolds number for the entire test section. The mean Nusselt number is calculated in terms of the mean heat flux and the mean value of wall to bulk fluid temperature differences with properties evaluated at mean fluid bulk temperature. Also shown for comparative purposes in Fig. 6(*a*) is the well-known Dittus-Boelter [8] correlation for developed pipe flow but based on the effective or hydraulic diameter of the triangular sectioned duct used. Typically, the mean Nusselt numbers at zero rotational speed were approximately 90 percent of the Dittus-Boelter values.

The data processing method used permitted local values of Nusselt number to be determined along the duct and Fig. 6(*b*) shows these variations for a range of throughflow Reynolds number values. The axial location is defined as a fraction of the actively heated test section, in other words normalized with respect to the length of the test section. The bandwidths shown in Fig. 6(*b*) encompass local data points from a number of test runs with different heating levels. It should be pointed out again that there was no systematically detectable girthwise variation of wall temperature during the rotating or nonrotating tests and that the wall temperature values used for data processing were those on the leading edge of the section. The lack of any girthwise temperature variation is probably due to the relatively high thermal conductivity of the material from which the test section was manufactured.

The variations of local Nusselt number were noticeably different from those determined by Morris and Ayhan [1] for the circular-sectioned tube fitted with a calming section. The region of relatively high local Nusselt number in the immediate entry region, associated with normal boundary layer development, was suppressed with the sharp-edged entry as shown in Fig. 6(*b*). This region of reduced heat transfer, which extended for approximately 20 percent of the test section, is probably caused by a zone of separated flow. It is interesting to note that Mills [9], who tested circular-sectioned tubes fitted with sharp-edged entrance conditions, detected similar reductions in local heat transfer in the immediate entry regions and that an axial distance equivalent to one hydraulic diameter was needed for this effect to die away. In the present case, an axial distance of approximately 3.5 equivalent diameters was needed for this region of reduced heat transfer to die away. Ainsworth and Jones [10] conducted tests on a stationary duct of triangular cross section (10 deg isosceles triangle) fitted with a bell mouth entry. These workers also detected a region of reduced heat transfer in the immediate entry zone which took approximately 15 equivalent diameters of axial length to recover, and this was ascribed to a laminar-turbulent transition phenomenon.

The variation of mean Nusselt number with rotational Reynolds number for four values of throughflow Reynolds number is shown in Fig. 7; the zero speed values of Nusselt number obtained with these values of throughflow Reynolds numbers are also shown. It should be noted that zero speed mean values at a Reynolds number of 45,500 were obtained by extrapolation from Fig. 6(*a*). The data spread indicated reflects the point that tests with nominally fixed values of throughflow and rotational Reynolds number were conducted with various heat flux levels and hence various rotational Rayleigh numbers. Even so, the following features are worthy of note as regards the influence of Coriolis acceleration. At the lowest value of throughflow Reynolds number (i.e., 6550), Coriolis acceleration appears to have a significant effect on the mean heat transfer in that the mean Nusselt number increases with increases in rotor speed. At a throughflow Reynolds number value of 14500, rotation had no detectable effect on heat transfer over the range of variables covered. However, heat transfer reductons relative to the zero speed condition were evident at the higher levels of throughflow Reynolds numbers.

In an attempt to separate out the individual influences of Coriolis acceleration and centripetal buoyancy, Fig. 8 shows the variation of mean Nusselt number with mean rotational Rayleigh number for lines of fixed throughflow and rotational Reynolds number. This figure shows that rotational buoyancy appears to have a small attenuating effect on mean heat transfer at the lowest values of throughflow studied but no noticeable effect at the higher values. Even so, a net reduction of heat transfer was possible at these higher values of throughflow Reynolds numbers.

As regards the influence of orthogonal-mode rotation on the present test geometry, it appears that centripetal buoyancy does not have such a strong influence on mean heat transfer as

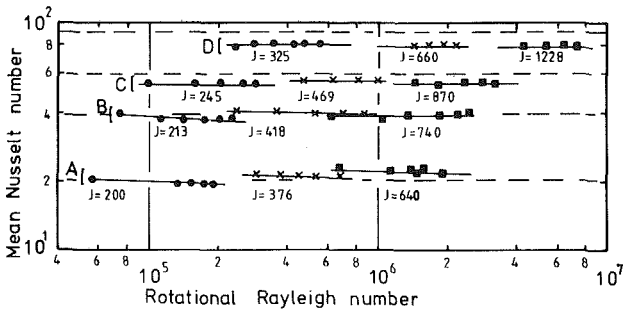

Fig. 8 Variation of mean Nusselt number with rotational Rayleigh number and rotational Reynolds number

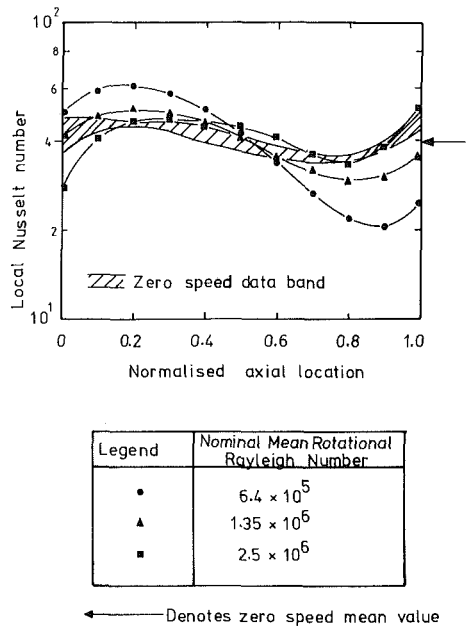

Fig. 9 Typical measured distributions of local Nusselt number with orthogonal-mode rotation (Re = 14,500, $J = 7.4 \times 10^2$)

indicated by the circular-sectioned tube work of Morris and Ayhan [1, 2]. Also, Coriolis acceleration produced an overall increase in mean heat transfer at the lower levels of throughflow Reynolds number but this trend was seemingly reversed at the highest value of throughflow Reynolds number tested.

Despite care in the control of the experimental program, it may be stated that the overall influence of rotation on mean heat transfer with the configuration studied is still confused. Although the physics of the problem is far from completely understood, there exists the possibility of significant reductions in mean heat transfer in relation to the zero rotational speed base lines.

Because local behavior is important from the viewpoint of rotor blade design, we now look at the distributions of local heat transfer obtained with the present investigation.

Although it may be argued from the mean heat transfer data presented that rotational buoyancy did not appear to have a large order effect over the range of variables studied, this was not found to be true in certain local regions particularly at the lower range of throughflow Reynolds numbers. Figure 9 typifies some of the more dramatic changes in local heat transfer distributions that were noted. In this figure, the zero rotational data are shown as the hatched band. Although the hatched bandwidth reflects the difficulties

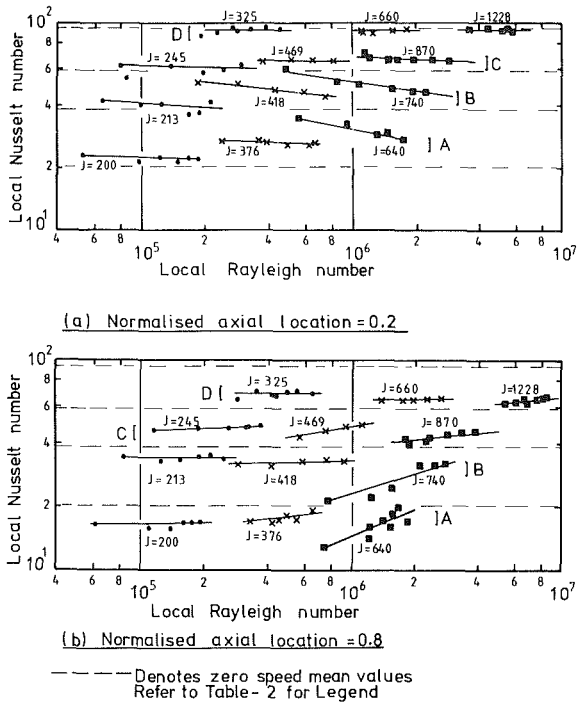

Fig. 10 Examples of the influence of orthogonal-mode rotation on local heat transfer

in the control of heat transfer experiments in that property changes are inevitable as heating rates are changed, the band is certainly less pronounced than the corresponding distributions for the local Nusselt numbers at the rotational Reynolds numbers shown suggesting a buoyant-type interaction. The individual lines reflect changes in the heating rate and consequently the rotational Rayleigh number mean values. What is interesting is the unexpected result that in the immediate entry region increasing the rotational Rayleigh number causes the expected reduction in heat transfer but that the trend is reversed in the exit section of the duct. To exemplify for the case shown at a normalized axial location of 0.2, an increase in local heat transfer relative to the zero speed mean value of about 59 percent was possible, whereas at a corresponding position of 0.8 a reduction of 44 percent was possible. This magnitude of local departure from a zero speed mean value could be potentially troublesome if design predictions are made without taking rotation into account. For all the tests undertaken, Fig. 10 typifies the overall trends which were noted. In this figure, the local Nusselt number is plotted against local rotational Rayleigh number (i.e., the local level of wall to fluid temperature difference is used as the representative driving potential) for fixed values of nominal throughflow and rotational Reynolds numbers. Two representative axial locations are shown by way of example and the following features are worthy of note. At a normalized location of 0.2, see Fig. 10(*a*), there is a progressive tendency of the local heat transfer to be reduced as the rotational Rayleigh number increased, and this effect progressively diminishes as the throughflow Reynolds number is increased. Indeed, at a throughflow Reynolds number of 45,500, the buoyancy appears to have little effect at this location, although a net reduction in heat transfer was evident. For each of the nominal throughflow Reynolds numbers, local heat transfer tended to increase with rotational Reynolds number at a specified value of local rotational Rayleigh number, although again this effect reduced as the throughflow Reynolds number increased.

At a normalized axial location of 0.8, Fig. 10(*b*) demonstrates a converse effect of rotational Rayleigh number and

rotational Reynolds number. For example, the local Nusselt number increases as the local Rayleigh number increases. Even so, the local Nusselt numbers at all values of the throughflow Reynolds number tested were noticeably lower than that suggested by a mean nonrotating value.

Closure

It is evident from the preliminary experiments presented in this paper that the mechanisms by which rotation influences flow and heat transfer in coolant channels appropriate to cooled gas turbine rotor blades are particularly complex and interactive. Although full and definitive explanations for all the effects detected are, as yet, not possible, it is nevertheless possible to identify some features that cause concern in the design context, and these are briefly itemized as follows.

1 The flow conditioning that occurs in the delivery ducting prior to the blade passages will itself be influenced by the fact that the delivery ducting is rotating. This means that the entry plane velocity profile can be different at different operational speeds. In the present work, it is evident, with the sharp-edged entrance used, that flow separation in the immediate entry region produces regions of reduced local heat transfer in the rotating as well as the nonrotating case. It is interesting to note that computational methods that require the entry plane velocity field to be specified in order to solve the governing conservation equations for locally prevailing flow and heat transfer will strictly need to incorporate the influences of upstream flow configurations.

2 In general terms, rotational buoyancy appears to have an adverse effect on local heat transfer in the immediate entry with radially outward flow. This is similar to the findings of Morris and Ayhan [1] for a circular-sectioned tube fitted with a calming section. The severity of this effect is dependent on the relative strength of the customary forced convection component, characterized by the throughflow Reynolds number. For rotational Rayleigh numbers less than approximately 10^7, the buoyancy effect will probably be insignificant for throughflow Reynolds number greater than 30,000.

3 In the exit region of the duct tested, the influence of rotational buoyancy was reversed in that increases in local Rayleigh number at fixed rotational Reynolds number produced attendant increases in the local Nusselt number. This feature has not been reported previously as far as the present authors are concerned. Indeed the severe rippling of local Nusselt number distribution was a notable feature when rotation was present and tends to reflect an additional complication involved with experimentation in this area which can be important in the turbine blade design context. Because the test model geometry was fabricated from brass sheet for manufacturing convenience, the large material thermal conductivity implies that axial conduction in the walls is important. This was taken into account by the numerical data processing, and the modification to the local heat flux to the fluid to some extent reflects this term. In other words the experimental model is not one that has the academic convenience of a uniformly heated wall as a thermal boundary condition. It is important, therefore, in the real engine situation that computational models should be treated on a systems approach which includes the interaction of the fluid mechanics on the coolant side with the wall conduction mechanism.

4 Although in many ways the results of this investigation have posed more unanswered questions in what is a clearly complex problem, it is prudent to note that although rotation may appear not to have a great effect on overall heat transfer, in some instances there could be regions of severely reduced heat transfer on a local basis resulting from the combined and interactive effect of upstream flow conditioning, blade wall conduction, Coriolis accelerations, and rotational buoyancy.

Acknowledgments

The authors acknowledge with thanks the financial aid given by the Ministry of Defence and the Science and Engineering Research Council for this work to be undertaken, and Rolls Royce Ltd. for valuable discussions and permission to publish this work.

References

1 Morris, W. D., and Ayhan, T., "Observations on the Influence of Rotation on Heat Transfer in the Coolant Channels of Gas Turbine Rotor Blades," *Proc Inst Mech Eng*, Vol. 193, No. 21, 1979, p. 303.

2 Morris, W. D., and Ayhan, T., "An Experimental Study of Turbulent Heat Transfer in a Tube Which Rotates About an Orthogonal Axis," presented at the XIVth ICHMT Symposium, Dubrovnik, Yugoslavia, Sept. 1982.

3 Clifford, R. J., Jones, T. V., and Dunne, S. T., "Techniques for Obtaining Detailed Heat Transfer Coefficient Measurements Within Gas Turbine Blade and Vane Cooling Passages," ASME Paper 83-GT-58, 1983.

4 Mori, Y., Fukada, T., and Nakayama, W., "Convective Heat Transfer in a Rotating Radial Circular Pipe (2nd Report)," *Int Jnl Heat and Mass Transfer*, Vol. 14, 1971, p. 1807.

5 Skiadaressis, D., and Spalding, D. B., "Heat Transfer in a Pipe Rotating Around a Perpendicular Axis," ASME Paper No. 77-WA/HT-39, 1977.

6 Lokai, V. I., and Limanski, A. S., "Influence of Rotation on Heat and Mass Transfer in Radial Cooling Channels of Turbine Blades," *Izvestiya VUZ Aviatsionaya Tekhika*, Vol. 18, No. 3, 1975, p. 69.

7 Zysina-Molozhen, L. M., Dergach, A. A., and Kogan, G. A., "Experimental Investigation of Heat Transfer in a Radially Rotating Pipe," HGEEE *High Temp*, Vol. 14, 1977, p. 988.

8 Dittus, F. W., and Boelter, L. M. K., *Univ Calif Publs. Engng*, Vol. 2, 1930, p. 443.

9 Mills, A. F., "Experimental Investigation of Turbulent Heat Transfer in the Entrance Region of a Circular conduit," *Jnl Mech Eng Sci*, Vol. 4, No. 1, 1962, pp. 63-77.

10 Ainsworth, R. W., and Jones, T. V., "Measurements of Heat Transfer in Circular, Rectangular and Triangular Ducts, Representing Typical Turbine Blade Internal Cooling Passages Using Transient Techniques," ASME Paper No. 79-GT-40, presented at the ASME Gas Turbine Conference, San Diego, Calif., Mar. 1979.

A Horseshoe Vortex in a Duct

J. Moore

T. J. Forlini

Department of Mechanical Engineering,
Virginia Polytechnic Institute and
State University,
Blacksburg, Va. 24061

A Rankine half-body is used to model the three-dimensional flow caused by a blunt obstruction in a flow passage. The body is located in a duct bounded by two plane endwalls and two side walls shaped like potential-flow streamlines. A thick turbulent boundary layer on the endwall forms a horseshoe vortex flow as it encounters the leading edge of the body. Flow measurements are presented showing the inlet flow and the three-dimensional flow downstream of the leading edge. Sufficient data are presented for this to be a test case for the development of three-dimensional viscous flow codes.

Introduction

Computational methods for three-dimensional viscous flow are being developed [1–3] to aid turbomachinery designers in their efforts to obtain better performance and durability, and an important part of this development process involves comparison with well-documented test cases. It is the object of this paper to provide a test case for leading-edge horseshoe vortex flow. This is a feature of turbomachinery flows, especially those in turbine blade rows which must be well modeled in order to accurately model the flow in the passage downstream. Indeed the calculations of Hah [3] for a linear turbine cascade suggest that quite small discrepencies in the calculated flow near the leading edge can lead to significant differences in the location and size of the passage vortex at the exit of the cascade.

Horseshoe vortices are formed in turbomachines when annulus wall boundary layers encounter the blunt leading edges of blades and support struts. Vortex lines from the boundary layer upstream are convected and stretched around the leading edge, forming a vortex that has a characteristic horseshoe shape with streamwise vorticity downstream. The boundary layer separates from the endwall in a complex three-dimensional flow, and there is reverse flow upstream of the leading edge.

This flow is known from engine experience [4, 5] to influence the endwall thermal field and to impact on durability problems in low aspect ratio vane rows in gas turbines. So it has been the subject of many visualization studies [6–9]. But, as has been noted recently by Briley and McDonald [10], for horseshoe vortex flow "little is available in the way of detailed flow measurements . . . particularly downstream of separation." There has not been a test case emphasizing leading-edge horseshoe vortex flow and suitable for testing turbomachinery flow codes.

The well-defined geometry of inviscid flow around a Rankine half-body provides the basis for the present study. The Rankine half-body is a thick obstruction with a rounded nose which can interact with an endwall boundary layer to produce large flow disturbances [11]. The well-known potential flow solution provides a primary velocity distribution upon which the secondary horseshoe vortex flow is imposed.

The body is placed between the parallel endwalls of a duct to model the situation in a turbomachine where struts and blades extend over the total passage height. The Rankine half-body duct then simulates the situation found in turbomachinery passages without the complication of cascade geometry, which introduces other flow phenomena due to curvature, acceleration of the flow, and trailing edges; it exhibits three-dimensional flow due solely to the horseshoe vortex.

In this paper, quantitative flow measurements are presented to define

(*a*) The inlet flow field upstream of the leading edge
(*b*) The static pressure distribution on the endwall and on the surface of the body
(*c*) The three-dimensional flow on two planes just downstream of the leading edge
(*d*) The exit flow field far downstream

These measurements are intended to provide experimental data in a well-defined flow field for testing calculation methods for three-dimensional turbulent flows in turbomachinery blade rows.

Duct Design

Figure 1 shows a schematic view of the Rankine half-body duct with overall dimensions. The duct is 1.19 m long with endwalls spaced 0.254 m apart. The duct side walls conform to potential-flow streamlines with no allowance for displacement due to boundary layers; at the inlet, the duct width is 0.356 m. The source location, 0.508 m downstream of the duct inlet, is at the origin of the cartesian coordinate system.

Rankine Half-Body—Potential Flow

The potential flow field is defined by the superposition of a line source of strength m in a uniform flow with velocity U_∞.

Contributed by the Gas Turbine Division of THE AMERICAN SOCIETY OF MECHANICAL ENGINEERS and presented at the 29th International Gas Turbine Conference and Exhibit, Amsterdam, The Netherlands, June 4–7, 1984. Manuscript received at ASME Headquarters January 18, 1984. Paper No. 84-GT-202.

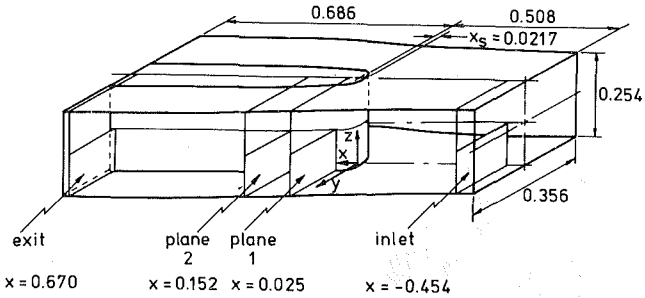

Fig. 1 Schematic of Rankine half-body duct showing measurement planes and overall dimensions in meters. Coordinate system origin located at source position.

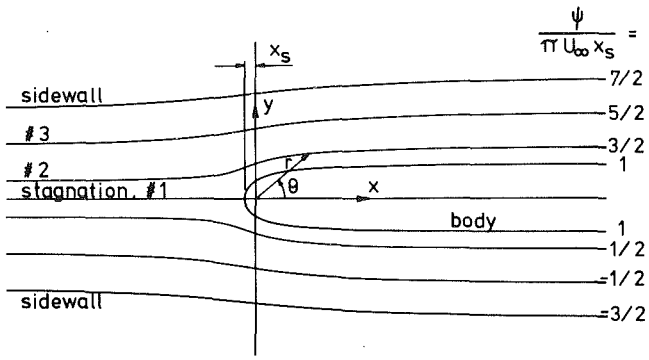

Fig. 2 Potential flow streamlines and geometry of Rankine half-body duct

In polar coordinates, the stream function ψ, as given by Vennard and Street [12] is

$$\psi = U_\infty r \sin\theta + m\theta/2\pi \tag{1}$$

Following the development in Vennard and Street, the length from the source to the stagnation point on the leading edge of the body is determined by

$$x_s = m/(2\pi U_\infty) \tag{2}$$

Substituting this into equation (1) gives

$$\psi/U_\infty = r\sin\theta + x_s\theta \tag{3}$$

which defines the potential-flow streamlines.

In the Rankine half-body duct, x_s = 21.7 mm. Figure 2 shows streamlines defined by equation (3) above, as well as positive values for the cartesian and polar coordinate systems located at the source position. The side walls are defined by $\psi/U_\infty = 7/2\ \pi x_s = 0.239$ m and $\psi/U_\infty = -3/2\ \pi x_s = -0.102$ m. The body is defined by $\psi/U_\infty = \pi x_s = 0.086$ m. Four intermediate streamlines defined by $\psi/U_\infty = 5/2\ \pi x_s$, $\psi/U_\infty = 3/2\ \pi x_s$, $\psi/U_\infty = 1/2\ \pi x_s$, and $\psi/U_\infty = -1/2\ \pi x_s$ are also shown in Fig. 2.

The velocity components in the axial, x, and transverse, y, directions are given by

$$u = \frac{\partial\psi}{\partial y} = U_\infty\left(1 + x_s\left[\frac{x}{x^2+y^2}\right]\right) \tag{4}$$

and

$$v = -\frac{\partial\psi}{\partial x} = U_\infty x_s\left[\frac{y}{x^2+y^2}\right] \tag{5}$$

and the velocity magnitude is given by

$$U = \sqrt{u^2+v^2} \tag{6}$$

Substituting the relations for u and v into equation (9) gives the velocity ratio

$$\frac{U}{U_\infty} = \sqrt{1 + 2x_s\left[\frac{x}{x^2+y^2}\right] + \left[\frac{x_s^2}{x^2+y^2}\right]} \tag{7}$$

Static Pressure Distribution—Potential Flow. A static pressure coefficient, C_{ps}, is defined as

$$C_{ps} \equiv \frac{P - P_r}{P_0 - P_r} \tag{8}$$

where P is the static pressure at the measurement point, P_0 is the upstream total pressure, and P_r is a reference static pressure. For potential flow, $P_r \equiv P_\infty$, the static pressure far upstream, and

$$P_0 - P_r = \frac{1}{2}\rho U_\infty{}^2 \tag{9}$$

Thus for the potential flow, the static pressure coefficient may be written as

$$C_{ps} = 1 - (U/U_\infty)^2 \tag{10}$$

so that C_{ps} may be determined from the velocity distribution. The static pressure distribution for potential flow is given by

$$C_{ps} = -2x_s\left[\frac{x}{x^2+y^2}\right] - \left[\frac{x_s^2}{x^2+y^2}\right] \tag{11}$$

Figure 3 shows this theoretical static pressure distribution along the duct streamlines.

Nomenclature

C_{ps} = static pressure coefficient, $(P-P_r)/(P_0-P_r)$
h = duct height, 0.254 m
H = boundary layer shape factor, δ_1/δ_2
m = source strength, 3.29m^2/s
P = static pressure
P_{atm} = atmospheric pressure
P_0 = reference total pressure measured at midheight on leading edge of body
P_r = reference static pressure measured at midheight on sidewall where $x = -x_s/2$
P_t = total pressure
r,θ = polar coordinates
R = ideal gas constant for air, 0.287 kJ/kgK
s = length along the body surface from leading edge
T_{atm} = atmospheric temperature
u,v,w = velocity components in cartesian coordinate directions
U = free-stream velocity magnitude
u' = fluctuating component of axial turbulent velocity
U_∞ = uniform velocity far upstream, 24.1 m/s
x,y,z = Cartesian coordinates
x_s = length from source to leading edge of body, $m/(2\pi U_\infty)$ = 21.7 mm
δ = boundary-layer thickness, $u/U = 0.99$
δ_1 = boundary-layer displacement thickness, $\int_0^\infty \left(1 - \frac{u}{U}\right)dy$
δ_2 = boundary-layer momentum thickness, $\int_0^\infty \frac{u}{U}\left(1 - \frac{u}{U}\right)dy$
μ = viscosity
ν = kinematic viscosity, μ/ρ
ρ = density, P_{atm}/RT_{atm}
ψ = stream function

Subscripts

e = exit plane
i = inlet plane
m = midheight in the duct

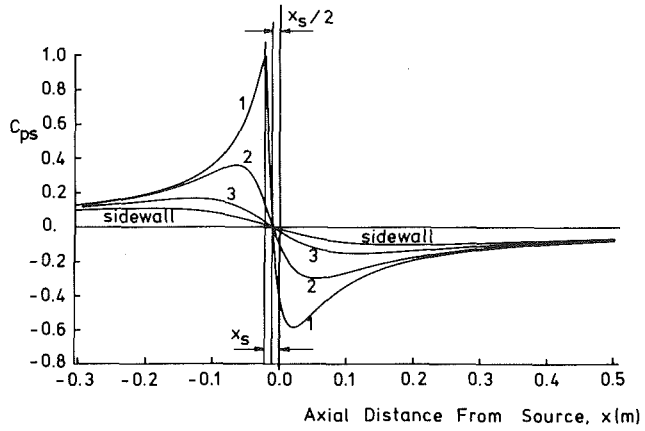

Fig. 3 Static pressure distribution for potential flow (equation (14)) along streamlines shown in Fig. 1

Figure 3 shows that far upstream and far downstream of the source at $x=0$, the static pressure in the duct approaches P_∞. The static pressure coefficient on the stagnation and body streamline, #1, rises to unity at the leading edge of the body (stagnation point), where $x = -x_s$, and then falls around the nose of the body. The pressure coefficient reaches a minimum value of -0.59 (a maximum velocity $U/U_\infty = 1.26$) at $x =$ 22.9 mm before rising to zero far downstream ($U/U_\infty = 1$). The static pressures on the other streamlines, #2, #3, and the sidewall, also fall near the leading edge and rise past the nose of the body.

One interesting feature of the static pressure distribution for the potential flow is that at $x = -x_s/2$, $P = P_\infty$ *for all values of* y, i.e., *on all streamlines* [13]. The existence of this plane of uniform static pressure allows the upstream value of static pressure, P_∞, and velocity, U_∞, to be measured in the duct.

Body Construction. The body is made of three 3-mm-thick plexiglass sheets formed to the Rankine half-body shape. The plexiglass walls are fastened at the top and bottom to a supporting wood frame. The frame consists of two plywood forms separated by wood supports near the body midsection, 0.254 m downstream of the leading edge of the body, and near the end of the body, 0.686 m downstream of the leading edge. The vertical seams between the plexiglass sheets are located at the forward supports, 0.254 m downstream of the leading edge, so that the nose of the body is a continuous surface. Further details of the duct and body construction are given in [13] and [14].

Wind Tunnel and Inlet Duct. The wind tunnel used as the air supply for the present tests is described by Tavakoli [15]. It ends with a straight test section 0.356 m wide, 0.254 m high and 1.24 m long. This test section was used as the inlet duct for the Rankine half-body duct. Wire screens were placed at the inlet to this section to thicken the boundary layers on the top and bottom endwalls in order to produce large horseshoe vortices at the leading edge of the Rankine half-body.

Flow Symmetry. The boundary layer screens were positioned in the tunnel to obtain a symmetrical flow at the inlet to the Rankine half-body duct. With a symmetrical flow, the amount of data necessary to define the flow are reduced, since planes of symmetry may be used as boundaries. The vertical plane along the duct centerline and the horizontal plane at the duct midheight are planes of symmetry that divide the duct into four quadrants. Care was taken to establish a symmetrical inlet flow so that data could be taken in any quadrant.

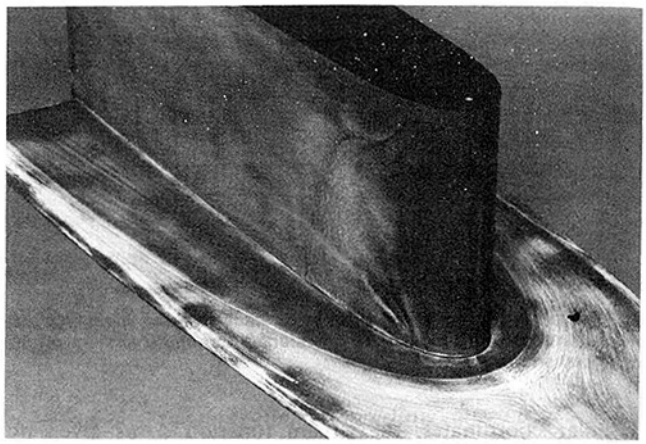

Fig. 4 Flow visualization of the limiting streamlines on the Rankine half-body and on the bottom endwall. The white dot on the top of the body, near the leading edge, is the location of the line source.

Flow Visualization

Before presenting the results of the detailed flow measurements, it is helpful to consider the overall flow development as revealed by surface flow visualization. Figure 4 shows oil-flow traces of the limiting streamlines on the horizontal (bottom) endwall of the duct and on the vertical surface of the Rankine half-body. The visualization was achieved by spraying a mixture of diesel oil and titanium dioxide onto an aluminum sheet on the endwall and onto a mylar sheet wrapped around the body; these sheets had previously been sprayed with mat black paint. The flow was then turned on for about 5 min, giving the picture shown.

The resulting flow patterns on the endwall show a classical horseshoe vortex flow that sweeps titanium dioxide away from the body revealing the dark surface beneath. The clearly defined boundary between the dark and light areas represents a line of three-dimensional flow separation which follows the vortex core.

A thin white line marks the stagnation line along the leading edge of the body. This is clearly seen at midheight, where the stagnation flow is nearly two-dimensional, but near the endwalls the horseshoe vortices induce flows which sweep the titanium dioxide towards the endwalls.

At midheight on the body, the titanium dioxide is swept around the leading edge by an apparently two-dimensional laminar boundary layer before it accumulates in a wide area which exhibits streaks vertically downwards. This is probably a region of laminar flow separation with correspondingly small shear stresses, where the oil flow is influenced by gravity. Downstream of this separation region, the oil streaks are essentially horizontal once more as the flow reattaches with a nearly two-dimensional turbulent boundary layer.

In the vicinity of the leading edge, the details of the traces on the endwall can be considered to correspond with the physical explanation of horseshoe-vortex flow given by Belik [7] and Baker [9]. In the discussion below, we have followed their procedure in marking "primary and secondary separation lines" at locations of accumulation of titanium dioxide. A close-up picture of the flow visualization in this region that shows these accumulations is given in [14] and [16]. In [16], which may be considered a companion paper to the present one, we present the results of inviscid rotational flow calculations that show reverse flow due to the horseshoe vortex upstream of the leading edge.

Flow Measurements

Measurements of the flow in the Rankine half-body duct are presented on four measurement planes normal to the duct

Table 1 Standard test conditions

P_{atm}	93.7 kPA
T_{atm}	295 K
U_∞	24.1 m/s
ρ_{air}	1.11 kg/m^3
μ_{air}	1.9 x 10^{-5} Ns/m^2
Source strength, m	3.29 m^2/s

axis (see Fig. 1) and three potential-flow streamlines defined below (see Fig. 2). Measurement of the axial flow on the inlet plane defines the inlet boundary layers on the duct endwall and side wall. Static pressure measurements on the potential-flow streamlines define the overall duct flow. Three-dimensional flow measurements on two intermediate planes downstream of the leading edge of the body define the secondary flow due to the horseshoe vortex. Measurement of the axial flow on the exit plane defines the downstream flow far from the leading edge.

Standard Test Conditions. The standard test conditions for this steady incompressible air flow and values of the fluid properties at the standard conditions are presented in Table 1. The reference static pressure, P_r, is defined as the static pressure measured on the side wall at the duct midheight where $x = -x_s/2$. This location was chosen from the potential-flow solution, presented earlier. The reference total pressure, P_0, is defined as the stagnation pressure measured at midheight on the leading edge of the body.

Measurement Locations. Flow measurements are presented on four planes; an inlet plane at $x = -0.454$ m, two intermediate planes at $x = 0.025$ m and $x = 0.152$ m, and an exit plane at $x = 0.670$ m. Figure 1 shows the locations of the measurement planes.

The figures with the results of the measurements on the four planes show a view, looking upstream, of the measurement plane bounded by the duct walls and planes of symmetry. The location of the measurement traverses are shown as well as the origin of the duct coordinate system. Dimensions in the y-direction are given in meters, while dimensions in the z-direction are fractions of the duct height, $h = 0.254$ m. The flow measurements are presented in the quadrant of the duct defined by $z/h \leq 0.5$ and $y \geq 0$, as shown in Fig. 1.

Inlet Plane Measurements

The inlet flow distribution was measured by traversing a total pressure probe with a flattened tip on the inlet plane. Total pressure, P_t, was measured at the probe tip and static pressure, P, was measured with a static pressure tap on the endwall at the inlet plane.

Velocity Distribution. Figure 5 shows contours of axial velocity ratio, u/U_i, on the inlet plane where $U_i = 23.3$ m/s is the measured free-stream velocity. The natural boundary layer on the side wall is shown as well as the thickened boundary layer on the endwall. The endwall boundary layer is uniform over the center half of the duct width where the flow interacts with the body. The boundary layer parameters for this region are presented in Table 2, together with the parameters for the side wall at midheight. Further details are given in [14].

Turbulence Intensity. The turbulence intensity was approximated by measuring the mean and RMS signals from a

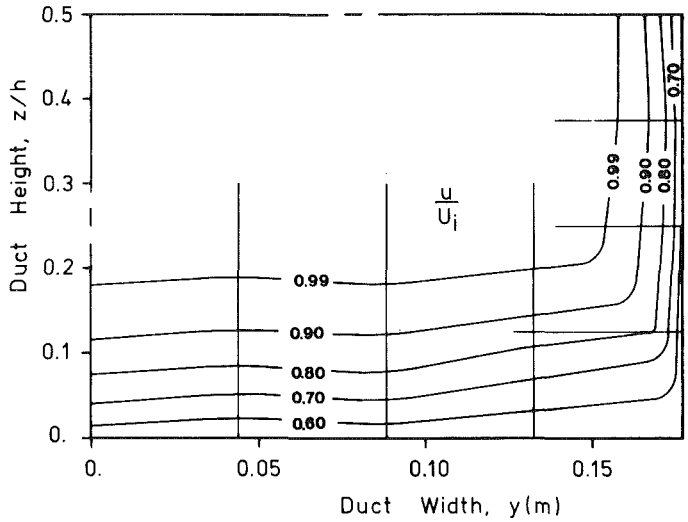

Fig. 5 Contours of axial velocity ratio (u/U_i) on the inlet plane. Free-stream velocity, $U_i = 23.3$ m/s.

Table 2 Inlet boundary layer parameters (endwall over center half of the duct width and side wall at duct midheight)

		Endwall	Sidewall
Thickness	δ	46.4 mm	19.1 mm
Displacement thickness	δ_1	9.0 mm	2.8 mm
Momentum thickness	δ_2	6.4 mm	2.1 mm
Shape Factor	H	1.42	1.30

single-wire, hot-wire anemometer that was traversed across the inlet plane. The distributions of turbulence intensity ($\sqrt{u'^2}/U_i$) in the endwall boundary layer showed little variation over the center half of the duct; the shape of the distribution in this region was quite similar to that reported by Klebanoff [17] for a turbulent boundary layer on a flat plate but the values were approximately 15 percent lower. The inlet free stream turbulence intensity was 0.5 percent of U_i.

Static Pressure Measurements

The static pressure distribution was measured with an inclined, multiple-tube manometer and also with a Statham pressure transducer. Multiple data points are shown where repeated pressure measurements gave slightly differing results.

Wall static pressure tappings are located along three of the potential-flow streamlines shown in Fig. 2. Streamline #1 is the stagnation streamline upstream of the body and the body streamline. Streamline #2 and streamline #3 are the two intermediate streamlines defined by $\psi/U_\infty = 3/2\ \pi x_s$ and $\psi/U_\infty = 5/2\ \pi x_s$. The static pressure taps on the stagnation streamline and on streamlines #2 and #3 are located on the duct endwall while the pressure taps on the body are located at the duct midheight. Pressure tappings are also located around the perimeter of the uniform pressure plane at $x = -x_s/2$. All of the static pressure tappings are nominally 0.5 mm dia.

Figure 6 shows the static pressure distribution measured in the duct compared with the calculated potential-flow distribution.

Stagnation Streamline. The static pressure on the stagnation streamline, measured on the endwall upstream of the body, is shown in greater detail in Fig. 7. Far from the leading edge, between 0.10 and 0.25 m upstream, the measured data deviates little from the potential flow solution. Less than 0.10 m upstream, the deviation of the measured data becomes larger with decreasing distance from the leading edge, ending at a stagnation value of $C_{ps} = 0.85$. This

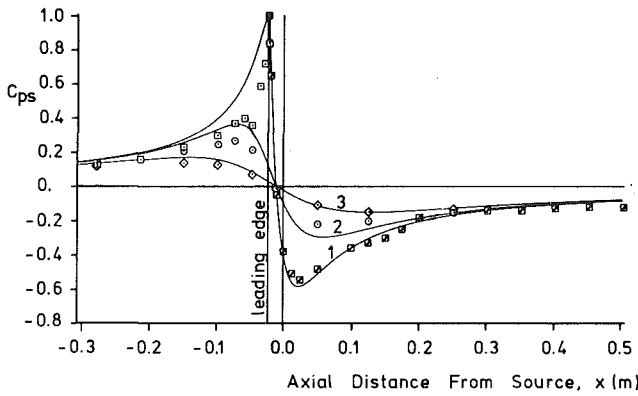

Fig. 6 Wall static pressure distributions along streamlines shown in Fig. 1: — potential flow, equation (14); □, measurements on endwall for streamline 1; □, measurements at midheight on body for streamline 1; ○, measurements on endwall for streamline 2; ◇, measurements on endwall for streamline 3

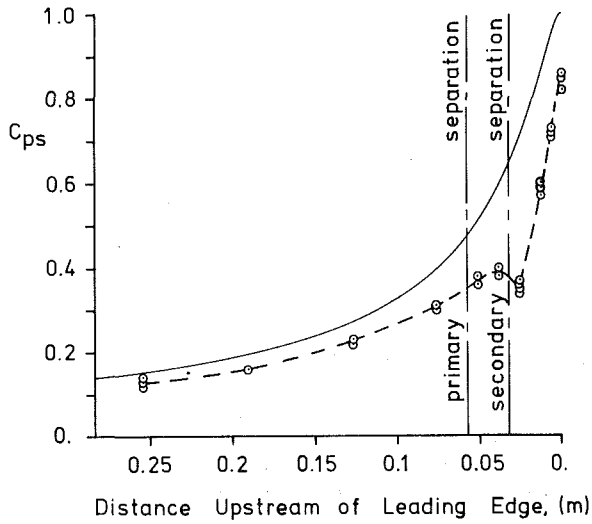

Fig. 7 Wall static pressure distribution along stagnation streamline (1) on duct endwall: — potential flow, equation (14); - - - mean line through data, 0; — - — saddle points of separation

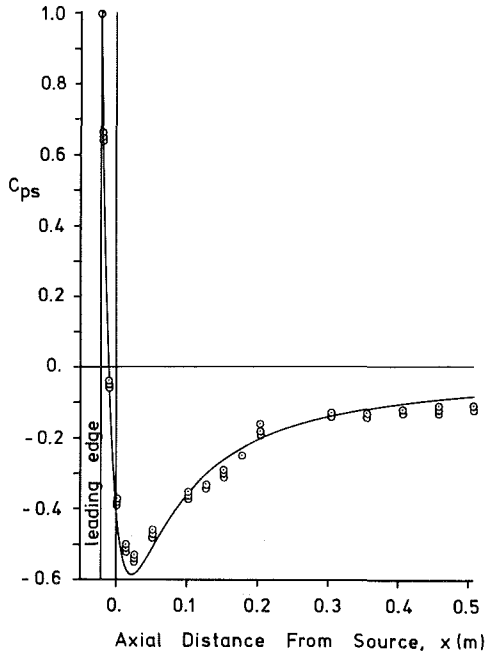

Fig. 8 Wall static pressure distribution at midheight on body: — potential flow, equation (14); 0, measurements

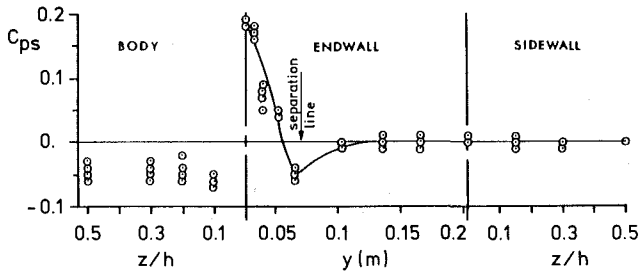

Fig. 9 Wall static pressure distribution on theoretical uniform-pressure plane at $x = -x_s/2$

low stagnation value may be due to low-velocity, boundary-layer fluid stagnating at the junction of the leading edge and the endwall.

A local minimum in the measured static pressure occurs 0.025 m upstream of the leading edge. This minimum has been assumed by Belik [7] to be adjacent to the core of the horseshoe vortex. From endwall flow visualization, the location of the secondary separation line, which according to Belik follows the course of the vortex core, was found to be 0.032 m upstream of the leading edge of the body; primary separation occurred 0.057 m upstream of the leading edge; the locations of the two corresponding saddle points are marked on Fig. 7. It is interesting to note the local peak in static pressure between the two saddle points; this is probably associated with a nodal point of reattachment [9].

Body Streamline. Figure 8 shows the static pressure distribution measured at midheight along the body. The measurements show the flow accelerating around the nose to a minimum of $C_{ps} = -0.54$ at $x = 0.025$ m, which corresponds to $U/U_\infty = 1.24$. This is compared to the potential flow maximum $U/U_\infty = 1.26$ at $x = 0.023$ m. The measured flow then decelerates to a relatively constant value of $C_{ps} = -0.12$ for $x > 0.3$ m; this small variation of static pressure may be due to the increasing displacement thickness of the wall boundary layers.

The region between $x = 0.10$ m and $x = 0.30$ m is interesting. The data points measured in this region suggest boundary-layer separation and reattachment, as discussed by Schlichting [18]. There is a section of slight pressure rise, which is less than for the potential flow solution, instead of the constant pressure described by Schlichting. Then there is a larger pressure rise that overshoots the potential flow solution before returning to the nearly constant downstream static pressure.

The construction of the body prevented measurements between $x = 0.20$ m and $x = 0.30$ m. The wood supports did not allow access to the body surface for a pressure tap, and the vertical seam between the plexiglass sheets was located here. The static pressure measurements on the body were unchanged when the vertical seam was covered with cellophane tape, so that the presence of the seam was not a probable cause for the flow disturbance. This region of the flow will be discussed further in the section that describes the calculation of the boundary layer on the body.

Uniform-Pressure Plane. Figure 9 shows the static pressure distribution measured around the perimeter of the theoretical uniform-pressure plane at $x = -x_s/2$. The value of C_{ps} at midheight on the sidewall is by definition equal to zero. The measured C_{ps} is uniform and equal to zero on the side wall and on the outer 60 percent of the endwall away from the body. C_{ps} decreases to a minimum of approximately

-0.05 at $y = 0.064$ m just inside the separation line at $y = 0.072$ m; it then increases to 0.18 at the junction of the body and endwall. The measured value of C_{ps} on the body is relatively uniform at about -0.05; this does not seem to be related to the endwall minimum, since the velocity gradient is large here and an error in C_{ps} of ± 0.05 corresponds to an error in the placement of the static pressure tap on the body of only ± 0.8 mm measured in the axial direction.

Secondary Flow Measurements

The flow distribution just downstream of the leading edge was determined by traversing a five-hole pressure probe on plane 1, at $x = 0.025$ m, and on plane 2, at $x = 0.152$ m.

Pressures were measured relative to the reference static pressure, P_r, at midheight on the side wall where $x = -x_s/2$. The static pressure, $P-P_r$, total pressure, P_t-P_r, pitch angle, measured in the vertical plane, and yaw angle, measured in the horizontal plane, were obtained from the five-hole probe measurements; and from these results, the three velocity components u, v, and w in the x-, y-, and z-directions, respectively, were calculated.

Method of Presenting Secondary Velocities. The secondary velocities and the corresponding velocity vectors for planes 1 and 2 are shown in Figs. 10–13. In order to present the data alone, the v components of velocity from the potential flow are not subtracted from the measured v values. This would involve the reader in calculating the local value of v for the potential flow and then correcting each point on the figures in order to obtain the actual measured values for v. Instead, the data are presented as $v-v_m$, where v_m is the measured v velocity at midheight ($z/h = 0.5$) for the particular vertical traverse considered. At each plane there are seven vertical traverses, and with this method of plotting the data, all the values, $v-v_m$, go to zero at midheight; the plots then show variations in secondary velocity relative to the value at midheight. At the endwall, all the velocity components are zero, and the value of $v-v_m$ plotted is simply $-v_m$, the negative of the velocity component v_m for that traverse at midheight.

Velocities at Midheight. The measured velocities at midheight were compared with the corresponding values from potential flow theory, found using equations (2), (4), and (5), with the source strength m and the free stream velocity U_∞ from Table 1.

At plane 1, the measured axial velocity component u/U_∞ was slightly higher by 1.1 percent ± 0.5 percent; at plane 2, the inner six points were consistently higher in u/U_∞, 2.3 percent ± 0.4 percent, while the outer point agreed with the potential flow value.

Apart from one point, the measured values of velocity component v at midheight were consistently less than those calculated from potential flow theory. At plane 1, all the values were smaller by -0.3 m/s ± 0.2 m/s and at plane 2 the outer six values were smaller by -0.4 m/s ± 0.1 m/s. This suggests a small secondary flow towards the body at midheight. The only point which showed a secondary flow away from the body at midheight was the point next to the body at plane 2. As discussed in the boundary layer section, below, this point was adjacent to a region of laminar flow separation on the body which may explain the small positive secondary velocity of 0.1 m/s (relative to the potential flow) and the significant difference of this point from the others at plane 2.

Secondary Velocities. The y and z components of secondary velocity, $v-v_m$ and w, on plane 1, at $x = 0.025$ m, are shown in Fig. 10. The velocity in the y-direction shows a region near the endwall where v is greater than v_m then a region where v is less than v_m before reaching the midheight value, v_m. The secondary flow in the y-direction extends approximately 30 percent of the duct height from the endwall. The maximum measured value of $v-v_m$ is 4.0 m/s at $y = 0.076$ m, $z/h = 0.019$. At this y-station v_m is 6.1 m/s and u_m is 26.4 m/s.

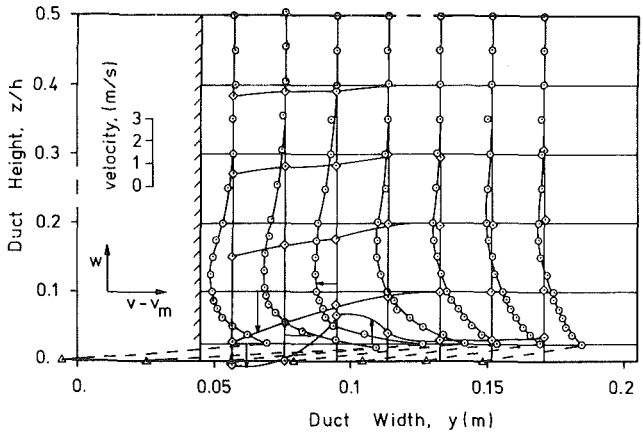

Fig. 10 Secondary velocities measured on plane 1: v_m = component of velocity in y-direction measured at midheight. Velocity components: 0, $v-v_m$; ◇, w; △, $v-v_m = -v_m$ at wall.

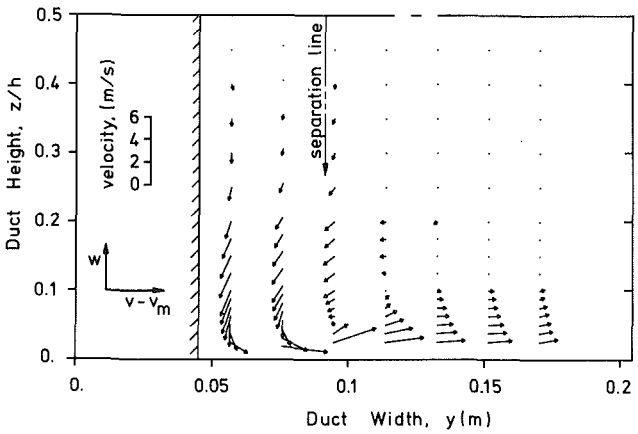

Fig. 11 Secondary velocity vectors measured on plane 1. v_m = component of velocity in y-direction measured at midheight.

The velocity in the z-direction shows flow towards the endwall near the body. At $z/h = 0.025$, there is a flow reversal between $y = 0.076$ m, where $w = -0.8$ m/s, and $y = 0.095$ m, where $w = 1.3$ m/s, which indicates the presence of the vortex with counterclockwise rotation. This is the direction of rotation associated with the boundary-layer vortex line stretched around the body.

Figure 11 shows the corresponding vector plot illustration of the secondary velocities on plane 1. Vectors with magnitudes less than 0.30 m/s are considered insignificant and are not shown. The location of the separation line on the endwall, at $y = 0.092$ m, is indicated on Fig. 11.

The secondary velocities, $v-v_m$ and w, on plane 2, at $x = 0.152$ m, are shown in Fig. 12. The region of secondary flow in the y-direction is limited to the 10 percent of the duct height near the endwall. Secondary flow away from the body is seen in this region. The secondary flow towards the body, seen on plane 1, is less significant on this plane. The maximum measured value of $v-v_m$ is 4.3 m/s, which occurs at $y = 0.133$ m and $z/h = 0.025$. At this y-station, v_m is 1.3 m/s and u_m is 26.6 m/s.

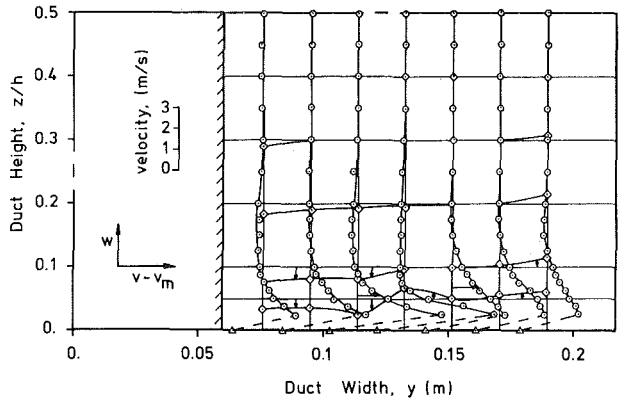

Fig. 12 Secondary velocities measured on plane 2. v_m = component of velocity in y-direction measured at midheight. Velocity components: 0, $v-v_m$; ◇, w; △, $v-v_m = -v_m$ at wall.

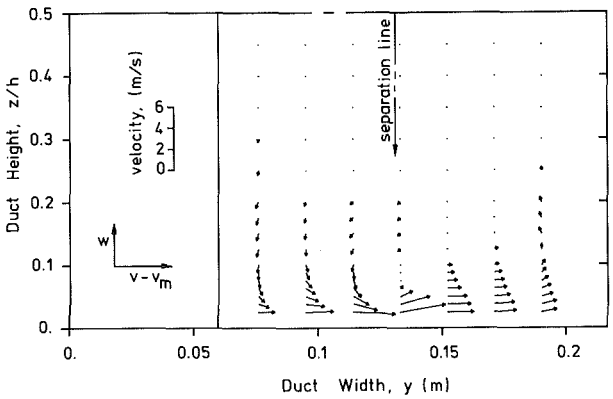

Fig. 13 Secondary velocity vectors measured on plane 2

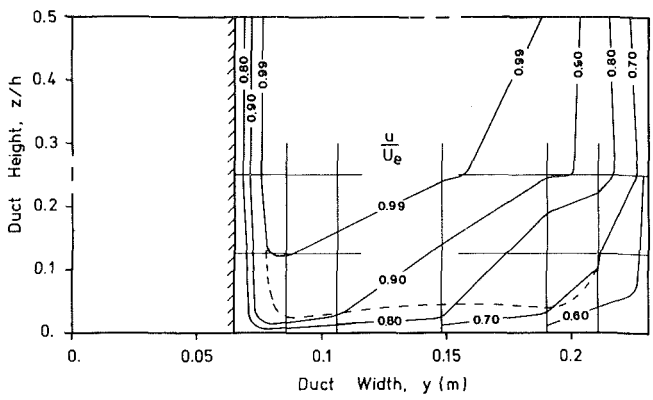

Fig. 14 Contours of axial velocity ratio (u/U_e) on the exit plane. Free-stream velocity, U_e = 25.7 m/s.

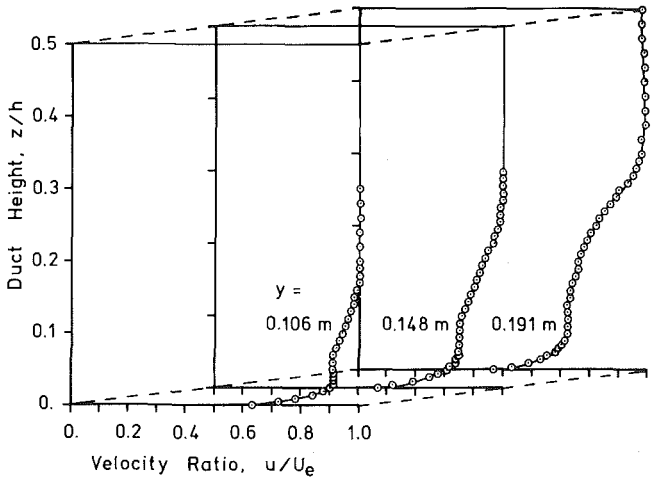

Fig. 15 Axial velocity profiles on the endwall at the exit plane

The secondary flow in the z-direction is towards the endwall near the body, as seen before. The flow reversal, which indicates the presence of the vortex, can be seen at z/h = 0.05, between y = 0.114 m, where w = −0.8 m/s, and y = 0.133 m, where w = 0.5 m/s. The vector plot in Fig. 13 illustrates these secondary velocities on plane 2.

Exit Plane Measurements

The exit flow distribution was measured as at the inlet by traversing the total pressure probe with a flattened tip on the exit plane. Total pressure, P_t, was measured at the probe tip. Static pressure, P, was measured with the static pressure portion of a pitot-static tube. The static pressure was measured at a single point in the free stream, since the exit static pressure was found to be uniform.

Velocity Distribution. Figure 14 shows the distribution of the exit velocity as a fraction of the exit free-stream velocity, u/U_e, where U_e = 25.7 m/s. The boundary layer on the body is approximately 11 mm thick and is uniform over the center 60 percent of the duct height. The boundary layer on the endwall is thinnest in the region near the junction of the body and the endwall. The endwall boundary layer profiles show a thin inner layer that reaches a constant velocity less than U_e, then an outer layer, that increases in velocity to U_e. Exit endwall boundary layer profiles are shown in Fig. 15. The dashed line on Fig. 14 shows the location of the edge of the inner endwall boundary layer.

The fluid near the edge of the outer endwall boundary layer at the exit plane is most likely from the thickened endwall boundary layer at the inlet, while the inner boundary layer originates midway along the duct, possibly downstream of the horseshoe vortex, behind the secondary separation line (the dark area on the endwall in Fig. 4). This situation is analogous to that reported by Langston, Nice, and Hooper [19], where the endwall boundary layer in the turbine cascade grows downstream of the separation line.

Boundary-Layer Analysis

A two-dimensional analysis was performed for the boundary layer on the body at duct midheight. The boundary layer analysis consists of a numerical laminar calculation around the nose of the body, and a flat-plate turbulent approximation after transition. The velocity distribution from the static pressure measurements on the body was used as the free stream, which must be known for the laminar calculation. The assumption of steady, incompressible flow is made in this analysis.

Laminar Integral Calculation

The laminar boundary layer was calculated using an integral technique [20] similar to that given by Tani [21]. It uses the momentum and mechanical-energy integral equations to solve for the shape factor, H, and the momentum thickness, δ_2, as a function of the distance, s, measured along the body surface from the leading edge.

Turbulent Flat-Plate Calculation

The well-known relation for the momentum thickness of a flat-plate turbulent boundary layer was used for the turbulent

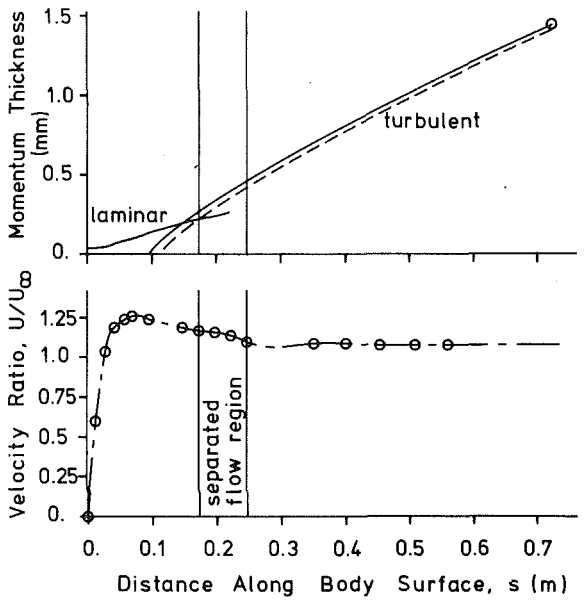

Fig. 16 Results of two-dimensional boundary layer calculation at midheight on body: — laminar and flat-plate turbulent boundary layer calculations to match measured momentum thickness (0) at exit; - - - flat-plate calculation from separation line found by flow visualization; — - — curve fit of free-stream velocity ratio (from measured wall static pressures) used in laminar boundary layer calculation; U_∞ = 24.1 m/s

calculation [22]. The exit velocity, U_e = 25.7 m/s, was the constant free-stream velocity imposed on the boundary layer.

The turbulent layer momentum thickness was calculated using the measured δ_{2e} as a known endpoint. This produced a flat-plate distribution which resulted in the measured δ_{2e} at the exit plane. Another calculation was performed using the value of δ_2 from the laminar calculation as a known initial condition at a chosen transition point.

Calculation Results

Figure 16 shows the momentum thickness calculated at midheight on the body. The measured velocity distribution is shown to the same scale for reference. The separated flow region, inferred from the measured static pressure distribution and flow visualization, is shown between s = 0.17 m and s = 0.25 m.

The two-dimensional laminar boundary layer calculation shows separation at s = 0.22 m, using H = 4.029 as the laminar separation criterion. The calculated laminar separation point is downstream of the inferred separation point, but upstream of the inferred reattachment point.

The turbulent flat-plate boundary layer calculation from the measured exit value of δ_2 = 1.45 mm is shown as the solid line in Fig. 16. This calculated curve intersects the laminar curve at s = 0.15 m, showing an effective transition point upstream of the inferred separation region.

An effective transition point at the inferred separation point, at x = 0.17 m, was obtained by matching the momentum thickness from the turbulent boundary layer calculation to the momentum thickness from the laminar boundary layer calculation. The result of this calculation is shown as the dashed line in Fig. 16 and gives an exit value of δ_2 = 1.40 mm. The difference between this calculated exit momentum thickness and the exit momentum thickness from the measurements is only 3.5 percent of the measured value.

Summary

This paper has presented measurements of the three-dimensional flow in a duct due to the horseshoe vortex at the junction of the duct endwall and a Rankine half-body obstruction. The inlet boundary layer on the duct endwall was artificially thickened to produce a relatively large horseshoe vortex. Measurements on four planes normal to the duct axis define the flow for comparison with the results of three-dimensional viscous flow calculation procedures. A symmetrical flow field was obtained to reduce the amount of measurement and subsequent calculation necessary to determine the duct flow.

A two-dimensional potential-flow analysis shows that at an axial location halfway between the source and the leading edge of the body, the velocity on all streamlines in the duct is equal to the uniform velocity upstream. The static pressure was measured on the duct walls around the perimeter of the plane at this axial location and found to be uniform except near the junction of the body and the duct endwall. In this corner region, the horseshoe vortex influenced the flow.

Variations in endwall static pressure upstream of the leading edge of the body are related to details of the horseshoe vortex flow. A local minimum in static pressure occurs near the saddle point on secondary separation, and a local maximum occurs between the saddle points of primary and secondary separation near a nodal point of reattachment.

Secondary flow velocities just downstream of the leading edge show the streamwise vorticity associated with the horseshoe vortex. The secondary velocities are largest near the endwall where the secondary flow is away from the body; at the duct midheight, a small secondary flow is observed towards the body. The core of the vortex occurs just inside the separation line on the endwall.

Velocity profiles measured on the exit plane show an inner boundary layer on the duct endwall. This result is similar to results reported in turbine cascades, where a new endwall boundary layer starts downstream of flow separation near the leading edges of the blades.

The two-dimensional laminar boundary layer calculation at midheight on the body predicts separation downstream of the location where static pressure measurements show characteristics of boundary layer separation. The boundary layer momentum thickness calculated by the laminar technique at the measured separation point was used to start a flat-plate turbulent boundary layer calculation. The exit momentum thickness calculated in this manner differed from the momentum thickness determined from the measured exit boundary layer by only 3.5 percent of the measured value.

References

1 Dodge, P. R., "Numerical Method for 2D and 3D Viscous Flows," AIAA Paper No. 76-425, 1976.

2 Moore, J. G., and Moore, J., "Lecture Notes on the Calculation of Three-Dimensional Viscous Flows Using Pressure Correction Methods," ASME Gas Turbine Division Short Course on 3-D Flows in Turbomachinery Blade Rows," Phoenix, Arizona, Mar. 1983.

3 Hah, C., "A Navier-Stokes Analysis of Three-Dimensional Turbulent Flow Inside Turbine Blade Rows at Design and Off-Design Conditions," ASME Paper No. 83-GT-40, 1983.

4 York, R. E., Hylton, L. D., and Mihelc, M. S., "An Experimental Investigation of Endwall Heat Transfer and Aerodynamics in a Linear Vane Cascade," ASME Paper No. 83-GT-52.

5 Gaugler, R. E., and Russell, L. M., "Comparison of Visualized Turbine Endwall Secondary Flows and Measured Heat Transfer Patterns," ASME Paper No. 83-GT-83.

6 Schwind, R. G., "The Three-Dimensional Boundary Layer Near a Strut," MIT Gas Turbine Laboratory Report No. 67, May 1962.

7 Belik, L., "The Secondary Flow About Circular Cylinders Mounted Normal to a Flat Plate," *Aeronautical Quarterly*, Vol. 24, No. 1, Feb. 1973, pp. 47–54.

8 Barber, T. J., "An Investigation of Strut-Wall Intersection Losses," *Journal of Aircraft*, Vol. 15, No. 10, Oct. 1978, pp. 676–681.

9 Baker, C. J., "The Turbulent Horseshoe Vortex," *Journal of Wind*

Engineering and Industrial Aerodynamics, Vol. 16, Nos. 1 and 2, July 1980, pp. 9–23.

10 Briley, W. R., and McDonald, H., "Computation of Three-Dimensional Horseshoe Vortex Flow Using the Navier Stokes Equations," Seventh International Conference on Numerical Methods in Fluid Dynamics, Stanford University & NASA/Ames, June 23–27, 1980.

11 Hawthorne, W. R., "The Secondary Flow About Struts and Airfoils," *Journal of the Aeronautical Sciences*, Vol. 21, No. 9, Sept. 1954, pp. 588–608.

12 Vennard, J. K., and Street, R. L., *Elementary Fluid Mechanics*, 5th ed., John Wiley & Sons, 1976, pp. 608–610.

13 Boblitt, W. W., "Horseshoe Vortices in a Duct," B.S. thesis, VPI&SU, June 1982.

14 Forlini, T. J., "Measurement of Three-Dimensional Horseshoe Vortex Flow in a Duct," M.S. thesis, VPI&SU, June 1983.

15 Tavakoli, A., "Design and Evaluation of a Pulsating Flow Wind Tunnel," M.S. thesis, VPI&SU, Sept. 1982.

16 Moore, J. G., and Moore, J., "Calculation of Horseshoe Vortex Flow Without Numerical Mixing," ASME Paper No. 84-GT-241.

17 Klebanoff, P. S., "Characteristics of Turbulence in a Boundary Layer with Zero Pressure Gradient," NACA Report 1247, 1955.

18 Schlichting, H., *Boundary Layer Theory*, 7th ed., McGraw-Hill, 1979, p. 220.

19 Langston, L. S., Nice, M. L., and Hooper, R. M., "Three-Dimensional Flow Within a Turbine Cascade Passage," JOURNAL OF ENGINEERING FOR POWER, Vol. 99, No. 1, Jan. 1977, pp. 21–28.

20 Moses, H. L., Unpublished notes, VPI&SU, Winter 1982.

21 Tani, I., "On the Approximate Solution of the Laminar Boundary Layer Equations," *Journal of Aeronautical Sciences*, Vol. 21, No. 7, July 1954, pp. 487–495.

22 Schlichting, H., *Boundary Layer Theory*, 7th ed., McGraw-Hill, 1979, pp. 636–638.

D. E. Metzger

C. W. Plevich

C. S. Fan

Mechanical and Aerospace Engineering Department, Arizona State University, Tempe, Ariz. 85287

Pressure Loss Through Sharp 180 Deg Turns in Smooth Rectangular Channels

Measured pressure distributions, pressure loss coefficients, and surface streamline visualizations are presented for 180 deg turns in smooth, rectangular cross-section channels. The flow geometry models situations that exist in multipass internal cooling of gas turbine engine airfoils. The turn geometry is characterized by parameters W^*, the ratio of upstream and downstream channel widths; D^*, the nondimensional channel depth; H^*, the nondimensional clearance height at the tip of the turn; and R^*, the nondimensional corner fillet radius. The present results cover a range of combinations of geometry parameters and Reynolds numbers to aid in prediction of coolant flow rates in present and future cooled airfoil designs.

Introduction

Internal cooling passage designs in gas turbine blades and vanes frequently employ multiple channels aligned with the airfoil spanwise direction. The channels are connected by 180 deg bends with cooling air thus traversing the inside of the airfoil in a multipass arrangement, as shown in Fig. 1. Frequently, the channels are roughened with ribs to enhance the convective heat transfer. Pin-fin arrays are often used in the narrow airfoil trailing edge region for similar heat transfer augmentation.

In a typical cooled airfoil, these different coolant passage regions are series-connected to produce a total flow resistance that determines the coolant flow rate for a given supply pressure. In each region, heat transfer rate is a strong function of coolant flow rate. Thus accurate predictions of cooling throughout the airfoil depend critically on the designer's ability to first accurately predict the passage flow resistance. It is well known that relatively large pressure losses are associated with flow turning in channel bends and that the total passage flow resistance is therefore strongly influenced by the turning losses. However, there is currently little information available to aid the designer in accurately predicting these turning losses for the range of geometries of interest in turbine design.

Most previous studies aimed specifically at measuring turning losses in piping systems consider only 45 and 90 deg turns in constant cross-sectional area ducts. References [1] and [2] are representative. Also, although the detailed nature of the flow, particularly secondary flow, in curved channels has been of fundamental interest for many years [3, 4], such studies generally provide scant guidance in predicting losses in the type of sharp bends depicted in Fig. 1.

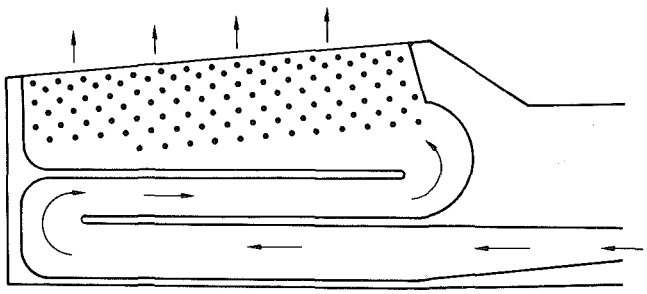

Fig. 1 Turbine airfoil multipass cooling arrangement

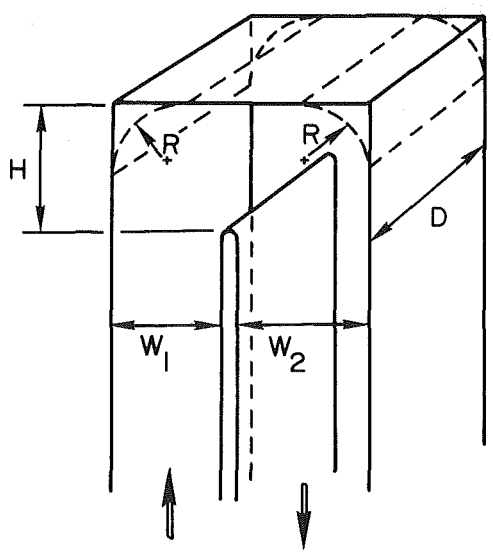

Fig. 2 Present turn geometry

The general configuration of this family of 180 deg bends is illustrated in Fig. 2. The geometry is characterized by four parameters, W^*, H^*, D^*, and R^*. The narrow dividing rib

Contributed by the Gas Turbine Division of THE AMERICAN SOCIETY OF MECHANICAL ENGINEERS and presented at the 29th International Gas Turbine Conference and Exhibit, Amsterdam, The Netherlands, June 4–7, 1984. Manuscript received at ASME Headquarters January 11, 1984. Paper No. 84-GT-154.

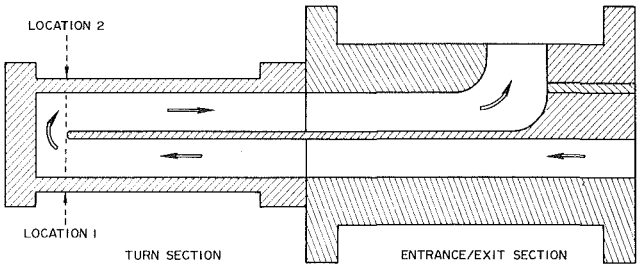

Fig. 3 Test rig cross section

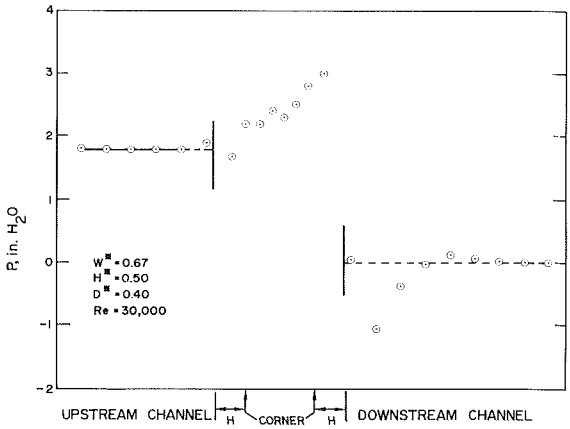

Fig. 4 Typical pressure distribution

between the upstream and downstream channels dictates that the inner radius flow will separate at the tip of the rib, creating a recirculation flow zone for some distance on the downstream side of the rib. Moreover, the centrifugally driven secondary flow creates a strongly three-dimensional flow field even in regions without recirculation. Such turbulent, three-dimensional separated flows are not yet generally predictable with the methods of numerical fluid mechanics, so design predictions of turning losses must be based on experimentally derived information.

Pressure loss information now in existence for turn geometries like those of Fig. 2 is largely in the form of proprietary data obtained from flow testing of actual fabricated airfoils or large-scale flow models of such airfoils. The geometrical range of such data is usually quite limited, which restricts the designer's ability to assess effects of even small changes in the cooling passage geometry. Moreover, the losses associated with the turns are usually determined indirectly, with considerable uncertainty, from overall passage pressure drop, which may include several significant loss regions in addition to turning loss. The open literature, to the author's knowledge, provides only one value [1] for pressure loss in a turn arrangement similar to Fig. 2. The single value is restricted to a constant cross-sectional area turn, and channel Reynolds number is unspecified.

In view of this generally unsatisfactory situation, the present study was initiated with several objectives in mind. The first was to design and fabricate a suitable test rig so that turning losses could be isolated and accurately determined over a large range of combinations of the geometrical parameters. Such information should be immediately useful in design for estimating smooth wall turning losses and assessing their acceptability. The information should also be useful in judging the relative effectiveness of present and future schemes (such as turning vanes) employed to reduce turning losses. A further objective was to design the test rig so that flow visualization studies could be carried out in conjunction with the pressure measurements. Of particular interest in this regard is the extent of recirculating flow zones which, in general, are undesirable from a heat transfer point of view.

Apparatus and Experimental Methods

The test rig is designed to be assembled from interchangeable component parts in order to allow assemblies covering a large range of different combinations of W^*, H^*, D^*, and R^*. The rig consists of two main sections, the test section itself and an entrance/exit section. The main component parts and their assembled relationship are shown in Fig. 3. The parts shown define the flow path and have been fabricated in three complete sets corresponding to values of D (normal to page) of 1.27, 2.54, and 3.81 cm. The sets are interchangeably located between top and bottom cover plates, forming the rectangular cross-section channels and turn region.

The dividing rib between the entrance and exit channels is of one-piece construction and extends from an attachment point in the entrance/exit section into the turn region, eliminating any possibility for leakage across the rib at a joint. In addition, the top and bottom edges of the divider are grooved for O-rings to provide an effective seal at the joint between the rib and top and bottom cover plates. All other possible leakage routes between mating parts are also O-ring sealed. The mating parts are positioned accurately through the use of locator pins, so that the resulting geometry is accurate and repeatable upon reassembly. The entire assembly is secured with machine screws.

For each channel depth, D, three different length divider ribs have been fabricated, corresponding to rib tip clearances of 2.54, 3.18, and 3.81 cm. The relative widths of the upstream and downstream channels is adjusted through the use of spacers at the rib divider attachment point. The total width between side walls is always 6.99 cm; the rib width is always 0.64 cm. The present rig allows operation with any combination of the following parameter values: $W^* = 0.67$, 1.0, 1.5; $H^* = 0.4$, 0.5, 0.6; $D^* = 0.2$, 0.4, and 0.6. In addition,

Nomenclature

A = flow cross-sectional area
D = channel depth
D_h = hydraulic diameter
H = divider tip-to-wall clearance
L = length of separated flow on divider
m = mass flowrate
P = pressure
ΔP = total pressure loss associated with turn
R = fillet radius
V = channel mean velocity
W = channel width
μ = fluid dynamic viscosity
ρ = fluid density

Subscripts

1 = quantity at location 1, upstream side of turn region
2 = quantity at location 2, downstream side of turn region
av = average of location 1 and location 2 quantities

Nondimensional Quantities

$D^* = D/(W_1 + W_2)$
$H^* = H/(W_1 + W_2)$
K = pressure loss coefficient, $2\Delta P/(\rho_{av} V_{av}^2)$
K_1 = pressure loss coefficient based on upstream values of ρ and V
$R^* = R/(W_1 + W_2)$
Re = Reynolds number = $\rho_{av} V_{av} D_{hav}/\mu_{av}$
Re_1 = Reynolds number based on upstream values of ρ, V, and D_h
$W^* = W_1/W_2$

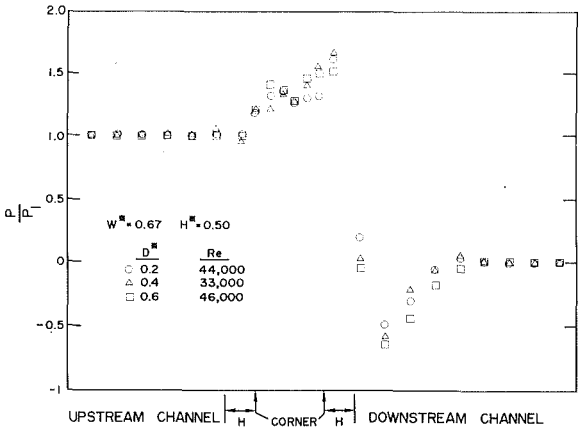

Fig. 5 Typical normalized pressure distribution

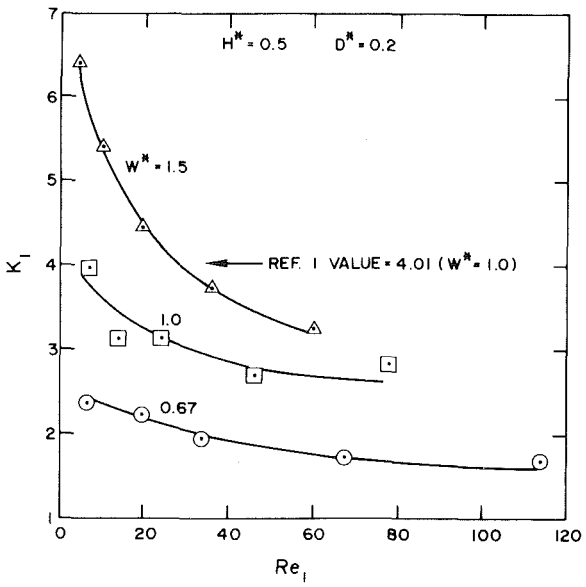

Fig. 6 Effect of W^* on K_1 versus Re_1

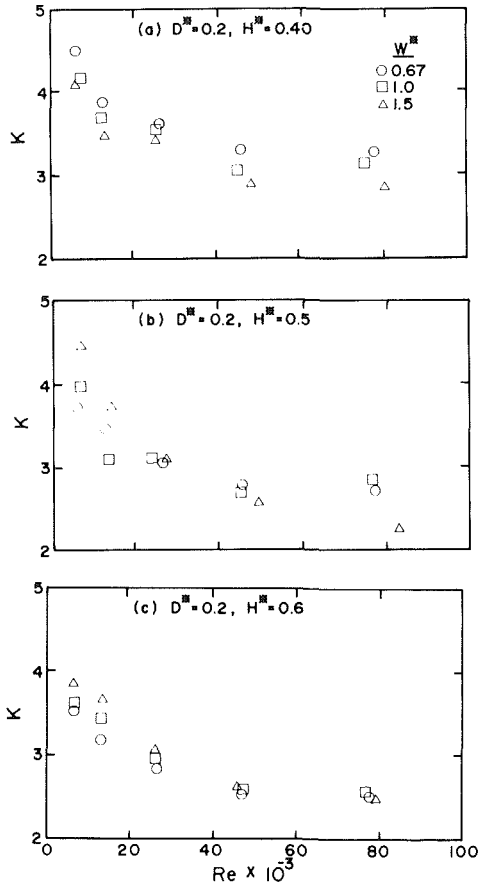

Fig. 7 Effect of W^* on loss coefficients

interchangeable corner fillets have been fabricated for use at $D^* = 0.2$, which provide R^* values of 0.1, 0.2, and 0.4.

Air flow to the test rig is provided by one of several laboratory compressors, depending on the desired mass flow rate. Compressor output, filtered and dried, is measured in an ASME standard orifice installation and supplied to a plenum chamber located immediately upstream of the test rig. The plenum contains a series of screen sections to settle the flow prior to its entry to the channel on the upstream side of the turn.

Flush pressure taps are located at intervals of 2.54 cm along both the upstream and downstream side walls, and at 1.27 cm intervals on the turn or end wall. The pressure taps are connected to a single solenoid activated rotating pressure switch for sequential reading on one of several manometers, depending on pressure level.

Figure 4 shows a representative sample static pressure distribution to illustrate the procedure used for determining loss coefficients associated with the turn region. In general, the pressure distribution in the upstream channel is expected to be linear. The turn highly disrupts the pressure distribution, and the disruption continues downstream of the turn as the flow separates from the center divider, reattaches, and redevelops. Eventually, a linear pressure drop is restored in the downstream channel. The upstream and downstream distributions are both extrapolated in the direction toward the turn to within a distance H of the corner; i.e., to locations 1 and 2 shown on Fig. 3. In both instances, the extrapolated value is the pressure that would have existed at that location if well behaved and if essentially fully developed flow was present within the entire entrance and exit channels. The difference in the two extrapolated pressures is associated with (*a*) the static pressure differential caused by the flow area change from upstream to downstream channels (when one exists), and (*b*) pressure losses caused by the turn. The extrapolated pressure difference is corrected for pressure differential caused by area change, yielding a net total pressure loss associated with the turn, ΔP. This total pressure loss is the overall combination of all phenomena associated with the turn including local accelerations and decelerations, separation and attachment, and the development and subsequent decay of secondary flows.

Results and Discussion

Pressure Distributions. Each turn geometry investigated was tested at five flow rates, covering a nominal Reynolds number range of 5000 to 80,000. Pressure distributions in all cases are typified by the test results shown in Fig. 4. The pressure remains nearly constant along the entrance channel, then begins to rise in the vicinity of the upstream corner. There is a general rise in pressure along the endwall, with the magnitude of the rise dependent upon the turn geometry. The rise in pressure abruptly ends just beyond the downstream corner and drops rapidly to a minimum before increasing to a nearly constant downstream value.

Examination of the individual pressure distributions for each test reveals that their shapes are highly independent of Reynolds number. If each distribution is normalized with the

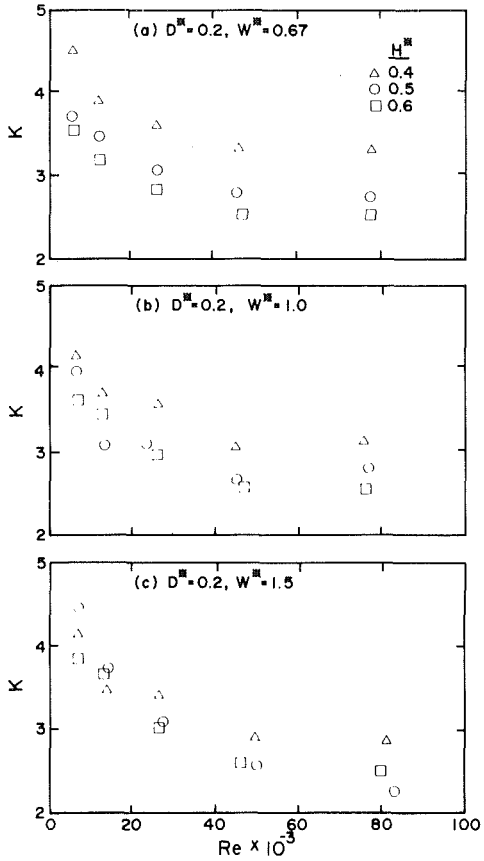

Fig. 8 Effect of H^* on loss coefficients

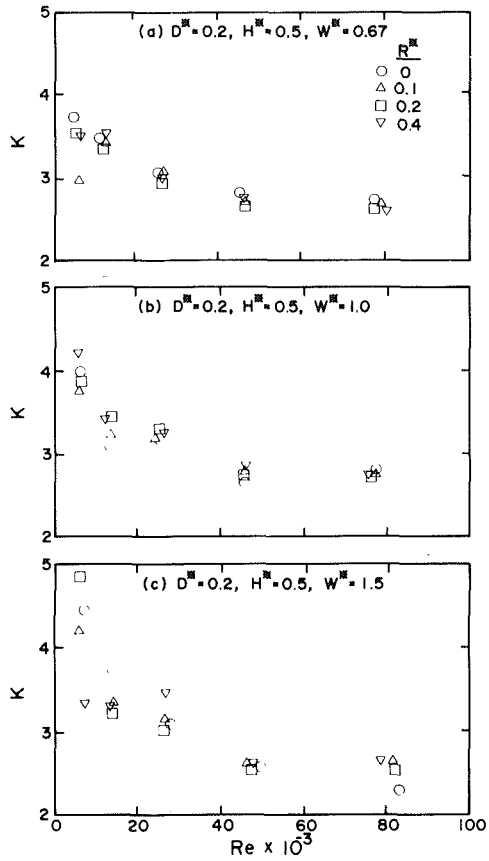

Fig. 10 Effect of R^* on loss coefficients

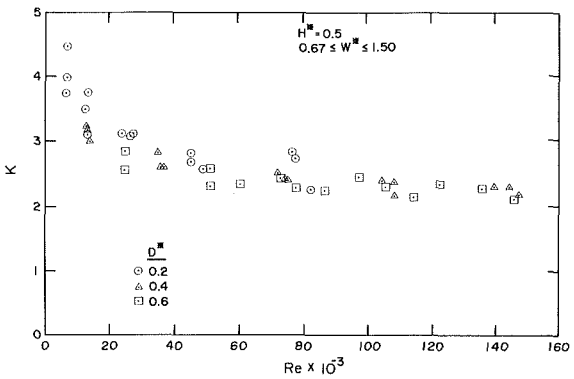

Fig. 9 Summary of K versus Re for $H^* = 0.5$

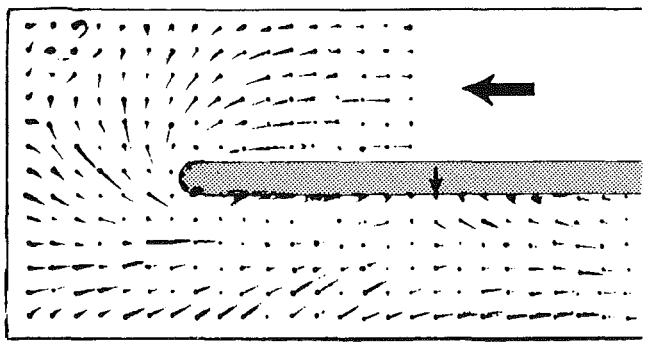

Fig. 11 Surface streamlines, $W^* = 1.0$, $H^* = 0.6$, D^* 0.2, Re = 40,000

value of P_1 for that test, the normalized distributions are virtually identical over the entire Re range for a given geometry. This behavior indicates that the flow pattern is stable, and that there are no abrupt flow regime transitions to be avoided in design. This similarity in pressure distributions extends even further, across the entire D^* test range. Figure 5 shows a typical comparison of such normalized pressure distributions obtained at the three values of D^*, with W^* and H^* held constant. This behavior suggests that turning losses also will not be strongly dependent on D^*, at least for the range of geometries covered.

Loss Coefficients. Figure 6 shows typical loss coefficients measured in the present study as a function of Reynolds number. In this presentation, both loss coefficient, K_1, and Reynolds number, Re_1, are defined in terms of characteristic lengths, velocities, and properties in the upstream channel. These definitions are conventional and correspond, for example, to those used in [1]. There is good correspondence between the single [1] value (for $W^* = 1.0$) and the present result at the lowest tested value of Reynolds number. However, the present results show that use of the [1] result would seriously overpredict pressure loss at higher Reynolds number.

The use of upstream based definitions for loss coefficients and Reynolds number can easily lead to the erroneous conclusion (as might be inferred from Fig. 6) that pressure loss is a strong function of W^*. Actually, for identical flow rates, the three geometrical arrangements covered in Fig. 6 produce nearly identical pressure loss. The differences in K mainly reflect differences in the location 1 velocity rather than differences in total pressure loss.

Figure 7(*b*) shows the same results redefined in terms of loss coefficients and Reynolds numbers based on averages of location 1 and location 2 quantities. These averaged quantities remain essentially constant as the turn geometry is varied for a given flow rate through the turn. On this basis, the values of

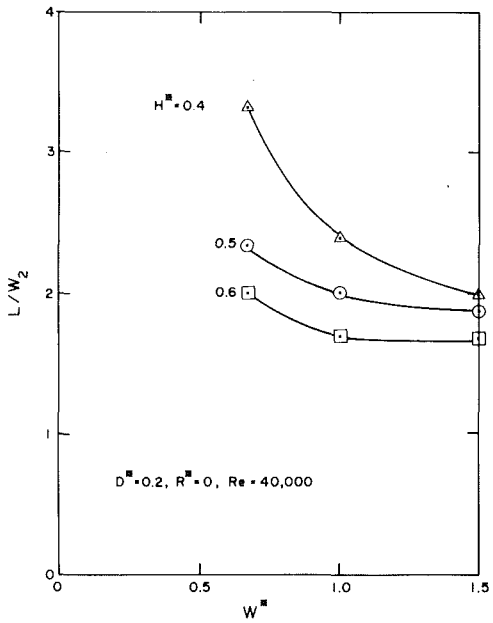

Fig. 12 Length of separated flow on divider

K obtained over the range of W^* agree to nearly within experimental uncertainty, which is estimated to be ± 8 percent by the methods of [6]. The same conclusion is reached for $H^* = 0.4$ and 0.6 at $D^* = 0.2$, as seen in Figs. 7(*a*) and 7(*c*).

Inspection of Fig. 7 reveals that there is a fairly consistent effect of H^* on the loss coefficients, and Figs. 8(*a–c*) show this trend for $D^* = 0.2$ and $W^* = 0.67$, 1.0, and 1.5, respectively. Within the test range $0.4 \leq H^* \leq 0.6$, there is a tendency for K to increase as H^* is decreased. The generally small effect is most pronounced at $W^* = 0.67$ and decreases with increasing W^*.

Figure 9 presents additional results for D^* values of 0.4 and 0.6, all at $H^* = 0.5$, combined with the results of Fig. 7(*b*). The $D^* = 0.4$ and 0.6 tests were carried out to larger flow rates and thus extend the Reynolds number range over which the independent influence of W^* can be seen to be small.

Close inspection of Fig. 9 shows a tendency for loss coefficients to be higher at smaller D^*, but the effect is minor and the present definitions of K and Re collapse all of the results for a single value of H^* to a relatively narrow band. It appears reasonable to expect that the same will hold for the other values of H^* as well. Therefore, the results of Figs. 7(*a*) and 7(*b*) are likely also to represent the entire range $0.2 \leq D^* \leq 0.6$.

All of the foregoing results and discussion are based on tests conducted with 90 deg sharp corners, both upstream and downstream. Figures 10(*a–c*) present results of similar tests conducted with various radii fillets installed in the corners. With the exception of a few of the lowest Reynolds number tests, the presence of fillets appears to have no significant effect on the loss coefficients.

Flow Visualization. Separate flow visualization tests were conducted for a variety of different turn geometries, mostly at $D^* = 0.2$, $R^* = 0$ and at intermediate Reynolds numbers of around 40,000. A few tests were conducted at other values of D^*, R^*, and Re and confirm that the basic flow pattern is essentially independent of these parameters. The method of visualization used provides surface streamlines through use of an ink-dot matrix and solvent film technique described in [5]. Figure 11 is a typical result. The ink from each dot migrates downstream under the influence of the wall shear forces, leaving a gradually thinning tracer line pointing in the direction of the surface flow. Several features of the turn flow field are clearly visible: separated flow regions in the upstream corner and along the downstream side of the divider rib, acceleration and convergence of the upstream surface flow toward the divider tip, and establishment of a radially inward wall surface flow within and downstream of the turn.

The technique shows quite well the length of the recirculation region on the downstream side of the rib. The downstream extent of this region is indicated in Fig. 11 as the point where the surface streamlines immediately adjacent to the rib shift from an upstream to downstream direction in their streamwise component (marked with an arrow on the figure). This point is of special interest, since it has been evident from the start of the investigation that the separated flow zone attached to the rib has a length which is relatively large and sensitive to changes in the turn geometry.

Figure 12 shows the variation in separation zone length on the rib as a function of H^* and W^* (for $D^* = 0.2$ and $R^* = 0$). It is probably to be expected that there is a correlation between the size of the separated flow zone and the loss coefficient, and a comparison of Fig. 12 with Fig. 8 shows the correspondence clearly. At $W^* = 0.67$, L has a large sensitivity to H^*, as does K in Fig. 8(*a*). As W^* increases, the sensitivity of both L and K to H^* decreases.

From a heat transfer point of view, the large separated flow zone on the downstream side of the rib that is observed at $H^* = 0.4$, $W^* = 0.67$ is likely to be undesirable. The flow in these zones is often less energetic and less effective in cooling than the adjacent unseparated flow. This situation can lead to hot spots and high temperature gradients in a cooled airfoil, both of which can contribute to early failure of the cooled part. Such conclusions are of course speculative, and indicate the need for actual heat transfer measurements in similar turn geometries. Nevertheless, the results of the present study do provide the designer with information that will allow accurate prediction of coolant flow rate, a necessary and extremely important prerequisite to the estimation of heat transfer rates.

Acknowledgment

The work reported herein was supported, in part, by Pratt and Whitney Aircraft, Commercial Products Division, East Hartford, Conn.

References

1 Kaminski, D. A., ed., *Fluid Flow Data Book*, General Electric Company, Schenectady, N.Y.

2 Madison, R. D., and Parker, J. R., "Pressure Losses in Rectangular Elbows," ASME *Transactions*, Vol. 58, 1936, pp. 167–176.

3 Dean, W. R., "Fluid Motion in a Curved Channel," *Proc. Royal Society of London*, Series A, Vol. 121, 1928, pp. 402–420.

4 Humphrey, J. A. C., Whitelaw, J. H., and Yee, G., "Turbulent Flow in a Square Duct with Strong Curvature," *Journal of Fluid Mechanics*, Vol. 103, 1981, pp. 443–463.

5 Langston, L. S., and Boyle, M. T., "A New Surface-Streamline Flow-Visualization Technique," *Journal of Fluid Mechanics*, Vol. 125, 1982, pp. 53–57.

5 Kline, S. J., and McKlintock, F. A., "Describing Uncertainties in Single Sample Experiments," *Mechanical Engineering*, Vol. 75, Jan. 1953.

Modeling of Three-Dimensional Flow in Turning Channels

I. M. Khalil

H. G. Weber

Cummins Engine Company, Inc.,
Columbus, Ind. 47202-3005

The structure of developing flows inside curved channels has been investigated numerically using the time-averaged Navier Stokes equations in three dimensions. The equations are solved in primitive variables using finite difference techniques. The solution procedure involves a combination of repeated space-marching integration of the governing equations and correction for elliptic effects between two marching sweeps. Type-dependent differencing is used to permit downstream marching even in the reverse-flow regions. The procedure is shown to allow efficient calculations of turbulent flow inside strongly curved channels as well as laminar flow inside a moderately curved passage. Results obtained in both cases indicate that the flow structure is strongly controlled by local imbalance between centrifugal forces and pressure gradients. Furthermore, distortion of primary flow due to migration of low momentum fluid caused by secondary flow is found to be largely dependent on the Reynolds number and Dean number. Comparison with experimental data is also included.

Introduction

The study of three-dimensional flow in curved channels continues to be a subject of significant importance in a large number of engineering disciplines. The flow through turbomachine blade passages, aircraft inlets, and interstage ducting of integrated propulsion systems are but a few examples. Among the important physical phenomena characterizing the flow inside these passages is the generation of secondary flow due to the turning of the main flow. Boundary layer growth, flow separation and reattachment, and the appearance of corner vortices represent other flow phenomena of practical interest. Besides contributing to the losses within a passage, these phenomena can also interact with the main flow to cause major distortions within the flow field. In multistage turbomachinery applications, the distortions become of great concern since variation in fluid properties have a direct effect on the performance of succeeding flow passages. Proper knowledge and ability to accurately predict or numerically simulate curved channel flows thus become of considerable value to the flow system designer. Not only is this information essential in optimizing the design of one flow component, but it is also needed if the overall performance of a multistage flow system is to be improved.

The accuracy and efficiency with which various flow phenomena can be simulated depend directly on the choice of a mathematical model and on the design of a numerical solution procedure. It is generally acknowledged that the solution of the full three-dimensional Navier Stokes equations (NSE) offers the most complete approach in numerical simulation. These equations are classified as being elliptic and can be solved as a boundary value problem. A number of algorithms have been recently developed for the numerical solution of such problem using different techniques, see for example references [1-3]. In general, these direct methods require excessive computer storage in addition to being expensive in terms of computation time. They are often used when no other viable alternative exists.

The potential disadvantages of large storage and computation time can be circumvented if the physical character of the curved channel flow is considered. In this case, the fluid exhibits a predominant flow direction even through crossflow recirculation may prevail. Accordingly, the NSE can be simplified by neglecting the diffusion in the main flow direction. The simplification allows the treatment of the NSE as an initial value problem in space and forward marching techniques can be used for their numerical solution with considerable savings in memory storage and computation time. However, the forward marching allows the flow conditions to be convected in the downstream direction only. Therefore, in solving the simplified NSE measures have to be taken in order to preserve the overall elliptic influence of the flow field. A number of approaches have been devised to address this problem. Briley and McDonald [4] developed the initial value correction approach based on the primary secondary velocity decomposition. The approach has been employed in a number of studies [4, 5] where the elliptic character of the flow field is accounted for through the imposition of an a priori known inviscid pressure field on the governing equations. The equations are then solved as an initial value problem using spatial marching techniques. The marching is performed only once to correct on the inviscid pressure field for viscous and secondary flow effects. Although it is computationally efficient to obtain a solution in a single sweep, it is not clear whether a single sweep correction

Contributed by the Gas Turbine Division of THE AMERICAN SOCIETY OF MECHANICAL ENGINEERS and presented at the 29th International Gas Turbine Conference and Exhibit, Amsterdam, The Netherlands, June 4-7, 1984. Manuscript received at ASME Headquarters, December 27, 1983. Paper No. 84-GT-49.

would provide satisfactory results for strongly turning flows having regions of large velocity gradient variations.

An alternative approach is to use iterated forward marching techniques. Such techniques have been introduced in an attempt to account for the elliptic character of the flow field by performing repeated marching sweeps. In reference [6], Pratap and Spalding start the sweeps by solving the momentum equations for a guessed pressure field. The resulting velocities for this field do not in general satisfy the continuity equation. To remove the imbalance, they introduce two pressure corrections. The first involves a one-dimensional global correction and the second is a two-dimensional local correction. Both corrections are coupled after each sweep so as to reflect the effects of downstream conditions and to modify the three-dimensional pressure field until the system of momentum and continuity equations are satisfied. Moore and Moore [7] have also suggested a somewhat related forward iterative method. However, unlike the procedures of reference [6], Moore and Moore do not couple the pressure corrections. Instead, they use the local two-dimensional pressure corrections to compute a three-dimensional elliptic correction for use in the next sweep. Recently, Fraser et al. [8] and Swanson [9] have extended the Pratap and Spalding procedures to obtain the flow details inside radial flow impellers.

Dodge [10] has proposed another iterated forward marching procedure in which the velocity field is resolved into potential and rotational components. The potential component is used to update the pressure field so as to satisfy the continuity requirements. Since the pressure is always obtained from a potential solution, the method of Dodge does not appear to be suitable for general flow applications having regions of rotational secondary flow.

The method used in the present work for flow simulation is an extension of the iterative forward marching procedures of reference [6] but differs in the following respects:

1. Boundary fitted coordinates are used to allow modeling of curved channels with arbitrary geometries.
2. Rigorous procedures are applied to develop and solve the pressure correction equations.
3. Type-dependent difference approximations are implemented to allow marching through small regions of separated flow.
4. An alternating direction implicit method is employed for numerical efficiency.
5. A modified two-equation turbulence model which accounts for streamline curvature is included.

The text which follows describes the above features. Applications of the present method to different curved channel flows are then presented and compared to experimental or previously published computed results.

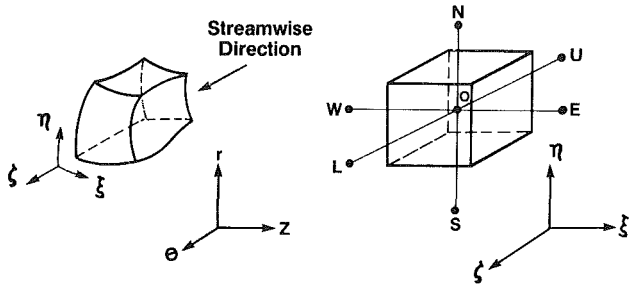

Fig. 1 Body-fitted coordinate and control volume representation

Analysis

Governing Flow Equations. The governing equations are derived from the Reynolds averaged Navier Stokes equations expressed in conservative form using cylindrical (z, r, θ) coordinates. In order to facilitate the implementation of a finite difference solution and the treatment of boundary conditions for general curved passages, the independent variables (z, r, θ) of these equations are transformed to a body-fitted coordinate system (ξ, η, ζ), Fig. 1. The coordinate ζ is taken along the predominant flow direction and ξ, η are the cross stream directions. The resulting set of transformed equations can be written in the following vectorized form [11, 12, 13]:

$$\hat{f}_\xi + \hat{g}_\eta + \hat{h}_\zeta + \bar{l} = \bar{m} \tag{1}$$

The vectors $\hat{f}$, $\hat{g}$, $\hat{h}$, are related to those defined on cylindrical coordinates by means of metrics:

$$\begin{aligned} \hat{f} &= \xi_z \bar{f} + \xi_r \bar{g} + \xi_\theta \bar{h}/r \\ \hat{g} &= \eta_z \bar{f} + \eta_r \bar{g} + \eta_\theta \bar{h}/r \\ \hat{h} &= \zeta_z \bar{f} + \zeta_r \bar{g} + \zeta_\theta \bar{h}/r \end{aligned} \tag{2a}$$

The metrics ξ_z, η_r, ζ_θ, . . . etc. are nondifferentiable transformation parameters relating the body fitted coordinates to the cylindrical coordinates.

The vectors, $\bar{f}$, $\bar{g}$, $\bar{h}$, $\bar{l}$, $\bar{m}$, are defined as follows:

Nomenclature

$C_1, C_2, C_k, C_\epsilon$ = constants in turbulence model
D = dissipation due to viscosity
De = Dean number = $\mathrm{Re}\sqrt{H/R}$
H = channel height $(R_0 - R_i)$, mm
k = kinetic energy of turbulence J/Kg
m = error in continuity equation
M = mass flow, Kg/s
p = static pressure, Kp/m^2
R_i, R_0 = channel inner, outer radius, mm
R = channel mean radius $(R_0 + R_i)/2$, mm
Re = Reynolds number = $\rho W_{\mathrm{in}}/\mu$
S = source terms
u, v, w = velocity components in the z, r, θ direction, m/sec
W = streamwise velocity, m/sec
ϵ = dissipation of kinetic energy of turbulence, J/Kg
ρ = static density, Kg/m^3
η, ξ = cross stream coordinate in the transformed domain
ζ = streamwise coordinate in the transformed domain
ϕ = denotes a general flow property
α, β, γ = transformation parameters (equation (4))

Subscripts

$0, N, S, E, W, U, L$ = denotes node location, Fig. 1
in = inlet conditions
$\zeta, \eta, \xi, z, r, \theta$ = denotes differentiation with respect to these variables

Superscripts

c = denotes corrective values

$$\bar{f}=\begin{pmatrix}\rho u\\ \rho u^2+p-\sigma_{zz}\\ \rho uv-\sigma_{rz}\\ \rho uw-\sigma_{\theta z}\end{pmatrix}\quad \bar{g}=\begin{pmatrix}\rho v\\ \rho vu-\sigma_{rz}\\ \rho v^2+p-\sigma_{rr}\\ \rho vw-\sigma_{r\theta}\end{pmatrix}$$

$$\bar{h}=\begin{pmatrix}\rho w\\ \rho wu-\sigma_{\theta z}\\ \rho wv-\sigma_{r\theta}\\ \rho w^2+p-\sigma_{\theta\theta}\end{pmatrix}\quad \bar{l}=\frac{1}{r}\begin{pmatrix}\rho v\\ \rho vu\\ \rho(v^2-w^2)\\ 2\rho vw\end{pmatrix} \tag{2b}$$

$$\bar{m}=\frac{1}{r}\begin{pmatrix}0\\ \sigma_{rz}\\ \sigma_{rr}-\sigma_{\theta\theta}\\ 2\sigma_{r\theta}\end{pmatrix}$$

Where u, v, w are the velocity components in z, r, θ; ρ is the density and p is the pressure field. The σ's represent the regular shear-stress which is expressed in terms of the velocity gradients and the viscosity μ.

For computational economy, the stagnation temperature is assumed constant and thus an energy equation is not required. The static temperature is obtained from the ideal gas law and the constant total temperature assumption.

For high Reynolds number flows, the diffusion of momentum in the predominant flow direction ζ can be neglected. This approximation is consistent with boundary layer theory and yet maintains the coupling between the inviscid and viscous regions that is critical in simulating interactive flows. With this thin layer approximation, the momentum equations (1) can be rewritten as [12]:

$$(\rho U\phi)_\xi+(\rho V\phi)_\eta+(\rho W\phi)_\zeta=(\omega\mu\phi_\xi)_\xi+(\Omega\mu\phi_\eta)_\eta+S+S^p \tag{3}$$

where ϕ may represent any dependent flow property such as u, v, or w. The contravariant variables U, V, and W are given by:

$$\begin{aligned}U&=\xi_z u+\xi_r v+\xi_\theta w/r\\ V&=\eta_z u+\eta_r v+\eta_\theta w/r\\ W&=\zeta_z u+\zeta_r v+\zeta_\theta w/r\end{aligned} \tag{4}$$

and

$$\begin{aligned}S^p&=\alpha p_\xi+\beta p_\eta+\gamma p_\zeta\\ \omega&=\xi_z^2+\xi_r^2+\xi_\theta^2/r^2\\ \Omega&=\eta_z^2+\eta_r^2+\eta_\theta^2/r^2\end{aligned}$$

In the foregoing equations, the α, β, γ, represent the metric coefficients ξ_z, η_z, ζ_z when $\phi\equiv u$ and represent ξ_r, η_r, ζ_r when $\phi\equiv v$ and ξ_θ, η_θ, ζ_θ when $\phi\equiv w$. The source term S contains first order as well as mixed derivative viscous terms [12] in addition to the appropriate component of the vector $\bar{l}$ of equation (2b).

It should be noted at this point that the pressure field in equation (3) is the same in all three momentum equations. This causes the equations to be coupled and as such, influences from downstream are transmitted upstream through the pressure field.

Turbulent Closure. The foregoing development of the governing equations is strictly applicable to laminar flow since the practical problem of grid size prevents resolution of small scale turbulent eddies. However, an inclusion of a turbulent model allows the range of the preceding equations to be extended to the fully turbulent regime. The two equation model proposed in [14] for the kinetic energy of turbulence k and its rate of dissipation ϵ is used in the present study with modifications to account for streamline curvature. The equations governing the transport of k and ϵ have a general form which includes convection, production, diffusion, and dissipation terms. These can be written in a form similar to that given by equation (3). However, in this case, the diffusion coefficient, μ, is replaced by μ/C_k for the k-equation while it is replaced by μ/C_ϵ for the ϵ equation. The source term S^p also takes the following form:

$$\begin{aligned}S^p&=D-\rho\epsilon \qquad \text{for } k\text{-equation}\\ &=\frac{\epsilon}{k}(C_1D-C_2\rho\epsilon) \quad \text{for } \epsilon\text{-equation}\end{aligned} \tag{5}$$

where D is the dissipation due to viscosity [14].

The numerical values of the constants in equation (5) are not optimized and are given by:

$$C_1=1.44, C_2=1.92, C_k=1.0, C_\epsilon=1.3$$

The Reynolds stresses are related to the mean flow variables using the viscosity coefficient

$$\mu=\mu_l+C_\mu\rho k^2/\epsilon \tag{6}$$

where the laminar viscosity μ_l is considered to be uniform and known. The curvature modification used in the present study is based on the algebraic stress model of Gibson [15]. This consists of a set of algebraic equations interrelating the Reynolds stress to the strain rates introduced by curvature. Solution of these equations results in a curvature dependent C_μ given by [16]:

$$C_\mu=11.11+6.31\frac{k^2}{\epsilon^2}\left(\frac{\partial W}{\partial N}+\frac{W}{R}\right)W/R \tag{7}$$

where R is the radius of curvature of the streamline; W is the velocity in the streamwise direction, and N is the streamline normal.

Discretization Scheme. Finite difference analogs of the governing differential equation (3) are obtained using finite volume spatial discretization approach. In this approach, the governing equations are integrated over the control volume $\Delta\xi\Delta\eta\Delta\zeta$ shown in Fig. 1 in the transformed domain. A fully staggered arrangement of control volumes is employed for the velocities and pressures. This arrangement is chosen in order to avoid the decoupling effect between velocities and pressures which is frequently observed with normal grid arrangements. In carrying out the necessary integration, variables at the control volume boundaries are interpolated between adjacent grid points. The nonlinear terms are linearized using either upstream values or values from the previous iteration. The streamwise convective terms are replaced with two point backward differences while three point central differences are used for the derivatives in the cross stream directions ξ, η. With this representation, a finite difference analog of the generalized governing equation (3) can be written as:

$$A_0\phi_0=A_N\phi_N+A_S\phi_S+A_E\phi_E+A_W\phi_W+B_U\phi_U+(S+S^p)\Delta\xi\Delta\eta\Delta\zeta \tag{8}$$

where the subscripts 0, N, S, E, W, and U denote locations as shown in Fig. 1. The A coefficients involve contribution due to the convective fluxes in ξ, η, ζ directions as well as diffusion in the ξ, η directions. The coefficient B_U represents the upstream convective contribution.

When flow reversal occurs, the streamwise convection may

be neglected and the coefficient B_U in equation (8) is set to zero. As compared to other techniques [6–9], this type-dependent approximation should allow the marching sweeps to be performed effectively for cases involving the presence of small but noticeable streamwise separation zones. It must be noted, however, that the approximation does not allow the prediction of the zone details to a high degree of accuracy. Local elliptic calculations using three-dimensional arrays of all flow variables are needed to handle the required details. Such refinements are beyond the scope of this study.

Pressure Correction Equations. An iterative marching procedure is used to advance the solution of the finite difference equations (8) toward a converged state. A feature directly associated with this procedure is the manner in which the pressure field is gradually established. In the present study, the pressure field is established by performing three levels of pressure adjustments so as to drive the solution of the momentum equations toward the one satisfying mass conservation.

In the first level, a one-dimensional pressure correction, $p^c(\zeta)$ is applied uniformly at each cross stream surface (where ζ is constant). The correction is determined iteratively to ensure global mass conservation:

$$\iint \rho W d\xi d\eta = M$$

where M is the total mass flow at the channel inlet, and W is the streamwise velocity component given by equation (4). As opposed to previous approaches [6–9] where approximate integral expressions are employed, the present iterative scheme makes use of the full momentum equations to arrive at the required pressure correction $p^c(\zeta)$. Besides being more general, this scheme is also found [12] to provide improved stability characteristics especially when massive stagnation regions exist in the upstream flow. The scheme is implemented as follows. The pressure field obtained from previous iteration is adjusted using two different sets of guessed values of $p_1^c(\zeta)$, $P_2^c(\zeta)$. The three momentum equations are then solved for these two guesses to obtain the corresponding values of W_1, W_2. Two sets of error, ER_1, ER_2, are also recorded. These errors are defined as follows:

$$ER_1 = M - \iint \rho W_1 d\xi d\eta \text{ and } ER_2 = M - \iint \rho W_2 d\xi d\eta \qquad (9)$$

The third and successive guesses for $p^c(\zeta)$ are obtained from the secant iterative formula:

$$p_q^c(\zeta) = p_{q-1}^c(\zeta) + \frac{ER_{q-1}(p_{q-1}^c - p_{q-2}^c)}{ER_{q-2} - ER_{q-1}} \qquad (10)$$

where q is the iteration parameter. For the flow cases considered here, the procedure converged after only two applications of equation (10) while accelerating the establishment of the correct pressure field.

During the second level of adjustment, two-dimensional pressure corrections $p^c(\xi,\eta)$ are applied on each cross stream surface to arrange for the satisfaction of local continuity at each grid point. These corrections are determined from the solution of a pressure Poisson equation. The further analysis required to arrive at an appropriate form of this equation involves the use of the momentum and continuity equations. Based on the momentum equation (3), the following relations are employed to relate the pressure corrections to velocity corrections.

$$\begin{aligned} A_1 u^c &= \alpha_1 p_\xi^c + \beta_1 p_\eta^c + \gamma_1 p_\zeta^c \\ A_2 v^c &= \alpha_2 p_\xi^c + \beta_2 p_\eta^c + \gamma_2 p_\zeta^c \\ A_3 w^c &= \alpha_3 p_\xi^c + \beta_3 p_\eta^c + \gamma_3 p_\zeta^c \end{aligned} \qquad (11a)$$

Where the A coefficients include contributions due to convection and viscous effects, and the superscript c denotes corrective values. Application of the continuity equation (1) dictates that the correction to the velocity field must satisfy:

$$\iiint [(\rho U^c)_\xi + (\rho V^c)_\eta + (\rho W^c)_\zeta + \rho v^c / r] d\xi d\eta d\zeta = -m \qquad (11b)$$

where the integral is carried over the control volume and m is the local mass imbalance in the continuity at the current iteration level. It is understood here that U^c, V^c, and W^c are related to u^c, v^c, and w^c through equation (4).

The following Poisson equation for pressure is obtained after substituting equation (11a) into (11b) and expressing the result in finite difference form.

$$A_0 p_0^c = A_N p_N^c + A_s p_S^c + A_E p_E^c + A_W p_W^c + B_U p_U^c + B_L p_L^c + S + m \qquad (12)$$

Where S contains all cross derivative terms.

It should be noted that equation (12) represents a three-dimensional pressure correction statement. This equation is solved during the second level of adjustment by neglecting the upstream and downstream influences; namely, setting B_U and B_L to zero. This procedure accelerates the establishment of the corrected transverse pressures $p^c(\xi,\eta)$ resulting from local effects such as local radii of curvature.

The third level of correction is performed after a complete marching sweep has been completed through the flow domain. During this level, the pressure field is corrected for three dimensional effects. The necessary corrections are obtained from the solution of the complete Poisson equation (12). It is worthy to mention here that the off diagonal terms in the momentum equations are not completely neglected while formulating equation (11a). Such consideration was found to bring a considerable accuracy improvement during the solution of the Poisson equation for problems in which continuity cannot be easily satisfied for the initial conditions.

Boundary Conditions. To initiate the space marching procedure, all dependent variables must be specified at the inflow boundary. This information is taken from experimental data where possible. At the outflow boundary, conditions are needed for the elliptic pressure correction equation. A linear extrapolation of pressure correction is used for this purpose. Since the other governing equations are rendered implicit in space (as a result of neglecting the diffusion of momentum in the streamwise direction), no extra conditions are required for the remaining flow variables at the same boundary.

Along the channel walls, the no slip conditions are enforced. For turbulent flow calculations, wall functions based on the constant stress layer [14] are applied to grid nodes next to the wall to match the interior flow with the imposed no slip conditions. This practice precludes the need for fine grids, which would otherwise be necessary to resolve steep gradients within the wall regions. The numerical procedures used to implement the wall function formulation for the velocities, turbulent kinetic energy, and dissipation rate are similar to those outlined in reference [17]. The remaining boundary conditions along the channel walls consist of zero normal derivative for the pressure corrections.

Numerical Solution Procedure. The global solution of the system of coupled difference equations (8, 12) is obtained by performing repeated sweeps through the flow domain. Each sweep consists of an implicit marching integration of the finite difference equations (8) followed by the solution of the three-dimensional elliptic pressure correction equation (12). During the marching procedure, the cross-stream surfaces are scanned one by one beginning from the upstream station where the flow variables are given. An alternating direction implicit (ADI) scheme is used to obtain a solution to the difference equations at each station during the scanning process. This scheme combines the convenience of one-dimensional easily invertible operators and the unconditional stability of implicit methods. Details of the ADI scheme are

similar to those given in references [17, 18]. The sequence of calculation steps to evaluate the flow variables at each station is outlined below.

1. The three momentum equations are solved simultaneously to obtain a tentative velocity distribution. The pressure field from an initial guess or a previous iteration is used with the momentum equations.
2. The density field is updated next using the equation of state and the total enthalpy definition.
3. The secant iterative procedure is employed in order to conserve the total mass flow at the current station. Global adjustments to pressures are enforced accordingly.
4. The two-dimensional version of the pressure correction equation (12) is solved next to arrange for the local satisfaction of continuity at each grid point. The pressure distribution for the station is then adjusted.
5. The computations described in Steps 1 to 4 are repeated iteratively until satisfactory convergence for the continuity is obtained. Typically, no more than 5 iterations were required in the present study and this ensured that the final change in the velocity components $\Delta u/w$, $\Delta v/w$ between two consecutive iterations was less than 0.002. The corresponding error in global mass flow was less than 0.003 of the inlet total flow.
6. The finite difference equations for the remaining variables k and ϵ are solved.

The foregoing procedures are repeated for all subsequent stations to the exit station. After one sweep of the forward marching, the three-dimensional elliptic pressure correction equation is solved. The results obtained from this solution provide corrections to improve the pressure distribution. The improved pressure field is used as input when repeating the marching procedure during the following sweep.

In general, fewer than seven sweeps were necessary to achieve convergence for the turbulent flow case studied here. The actual criterion used to judge convergence was chosen such that the maximum relative change in pressures between two sweeps $\Delta p/p$ was less than 0.0005.

Remarks on the Computational Method. To obtain useful flow prediction, the problem of solving the pressure Poisson equation (12) with the imposed derivative boundary conditions (Neumann problem) should be properly addressed. Careful numerical investigations [19, 20] indicate that unless the boundary gradients are compatible with the source term in the Poisson equation, the solution of the Neumann problem can lead to significant errors. In the present study, these errors can easily result in poor satisfaction of continuity and hence obscure the prediction of important physical processes. To optimize the accuracy and the convergence rate of the present numerical procedures, the necessary compatibility constraints are enforced by satisfying Green divergence theorem. This practice, which was first suggested by Briley [20], has apparently been overlooked in other previous studies [6–9]. It is implemented here by requiring that the area integral of the velocity field divergence m and the line integral of the normal pressure gradient $\partial p^c/\partial N$ must satisfy the following relation:

$$E = \int\int_A m dA - \int_L \frac{\partial p^c}{\partial N} dL = 0 \qquad (13)$$

Where the integrals are evaluated over the cross stream surface total area A and its contour L. Numerical implementation of the above constraint is achieved iteratively using similar procedures as those outliend in reference [20].

Artificial Dissipation. A major problem associated with the central differencing of convective terms for high Reynolds number flows is the appearance of spatial oscillations during the solution. To suppress these oscillations, some form of nonphysical diffusion mechanism must be included in the numerical scheme. The mechanism can be included implicitly through the use of upwind differencing of the convective terms [17] or explicitly through addition of smoothing terms [13]. The explicit form of artificial dissipation scheme presented in [13] was implemented here. Since the techniques add a smoothing term that is proportional to the fourth power

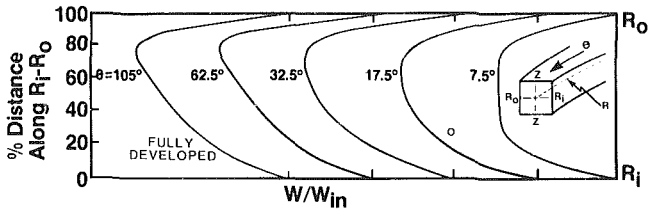

Fig. 2(a) Development of streamwise velocity profiles along ($R_i - R_0$)

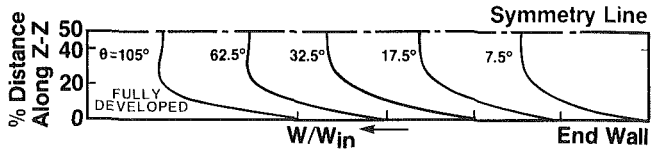

Fig. 2(b) Development of streamwise velocity profiles along ($Z-Z$)

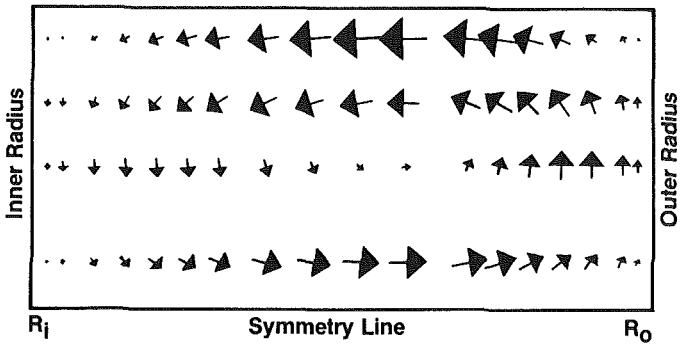

Fig. 3 Secondary velocity vectors for fully developed flow (θ = 105 deg)

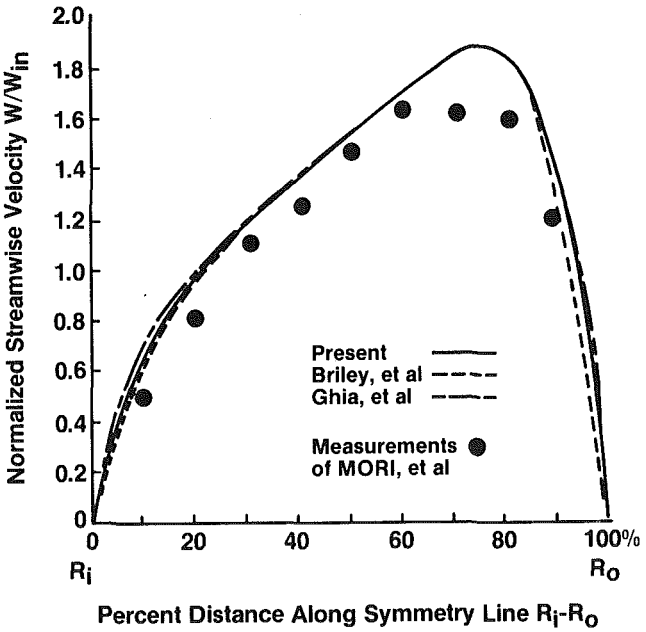

Fig. 4 Radial variation in streamwise velocity along symmetry line ($R_i - R_0$)

of the coordinate spacing, its global impact on the solution accuracy should be minor.

Results

The present method of solution has been tested to illustrate its capability in predicting the actual flow behavior within different curved passages. The cases investigated include laminar flow in a moderately curved channel, turbulent flow in a strongly curved channel, and flow inside a turbine volute housing.

Laminar Flow Results. The laminar flow in a circular arc channel of square cross section under conditions of low Reynolds number and small channel curvature was investigated. The calculations simulated the experimental conditions reported by Mori et al. [21] in which the flow Reynolds number, $\mathrm{Re} = \rho W_{in} H/\mu$ was 205, where H is the radial channel height. The corresponding Dean number defined as $\mathrm{De} = \mathrm{Re}\sqrt{H/R}$ was 55, where R is the channel mean radius of curvature. A 20 × 20 nonuniform grid was used at each cross section, and 30 streamwise stations were required for the numerical solution which was performed in the transformed domain. The grid geometry and transformation parameters were generated analytically for this simple case. Since no experimental data were available at the upstream boundary, all flow properties were assumed to be uniform at the inlet station. This is believed to be a reasonable assumption since the supply air in the experimental set up was fed through a large plenum chamber. An initial guess of the pressure field is needed to start the computation and for this purpose the pressure field was assumed uniform. The computations were run on a Honeywell CP6 machine and the run time was ten minutes.

Computed flow results are presented in Figs. 2–4. Figures 2(*a*) and 2(*b*) show the development of streamwise velocity profiles along the horizontal and vertical channel centerlines. The profiles in Fig. 2(*a*) indicate that near the channel inlet, curvature has little effect on the streamwise velocities. The thick boundary layers in this region generate a rapid and strong secondary flow motion similar to the one shown in Fig. 3. The radial velocities associated with this motion counteract the effects of pressure gradients set up by radius changes and result in the nearly symmetrical velocity profiles noted at inlet. As the flow progresses downstream, the predicted profiles become more asymmetric. The asymmetry can be directly related to the spatial development of the secondary flows which induce a helical flow motion into the fluid as it moves downstream. This motion draws low momentum fluid from the sidewalls and convects it toward regions adjacent to the inner radius. High streamwise velocities existing near the channel center are displaced accordingly toward the outer radius as indicated in Fig. 2(*a*). The presence of a hump in the calculated symmetric velocity profiles along the channel centerline in Fig. 2(*b*) is also a manifestation of the helical motion.

To assess the accuracy of the present solution, computed results for the fully developed streamwise velocity profiles are compared with other predictions [5, 19]. The results shown in Fig. 4 by Briley were obtained using the primary-secondary velocity decomposition method, whereas those of Ghia were obtained from the solution of the parabolized Navier Stokes equations. In general, the differences observed between the three solutions are small and presumably reflect the differences in the numerical approaches used. Also shown in Fig. 4 are the experimental measurements of Mori [21] which qualitatively agree with the computed results. The discrepancy between the measurements and various calculations has not as yet been fully explained although some doubt has been cast recently regarding the accuracy of measurements [22].

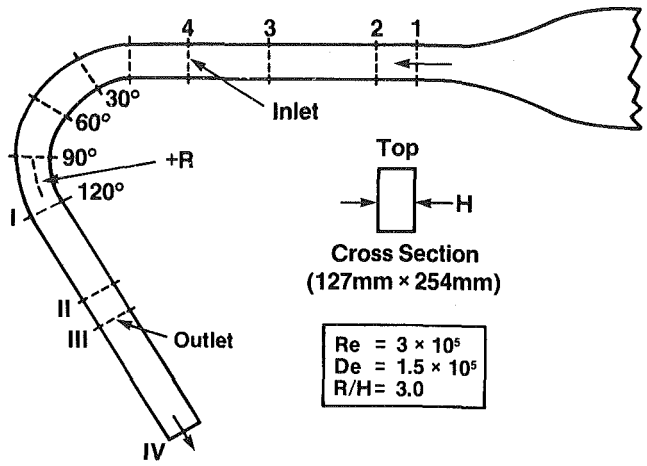

Fig. 5 Flow configuration for the turbulent case

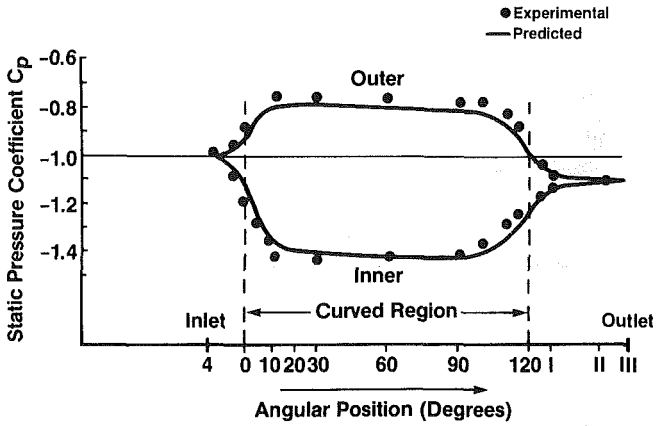

Fig. 6 Streamwise variation in static pressure coefficient

Turbulent Flow Results. To further check the predictive capability of the present analysis, turbulent flow in a strongly curved channel was considered. This case was computed for comparison with the experimental measurements of Brunn [23]. The channel geometry is shown in Fig. 5. Because of the accentuated curvature variation between the straight and curved section of the channel, this geometry represents a good test case whereby the accuracy of the numerical procedures can be assessed. The Reynolds number of the experimental flow was 3.0×10^5. The corresponding Dean number was 1.5×10^5. In the computations, the inflow boundary was located at station 4 upstream of the curved section and the outflow boundary was at station III downstream. The flow conditions obtained from the experimental data at station 4 were used as input to start the calculations. The calculations were performed using 20 × 30 nonuniform grid at each cross-section and 50 streamwise stations were required to scan the whole flow domain. As in the laminar flow case, the boundary fitted coordinates were generated analytically and consisted of Cartesian and cylindrical grids for the straight and curved sections, respectively. To remove the discontinuity in coordinate curvature at the junction of the two sections, the curvature and its derivative with respect to the coordinates were smoothed over two streamwise stations. The initial guess for the pressure distribution within the domain consisted of uniform pressures in the straight sections and pressures corresponding to free-vortex flow behavior in the curved section. The computer CPU time for this case was approximately 140 min.

Figures 6 through 9 show comparisons of the predicted flow results against the measurements of [23]. In Fig. 6, the

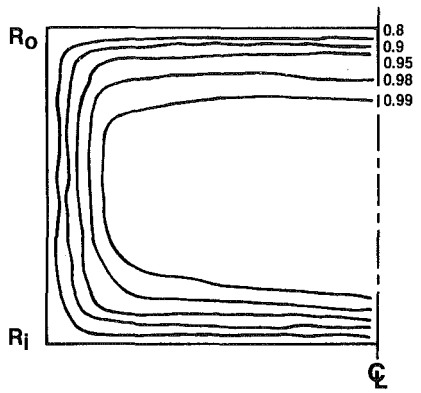

Fig. 7 Inlet velocity contours, W/W_{in}

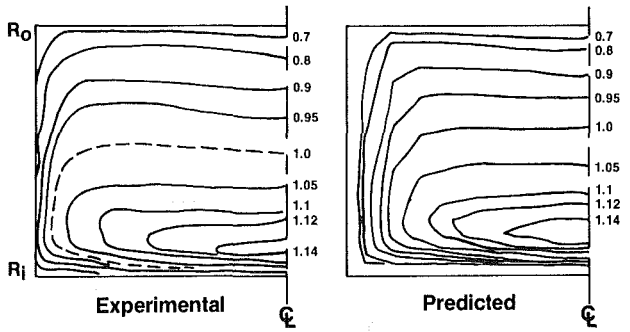

Fig. 8(*a*) Streamwise velocity contours, W/W_{in} at 30 deg

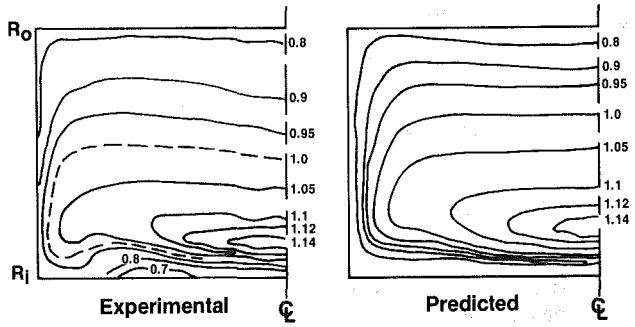

Fig. 8(*b*) Streamwise velocity contours, W/W_{in} at 60 deg

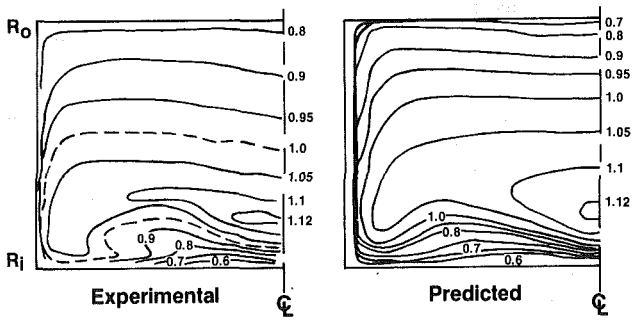

Fig. 8(*c*) Streamwise velocity contours, W/W_{in} at 90 deg

streamwise variation of static pressure coefficient is shown along the midchannel width of both the inner and outer walls. The results show that the flow rapidly adjusts itself to the radial pressure gradients set up by the radius change. The adjustment region of the flow field is seen to extend both upstream (Station 4 to $\theta = 0$) and downstream into the curved section ($\theta = 0$ to 15 deg). The pressure field at mid-width remains virtually constant from (15 deg $< \theta <$ 90 deg) after which the flow adjusts itself to the exit conditions. The

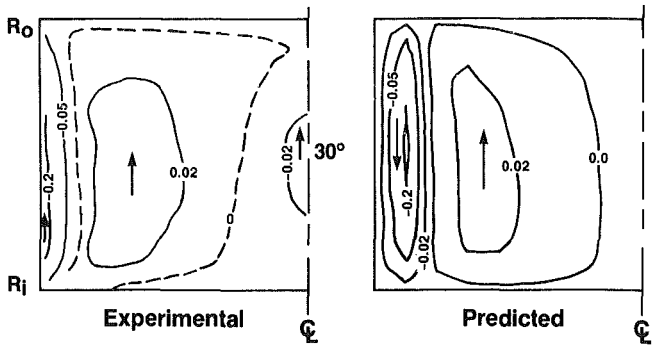

Fig. 9(*a*) Radial velocity contours, v/W_{in} at 30 deg

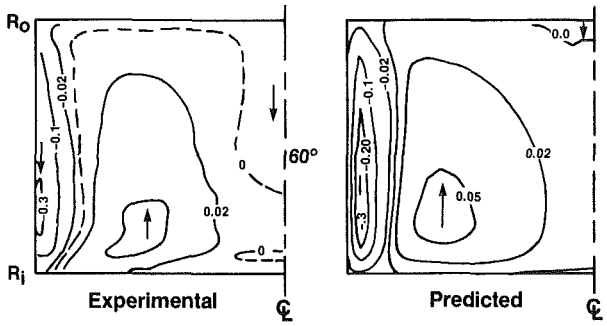

Fig. 9(*b*) Radial velocity contours, v/W_{in} at 60 deg

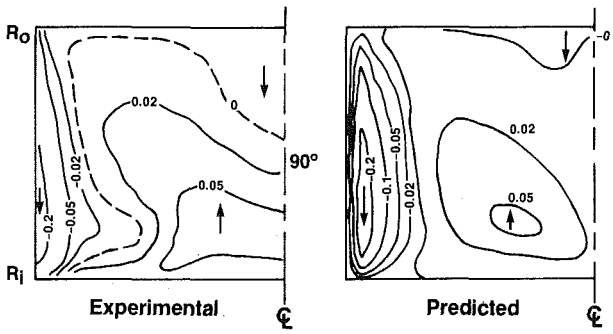

Fig. 9(*c*) Radial velocity contours, v/W_{in} at 90 deg

variation of the radial pressure gradients between the inner and outer walls within the two regions of adjustments confirms the existence of strong elliptic pressure effects. The essentially good level of agreement noted in Fig. 6 between the predicted results and experimental data indicates that these elliptic effects are accurately resolved.

The development of streamwise velocity is displayed in Fig. 8 as contour plots. The inlet velocity profiles used as input are shown in Fig. 7. The computed flow structure at 30 deg (Fig. 8(*a*)) displays an acceleration of the fluid moving near the inner radius in accordance with the initial favorable streamwise pressure gradient noted in Fig. 6. Simultaneously, the fluid moving near the outer radius is decelerated in response to the unfavorable streamwise pressure gradients. The patterns are also present in the experimental data and the level of agreement at this station is generally good. The predicted contours of the 60 deg location (Fig. 8(*b*)) indicate that the locus of maximum streamwise velocity is still located near the inner radius although the velocity gradients are not as steep as at 30 deg. Accumulation of low momentum fluid near the inner radius under the action of secondary flow motion is responsible for this as well as in the slight distortion of the velocity contours predicted near the inner radius corner. At the 90 deg location (Fig. 8(*c*)), the effects of secondary flow

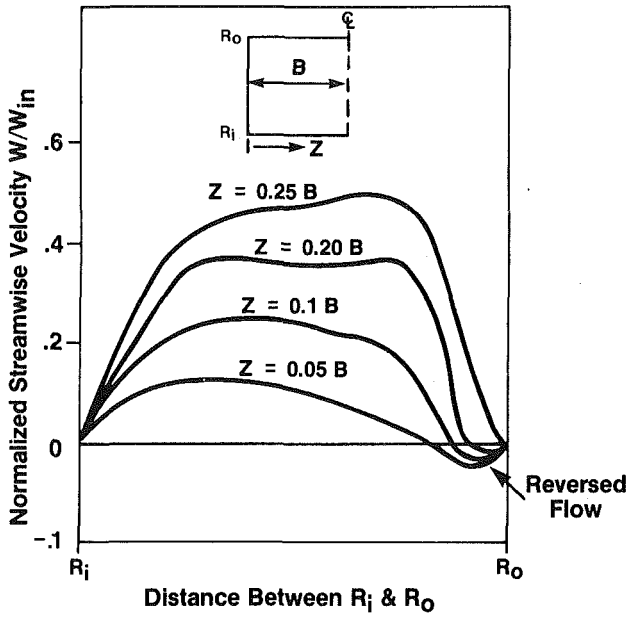

Fig. 10 Streamwise velocity profiles at 30 deg for the reversed flow case

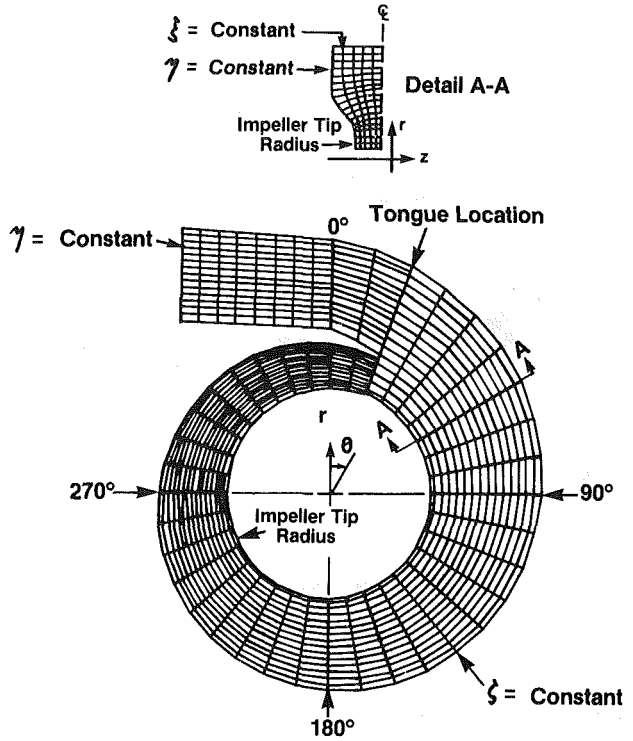

Fig. 11 Turbine housing geometry with body-fitted coordinate system

on the distortion of streamwise velocity contours becomes more pronounced. The computation also shows that high speed flow has been displaced toward the center of the channel. On the whole, the present computational results correlate well with the experimental data. In fact, the level of agreement is perhaps better than might be expected considering that the current turbulent flow calculations were performed with no sublayer resolution and with the relatively coarse grid of $20 \times 30 \times 50$.

The predicted radial velocity distribution is plotted in Fig. 9 giving the magnitude and direction of secondary flows. Note that at the inflow boundary, no significant radial velocities are present. At the 30 deg station (Fig. 9(*a*)), the computed radial velocities display a very strong inward flow near the end walls with peak velocities up to 20 percent of the mean streamwise velocities. Near the symmetry plane, the corresponding outward flow is diffusive and weak. These two distinctive features are also clearly shown by the experimental measurements. As the flow moves through the channel (Fig. 9(*b*)), the secondary flow grows in strength and region of maximum radial velocity remains close to the side walls but shifts toward the inner radius. Toward the channel exit at 90 deg (Fig. 9(*c*)), the regions of inward radial velocities grow into the main flow near the inner radius. In general, the computed radial velocities at all three stations seem to be predicted well, considering the difficulty of predicting turbulent secondary flows. The only significant disagreement occurs at the 90 deg station for the predicted velocity contours of 0.0 and 0.02. These contours do not duplicate the bulging noticed in the measured contours near the inner radius. Recent studies suggest that the bulging is a manifestation of a weak corner vortex caused by the differences of turbulent normal stresses in this region. The standard k-ϵ model used here could not predict this vortex motion since the isotropic viscosity assumption inherent in the model neglects the anisotropy effect of the turbulence.

Discussion of Curved Channel Results. Comparison between the laminar and turbulent flow results indicates that the flow patterns for each case have their own distinctive features. The laminar flow under the effect of centrifugal forces and radial pressure gradients develops secondary flow velocities more rapidly near the channel inlet. The interaction between these secondary velocities and end wall boundary layers displaces regions of maximum streamwise velocities toward the outer walls as the flow progresses downstream. On the other hand, regions of high streamwise velocities in the turbulent flow are predicted to slowly migrate toward the channel center under the effects of strengthening secondary flow motion. The difference in behavior as compared to the laminar flow can be related to the difference in Reynolds number, Dean number, inlet boundary layer thickness, and length of the flow path.

An analysis to determine the effects of all the above parameters on the varying degrees by which the strength and subsequent development of secondary flow influence the flow structure is a study by itself. However, one phenomenon which can arise under certain combinations of geometry and inlet conditions is a reversal of the streamwise flow. In order to perform a preliminary check on the validity of the numerical procedures to deal with this situation, the geometry shown in Fig. 5 was modified by decreasing R/H to 2.2. The same passage cross section was preserved. The Reynolds number was also reduced to 2000, and fully developed laminar velocity profiles were imposed at the passage inlet. Under these conditions, the analysis predicted a small but noticeable reversed flow region at the duct's outer radius corners. This region extended between the channel angular coordinates of 5 and 40 deg. Figure 10 shows the predicted streamwise velocity profiles at a passage angular coordinate of 30 deg.

The ability to predict this local streamwise flow reversal is related to the use of the type-dependent difference approximations discussed earlier. The authors feel that while this approximation appears to give satisfactory results for small regions of flow reversal, its accuracy cannot be determined without careful comparisons to experimental data. Nevertheless, the possibility of marching through regions of reversed primary flow with the code is promising.

Turbine Volute Housing Results. The solution techniques described have also been used to predict the flow behavior

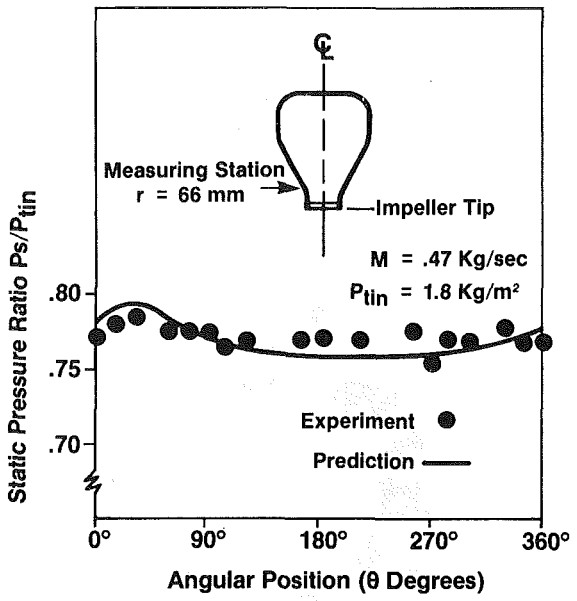

Fig. 12 Circumferential variation in static pressure at r = 66 mm

within a radial inflow turbine volute housing. This case was chosen to demonstrate the capability of the present method to handle arbitrary curved passages with changing cross section. Figure 11 shows a computer output simulating the housing geometry. The details of the actual housing design may be found in [24, 25].

The inlet flow conditions to the housing which were used for the computation were obtained from experimental measurements. The inlet Reynolds number was 4.4×10^5. The initial pressure distribution guess was calculated using free vortex flow assumptions. To reflect the influence of the presence of the turbine impeller along the outflow boundary circumference, it is necessary to allow for the variations of flow properties along this boundary. This was achieved through the incorporation of a simple impeller model. The model requires that the centrifugal force produced by the impeller is such that the mass efflux along the outflow boundary is equal to the mass flow entering the housing. The boundary fitted coordinates shown in Fig. 11 and used to map the housing geometry into the computational domain were generated numerically. A transformation package similar to the one described in reference [26] was used for this purpose. A total of 48 stations were used in the streamwise direction and each station was overlayed with 20×30 grid meshes. A total of 270 minutes of CPU time was required to obtain a solution on a Honeywell CP6 computer.

The predicted wall static pressures around the housing circumference are compared to experimental data in Fig. 12. As explained in [24, 25], the housing was designed to produce uniform pressure field at its exit. Both the experimental and computed results verify this aspect of the design and the level of agreement is satisfactory. Although this preliminary result suggests that the techniques described can be used successfully for generalized geometries, additional detail experimental data for the present case are now being obtained for further comparison and to fully qualify the analysis accuracy.

Conclusions

A numerical method has been presented for the prediction of the three dimensional viscous flow in curved channels. The field analysis was based on the solution of the Reynolds-Averaged Navier-Stokes Equations. The solution procedure involved the use of a combination of repeated space marching integration of the governing equations and correction for elliptic effects between the two marching sweeps. Numerical integration was performed using an alternating direction implicit procedure with careful treatment of different boundary conditions. A boundary fitted coordinate system has been incorporated for the efficient manipulation of channels of arbitrary configuration. Effects of turbulence were modelled using a two equation closure model with provisions to account for streamline curvature.

Solutions have been presented for laminar flow inside a moderately curved passage, turbulent flow in a strongly curved channel, and for pressures inside a turbine volute housing. Computed results were compared to other theoretical solutions and detailed experimental measurements to establish the validity and accuracy of the present analysis. The essentially fair agreement achieved suggests that the analysis can be used to obtain viscous flow details inside curved channels with an acceptable degree of accuracy. The demonstrated capability cannot be attributed to a single element of the analysis but results from the combination of many factors. The major one is believed to be the careful treatment of the pressure Poisson equation with the Neumann boundary condition. Future plans include further checks of the model against detailed experimental data to determine its accuracy for cases of arbitrarily curved passages and primary flow reversals.

Acknowledgments

The authors would like to thank John Mulloy and Robert Cox for obtaining the experimental data for the turbine volute housing. The encouragement from Sir William R. Hawthorne, Gerry Donnellan, and Patrick Flynn is gratefully acknowledged. The skilled secretarial assistance of Patricia Wilson is sincerely appreciated. Finally, the authors would like to thank Cummins Engine Company, Inc. for their permission to publish the findings of this study.

References

1 Briley, W. R., and McDonald, H., "Solution of the Multidimensional Compressible Navier Stokes Equations by a Generalized Implicit Method," *J. Comp. Physics*, Vol. 24, 1977.

2 Spradley, L. W., Stalnaker, J. T., and Ratliff, A. W., "Computation of Three Dimensional Viscous Flows with the Navier Stokes Equations," AIAA Paper No. 80-1348.

3 Humphrey, J. A. C., "Numerical Calculation of Developing Laminar Flow in Pipes of Arbitrary Curvature Radius," *Can. J. Chem. Eng.*, Vol. 56, p. 151.

4 Briley, W. R., and McDonald, H., "Analysis and Computation of Viscous Subsonic Primary and Secondary Flows," AIAA Paper No. 79-1453.

5 Kreskovsky, J. P., Briley, W. R., and McDonald, H., "Prediction of Laminar and Turbulent Primary and Secondary Flows in Strongly Curved Ducts," NASA CR3388, 1981.

6 Pratap, V. S., and Spalding, D. C., "Fluid Flow and Heat Transfer in Three-Dimensional Duct Flows," *Int. J. Heat and Mass Transfer*, Vol. 19, 1976, p. 1183.

7 Moore, J., and Moore, J. G., "A Calculation Procedure for Three-Dimensional Viscous Compressible Duct Flows, Part I and II," ASME *Journal of Fluid Engineering*, Vol. 101, 1979, p. 415.

8 Swanson, B. W., "Solution of the Three-Dimensional Navier Stokes Equations in Non-Orthogonal Coordinates to Calculate the Flow in a Log Spiral Impeller," ASME Paper No. 82-GT-268.

9 Fraser, D. A., Howard, J. H. C., and Lennox, W. C., "A Three-Dimensional Turbulent Flow Analysis Method for the Rotating Channels of a Centrifugal Turbomachine," ASME Paper No. 82-GT-221.

10 Dodge, P. R., "A Numerical Method for 2-D and 3-D Viscous Flows," AIAA Paper No. 76-425.

11 Walkden, F., "The Equations of Motion of a Viscous Compressible Gas Referred to an Arbitrarily Coordinate System," Royal Aircraft Establishment, RAE-TR-66140, ARC R/M-3609, 1969.

12 Khalil, I. M., "A Calculation Procedure for the Three-Dimensional Flow in Turbomachines," CTR #0778-83002, Cummins Technical Center, 1983.

13 Pulliam, T. H., and Steger, J. L., "On Implicit Finite Difference Simulation of Three Dimensional Flow," AIAA Paper No. 78-10.

14 Launder, B. E., and Spalding, D. B., "The Numerical Computations of Turbulent Flows," *Computer Methods in Applied Mechanics and Engineering*, Vol. 3, 1974, pp. 269–289.

15 Gibson, M. M., "An Algebraic Stress and Heat-Flux Model for Turbulent Shear Flow with Streamline Curvature," *Int. J. of Heat and Mass Transfer*, Vol. 21, 1978, pp. 1609–1617.

16 Leschziner, M. A., "Separated Flows in Turbomachinery Components," in *Von Karman Lecture Series 1981-1*, Vol. 1, pp. 11–29.

17 Khalil, I. M., "A Study of the Viscous Flow in Turbomachines," Ph.D. thesis, University of Cincinnati, OH, 1978.

18 Davis, R. T., "Numerical Solutions of the Navier Stokes Equations for Symmetric Laminar Incompressible Flow Past a Parabola," *Journal of Fluid Mechanics*, Vol. 51, Part 3, 1972, pp. 417–433.

19 Ghia, K. N., Sokhey, J. S., "Analysis and Numerical Solution of Viscous Flows in Curved Ducts of Rectangular Cross Section," Numerical/Laboratory Computer Methods in Fluid Mechanics.

20 Briley, W. R., "Numerical Methods for Predicting Three-Dimensional Steady Viscous Flow in Ducts," *J. Comp. Physics*, Vol. 14, 1974, pp. 8–28.

21 Mori, Y., Uchida, Y., and Ukon, T., "Forced Convective Heat Transfer in a Curved Channel with a Square Cross Section," *Int. J. Heat and Mass Transfer*, Vol. 14, 1971, p. 1782.

22 Ghia, K. N., Ghia, U., Shin, C. T., and Reddy, D. R., "Multigrid Simulation of Asymptotic Curved—Duct Flows Using a Semi-Implicit Numerical Technique," Computers in Flow Predictions and Fluid Dynamics Experiments.

23 Brunn, H. H., "An Experimental Investigation of Secondary Flow Losses in Bends with Rectangular Cross Sections," CUED/A-Turbo/TR 95, Cambridge University.

24 Chapple, P. M., Flynn, P. F., and Mulloy, J. M., "Aerodynamic Design of Fixed and Variable Geometry Nozzleless Turbine Casings," ASME JOURNAL OF ENGINEERING FOR POWER, Vol. 102, No. 1, Jan. 1980.

25 Chapple, P. M., "Casing for a Turbine Wheel," United States Patent No. 4,381,171, Apr. 26, 1983.

26 Khalil, I. M., and Tabakoff, "A Study of the Viscous and Nonadiabatic Flow in Radial Turbines," ASME JOURNAL OF ENGINEERING FOR POWER, Vol. 103, No. 3, July 1981.

Turbofan Mixer Nozzle Flow Field—A Benchmark Experimental Study

R. W. Paterson
Manager,
Aeroacoustics and Experimental
Gas Dynamics Section,
United Technologies Research Center,
East Hartford, Conn. 06108

An experimental investigation of the three-dimensional flow field within a multilobed model turbofan forced-mixer nozzle was conducted. The objective of the study was to provide detailed velocity and thermodynamic state variable data for use in assessing the accuracy and assisting the further development of computational procedures for predicting the flow field within mixer nozzles. Velocity and temperature data suggested that the nozzle mixing process was dominated by large-scale secondary circulations that were associated with strong radial velocities observed near the lobe exit plane. Flow field similarity for variable inlet temperature conditions was also observed, although unanticipated.

Introduction

The two important characteristics of mixer nozzles are the ability to achieve thrust augmentation as well as a more uniform nozzle exit plane velocity profile relative to either separate primary and secondary stream discharge configurations or common tailpipe configurations having no forced-mixing element. Exit velocity profile modification can cause a significant reduction in an engine's jet noise signature. Because of the lack of a reliable analytical procedure for predicting thrust augmentation and the degree of exit velocity profile uniformity for arbitrary mixer lobe and downstream duct geometries, the mixer nozzle development process, to date, has been largely empirical. While this approach has been reasonably successful, increased use of computational procedures as an adjunct to testing would be expected to accelerate the development of improved mixer designs and reduce development costs. This is particularly evident when one considers the number of free parameters available to a mixer designer. Among these are the number of lobes, degree of radial penetration, lobe contour, lobe cutback angle, use of scalloping and/or vortex generators, plug angle and length, tailpipe length, and convergence, etc. The designer's objective is to select the combination that maximizes the mixing benefit (performance and noise) and minimizes total pressure loss, weight, and cost.

Critical to the code development process is the availability of suitable experimental data. Although existing thrust and exit plane total pressure and temperature data can be used to assess the overall accuracy and hence the usefulness of a given mixer code, insufficient detail (such as data at the lobe exit used as code input) exists to identify the cause of a failure to predict these properties. In the present study, the selection of measured parameters and measurement locations, the degree of spatial resolution, and the experimental accuracy were dictated by code input and assessment requirements. A more detailed report of this experiment (including turbulence measurements) is given elsewhere [1], while [2] and [3] provide comparisons of the present experimental results with prediction.

Contributed by the Gas Turbine Division for publication in the JOURNAL OF ENGINEERING FOR GAS TURBINES AND POWER. Manuscript received by the Gas Turbine Division October 25, 1983.

Previous Investigations

In a series of recent publications by NASA Lewis Research Center [4–6], results of a joint analtyical and experimental mixer research program have been documented. In [4], by Povinelli, Anderson, and Gerstenmaier, predictions of a three-dimensional, viscous calculation procedure were compared to data obtained with an eighteen-lobed, bypass ratio four, model mixer. Temperature data indicated the existence of large-scale secondary flows in the radial-azimuthal plane and suggested that such flows contributed significantly to the mixing process. Preliminary LDV secondary flow data from the present study, obtained at the lobe exit plane, were cited as further support for this hypothesis regarding the role of large-scale secondary flows in determining the degree of mixing. In [5], additional comparisons between analytical predictions and experiment were reported for one mixer configuration. Flow angularity measurements obtained at the lobe exit plane were used to develop a representation of the lobe exit plane secondary flow field. Predictions employing these initial conditions were found to yield much better agreement with data than those in which lobe exit plane secondary flows were neglected. In [6], inclusion of additional lobe exit plane vorticity, associated with a "passage vortex" in the primary stream at the base of the fan trough, was found to improve agreement with data relative to a calculation which included only the larger-scale secondary flow field. From these code prediction comparisons, it was concluded that pressure-driven secondary flow patterns within the nozzle play a dominant role in the mixing process. The first analytical and experimental study of mixer nozzle flows was reported by Paynter, Birch, Spalding, and Tatchell in 1977 [7]. A three-dimensional, viscous

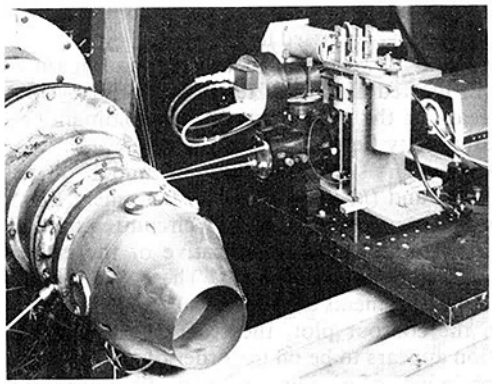

(a) EXHAUST NOZZLE INSTALLED

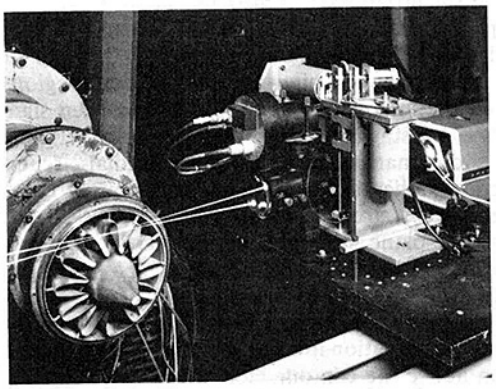

(b) EXHAUST NOZZLE REMOVED

Fig. 1 Model mixer test arrangement

analysis was applied to predict exit plane total temperature and total velocity distributions. Initial conditions were not measured although an approximate scheme was applied to input radial velocities at the lobe exit. Agreement between predictions and data at the nozzle exit plane was encouraging given the lack of experimentally determined initial conditions.

In addition to these joint analytical and experimental efforts, model mixer parameter variation studies, directed toward peformance improvement rather than code development, have recently been reported [8–10].

Description of the Experiment

Approach. Considering the code assessment objective, a model turbofan forced mixer nozzle having a mixer lobe geometry representative of those used in current production low-bypass-ratio commercial engines, was selected as the test model. The parameters selected for measurement within the mixer flow field were the three mean velocity and three turbulent velocity components, two of the three second-order turbulent component correlations, total pressure, total temperature, wall static pressures, and primary and secondary stream mass flow rates. The mean flow field parameters selected for measurement (**U**, P_T, and T_T) were sufficient to define, uniquely, Mach number and all thermodynamic state variables.

Experimental Arrangement. Photographs of the test nozzle installation with and without the convergent nozzle installed are shown in Fig. 1. Figure 2 provides a cross-sectional view of the nozzle in a plane passing through the nozzle centerline. The mixer consisted of twelve primary stream lobes centered at intervals of 30 deg in the circumferential direction, which projected into the secondary stream annulus, and a corresponding twelve secondary stream

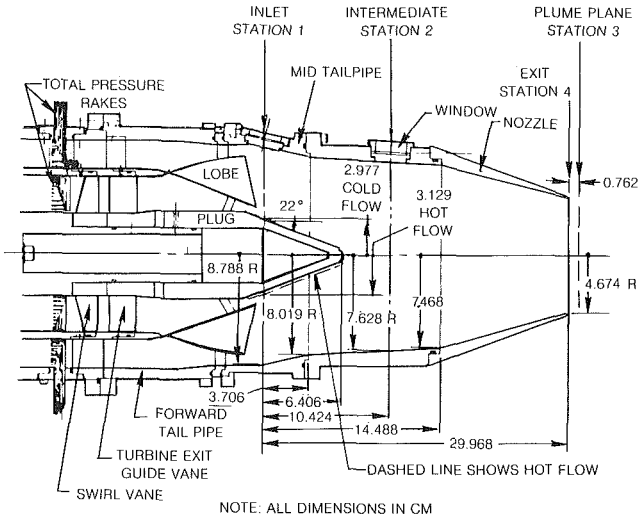

Fig. 2 Model mixer nozzle

lobes. Downstream of the lobes was a "mixing duct" region bounded on the outside by the tailpipe and convergent nozzle and initially on the inside by the nozzle plug, which terminated within this duct. The test conditions selected for the experiment were a primary stream pressure ratio of 2.6, a primary-to-secondary stream total pressure ratio of 1.04, a primary-to-secondary temperature ratio of 2.5 for hot flow testing, and a temperature ratio of unity for cold flow testing. These pressure ratios and the hot flow temperature ratio are representative of full-scale engine cruise conditions.

Selection of Measurement Locations. To meet code requirements, a "benchmark" mixer experiment must, as a minimum, provide data at a location to start the computation and at a relevant downstream location to check results. Axial measurement station 1 (Fig. 2), just downstream of the lobe exit, was selected to meet the former need and station 3, just downstream of the nozzle exit was chosen for the latter. A complete set of data was also obtained at an intermediate plane (station 2) within the tailpipe region. This provided an assessment of code accuracy in predicting the initial mixing out of the lobe-induced velocity gradients. Some data were also acquired in the plane of the nozzle exit (station 4). At each of the three principal axial measuring stations (1, 2 and 3), data were acquired over one lobe segment of the nozzle encompassing one-half of a primary and one-half of a secondary lobe. Velocity, pressure, and temperature measurements were obtained along radial lines differing in circumferential angle, ϕ.

Instrumentation. Total pressure and temperature data were acquired with conventional stagnation probes while LDV was employed for velocity measurements. The LDV system consisted of an Argon-ion laser, optical system, counter-type signal processor and on-line computer. A serious seed particle lag problem was encountered in the initial stage of the present study at axial station 3 due to the high accelerations in this transonic flow region. This resulted in velocity measurement errors on the order of 20 percent. Forward scatter collection in conjunction with seeding system development efforts were found necessary to eliminate this lag problem as described in [11].

Results and Discussion

Axial Mean Velocity Field. The axial velocity field at inlet station 1, located less than one-half of a primary lobe width downstream of the mixer lobes is characterized by high and low velocity regions separated by the lobe interface, as would be anticipated. This is shown in Fig. 3(*a*) where the ratio of

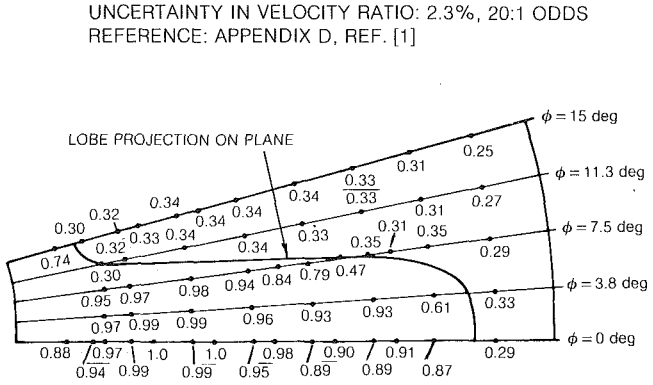

(a) HOT FLOW Ux/U_{REF} DISTRIBUTION, U_{REF} = 163.6 m/sec, INLET STATION 1

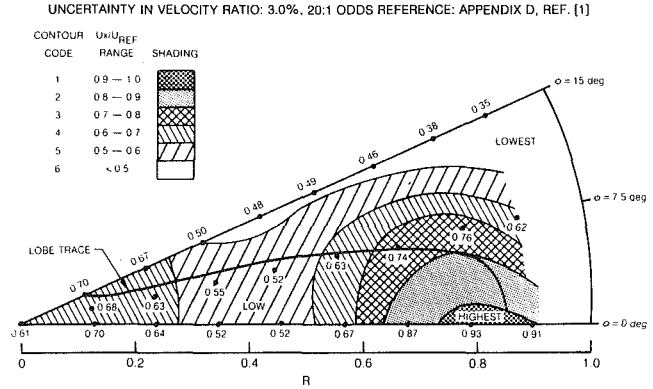

(b) HOT FLOW Ux/U_{REF} DISTRIBUTION, U_{REF} = 163.6 m/sec INTERMEDIATE STATION 2

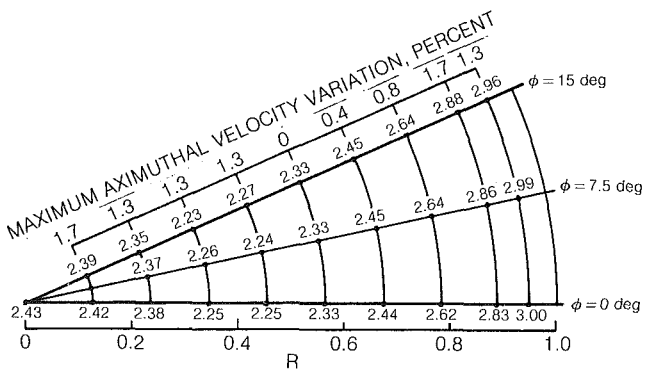

(c) HOT FLOW Ux/U_{REF} DISTRIBUTION, U_{REF} = 163.7 m/sec; PLUME PLANE STATION 3

Fig. 3 Axial velocity distributions

axial velocity to a reference velocity in one lobe segment is given as a function of circumferential angle ϕ and nondimensional radius R. Nondimensional radius, as defined here, is equivalent to fractional gas path height, that is: $R = (r - r_{min})/(r_{max} - r_{min})$ for station 1 and r/r_{max} elsewhere.

Within the majority of the secondary lobe region, the velocity field is relatively uniform. Velocities decrease in the tailpipe wall boundary layer at large radius. Within the inner half of the primary lobe region, the velocity field is also relatively uniform. A significantly lower velocity is observed, however, at larger radius (R = 0.78, ϕ = 3.75). This is believed due to a small clockwise-circulating vortex located in the peak region of (this half of) the primary lobe that transported secondary stream fluid into the primary lobe. The probable origin of such a vortex is a horseshoe vortex formation process as discussed in [1].[1]

At the next downstream measuring station (intermediate station 2) located approximately seven primary lobe widths downstream of the mixer, the two predominant features of the axial velocity field are: (*i*) strong penetration of low axial velocity secondary stream fluid into the middle of the primary lobe region, and (*ii*) an outward displacement of high axial velocity primary stream fluid. Such circumferential and radial transport of momentum is indicative of the existence of a large scale, secondary flow field. These two features of the station 2 measurements are shown in Fig. 3(*b*).

From the contour plot, the scale of the secondary flow circulation appears to be on the order of the lobe dimensions. This circulation, of counterclockwise orientation, divides the primary lobe region into two high axial velocity regions, the highest velocity region at large radius and a somewhat lower one near the nozzle axis. It also appears to be responsible for the upward transport of primary stream fluid into the secondary lobe region observed for $R > 0.55$. In summary, the interface between high and low velocity regions, which followed the lobe trace[2] at station 1, has been significantly contorted by station 2; this suggests a two-stream mixing process dominated by large-scale, radial-circumferential convection rather than turbulent diffusion at the interface between the two streams.

At plume-plane station 3, located approximately sixteen primary lobe widths downstream of the mixer, the axial velocity field has totally mixed out in the circumferential direction, as shown in Fig. 3(*c*). The maximum circumferential variation in axial velocity is listed for each radial position above the contour plot; the average circumferential variations for hot and cold test conditions were 1.1 and 0.9 percent, respectively.

Radial and Circumferential Velocity Field. At inlet station 1, the predominant featues of the radial-circumferential velocity field (secondary flow field) are: (*i*) a strong radial velocity field directed inward toward the hub in the secondary lobe region, (*ii*) a weaker radial velocity field directed toward the tailpipe wall in the primary lobe region, and (*iii*) circumferential velocity components in the lobe interface region suggesting (*i*) and (*ii*) are linked by a large-scale, counterclockwise circulation of the type inferred previously from axial velocity measurements. This inlet station secondary flowfield is shown for hot and cold test conditions in Fig. 4, parts (*a*) and (*b*), respectively.

Hot and cold flow results are observed to be generally consistent and satisfy symmetry arguments within experimental error bounds. Except for inwardly directed vectors at $R = 0.78$, $\phi = 3.75$ deg in hot and cold flow, a general counterclockwise secondary flow field is indicated. This exception is believed caused by a clockwise-oriented horseshoe vortex, the position of which is shown approximately by the circled HV symbol. The presence of this vortex was previously suggested by axial velocity data and directly confirmed by a vorticity meter survey.

[1] A pair of contrarotating vortices was found in both the peak region of the primary lobes and the trough region of the secondary lobes; the strength of the secondary stream vortices was weaker, as expected, and observed directions of rotation were consistent with a horseshoe vortex hypothesis.

[2] Mixer lobe traces at stations 2 and 3 are plotted with the same R, ϕ coordinates as station 1. An alternative procedure would be to plot the trace on the basis of constant percent flow area. For fixed ϕ, this would result in trace R coordinates being shifted from values of .1, .3, .5, and .9 at station 1 to values of .24, .45, .65, and .93 at stations 2 and 3. The latter method would be clearly preferable in a two-dimensional flow without density changes, but both methods are somewhat arbitrary here. The high clockwise swirl shown in Fig. 4(*c–e*) near the axis, however, is more consistent with an area trace coordinate (R = .28) than the linear coordinate shown (R 0.13) at ϕ = 15 deg.

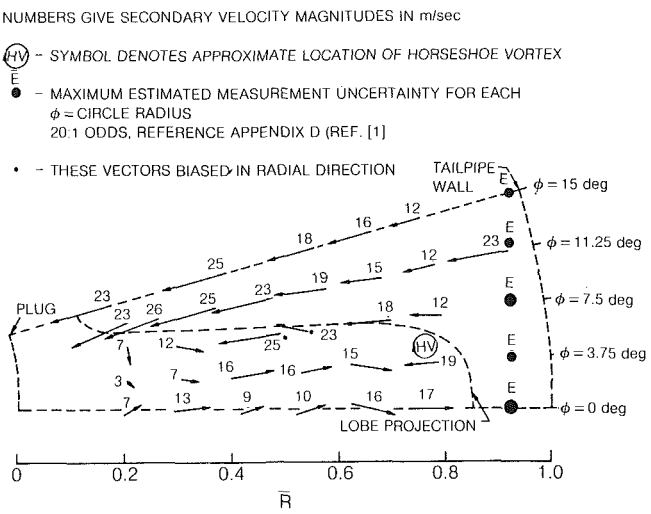

(a) HOT FLOW, INLET STATION 1

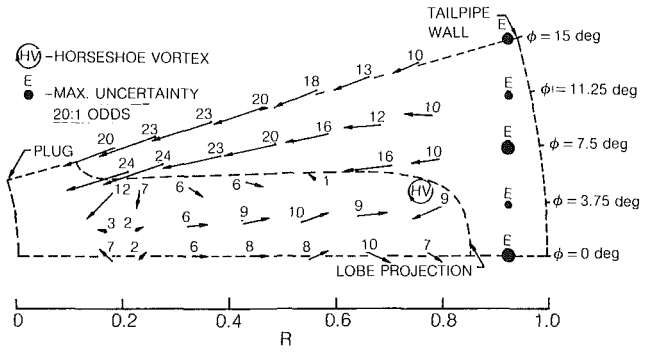

(b) COLD FLOW, INLET STATION 1

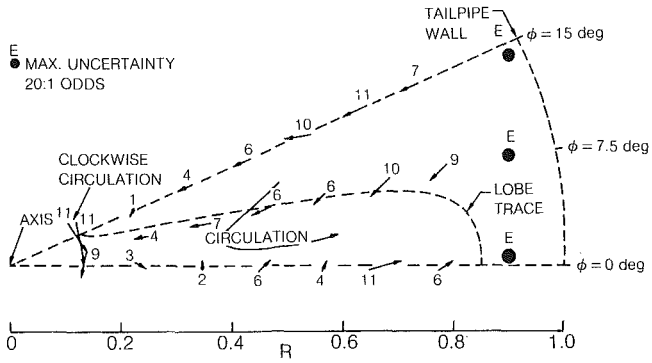

(c) HOT FLOW, INTERMEDIATE STATION 2

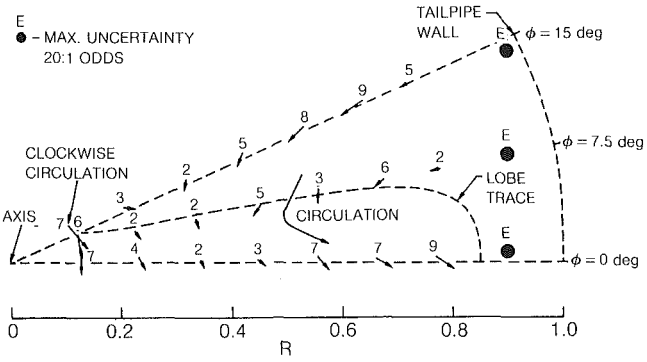

(d) COLD FLOW, INTERMEDIATE STATION 2

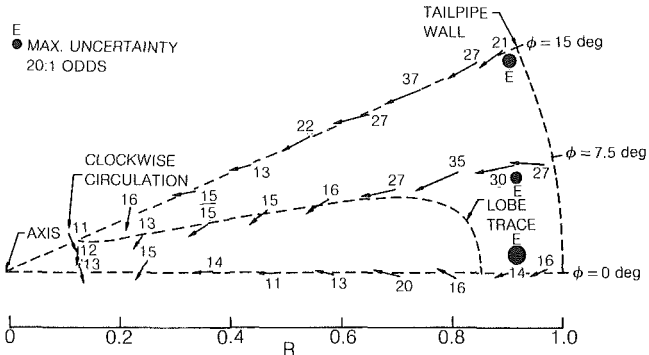

(e) HOT FLOW, PLUME PLANE STATION 3

Fig. 4 Secondary flow velocity vectors

Also of interest is the relationship between the measured radial velocity magnitude and the lobe geometry (lobe penetration angle). In the absence of detached flow within the lobe, the magnitude of the radial velocity component would be expected to be proportional to the slope of the lobe. For the secondary stream lobe this is found to be approximately correct, since the average value of the ratio of radial-to-axial velocity along the center of the secondary lobe ($\phi = 15$ deg) for both hot and cold flow is about 0.37. This is close to the tangent of the 22-deg lobe penetration angle, which is 0.4. Similarly, the ratio of primary lobe radial-to-axial velocity along the center of the primary lobe ($\phi = 0$ deg) for both hot and cold flow is close to the slope of the primary lobe at the trailing edge (outward projection at 5 deg). The only exception to this trend is the inward vector at $R = 0.78$, $\phi = 3.75$ deg, which is believed associated with a horseshoe vortex, as previously discussed.

These oppositely directed radial velocities in the primary and secondary streams mean that the dividing surface between the two streams at the lobe exit plane constituted a rotational flow region possessing axial vorticity of counterclockwise orientation. This can be viewed as a vortex layer (or vortex sheet when the limit of zero thickness is taken). Vorticity components also exist in the R, ϕ plane, tangent to the lobe trace, due to the discontinuity in axial velocity at the lobe trailing edge. The shear layer emanating from the lobe trailing edge, therefore, constitutes a complicated rotational flow region possessing vorticity components in all three coordinate directions.

In summary, radial and circumferential velocity component measurements obtained at *station 1* confirm the existence of a large scale counterclockwise lobe circulation previously inferred from axial velocity measurements at *station 2*.

The secondary flow circulation pattern observed at inlet station 1 also exists at station 2 as shown in Fig. 4, parts (*c*) and (*d*) for hot and cold flow test conditions, respectively. Both hot and cold flow data indicate that a radially inward flow occurs in the center of the secondary lobe ($\phi = 15$ deg) and radially inward and downward flow exists at $\phi = 7.5$ deg. At $\phi = 0$ deg, hot and cold flow data both show outwardly directly radial components while the circumferential components tend to be of opposite sign and violate symmetry arguments. This is indicative of measurement error. In addition to this flow pattern, a relatively intense clockwise vortex is also indicated near the nozzle axis, presumably associated with residual swirl that was not removed by the simulated turbine exit guide vanes located upstream of the mixer. While the primary mixer lobes would be expected to attenuate residual swirl at moderate-to-large radius due to their axial orientation, the gap between the hub and the trough of the secondary stream lobe provides an unobstructed

passage for convection of residual swirl downstream into the on-axis region at station 2.[3]

At station 3, the secondary flow field is, in the main, radially inward, in response to the nozzle convergence. As shown in Fig. 4, part (*e*), the circulatory flow observed at stations 1 and 2 is not evident. Some effect of this circulation may be present in that inward velocities along $\phi = 0$ are lower than along the other two lines and vectors along $\phi = 7.5$ deg tend to have downward circumferential components. Near the axis ($R < 0.3$), a clockwise oriented vortex is evident as was the case at station 2. The presence of this vortex was confirmed by a vorticity meter survey.

Nozzle Total Temperature Field. At inlet station 1, the temperature field, as expected, consists of a hot primary region and cold secondary region with the intervening temperature gradient region roughly centered on the lobe projection. This is shown in Fig. 5 where part (*a*) displays T_T/T_{op} contours[4] and part (*b*) shows the relationship of the contours to the lobe projection. In apparent confirmation of velocity data, an upward penetration of hot fluid into the secondary stream near $R = 0.65$ and downward penetration of cooler fluid into the primary stream at somewhat larger R indicates the presence of a small, clockwise-oriented vortex (horseshoe vortex) in the primary lobe. The presence of cold fluid within the primary lobe near the trough of the secondary stream lobe is the result of inward convection of secondary stream fluid by the strong radial velocity field during the time interval between leaving the lobe and arriving at station 1. This is based on a calculation (using measured axial and radial velocities) that predicts an inward penetration of the 0.48 contour much as shown.

Intermediate Station 2 Contours. Temperature contours at intermediate station 2 unequivocably confirm the existence of the large-scale circulation inferred previously from velocity data. In Fig. 6, cool fluid is seen to have penetrated the primary lobe region, extending all the way to the lobe centerline ($\phi = 0$) between $R = 0.3$ and 0.5. Consistent with a large-scale circulation of counterclockwise orientation, there is a corresponding transport of hot primary stream fluid outward and upward into the otherwise cool secondary stream region. The only station 2 region that is mixed-out circumferentially is a hot flow area near the axis where the previously discussed on-axis vortex as well as the close proximity of the segment boundaries (small lobe width) favor mixing.

At the nozzle exit the temperature field is reasonably well mixed-out in the circumferential direction as shown in Fig. 7. There is some radial stratification; the largest radial temperature gradients occur in the vicinity of the axis, where, as in the case of station 2, a relatively hot spot exists. A comparison of station 2 and 3 contours (Figs. 6 and 7) for the outer portion of the segment ($R > 0.4$) suggests that the large-scale, counterclockwise circulation that exists between stations 1 and 2 also plays an important role in the mixing occurring downstream of station 2. While the coolest region of station 2 is in the upper right corner of the contour, the coolest region at station 3 is to the left and downward; similarly, the hot region at station 2, contained within the 0.79 contour, by station 3, has been displaced upward and to the right. Temperature data, therefore, provide an indication of the continued importance of secondary flow-induced convective mixing downstream of station 2; this could also be inferred, but less clearly, from axial velocity data.

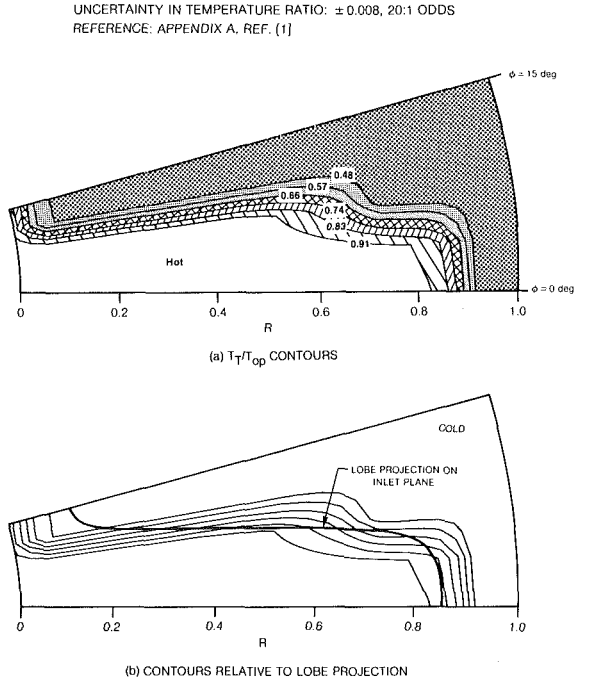

Fig. 5 Total temperature contours at inlet station 1

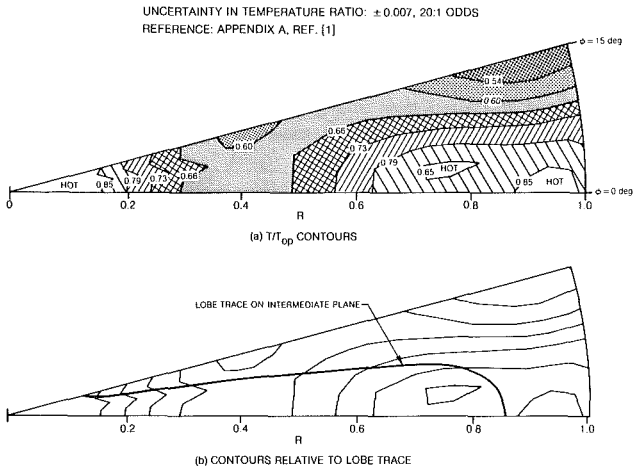

Fig. 6 Total temperature contours at intermediate station 2

Nozzle Mixing Mechanisms

A simplified view of mixing in turbulent flow results in the following three transport mechanisms: (*i*) convection by the mean velocity field, (*ii*) convection by large-scale turbulent motions, and (*iii*) gradient-type turbulent diffusion by small-scale turbulent motions. Velocity and temperature data presented in the previous sections strongly indicate that the first mechanism, convection by the mean radial-circumferential velocity field, represents the dominant mechanism for nozzle mixing. It provides the rapid transport of heat and axial momentum at length scales comparable to the nozzle radius and contorts the mixing layer interface. This secondary flow field is characterized by a circulatory flow in each lobe segment established by oppositely directed radial flows in the primary and secondary stream lobes. In a simplified view of this field, the interface between the two streams can be viewed as a thin vortex layer or sheet and the circulation around the contour taken as the sum of the two radial velocity components. From Kelvin's theorem, which

[3] The advisability of providing swirl and simulated turbine exit guide vanes can be questioned relative to unnecessary complexity in such a code assessment experiment; in this case, however, previous performance data with this vaned model were to be used to relate the present detailed measurements to overall mixing and thrust performance (see [2]).

[4] T_{op} is total temperature in the primary stream, the reference value for which is 755K.

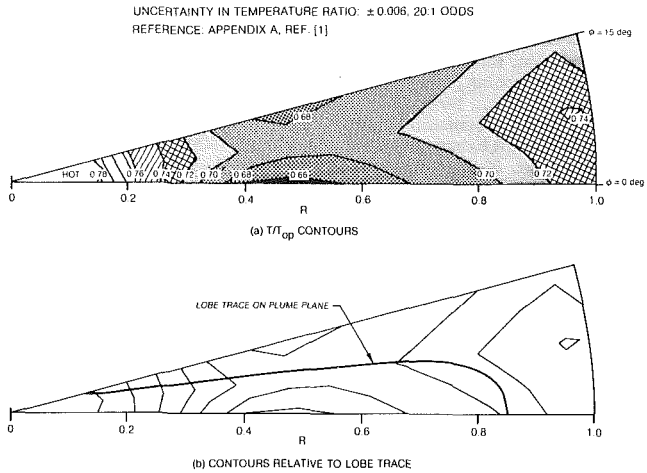

Fig. 7 Total temperature contours at plume plane station 3

would be expected to apply approximately to this case, this circulation persists downstream of the lobes causing radial-circumferential mixing of the two streams throughout the axial extent of the nozzle.

This circulation can be considered a pressure-driven secondary flow, since the oppositely directed radial components are established by radial pressure gradients in the lobes. Circumferential components are established near the hub and tailpipe wall by a stagnation-type flow. The extent of nozzle mixing by this circulation would appear to be dependent upon the ratio of radial to axial velocity (U_r/U_x) rather than on the absolute magnitude of the radial velocity component. The greater this ratio, the greater will be the radial and circumferential displacement of a fluid element in the time required to transit the nozzle, and presumably the greater the convective transport (mixing). Since radial velocity magnitude would be expected to be proportional to lobe penetration angle, in the absence of separation within the lobes, penetration angle appears to be an important parameter. Effects of other parameters such as the extent of radial lobe penetration l, lobe width, and the proximity of the hub and tailpipe wall to the lobe trough and peak, respectively, would also be expected to be important, since these parameters affect the scale of the secondary circulation. These conclusions regarding the importance of the lobe exit plane secondary flow field are consistent with the study in [5]. In that study, analytical predictions employing a representation of this secondary field were found to yield much better agreement with data than those in which lobe exit secondary flows were neglected.

In this simplified description of the mixing process, convection by large-scale turbulent motions (the second mixing mechanism listed above) would be expected to be responsible for mixing at the next smaller scale. These turbulent motions are expected to cause the lateral spreading of the shear layers shed at the lobe trailing edge and which are imbedded in the larger-scale circulations. These broadened shear layers are contorted by the mean velocity field in a complicated three-dimensional manner. At the smallest scale of mixing, gradient-type diffusion by small-scale turbulent motions are expected to progressively attenuate remaining gradients.

While this picture of the mixing process is very simplified, it provides some indication of why lobed mixers are efficient. The lobed geometry not only produces a circumferentially and radially varying flow field from an initially axially symmetric field, but sets up large-scale secondary circulations to mix-out the resultant axial and radial variations. While the lobed geometry also increases the length of the shear layer interface between the two streams, resulting in enhanced mixing by virtue of shear layer broadening, this study suggests that the large-scale circulations play a major role in the mixing process. This view is consistent with [4], in which it was concluded that large-scale mixing associated with secondary flow downstream of the lobe exit is an important nozzle mixing mechanism. It also appears to be consistent with Shumpert's [8] finding that injection and vortex generator mixer configurations (which would not be expected to induce strong radial velocities) were less effective than multilobed chute configurations (which do induce a radial velocity field).

Mach Number and Total Pressure Field Similarity

An observation made in this study and described in detail elsewhere [1] was that the vectorial Mach number and total pressure distributions throughout the nozzle were effectively identical for both the cold and hot flow tests. As noted in [1], such behavior would be predicted by the Munk and Prim substitution theorem [12, 13], which applies to isentropic flows (inviscid, nonheat conducting). Since the mixer flow clearly violated these assumptions, an apparent paradox existed that could not be explained by present theory. This issue is dealt with in [14], where an extended Munk and Prim principle is developed. Its basis is a previously unanticipated balance of heat transfer and viscous effects that appears to exist for a class of flows more general than those occurring in turbofan forced mixer nozzles. Where applicable, it appears to have important implications for the design and scaling of experiments involving mixing phenomena.

Conclusions

1 The multilobed mixer employed in the present study produced a system of adjacent, contrarotating circulatory flows at the exit of the mixer lobes. These secondary flows were located in the radial-circumferential plane (axially oriented vortices) and had a scale on the order of one lobe segment.

2 The large-scale circulations previously discussed provided the dominant mechanism by which transport of heat and axial momentum occurred at length scales comparable to the nozzle radius. This large-scale mixing would be expected to control the rate of mixing within the nozzle. In their absence, mixing rate would be expected to be lower, being controlled by the small-scale turbulent eddy interactions within the shear layers emanating from the trailing edge regions of the lobes. If, as suggested here, large-scale circulations control the overall mixing rate, it should be possible to explain why certain geometry changes (e.g., lobe scalloping) have a larger effect on mixing in some mixer applications than in others.

3 Production of the observed large-scale secondary flows was dependent upon the existence of radial flows of opposite direction in the primary and secondary lobes, which were in turn established by radial pressure gradients within the lobes. The secondary flow consists of a large-scale irrotational flow region within which are embedded smaller rotational regions containing vorticity shed at the lobe trailing edge.

4 Mixer designs which induce no net circulation but generate secondary flows having a scale on the order of the annular gap between the plug and tailpipe wall would be expected to be more effective than mixers having small secondary flow patterns or none. For a multilobed mixer, lobe penetration angle and depth would be expected to be the parameters that most affect secondary flow velocity and scale, respectively.

5 The Mach number and total pressure field similarity observed in hot and cold flow testing has potentially important implications for the design and scaling of mixing experiments.

Acknowledgments

The author wishes to acknowledge helpful discussions with Professor E. M. Greitzer (M.I.T.), Dr. L. A. Povinelli (NASA), Dr. W. M. Presz, Jr. (Pratt & Whitney Aircraft), and Dr. M. J. Werle (UTRC).

References

1 Paterson, R. W., "Turbofan Forced Mixer-Nozzle Internal Flow Field, Vol. 1—A Benchmark Experimental Study," NASA Contractor Report 3492, Apr. 1982.

2 Werle, M. J., and Vatsa, V. N., "Turbofan Forced Mixer-Nozzle Internal Flowfield, Vol. 2—Computational Fluid Dynamic Predictions," NASA Contractor Report 3493, Apr. 1982.

3 Anderson, O. L., and Hankins, G. B., "Development of a Parabolic Finite Difference Method for Three-Dimensional High Reynolds Number Viscous Internal Flows," presented at the ASME 102nd Winter Annual Meeting, Washington, D.C., Nov. 15-20, 1981.

4 Povinelli, L. A., Anderson, B. H., and Gerstenmaier, W., "Computation of Three-Dimensional Flow in Turbofan Mixers and Comparison With Experimental Data," AIAA Paper 80-0227, 1980.

5 Anderson, B., Povinelli, L., and Gerstenmaier, W., "Influence of Pressure Driven Secondary Flows on the Behavior of Turbofan Forced Mixers," AIAA Paper 80-1198, 1980.

6 Anderson, B. H ., and Povinelli, L. A., "Factors Which Influence the Behavior of Turbofan Forced Mixer Nozzles," NASA TM 81668, 1981.

7 Paynter, G. C., Birch, S. C., Spalding, D. B., and Tatchell, D. G., "An Experimental and Numerical Study of the Three-Dimensional Mixing Flows of a Turbofan Engine Exhaust System," AIAA Paper 77-204, 1977.

8 Shumpert, P. K., "An Experimental Model Investigation of Turbofan Engine Internal Exhaust Gas Mixer Configurations," AIAA Paper 80-0228, 1980.

9 Kozlowski, H., and Kraft, G., "Experimental Evaluation of Exhaust Mixers for an Energy Efficient Engine," AIAA Paper 80-1088, 1980.

10 Kuchar, A. P., and Chamberlin, R., "Scale Model Performance Test Investigation of Exhaust System Mixers for an Energy Efficient Engine Propulsion System," AIAA Paper 80-0229, 1980.

11 Patrick, W. P., and Paterson, R. W., "Seeding Technique for Laser Doppler Velocimetry Measurements in Strongly Accelerated Nozzle Flowfields," AIAA Paper 81-1198, 1981.

12 Munk, M., and Prim, R. C., "On the Multiplicity of Steady Flows Having the Same Streamline Pattern," *Proc. U.S. National Academy of Sciences*, Vol. 33, No. 5, 1947, pp. 137-141.

13 Tsien, H. S., "The Equations of Gas Dynamics," *Fundamentals of Gas Dynamics*, edited by H. W. Emmons, Princeton University Press, Princeton, 1958, pp. 41-43.

14 Greitzer, E. M., and Paterson, R. W., "An Approximate Substitution Principle for Viscous Heat Conducting Flows," Report UTRC 84-18, United Technologies Research Center, East Hartford, Conn., 1984.

R. Digumarthi

Chung-Nan Chang

International Power Technology,
Sunnyvale, Calif. 94086

Cheng-Cycle Implementation on a Small Gas Turbine Engine

The Cheng-Cycle turbine engine is a superheated steam injected gas turbine cycle system. This work is based on the Garrett 831 gas turbine. The development effort involved the design and manufacture of an experimental heat recovery steam generator, a steam injection system, and system controls. Measured performance data indicate the 26 percent efficiency improvement has been obtained compared to that of the basic turbine engine at its continuous power rating.

1 Introduction

A couple of decades ago, fuel was cheap and the supply seemed so plentiful that incentives were lacking for the development of more efficient energy converters. Now as the situation has changed, even relatively modest increases in efficiency are economically attractive. The Cheng-Cycle turbine is an engine recently developed to meet the need for greater efficiency. This paper describes the development and experimental results of the Cheng-Cycle turbine based on a small gas turbine.

The Cheng Cycle, a patented thermodynamic power cycle of International Power Technology, combines the Brayton and the Rankine cycles in a unique manner, utilizing the exhaust heat in the form of superheated steam at a moderate pressure. This unique cycle was applied to the Garrett IE831 Engine consisting of a 600-kW generator packaged by Onan Corporation.

The Onan 560 Gtu set was attached with an experimental (Onan 560 Gtu Set) heat recovery steam generator (HRSG). This combination of the Garrett 831 turbine with the HRSG is a typical Cheng-Cycle turbine. This paper will show the development of Cheng-Cycle turbine involving the performance matching of the components, fabrication of the HRSG and the system control unit. The development of steam injection manifold will also be discussed. The comparison of the CC-Turbine performance and Brayton cycle will be discussed.

Water injection is a well-known method of augmenting the power output with some penality of inefficiency. The Cheng-Cycle engine was developed on a patented process by International Power Technology Inc. [1-4] in the period from 1976 to 1981. The working fluid in the turbine is thus a combination of combustion gases and superheated steam. Increasing the mass flow and the specific heat of the working fluid increase work output dramatically.

Dr. Cheng of International Power Technology, analyzed the thermodynamics of the cycle and discovered that an optimum occurred in efficiency at large steam to fuel ratios. At this optimum ratio, the overall efficiency of the engine increased significantly. In this condition, the engine has all the advantages of a Rankine-cycle steam turbine operating as a topping cycle from the exhaust of a Brayton-cycle turbine. The engine has the mechanical simplification of a single shaft output and no increase in rotating machinery.

The improvement in the power output is based on the increased mass flow through the turbine when compared with the compressor mass flow. The increased mass flow through turbine in return would require higher compressor pressure ratio. The improvement in the power generated in the turbine will more than offset the requirement of the compressor work for higher compressor pressure ratio. Thus the steam injected gas turbine would produce more power at a higher efficiency but would utilize the same rotating machinery. The steam injection into the combustion chamber also reduces the generation of No_x [5].

Additional fuel burned in the combustion chamber to bring the superheated steam to the turbine inlet temperature is offset by the increase in the power output. For the same fixed power output of the basic engine, the addition of the superheated steam reduces the turbine inlet temperature and thus increases the life of the gas turbine.

The presence of the superheated steam in the exhaust gas flow enables the HRSG to extract more heat for the same temperature drop of the exhaust gases. The ratio of the injected steam, generated from the exhaust heat, to the compressor inlet air flow is coupled to the cycle parameters. The HRSG surface area, the turbine exhaust gas temperature, along with the evaporator exit temperature pinch have critical influence in achieving the peak efficiency of the gas turbine.

An important economic factor is that the Cheng-Cycle engine can be constructed with minor modifications to existing gas turbines. The modification consists of a waste heat recovery steam generator to provide the superheated steam and the modification to the combustion chamber to provide for the controlled steam injection at the proper fuel and air mixture ratios.

Contributed by the Gas Turbine Division of THE AMERICAN SOCIETY OF MECHANICAL ENGINEERS and presented at the 29th International Gas Turbine Conference and Exhibit, Amsterdam, The Netherlands, June 4-7, 1984. Manuscript received at ASME Headquarters January 9, 1984. Paper No. 84-GT-150.

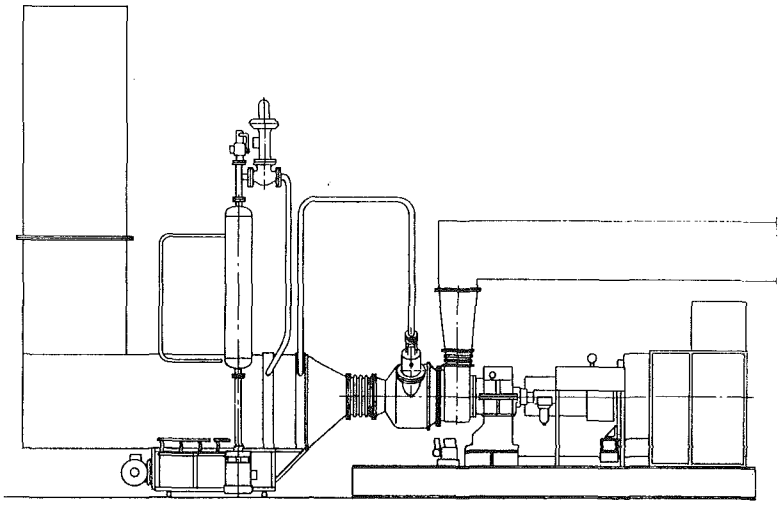

Fig. 1 Onan 560 GTU configured as Cheng-Cycle turbine

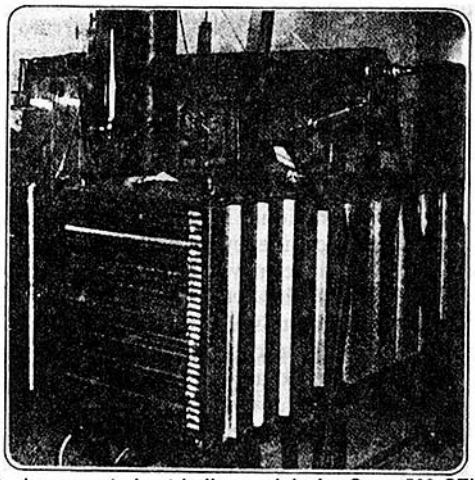

Fig. 2 Package waste heat boiler module for Onan 560 GTU Cheng-Cycle genset (superheater section in foreground is stainless steel fin tube, followed by conventional horizontal U-tube evaporator and economizer sections)

2 Onan 560-GTU (Garrett 831) Gas Turbine Generator

The 831 gas turbine is comprised of two radial outflow compressor stages with a single burner can with dual orifice atomizer for liquid fuel and a three-stage axial turbine. Though the 831 can utilize gaseous fuel, current experiments were conducted with liquid fuel DF-2 only.

The 831 turbine operates at a nominal compressor pressure ratio of 11 with 7.91bm/s of inlet air and turbine inlet temperature of 1760 °F. The Onan 560/Gtu Generator set consists of a Garrett IE831-800 gas turbine prime mover directly coupled to Onan "UV" generator. The gearbox is an integral part of the engine assembly, and the turbine speed is reduced to generator speed by double reduction spur gears. The generator is an Onan type "UV," 12-lead, 4-pole, revolving field, brushless unit wired for 277/480 volts, three-phase operation.

The Garrett IE831-800 gas turbine is an open-cycle, single-shaft, constant-speed gas turbine. Nominal rpm of 41,730 is reduced through the gear box to 1800 rpm as required by the generator. The Garrett 831 has a nominal shp rating of 800 shp as standby and 690 shp as continuous. With a nominal efficiency of 94 percent of the gearbox, the Onan-560 generates 560 kW at standby and 490 kW at continuous operation.

The Onan-560 generator set is equipped with relay control logic to provide basic operational control, fault shutdown of the gas turbine, and proper sequencing of the engine electrical system. This control system was utilized as local controller in the control schematic.

Based on the engine basic characteristics and assumed matching HRSG performance, the maximum operating characteristics of Cheng Cycle Turbine of 1-MW output at a thermal efficiency of 34 percent was projected at standard condition. A comparable thermal efficiency of 22.5 at the nominal rating of 520 kW was also predicted.

3 Steam Generating and Injection Equipment

3.1 Heat Recovery Steam Generator. The heat recovery steam generator consists of superheater, evaporator, and economizer/feed water heater (Fig. 2). City water was fed through deionizing system before being pumped into the feedwater heater. The feedwater heater is one bank of cross-flow heat exchanger. The water was then fed into an evaporator drum through a control valve. The evaporator consisted of four crossflow heat exchanger banks that were fed by a common header. The flow from the evaporator sections was fed into a vertical steam separator. The saturated steam was then separated into the superheater. The superheated steam was injected into the combustor can and the steam flow was measured utilizing an orifice meter and a vortex shedding meter.

The maximum operating pressure of the drum is about 200 psig. This pressure range was enough to maintain a 20 psi higher drum pressure than the compressor discharge pressure at the maximum operating point. The HRSG can generate a maximum of 3000 lbs/hr steam based on the surface area.

3.2 Steam Injection Manifold. The superheated steam from the HRSG was injected in the outer annules around the combustion chamber. The injection was made through eight steam tube nozzles in the secondary dilution region, with the nozzle pointing towards the compressor discharge region. The nozzle set up with the combustion chamber is shown in Fig. 3. With the steam tubes pointing in circumferential direction, the compressor discharge air has enhanced mixing of the injected steam.

4 Test Facility

The experiment was monitored utilizing the HP-9835. The software required for the data acquisition system was generated in-house. The software provides the opportunity to

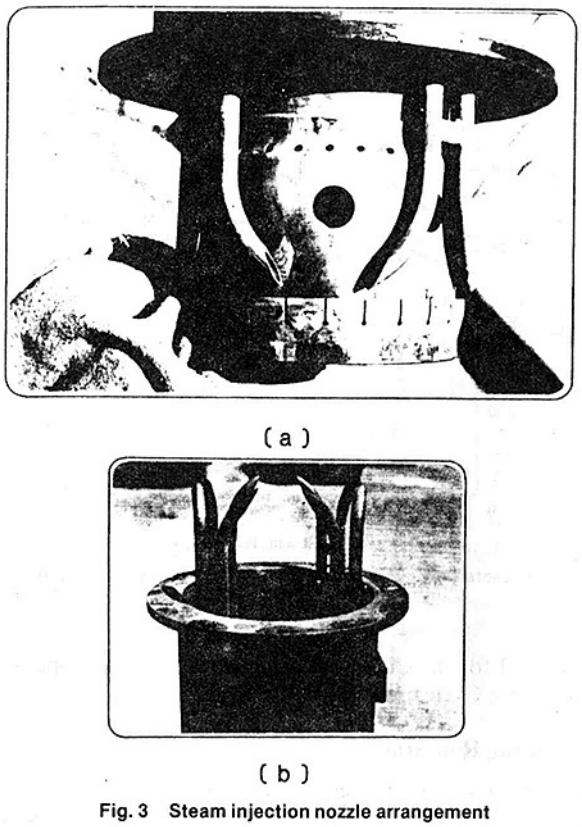

Fig. 3 Steam injection nozzle arrangement

monitor 80 data channels. In this experiment, only 40 channels were utilized and the collected data were stored on floppy disks and displayed on a graphic screen showing the current state of the experiment.

The Onan 560 turbine generator was loaded using a resistive load bank. The load on the system was changed in 50-kW steps and was increased in a linear fashion. The voltage and the amperage at the load was monitored.

5 Experimental Results

The turbine generator was run at a various load and ambient conditions. It was found that the results were insensitive to ambient conditions over the range investigated.

Figure 4 shows the generating efficiency of the system as a function of power output for loads up to 500 kW, and for a variety of ambient temperatures ranging from 60 to 90 °F. Generating efficiency increased from about 9 percent at the 100-kW load to nearly 27 percent of the 500-kW load. The results are practically independent of the ambient temperature.

For comparison, the nominal engine efficiency operating in the usual Brayton-cycle mode, is also shown in Fig. 4. The Cheng-Cycle operation gives a significant increase in efficiency at all loads; for example, at the 400-kW load efficiency has increased from 17.5 percent for the usual Brayton-cycle operation to about 23 percent in the Cheng-Cycle operation, an increase of 23 percent in the relative efficiency.

It may be noted that calculations of thermal efficiency, using 94 percent as the combined gear box/generator efficiency, gives almost the identical curve. Efficiency and power output are both slightly increased by the correction, such that the functional relation remains nearly the same.

One of the important characteristics of turbine operation is exhaust temperature. Figure 5 shows the measured exhaust temperature for the Cheng-Cycle operation of the test unit as a function of power output. The nominal Brayton-cycle

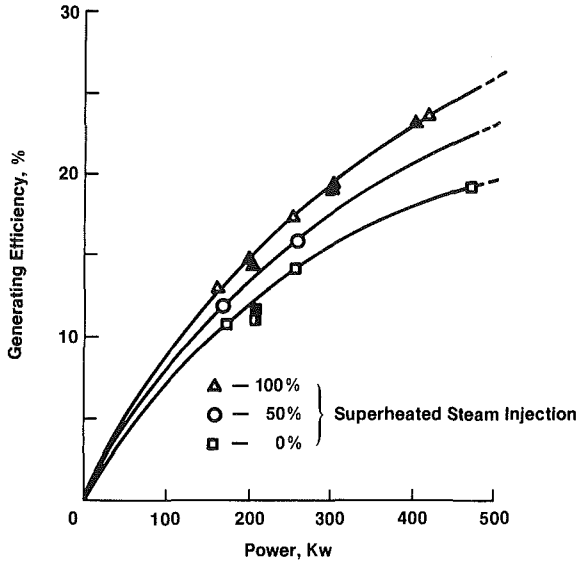

Fig. 4 Comparison of Cheng-Cycle turbine with basic turbine (△, □: $T_a = 60°F$; ▲, ■: $T_a = 80°F$; ▲, ■ : $T_a = 90°F$)

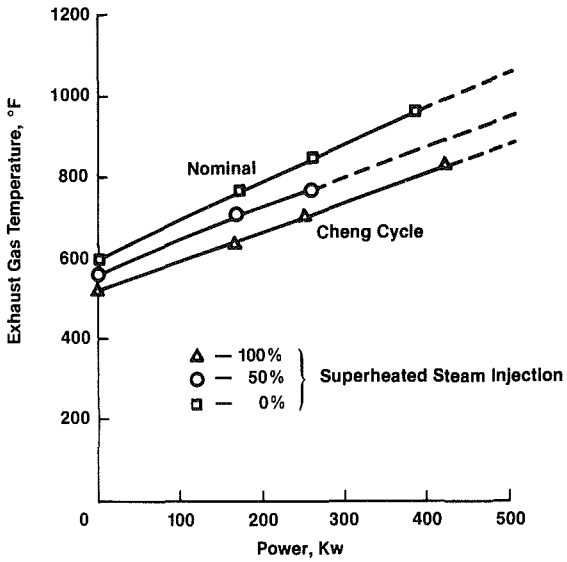

Fig. 5 Comparison of the exhaust flow temperature between Cheng-Cycle turbine and basic turbine

exhaust temperature is also shown for comparison. The Cheng-Cycle exhaust flow was 50°F cooler at low loads to nearly 100°F cooler at 400 kW.

For turbines, the crucial factor is generally the fuel cost, since initial capital cost is not such a large factor as for other types of energy converters. Figure 6 shows the percentage fuel saved as a function of load for the Cheng-Cycle operation compared with the nominal Brayton-cycle operation of the engine. The fuel saving varies from 10 percent at idle to 28 percent at the rated basic engine full continuous load.

A matched heat exchanger steam generator design would allow the turbine to operate at still higher load values. Peak power output could be increased from 560 kW to an estimated 1.1 MW with a thermal efficiency of 34 percent. This means that capital investment per kW-hour peak load could be reduced as much as a factor of 2 for this unit, as the modification costs are modest. The Cheng-Cycle modification thus renders smaller turbines attractive for higher load handling duty.

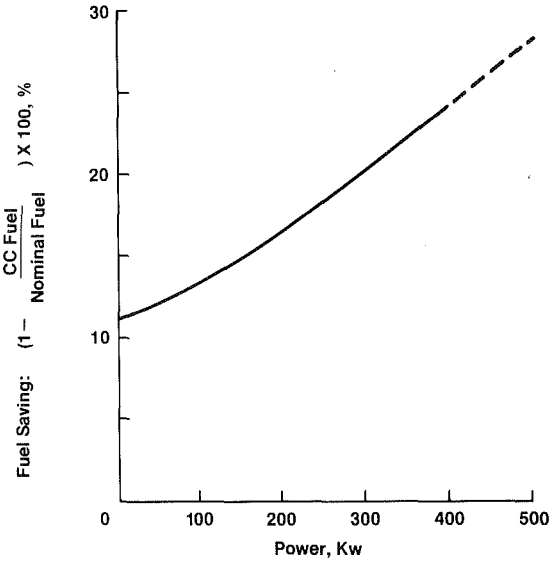

Fig. 6 Fuel saving for Cheng-Cycle turbine

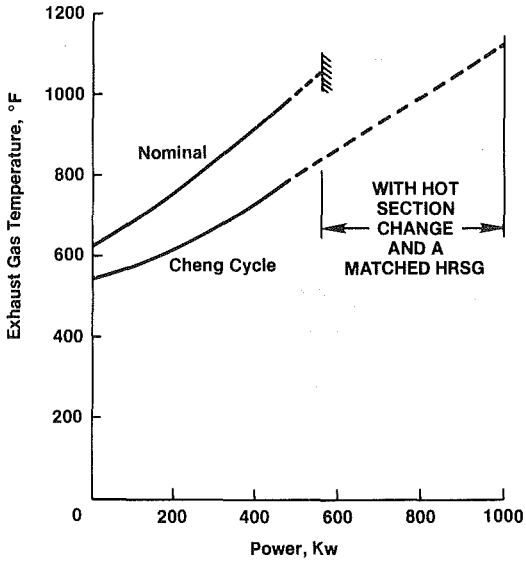

Fig. 8 Projected exhaust flow temperature for Cheng-Cycle turbine

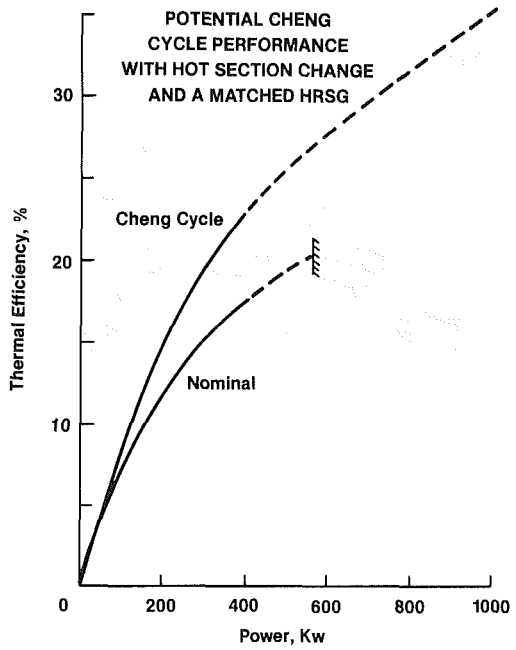

Fig. 7 Projected performance of Cheng-Cycle turbine

Figure 7 shows the extension of results in Fig. 4 to include a waste heat steam generator that would permit operation at higher loads. Figure 8 includes the extension of results in Fig. 5 to show the effect of the matched steam generator on exhaust temperature. The limits shown in these figures could be achieved for the Garrett IE831-800 turbine when operated in the Cheng-Cycle mode.

Concluding Remarks

In summary, the test results confirm the efficiency gains predicted from thermodynamic analysis of the Cheng Cycle when applied to the small turbine. The efficiency increases appreciably, fuel need for a given load decreases, exhaust temperature decreases and the maximum load capacity of the turbine increases markedly. Thus both the capital investment and the operating cost per unit of energy are reduced as compared with the usual Brayton-cycle mode to turbine operation. Thus the Cheng-Cycle engine simultaneously meets the need for more efficient and less polluting energy converters.

Acknowledgments

The authors appreciate the support and encourgement of the Onan Corporation in allowing them to utilize the Onan 560 Gtu Set.

References

1 Cheng, D. Y., "Parallel-Compound Dual-Fluid Heat Engine," Patent No. 3978661, Sept. 7, 1976.

2 Cheng, D. Y., "Regenerative Parallel Compound Dual-Fluid Heat Engine," Patent No. 4128994, Dec. 12, 1978.

3 Cheng, D. Y., "Regenerative Parallel Compound Dual-Fluid Heat Engine: Continuation of Patent No. 4128994 is a Separate Patent," Patent No. 4248039, Feb. 3, 1981.

4 Cheng, D. Y., "Dual-Fluid Approximation," International Power Technology internal report.

5 Chang, C. N., and Digumarthi, R., "Measurements of Low-Level No_x Emission from a Cheng Cycle Gas Turbine,"

A New Generation of Allison Model 250 Engines

J. A. Byrd
Chief Project Engineer,
Allison Gas Turbine Operations,
Indianapolis, Ind. 46206

Allison is actively developing two new additions to the Model 250 product line, the C34 and C24 engines, targeted for mid-1980s production. The C34 engine is a growth version of the Model 250-C30 and will provide a 10 percent power increase throughout the flight envelope. The C24 engine features decreased fuel consumption, one-engine-inoperative (OEI) ratings, and substantial increases in hot day performance compared to its predecessor, the highly successful C20B. Both engines incorporate single-stage turbines, digital electronic control units, and new shafting arrangements and are designed for increased reliability and durability, reduced complexity and part count, less maintenance, and decreased operating costs.

Introduction

Allison Gas Turbine Operations has recently announced two new additions to the Model 250 series of turboshaft engines, which currently power a wide variety of single and twin helicopters. As shown in Fig. 1, the Model 250 series of engines has grown from the original T63 engine for the U.S. Army's original light observation helicopter (LOH) to a production base of 20,000 engines selected in some 27 installations and has accrued 29,000,000 flight hrs. The Model 250-C34 engine, at 735 shaft horsepower (shp), will replace the C30 engine in late 1985 as the largest powerplant of the series and will be available either as a new engine or through a turbine conversion kit for the C30 engine. The Model 250-C34 engine derives its increase in power from the increase in turbine inlet temperature made possible by the replacement of an uncooled, two-stage gasifier turbine with a single-stage turbine employing an air-cooled nozzle. The engine also includes a new shafting arrangement available from damped bearing technology. This simplifies the mechanical arrangement of the main shafting configuration, reducing both part count and maintenance activities while improving the overall system reliability. The new gasifier turbine, the hardware necessary to accommodate the shafting modification, and larger capacity power output gears comprise the conversion kit.

In addition, Allison has recently committed to the design and development of a new small turboshaft engine, the Model 250-C24 engine, scheduled for 1986 introduction and designed for the rapidly expanding light twin helicopter market to replace the Model 250-C20B engine. Relative to the C20B, the Model 250-C24 engine features decreased fuel consumption, sufficient flexibility in thermodynamic power to permit OEI ratings, and substantial increases in hot day performance. Like the C34 engine, which precedes the C24 into production by a year, the engine also incorporates a single-stage gasifier turbine and a new shafting configuration but derives its reduced fuel consumption from an increased pressure ratio, increased efficiency axial-centrifugal compressor, and a decreased pressure loss exhaust system.

Both the C34 and C24 engine designs and development programs emphasize reduced system complexity, increased durability and reliability, and decreased operating costs. This new generation of Model 250 engines represents the conscious blend of Allison's extensive commercial and U.S. military engine experience with modest, proven increases in technology.

Model 250-C34 Engine

The increased-power C34 engine, shown in Figs. 2 and 3, maintains more than 90 percent individual part commonality with the parent C30 production engine.

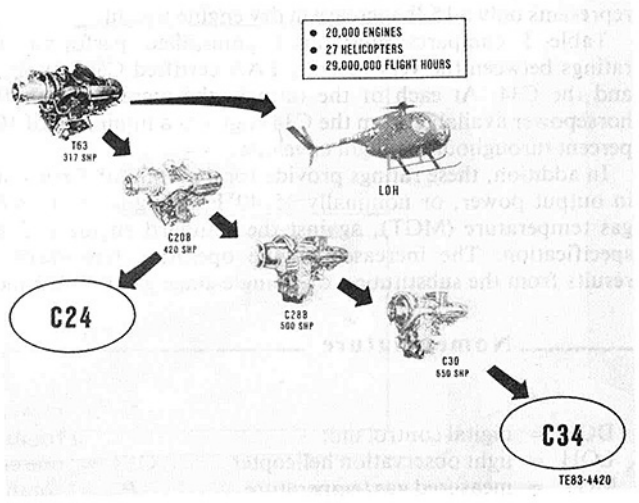

Fig. 1 Model 250 engine series

Contributed by the Gas Turbine Division of THE AMERICAN SOCIETY OF MECHANICAL ENGINEERS and presented at the 29th International Gas Turbine Conference and Exhibit, Amsterdam, The Netherlands, June 4–7, 1984. Manuscript received at ASME Headquarters January 18, 1984. Paper No. 84-GT-197.

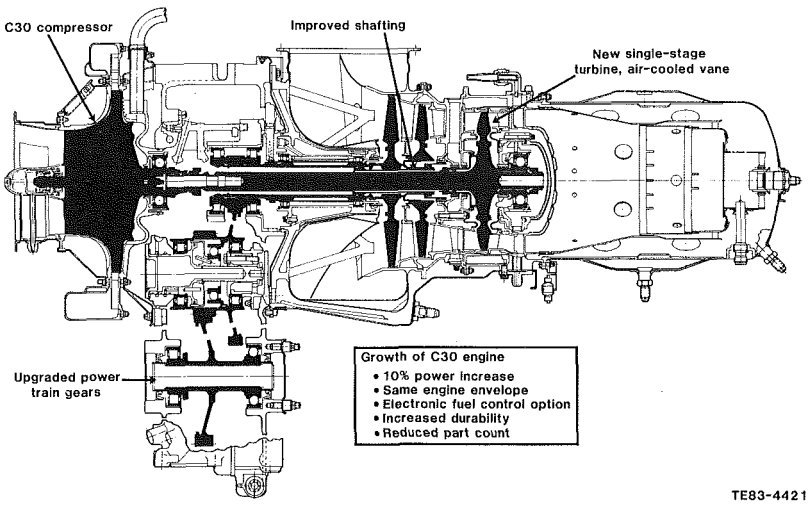

Fig. 2 Model 250-C34 engine features

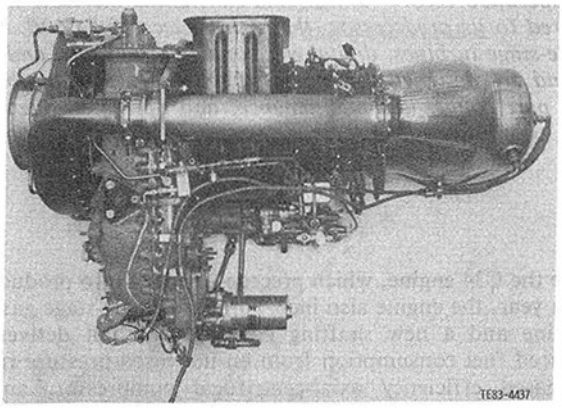

Fig. 3 Model 250-C34 demonstration test engine, July 1982

Particularly, the compressor assembly (comprised of the front and rear supports, the centrifugal impeller, diffuser, scroll, mount, and bearings) and, for the most part, the power and accessory gearbox assembly are identical on the two engine models. Only the power output gear, torquemeter gear, and bearings have been redesigned to accommodate the increased shaft horsepower available from the C34 engine. The major component change is the adaptation of a new gasifier turbine assembly to provide a minimum of 10 percent increase in output power. The resultant C34 engine preserves the C30 interface connection points and engine mounts and, at 255 lb, represents only a 15-lb increase in dry engine weight.

Table 1 compares guaranteed uninstalled performance ratings between the very recently FAA-certified C30S engine and the C34. At each of the ratings, the increase in shaft horsepower available from the C34 engine is a minimum of 10 percent throughout the flight envelope.

In addition, these ratings provide for a margin of 5 percent in output power, or nominally 35–40°F in engine measured gas temperature (MGT), against the standard engine rating specification. The increased engine operating temperature results from the substitution of a single-stage gasifier turbine

Table 1 Comparative ratings – Model 250-C30S versus C34 guaranteed uninstalled engine performance, sea-level standard

Ratings	C30S	C34	
2-1/2-min OEI			
• shp (min)	700	770	+10%
• sfc (max) – lb/shp-hr	0.588	0.591	+0.5%
• MGT*	1386°F	1502°F	+116°F
Takeoff, 30 min			
• shp	650	735	+13%
• sfc	0.592	0.596	+0.67%
• MGT	1337°F	1468°F	+131°F
Normal cruise			
• shp	557	629	+13%
• sfc	0.607	0.611	+0.66%
• MGT	1261°F	1369°F	+108°F
Weight (lb)	240	255	

*Measured rated gas temp (max)

Table 2 C34/C30 gasifier turbine performance

	C30	C34
Stages	2	1
Efficiency	87.5%	86.5%
Takeoff power, shp	650	735
Equivalent work/stage	16.0 BTU/1 bm	31.0 BTU/1 bm
Rotor inlet gas temperature	1930°F	2040°F
Relative gas temperature, rotor	1800°F	1760°F
Gas relative temperature – total temperature ratio	0.946	0.881

rotor and air-cooled nozzle for the standard Model 250 non-air-cooled two-stage turbine.

Single-Stage Turbine. The Allison single-stage turbine has been developed from privately funded and U.S. Government-sponsored research on high-work, high-load-coefficient turbines. In spite of the inherent reduction in realizable gasifier turbine efficiency, the permitted increase in temperature provides for an increase in rated power with only a ½ percent increase in specific fuel consumption (sfc). As shown in Table 2, the gasifier turbine efficiency is lower by 1

Nomenclature

DCU = digital control unit
LOH = light observation helicopter
MGT = measured gas temperature
N_1 = gasifier speed of rotation
N_2 = power turbine speed of rotation
OEI = one engine inoperative
P_c = compressor discharge pressure
Py = governor servo pressure
sfc = specific fuel consumption
SFE = simulated flight endurance
shp = shaft horsepower
T.O. = takeoff

percent in the C34 to account for losses associated with the air-cooled vane discharge flow and the increased stage loading coefficient. The real merit of the single-stage turbine, however, is the reduction in operational metal temperatures. Although the turbine rotor inlet gas temperature has increased 110°F for the takeoff rating in the C34, the higher blade work level lowers the relative blade temperature approximately 6 percent and allows increased power while maintaining acceptable airfoil stress rupture life. The C34 turbine design is matched to the same compressor operating line as the C30, thereby maintaining the same speed, pressure ratio, and mass flow relationships.

The reduction in the gas relative temperature translates directly, of course, to lower metal temperatures. Figure 4 compares the wheel and blade metal temperatures of the first-stage gasifier turbine for the C30 with the single-stage C34. The C34 turbine operates at a 15°F lower rotor airfoil temperature than the C30 at the most critical radial location for rupture. Similarly, the turbine wheel rim operates at a 40°F lower temperature, which improves the durability of the rotor by retarding the rim-cracking induced by thermal cyclic operations. In addition, substituting a fine-grained nickel-base MARM-247 for the conventional coarse-grained MARM-246 improves both the fatigue and stress rupture capacity of the rotor.

An uncooled C34 gasifier nozzle, however, would react adversely to the increase in turbine inlet temperature required by the engine cycle for the power increase. Additional compressor discharge cooling air (1.6 percent) has been added to the gasifier turbine secondary flow system to permit cooling of the nozzle. A simple, yet effective, cooling technology has been employed.

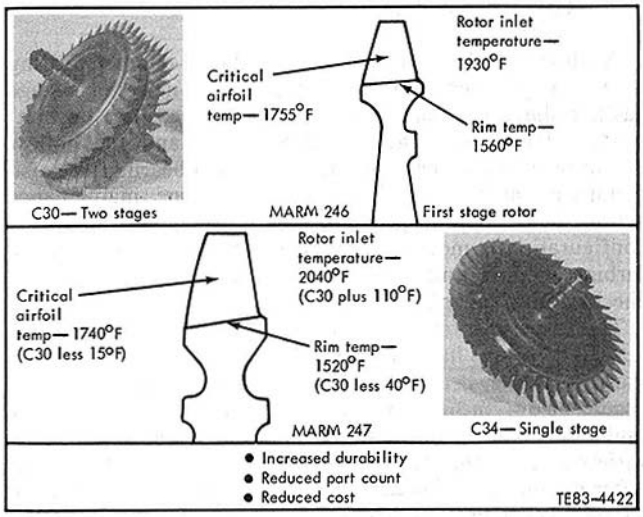

Fig. 4 Gasifier turbine wheel metal temperatures

The nozzle has a three-compartment impingement-cooled vane, as shown in Fig. 5, with cooling air fed from the outer nozzle band and discharged on the trailing edge pressure surface of the airfoil. The C30 nozzle reaches a maximum trailing edge metal temperature equal to the maximum burner outlet temperature impinging on the nozzle, including the effects of the circumferential temperature distortion from the combustor liner. While the C34 nozzle, made from the same material as the C30 nozzle, operates with an inlet gas temperature that is 120°F hotter, the trailing edge of the vane reaches metal temperatures 10 percent lower than the C30. Again, a design change improves turbine durability.

Most critical to the concept of a single-stage turbine, however, is the increased performance sensitivity to clearances between the rotor tip and the blade track. Historically, smaller gas turbine engines have experienced more problems than their larger counterparts with thermal distortion of ringed structures. Accurately controlling the hot-running tip clearance in any engine is critical, but in a small engine, because of the relatively large percentage of blade length that is represented by realistic tip clearances, the problem becomes more acute. Figure 6 contrasts the increased loss in gasifier turbine efficiency of the single-stage C34 with the current C30 for increases in blade tip clearance. The single-stage turbine loses 50 percent more in gasifier efficiency than the two-stage turbine for a given increase in hot-running tip clearance. In terms of typical small engine cycle performance sensitivities, each percentage point loss in gasifier turbine efficiency is at least 2 percent in output shaft horsepower (at a constant turbine temperature) and, of course, 1 percent in increased fuel flow.

In the C34 turbine, the increased cooling air necessary to cool the gasifier nozzle is utilized first to cool the rotor blade track. This cooling air is impinged directly into the blade track through a series of circumferential holes, substantially lowering the maximum operating temperature of the ring. The radial growth characteristics of the rotor are dictated by its thermal and mechanical inertia, dependent upon rotational speed and gas and cooling air temperatures, and are extremely difficult to change. The most critical engine operational events determining the clearance are either a slam deceleration from maximum power or a rapid second acceleration. In both of these flight conditions, the larger, massive rotor with the higher thermal inertia reacts slowly, maintaining near-maximum radial deflection. The thin ring, on the other hand, cools more rapidly, potentially shrinking onto the blade tip.

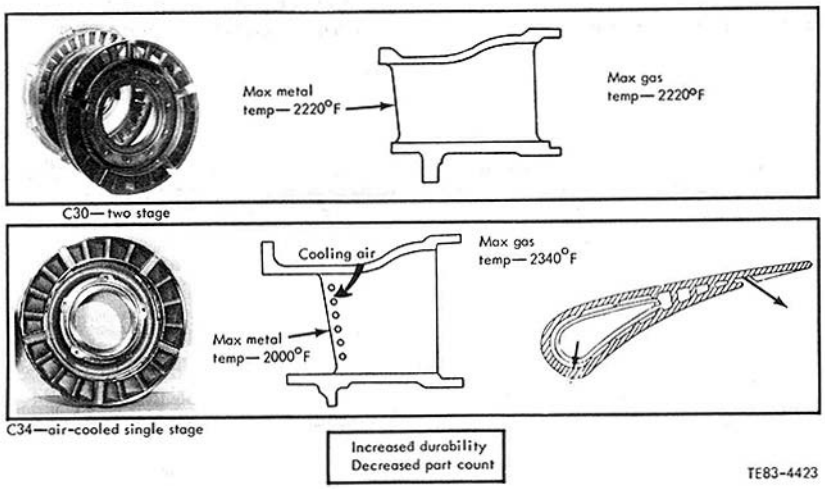

Fig. 5 Gasifier turbine nozzle temperatures

Adequately cooling the thinner ring is then paramount to controlling the rotor blade tip clearances and thereby ensuring maximum aerodynamic efficiency from the single-stage turbine. The C34 design provides sufficient cooling to minimize the relative increase in blade track temperature, thereby retarding the response rate of the ring and providing proper clearance control for the single-stage turbine.

The resultant C34 gasifier turbine has eliminated the second-stage wheel and nozzle, a turbine tie bolt, and a curvic coupling, along with the attendant assembly and balance operations, thereby providing increased power and yet a design that is more durable and less expensive.

New Shafting Arrangement. The basic shafting configuration of the Model 250 series of engines was conceived during the design of the T63 engine and was modified during the C20B engine development to add a spline coupling and main shaft bearing that has been retained throughout the development of the C28B and C30 engines. When work was begun on the C34 engine with the larger turbine, it became apparent that difficulty would be encountered in maintaining critical speed margins consistent with Allison's design practice with the standard shafting configuration. Studies were conducted that revealed the suitability of supercritical shafting to the gas generator. It was also recognized that many other advantages could be readily realized, provided an acceptable supercritical design could be determined. A comprehensive analytical and experimental program was conducted over a 12-month period. The result of these efforts has been a shafting system designed to reduce maintenance of the engine as well as the cost of ownership. The new shafting system is a simpler configuration than its predecessor, with fewer parts and the following features:

- Part count reduction
  - Gasifier coupling assembly – five parts to two parts
  - Two main shaft bearings eliminated
  - Power turbine oil sump removed
- Reduced maintenance
- Reduced balance requirements
- Improved alignment characteristics
- Reduced smoke and carbon formation
- Less oil flow and heat rejection
- Reduced vibration level
- Performance improvements
  - Exhaust collector pressure drop
  - Balance piston losses
  - Gas-path blockage

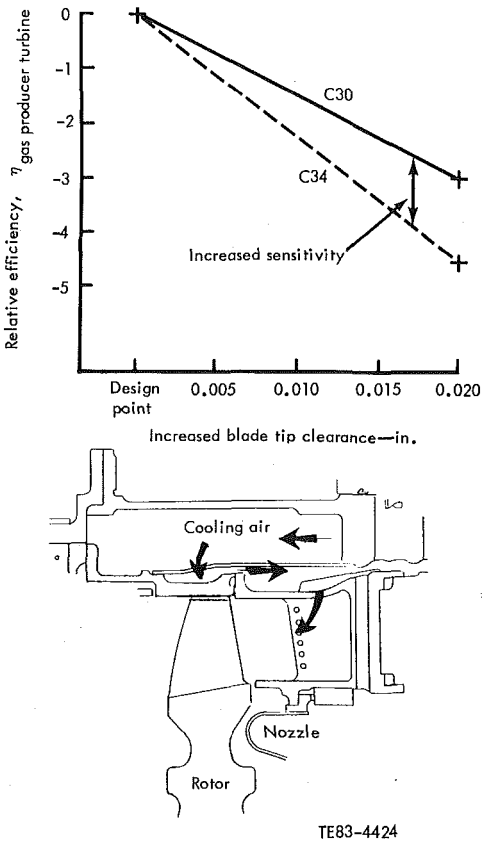

Fig. 6 Effects of turbine rotor tip clearance

As shown in Fig. 7, the inclusion of the oil-damped bearing at the gas producer support provides for a new single-stage gasifier shaft assembly that eliminates the gasifier tie bolt, spline adapter, spur adapter gear shaft, and the hollow compressor-to-turbine coupling shaft. Two bearings are also eliminated along with the required routine maintenance actions of periodic inspections and cleanings. The modified configuration is more tolerant to potential unbalance in the turbine module and less restrictive to exacting alignment checks during assembly.

The experimental program conducted on a series of development rigs has been extensive. In addition to verifying that the first two critical speeds (21 and 42 percent speed) occur below the engine idle rotational speed, the test evaluation of the configuration considered the impact of a variety of potential field-service problems or abuses (Fig. 8). After the initial testing to define the detailed geometry of the damper configuration and to determine the sensitivity to unbalance, tests were conducted with extremely hot and cold oils to examine viscosity effects; to examine the ability of the damper to operate for periods of time without oil; to simulate

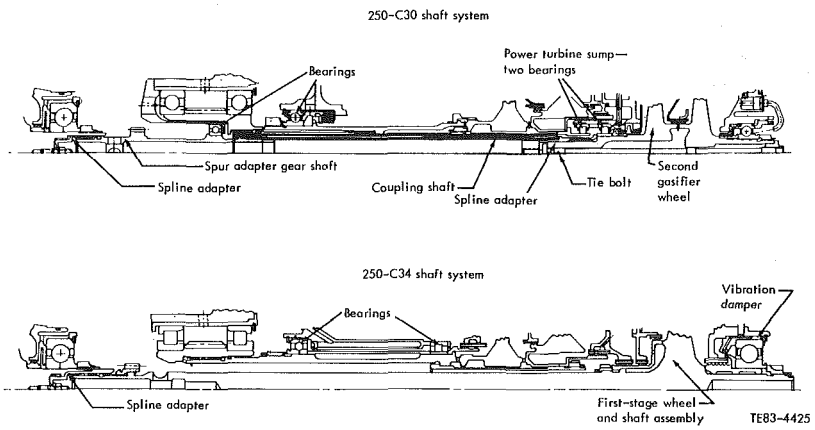

Fig. 7 Comparison of shafting systems

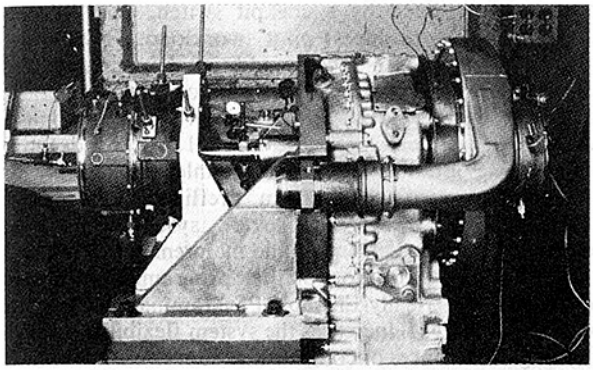

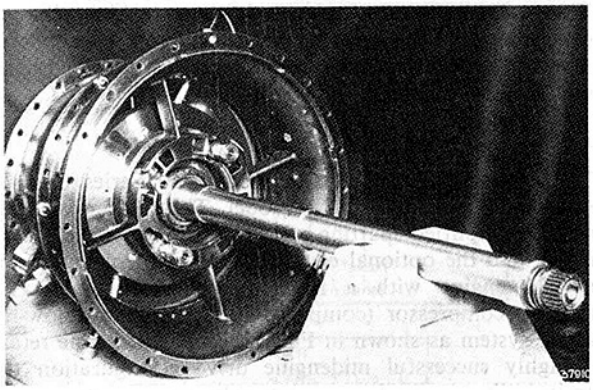

Testing profile

- Damper definition
- Unbalance sensitivities
  - Turbine
  - Shaft
- Oil viscosity effects
- Simulated coking
- Loss of oil
- Spline torque/lockup
- Damper wear, out-of-spec
- Axial thrust loads
- Misalignment
- Landing shocks

TE83-4426

Fig. 8 C34 shafting development rig

and evaluate a coked damper; to subject the system to landing shocks up to 17 g's at both sub-idle resonances and at maximum speeds; and to test the effects of mismanufactured dampers or dampers that were worn beyond expected limits. While some of these tests were abusive in nature, the new shafting configuration proved superior in each instance to the conventional arrangement.

The predicted third response mode, expected to occur near 134 percent rotational speed, was never encountered for test speeds routinely as high as 110 percent. Vibratory response levels were found to be acceptable with unbalance levels up to 30 times normal balance limits at the center of the shaft and in excess of 130 times balance limits at the turbine. Testing has also verified that the gas generator shaft could be balanced using a conventional, low-speed approach. The changes comprising the new shafting arrangement all serve to reduce spare parts and maintenance costs and improve reliability.

Digital Electronic Fuel Control. In July 1983, Allison received FAA certification for a digital electronic fuel control for operation on the C30L and C30R engines. The C30R engine is currently undergoing development testing as part of the U.S. Army's Advanced Helicopter Improvement Program in the OH58D, the Bell Helicopter Model 406. Certification was the culmination of an intensive control development effort that was initiated in 1979 and has proceeded through three hardware phases – breadboard, prototype, and certification. Over 1200 hrs of flight testing, 1000 hrs of engine

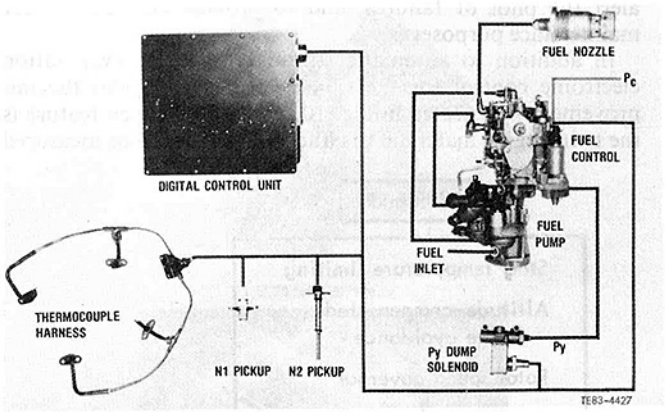

Fig. 9 Model 250-C30L electronic fuel control schematic

testing, and several thousand hours of bench testing have been completed as part of that effort. Since its initial demonstration in July 1982, the C34 engine has completed in excess of 1500 hrs of operation with an electronic control. The C34 engine will be offered with the option of selecting an electronic control or the standard pneumatic system.

The principal components of the Model 250 electronic fuel control system are shown in Fig. 9, with the digital control unit (DCU) as the new component in the system. The fuel control unit is shown in the installed position on the fuel pump. The remaining components comprising the new electronic system are the thermocouple harness, gas generator and power turbine speed pickups, pneumatic control pressure (P_Y) dump solenoid, and the fuel pump and fuel nozzle. The DCU conditioning circuit is compatible with the standard temperature indication systems utilizing measured gas temperature.

The electronic control is airframe-mounted and microprocessor-based. Off-engine mounting of the electronics was selected to promote increased system reliability due to lower ambient temperatures and a more benign vibrational environment. The digital microprocessor technology developed for the commercial automotive market is combined with the use of highly reliable military derived components to maximize operational reliability, yet minimize cost.

The principal features of the first-generation control for the C30 engines are shown in Fig. 10. In the start regime, the control limits engine temperature. This function replaces manual modulation and eliminates the need to adjust the fuel control for varying ambient temperature and altitude conditions. In the testing to date, the improvement in starts is noteworthy. Starting times have been consistent with the preset values, and start temperatures have been topped at the reference level over a wide range of ambient conditions for both hot and cold engines and for various battery conditions. Engine starting performance such as this has a positive impact on engine hot-section life. The C34 control will abort hot starts automatically and enable fuel flow only after proper light-off speed is reached, but manual modulation will be retained for backup.

The production C28B and C30 engines presently employ a compressor bleed valve system to provide increased surge margin during transient operation but operate closed-bleed under steady-state conditions. The electronic control eliminates the need for the bleed valve by altitude-compensated fuel scheduling during accelerations. Accelerations to date with the electronic control have been not only surge-free but have been faster than with the standard system. For safety, the electronic control has two levels of backup – both analog and manual – and contains self-diagnostic circuitry to detect malfunctions of the control, to

alert the pilot of failures, and to provide information for maintenance purposes.

In addition to automatic starting, the second-generation electronic control for the C34 engine incorporates the improvements illustrated in Fig. 10. The major added feature is the twin engine matching to either torque output or measured temperature, selected by a cockpit switch. The automatic engine matching reduces pilot workload. The second-generation system also accepts additional input data, both rotor speed input and engine compressor inlet temperature. Access to helicopter rotor speed data improves the response of the control and enhances the overall system decoupled stability. The addition of compressor inlet temperature data enables the control to perform preflight engine power-assurance monitoring. Improved system modularity facilitates both initial assembly and maintenance of the DCU, while the addition of nonvolatile, programmable memory such as Electrically-Erasable-Programmable-Read-Only-Memory (EEPROM) increases the system flexibility to permit recording exceedances or control fault codes.

These three features – the single-stage turbine, the improved main shafting system, and the optional electronic fuel control – represent the principal changes incorporated in the Model 250-C34 engine.

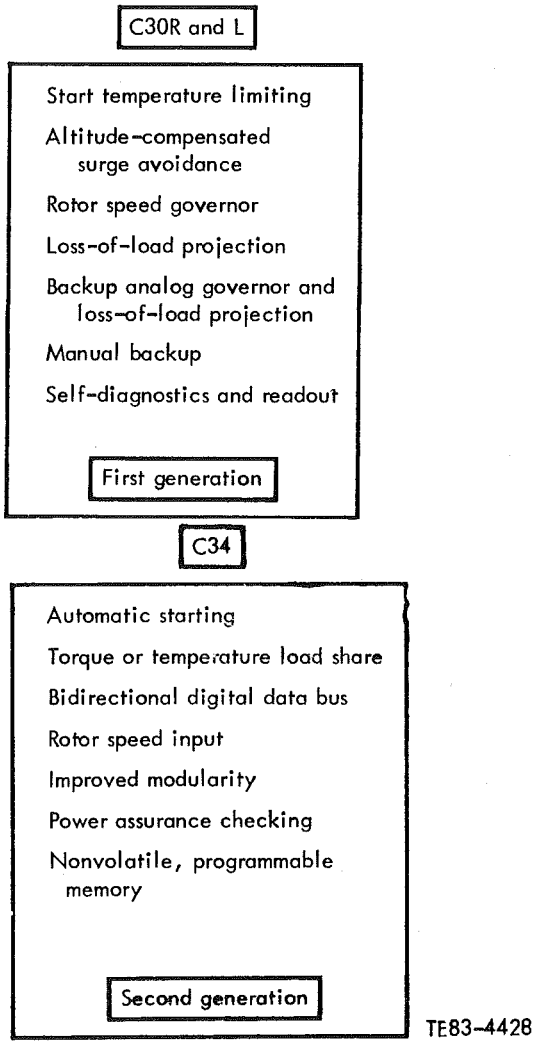

Fig. 10 Electronic control system features

Model 250-C24 Engine

The second addition to the Model 250 Series of small turboshaft engines is the C24 model. The C24 engine combines the simplified shafting system, the single-stage gasifier turbine, and the optional electronic fuel control features of the C34 engine with a higher-pressure-ratio, increased-efficiency compressor (compared to C20B) and a low-loss exhaust system as shown in Fig. 11. The new engine retains the highly successful midengine drive configuration that permits both front and rear power splitting from the gearbox with a simple fuel delivery system and a single can combustor. The engine mount locations are identical to the parent Model 250-C20B, preserving installation commonality even though the turbine assembly has been lengthened by 2 in. While substantial increases in performance are the basis for the new C24 engine, simplicity and ruggedness of construction and increased reliability and durability have been the emphasis of the design philosophy.

The design goals of the C24 engine focus on aspects that economically impact the commercial engine and are as follows:

- sfc – 12.5 percent lower than C20B
- Reliability – twice current C20B
- Durability – double gasifier component lives
- Maintenance cost – 70 percent of C20B
- Specific weight – same as C20B
- Performance margin – same as C20B

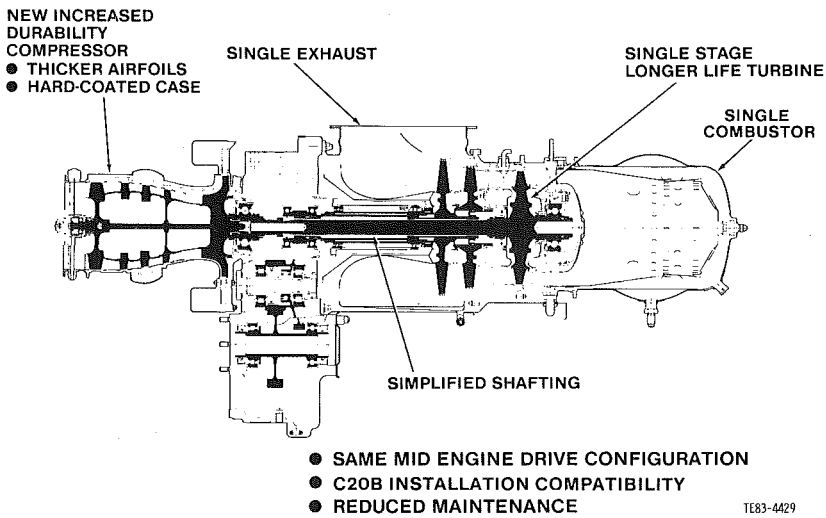

Fig. 11 Model 250-C24 cross section

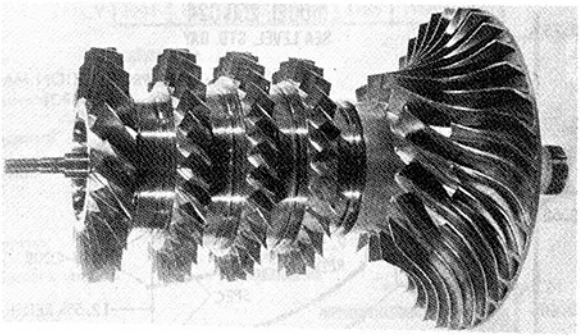

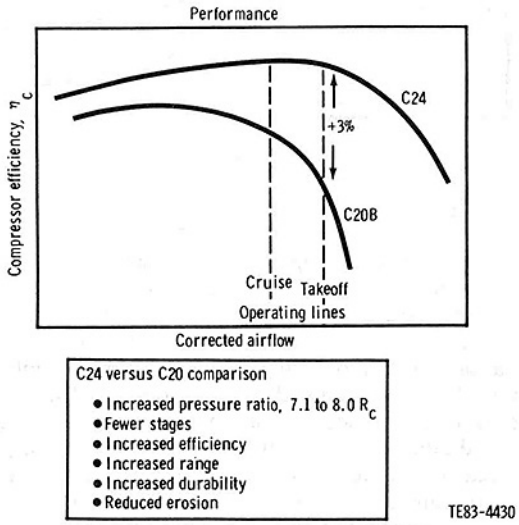

Fig. 12 C24 compressor features

C20 bifurcated exhaust

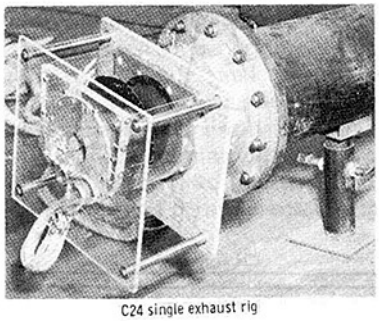

C24 single exhaust rig

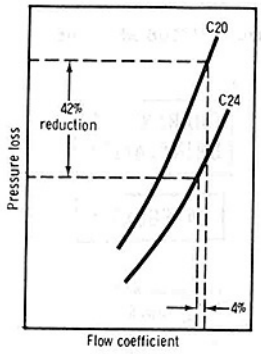

Fig. 13 C24 exhaust collector

The parent C20B engine has established a design maturity and evolved a maintenance philosophy that has made it the current workhorse of the industry. The Model 250-C24 design problem list, which resulted in component improvements to be accommodated in the C24, has been constructed from the history of service experience logged against the C20B in worldwide operation in varied climates and environments. Particular attention has been given to the reduction of corrosion and erosion damage in the gas path; incorporation of larger, more durable bearings and gears better able to resist the wear and distress that activate metal chip detectors; and new, improved coatings and seal designs. The design process has been expanded beyond the normal parochial limits, formally assessing current and future component and future component processing and quality control, to guard against unforeseen increases in initial acquisition and spare parts cost at a future date.

The C24 axial-centrifugal compressor is identical in length to the C20B (Fig. 12) but achieves a 3 percent increase in adiabatic compressor efficiency and an additional atmosphere in pressure ratio.

Rig tests on the new compressor have not only verified the increases in efficiency and loading but have demonstrated both adequate surge margin and the predicted broader range. The good high-speed flow characteristics of the C24 compressor, as opposed to the limited-flow characteristic of the C20B, provide increased cycle flexibility. The resultant engine enjoys increased hot day power and is more flexible for potential growth derivatives.

The axial compressor has two fewer stages with thicker, coated, more erosion-resistant airfoils, which are designed to meet unprotected ingestion requirements, and a corrosion-resistant case. The compressor disks have been designed to lower stress values to achieve twice the fatigue life in the C24 compressor as currently experienced in the C20B. To minimize hardware costs in the compressor, all the disks and compressor case halves are fabricated from castings.

The second major modification to the Model 250-C24 engine is the conversion from the C20B bifurcated exhaust to a longer, more efficient single exhaust duct. Historically, the midengine configuration, while a preferred arrangement for many installations, has prevented significant improvements in sfc. The mass flow rate in the C24 engine is identical to that in the C20B, and without a newly configured exhaust collector, the pressure drop across the collector would be approximately the same for modest changes in the power turbine flow path. The new shafting arrangement with the oil-damped bearing in the gas producer support permits a longer bearing span and provides for increased length in the exhaust system.

As shown in Fig. 13, the single-duct C24 exhaust collector reduces the exhaust pressure loss in excess of 42 percent. This reduction in pressure loss represents nearly a 4 percent gain in both sfc and power. The previously mentioned increase in turbine assembly length for the C24 is due primarily to the improved exhaust system.

While the C24 engine also employs the single-stage turbine, the available reduction in gas relative temperature is used to increase stage durability rather than increase power as in the case of the C34. At the same rotor inlet temperature, the operating metal temperatures of the critical blade section and the center of the wheel rim are reduced 145°F and 260°F, respectively, as illustrated in Fig. 14. Independent of potential material changes or alternate disk rim construction currently under consideration for the C24 engine, these temperature reductions represent significant increases in component life.

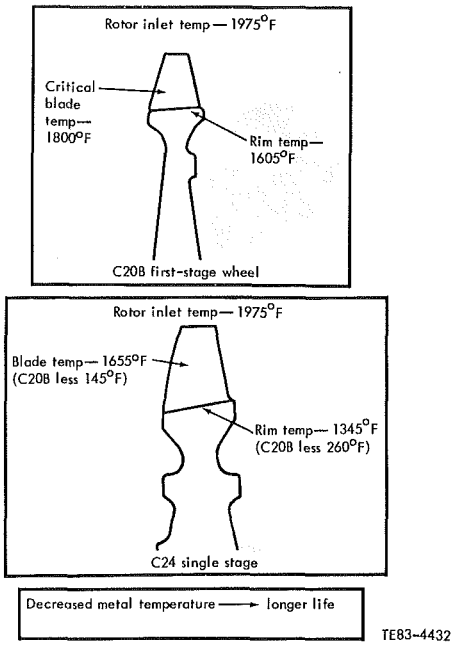

Fig. 14 Comparative C24/C20B wheel metal temperatures

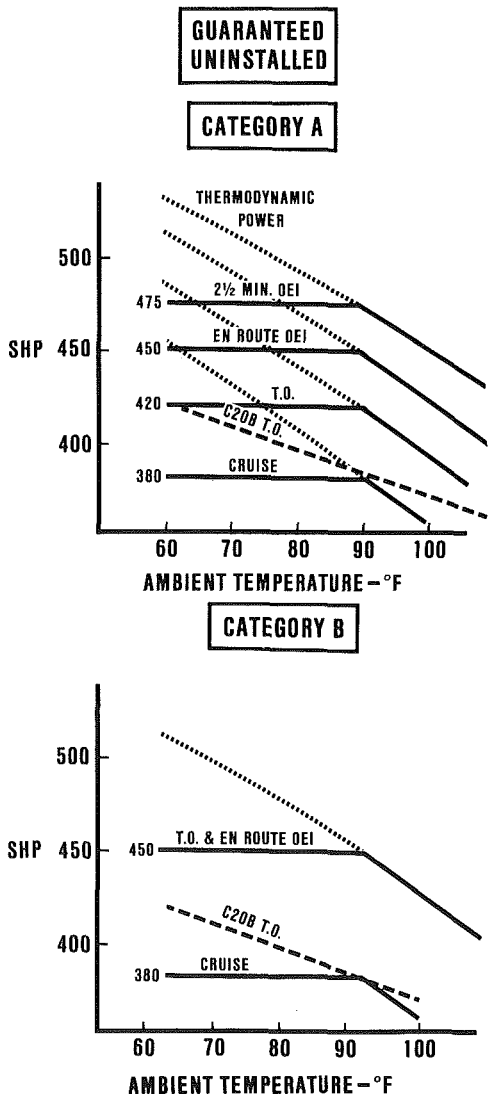

Fig. 15 Model 250-C24 potential ratings

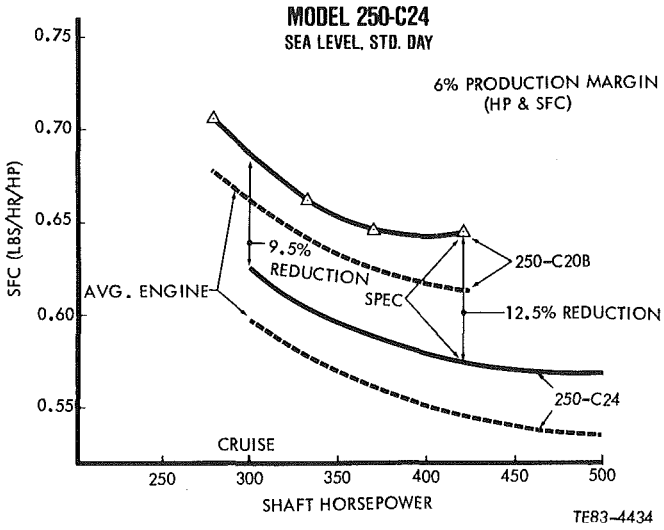

Fig. 16 Model 250-C24 – sea level, standard day

The Model 250-C24 engine, while designed for the same airflow characteristics as the C20B, offers characteristic increases in guaranteed uninstalled power (Fig. 15), and the thermodynamic cycle is sufficiently flexible to provide for either a category A or category B rating philosophy. The engine is flat-rated to hot day conditions (90°F), providing power in circumstances consistent with typical helicopter flight conditions without adding considerable weight penalty to the gearbox. Like the C34 ratings, the C24 ratings will provide for an additional 5 percent margin in power. The increased component efficiencies permit these powers at decreased rotational speeds and temperatures, again providing the basis for significant improvements in durability.

In addition to potential OEI ratings, the engine provides increases of 10–20 percent in hot-day takeoff power compared to the C20B. The increased thermodynamic power available increases the flexibility for alternate customer ratings and derivative models.

The C24 engine also offers a decrease in fuel consumption compared with the C20B (Fig. 16). At a comparable takeoff rating of 420 shp, the newer engine provides a decrease of 12.5 percent in guaranteed maximum fuel consumption, with average production engines lower by an additional 4 percent. At a cruise rating of perhaps 300 shp, where the most fuel would be consumed, the decreases in sfc would be 9.5 and 13 percent for the respective specifications and average engines.

These improvements in performance in the C24 engine will significantly improve the payload-range characteristics of the next generation of helicopters over C20B-powered aircraft, particularly under hot-day conditions. From the perspectives of increased productivity of the aircraft, decreased fuel consumption, and increased reliability of the engine, the Model 250-C24 provides the basis for significant reductions in direct operating costs to the system owner/operator.

Engine Development Testing

While both advanced Model 250 engines, the C34 and C24, are scheduled for near-term production, considerable emphasis has been placed on increasing the amount of in-house testing on the engines prior to production. As shown in Fig. 17, the C34 engine is expected to be certified by the FAA in the spring of 1985 and into production later in the year after about 7500 hrs of abusive engine testing. The C24 engine, because of the similarity of design in the shafting arrangement and turbine section, benefits directly from the C34 program and will be certified 18 months later than the C34. Of utmost

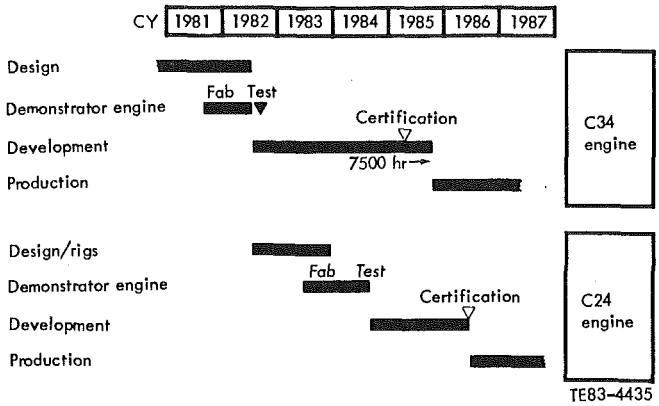

Fig. 17 Model 250-C34/C24 program schedules

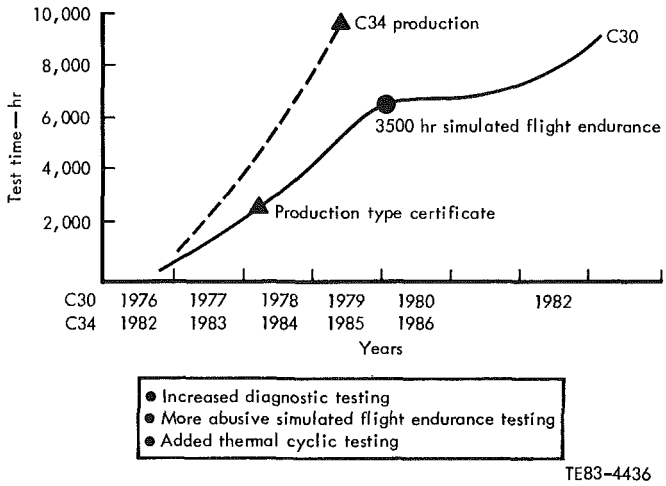

Fig. 18 In-house engine development testing

priority in both engine programs is to realize drastic increases in reliability over predecessor Model 250 engines at all phases of their service life – from initial introduction to maturity.

In terms of program contrasts, the next generation of Model 250 engines will feature increased in-house test time over their respective parent engines. As shown in Fig. 18, the Model 250-C30 engine was certified and released to production after some 2400 hrs of diagnostic and preliminary simulated flight endurance (SFE) testing. The in-house test evaluation continued after production at increased test severity levels and provided a basis for comparison of in-house testing with field experience. Recent increased C30 testing has been undertaken to validate design improvements. The C34 program schedule accelerates that in-house testing profile by a factor of three to four times the number of hours to provide for incorporation of improvements prior to production. Although the C34 engine (which adopts changes released for the C30 engine) involves only a turbine change, the increased testing is intended to ensure initial production reliability at near maturity levels. The additional scheduled test hours provide for more diagnostic testing, an added level of SFE testing at increased severity ratios (cyclic content and high-temperature operation), and particularly abusive thermal cyclic tests in which the engine is rapidly accelerated to takeoff power, quickly shut down, and blown cold. This combination of tests will determine design inadequacies for a variety of failure modes prior to production, identify items with high rates of wear, and permit preproduction correction actions.

Summary

While the new generation of Model 250 engines, the C34 and C24, are designed for significant increases in performance – namely, increased power and decreased fuel consumption – the design of these engines reflects a commitment to increased durability and reliability, reduced complexity and part count, less maintenance, reduced pilot work load, and decreased operating costs. This new generation of engines represents a deliberate blending of new, proven technologies with millions of hours of actual flight experience and provides a logical transition between Allison's production engines of today and its high-technology engine under development for the U.S. Army LHX competition.

References

1 Helton, D. J., Lueders, H. G., and Arvin, J. R., "An Experimental Investigation of a Subscale Variable Pressure Ratio High Thru Flow Turbine," Air Force Aero-Propulsion Laboratory Technical Report 77-7, Feb. 1977.

2 Byrd, J. A., and Harvey, R. F., "Designing Turboshaft Engines for the Commercial Operator," Ninth European Rotorcraft Forum, 13-15 Sept. 1983, Paper No. 86.

3 Herman, W., Weber, J., and Ervin, E., "Electronic Control for Small Engines," American Institute of Aeronautics and Astronautics 18th Joint Propulsion Conference, Paper No. AIAA-82-1126, 1982.

Journal of Engineering for Gas Turbines and Power
Formerly: Journal of Engineering for Power

Technical Briefs

Blockage in Axial Compressors

R. P. Dring[1]

C_x = axial flow speed
P_T = relative total pressure
P_S = static pressure
$P_{T,\text{rot}}$ = rotary total pressure ($P_T - 1/2\ \rho\ U^2$)
r_h = hub radius
r_t = tip radius
U = wheel speed
ρ = density
θ = yaw angle from axial
ϕ = pitch angle from axial

Superscripts

$-a$ = circumferential area average
$-m$ = circumferential mass average

The "throughflow" analysis in compressor design is a two-dimensional axisymmetric calculation describing the spanwise variation of the flow at streamwise locations, both within and between blade rows from the inlet of the compressor to its discharge. The input required by the analysis includes the total pressure loss and the exit flow angle for each blade row (or their equivalents: stage pressure ratio, reaction, efficiency, and so on). This information is sufficient to completely describe the absolute and relative velocity triangles. In the design mode, these results are used to define airfoil inlet and exit metal angles for optimum performance, and in the off-design mode, they are used to describe the approach to choking or stall. If the flow in a compressor were truely axisymmetric this would be the end of the problem. However, actual compressor flows are not axisymmetric and this nonaxisymmetry must be accounted for in order to describe the flow with sufficient accuracy. This is achieved by the introduction of "blockage" into the analysis. Errors in estimated blockage are one of the primary reasons for compressors initially not achieving their design goals of flow, pressure rise, and efficiency.

In the sense that blockage accounts for nonaxisymmetry in the flow, the displacement effects of an axisymmetric (gap-averaged) boundary layer are not included in it. This kind of "endwall blockage" [1, 2] does not reflect a departure from axisymmetry, but rather it is an item of convenience to account for the use of a relatively small number of computational stream tubes in the throughflow analysis to accurately account for the endwall boundary layers. This type of endwall displacement effect can be accounted for either by coupling the throughflow analysis to an endwall boundary layer analysis, or by a simultaneous solution of the inviscid and viscous portions of the flow as in the method of Anderson [3].

In the sense that blockage accounts for the nonaxisymmetry in the flow, it corresponds to what has been called "tangential blockage" [1], that is, the blockage due to blade wakes, corner stall, tip leakage, and to the extent that they depart from axisymmetry, the endwall boundary layers and secondary flows. The essence of the problem is that the nonaxisymmetry of the flow causes a significant difference between circumferential mass and area averages at any radius. For example, the mass-averaged total pressure is usually higher than the area-averaged total pressure, since the low total pressure region in a wake usually has associated with it a low axial velocity, i.e., a low mass flux.

Throughflow analyses are generally considered to provide the distributions of mass averaged quantities, the virtue here being that quantities such as work depend on mass averages. The mass flow, however, is an area-averaged quantity, i.e., the integral of mass flux (ρC_x) over area. Blockage provides the link between these two types of averages. The mass flow M through an annulus may be expressed as follows.

$$M = 2\pi \int_{r_h}^{r_t} \rho \bar{C}_x^a r dr = 2\pi \int_{r_h}^{r_t} \bar{K} \rho \bar{C}_x^{PT} r dr$$

The blockage factor $\bar{K}$ may be expressed as the ratio of the circumferentially area-averaged axial flow speed $\bar{C}_x^a$ to the axial flow speed based on the circumferentially mass-averaged total and static pressures and flow yaw and pitch angles $\bar{C}_x^{PT}$. This is expressed as follows:

$$K \equiv (\bar{C}_x^a / \bar{C}_x^{PT}) = f(r)$$

where, for incompressible flow

$$\bar{C}_x^{PT} \equiv \sqrt{(\bar{P}_T^m - \bar{P}_s^m)/\frac{1}{2}\rho} \qquad \text{Cos}\bar{\theta}^m \text{Cos}\bar{\phi}^m$$

Note that $\bar{K}$ is a function of radius and that when the flow is

[1]Manager, Gas Turbine Technology, United Technologies Research Center, East Hartford, Conn. 06108

Contributed by the Gas Turbine Division for publication in the JOURNAL OF ENGINEERING FOR GAS TURBINES AND POWER. Manuscript received by the Gas Turbine Division June 6, 1983.

axisymmetric the mass and area averages are equal, and $\bar{K}$ is equal to unity.

Normally, a compressor analyst would be hard pressed to calculate blockage on this basis. The only measured data at his disposal are typically spanwise distributions of total pressure, total temperature, and flow angle. Blockage would then be inferred by using a throughflow analysis to match the known mass flow to measured static pressures on the flow path hub and/or tip. This approach provides at best a rough indication of blockage and no indication as to its variation with span.

Recently, however, efforts have been underway to obtain more exhaustive data from compressor flows. Two examples of such efforts are those by Dring, Joslyn, and Hardin [4, 5] and by Wagner, Dring, and Joslyn [6] where full-span, radial-circumferential arrays of total pressure, static pressure, and yaw and pitch data have been acquired in the rotating frame of reference downstream of a compressor rotor. An example of this type of data is shown in Fig. 1. This figure illustrates the full-span, blade-to-blade distribution of rotary total pressure measured in a plane 30 percent chord downstream of the rotor. The profile wake, the hub corner stall, and the combined tip boundary layer and leakage flow are evident in the figure. Note that the data shown in Fig. 1. covers 1.32 rotor blade pitches and that the rotor was operating at its design incidence. The flow entering this rotor was axial and had a constant absolute total pressure. This is the reason for the large region of constant rotary total pressure between the wakes. Using the foregoing definitions, the spanwise distribution of blockage was calculated for these data (30 percent aft) as well as for three other axial measurement planes (located 10, 50, and 110 percent aft of the rotor). The major contribution to the blockage was due to the difference between the mass and area averages of relative total pressure. The mass and area averages of the static pressure, yaw, and pitch were very nearly equal. These blockage results are presented in Fig. 2. The data show relatively high levels of blockage in the hub and tip regions and very low levels in the midspan region. There is a rapid decay in blockage in the endwall regions with increasing downstream distance. The curve for the data 10 percent aft is shown dashed near the hub, because the hub corner stall extended into this plane and the existence of the backflow region here prevented data acquisition in the wake (see [5], Fig. 12). The dashed portion of the curve at the 10 percent aft location is based on the assumption that the flow velocity is zero in this backflow region. Using this assumption, the blockage approaching the hub at this axial location was calculated to be 39 percent. Recall that the high levels of blockage in the endwall regions are not a result of displacement due to endwall boundary layer growth, but rather they represent the departure of the endwall flows from axisymmetry.

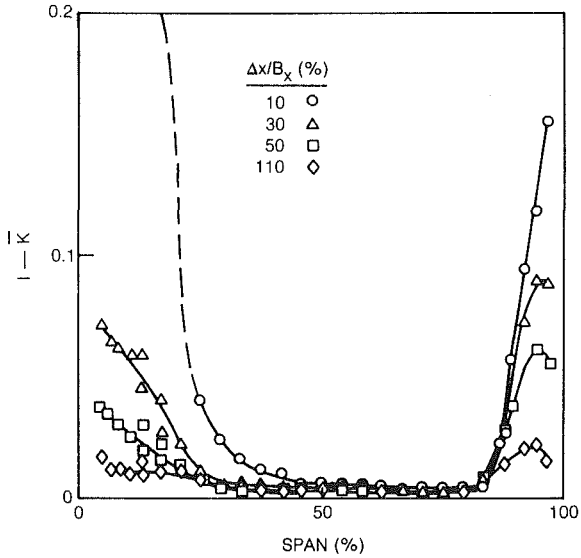

Fig. 2 Spanwise distributions of blockage, design incidence

The definition of blockage presented here is by no means unique. Operational experience in the analysis of compressor performance data may lead to a better definition. It is noteworthy, however, that the present definition of blockage can be rewritten in terms of velocity components. Thus blockage can be calculated not only from the type of detailed pneumatic probe data presented in [4–6], but it could also be calculated from the large amount of hot-wire and laser anemometry data presently available in the open literature.

The objective of this note was to provide a better understanding of the nature of blockage in axial compressors. The treatment of the aerodynamic data as described above provides a physically meaningful approach to the comparison of computed throughflow results with measured data. The fact that spanwise distributions of loss, deviation, and blockage can be specified provides, at long last, a firm basis for the detailed assessment of throughflow calculation methods. The present data will also allow one to estimate the magnitude of the errors associated with inferring blockage and perhaps provide a more sound foundation on which to base this inferrence in the future. Finally, it is anticipated that the specification of the spanwise distribution of blockage will result in more precise predictions of airfoil incidence and that through this they will have an impact on the airfoil design.

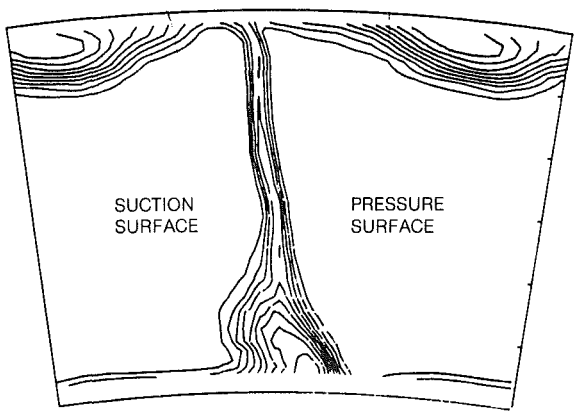

Fig. 1 Compressor rotor exit flow field, design incidence

Acknowledgment

The experimental data shown here were acquired under Air Force contract under the direction of C. Herbert Law (AFWAL/POTX), project engineer, Contract Number F33615-77-C-2083.

References

1 "Propulsion and Energetics Panel Working Group 12 on Through-Flow Calculations in Axial Turbomachines," AGARD-AR-175, Oct. 1981, p. 329.

2 Johnsen, I. A., and Bullock, R. O., *Aerodynamic Design of Axial-Flow Compressors*, Ch. 3 and 8, NASA SP-36, 1965.

3 Anderson, O. L., "Calculation of Internal Viscous Flows in Axisymmetric Ducts of Moderate to High Reynolds Numbers," *Computers and Fluids*, Vol. 8, 1980, pp. 391–411.

4 Dring, R. P., Joslyn, H. D., and Hardin, L. W., "Experimental Investigation of Compressor Rotor Wakes," AFAPL-TR-79-2107, Air Force Aero Propulsion Laboratory, Technology Branch, Turbine Engine Division (TBX), Wright-Patterson Air Force Base, Ohio.

5 Dring, R. P., Joslyn, H. D., and Hardin, L. W., "An Investigation of Compressor Rotor Aerodynamics," ASME JOURNAL OF ENGINEERING FOR POWER, Vol. 104, Jan. 1982, pp. 84–96.

6 Wagner, J. H., Dring, R. P., and Joslyn, H. D., "Axial Compressor Middle Stage Secondary Flow Study," NASA Lewis Research Center, Contract No. NAS3-23157, Contractor Report 3701, July 1983.